Les granites à métaux rares : origine, mise en place et mécanismes de la transition magmatique-hydrothermale

Julie Michaud

UNIVERSITÉ D'ORLÉANS

ÉCOLE DOCTORALE

ÉNERGIE, MATÉRIAUX, SCIENCES DE LA TERRE ET DE L'UNIVERS

Institut des Sciences de la Terre d'Orléans

THÈSE présentée par : **Julie MICHAUD**

soutenue le : **26 février 2019**

pour obtenir le grade de : **Docteur de l'université d'Orléans**

Discipline/ Spécialité : Sciences de la Terre

LES GRANITES A METAUX RARES :

ORIGINE, MISE EN PLACE ET MECANISMES DE LA TRANSITION MAGMATIQUE-HYDROTHERMALE

THÈSE dirigée par :

Éric MARCOUX	Professeur, ISTO

RAPPORTEURS :

Alain CHAUVET	Directeur de Recherche CNRS, Géosciences Montpellier
Robert LINNEN	Professeur, Western University Canada

JURY :

Michel PICHAVANT	Directeur de Recherche CNRS, ISTO, Président du jury
Alain CHAUVET	Directeur de Recherche CNRS, Géosciences Montpellier
Robert LINNEN	Professeur, Western University Canada
Sarah GLEESON	Professeur, GFZ Potsdam
Robin SHAIL	Docteur, Cambornes School of Mines, Université d'Exeter
Karel BREITER	Docteur, Czech Academy of Sciences
Éric MARCOUX	Professeur, ISTO
Charles GUMIAUX	Docteur, ISTO

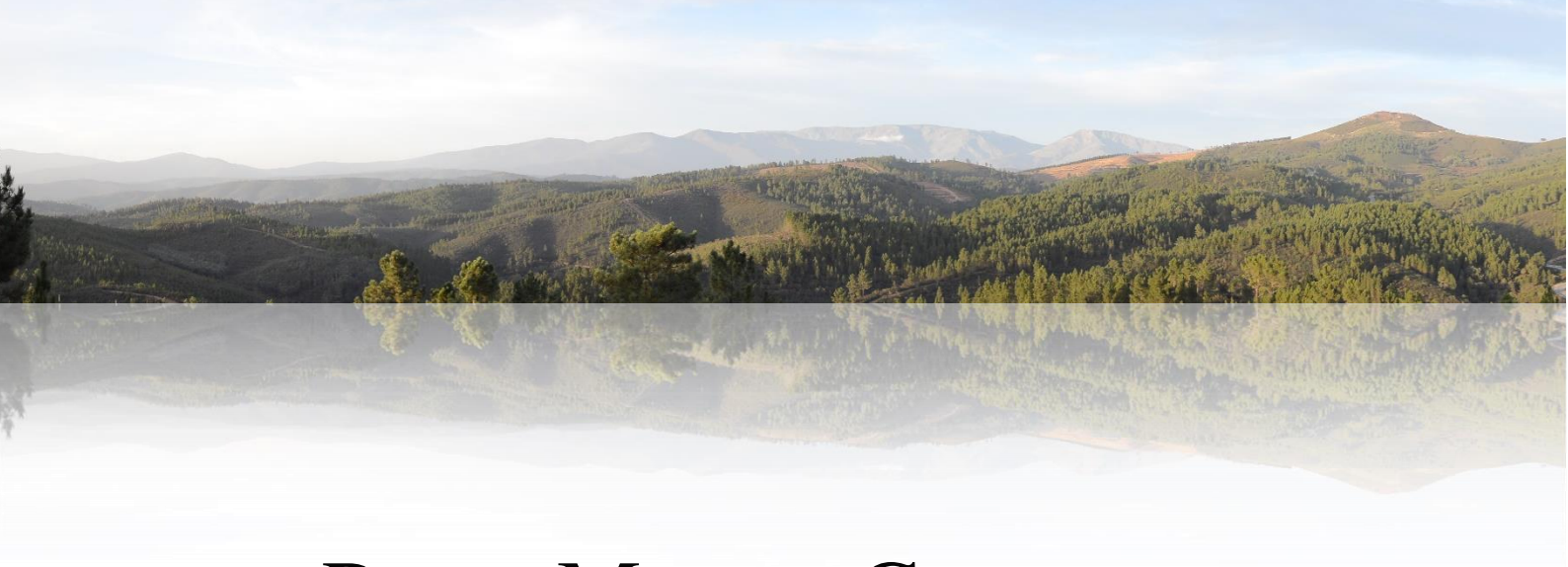

RARE METAL GRANITES

ORIGIN, EMPLACEMENT AND MECHANISMS OF THE MAGMATIC-HYDROTHERMAL TRANSITION

- Insights from the Argemela Rare Metal Granite (Portugal) and an experimental study -

« Le vin est un professeur de goût, il est le libérateur de l'esprit et l'illuminateur de l'intelligence »
Paul Claudel

« Il y'en a qui sont faits pour commander et d'autres pour obéir. Moi je suis fait pour les deux : ce midi, j'ai obéi à mes instincts en commandant un deuxième pastis »
Pierre Dac

« 06h33, je m'entrave dans une fougère »
La Palombière

REMERCIEMENTS

TROIS ANS… *(et quelque), ça parait long au départ, mais finalement ça passe très vite. Au début on se met dans le bain, on rencontre des copains, on choisit un quartier général, on se réjouit de cette nouvelle aventure qui commence. A la fin, on a plus le temps, il faut écrire, finir et rapidement l'heure de la soutenance arrive. On est enfin soulagé mais tout de même un peu triste de penser qu'on va quitter ce cocon, cette ambiance, toutes les personnes avec qui on a pu discuter, rire et qui nous ont soutenu. Mais l'aventure continue et ces superbes années passées à Orléans resterons gravées dans ma mémoire…*

Pour commencer, je tiens tout d'abord à remercier Eric Gloaguen, Charles Gumiaux et Sarah Deveaud qui m'ont permis de mettre un pied à Orléans. Pour ces moments passés sur le terrain, au routier de Limoges, pour ces discussions au labo ou au V&B, et pour leur aide. Je remercie également Yannick Branquet qui m'a acceuilli dans son bureau à mon arrivée.

En ce qui concerne ces années de thèse, je tiens à remercier mon directeur de thèse Eric Marcoux pour sa confiance, pour ces moments sur le terrain et pour m'avoir permis de terminer dans les meilleures conditions qui soient.

Ensuite, je tiens tout particulièrement à remercier Michel Pichavant sans qui cette thèse n'aurait pas été possible, bien que le banquier soit tombé dans un trou pendant un an ! Merci pour ta confiance, ta patience, ta grande pédagogie et pour tout ces vendredi V&B, là où toutes les grandes discussions se prennent . C'était pas gagné, j'ai donc inventé la géochimie pour les nuls ! On a passé de superbes moments au Portugal, autour d'une bouteille de vinho verde, dans la voiture de Fernando, chez o Pipo et tu as pu orienter ton premier échantillon ! Plus sérieusement, merci pour ta présence, ta disponibilité et ton accompagnement tout au long de la thèse. J'espère qu'on se reverra après mon départ autour d'un petit ricard en terasse ou d'un verre de Picpoul accompagné d'huîtres de Bouzigues!

J'adresse également un immense merci à Charles qui m'a accompagné tout au long de ces années. Merci pour ta patience, pour ces super moments sur le terrain à chercher la S1, à inventer des zones de cisaillement (en plein cagnard parfois, hé mais où est la piscine ?), à discuter, en encadrer Ricardo… ! Je crois que nous avons un problème en commun… les noms et prénoms ! On se rappelera d'ailleurs du fameux Paulo Pinto ! Merci pour ces apéros, cafés, V&B et ta bonne humeur. On se reverra très certainement après mon départ, à Orléans ou ailleurs autour d'une petite bière.

Un grand merci également à Eric (Gloaguen) pour ces discussions, ton enthousiasme et ta confiance; à Fernando Noronha et Alexandre Lima pour avoir faciliter l'accès à Argemela, pour leur accompagnement sur le terrain et à Porto et pour ces supers moments autour d'un bon repas accompagné de vinho verde. Merci à Filipe Pinto et Paulo Ferraz pour leur aide et les bon moments passés à Panasqueira et à so Grelhados. Merci à Paulo Pinto et Paulo Moutela de m'avoir permi d'accéder aux carottes et à la carrière. Merci à Ricardo Ribeiro pour son super travail, pour son aide ; je pense en particulier à ce changement de roue à Porto !

J'en profite également pour remercier tous les membres du jury qui ont accepté de lire et juger cette thèse, pour leurs remarques constructives et pour ce bon moment passé à discuter après la soutenance autour d'un verre. J'espère que nous pourrons nous revoir et travailler ensemble dans le futur.

Je remercie toutes les personnes qui m'on aidé et avec qui j'ai passé de supers moments au labo : Ida Di Carlo pour son aide précieuse et nos super discussions, Patricia Benoist, Rémi Champallier (superbe moment avec la presse Paterson !), Frédéric Savoie, Esteban Le Moing, Didier Bellenoue, Aneta Slodczyk... Je remercie également Jean-Luc Devidal, Philippe Lach, Thomas Rigaudier, Christian France-Lanord et Louis Hennet.

Un grand merci à la famille avec une pensée particulière à ma maman pour se soutient pendant toute la durée de ces longues études.

Enfin merci du fond du cœur à tous les copains sans qui ça aurait été beaucoup moins drôle, pour toutes ces soirées au Charbon, au V&b, au boui-boui, au fût de trop, à la sardine, à Montpellier, à Lexy, en Cornouailles... pour tout ces moments passés en votre compagnie à rire et parfois pleurer ! Merci à toi Alice d'avoir été là depuis toutes ces années. Merci à vous tous : Charlène, Rabi, Bryan, Cheval (ou princesse Sisi), Rabi, Max, Jérôme, Kévin, Meïssou, Ptit Gui, Ananas, Morgane, Thomas², Nico⁴, Arnaud², Jeff, Armel, Alex, Leïla, Hugo, Chris, Sam, Yann, Antoine, Céline et Stéphane, Adoum, Cédric, Tiago, Lauriane, Claudie, Lucille, Antoine, Maria, Jonas, Juan, Clément, Benjamin... (j'espère que j'oublie personne…). Une pensée particulière pour Virginie que je connais depuis mon stage (vive Lancelot !), pour Zineb et Arnaud mes supers cobureau, Chloé et Eloïse, avec qui j'ai rit, dansé et beaucoup bu l'apéro ! On s'est soutenu du début jusque dans la dernière ligne droite !

Le dernier merci revient à Nico grâce à qui j'ai tenu le coup, qui m'a supporté et soutenu pendant ces 7 dernières années. Une nouvelle aventure commence maintenant...

RESUME

Les granites à métaux rares (GMRs) sont l'expression du magmatisme à métaux rares au même titre que les pegmatites et autres équivalents volcaniques (e.g., rhyolites à métaux rares, macusanites, ongonites) et se rencontrent dans le monde entier (e.g., Chine: Belkasmi et al., 2000 and Zhu et al., 2001; Finlande: Haapala and Likkari, 2005; Algerie: Kerriou et al., 2000; Namibie: Schmitt et al., 2000; Nigeria: Kinnaird et al., 1985; Egypte: Renno, 1997; Canada: Kontak, 1990, Pillet et al., 1992; Russie: Raimbault et al., 1995; Mongolie: Kovalenko et al., 1995; Europe de l'Ouest: Charoy and Noronha, 1996; Breiter et al., 2017; Manning and Hill, 1990). Egalement désignés sous le nom de granites à éléments rares, granites à étain, granites à topaze, à zinnwaldite ou granites Li-F, ils résultent de la cristallisation de magmas très évolués et sont caractérisés par une signature géochimique particulière qui diffère des autres types de granites. Les granites à métaux rares montrent communément de forts enrichissements en volatiles et fondants (e.g. F, Li, P, B) et en métaux tels que Li, Sn, Nb et Ta se présentant sous la forme de minéralisations disséminées. Les GMRs peuvent avoir des compositions (i.e., péralcalin à très péralumineux) et minéralogies relativement variables en fonction, par exemple, du contexte géodynamique de mise en place. Depuis les années 80, plusieurs classifications ont été proposées tel que celle de Beus (1982) relativement complexe comptant 8 types de GMRs. En 2005, Linnen et Cuney, proposent une classification simplifiée basée sur des arguments minéralogiques et géochimiques. Les GMRs y sont classés en trois groupes principaux : (i) péralcalins ; (ii) métalumineux à péralumineux ou péralumineux faiblements phosphorés et (iii) péralumineux très phosphorés. Le groupe péralcalin fait référence aux GMRs caractérisés par de très fortes concentrations en F, REE, Y, Zr, Nb et de fortes concentrations en Th, Sn, Be, Rb et U, se mettant en place dans un contexte anorogénique. Les GMRs péralcalins sont particulièrement enrichis en Fe, modérément en Li et appauvris en P. Ils sont principalement minéralisés en Zr, Nb (pyrochlore), REE, U et Th. Les granites métalumineux à péralumineux sont principalement minéralisés en Nb-Ta (colombite) et Sn (cassitérite) et peuvent se mettre en place à la fois dans un contexte anorogénique ou post-orogénique. Ils sont généralement caractérisés par un profil de terres rares plat avec une forte anomalie négative en Eu et les

rapports Nb/Ta, Zr/Hf sont relativement bas comparés aux rapports observés dans le cas des granites péralcalins. Enfin, les GMRs péralumineux très phosphorés sont caractérisés par des concentrations très faibles en terres rares, inférieures aux concentrations moyennes observées pour la croûte supérieure. Les concentrations en Y, Zr, Hf, Th, Sc, Pb sont faibles tandis que Rb et Cs sont très enrichis. Ces granites se mettent en place dans un contexte tardi à post-orogénique dans les chaînes de collision continentale. Ils sont principalement minéralisés en Sn, Nb, Ta et Li portés par les colombite-tantalites, cassitérites, micas et phosphates de lithium de la série amblygonite-montébrasite.

De manière générale, les GMRs se mettent en place très haut dans la croûte (e.g., 1-2 km) et sont caractérisés par une texture subvolcanique marquée par la présence de phénocristaux (e.g., quartz snowball, micas) entourés d'une matrice très finement cristallisée. Ils sont de taille restreinte en carte (i.e., quelques centaines de mètres ou moins) et impliquent de petits volumes de magma (i.e., 0.02-0.2 km^3) comparés aux intrusions de type laccolite ou batholite (i.e., plusieurs km en carte et 200-5000km^3). Une autre caractéristique commune aux GMRs est la présence d'un faciès de bordure au toit de l'intrusion, au contact avec les roches encaissantes. Ce faciès de bordure, également nommé stockscheider par certains auteurs, correspond à des textures de solidification unidirectionnelle pointant vers le centre de l'intrusion. Ce faciès spécifique est souvent composé d'une alternance de zones aplitiques et pegmatitiques, les termes aplitique et pegmatitique référant à la taille des cristaux et non à une définition spécifique.

Depuis les années 60, de nombreuses études ont été consacrées à la compréhension de ces granites évolués et en particulier dans la chaîne Varisque, cependant, plusieurs questions restent en suspend et certains points sont encore largement débattus. L'un de ces points concerne la genèse de ces magmas à métaux rares et l'acquisition de leur signature particulière. Le premier débat fut de savoir si cette signature résultait de processus magmatiques ou de changements subsolidus tardifs. Plusieurs études sur des équivalents volcaniques ont montrées que les métaux pouvaient être concentrés au stade magmatique (e.g., Ongonites et Macusanites ; Kovalenko et al., 1970; Kovalenko et Kovalenko, 1976 et Pichavant et al., 1988). L'importance des processus magmatiques sera, par la suite, largement acceptée par la communauté, ceci n'excluant pas des changements tardi-magmatiques, souvent significatifs dans ces systèmes (e.g., redistribution des éléments liée à la circulation de fluides

hydrothermaux ou altération). Considérant une origine principalement magmatique, deux modèles s'affrontent. D'après certains auteurs, les magmas à métaux rares résultent de la différenciation extrême d'un magma granitique parent (e.g., Černȳ, 1991b, Černȳ 1992a; Raimbault et al., 1995; Černȳ et al., 2005), les fondants, les lithophiles et les métaux étant préférentiellement partagés dans le magma résiduel au cours de la cristallisation fractionnée. D'autres auteurs (e.g., Burt et al., 1982; Christiansen et al., 1986; Manning et Hill, 1990; Cuney, 1990; Cuney et al., 1992; Nabelek et al., 1992a; b, Simmons et al., 1995; 1996; Falster et al., 1997; 2005; Roda et al., 1999; Marignac et Cuney, 1999) proposent un modèle alternatif mettant en jeu la fusion partielle à faible taux ou la fusion partielle de sources enrichies comme processus principaux permettant le genèse des magmas à métaux rares. Ces deux modèles restent encore au centre des discussions, l'efficacité des processus de fusion (e.g., différenciation par fusion) n'ayant pas encore été démontrée.

Bien que les processus magmatiques jouent un rôle majeur, la signature finale des GMRs résulte d'une combinaison de processus magmatiques et hydrothermaux. L'importance relative et le rôle des fluides, qui peuvent être d'origine diverses (i.e., magmatiques, métamorphique ou météorique), restent encore mal compris et en particulier les processus à la transition magmatique-hydrothermale restent à préciser (i.e., exsolution des fluides magmatiques). La principale difficulté réside dans le fait que dans la majorité des systèmes naturels, l'expression des processus magmatiques et hydrothermaux précoces soit partiellement effacée par les processus tardifs d'altération hydrothermale ou météorique (e.g., greisenisation, kaolinisation). La compréhension de ces processus nécessite donc des études complémentaires. Ces processus ont également un rôle important sur la distribution des métaux, sur l'expression des minéralisations (e.g., magmatiques disséminées, hydrothermales précoces ou hydrothermales tardives de type veine) et sur le comportement des métaux au cours de la transition.

Même si certaines questions persistent, l'attention de la communauté s'est principalement portée sur les spécificités minéralogiques et géochimiques des GMRs (e.g., Pichavant and Manning, 1984; Cerný et al., 1985; Raimbault et al., 1995; Charoy and Noronha, 1996; Linnen and Cuney, 2005; Breiter et al., 2017). En comparaison, les contrôles structuraux permettant la mise en place des GMRs, le comportement mécanique et la géométrie des GMRs sont rarement abordés. Le nombre limité d'études de ce type sur les GMRs contraste fortement avec le grand nombre d'études menées sur les

autres granites Varisques (e.g., étude structurale couplées aux méthodes géophysiques). Aux vues des singularités des GMRs (e.g., signature géochimique, volume de magma, niveau de mise en place), le comportement des magmas à métaux rares et les mécanismes de mise en place sont supposément différents des autres granites de la chaîne Varisque.

Ce travail a pour but de mener une étude intégrée afin d'avoir une compréhension complète des GMRs. Les objectifs principaux sont d'appréhender les processus et mécanismes à la fois magmatiques, hydrothermaux et structuraux responsables de : (i) la genèse des magmas à métaux rares, (ii) la mise en place et la géométrie des GMRs et (iii) leur signature géochimique spécifique et leur enrichissement en métaux. Ces différents aspects sont étudiés sur l'exemple exceptionnel du GMR Varisque d'Argemela (Zone Centro Ibérique, Portugal) en utilisant différentes approches et échelles. Une étude expérimentale a été également menée en complément. Ce manuscrit compte 7 chapitres, les chapitres I et VII étant l'introduction générale et la partie synthèse/conclusion, respectivement. Le chapitre II s'intéresse au contexte structural et aux mécanismes de mise en place du granite à métaux rares d'Argemela *via* une analyse structurale multi-échelles couplée à une étude gravimétrique. Le chapitre III traite de la caractérisation et des mécanismes de mise en place des minéralisations associées spatialement et/ou génétiquement au granite d'Argemela, au cours de la transition magmatique-hydrothermale. Dans le chapitre IV, un modèle de dépôt de la wolframite a été établi dans le cas d'Argemela et une comparaison à d'autres gisements est proposée. Le chapitre V est consacré à l'étude des mécanismes à la transition magmatique-hydrothermale et plus particulièrement au comportement des métaux à l'aide des compositions en majeurs et traces des minéraux et des isotopes stables. Enfin, le chapitre VI décrit les résultats de l'étude expérimentale menée dans le but de tester la fusion partielle à faible taux comme mécanisme possible à l'origine de la genèse des magmas à métaux rares.

La chaîne Varisque d'Europe de l'Ouest, du Portugal à la Bohème, est une province métallogénique notoire dans laquelle plusieurs GMRs ont été reconnus et étudiés depuis un certain nombre d'années. Elle résulte de la collision continentale, au Paléozoïque, du Gondwana au Sud et du Laurussia au Nord (Autran et Cogné 1980; Bard et al. 1980; Matte 1986, 1991) et d'autres blocs crustaux

satellites d'extension limitée, dont l'existence est reconnue (e.g., Armorica) ou supectée (e.g., Léon). Une évolution géodynamique polycyclique est amplement acceptée par la communauté scientifique, cependant, les âges et la signification des évènements tectoniques, magmatiques et métamorphiques restent débattus. Plusieurs modèles d'évolution ont été proposés depuis plus de 30 ans (Holder and Leveridge, 1986; Ledru et al., 1989; Matte, 1991; Faure et al., 1995; Franke, 2000; Faure et al., 2005; Martínez-Catálan et al., 2007; Matte, 2007). D'après l'étude relativement récente de Ballèvre et al. (2014) à l'échelle régionale pour l'Arc Ibéro-Armoricain, plusieurs stades d'évolution peuvent être reconnus comme suit. Au Devonien, - de 405 à ~370 Ma - la convergence des plaques lithosphériques Gondwana et Laurussia est accommodée par les marges actives et le développement de systèmes d'arcs (e.g. Ducassou et al., 2014). L'accrétion des unités d'arcs aux blocs continentaux entraine la formation d'unités éclogitiques de HP/HT (Stosch and Lugmair, 1990, Ordóñez Casado et al., 2001, Roger and Matte, 2005) et l'accrétion d'ophiolites formées en contexte de supra-subduction (e.g. Sanchez Martinez et al., 2007, Ballèvre et al., 2014, Paquette et al., 2017). Ces évènements sont suivis par la subduction vers le Nord et le Nord-Ouest de la marge passive Gondwana entrainant la formation d'éclogites de HP/BT (e.g. Bosse et al., 2000). Lorsque la subduction continentale est vérouillée à ~365-360Ma, la phase de collision continentale débute, évènement marqué par l'empilement de nappes (Burg et al., 1987, Faure et al., 2008, Pitra et al., 2010, Paquette et al., 2017) et un épaississement crustal. Les bassins compressifs synchrones de l'orogenèse se forment à partir de ~335Ma alors que la déformation compressive et les chevauchements se propagent dans les domaines externes. Les domaines internes sont marqués, à cette période, par un épisode de fusion crustale et la mise en place de dômes migmatitiques. Il est à noter que le magmatisme tardi-magmatique semble avoir migré depuis les zones internes vers les zones les plus externes de 335 à 280Ma (see Cochelin, 2016). L'évolution tardi-Varisque est ainsi marquée par : (i) une extension syn-convergence dans les domaines internes (Burg et al., 1994; Gapais et al., 2015), (ii) le développement de zones de cisaillement d'échelle crustale (Arthaud and Matte, 1975; Matte, 1986) et (iii) l'intrusion de granites péralumineux syn-cinématiques ((Lagarde et al., 1992; Faure, 1995; Marignac and Cuney, 1999). Le magmatisme à métaux rares ainsi que les minéralisation Sn-W-Li-Nb-Ta se mettent en place à la fin de cette épisode tardi-Varisque, généralement du Westphalien au Stéphanien.

Le district d'Argemela (CIZ, Portugal) se situe à ~15 km à l'est de la mine de tungstène de Panasqueira d'importance mondiale, au sud de la Serra Da Estrela et à l'ouest du granite composite de Fundão et de son auréole de contact (Serra Do Gomes). Ce district est composé de deux systèmes minéralisés mis en place dans les schistes de Beira faiblement métamorphisés dans le facies schiste vert : (i) l'ancienne mine d'étain et (ii) le granite à métaux rares. L'ancienne mine d'Argemela consiste en un ensemble de veines à Sn-Li mis en place dans les schistes. Le granite d'Argemela, situé à quelque centaines de mètres de la mine, forme une petite intrusion caractérisée par des minéralisations à la fois disséminées et de type veine.

L'étude structurale de terrain couplée à une analyse du champ de déformation à l'échelle régionale et à de la modélisation gravimétrique ont permis de contraindre la structure et la géométrie du granite d'Argemela et le contexte mécanique de mise en place. Ceci a permis de mettre en évidence le contexte particulier de mise en place du district d'Argemela incluant le GMR et les systèmes minéralisés associés. Les résultats principaux sont brièvement décrits ci-après. (i) A l'échelle régionale, la stratification S0 est affectée par une phase de compression coaxiale NE-SW homogène entrainant la formation de pli droits N130-140°E (F1) décimétriques à plurikilométriques et la mise en place d'une schistosité S1 d'axe de pli pénétrative orientée ~N135°E à fort pendage. (ii) Le district d'Argemela se met en place dans une ombre de pression d'échelle régionale (plurikilométrique) mise en évidence par la réorientation de la S1 autour du granite composite de Fundão et de son auréole de métamorphisme. L'ombre de pression, agissant comme une zone de relâchement des contraintes durant la déformation Varisque, a joué un rôle important dans la mise en place d'Argemela favorisant la chenalisation du magma et son ascension dans cette zone. (iii) La modélisation gravimétrique a révélée la géométrie particulière du granite d'Argemela en forme de tuyau (« pipe »). Ce type de géométrie est en accord avec une ascension verticale du magma vers des niveaux subvolcaniques. (iv) Des zones de cisaillement dextres N170°E-NS viennent se surimposer à l'ombre de pression régionale, ce qui est cohérent avec une direction de raccourcissement NE. A l'échelle régionale, les zones de cisaillement entrainent la formation de plis aux axes modérément à fortement pentés et localement une schistosité d'axe de pli S2 se développe. La localisation de la déformation le long des plans cisaillants entraine une réorientation passive de la S1. La bordure nord-est du granite d'Argemela est affectée par une de ces zones de

cisaillement jouant un rôle important au moins dans les derniers stades de mise en place. La zone de cisaillement est mieux exprimée que celles affectants les schistes encaissants et se localise fortement le long du contact. Ceci illustre bien le rôle du comportement rhéologique des roches sur la localisation de la déformation. De plus, la localisation de la déformation pourrait avoir induit la rotation horaire de l'intrusion. (v) A l'échelle de la modélisation gravimétrique, l'intrusion n'est pas enracinée sur la zone de cisaillement ce qui suggère que le cisaillement n'a affecté que la forme du granite au niveau de mis en place. Il n'est cependant pas impossible que ces zones de cisaillement aient une continuité en profondeur et se branchent sur des structures d'échelle plus importante favorisant la chenalisation du magma. (vi) Les caractéristiques géométriques et texturales du granite d'Argemela suggèrent une remontée verticale rapide et canalisée du magma vers des niveaux subvolcaniques. Ceci est cohérent avec les faibles viscosités généralement attribuées à ce type de magma. Les autres GMRs de la chaîne montrent des géométries et des volumes similaires à ceux d'Argemela. De ce fait, il est proposé que les magmas à métaux rares, de manière générale, ont un comportement du même ordre qui inhibe les flux horizontaux communément observés dans le cas des autres types de granites (e.g., laccolithes). (vii) Le mode de mise en place des veines, appartenant au district minéralisé d'Argemela, est cohérent avec le régime de déformation régional. Le système de veines intragranitiques limité au GMR d'Argemela est composé de trois générations. Les deux premiers types s'ouvrent sous forme de fentes de tension et leurs géométries mettent en évidence le comportement encore légèrement ductile de l'intrusion. En revanche, les veines de la dernière génération sont très rectilignes avec des contacts francs avec le granite et la structure interne indique un mouvement apparent senestre. Ceci suggère un comportement plus cassant du granite encaissant. Dans leur position actuelle l'orientation des veines n'est pas cohérente avec la direction de raccourcissement régionale NE. Or, dans la mesure où le granite d'Argemela est affecté par une zone de cisaillement dont la direction et le jeu sont cohérents avec le régime de déformation et les contraintes régionales, il est possible que l'ensemble de l'intrusion ai subit une rotation horaire d'environ 20° autour d'un axe vertical sous l'effet d'un cisaillement dextre. Cette hypothèse est en accord avec le comportement rigide du granite comparé à l'encaissant schisteux. Ce type de rotation a d'ailleurs été décrit sur des plutons de taille plus importante. Au niveau de la mine d'Argemela, l'évolution des directions et des géométries des veines est cohérente avec le développement d'un cisaillement simple

sous l'effet d'une direction de raccourcissement incrémentale NE. Les directions et les variations des contraintes finies du système mettent en évidence un cisaillement non coaxial compatible avec les zones de cisaillement dextres N170°E-NS décrites auparavant. Les veines s'ouvrent sous forme de fentes de tensions, tournent et se font plisser au cours du cisaillement simple, le plissement étant possible cette fois du fait du comportement ductile des schistes encaissants. Le mode de mise en place des veines du district d'Argemela souligne le rôle du comportement des roches encaissantes sur la distribution de la déformation et sur le développement des minéralisations de type veine.

Argemela est un exemple exceptionnel qui nous a donné l'opportunité d'étudier en détail l'expression de la transition magmatique-hydrothermale et de mieux comprendre le rôle de cette transition sur le transport/distribution des métaux et sur le dépôt des minéralisations. Les observations de terrain ont été combinées à une étude pétrologique, à des analyses roches totales et sur minéraux et à une étude des isotopes stables (O, H). L'étude de terrain a permis de mettre en évidence trois faciès principaux recoupés par les trois générations de veines. Les relations d'intersection claires ont permis d'établir une chronologie détaillée avec la mise en place : (1) du faciès granitique et du faciès de bordure (stockscheider), (2) du faciès gris sous forme de dyke, (3) des veines I, (4) des veines II, (5) des veines III et (6) des sulfures. Les isotopes stables réalisés sur micas et quartz couplés aux études minéralogiques et géochimiques suggèrent une forte affinité magmatique du fluide sans contribution externe (i.e., fluide métamorphique et/ou météorique) à l'exception de la bordure nord-est du granite affectée par le cisaillement. La géochimie roche totale, l'identification des zonations et l'analyse des éléments majeurs et traces des minéraux clés (présents à la fois dans le granite et dans les veines à l'exception des micas) ont rendu possible la reconnaissance de cinq stades principaux au cours de la transition magmatique-hydrothermale. (1) Le stade précoce dominé par le magma correspond à la phase majeure de cristallisation des minéraux principalement anhydres - en dehors des micas et des phosphates de lithium - qui vont former 90% du bâti granitique. La transition entre le stade dominé par le magma et le stade « crystal mush » a probablement impactée le comportement mécanique de l'intrusion. Le style de zonations observées dans les minéraux suggère que le magma a cristallisé *in-situ* sans variations de premier ordre de l'environnement de cristallisation. Les concentrations significatives en éléments rares observées dans les quartz et les micas (en particulier Sn, Li, Nb, Ta, W, P) indiquent que

l'enrichissement en ces éléments résulte en premier lieu de processus magmatiques. Les zonations, la signature géochimique et les textures des premières générations de cassitérite et colombite-tantalite suggèrent que ces minéraux ont cristallisés à ce stade. De manière générale, les concentrations en métaux significatives enregistrées par tous les minéraux indiquent que l'environnement de cristallisation était concentré en ces éléments à ce stade. (2) Le second stade correspond à un moment décisif de la transition magmatique-hydrothermale. Une chute drastique et uniforme des concentrations en éléments est observée dans les micas (en particulier Sn, Li, Nb, Ta, W à l'exception de Rb et Cs qui restent stables) ce qui indique une modification importante de l'environnement de cristallisation. Ceci combiné aux critères texturaux et chimiques des autres minéraux (Qtz_{III}, Cst_{II}, CT_{II}) indique que le granite cristallise en présence d'une phase fluide. Ainsi, ce changement drastique d'environnement marque le début de l'exsolution des fluides magmatiques, les métaux étant partagés dans la phase fluide. A ce stade, la cristallisation de cristaux squelettiques indique que mécaniquement le fluide est encore capable de percoler à travers le « crystal mush ». Suite à cette chute drastique uniforme des concentrations, une ré-augmentation sélective des éléments (Sn, Nb, Ta, Mn) est observée accompagnée d'une hausse drastique du bore. Ce changement pourrait s'expliquer par la condensation d'un matériau enrichi en soluté sous l'effet du refroidissement et/ou de la dépressurisation du fluide, comme cela a été observé expérimentalement. Ce mécanisme pourrait expliquer le fractionnement des éléments et la cristallisation du faciès gris anormalement riche en métaux. Cela mis à part, le faciès gris se trouve sous la forme de « dykes » fortement pentés ce qui signe le début de la chenalisation des fluides et représente un intermédiaire entre la circulation des fluides par percolation et l'ouverture des veines. (3) Ce stade est marqué par la mise en place des veines intragranitiques ce qui indique que les fluides sont totalement chenalisés. Les fluides n'interagissent plus avec le granite comme le suggèrent les analyses roches totales en bordure de veines. A ce stade le granite est entièrement cristallisé, cependant les géométries des veines Types I et II traduisent un comportement encore légèrement ductile de la roche. Les analyses et la minéralogie des veines indiquent que les éléments rares sont transportés par la phase fluide. Toutefois, les quartz des veines I à III enregistrent une diminution générale de la concentration en éléments qui peut s'expliquer soit par la cristallisation de minéraux porteurs ou par une perte liée à l'extraction du fluide. (4) Ce stade est interprété comme l'expression limitée de processus d'altération

hydrothermale. L'enrichissement important en Li et F de la dernière génération de micas peut être l'expression de la remobilisation des éléments suivie d'une phase de cristallisation subsolidus. (5) La cristallisation de sulfures, limitée à la bordure nord-est cisaillée, marque la contribution d'un fluide externe riche en soufre et arsenic.

L'étude pétrographique et géochimique détaillée de la transition magmatique-hydrothermale a également permis de proposer une séquence de minéralisation mettant en évidence le comportement contrasté de l'étain et du tungstène au cours de cette transition. La cassitérite cristallise principalement au stade magmatique ou très tôt dans la transition alors que la wolframite cristallise dans les derniers stades hydrothermaux. Ainsi, les minéraux à Sn et W résultent de mécanismes de dépôt différents. Par ailleurs, les variations de composition de la wolframite sont apparus comme clés pour comprendre les mécanismes de dépôt. En effet, nos résultats suggèrent que le rapport H/F (Hübnérite/Ferbérite) peut être utilisé comme indicateur des environnements de dépôt contrastés dans les systèmes péri-granitiques à wolframite. Ce rapport peut également être utilisé comme outil de prospection. L'étude de la transition magmatique-hydrothermale montre aussi qu'un enrichissement primaire en métaux dans le magma ne résulte pas nécessairement sur la formation d'un gisement. En effet, le granite d'Argemela est très enrichi en Li, Sn, Nb et Ta comparé au granite à Zinnwaldite de Cínovec (Erzgebirge), cependant, les métaux ne font pas l'objet d'un intérêt économique. Les processus d'altération hydrothermaux tardifs, très limités à Argemela, jouent un rôle clé dans la formation de concentrations économiquement attractives.

Le dernier volet de cet étude a eut pour objectif de tester l'efficacité de la fusion à faible taux à générer des magmas à métaux rares et la fusion par déshydratation comme mécanisme principal permettant la concentration des métaux expérimentalement. Afin de coller au plus près aux processus naturels, nous avons choisit des échantillons naturels ayant des caractéristiques minéralogiques, texturales et chimiques différentes. Les résultats de l'étude expérimentale ont mis en évidence le rôle de l'assemblage minéralogique, de la distribution des minéraux et de la schistosité sur la distribution du liquide silicaté. Pour des assemblages minéralogiques et une chimie initiale différente, les mécanismes de fusion sont similaires aux mêmes conditions de pression et température. En revanche, la proportion modale initiale de biotite et muscovite est un facteur majeur contrôlant le pourcentage de fusion et la

redistribution des métaux. Cette étude montre également qu'une teneur importante en métaux dans le protolithe ne résulte pas nécessairement en un enrichissement en métaux dans le liquide silicaté généré. Même dans le cas des plus faibles taux de fusion, le liquide silicaté est que légèrement enrichi, les métaux étant séquestrés dans les phases restitiques. Ces résultats ont des implications majeures et suggèrent qu'un seul épisode de fusion ne permet pas de former des liquides silicatés enrichis. En revanche, une fusion répétée impliquant la déstabilisation des restites enrichies pourrait conduire à la genèse de liquide enrichis.

Enfin, cette étude démontre la nécessité de combiner différentes approches, à différentes échelles, afin d'avoir une vue d'ensemble et une meilleure compréhension des systèmes minéralisés. Les granites à métaux rares résultent d'une combinaison de processus magmatiques, hydrothermaux et structuraux, jouant tous un rôle non négligeable. De plus, chaque grand type de processus va influencer les autres, d'où l'importance de réaliser une étude intégrée.

TABLE OF CONTENT

CHAPTER I:

GENERAL INTRODUCTION

GENERAL INTRODUCTION

I.1. RARE METAL GRANITES: DEFINITION AND CLASSIFICATIONS

I.1.1. Definition

Rare Metal Granites are one expression of the so called “rare metal magmatism” and occur worldwide at different ages (e.g., China: Belkasmi et al., 2000 and Zhu et al., 2001; Finland: Haapala and Likkari, 2005; Algeria: Kesraoui et al., 2000; Namibia: Schmitt et al., 2000; Nigeria: Kinnaird et al., 1985; Egypt: Renno, 1997; Canada: Kontak, 1990, Pillet et al., 1992; Russia: Raimbault et al., 1995; Mongolia: Kovalenko et al., 1995; Western Europe: Charoy and Noronha, 1996; Breiter et al., 2017; Manning and Hill, 1990). Other product of this magmatism includes granitic pegmatites and volcanic equivalent (e.g. rare-metal rhyolite, macusanite or Ongonite). Also designated as rare elements, tin, topaz, zinnwaldite or Li-F granites, RMGs result from the crystallization of highly evolved magmas and are characterized by a specific geochemical signature which differs from other granites. RMGs commonly show strong enrichment in volatiles and fluxing elements (e.g. F, Li and/or P, B) and in metals such as Li, Sn, Nb and Ta found as disseminated mineralization dispersed in the granitic mass. Depending on the location and especially the source (i.e. geodynamical context and position within an orogen) RMGs can be peralkaline to highly peraluminous and thus differs strongly in terms of composition and mineralogical assemblage (e.g. A/CNK, REE pattern and content, P and F content, related metal mineralization). Emplaced in shallow crustal levels (i.e. 1-2 km deep), these intrusions show a subvolcanic texture being mainly made of snowball quartz phenocrysts embedded in very fine-grained albitic matrix. RMGs are of restricted size, in map view (i.e. several hundred meters or less), and volume (i.e. 0.02-0.2 km^3) compared to laccolithic intrusions or batholiths (i.e. several km and 200-5000 km^3 to even > 10 000 km^3). Another characteristic feature is the presence of a border facies at the top and upper borders of the intrusion (i.e. upper contacts with the surrounding rocks). Border facies, also designated as stockscheider, consist in unidirectional solidification textures with crystals growth

pointing toward the center of the intrusion. This specific facies is generally composed of aplitic and pegmatitic zones, the terms aplitic and pegmatitic referring only to crystal size here and not to specific definitions.

I.1.2. Classifications

Several classifications have been proposed up to now with various complexities and up to eight types proposed for RMGs by Beus (1982). A simpler classification has been proposed by Linnen and Cuney (2005) based on highly specific mineralogical and geochemical arguments. RMGs are grouped into three main types: (i) peralkaline, (ii) metaluminous to peraluminous or peraluminous low-phosphorus and (iii) peraluminous or peraluminous highly phosphorous.

(i) The Peralkaline group (PLK, ASI<1) refers to granite typically emplaced in anorogenic settings. These RMGs are characterized by very high content of F, REE, Y, Zr and Nb and high content of Th, Sn, Be, Rb and U. Nb/Ta and Zr/Hf ratios are high while P content is very low. Peralkaline RMGs are particularly enriched in Fe and moderately in Li. The most present Li-F micas are zinnwaldite and polylithionite. PLK granites are generally mineralized in Zr, Nb (pyrochlore), REE, U and Th.

(ii) The Peraluminous Low Phosphorous (PLP) granites are characterized by intermediate content of REE with a typical flat pattern and a strongly negative anomaly in Eu, Y, Zr, Hf, Th and Pb. Nb/Ta and Zr/Hf ratios are relatively low compared to PLK granites and the main Li-bearing mica is zinnwaldite. Spatially related to metaluminous to weakly peraluminous less fractionated intrusions, these granites can occur either in post-orogenic or anorogenic geodynamical settings and are typically mineralized in Nb-Ta (columbite group) and Sn (cassiterite).

(iii) The Peraluminous High Phosphorous (PHP, molar Al / [Na+K] >1.15) granites are characterized by REE content much lower than the upper crust, low Y, Zr, Hf, Th, Sc and Pb and very high Rb and Cs content. Nb/Ta and Zr/Hf ratios are very low and the most common micas are Li-

muscovite to lepidolite. Associated with two micas S-type peraluminous granite, PHP granites occur as late to post-orogenic intrusions in continental collisional belts. These granites are commonly mineralized in Sn, Nb, Ta and Li occurring in columbite-tantalite, cassiterite, micas and Li-bearing phosphates from the amblygonite-montebrasite serie.

I.2. RARE METAL GRANITES WITHIN THE VARISCAN BELT

I.2.1. The Variscan belt

Development of the Paleozoic Variscan belt of Western Europe (Fig. 1) results from the convergence of two major lithospheric plates – Gondwana to the south and Laurussia to the north – (Autran and Cogné 1980; Bard et al. 1980; Matte 1986, 1991) with known (e.g. Armorica) or suspected satellite crustal blocks of rather limited extension squeezed in between. A polycyclic geodynamical evolution for the Variscan belt is now widely accepted but timing and general meaning of the tectonic-magmatic-metamorphic events remain controversial. Several models of evolution have been proposed for more than thirty years (Holder and Leveridge, 1986; Ledru et al., 1989; Matte, 1991; Faure et al., 1995; Franke, 2000; Faure et al., 2005; Martínez-Catálan et al., 2007; Matte, 2007). Following a recent regional-scale review made for the Ibero-Armorican arc evolution (Ballèvre et al., 2014), tectonic stages can be recognized, as follows. During Devonian – from 405 to ~370 Ma – Early Variscan Gondwana-Laurussia convergence is firstly accommodated by active margins and arcs development (e.g. Ducassou et al., 2014); a stage also referred as the Acadian cycle. Accretion of arc units to continental blocks leads to the formation of HP/HT eclogite units (Stosch and Lugmair, 1990, Ordóñez Casado et al., 2001, Roger and Matte, 2005) and of accretion of ophiolites formed in supra-subduction settings (e.g. Sanchez Martinez et al., 2007, Ballèvre et al., 2014, Paquette et al., 2017). It follows northward to northwestward subduction of the Gondawana passive margin leading to the formation of HP/LT eclogite units (e.g. Bosse et al., 2000). When continental subduction locked, at ~365-360 Ma, continental collision *s.s.* began with nappe stacking (Burg et al., 1987, Faure et al., 2008, Pitra et al., 2010, Paquette et al., 2017) and continental crust thickening. It is noteworthy that structure of the Western European Variscan belt may not be fully cylindrical leading to discordant ages of the eclogite-facies metamorphism from massif to massif (see Paquette et al., 2017 and Lotout et al., 2018 for recent results and discussions).

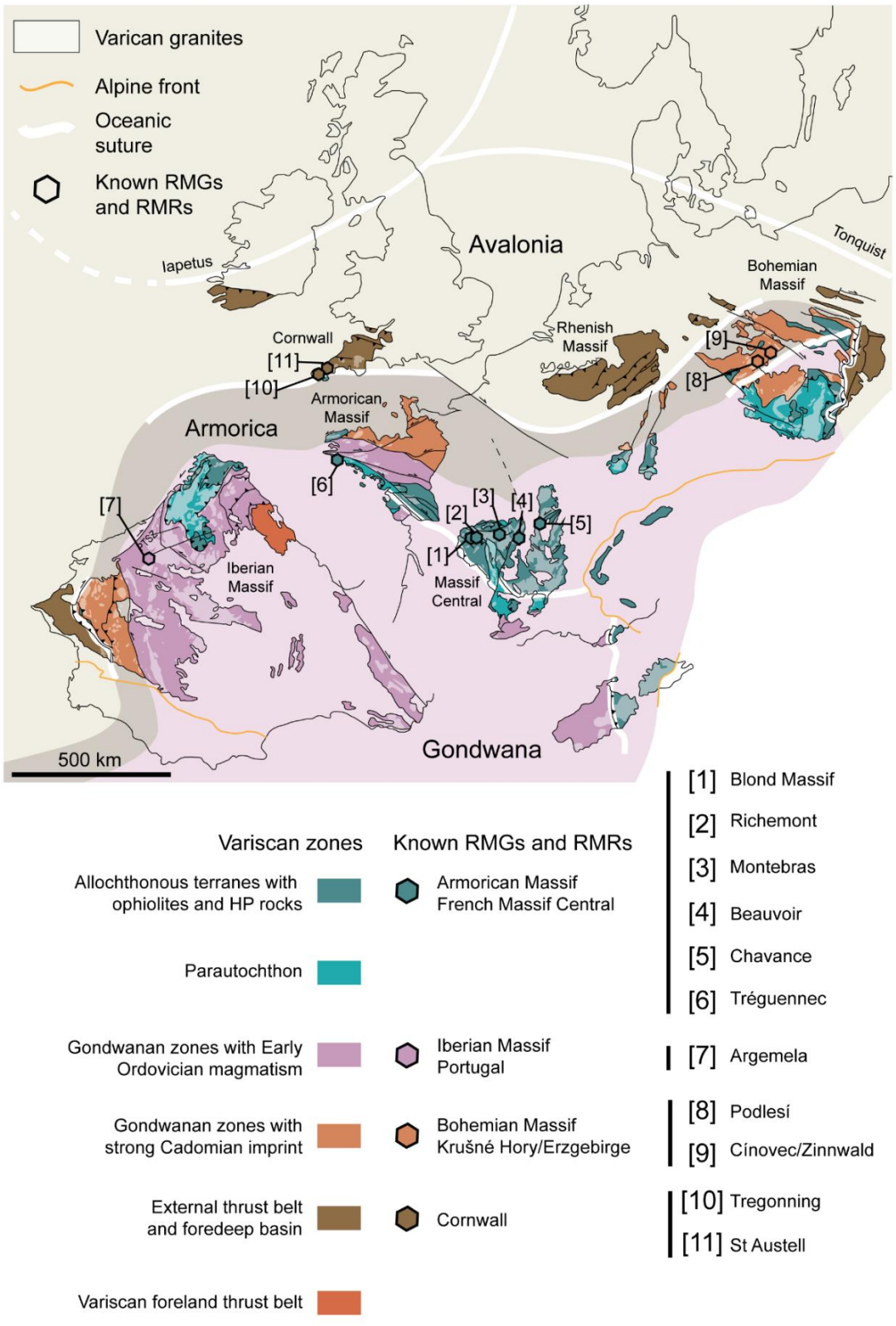

Fig 1 *Outstanding examples of RMGs and RMR across the Western Europe Variscan belt. Modified after Ballèvre et al. (2014)*

Syn-orogenic compressive basins formed and from ~335 Ma, while compressional deformation/thrusting propagated to the external domains of the range, internal parts underwent partial melting in the lower crust and migmatitic domes (Jones and Brown, 1990) and extensional detachments (Gapais et al., 1993) formed. It is noteworthy that felsic late Variscan magmatism looks to have migrated from internal to external zones of the range from 335 to 280 Ma (see compilation in Cochelin, 2016 and references therein). Late tectonic evolution, from 335 to ~290 Ma, is thus marked by coeval (i) syn-converging extension in the internal domains (Burg et al., 1994; Gapais et al., 2015), (ii) development of crustal scale transcurrent shear zones (Arthaud and Matte, 1975; Matte, 1986) and (iii) intrusion of syn-kinematics peraluminous granites (Lagarde et al., 1992; Faure, 1995; Marignac and Cuney, 1999). Examples of such syn-tectonic plutons can be found in Portugal, along the NW trending sinistral shear zones (Pereira et al., 1993), along the South Armorican Shear Zone (NW France; Berthé et al., 1979, Jegouzo, 1980, Tartèse et al., 2011) and along extensional shear zones (Gapais et al., 1993, Lagarde et al., 1994, Turillot et al., 2009). During this late Variscan orogenic phase, rare metal magmatism – including RMG generation – mainly occurred during the Westphalian and the Stephanian (Marignac and Cuney, 1999; e.g. 308 ± 2Ma for the Beauvoir RMG, FMC, Cheilletz et al., 1992 and 303 ± 6Ma for the Argemela RMG, CIZ, Noronha et al., 2013). Expressions of deformation, metamorphism and magmatism can be discontinuously observed all over Western Europe through several massifs preserved from Alpine tectonics in their core: the Iberian Massif, the Armorican Massif, Cornwall, the French Massif Central, Ardennes, the Rhenish Massif and the Bohemian Massif.

I.2.2. Correlations and subdivision

Based on several key features (e.g. lithological associations, sedimentary and faunal records, chemical affinities, magmatism, distribution of ophiolitic and HP units, metamorphic evolution, tectonic or ages), many attempts have been undertaken over the years to correlate the different zones or terranes involved in pre-Variscan and Variscan orogenies (e.g. Holder and Leveridge, 1986; Matte, 1991; Faure, 1995; Franke, 2000; Matte, 2001; Franke and Żelaźniewicz, 2002; Faure et al., 2005; Martínez-Catálan et al., 2007; Ballèvre et al., 2009; Martínez-Catálan et al., 2011; Shaw et al., 2012; Ballèvre et al., 2013;

Kroner and Romer, 2013). Strong lasting controversies include the number and location of involved microcontinents or terrane and oceanic sutures (i.e. number of oceans and timing). Main difficulties are derived from discontinuous outcrops and crust blocks splitting related to late and/or post Variscan events (e.g. formation of post orogenic oroclines, erosion, Alpine and Pyrenean orogenies). More recently, backed up by previous works, Ballèvre et al. (2014) attempted to produce a new correlation map for Western Europe involving five main zones: (i) internal domains including the allochtonous and parautochtonous units, (ii) Gondwanan zones with Early Ordovician magmatism, (iii) Gondwanan zones with strong Cadomian imprint, (iv) the Variscan foreland thrust belt and (v) the external thrust belt and foredeep basins. Internal domains are characterized by autochtonous units overlain by both the parautochtonous thrust sheets and allochtonous nappe stacking units. The autochton is made up of Neoproterozoic to Paleozoic sediments and volcanic materials deposited on the northern passive margin of Gondwana (Martínez-Catálan et al., 2004). The parautochtonous units correspond to a more distal part of the north Gondwanan continental margin. The allochtonous nappe stack is composed of three main units (i.e. Lower, Middle, Upper allochtons; Martínez-Catálan et al., 2007 and Ballèvre et al., 2014) separated by thrust faults or shear zones. Each allocthonous units has undergone its own tectonometamorphic evolution and is characterized by specific lithologies. The Lower allochtonous unit is characterized by Cambrian to Early Ordovivian mainly metaluminous granites rather than alkaline or peralkaline, surrounded by a Late Proterozoic terrigenous sequence. The Middle allochton correspond to discontinuous terranes which are characterized by oceanic affinities with some true ophiolitic units, others being interpreted as accretionary prisms terrane. Rocks of the blueschist to eclogitic facies, occurring locally, are generally overprinted. The Upper allochtonous unit derives from a Late Cambrian continental arc on the northern Gondwanan margin. Evidences of a HP-HT (granulitic to eclogitic facies) early metamorphic event are preserved in the lower part of this unit. The second and third main Variscan zones (Martínez-Catálan et al., 2007 and Ballèvre et al., 2014) correspond to autochnonous units which belonged to the proximal and distal northern gondwanan shelf, respectively. The main difference between these two zones is that one is broadly affected by Ordovcian magmatism while the others preserve a strong Cadomian imprint. The thrust belt and foredeep basin zone develop during the Middle Devonian and Carboniferous, probably on the Avalonian crust.

The internal domains outcrop discontinuously along the Iberian-Armorican, French Massif Central and Bohemian oroclines (i.e. arcs). Allochtonous and parautochonous units are mainly recognized in the Galicia-Trás-os-Montes Zone (GTMZ, Iberian Massif), in the South Armorican domain (Armorican Massif), in most of the French Massif Central (FMC) and in the southern part of the Bohemian Massif (BM). Gondwanan zones affected by Ordovician magmatism occur mostly in the southwestern part of the belt (Central Iberian Zone, CIZ; Central Armorican domain, Pyrenees, South FMC and Corsica). No equivalent is highlighted in the northeastern part. Gondwanan zones preserving a strong Cadomian imprint correspond to the Ossa Morena Zone (OMZ, Iberian Massif), the Northern Armorican Domain (Armorican Massif) and in the north of the BM. The external thrust belt and foredeep basins zone wraps around the others in the arcs from eastern BM through the Rhenish Massif and Cornwall to the South Portuguese Zone (SPZ). The second Variscan foreland thrust belt (i.e. between Gondwana and Armorica) cores the Iberian-Armorican orocline. Correlations between Iberia and the Armorican Massif (i.e. the Iberian-Armorican arc) and even up to the French Massif Central are better and better constrained and accepted by the community even if some controversies remain. Most authors agree on the correlation of the Ossa Morena Zone with the North Armorican Massif (i.e. being part of the Gondwanan margin with a strong Cadomian imprint) but some others (e.g., Franke, 2014) proposed to correlate almost all of the northern Armorican Massif (lying north of the South Armorican Shear Zone and the Nort-Sur-Erdre suture) with the CIZ. In such case, the OMZ equivalent in the Armorican Massif is almost nonexistent. Relationships between the Iberian-Armorican arc and FMC with the Bohemian Massif are still controversial. The main discussed point is the position of the Saxo-Thuringian Zone. Indeed, it has been either attributed to Gondwanan zones with Cambro-Ordovician magmatism (e.g., Martínez-Catálan et al., 2007; Franke, 2014) or Gondwanan zones with a strong Cadomian imprint (Ballèvre et al., 2014) which is like debating whether or not the Saxo-Turingian zone comprises evidences of Ordovician rifting and subduction according to the classification (e.g., magmatism, sedimentation, HP rocks). Another proposition is that both the Léon and the Saxo-Thuringian zone are intermediate blocks or microcontinents. The main difficulty to correlate the Saxo-Thuringian zone with other part of the belt resides in several key features. On the northern and western part, the Cadomian basement is widely intruded by syn- to post-tectonic Variscan granitoïds which could be correlated with

Gondwana zone with a strong Cadomian imprint. Conversely, the southeastern part is characterized by both pre and Carboniferous authochtonous and HP rocks/meta-ophiolites occurring in allochtonous nappes. Allochtonous could be correlated with internal domains but protoliths ages are younger (Kroner and Romer, 2013). Evidences of the Ordovician rifting and later subduction down to the mantle have also been highlighted in the Saxo-Thuringian zone which can led to the correlation with the Gondwanan zones affected by Cambro-Ordovician magmatism.

I.2.3. Overview of Variscan magmatism

The Variscan orogeny is accompanied by melting episodes associated with the geodynamical evolution of the belt, this results in voluminous amount of magmas. According to Faure et al. (2005), the Variscan magmatism can be divided into four major periods. The Middle/Late Devonian event is characterized by different types of magmatic rocks exhibiting a significant mantle contribution. Calkalcaline and tholeiitic affinities of plutonic (e.g. diorite, tonalite, gabbros) and volcanic/volcano-clastic rocks are markers of a magmatic arc related to subduction zone, representing the deep and shallow levels of the arc, respectively. Oceanic rocks are also formed during this event (e.g., tholeiitic and alkali basalts, dolerite) and could result from supra-subduction settings (see Ballèvre et al., 2014 and references therein). The second magmatic event is pre to Late Visean in age and corresponds to aluminous magmatism originated from partial melting of the continental crust. This melting event is generally related to crustal thickening. The Late Visean magmatic event comprises lavas flows, ignimbrites, pyroclastic, rhyolitic and dacitic dykes, hypovolcanic microgranite and granites. Geochemical signatures suggest a mantle contribution and that crustal melting resulted from a heat input from the mantle (Pin and Duthou, 1990). The Namurian-Westphalian magmatism (325-310 Ma) was a productive period for magma generation. This includes the massive production of peraluminous magmas (i.e. two micas to muscovite granites) originated from partial melting of the continental crust. Rare Metal magmatism is thought to be slightly posterior with ages ranging between Westphalien and Stephanian (e.g., Bray and Spooner, 1983; Darbyshire and Shepherd, 1985; Duthou and Pin, 1987; Cheilletz et al., 1992; Cuney et al., 1992; Cuney et al., 2002; Noronha et al., 2013; Zhang et al., 2018) which also

correspond to the age span of Sn-W mineralization. This partial melting episode has been attributed to process of lithospheric delamination at the end of the Variscan orogeny (e.g. Marignac and Cuney, 1999).

I.2.3. Distribution, ages and geochemical signature of Rare Metal Granite

RMGs are scarce and distributed across the Western Europe Variscan belt from Iberia to the Bohemian Massif (Fig. 1). The limited occurrence of these granites could be either due to the structural level of exposure and their limited size (i.e. eroded or non-outcropping RMGs) or truly to their limited number. Another explanation may be the limited effort to discover new occurrences apart from the already known RMGs. Known RMGs occur either in the internal to the most external domains of the belt.

At least four RMGs occur in the internal domains distributed in the westernmost part of the AM (i.e., Tréguennec: Chauris, 1988) and the northern part of the FMC (i.e., Mont de Blond: Raimbault, 1998; Montebras: Aubert, 1969; Raimbault et al., 1991 and Raimbault et al., 1995; Beauvoir: Aubert, 1969; GPF, 1987; Cuney et al., 1992; Raimbault et al., 1995; Chavance; Fig. 1). Rare Metal Rhyolites (RMRs) are also recognized in the FMC such as Richemont occurring close to the Blond complex (Raimbault and Burnol, 1998) or the rhyolite of Beauvoir, formerly called microgranite. Characteristics of the outstanding Beauvoir and Montebras RMGs are detailed thereafter.

Beauvoir

The Beauvoir granite, located in the FMC, east of Sillon Houiller, has been the subject of many studies over the years and was first identified as RMG in Aubert et al. (1965). This RMG is intrusive into the low grade Parautochtonous unit (i.e., micaschists, metagreywackes and quartzites) and the La Bosse W-bearing stockwork in the south and cuts the Colette two micas cordierite granite northward (Aubert, 1969; Raimbault, 1995). In this area, the parautochtonous unit form a ~NS trending antiform into the Sioule nappes. The Beauvoir granite outcrops are quite restricted but the national deep drilling program (GPF, 1987) revealed its greater extent at depth over 880m. Mineralogical, geochemical and

structural studies on drill cores (Bouchez et al., 1987; Jacquot and Gagny, 1987) allowed the recognition of three main units B1 to B3 from top to bottom indicating a multistage intrusion (i.e., at least three magma batches). Several attempts of dating have been undertaken using several alternative methods, zircon and monazite crystals being almost absent or too small. Rb-Sr whole rock analyses gives 299 ± 9 Ma and 308.3 ± 0.3 Ma for the B1 and B2 facies respectively (Duthou and Pin, 1987) while ^{40}Ar-^{39}Ar dating on lepidolite gives 307.6 ± 5 Ma and 308.3 ± 0.3 Ma (Cheilletz et al., 1992). More recently, in situ U-Pb dating on columbite-tantalite gave a much older age of 317 ± 6 Ma (Melleton et al., 2011). The Beauvoir granite is moderately to highly peraluminous depending on the facies (i.e., A/CNK B1 = 1.3-1.7; A/CNK B2 ~ 1.3 and A/CNK B3 1.1-1.3; Raimbault et al., 1995). It is characterized by high P (i.e., mainly > 1 wt% for B1 and B2), F (i.e., mostly > 1.5 wt% for B1 and B2), Li and Sn content (e.g., Aubert, 1969; Cuney et al., 1992; Raimbault, 1995) and thus belong to the Peraluminous Highly Phosphorous class of Linnen and Cuney (2005). Li is constitutive of both Li-micas and Li-phosphates from the amblygonite-montebrasite series. Sn, Nb and Ta occur in disseminated cassiterites and columbite-tantalites distributed in the whole granitic mass. Geochemical features vary from the less (B3) to the highest (B1) evolved units. Hydrothermal alteration is limited to small greisen, no hydrothermal veins have been described.

Montebras

The Montebras RMG occurs in the northern part of the FMC and belongs to the eastern *Marche* peraluminous granite complex (Belkasmi and Cuney, 1991) which is bordered by the anatexites of Boussac to the North and Lépaud to the South (Aubert, 1969). The cupola is intrusive into the Chanon biotite granite and is composed of two units: the microgranite forming the larger volume and the albite-muscovite granite wrapping around the microgranite. The Montebras granite is peraluminous (A/CNK = 1); it has been dated at 310.1 ± 1.3 Ma by ^{40}Ar-^{39}Ar on lepidolite (Cuney et al., 2002) and at 314 ± 4 Ma by U-Pb on columbite-tantalite (Melleton et al., 2011). The albite-muscovite granite has formerly been considered as a specific facies of the microgranite but Aubert et al. (1962) demonstrated the intrusive character of the contact between the two units. The microgranite is enriched in F to up to 7190 ppm and in Li up to 3400 ppm while the albite-muscovite granite is only moderately enriched (i.e., F

~2050 and Li ~1120 ppm, Aubert, 1969). On the other hand, according to analyses made by Aubert (1969) Sn is more than twice as rich in the albite-muscovite granite compared to the microganite. In more recent studies, geochemical analyses refer to the Montebras RMG without distinction between the two units. Depending on the study, the P content looks highly variable. The analyses of P in Aubert (1969) gives 0.32-0.58 and 0.18-0.34 wt% for the microgranite and the albite-muscovite granite, respectively, while more recent analyses give 1.49-1.82 wt% (i.e., Raimbault et al., 1991; Raimbault et al., 1995). Thus, depending on the study, Montebras can be either attributed to peraluminous intermediate or high phosphorous RMG (Linnen and Cuney, 2005).

Argemela

The Argemela microgranite is another outstanding example of RMG lying within the southern part of the Central Iberian Zone. This domain corresponds to the deformed sedimentary series of the north Gondwana margin with Cambro-Ordovician magmatism (Ballèvre et al., 2014). The Argemela RMG is intrusive in the Neoproterozoic to Cambrian Schist and Greywacke Complex (Fig. 1). Locally called the Beira schist, it consists of low grade metasediments (i.e. greenschist facies conditions). The granite, outcropping over a restricted area, lies south of the Serra Da Estrela granitic complex, ~13 km east of the Panasqueira W-world class mine and close to the Fundão composite granite (monzogranite to two micas granites, Ferreira et al., 1985). The intrusion has been dated at 303 ± 6 Ma (Noronha et al., 2013) using the K-Ar method on muscovite and at 326 ± 3 Ma using U-Pb on columbite-tantalite (Melleton et al., 2011). Main petrographic and geochemical features have been described in Charoy and Noronha (1991; 1996). The Argemela RMG is highly peraluminous (A/CNK 1.3-1.5; Charoy and Noronha) and show high concentration of volatiles (F), fluxing elements such as Li, P and Al and rare metals (i.e., Sn, Nb and Ta). P content is very high and can vary from 1.37 to 1.73 wt% (Charoy and Noronha, 1996) belonging to the PHP RMG of Linnen and Cuney (2005). Tin, niobium and tantalum occur mainly as disseminated cassiterite and columbite-tantalite while Li occurs either in Li-micas and Li-phosphates from the amblygonite-montebrasite series.

Krušné Hory/Ergebirge

In the Saxo-Thuringian zone and especially intruding the Krušné Hory/Ergebirge massif, two types of RMGs were recognized: the strongly and the slightly peraluminous. The Krušné Hory/Ergebirge area is a good example where many albite Li-micas granites were recognized (e.g., strongly peraluminous: Krásno and Horni Blatná; slightly peraluminous: Krupka, Seifen, Sadisdorf, Sachsenhohe-Altenberg, Hora svaté Kateřiny and Markesbach) but only little studied except for the strongly peraluminous Podlesí and the slightly peraluminous Cínovec granites. As previously discussed, the correlation of the Saxo-Thuringian zone with the other Variscan Massifs is still strongly debated; it has been either attributed to the Gonwanan zones with Cambro-Ordovician magmatism or to the Gondwanan zones with strong Cadomian imprint. According to Mingram et al. (2004 and reference therein) the Krušné Hory/Ergebirge massif is made of several thrust units (i.e., from deeper to upper structural levels: MP-MT gneiss, HP-HT Gneiss / Eclogite, HP-LT micaschists / Eclogite, garnet-phyllite and phyllite) and is often called the nappes complex referring to its allochtonous character (e.g., Kroner et al., 2007; Hofmann et al., 2009). The nappes complex structurally overlies pre-Carboniferous autochtonous units and on a Cadomian basement (Franke, 2014). The Podlesí RMG is located in the western part of the Krušné Hory/Ergebirge massif and is intrusive into the phyllite unit and into the Nejdek-Eibenstock granite. The Podlesí granite is composed of the granitic stock which peraluminous (A/CNK 1.15-1.25) and of intercalated sub-horizontal albite-zinnwaldite-topaz granite which is more enriched in Al (A/CNK 1.2-1.4; Breiter et al., 2005). The stock granite shows intermediate P content of ~0.45 wt% while dyke can show P content of 0.5-0.85 and up to 1 wt% (Breiter et al., 2005). Compared to the previously described RMGs, this RMGs is less enriched in Li and its Sn content is quite low. The geochemical characteristics of Podlesí classify it in the PIP RMGs (Linnen and Cuney, 2005). According to Förster (2001), the Podlesí stock is ~320 Ma old. The Cínovec/Zinnwald granite is located in the eastern part of the Krušné Hory/Ergebirge massif and is intrusive in the Teplice rhyolite relying on the MP-MT gneiss unit and on muscovite gneisses. The zinnwaldite granite of Cínovec is slightly peraluminous (A/CNK = 1-1.35; Breiter et al., 2017) low phosphorous (0.006-0.024 wt%; Breiter et al., 2017) and, mostly, more enriched in Nb and Li than in Sn. However, Sn is highly enriched in greisen.

Cornwall

In Cornwall, which belongs to the external thrust belt and foredeep basin domain (e.g., Ballèvre et al., 2014), several intrusions have been identified as RMGs (e.g., Nanpean stock, Hensbarrow stock, Meldon aplite, albite microgranite and the Tregonning-Godolphin granite). Granites of the St Austell district are intrusive in the St Austell biotite granite and are slightly peraluminous to metaluminous (A/CNK 1.15-0.85; Manning and Hill, 1990; Müller et al., 2006) low to intermediate phosphorous (0.06 to 0.55 wt%, Manning and Hill, 1990; Müller et al., 2006). St Austell granites are younger compared to others RMGs occurring within the Variscan belt (i.e., 260-301 Ma; Miller and Mohr, 1964; Darbyshire and Shepherd, 1985).

Main geochemical characteristics of the known RMGs seem to differ according to their location within the belt (i.e., internal domains to external most domains; Fig. 2). Most of the RMGs occurring in the French Massif Central, Armorican Massif and Portugal (e.g., Blond, Montebras, Beauvoir, Tréguennec and Argemela) are highly to intermediate phosphatic and highly peraluminous. These granites show extreme enrichment in Li and Sn, high Rb and very low Nb/Ta. Contrariwise, geochemical signature of RMGs occurring in the Bohemian Massif and in Cornwall (e.g., Podlesí, Cínovec, Tregonning and granites occurring on the St Austell) tends to lower P, Li, Sn and Rb and to higher Nb/Ta. These RMGs are also less peraluminous to metaluminous. Such geochemical trend from internal domain to external most part of the belt could be either due to real differences (e.g., variations of source rock, melting processes and temperature) or to a non-representative study of RMGs (e.g., hidden RMGs, focused studies on outstanding historical examples). The Krušné Hory/Ergebirge massif is a good example: the Podlesí and Cínovec intrusions have been extensively studied over the years while almost no recent data are available on the other know RMGs of this region (e.g., Krásno, Horni Blatná, Krupka, Seifen, Sadisdorf, Sachsenhohe-Altenberg, Hora svaté Kateřiny and Markesbach).

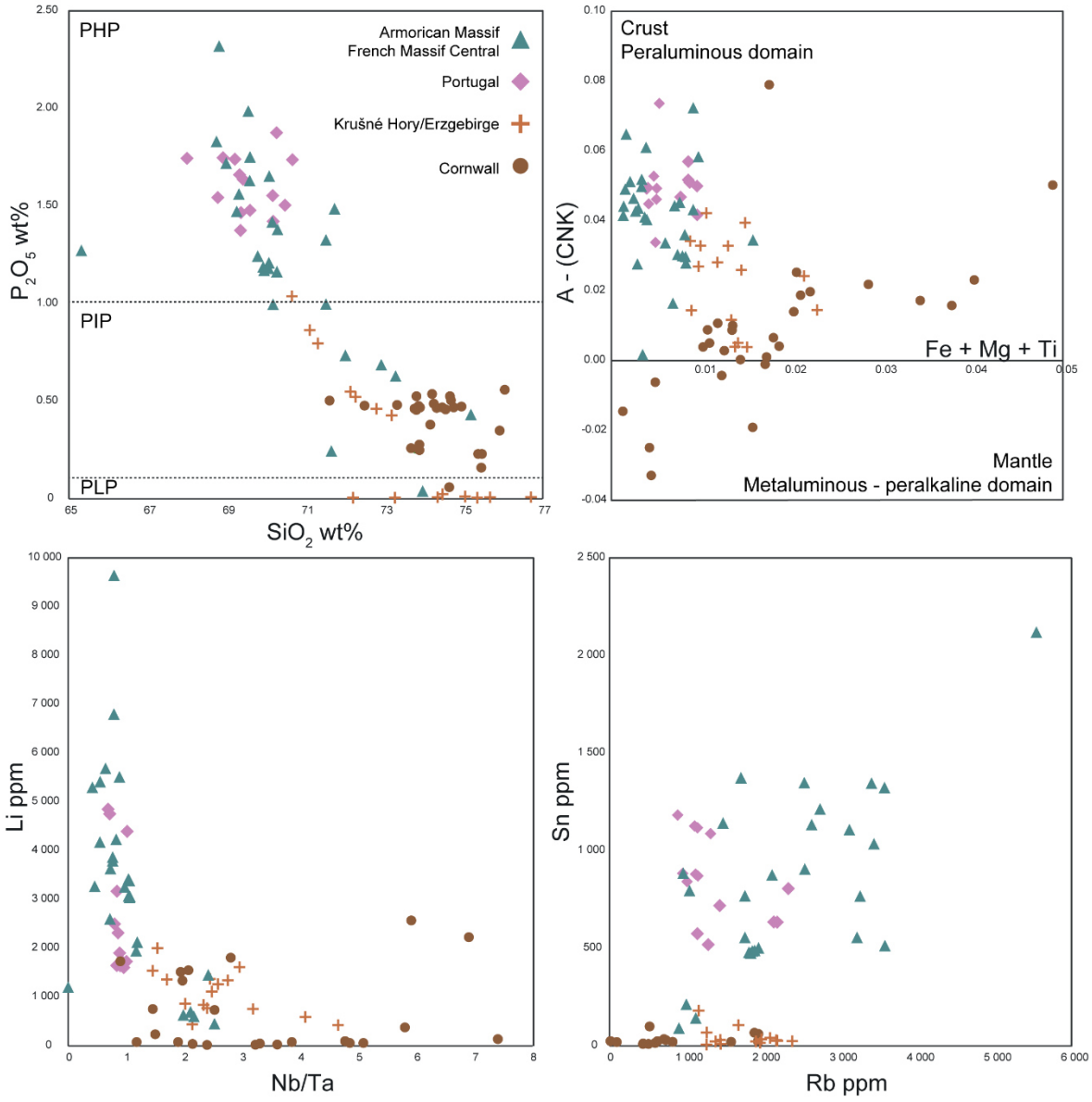

Fig 2 *Geochemical signatures of RMGs across the Western Europe Variscan belt from internal to external domains. Armorican Massif and French Massif Central: Raimbault, 1987, Chauris, 1988, Raimbault et al., 1995, Raimbault and Burnol 1998; Portugal: Charoy and Noronha, 1996 and this study; Krušné Hory/Ergebirge: Müller et al., 2002, Breiter et al., 2005, Breiter et al., 2017; Cornwall: Manning and Hill, 1990 and Müller et al., 2006*

I.3. QUESTIONS UPON THE GENESIS MODELS

I.3.1. Origin of metals: metasomatic vs magmatic

Since the 60's, the origin of metals, such as Li, Sn, W, Nb, Ta, occurring as disseminated mineralization in highly evolved granites, has been a burning topic and remains controversial. The central question was: do these granites owe their specific geochemical signature to early magmatic processes or to late subsolidus changes. On one hand, early workers (Beus et al., 1962; 1964; Beus and Zhalashkova, 1964; Zhalashkova and Sitnin, 1967; Hu et al., 1984) have emphasized the role of subsolidus metasomatic transformation (i.e., late magmatic transformation) of the granite by incompatible elements-rich hydrothermal fluids (Beus et al., 1962). This model would explain the metal occurrence zonation at the top of the pluton. On the other hand, Kovalenko et al. (1970) Kovalenko and Kovalenko (1976) and Pichavant et al. (1988) demonstrated the importance of magmatic processes for metal concentration through the study of Ongonite and Macusanite volcanic glass. The Richemont rhyolitic dyke (French Massif Central; Raimbault and Burnol, 1998) and the Beauvoir rhyolite (French Massif Central, this study), formerly identified as a microgranite, are other outstanding examples of metals concentrations having a magmatic origin. This model is also supported by melt inclusion studies on peraluminous granite and pegmatites (Webster et al., 1997; Thomas and Webster, 2000). Even if a magmatic origin for metal concentration is now widely accepted, late metal remobilization *via* circulation of hydrothermal fluids or throught late alteration is not excluded. Indeed, few RMGs are affected by late alteration mechanisms such as greisenization or kaolisation. For example, the zinnwaldite granite of Cínovec (Breiter et al., 2017) is affected by intense greisenization leading to an extreme enrichment in Li, Sn and W through element remobilization.

I.3.2. Genesis models: parental granite vs low degree melting

Considering a magmatic origin for the specific RMGs signatures and for their metal enrichment, two models confront. According to several authors, rare metal magmas are products of an extreme differentiation of a parental granitic magma (e.g., Černȳ, 1991b, Černȳ 1992a; Raimbault et al., 1995; Černȳ et al., 2005), fluxing, litophile elements and metals being partitioned in the residual melt during fractional crystallization. The parental granite model implies a direct genetic link between granite of larger size and RMGs. Rossi et al. (1988) have concluded from the study of Sn-W granites that fractional crystallization can achieve one order of magnitude of enrichment in Sn and W passing from a monzogranite to leucogranites. Raimbault (1987) suggests a similar process for rare metal magmas. Several studies on pegmatites (e.g., Jahn and Burnham, 1969; Breaks et al., 2005; Černȳ et al 2005, Roda-Robles et al., 2018), coarse-grain equivalent of RMGs, clearly invoke the *parental granite* model and thus, extreme fractionation-crystallization of a parental magma as a main mechanism for metal concentration and pegmatitic magma generation.

However, it has been noted that mechanisms of crystallization-differentiation cannot achieve such high rare metals concentration. Furthermore, spatial relationships between peraluminous granites and RMGs are not always clear even if the presence of concealed granites at depth is often invoked. Therefore, direct low degree partial melting and/or partial melting of a rare-elements rich source have been proposed as an alternative model to generate highly evolved magmas (e.g., Burt et al., 1982; Christiansen et al., 1986; Manning and Hill, 1990; Cuney, 1990; Cuney et al., 1992; Nabelek et al., 1992a; b, Simmons et al., 1995; 1996; Falster et al., 1997; 2005; Roda et al., 1999; Marignac and Cuney, 1999). Rare-element fractionation enhanced by melting mechanisms could results in rare-elements enrichment in the segregated melt. Partial melting is a main process in magma generation and leads to the redistribution of elements within the continental crust. However, behavior of rare-elements according to melting mechanisms, melting degree and protolith mineralogy and geochemistry has been only little investigated. Thereby, in order to constrain rare-element behavior during melting and the possible efficiency of melting mechanism to concentrate rare-elements, it is of growing interest to better understand the role of these mechanisms. Over the years, only few experimental studies have been

performed (e.g., Icenhower and London, 1995; Patiño Douce and Harris, 1997; Tumarkina et al., 2011; Konzett et al., 2018), however, most experiments focused on major elements behavior and only a few trace elements are considered. Furthermore, synthetic starting materials are mostly used, and melting degrees are generally higher than what could be expected for low degree melting. Theorical trace element melting models have also been performed (Harris et al., 1992: Harris and Inger, 1995 and more recently Wolf et al., 2018) but behavior of Li, Nb, Ta and W are not detailed. Performing a new experimental study would be likely, considering: (i) low degree melting; (ii) natural samples to get as close as possible to real mechanisms; (iii) the geochemistry (i.e., initial rare-elements concentration) and mineralogy of the protolith; (iv) melting mechanisms; (v) minerals involved during melting and (vi) behaviors of both major elements and metals.

I.4. MINERALIZATION

I.4.1. Mineralization within the Variscan belt

The Variscan belt of Western Europe is a renowned, well defined, metallogenic province. It is widely accepted that Li, Sn, Nb, Ta and W mineralization are spatially related to granitic intrusions and volcanic equivalent (Cuney et al. 1990; Cuney et al. 1992; Černý et al. 2005; Štemprok and Blecha 2015; Harlaux et al. 2017). Various types of mineralization occur and include disseminated, veins, greisens, skarns and breccias, among others. Disseminated mineralization are characteristic of highly evolved granites. Metals-bearing minerals such as cassiterite and columbite-tantalite occur homogeneously dispersed in the whole mass of granite bodies or stocks, as observed for example at Beauvoir (France; Cuney et al. 1992; Raimbault et al. 1995), Argemela (Portugal; Charoy and Noronha, 1996) and Cínovec (Czech Republic; Breiter et al. 2017). In vein-type mineralization which are economically the most important after W-bearing skarns, Sn- Nb- Ta- Li- W-bearing minerals occur in quartz-veins. Representative examples include Panasqueira (Portugal; e.g., Kelly and Rye 1979; Neiva 2008), Hemerdon (United Kingdom; Cameron 1951; LeBoutillier 2002), Logrosán (Spain; Chicharro et al. 2016), La Bosse (France; Aubert 1969; Harlaux et al. 2018) and W deposits from the southern part of French Massif Central (Béziat et al. 1980; Noyé and Weisbrod 1988; Demange et al. 1988; Lerouge et al. 2000; Harlaux et al. 2018). Ore-bearing vein systems can be intragranitic as observed at Cligga Head (Cornwall U.K.; Smith et al. 1996), at Cerro de San Cristóbal (Spain; Chicharro et al. 2016) and in the Jálama batholith (Spain; Llorens and Moro 2012); they can also be emplaced in country rocks at some distance from the granite body (Chicharro et al. 2016), or a combination of both. RMGs show especially Sn-Li-Nb-Ta disseminated mineralization crystallizing as a magmatic phase whitin the granite and are mostly exploited to provide ceramic raw materials. In some cases, late hydrothermal alteration occurs, such as greisenization or kaolinization, resulting in the remobilization and concentration of rare-elements. The Beauvoir granite is, for example, affected by intense kaolinization and is exploited for both kaolin and metal concentrates as by products. Also, the zinnwaldite granite of Cínovec is strongly

affected by late greisenization and rare elements are strongly enriched in the greisen zones. Apart from disseminated mineralization, RMGs can occur in close spatial association with vein-type or stockwork ore-deposits. One outstanding example is the La Bosse W-stockwork (FMC) which is intersected by the Beauvoir intrusion. However, significant Sn-W vein-type deposits are not considered as genetically linked to small intrusions such as RMGs, hydrothermal veins system related to RMGs being generally of limited importance. Nevertheless, these intrusions can show high Li content carried by Li-phosphates or Li-Micas occurring as disseminated phases in the granite or concentrated in greisens. As providing Li for new technologies becomes of primary importance, finding Li-ore-deposits such as RMGs is of growing interest in Europe.

I.4.2. Origin of W and wolframite deposition mechanisms

As emphasized above, the origin of metals associated to RMGs has been strongly controversial since decades. A magmatic origin is now widely accepted for rare element concentration including Li, Sn, Nb and Ta. Indeed, these elements occur as magmatic disseminated mineralization in RMGs either as ore-minerals (i.e., cassiterite, Li-phosphates and columbite-tantalite) or as elements incorporated in the main granite forming minerals (i.e., micas). On the other hand, the origin of W is still a matter of debate. RMGs show slight W enrichment in whole rock analyses, however, no W-minerals occur as a magmatic phase. Wolframite, which is one of the main W-ore minerals, crystallizes almost exclusively during late hydrothermal stages (Che et al., 2013). A genetic link between W and RMGs is thus difficult to demonstrate and there is still uncertainty as to whether W can be concentrated *via* magmatic processes or provided by external sources. This is part of the broader issue concerning the source of W in granite-related mineralization (Heinrich 1990; Lehmann 1990; Štemprok 1995; Marignac and Cathelineau 2009; Harlaux et al. 2018). In hydrothermal systems, source of fluids transporting and/or providing W can be diverse. Fluids can be either magmatic in origin, resulting from magma exsolution at the beginning of the magmatic-hydrothermal transition, metamorphic (i.e., fluid convection in the contact metamorphic aureole of granites), meteoric, or a complex combination of these sources (Kelly and Rye 1979; Dominy

et al 1995; Smith et al 1996; Rickers et al 2006; Lecumberri-Sanchez et al 2017). In addition to W, wolframite necessitates Fe (i.e., ferberite) and/or Mn (i.e., hübnerite) to precipitate. Variations in wolframite composition has been as controversial as the origin of W. Since the 50's, several authors focused their attention on the Mn/Fe ratio in wolframite. Deposition style, source of Mn and Fe, distance from the heat/fluid source and temperature were invoked as controlling factors governing the Mn/Fe ratio (e.g., Oelsner, 1944; Hosking and Polkinghorne, 1954; Leutwein 1952, Taylor and Hosking 1970; Moore and Howie, 1978; Amossé, 1978). More rencently, high Fe content in wolframite has been attributed to fluid/country rock interaction (e.g., Lecumberri-Sanchez et al., 2017), however, there is still no comprehensive model to explain hübnerite precipitation.

I.4.3. The magmatic-hydrothermal transition

Mechanisms at the magmatic hydrothermal transition are of major importance in granite-related mineralized systems but evaluating the relative importance of magmatic and hydrothermal processes is a difficult task. Indeed, in most natural cases, only expressions of the two *end members* are still preserved (i.e., magmatic and late hydrothermal) and expression of detailed mechanisms operating at the transition are overprinted. Furthermore, the term hydrothermal refers to several different processes involving various fluid sources (i.e., magmatic, hydrothermal, metamorphic, meteoric) and is also used in the case of late subsolidus alteration. The transition, strictly speaking (i.e., exsolution of fluids from the magma) must occur relatively late during magma crystallization but rather early in the overall cooling and consolidation of the granitic body and will control the transfer of trace elements and metals from the magma toward the fluid phase. Main constraints on the transition mechanisms comes from melt and fluid inclusion studies (Thomas et al., 2003; 2005; Rickers et al., 2006; Zajacs et al., 2008; Borisova et al., 2012; Harlaux et al., 2018) and from element zonation in minerals (Siegel et al., 2016; Kaeter et al., 2018; Monnier et al., 2018). Nevertheless, the transition from a melt- to a fluid-dominated differentiation regime is still unclear and needs further investigations.

I.5. RMG EMPLACEMENT AND GEOMETRY

Up to now, attention was focused on the specific mineralogy of RMGs and on the origin of their geochemical signature (e.g., Pichavant and Manning, 1984; Cerný et al., 1985; Raimbault et al., 1995; Charoy and Noronha, 1996; Linnen and Cuney, 2005; Breiter et al., 2017). In comparison, structural controls on RMGs emplacement, mechanical behavior and origin of specific geometries are rarely addressed. In 1984, Pichavant and Manning emphasized some of the common characteristics of RMG intrusions: (i) occurrence as small stocks or dykes, (ii) shallow emplacement levels and (iii) the small volumes of magma involved. Lack of structural and geophysical investigations on RMGs, except for some rare examples (e.g., Beauvoir, Cuney and Autran, 1987), strongly contrasts with the great number of studies on other Variscan granites. Numerous granites of various geochemical affinities and provenances along the Variscan belt have been characterized using a combination of geological, structural, magnetic susceptibility (AMS) and gravimetric approaches (e.g., Vigneresse, 1995; Vigneresse and Bouchez, 1997; Druguet and Hutton, 1998; Román-Berdiel et al., 1997; Sant'Ovaia et al., 2010). Due to their specific signature (e.g., high fluxing elements content) strongly differing with other Variscan granites, rare metal magmas are expected to have unusual low intrusion temperatures and to exhibit an anomalously fluid-like mechanical behavior. These important characteristics could possibly lead to specific emplacement mechanisms and geometries common to all RMGs. A detailed study of the structural context and emplacement mechanisms of RMGs must be undertaken, volume and geometries of RMGs being as unusual as their specific geochemical signature.

I.6. OBJECTIVES AND STRUCTURE OF THE MANUSCRIPT

The present work aims at providing an integrative study and a comprehensive understanding of RMGs. The main objectives are to apprehend the magmatic, hydrothermal and tectonic processes/mechanisms responsible for: (i) rare metal magma generation, (ii) RMGs emplacement and geometries, (iii) RMGs specific geochemical signature and metal enrichment. These different aspects are studied on the outstanding example of Argemela (CIZ, Portugal), using several approaches. In addition, an experimental study has also been performed. The manuscript is divided into 7 chapters, chapter I, being the introduction and chapter VII, the general synthesis and conclusions. Chapter II focuses on the structural context and mechanisms of emplacement of the Argemela RMG using a multiscale structural analysis with gravimetric survey and modelling. The gravimetric study has been performed as part of the Ricardo Ribeiro Master thesis (see Ribeiro, 2017). Chapter III deals with the type and emplacement mechanisms of mineralization spatially and genetically associated to Argemela along the magmatic-hydrothermal transition. Chapter IV emphasized wolframite deposition mechanisms on the example of Argemela and a comparison with other Variscan and worldwide deposits is proposed. Chapter V focuses on the mechanisms at the magmatic-hydrothermal transition and especially on fluid exsolution and metal transfer using major and trace elements mineral compositions and stable isotope data. Finally, chapter VI describes results and interpretations from the experimental study focusing on low degree melting as possible mechanism for rare metal magma generation.

CHAPTER II:

STRUCTURE AND EMPLACEMENT OF RARE-METAL GRANITES: INSIGHTS FROM AN INTEGRATED STUDY OF THE ARGEMELA GRANITE (CIZ, PORTUGAL)

ABSTRACT

Rare metal granites (RMGs) from the Variscan belt of Western Europe have been the subject of numerous mineralogical and geochemical studies but, comparatively, little attention has been placed on their mechanical behavior and emplacement mechanisms. The Argemela granite (Central Portugal) is a typical RMG showing a subvolcanic texture and high contents of fluxing elements (F, Li, P) and metals (Sn, Nb, Ta). It forms a small body intruded into low grade metamorphic rocks of the Schist and Greywacke Complex. Cleavage orientation measurements from country rocks have been analysed and interpolated to produce automatic trajectories and a picture of the finite strain linked to the granite emplacement. In particular, the existence of a pressure shadow related to the nearby Fundão pluton is evidenced by a deflection of the ~N140°E trending S1 mean cleavage. Regionally expressed ~N170°E trending dextral shear zones are superimposed on this deflection, both structures favoring magma channeling. Gravity survey and modelling reveals a pipe-like shape of the intrusion, consistent with shallow level emplacement and volcanic type processes. Our results, combining structural, geostatistical and geophysical approaches, stress the specific structural context of the Argemela granite and emphasize the particularities in RMG emplacement mechanisms.

STRUCTURE AND EMPLACEMENT OF RARE-METAL GRANITES: INSIGHTS FROM AN INTEGRATED STUDY OF THE ARGEMELA GRANITE (CIZ, PORTUGAL)

II.1. INTRODUCTION

Rare Metal Granites (RMGs, also designated as tin granites, topaz, zinnwaldite or Li-F granites) occur all along the Variscan belt of Western Europe, from Portugal to the Bohemian Massif (Cuney et al., 1992; Charoy and Noronha, 1996; Breiter et al., 1997). RMGs display highly evolved geochemical signatures marked by depletions in Ca, Fe, Ba, Sr and enrichments in Na, Rb, Cs as well as in fluxing elements (F, B, P, Li) and metals (Sn, W, Nb, Ta). RMGs are commonly, although not always, associated with Sn, W, Nb, Ta, Li mineralization of different types such as quartz veins, massive greisens and breccia pipes. In spite of their elevated bulk rock metal concentrations, RMG bodies are presently exploited mostly for ceramic raw materials (e.g., clay minerals, quartz, feldspar). In rare cases (e.g., Beauvoir, French Massif Central, FMC), Sn, Nb and Ta minerals are separated and sold as by-products. As lithium market prices are rising, there is growing interest in RMGs and for their detection, especially under cover.

Mineralogical and geochemical studies of RMGs have been numerous in the past (e.g., Pichavant and Manning, 1984; Cerný et al., 1985; Raimbault et al., 1995; Charoy and Noronha, 1996; Linnen and Cuney, 2005; Breiter et al., 2017). In comparison, much less attention has been placed on their geometry, structure and mechanical behavior during, and after, emplacement. Historically, the first information on RMGs has coming out from mining districts, mostly Cornwall and the Bohemian Massif. Pichavant and Manning (1984) stressed some common characteristics of RMG-like (tourmaline and topaz) granites such as (i) their occurrence as small stocks or dykes, (ii) their shallow emplacement levels and (iii) the small volumes of magma involved. The Beauvoir granite, an emblematic example of

RMG from north Massif Central, France, was subjected to an integrated structural and geophysical investigation during the late 80s (e.g., Cuney and Autran, 1987). Results emphasized the small volume (< 1 km^3) despite the composite nature of the granite and the steeply deeping and tongue-like aspect of the successive intrusions (Bouchez et al., 1987; Jacquot and Gagny, 1987; Cuney et al., 1992).

The near lack of structural and geophysical investigations on RMGs contrasts with the large number of studies of this type performed on other Variscan granites. Numerous granites of various geochemical affinities and provenances along the belt have been characterized using a combination of geological, structural, magnetic susceptibility (AMS) and gravimetric approaches (e.g., Vigneresse, 1995; Vigneresse and Bouchez, 1997; Druguet and Hutton, 1998; Román-Berdiel et al., 1997; Sant'Ovaia et al., 2010). Despite particularities related to magma type and local/regional context, granite shapes, geometries and volumes were found to be globally diverse (e.g., Vigneresse, 1995; Aranguren et al., 2003; Chicharro et al., 2015). Numerous granite plutons exhibit laccolithic (i.e. flat lying; Petford et al., 2000) shapes, but dyke-like or batholitic shapes (large granitic bodies corresponding to several magma batches) have been also encountered (e.g., the Cornubian batholith: Pownall et al., 2013; the Jálama batholith: Llorens and Moro, 2012). Granitic intrusions are often associated with shear zones and/or large-scale faults, i.e. magma ascent is guided by the specific regional or local structural context (Román-Berdiel et al., 1997; Weinberg et al., 2004). Geometries of granite bodies are correlated with the deformation regime (Vigneresse, 1995). For example, granites emplaced along transcurrent shear zones show typical elongated elliptical or tear shapes in map view with various obliquity angle to the shearing direction (Courrioux, 1983; Vigneresse and Brun, 1983; Tartèse et al., 2011). Extensional structures can be responsible for either dome-like (Faure and Pons, 1991) or pull apart sigmoidal geometries (Rolin et al., 2014, Ciancaleoni and Marquer, 2006), whereas magma ascent in extensional cracks produces dyke shapes (Castro, 1986; Hutton, 1988). At last, volumes of Variscan granitic plutons vary by orders of magnitude from < 1 to more than 1000 km^3 in some examples (see Vigneresse, 1988) although the largest most probably represent aggregates of several smaller individual intrusions.

Due to their high concentrations of fluxing elements, RMGs have exceptionally low crystallization temperatures (Pichavant and Manning, 1984; Burnham and Nekvasil, 1986; Pichavant et al., 1987a; Weidner and Martin, 1987) and viscosities (Holtz et al., 1993; Bartels et al., 2011; 2013).

Therefore, their parent magmas are expected to have unusually low intrusion temperatures and to exhibit an anomalously fluid like mechanical behavior, both factors potentially leading to specific emplacement mechanisms and geometries. To test this hypothesis, a detailed geological, structural and geophysical study of a representative RMG has been undertaken and is presented below. Results constrain the mechanism of emplacement and emphasize the specificities in shape, geometry and volume of the studied RMG when compared to other granites, especially those from the Variscan Belt.

The Argemela area (Central Iberian Zone, CIZ, Portugal), a Li, Sn, Nb, Ta, W mineralized district (see Chapter III for details), hosts an outstanding example of Variscan RMG, the Argemela granite (Charoy and Noronha, 1996). As part of investigations in the area, new geological and structural data have been collected on the granite and associated country rocks. A new gravimetric survey has been carried out with the objective to constrain the shape and vertical extension of the Argemela granite. Below, the geological, structural and geophysical results on the Argemela area are detailed. Focus is placed on (i) the 3D geometry of the Argemela granite intrusion, (ii) the role of the local- to regional-scale deformation regime and (iii) the identification of emplacement mechanisms. This study provides a model for RMG emplacement in the Variscan belt with potential applications in the targeting of such bodies at sub-surface conditions.

II.2. STATE OF THE ART & GEOLOGICAL SETTING

Since the 70's, highly evolved granitic rocks (e.g. RMG stocks and dykes, pegmatites) and volcanic equivalents (e.g. rhyolites, Macusanites and Ongonites) have been extensively studied (Kovalenko and Kovalenko, 1976; Pichavant and Manning, 1984; Cerný et al., 1985; Pichavant et al., 1987b; Cuney et al., 1992; Raimbault et al., 1995; Charoy and Noronha, 1996; Breiter et al., 1997; Linnen and Cuney, 2005; Breiter et al., 2017). These rocks are enriched in Sn, Nb, Ta, Rb, Cs and depleted in Ca, Fe, Sr, Ba. They can show high contents of volatiles and fluxing elements (e.g., F, B Li, P) which reduces their solidus temperature, lowers magma viscosity and favors magma ascent (Bartels et al., 2011; 2013). RMGs are present all along the Western Europe Variscan belt although their geochemical signature can be highly variable depending on their location. Unlike pegmatites (that commonly form pegmatite fields) and other Variscan granites (that locally can be numerous and with large spatial extensions), RMGs occur in limited number as isolated bodies. They are of limited size (i.e. outcropping on a surface of up to several hundred m²) and emplaced at shallow crustal levels (e.g. 1-2 km, Müller and Seltmann, 1999; Poutiainen and Scherbakova, 1998; Müller et al., 2002a). Inferred RMG geometries can vary from elongated sub-vertical (e.g. Beauvoir, Cuney et al., 1992) to dyke-like bodies (e.g. Richemont, Raimbault and Burnol, 1998, Tréguennec, Chauris, 1988) or tongue-like intrusions (e.g. Podlesí, Müller et al., 2011; Montebras, Aubert, 1969).

Development of the Paleozoic Variscan belt of Western Europe results from the convergence of two major lithospheric plates – Gondwana to the south and Laurussia to the north – (Autran and Cogné 1980; Bard et al. 1980; Matte 1986, 1991) with known (e.g. Armorica) or suspected satellite crustal blocks of rather limited extension squeezed in between. Following a recent regional-scale review made for the Ibero-Armorican arc evolution (Ballèvre et al., 2014), tectonic stages can be recognized, as follows. During Devonian – from 405 to ~370 Ma – Early Variscan Gondwana-Laurussia convergence is firstly accommodated by active margins and arcs development (e.g. Ducassou et al., 2014). Accretion of arc units to continental blocks leads to the formation of HP/HT eclogite units (Stosch and Lugmair, 1990, Ordóñez Casado et al., 2001, Roger and Matte, 2005). It follows northward to northwestward subduction of the Gondawana passive margin leading to the formation of HP/LT eclogite units (e.g.

Bosse et al., 2000). When continental subduction locked, at ~365-360 Ma, continental collision *s.s.* began with nappe stacking (Burg et al., 1987, Faure et al., 2008, Pitra et al., 2010, Paquette et al., 2017) and continental crust thickening. Syn-orogenic compressive basins formed and from ~335 Ma, while compressional deformation/thrusting propagated to the external domains of the range, internal parts underwent partial melting in the lower crust and migmatitic domes (Jones and Brown, 1990) and extensional detachments (Gapais et al., 1993) formed. It is noteworthy that felsic late Variscan magmatism look have migrated from internal to external zones of the range from 335 to 280 Ma (see compilation in Cochelin, 2016 and references therein). Late tectonic evolution, from 335 to ~290 Ma, is thus marked by coeval (i) syn-converging extension in the internal domains (Burg et al., 1994; Gapais et al., 2015), (ii) development of crustal scale transcurrent shear zones (Arthaud and Matte, 1975; Matte, 1986) and (iii) intrusion of syn-kinematics peraluminous granites (Lagarde et al., 1992; Faure, 1995; Marignac and Cuney, 1999). Examples of such syn-tectonic plutons can be found in Portugal, along the NW trending Sulco Carbonífero sinistral shear zone (Pereira et al., 1993), along the South Armorican Shear Zone (NW France; Berthé et al., 1979, Jegouzo, 1980, Tartèse et al., 2011) and along extensional shear zones (Gapais et al., 1993, Lagarde et al., 1994, Turillot et al., 2009). During this late Variscan orogenic phase, rare metal magmatism – including RMG generation – mainly occurred during the Westphalian and the Stephanian (Marignac and Cuney, 1999; e.g. 308 ± 2Ma for the Beauvoir RMG, FMC, Cheilletz et al., 1992 and 303 ± 6Ma for the Argemela RMG, CIZ, Noronha et al., 2013).

The Argemela District is part of the southern CIZ (Central Portugal) which consists in mainly autochtonous Gondwana terranes showing low grade metamorphic conditions and corresponding to external zones in the belt. These include the Schist and Greywacke Complex (SGC) of Neoproterozoïc to Cambrian age, which outcrops in the southern part of the CIZ and is intruded by numerous granites (Fig. 1; 2). This region has undergone continuous deformation during Variscan tectonic evolution with three distinct stages classically recognized (see Diez Balda et al., 1990; Ribeiro et al., 1990; Dias and Ribeiro, 1995; Martínez Poyatos et al., 2001; Ábalos et al. 2002). The main and first stage of deformation is characterized by penetrative folding of the sedimentary series and coeval development of a pervasive subvertical S1 cleavage. A subsequent D2 event consists in development of localized subhorizontal

ductile-brittle shear zones and recumbent folds; such structures are restricted to the north of the SGCD and are lacking in the Argemela area (Diez Balda et al., 1990; Ábalos et al. 2002).

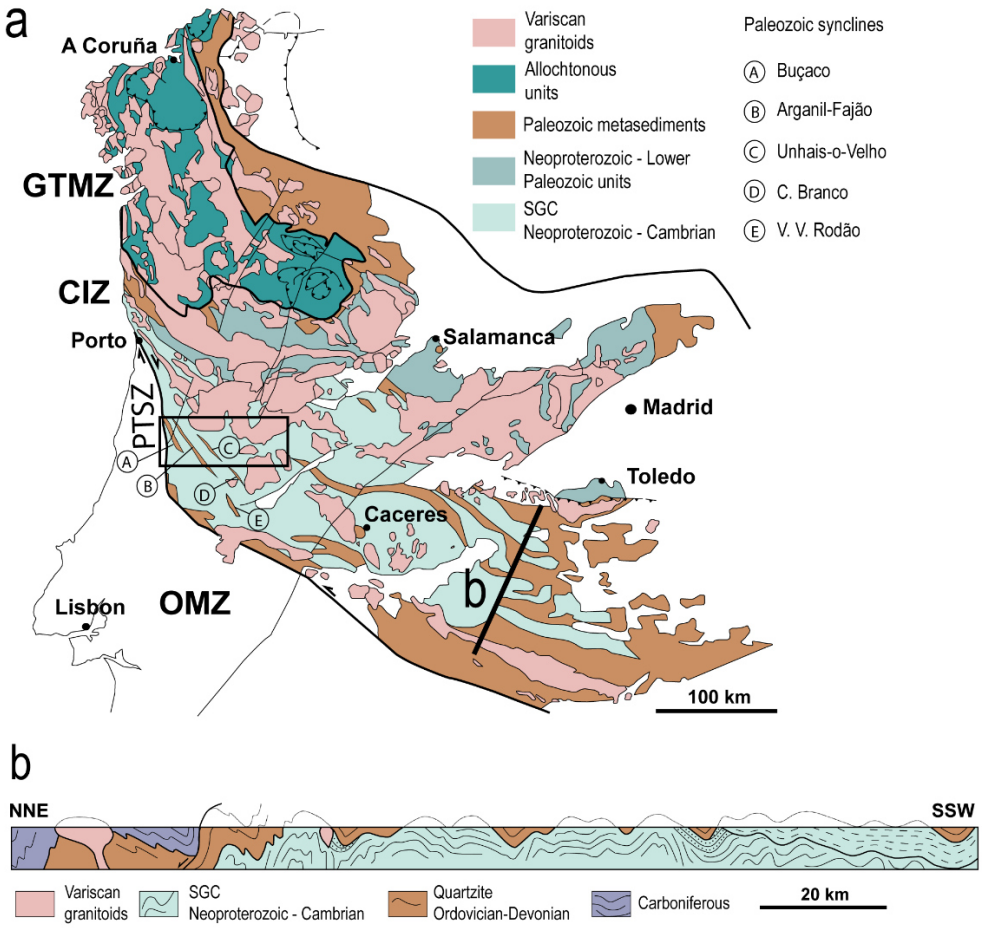

Fig 1 *(a) Geological map of the Iberian Massif showing the main geological unit of the Central Iberian Zone (CIZ) and the Galicia Trás-os-Montes Zone (GMTZ) modified after Roda-Robles et al. (2016) and (b) cross-section of the southeastern part of the CIZ modified after Martínez Poyatos et al. (2011). The black rectangle corresponds to Fig. 2a*

Subsequently, D3 deformation is marked by the development of large (pluri-km) open folds, homoaxial with those of the D1 phase (Diez Balda et al., 1990). This last stage is also marked by wrench tectonics with development of localised ENE-WSW sinistral strike slip shear zones and NW-SE (not shown on Fig. 1) to NNW-SSE dextral subvertical ones (see details in Pereira et al. 1993); such conjugate structures are consistent with a large-scale NE-SW subhorizontal shortening (Diez Balda et

al., 1990; Ribeiro et al., 1990). Whereas the succession of the different deformation stages is common to most authors, the timing of D1 deformation has been interpreted either as Upper Devonian to Lower Carboniferous (e.g. Ribeiro et al., 1990; Ábalos et al. 2002) or as Upper Carboniferous (Martinez Poyatos et al., 2001, 2011). D3 occurred during Uppermost Carboniferous to Lowermost Permian times (Ribeiro et al., 1990; Dias and Ribeiro, 1995; Martínez Poyatos et al., 2001). Finally, latest structures (Permian; Dias and Ribeiro, 1995) correspond to a conjugate system of NE-SW to NNE-SSW sinistral (Fig. 1b) and NW-SE dextral strike-slip faults associated with a N-S to NNW-SSE shortening direction (Pereira et al 1993). This late event, of rather limited deformation amount and of unknown age, is clearly not compatible with the main deformation setting observed.

The Argemela District is located ~ 13 km east from the Panasqueira world class W mine and south of the Serra de Estrela (Fig. 2a). The RMG is surrounded by rocks from the SGC which consist mostly in low grade turbiditic sediments metamorphosed in the greenschist facies. The Fundão composite granite (from monzogranite to two micas granite; Ferreira et al., 1985), ~15 km long and 10 km wide, outcrops ~1.5 km east of Argemela (Fig. 2a). East of Argemela (i.e. along the western border of the Fundão pluton), the country rocks are spotted and form an arc-shaped hill (i.e. Serra Do Gomes) while the granite is highly weathered and form a topographic depression (Fig. 2b). The Argemela District is composed of the Argemela Tin Mine (ATM) which consists of a vein swarm and the Argemela Hill Top (AHT) mainly consisting of the Argemela RMG, both systems being surrounded by the Beira schists belonging to the SGC (Fig. 2b). The Argemela RMG looks as a small (~250 m long and 125 m wide) intrusion outcropping at the top of a ~700 m high hill; it looks mostly circular in map view. Rocks forming the intrusion are typical of RMG and characterized by marked metal enrichments and a subvolcanic texture indicating a shallow emplacement level (1-2 km).

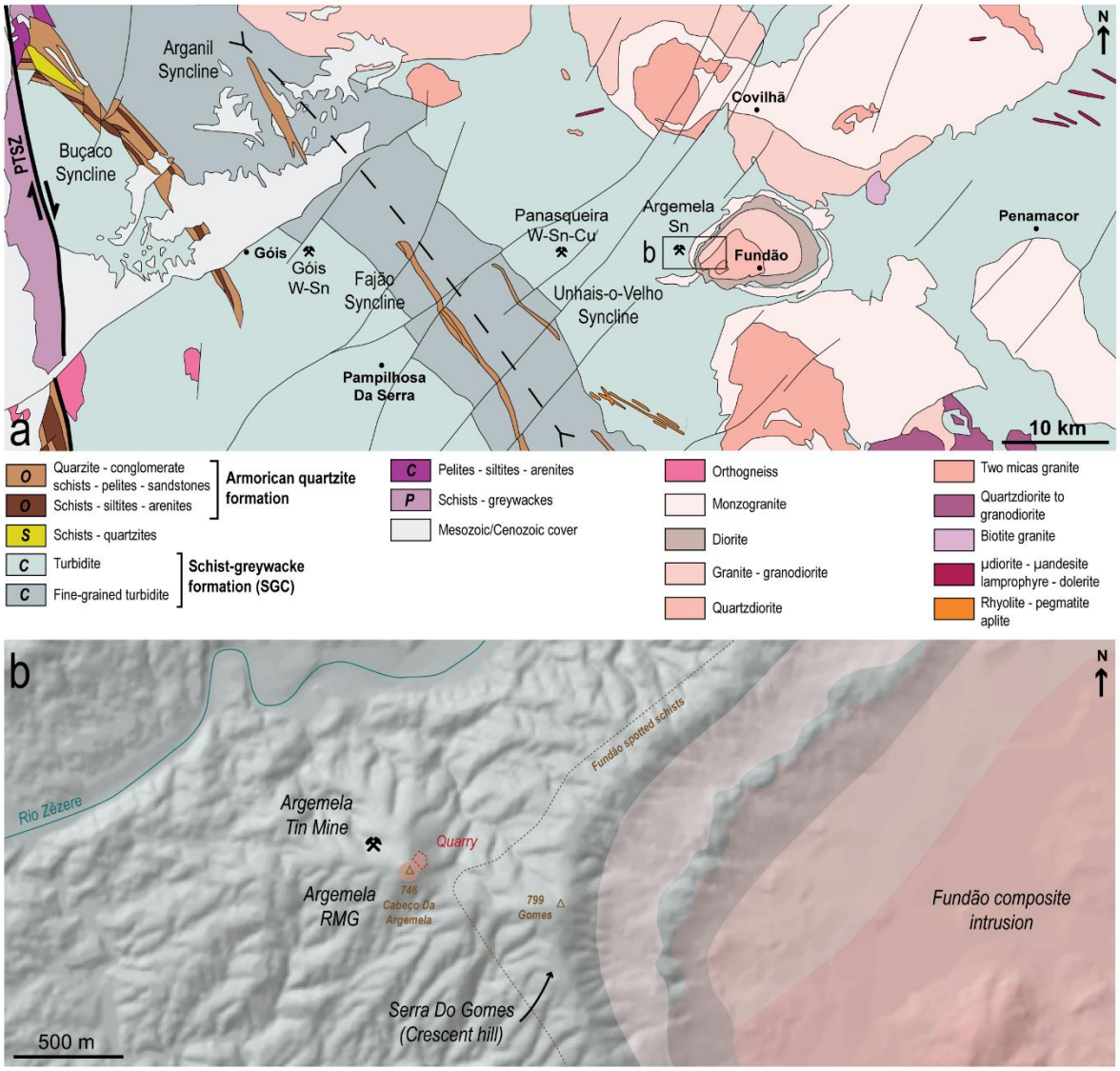

Fig 2 *Geological context of the Argemela RMG. (a) Larger scale geological map showing the location of the PTSZ, tight synclines and the Panasqueira mine; modified after the 500 000 geological map (LNEG); (b) zoom in the location of Argemela RMG, the Argemela ancient tin mine and the Serra Do Gomes*

II.3. MULTISCALE STRUCTURAL ANALYSIS

A multiscale structural analysis combining field structural analysis with geostatistical modelling is carried out in order to provide a full structural picture of the studied area. It consisted in (i) the study of outcrop scale deformation criteria, (ii) the description of macro-structures and analysis of orientation data and (iii) the interpolation of the strain field at the regional scale (i.e. distribution of deformation resulting from regional strain).

II.3.1. Structures and deformation regime

In addition to numerous syn- to post-tectonic granitic intrusions, the CIZ is made of autochthonous sedimentary units deposited along the north Gondwana passive margin; it is characterized by very low-grade (greenschists) and very stable metamorphic conditions over the entire zone (Diez Balda et al., 1990; Martinez Poyatos et al., 2001 and references therein). The southern part of the CIZ – also known as the Schist-Greywacke Complex Domain (SGCD; see Vilas & de San Jose, 1990 and references therein) – displays a remarkably monotonous succession of sedimentary units over more than 400 km long by ~150 km wide (Fig. 1a) with (i) Neoproterozoic to Cambrian series (Schist and Greywacke complex; de San Jose et al., 1990) and (ii) a continuous succession of Ordovician to Devonian siliclastic deposits (Gutierrez Marco et al., 1990). Such continuity clearly highlights a constant structural level, with very limited differential vertical movements, across this large Variscan domain. Although pre-Ordovician folding has been pointed out, deformation of this domain mainly occurred during Variscan evolution (see Diez Balda et al., 1990 and references therein). At regional scale, the most prominent structures of the SGCD (i.e. South CIZ) consist in NW to WNW trending upright folds affecting the overall sedimentary pile (Diez Balda et al., 1990, Ribeiro et al., 1990, Dias and Ribeiro 1995, Martinez Poyatos et al., 2011). At the base of this latter succession, the Lower Ordovician Armorican Sandstones – forming up to 500m of quartzitic layers – makes a continuous guide for mapping. In map view, its outlines highlight cylindrical synclines whose axial trace can sometimes be

followed over tens kilometers (Fig. 1a, b; see Diez Balda et al., 1990). As a whole, the sedimentary series displays disharmonic and symmetrical upright folds with a regional-scale sub-horizontal envelope (Fig. 1b). Besides, in contrast with the transpressive shear-zone described along the southern border of the domain (see Tomar-Badajoz-Córdoba shear zone, Romao et al., 2009), no evidence for simple shearing or cartographic en échelon structure has been described into the SGCD. Such structural features are compatible with a very homogenous pervasive horizontal shortening, at a rather high structural level in the crust, during Variscan tectonics.

Around Argemela and Panasqueira areas (Fig. 1a and Fig. 2a), four of the km-scale synclines of post-Cambrian series, trending N130-140°E, are recognized: the Buçaco, Arganil, Fajão and Unhais-o-Velho (Fig. 2a; see Meireles et al., 2013). In between, the Schist-Greywacke Complex – locally known as the Proterozoic Beira Group – exhibits well-preserved sedimentary bedding of alternating pelitic and quartzo-feldspathic lithologies, from millimeter to meter thick (Fig. 3a, b). In some outcrops, sedimentary figures are still visible and alternating laminations are of millimetric to centimetric scale (Fig. 3a). Bedding (S0) displays systematic upright similar folds (F1) of various wavelengths and interlimb angles (compare Fig. 3d and 3e). Axial-planar cleavage (S1) develops in the schists and can be measured everywhere across the Beira Group; it displays as very pervasive and is steeply dipping (Fig. 3b, d).

From the above described features, structures of the main deformation phase of the west SGCD are compatible with NE trending horizontal shortening, normal to the main belt orientation (see Diez Balda et al. 1990), in a rather pure shear regime, with subvertical principal stretching (Ribeiro et al., 1990). Even though some map-scale faults exist in the domain, the strictly horizontal envelope of the folds attests for a very homogeneous strain at regional-scale. For a large part, Variscan compression is thus accommodated by disharmonic upright folding and development of a sub-vertical cleavage across the entire study area.

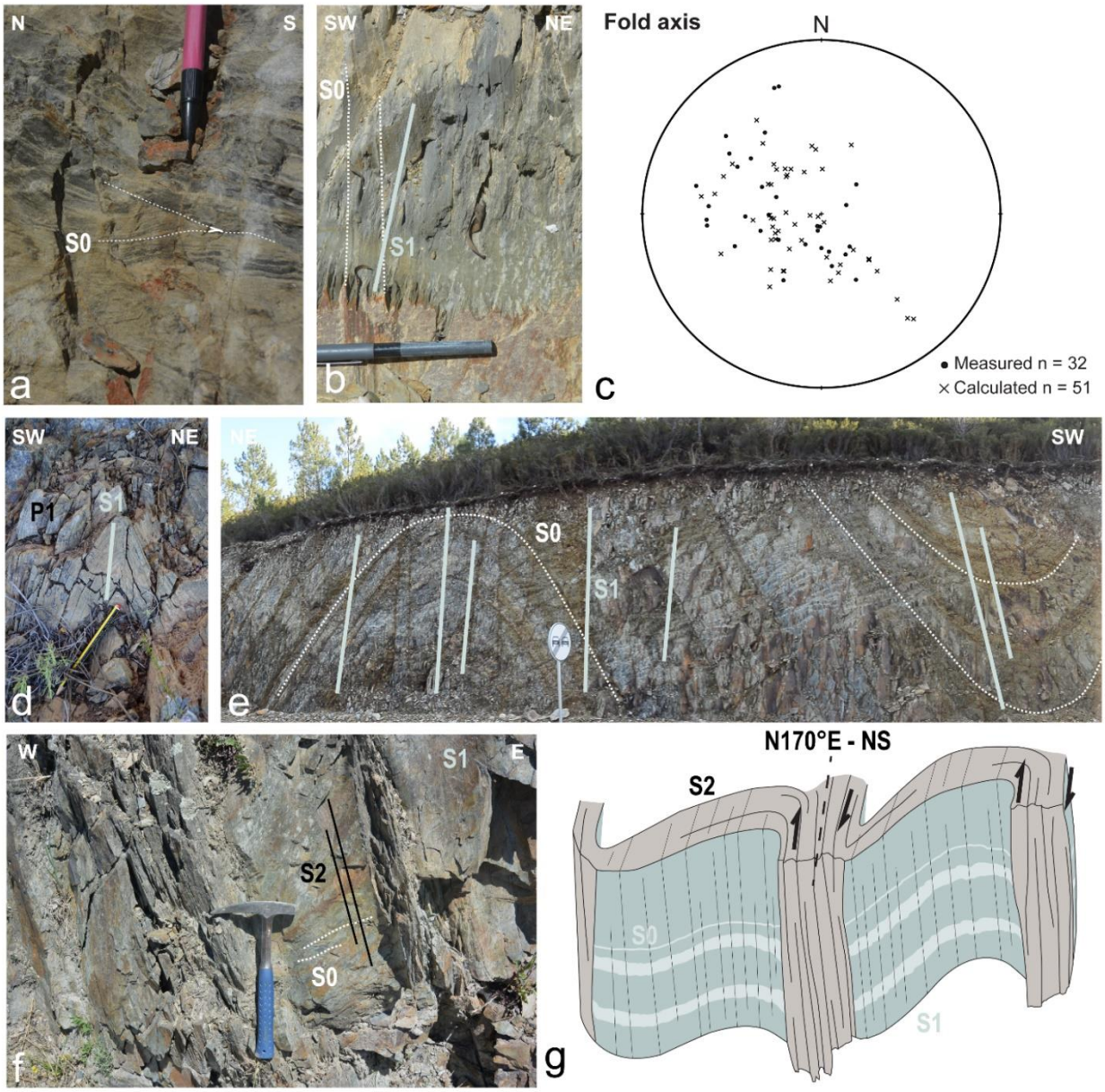

Fig 3 *Structures and deformation criterias of the studied area. (a) sedimentary bedding S0, (b) intersection between S0 and axial planar S1; (c) fold axis plot of the region; (d) pluricentimetric F1 upright fold and relation with S1; (e) plurimetric F1 upright folds and axial planar S1 intersecting folded S0; (f) F2 folds with steeply deeping axis formed in the vicinity of a N170°E-NS dextral shear corridor and local development of S2 parallel to the shear zone azimuth and (g) schema representing the main features of (f)*

In more details, a second stage of deformation can be deciphered from field structural data. Indeed, discrete N170°E to NS shear bands can be observed in some outcrops where S1 is systematically deflected on each side of those structures. Locally, such bending gives rise to secondary folds (F2) with moderate to steeply dipping axis (Fig. 3c, f) and the development of a dissolution type cleavage, oblique to the principal/pervasive S1 fabric (Fig. 3f, g). Even though no stretching lineations could have been observed in such bands, general structure and the systematic deflection sense highly suggest the development of late dextral shear bands (Fig. 3g). After the first and main stage of upright folding corresponding to shallow-dipping axes (Diez Balda et al., 1990, Ábalos et al. 2002) late simple shearing may have induced some statistical dispersion of the fold axes measured in the field or deduced from the S0/S1 intersection lines (Fig. 3c). While rather limited for Ordovician-Devonian series, such dispersion is particularly marked in pre-Ordovician formations; this may relate to the finely layered character of the pre-Ordovician turbiditic series but also to the existence of pre-Variscan folding (Diez Balda et al., 1990).

II.3.2. Statistical analysis of cleavage directions

In order to analyse spatial variations of the regional-scale strain, cleavage (S1) orientation measurements have been treated for 130 outcrops localised around Argemela, in a ~24 by 18 km wide zone (Fig. 4a). As much as can be done, some structural measurements have intentionally been distributed over the study area, but some others come from focus studies made on features of particular interest (e.g. around Argemela). As quite usual, this results in a spatially heterogeneous dataset with (i) several measurements available for a single outcrop (at a maximum ~10m distance) and/or (ii) too close outcrops for a given scale considered. When appropriate, and in order to avoid statistical overrepresentation and bias, cleavage orientation measurements have been averaged using a vectorial mean formulae adapted to circular data (see Upton and Fingleton, 1989). For the regional-scale analysis, the 43 measurements made at 12 outcrops around the AHT quarry have for instance been converted to one single data point. As a whole, 98 cleavage orientations have been extracted from the 130 outcrops in our set (see Fig. 4b).

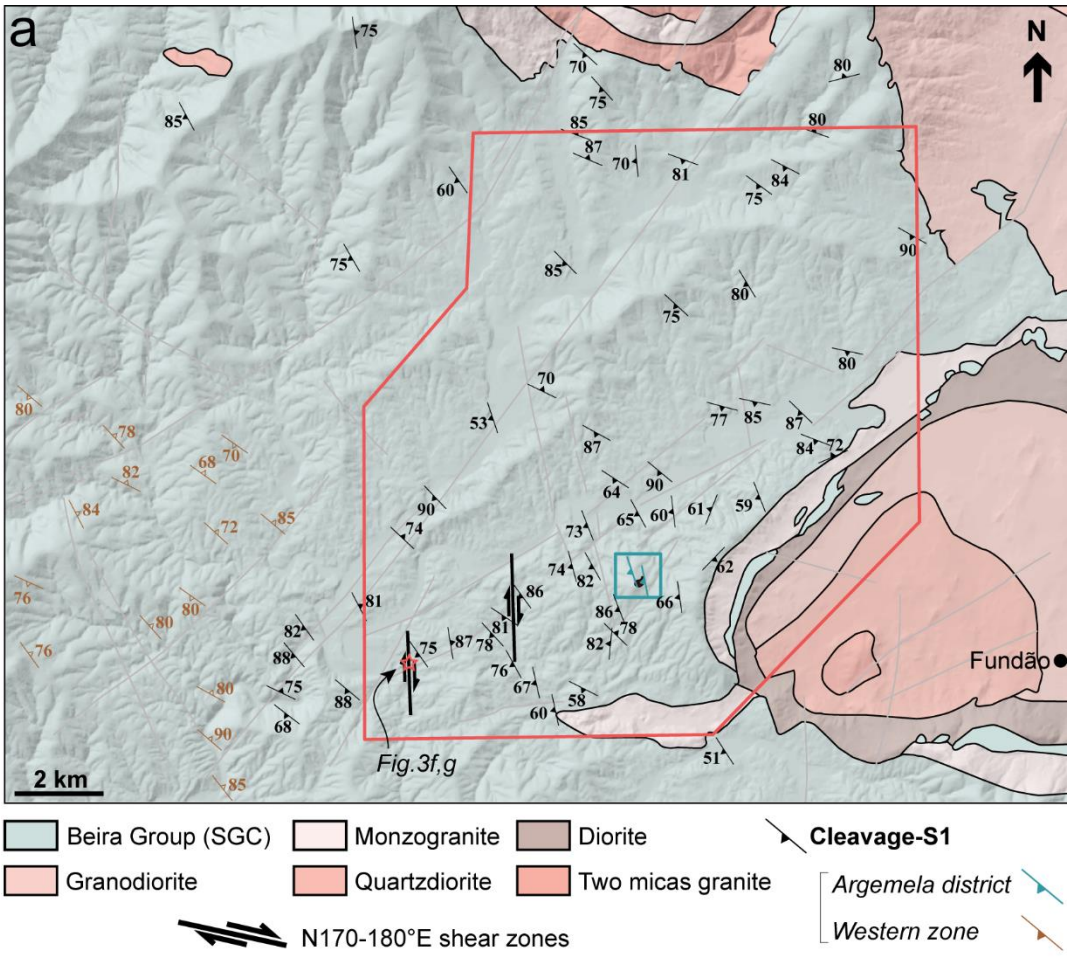
a
N
2 km
Fig.3f,g
Fundão
Beira Group (SGC)
Granodiorite
Monzogranite
Quartzdiorite
Diorite
Two micas granite
Cleavage-S1
Argemela district
Western zone
N170-180°E shear zones

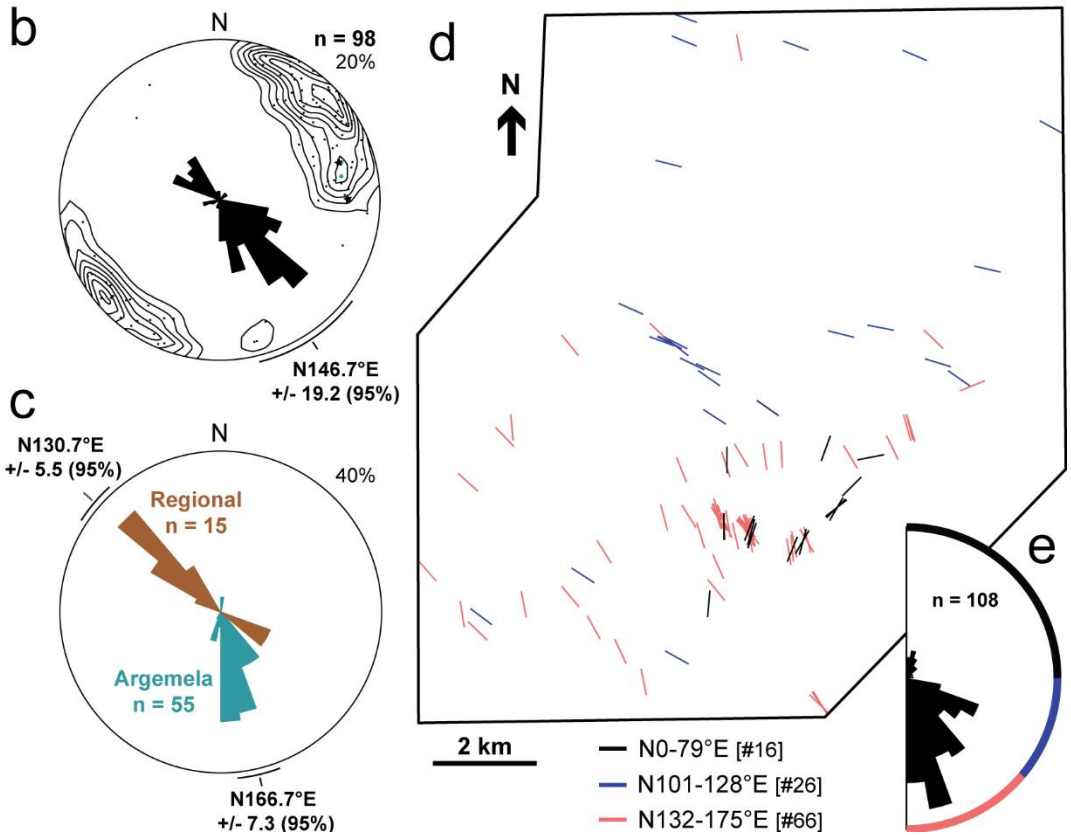
b
N
n = 98
20%
N146.7°E
+/- 19.2 (95%)
c
N
N130.7°E
+/- 5.5 (95%)
40%
Regional
n = 15
Argemela
n = 55
N166.7°E
+/- 7.3 (95%)
d
N
2 km
N0-79°E [#16]
N101-128°E [#26]
N132-175°E [#66]
e
n = 108

Fig 4 *Location of measurements and statistical analysis of cleavage directions. (a) Distribution and location of structural measurements and structures within the Argemela region; (b) stereogram and rose diagram plot of cleavage directions of the 98 data extracted from the 130 visited outcrops; (c) rose diagram plot of measurements in the Argemela are in blue and away from Argemela in brown, (d) cleveage direction data in the Argemela centered area grouped into 3 main class; (e) rose diagram plot showing the dispersion of cleavage data in each class. Map projection in Lisboa Hayford Mercator (m).*

The overall regional-scale dataset shows systematic vertical to steeply dipping cleavage planes (Fig. 4b) which is fully compatible with horizontal shortening, as described above. The study of spatial variations of the maximum shortening orientation can thus be simplified in two dimensions dealing with striking values analysis, in map view. General cleavage has an average trend of N146.7°E with significant angular dispersion, up to +/-20° (Fig. 4b). Indeed, in details, three main orientation classes can be distinguished: (i) from N100°E to N130°E, (ii) from N130°E to N150°E, which is the most represented one, and (iii) from N150°E to N trending. A plot of the cleavage measurements selected from the ATM and AHT (Fig. 4c) shows that, in this focus area (blue square area, Fig. 4a), cleavage is oblique to the average trend computed for the overall data-set. The N160-175°E average striking well corresponds to the N150-180°E class highlighted in the general rose diagram (Fig. 4b). In turn, and for comparison, cleavage striking directions measured away to the west of the Argemela District (Fig. 4a, orange symbols) display a single and prominent mode at N130-135°E (Fig. 4c). This direction corresponds to (i) the cleavage general trend described across the west SGCD (see details before) and (ii) the trend of km-scale upright folds as underlined by the map outlines of the four abovementioned synclines in post-Cambrian quartzitic series (Fig. 2a). Thereby, the N130-135°E direction can be considered as representative of the regional structural trend in the SGCD, normal to the principal maximum shortening direction. Fabric striking in the Argemela district thus looks clearly anomalous compared to the regional-scale setting (Fig. 4c).

Considering a restricted area of ~150km² centered on the Argemela District (Fig. 4a, red outline, and Fig. 4d), the resulting 108 direction values – averaged from a total of 228 initial measurements – of this zone group in distinct classes (Fig. 4e). Cleavage directions look rather scattered in this area and it

is to be noticed that, surprisingly, the N130-135°E regional trend is very poorly represented here (Fig. 4d, e). In figure 4d, measurements from three direction classes are displayed with distinct colors with (i) N0°E to N079°E directions in black line segments, (ii) directions from N101°E to N128°E (i.e. below the N130°E regional trend) in blue and (iii) directions from N0132°E to N175°E (i.e. above the N130°E regional trend) displayed as red line segments. It comes out from this map that, in the Argemela restricted area (Fig. 4a, red outline), the cleavage direction shows a clear domainal distribution (Fig. 4d) with (i) N to NE trending fabric occurring clustered along the Serra Do Gomes (crescent hill bordering the Fundão intrusion), (ii) the E to ESE striking cleavage planes restricted to the northern part of the area and (iii) the SE to S trending class (which is the more represented one) corresponding to measurements made in the southern part of the Argemela District and in the spotted schists bordering the Fundão granite. The obliquity to the regional trend of the cleavage and folds together with the peculiar spatial distribution highly suggests some deflection in the trend of the finite strain in this area.

II.3.3. Geostatistical interpolation of cleavage trajectories

Method and dataset

Analysis of strain field allows evaluating the role of localizing structures, of rheological contrasts or superimposed deformation on the structural pattern of a given area and at a given scale (see Cochelin et al., 2018). For ductile deformation, strain fields are usually evidenced *via* the drawing of cleavage trajectories considering cleavage or foliation planes as good proxies for measuring maximum shortening orientation. Trajectory maps can, thus, be drawn for domains showing vertical to steeply dipping foliation/cleavage planes. Trajectories curvature and their converging vs. parallel patterns reveal the distribution of strain gradients at map scale. While trajectory maps are traditionally extrapolated manually, leading to some possible subjective interpretations, an alternative approach consists in using geostatistics to quantitatively analyze and interpolate spatial variations of the cleavage orientation measurements (Gumiaux et al., 2003, Cochelin et al., 2018). For a given field structural geo-database, the two-step approach consists in (i) quantifying natural spatial variations and correlations between data-

point values based on the computation of experimental variograms and (ii) interpolating (Kriging) continuous variations of the cleavage trend leading to automatic trajectory maps (see Gumiaux et al. 2003 for details). From a single spatialised structural dataset, such approach allows modelling strain fields/trajectories for a given scale range (Cochelin et al., 2018).

Has described above, cleavage measurements look quite scattered in direction in the surroundings of Argemela (Fig. 4d, e). In order to better constrain finite strain spatial variations, the geostatistical approach is applied to the 228 cleavage striking values extracted from the 'restricted area' centered on the Argemela district, as described before (see red outline, Fig. 4a). Structural data is rather well dispersed in the area, but some are clustered and in particular close to the Argemela RMG (Fig. 4d). However, during Kriging interpolation, local 'averaging' of such clustered data is automatically taken into account by adjusting the *nugget effect* value (see Cochelin et al., 2018).

Variogram analysis

The experimental computed omnidirectional variogram can be fitted to a theoretical model one (see dots and continuous curve in Fig. 5a, resp.). At first, the variogram shows a non-null ordinate value at the origin (the "nugget effect") that corresponds to some possible measurements errors in the dataset or to very local orientation variations that are not relevant at the scale of the study. This latter represents only ~20% of the total variance for this dataset. Increasing values with distance highlight decreasing correlation between distant measurements and the cleavage direction can thus be considered as a regionalized variable (i.e. variations can be linked to a spatial pattern). The variogram continuously increases until a constant sill value of ~950 square degrees at a range of about 3 km (Fig. 5a). Such stationary variogram pattern highlights that the mechanism(s) controlling the strain field variations – and relative structures – has a characteristic distance of influence smaller than the study area. Kriging interpolation can thus be performed in that case with no bias. The best fitted variogram model is of *stable* type with moderate steepness of the initial variogram slope. Such feature highlights that even though the considered area is relatively small around the Argemela disctrict, the cleavage direction changes must be very smooth at that scale. It is thus unlikely that the measured cleavages may result

from the superposition of several oblique cleavage generations. Finally, when reaching the sill value, the variogram shows undulations that can either be due to a non-optimal spatial distribution of the data points (cf. “hole effect”) or to the presence of a structure inducing a certain wavelength in the strike variations (Fig. 5a). These latter have not been included in the model variogram.

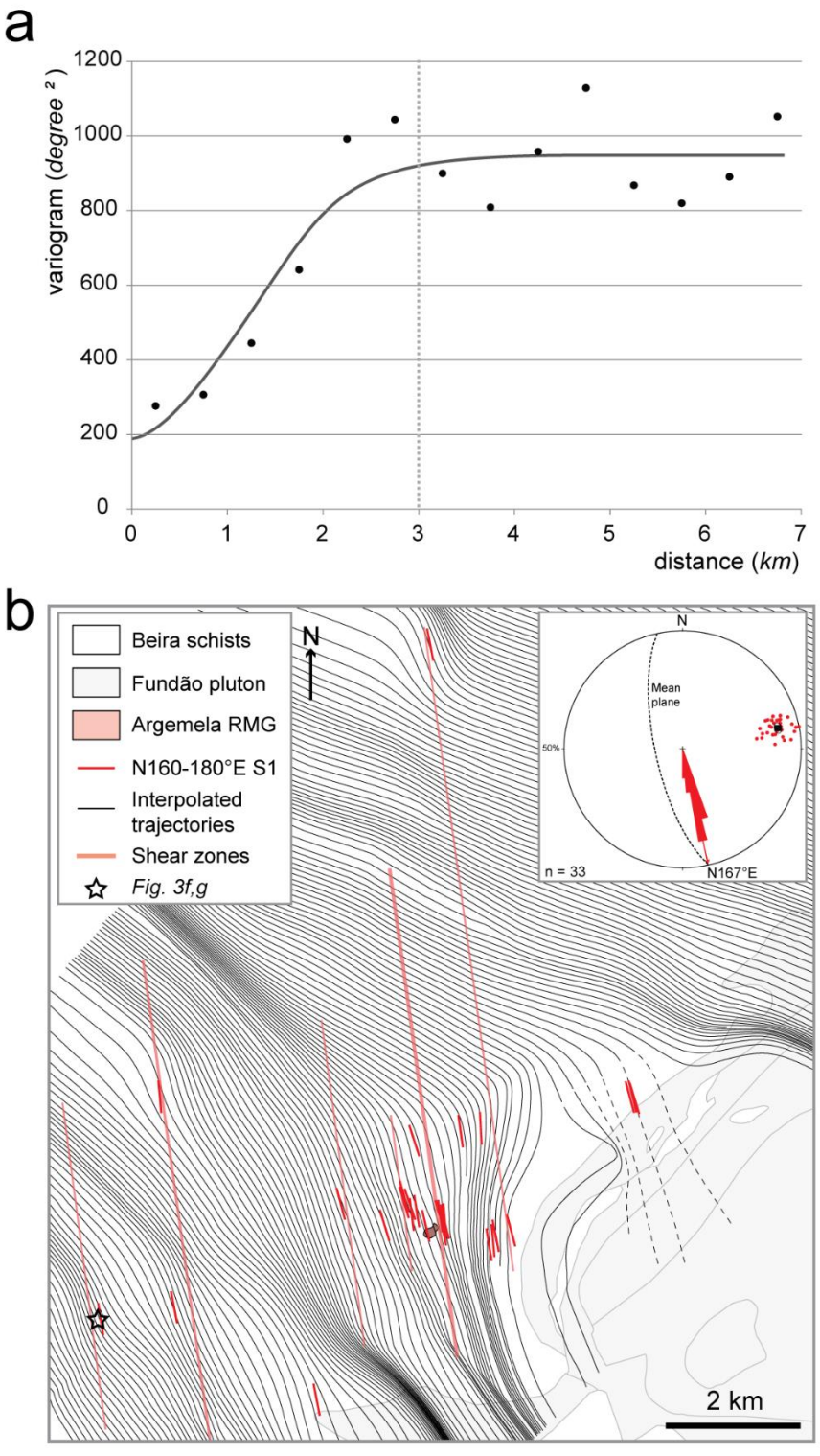

Fig 5 *Geostatistical interpolation of cleavage trajectories. (a) omnidirectional variogram and (b) cleavage trajectories map. See text for description*

Trajectory maps

From the above described variogram parameters, kriging interpolation of the cleavage directions has been undertaken (see Gumiaux et al., 2003 for details). The resulting interpolated trajectories (Fig. 5b) highlight spatial variations in cleavage/strain orientation at the scale fixed by the study area. Trajectories pattern confirms that the angle range of the dataset is rather large but not randomly distributed throughout the study area, around the Argemela district (Fig. 4a, 5b). This is fully compatible with the stationary nature of the experimental variogram (Fig. 5a). To the West, the cleavage steadily strikes ~N130-135°E, consistent with the average direction of the regional-scale maximum shortening direction (compare Fig. 2a, 4a, 4c and 5b). When approaching the Argemela district and the Serra Do Gomes (i.e. the Fundão contact aureole), cleavage trajectories are deflected. North of the hill, the S1 cleavage strikes ~N115°E while in the south it trends ~N170°E on average (Fig. 5b). As a whole, trajectories look draping and wrap around outlines of the Fundão granite, to the east. Besides, at a larger scale, trajectories display undulations and convergence forming sigmoid like structures (Fig. 5b). These latter coincide with places where high striking angles of the cleavage have been measured (Fig. 5b). Both sigmoids and cleavage data points from the N160-N180° direction class form N170°E to NS trending alignments that can be followed over several kilometers in the map (Fig. 5b); these correspond to the location of some shear bands observed in the field, as described above (see Fig. 3f, g and location in 5b). This is in particular the case within the Argemela district (Fig. 5b) where anomalous N160-175°E cleavage striking has been pointed out (Fig. 4a, blue square area and Fig. 4c). We thus infer that the study area is affected by N170°E to NS trending shear bands with deflection of the cleavage trajectories compatible with a dextral sense of shear. These look as localized, rather late structures with more than a kilometer-scale spacing (Fig. 5b).

II.4. STRUCTURE AND 3D GEOMETRY OF THE ARGEMELA GRANITE

II.4.1. Structure of the Argemela intrusion

The Argemela Rare Metal Granite is part of the AHT, within the Argemela District. The intrusion comprises two distinct facies (Fig. 6). (i) In its core, the more represented one shows a granitic to microgranitic (typically subvolcanic) texture with millimetric snowball quartz and white micas phenocrysts embedded in a fine-grained white matrix composed mainly of albite, Li-bearing phosphastes of the amblygonite-montabrasite serie and scarce K-feldspars. (ii) Along its border, alternating aplitic and pegmatitic rocks of similar composition discontinuously appear; these are particularly well exposed within the quarry exploited to date, to the NE (Fig. 6a and b). The granite (i.e., granitic and border facies confounded) is isotropic, i.e., no ductile fabric has been observed either in the field or in thin section. However, the intrusion contains a network of sub-parallel intragranitic veins which highly suggest that the granite has undergone late brittle deformation (see white line segments in Fig. 6b). In map view, the intrusion displays as a disk – 160 m in diameter – at the top of a hill with a northeast apophysis corresponding to the outline of the quarry (Fig. 6a, b). Such isotropic map shape is fully compatible with the unsheared character of the granite and, around the "disk" part (Fig. 6b), tree-like intrusive type geometries can be observed along its contacts (Fig. 6d). It is noteworthy that the hill slope is quite steep (~20-25°). As the intrusive contacts delineate the very top of the hill (Fig. 6a) with no granite outcropping below, this suggests steep intrusive contacts too (at least steeper than 20-25°).

At regional scale, the Argemela RMG owns to one of the N170-N175° striking shear bands highlighted from the structural analysis and trajectories interpolation presented here-before. In the close vicinity around the granite, the surrounding Beira schists display subvertical cleavage with a c.a. N166.7°E average striking.

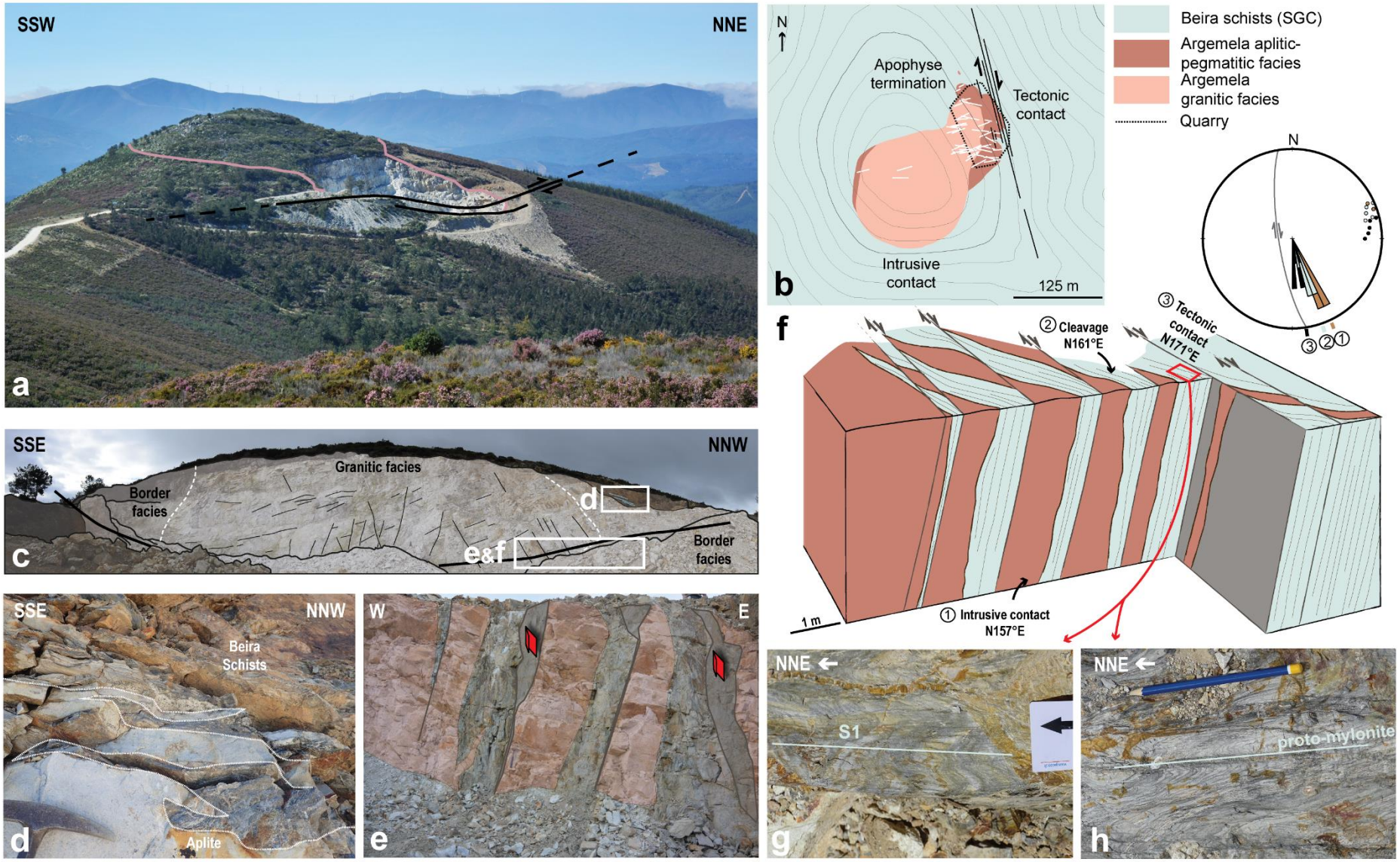
SSW
NNE
a
SSE
NNW
Granitic facies
Border facies
d
e&f
Border facies
c
SSE
NNW
Beira Schists
Aplite
d
W
E
e
N
Apophyse termination
Tectonic contact
Intrusive contact
125 m
b
Beira schists (SGC)
Argemela aplitic-pegmatitic facies
Argemela granitic facies
Quarry
N
f
② Cleavage N161°E
③ Tectonic contact N171°E
1 m
① Intrusive contact N157°E
NNE
S1
g
NNE
proto-mylonite
h

Fig 6 *Structure of the Argemela intrusion and contacts with the Beira surrounding schists. (a) photo of the Argemela RMG standing at the top of the hill, illustrating the steepness of the slopes, the steeply deeping southwesten contacts and the position of the shear zone; (b) map of the Argemela granite with location of the different type of contact; white segments are intragranitic veins; contours are every 10 m and the thick line is 700m; (c) panorama of the Argemela quarry and location of the granitic and border facies occurrences; (d) intrusive contact showing a tree-like geometry; (e) photo of the northeastern contact where the border facies is affected by a dextral shear corridor; (f) 3D block and rose diagram schematizing the main important features of the northeastern contact and showing main orientations; (g) and (f) protomylonitic to mylonitic dissolution cleavage.*

The systematic obliquity of the local-scale cleavage to its regional-scale trend is compatible with some local reorientation of the fabric during N170-175°E striking dextral shearing (see bending of the trajectories, Fig. 4b). Around the northeastern apophysis of the granite, schists are affected by protomylonitic to mylonitic dissolution cleavage occurring mostly as axial planes of tight folds (Fig. 6g, h). The contact zones itself consists in an alternation of meter-scale parallelepiped slabs of schists and granite (Fig. 6e, f). These are formed by subvertical intrusive contacts (striking ~N155°E, almost parallel to the cleavage in the schists) and by vertical shear planes, striking N171°E on average (Fig. 6e, f). Protomylonitic to mylonitic fabric and deflection of the cleavage of the schists – forming sigmoids – along C planes is compatible with dextral shearing localized along the NE apophysis of the granite. The several dextral shear planes (i.e. the shear corridor) affects only the border facies of the granite over several meters. The fact that only the border facies is affected suggests no continuation of the granite on the eastern side of the structure (Fig. 6a, b, f).

II.4.2. Gravity survey

Gravity modeling is a geophysical method which allows constraining the depth and sub-surface geometry of geological features of contrasting densities. This method is thus well adapted for imaging the structure of contacts between lithological units presenting various densities. In this study, gravity

modeling has been applied to constrain the shape, volume and vertical extension of the Argemela granite intrusion (Fig. 7). The gravity survey was conducted in the Argemela area throughout the granitic intrusion and its host rocks. Ground measurements were performed using a SCINTREX CG-5 micro-gravimeter (reading resolution of 0.001 mGal) in 43 stations spaced by 50 to 150 meters (Fig. 7a, b).

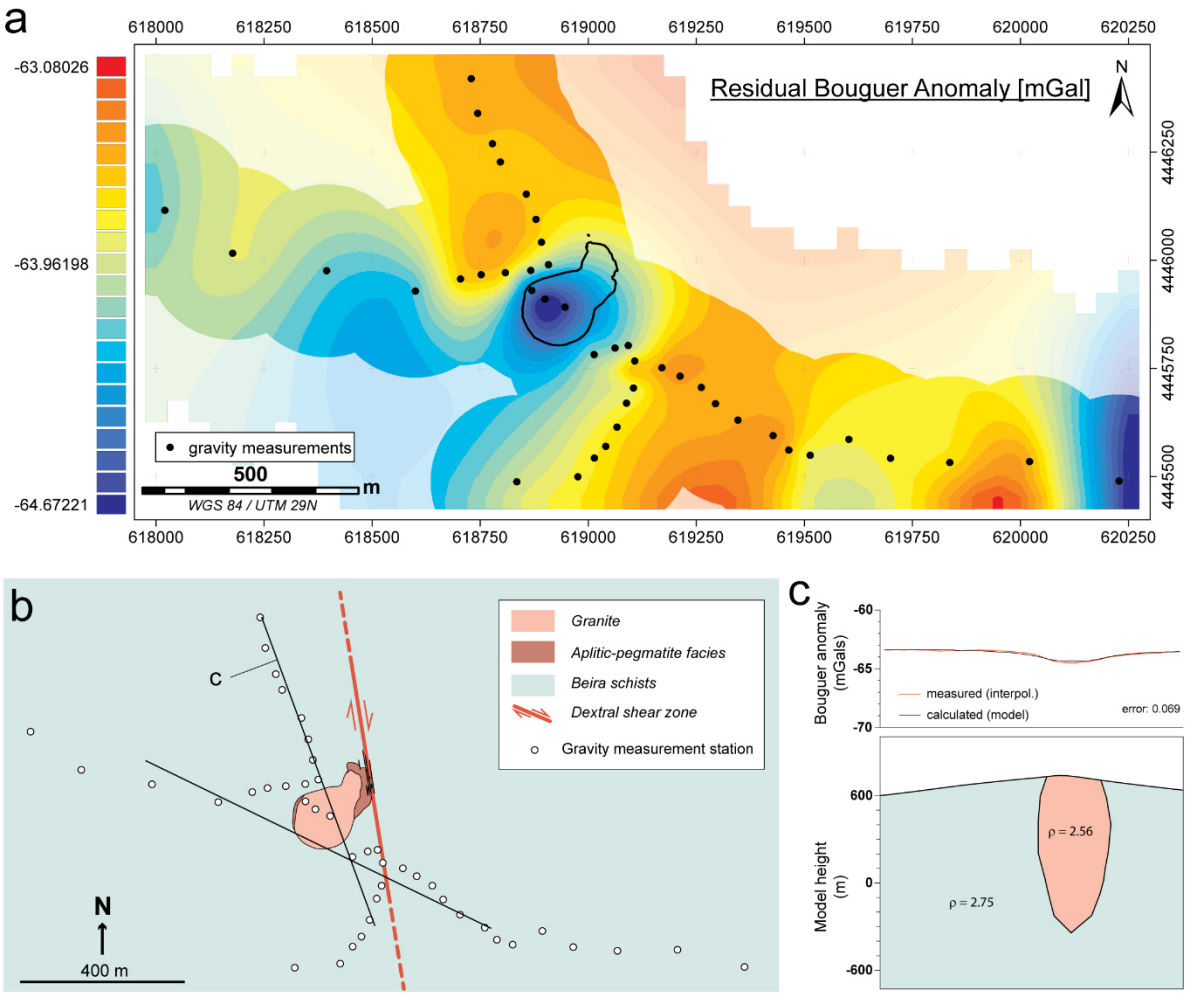

Fig 7 *(a) position of the stations spaced by 50 to 150m on the residual Bouguer anomaly map; the area of 200m around stations represent interpolated data; shaded zones represent pure extrapolation zones and should not be considered; (b) position of stations and chosen profiles for 2D modelling; (c) cross-section illustrating the best fitting shape of Argemela (i.e., showing the lowest error of 0.069)*

The measurements were distributed radially around the granite. Measurements sites have been carefully selected with hard and stable ground, for the most limited slope possible and at distance from existing tailings. Given these constraints with the local landscape configuration and accessibility the

measurement stations distribution results in roughly two profiles trending NNW-SSE and WNW-ESE across the granite (Fig. 7a). To minimize uncertainties and ensure control on the raw data, 3 ground measurements of 90 seconds each were collected at each station; for all the dataset, differences between any two of these three values are less than 5 μgal. One of the measurement stations (ETRS89: Lon. W7.601523°, Lat. N40.15382°) served as a unique base reference station to check and control the instrumental temporal drift during the entire surveying period. Determining precise location and, more particularly, elevation for each station of gravity measurements is of prime importance for a gravity survey. A differential Global Positionning System (GPS Trimble R6) was used in this study to measure the geographic coordinates and absolute elevation of each station; error on the elevation is of 0.02 m on average. Gravity anomalies were computed using the theoretical formula of g on the GRS-1967 ellipsoid. Bouguer anomaly values are computed based on standard corrections (i.e. drift, tidal, latitude, free air, plateau and terrain corrections) and on a 2.67 $g.cm^{-3}$ reference density value – corresponding to an average density value for continental crust – for reduction. Measures for inner terrain correction (up to 50m around stations) were directly made in the field using DGPS and based on Hammer charts (Hammer, 1939). Outer terrain corrections – from 50m and to 167 km away from stations – were computed numerically (see procedure in Martelet et al., 2002) based on a 20x20 meters free access DEM. To isolate the residual anomaly of the studied area, the Iberian Peninsula Bouguer Anomaly (Gómez-Ortiz et al., 2011) was subtracted to the Complete Bouguer anomaly values (see Martínez-Moreno, 2015).

II.4.3. Gravity model

From the individual point data, a continuous grid of the residual Bouguer anomaly can be interpolated using Kriging (Fig. 7b). As the regional-scale effects have been removed from the anomaly values, the residual Bouguer map highlights the density variations and contrasts in a rather close subsurface at the study scale. However, spatial distribution of the measurement stations is not optimal (see above) and while some parts of the resulting grid map are correctly interpolated, some others are instead extrapolated where data points are missing (Fig. 7b).

The residual anomalies (Fig. 7b, c) obtained after correction of the gravity data highlights an almost circular negative anomaly centered on the Argemela RMG, with a gravity low of -64.3 mGal while the surrounding schist anomaly ranges between -63.2 and -63.7 mGal. The second negative anomaly appearing east of Argemela is an extrapolation from the modeling (i.e. there are no gravity measurements in this area) and thus has probably no physical reality. The first negative anomaly fits the southwestern circular shape of the granite where it coincides with the relatively steep intrusive contacts described above. In comparison, this anomaly is less negative (~ -63.7 mGal, similar to the schist minimum anomaly) in the area of the northeastern apophyse.

In order to avoid over or misinterpretation of the Bouguer anomalies, gravity modeling is performed in this study based on the original data points along profiles (Fig. 7c). Two-dimensional gravity modeling was thus performed using the 'Geosoft-GMSYS' software (fig. 7c). The calculated modeled gravity values depend on two parameters: the density values contrast between the different geological units defined and the structure (i.e. geometry) of these geological units in depth. Here, densities were fixed, and geometry was thus the only remaining variable adjusted during the modeling process. For the Argemela RMG, a density of 2.566 g/cm^3 has been used; this results as the average from density measurements performed in lab on five granite samples. In order to minimize the effect of weathering which is particularly marked in the surrounding rocks, density of the Beira schist has been taken from measurement performed on drill cores after the drilling program (i.e., data from the LNEG, Porto); these gave a 2.75 g/cm^3 density. During modeling, the computed anomaly value is compared to the measured residual Bouguer one and adjusted by trials and errors. As several models may fit the data, further information has been used such as the precise map shape of the granite and the geometry of contacts between the granite and host rocks. Following such approach, several granite geometries have been tested to find the best fit between model and observed data. The choice was based on suspected and possible geometries for RMG, including the rootless body with feeder dykes proposed by Charoy and Noronha, (1996). The best fit model (Fig. 7c; with an error of 0.069 and 0.109 for profiles 1 and 2 respectively) corresponds to a tubular geometry centered on the circular anomaly and with an apparent maximum vertical extension of 1 km.

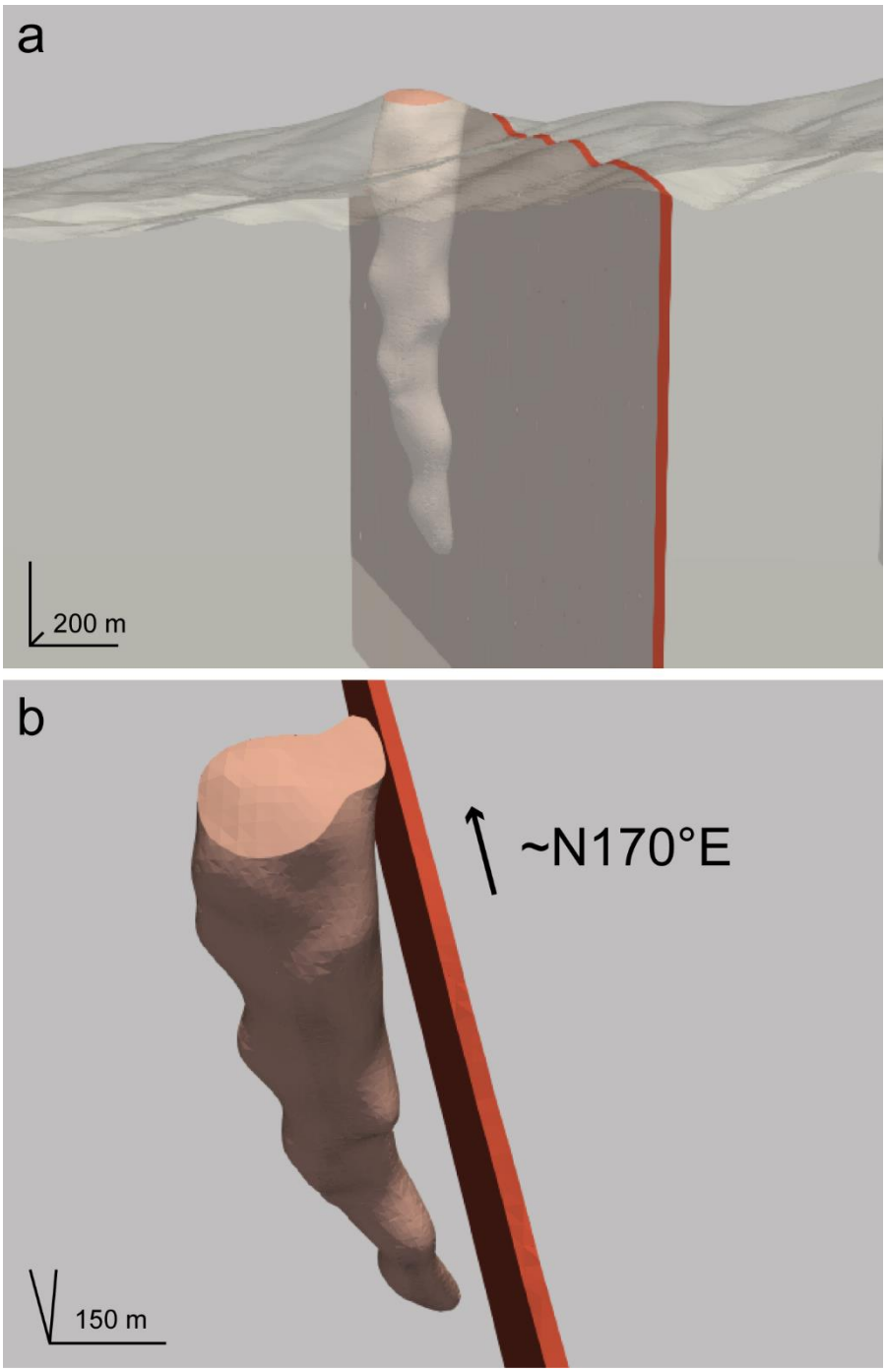

Fig 8 *Results of 3D modeling of the Argemela intrusion using the 3D Geomodeller software. See text for description*

Using the 3D Geomodeller software (Calcagno et al., 2008; Guillen et al., 2008), a 3D modeling of the Argemela RMG geometry was performed (Fig. 8) based on (i) the best fit models of the 2D gravity profiles, (ii) precise map outlines of the intrusive and tectonic external contacts of the granite, (iii) DEM available for the area and (iv) field structural measurements of the contact orientation (Fig. 7). The

computation principle consists in interpolating implicit surfaces along geological contacts based on a joint inversion of discrete contact points or lines and available orientation data in the whole 3D space (see Lajaunie et al., 1997; Calcagno et al., 2008 or Guillen et al., 2008 for details). It results in minimum curvature geological surfaces passing through corresponding individual contact points. The interpolated 3D geometry shows that the Argemela RMG is a pipe-like intrusion extending to a maximum of 1 km at depth (Fig. 8a, b). The maximum extension corresponds to the maximum depth resolution of the gravity study. The dip of the shear zone being subvertical, the Argemela intrusion is not rooted on the structure at depth. The flat apophyse in the northeastern part of the granite appears to lack continuation at depth and is interpreted as the result of shallow local magma displacement due to shearing localizing along this plane (Fig. 8).

II.5. INTERPRETATION AND DISCUSSION

II.5.1. Structural context of granite emplacement

Taken together, the field relations, multiscale structural analysis and gravity modelling results lead to a detailed picture of the structural context of emplacement of the Argemela granite. At the regional scale, the stratification S0 is affected by open to isoclinal upright folds and a penetrative axial planar S1 cleavage developped. In the western part, away from the Argemela district, cleavage strikes N130-135°E, parallel to the orientation of the large-scale isoclinal syncline of Ordovician quartzite formations located in the southwestern part of Argemela. These structures are compatible with a penetrative coaxial compression with NW-SE oriented horizontal shortening, as presented in previous studies. In the eastern part, variogram analysis of measured cleavage directions highlights regional-scale variations and heterogeneous shear; the resulting interpolated trajectories well display a fan like map pattern (Fig. 9). Indeed, the strain field is affected by the large Fundão intrusion and associated hornfels, leading to the formation of a map scale pressure shadow and rather scattered cleavage orientation in this peculiar area (Fig. 9). It is then evidenced that the Argemela RMG precisely emplaced within this regional scale pressure shadow. In several outcrops, the strain migrates to become localized along dextral ~ N170-NS°E shear corridors and a secondary cleavage sometimes develops as axial-planar fabric of steeply dipping folds superposed on early developed upright ones. The Argemela district is precisely located in such ~N170-180°E striking band and affected by dextral simple shearing: although no secondary cleavage appears in the zone, the cleavage observed corresponding either to the pre-existing cleavage deflected during shearing or to a newly-formed feature, alternatively. Strain field calculations show that a ~N162°E direction is easy to form *via* passive reorientation of a pre-existing cleavage during shearing. Furthermore, the absence of S2 in this area strengthens the former interpretation. Thus, the reorientation of cleavage in the Argemela District is interpreted to result from dextral N170°E-NS shearing which is consistent with NE-SW principal shortening and subhorizontal maximum stretching direction. Cleavage trajectories show undulation anisotropies that are also

compatible with the presence of ~N170°E-NS shear bands dispersed in the western part of the study area (Fig. 4).

Additional information on the local structural environment is provided by the Argemela intrusion. Its south, west and northwest part is circular in map view. Contacts with country rocks are intrusive and the granite is isotropic. Conversely, the eastern and northeastern border contacts are tectonic, being controlled by locally dominant N170°E-NS subvertical planes. Imbrication of parallelepiped slabs of schist and granite together with the late bending of the main cleavage forming sigmoids indicate a dextral sense of shear. The relatively flat contacts in the northeastern part are local features and the structural data suggest that the northeastern granite apophyse extends neither very far nor very deep, in agreement with the 3D modeling results. The presence of the border facies all along the sheared granite rim indicates that no part of the intrusion may have been shifted vertically. This is consistent with the absence of ductile deformation criteria in the granite along the shear. Thus, either the granite has undergone only brittle deformation or granite cooling was too fast for ductile deformation to be recorded. To summarize, the northeastern part of the granite clearly reveals the influence of the ~N170-NS striking shear corridor. However, its influence appears restricted to the granite apophyse and does not extend further west within the granite.

Overall, the data highlight the specific structural environment controlling the emplacement of the Argemela RMG and a synthetic 3D block has been drawn (see Fig. 9). The intrusion was emplaced within a large-scale pressure shadow where the local stress field might have been lowered during the entire regional-scale Variscan deformation, thus promoting magma channeling (Fig. 9). Indeed, a pressure shadow can facilitate fluid channeling as illustrated for example by the Príncipe Gold Deposit, Central Brazil (Siqueira Corrêa et al., 2015). There, the Príncipe Granite acted as an obstacle for hydrothermalism and deformation, producing two pressure shadows that acted as stress release zones and structural traps for the ore, concentrating the hydrothermal fluids (Siqueira Corrêa et al., 2015). The occurrence of stress release zones has apparently not been formally invoked for magma channeling, although other rare-metal granite systems have geometries and field relations similar to the Argemela-Fundão pair (e.g., Beauvoir-Colettes, Cuney and Autran, 1987). It is also possible that such stress release

zones have the greatest channeling efficiency when highly fluid media (either hydrothermal solutions or low viscosity melts) are involved, as expected at Argemela.

While the regional structural pattern seems to be controlled by the D1 deformational event (Ábalos et al. 2002) involving NE-SW shortening and subvertical stretching, the Argemela intrusion looks controlled by a subvertical ~N170°E dextral shear zone compatible with NE-SW shortening and subhorizontal stretching (Fig. 9). Additionally, the area hosts several N170°E-NS shear planes acting to reorient the pre-existing S1. Their striking direction and sense of shear are similar to the PTSZ westward, chronologically related to the late deformation event in the CIZ (Ábalos et al. 2002 and references therein). Other similar shear zones are well described in the southeastern part of the CIZ (e.g., Martínez Poyatos et al., 2011). These structures are interpreted as part of the D3 event (i.e., post S1) enhancing S1 cleavage reorientation. Thus, all these N170°E-NS structures may have been coeval and those observed at Argemela could be smaller scale distributed "replicas" of the plurikilometric scale PTSZ (see also Ribeiro et al., 1990).

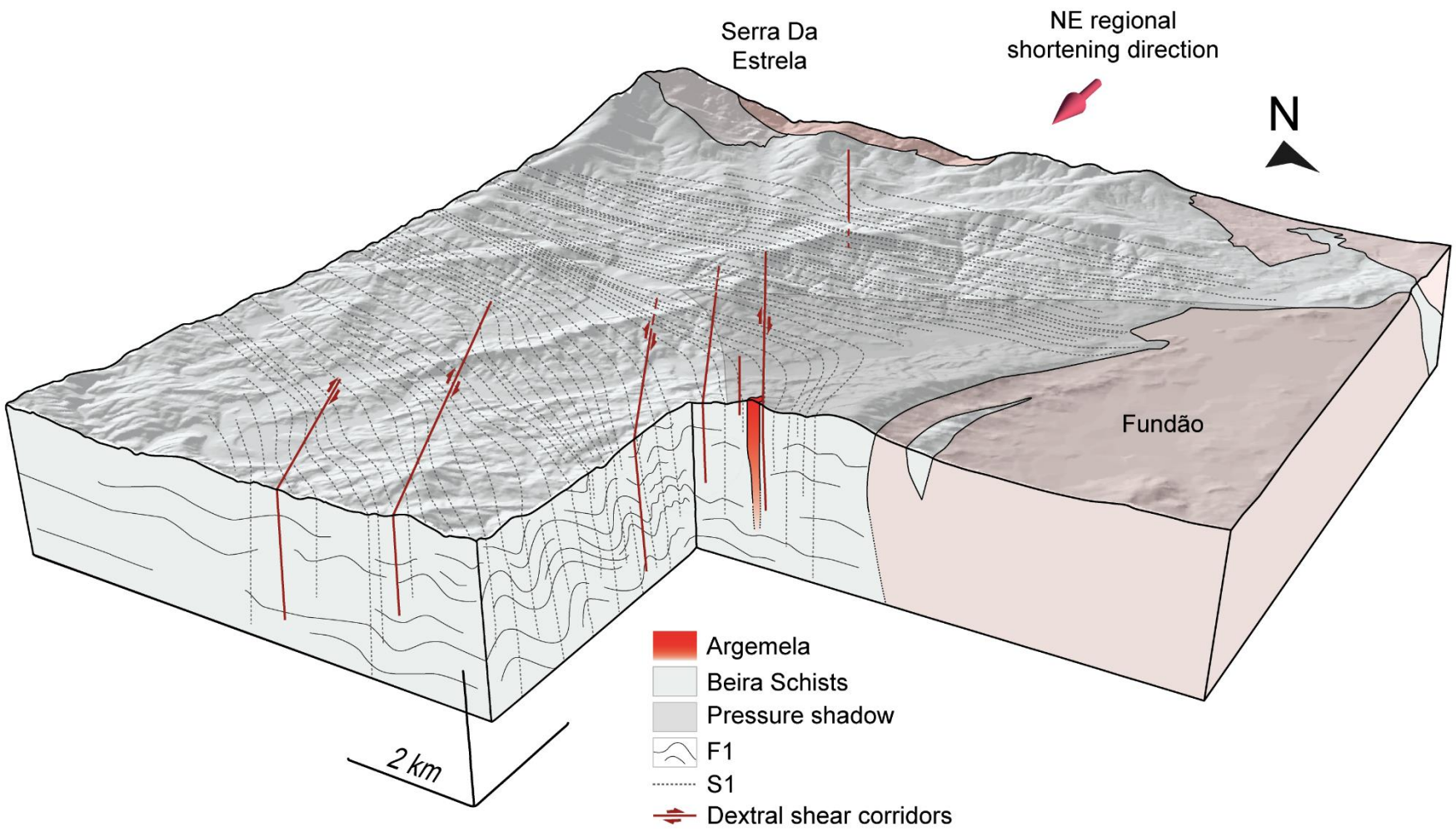
Serra Da
Estrela
NE regional
shortening direction
N
Fundão
2 km
Argemela
Beira Schists
Pressure shadow
F1
S1
Dextral shear corridors

Fig 9 *Synthetic 3D block stressing the special structural context of emplacement of the Argemela RMG and illustrating its unusual geometry*

II.5.2. Geometry of Argemela

The geometry of the Argemela granite is precisely constrained by the coupling of gravity measurements with field structural mapping. The resulting interpolated 3D model highlights a subvertical pipe-like structure for the Argemela granite intrusion, centered on the granite in map view (Fig. 8 and 9). They also emphasize the absence of continuation at depth of the northeastern granite apophyse. The remarkable 3D geometry inferred is consistent with field relations, in particular with the respective orientations of the intrusive contacts (in the south, west and north parts) and the topography which clearly rule out laccolithic or dyke-like geometries for the intrusion. Our gravity results establish the vertical continuity of the granite body at depths up to 1 km which excludes the near-surface bubble-like shape proposed by Charoy and Noronha (1996) for the Argemela granite. The 1 km value correspond to maximum depth resolution of the gravity surveying for the chosen scale. This means that deeper continuation is possible. Thus, even if the Argemela RMG forms an intrusion of restricted size in map view, it has a large extension at depth. It is also worth stressing that the pipe is not rooted on the subvertical shear zone which affects only the subsurface northeastern border of the granite, resulting in a quite flat pancake-like apophyse. Even though Argemela RMG clearly owns to one of the particular N170-NS°E trending shear zones highlighted in the area, the structural/gravimetric modelling suggests that the shear plane itself does not control magma channeling during ascent in the surrounding schists (Paterson and Schmidt, 1999; Vigneresse, 2004); only the near-surface geometry of the granite during late stages of emplacement is affected.

II.5.3. Comparison with other RMGs

Since little attention has been paid on RMGs emplacement mechanisms and shapes, it is difficult to compare Argemela with other RMGs. However, several geometrical characteristics of Variscan

RMGs are similar to the Argemela granite such as, for example, the predominance of near vertical structures and the lack or minor importance of horizontal flow during magma emplacement. This is illustrated by the Beauvoir granite taken as a whole (i.e., the 3 successive intrusions being considered together) which shows a subvertical tubular shape that extends up to at least 0.7 km (Cuney and Autran, 1987; Cuney et al., 1992). Further, the surface expression of the Beauvoir granite does not reflect its vertical extension, and both intrusions, Beauvoir and Argemela, also have quite small volumes. Jacquot and Gagny (1987) proposed a mechanism of cauldron subsidence for the Beauvoir granite (see Myers, 1975; Burchardt et al., 2012, for applications to shallow magma emplacement outside the Variscan belt) but the structural data allow their model to be ruled out in the case of Argemela. The Podlesí stock (Bohemian Massif) is a small elliptical intrusion in map view (i.e. 250 x 400 m; Müller et al., 2011) with a geometry only constrained from drillings. The published cross-section highlights the tubular geometry of the stock tilted to the north (Breiter et al., 2007; Müller et al., 2011). No subhorizontal flow direction is observed. Both the Richemont rhyolite (Raimbault and Burnol, 1998) and the Tréguennec aplite, representing rare sub-volcanic equivalents of RMGs, occur as dykes, which also implies essentially vertical magmatic flows. The Montebras and Cínovec RMGs are both roughly tongue-like intrusions (Aubert, 1969; Breiter et al., 2017). Their geometries are consistent with emplacement in weak zones (between two other granitic units) but strictly horizontal flow directions as observed in case of laccoliths are apparently lacking. Overall, vertical magma channeling, with limited subhorizontal flow, might be a characteristic common to most RMGs suggesting similar behavior of rare metal magmas. Such 3D geometry is consistent with shallow level of emplacement inferred for RMGs (i.e., 1-2 km at the maximum).

II.5.4. Implications for granitic-magma ascent mechanisms

The 3D geometry of Argemela, which indicates only an upward rise of the magma, is quite unusual and differs from other large granitic intrusions of the Variscan belt. Most granites occur as flat laccoliths or batholiths (Vigneresse and Bouchez, 1997; Petford et al., 2000; Vigneresse, 2007) and

show one to several subvertical roots, relics of feeding zones. Such felsic intrusions record an important vertical flow component. For example, the St Sylvestre Massif (Limousin, FMC) is a composite Variscan leucogranite with an overall laccolithic shape. Granite emplacement results from the transition between upward magma channeling and horizontal flow (Petford et al., 2000). Numerous mechanisms have been invoked to explain the transition between vertical and horizontal flow including neutral buoyancy, contrast of temperature and rheological changes (Ramsay and Huber, 1983; Vigneresse, 2004 and references therein). The Argemela RMG doesn't show such horizontal flow except for the little apophyse on the northeastern part. It is difficult to evaluate the relative importance of mechanisms responsible for the tubular geometry of Argemela. A horizontal rheological barrier (i.e. not evidenced from the field study) is unlikely in this case but the temperature contrast between the crustal magma and the greenschist facies Beira schists can have play a role to stop the magma ascent. The volume of magma may also be an important factor controlling the 3D geometry of intrusions. Laccolithic and batholitic intrusions result from several significant batches of magma involving final estimated volumes of 200 - 5000 km^3 (e.g. 1000-1500 km^3 for the Saint-Sylvestre Complex, FMC; Vigneresse, 1995) and >10 000 km^3, respectively (Vigneresse, 1999; Petford et al., 2000; Vigneresse, 2004). In comparison, the Argemela RMG estimated volume (considering a cylinder of 150 x 900 m) is <0.02 km^3. RMGs also result from several batches but the volume of magma may not be sufficient to induce subhorizontal flow. Indeed, the Beauvoir RMG as a whole (FMC; Cuney et al., 1992) is made of at least 3 intrusions and has an estimated volume of ~0.1 to 0.2 km^3 considering map and cross section extension (i.e. 500 x 300 x 900 m). The volume is greater than the estimated volume for Argemela but is still in the range of "small" volumes. Relatively small volumes are also highlighted for less evolved units such as the Chateauponsac peraluminous units, intrusive in the Brâme granite (St Sylvestre granitic complex). These intrusions show an important subvertical extension of ~2km at depth (Audrain, 1989) as well as limited horizontal flows in map view compared to the St Sylvestre laccolith. For such small amount of magma, crystallization should be quick compared to larger intrusions. The magma may begin to crystallize when reaching a sufficient contrast of temperature and when it is still rising in vertical path. Another hypothesis to inhibit subhorizontal flows is that the ascending magma never reached the neutral buoyancy and thus continued to rise upward. Thus, density of the magma would be of importance.

However, density and viscosity are influenced by the same parameters. It has been proposed that RMGs and pegmatites viscosity is low (Charoy and Noronha, 1996; Thomas et al., 2005; Bartels et al., 2013; Breiter et al., 2017) due to the presence of fluxing elements and volatiles but calculations are only based on estimated temperature and H_2O content (i.e. temperature and H_2O content are unknown parameters). Thus, it is difficult to constrain the viscosity of such evolved granite and thus the density. Also, evaluate the role of these two parameters on 3D geometry of an intrusion remain difficult even if it is likely that low viscosity enhances upward flow to subvolcanic level classical inferred to RMGs.

Overall, Argemela is an original example of RMG which was emplaced in a large-scale pressure shadow which promoted vertical magma channeling during magma ascent to subvolcanic level. To this special context is superimposed a ~N170°E-NS dextral shear zone that influence the geometry of the intrusion during the final stages of emplacement. The original pipe-like geometry may result from a combination of mechanisms. When ascending vertically within the pressure shadow, the magma could have never reached the neutral buoyancy and began to crystallize due to temperature contrast with the host rocks. These parameters together with the little volume of magma may have inhibited subhorizontal flows.

II.7. CONCLUSION

Our detailed multiscale field structural analysis combined with gravity modelling allows highlighting mechanisms responsible for Argemela emplacement. Argemela is an original example of RMG which was emplaced in a large-scale pressure shadow which promoted vertical magma channeling during magma ascent to subvolcanic level. To this special context is superimposed a ~N170-NS dextral shear zone that influence the geometry of the intrusion during the final stages of emplacement. Branching of shear zones on larger and more localized structures of the basement, at depth, is though possible and could have promoted magma channeling in the first place. The original pipe-like geometry may result from a combination of mechanisms. When ascending vertically within the pressure shadow, the magma could have

never reached the neutral buoyancy and began to crystallize due to temperature contrast with the host rocks. These parameters together with the little volume of magma may have inhibited subhorizontal flows. The restricted size of outcropping RMG does not reflect their vertical extension. Overall, our study gives new insights on emplacement mechanisms for RMGs on the original example of Argemela and emphasizes the importance of multiscale structural study coupled with gravity modelling.

CHAPTER III:

FROM MAGMATIC TO HYDROTHERMAL SN-LI-NB-TA-W MINERALIZATION: THE ARGEMELA DISTRICT (PORTUGAL)

ABSTRACT

The Argemela district, central Portugal, exhibits an almost complete sequence of magmatic to hydrothermal ore-forming sequence typical of the Variscan metallogenic province. Disseminated and vein-type mineralizations are distributed in two systems, the Argemela tin mine (ATM) and the Argemela hill top (AHT). Disseminated mineralization include Li- and P-, Sn-, Nb- and Ta-bearing phases dispersed in rare metal granites. Vein-type mineralizations occur both in granites and country rocks. The AHT exposes three generations of intragranitic veins with Li and P in the two earliest and Li, P, W, (Nb), (Ta) and (Sn) mineralization in the latest, interpreted as the expression of the magmatic-hydrothermal transition. Country rock veins include a swarm of Sn-Li-bearing veins (ATM) and rare isolated W-bearing veins (AHT). Disseminated cassiterites are enriched in Ta_2O_5 and Nb_2O_5 compared to vein cassiterites. Disseminated colombo-tantalites evolve toward Mn- and Ta-rich compositions that contrast with more Fe- and Nb-rich phases in intragranitic veins. In the AHT, both intragranitic and country rock veins crystallize early Mn-rich wolframites followed by late more Fe-rich compositions. Structural data show that the magmatic, magmatic-hydrothermal and hydrothermal events all developed in the same context and form part of the same integrated ore-forming process. Cassiterite, colombo-tantalite and wolframite, and the occurrence of stannite, demonstrate progressive dilution of the magmatic signature from Type I and II to Type III intragranitic veins. The Argemela district illustrates the contrasted behavior of Sn and W in Variscan granite-related mineralizations. In particular, early wolframite deposition at Argemela is clearly associated with granite crystallization and fluid exsolution.

FROM MAGMATIC TO HYDROTHERMAL SN-LI-NB-TA-W MINERALIZATION: THE ARGEMELA DISTRICT (PORTUGAL)

III.1. INTRODUCTION

Extending from Iberia to the Bohemian massif, the Western Europe Variscan belt is a renowned, well-defined metallogenic province (Marignac and Cuney 1999; Romer and Kroner 2016). The Li, Sn, Nb, Ta and W mineralization that occur along the belt are spatially related to granitic intrusions and their volcanic counterparts (Cuney et al. 1990; Cuney et al. 1992; Černý et al. 2005; Štemprok and Blecha 2015; Harlaux et al. 2017). Mineralization are of various types and include disseminated concentrations, quartz veins, greisens, skarns and breccias, among others. In disseminated mineralization, ore-bearing minerals such as cassiterite or columbite-tantalite occur homogeneously dispersed in the whole mass of granite bodies or stocks, as observed for example at Beauvoir (France; Cuney et al. 1992; Raimbault et al. 1995) and Cínovec (Czech Republic; Breiter et al. 2017). In vein-type mineralization which are economically the most important after W-bearing skarns, ore-bearing minerals occur in quartz-veins of various thickness and extension. They comprise wolframite together with other Sn, Nb, Ta, Li minerals and are often accompanied by sulfides. Representative examples include Panasqueira (Portugal; e.g., Kelly and Rye 1979; Neiva 2008), Hemerdon (United Kingdom; Cameron 1951; LeBoutillier 2002), Logrosán (Spain; Chicharro et al. 2016), La Bosse (France; Aubert 1969; Harlaux et al. 2018) and W deposits from the southern part of French Massif Central (Béziat et al. 1980; Noyé and Weisbrod 1988; Demange et al. 1988; Lerouge et al. 2000; Harlaux et al. 2018). Ore-bearing vein systems can be intragranitic as observed for example at Cligga Head (Cornwall U.K.; Smith et al. 1996), at Cerro de San Cristóbal (Spain; Chicharro et al. 2016) and in the Jálama batholith

(Spain; Llorens and Moro 2012), be emplaced in country rocks at some distance from the granite body (Chicharro et al. 2016), or a combination of both.

From a genetic point of view, there is a consensus that Variscan Li, Sn, Nb, Ta, W mineralization has a dual origin, both magmatic and hydrothermal (e.g., Cuney et al., 1990; Breiter et al., 2017; Lecumberri-Sanchez et al., 2017; Harlaux et al., 2018; Michaud and Pichavant, 2019). The imprint of magmatic processes is particularly clear in disseminated mineralization. Granite stocks hosting this type of mineralization display specific geochemical signatures. They include the peraluminous low (PLP), intermediate (PIP) and high phosphorous (PHP) rare metal granites classes (Linnen and Cuney 2005; Černý et al. 2005). As defined by those authors, PHP RMG are peraluminous [$1 < Al/(Na + K) > 1.15$], strongly enriched in P, F and, to variable proportions, in Li, Rb, Cs, Sn, Ta ($Ta/Nb \geq 1$), Be, and W. Conversely, they are depleted in Mg, Ti, Th, Y, Zr, Hf, Sc, Pb and have close to or below chondritic values for REE. These highly specialized granites are rather scarce but are present all along the Variscan belt, from Portugal to the Bohemian massif (Linnen and Cuney 2005). Vein-type mineralization mainly results from the action of hydrothermal systems developed within and around granite bodies. Sources of fluids can be diverse and include (i) magmatic fluids transferred from the granite at the magmatic-hydrothermal transition, (ii) contact metamorphism fluids and/or (iii) meteoric fluids (Kelly and Rye 1979; Dominy et al 1995; Smith et al 1996; Rickers et al 2006; Lecumberri-Sanchez et al 2017).

Evaluating the relative importance of magmatic and hydrothermal events in the sequence of ore-forming processes remains a critical subject of research (Taylor and Hosking 1970; Kelly and Rye 1979; Cuney et al. 1992; Smith et al 1996; Rickers et al 2006; Lecumberri-Sanchez et al 2017; Breiter et al. 2017). One difficulty is that most mineralized systems in the Variscan belt only exhibit a limited part of the overall theoretical metallogenic evolution. For example, the Beauvoir granite is characterized by disseminated mineralization (Raimbault et al. 1995) but mineralized veins genetically linked to the emplacement of the granite are lacking. Indeed, the neighboring W-bearing stockwork of la Bosse, which is cross-cut by the Beauvoir granite, is interpreted as an older vein system (De Rosen 1966; Aubert 1969). Reciprocally, Panasqueira is well known for its well-developed vein system but there is up to now no clear evidence that fluids and metals have been supplied by a rare metal granite. The Argemela

district, as highlighted in the present paper, is one of the few mineralized Variscan districts that display an entire sequence of mineralizing events from the magmatic to the hydrothermal stages.

Among the various metals concentrated in Variscan granite-related mineralization, Sn and W have contrasting behaviors. Cassiterite is present both in disseminated (Černý et al. 2005) and vein-type mineralization. In disseminated mineralization, there is both textural and chemical evidence that there is cassiterite of magmatic origin (e.g. presence of significant Nb and Ta concentrations, Breiter et al. 2007). Cassiterites of hydrothermal origin are generally depleted in these two metals, showing almost pure SnO_2 (Neiva 1996) or slightly Fe-rich compositions (Breiter et al. 2007). In comparison, wolframite crystallization is almost exclusively associated with hydrothermal deposition stages (Che et al. 2013). There is still uncertainty as to whether W can be concentrated at the magmatic stage, as part of the broader issue concerning the source of W in granite-related mineralization (Heinrich 1990; Lehmann 1990; Štemprok 1995; Marignac and Cathelineau 2009; Harlaux et al. 2018). Such features further stress the particular interest of districts such as Argemela which offer the opportunity to continuously track the behaviors of Sn and W during the magmatic to hydrothermal evolution.

This paper combines structural and mineralogical data to describe and interpret the different components of the Argemela mineralized district. A complete sequence of mineralizing events, from the magmatic, magmatic-hydrothermal transition and to the hydrothermal stages is proposed and the respective behaviors of Sn and W are detailed. This study is backed up, on the one hand, by a geophysical and multiscale structural analysis (see Chapter II) and, on the other hand, by a petrological and geochemical characterization of the Argemela granite (see Chapter V) which is a representative example of Variscan RMG (Charoy and Noronha 1996).

III.2. GEOLOGICAL SETTING

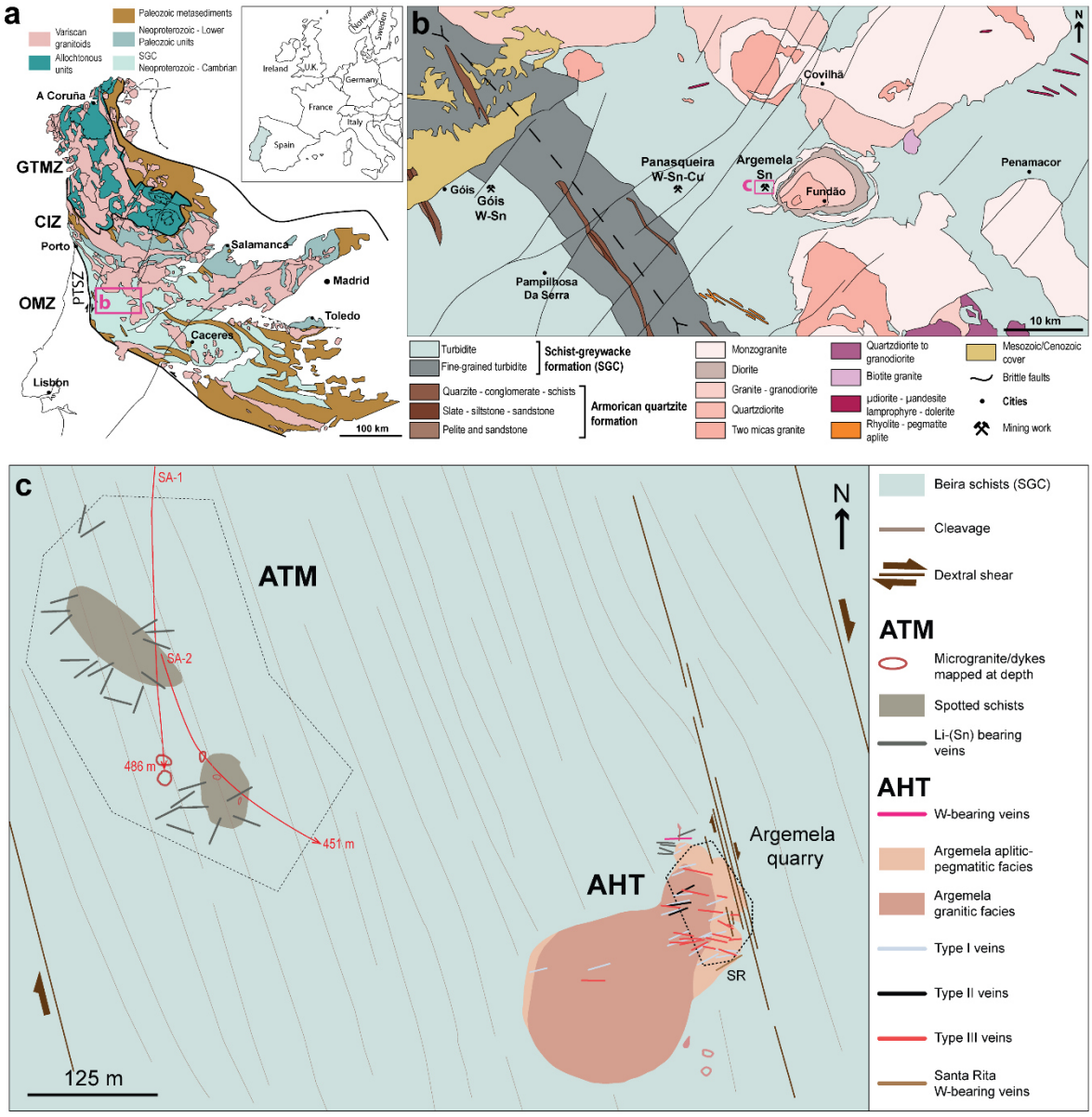

Fig 1 *Location and geological setting of the Argemela Mineralized District. (a) Sketch map of the Iberian Massif modified after Villaseca et al (2008) showing the main geological units (CIZ: Central Iberian Zone) and the location of the Porto-Tomas Shear Zone (PTSZ). (b) Regional geological map (modified after the 1992 1:500 000 map). (c) Local geological map of the Argemela Tin Mine (ATM) and Argemela Hill Top (AHT) systems with location of the SA-1 and SA-2 drillings (modified after Charoy and Noronha 1996 and Inverno 1998)*

The Argemela mineralized district (AMD) is part of the Central Iberian Zone (CIZ) Sn-W metallogenic province (Fig. 1a), in the southwestern part of the Variscan belt. The Western Europe Variscan belt extending from Iberia to the Bohemian massif results from the continental collision between Gondwana, Laurussia and some intercalated satellite microcontinents during Paleozoic times (Autran et Cogné 1980; Bard et al. 1980; Matte 1986; Faure et al. 1997). Crustal thickening is followed, during the Carboniferous, by intense partial melting and syn to late orogenic extension accompanied by voluminous peraluminous granitic intrusions (e.g. Faure 1995). Rare-metal enriched granites and Sn-W ore deposits are generally related to this late orogenic stage (Marignac and Cuney 1999) and their origin have been proposed to be linked with granulite metamorphism (Cuney and Barbey 2014).

The Argemela area is located in the southwestern part of the CIZ (Fig. 1a) which consists in autochtonous Gondwanian units and is characterized by numerous granitic plutons intruded into Neoproterozoic to Cambrian metasediments (namely the Schists and Greywackes Complex, SGC; Fig. 1).

This region has undergone a polyphased deformation history including four main phases, from D1 to D4 (see Ábalos et al. 2002 and references therein for details). The D1 phase (Devonian; Dias and Ribeiro 1995) led to narrow NW-SE trending subvertical synclines cored by Armorican quartzites and to anticlines formed of pre-Ordovician rocks (Fig. 1b). This main and pervasive deformation resulted from coaxial subhorizontal NE trending shortening normal to the main belt trending (Díez Balda et al. 1990). The D2 event (Visean to Namurian), which consists in normal ductile-brittle shear zones and subhorizontal folds, is absent in the Argemela area (Ábalos et al. 2002). The D3 event (Carboniferous in age; Dias and Ribeiro 1995) corresponds to the formation of ENE-WSW sinistral strike slip shear zones and of NW-SE (not shown on Fig. 1) to NNW-SSE dextral subvertical shear zones (see details in Pereira et al. 1993), consistent with a large scale NE-SW subhorizontal shortening. The North trending, dextral, Porto-Tomar shear zone (PTSZ, Fig. 1a), which forms the western limit of the CIZ, might have been active during this period (Ábalos et al. 2002). While the principal maximum shortening axis remains stable from D1, in a continuous deformation setting, the principal stretching shifted from vertical to horizontal. Finally, the D4 event (Permian; Dias and Ribeiro 1995) corresponds to a conjugate

system of NE-SW to NNE-SSW sinistral (Fig. 1b) and NW-SE dextral brittle strike-slips associated to a N-S/NNW-SSE shortening direction (Pereira et al 1993).

As part of the Gois-Panasqueira-Argemela-Segura mineralized axis (Inverno and Ribeiro 1980, Fig. 1b), the Argemela mineralized district (AMD) developed in the low-grade metamorphic Beira schists which belong to the SGC. It lies about 13 km east from the Panasqueira world class tungsten mine (Fig. 1b) in the western aureole of the composite Fundão pluton (monzogranite to two micas granite; Ferreira et al. 1985). Chapter II described in detail the specific structural setting of the AMD controlled both by the pressure shadow of the Fundão pluton and the development of a late ~N170-175°E trending dextral shear zone. The AMD is composed of two distinct mineralized systems (Fig. 1c): the Argemela Tin mine system (ATM) and the Argemela Hill Top system (AHT). Following Inverno and Ribeiro (1980) among others, the ATM system is made of a swarm of Sn-Li-bearing veins emplaced in the vicinity of a granitic apophyse hidden at depth. The AHT is mainly made of the Argemela granite which is a representative example of PHP RMG (Charoy and Noronha 1996) and of a few individual veins (Fig. 1c). Originally interpreted as a rootless body, new gravimetric data (see Chapter II) underline a pipe-like geometry for the Argemela granite, which is in good agreement with a process of vertical magma channeling.

III.3. METHODS AND ANALYTICAL TECHNIQUES

Field work in the AMD lasted for a total of one and a half months and was complemented by studies of two cores (SA-1 and SA-2) stored at the Portuguese Geological Survey (LNEG, Porto). These cores were drilled during the late 70's as part of an exploration campaign targeted on the ATM Sn-Li vein system.

A total of 118 rock samples were collected from in-situ outcrops and 28 more from the cores. These were prepared to produce thin and polished sections. Preliminary petrographic and textural observations were made using a petrographic microscope. Bulk rock analyses were performed at the Service d'Analyse des Roches et des Minéraux (SARM, Nancy). Detection limits are given in Table 1. Samples analyzed include the granitic facies and the border facies. Samples of veins (i.e. core of the veins) and granite at vein margins were also analyzed to track potential chemical variations. Backscattered electron (BSE) images and Energy Dispersive Spectroscopy (EDS) element mapping were obtained using a Merlin compact ZEISS Microscope equipped with a Bruker EDS detector and working under an acceleration voltage of 15 kV. All analyses of ore minerals were conducted at the Institut des Sciences de la Terre d'Orléans (ISTO, France). Punctual analyses, traverses and elements distribution maps for major and minor elements were obtained using a CAMECA SX Five microprobe operated under an acceleration voltage and a beam current of 20 kV and 40 nA respectively. Standards included Al_2O (Al$K\alpha$), apatite (P$K\alpha$), topaze (F$K\alpha$), cassiterite SnO_2 (Sn$L\alpha$), hematite Fe_2O_3 (Fe$K\alpha$), synthetic $MnTiO_3$ (Mn$K\alpha$ and Ti$K\alpha$) and pure Nb (Nb$L\alpha$), Ta (Ta$L\alpha$) and W (W$L\alpha$) metals. A homogeneous cassiterite crystal was used as a secondary standard and the error corresponds to the standard deviation calculated for each element on 25 analyses: 1.04 wt% for SnO_2, 0.28 wt% for Nb_2O_5, 0.18 for Ta_2O_5, 0.09 wt% for FeO, 0.28 for WO_3, 0.01 for MnO and 0.15 for TiO_2. Standard deviations were calculated on 11 analyses of CTI and are as follow: 0.2wt% for TiO_2, 0.8wt% for MnO, 0.6wt% for FeO, 2.1wt% for Nb_2O_5, 0.8wt% for SnO_2 and 2.5wt% for WO_3. Relative errors for wolframites are calculated as ((standard deviation x 100) / mean) for each major element using a homogeneous population and are: 3.7% for MnO, 8.5% for

FeO and 0.6% for WO_3. Relative errors for montebrasites are calculated the same way as wolframites and are 1.9% for Al_2O_3, 2.7% for P_2O_5, 29.5% for F.

Field and petrographic observations were supplemented by a structural analysis based on (i) detailed mapping of structures, veins and outline of the Argemela intrusion, (ii) statistical analysis of veins orientations and geometries and (iii) characterization of veins finite deformation.

III.4. RESULTS: PETRO-STRUCTURAL ANALYSIS

III.4.1. The Argemela district: a dual mineralized system

Mineralization in the AMD can be divided in two types: (i) Li-Sn-Nb-Ta disseminated mineralization spread in rare metal granite intrusions and (ii) Li-Sn-Nb-Ta-W vein-type mineralization occurring both in granite and surrounding rocks. Both types are expressed in the ATM and AHT, these two systems being located ~200 m apart. Mineralization in the ATM includes: (1) a network of previously mined Sn- and Li-bearing veins emplaced within the Beira schists, (2) granitic rocks (ATM RMG) only encountered at the tip of the SA-1 drill core (from 455 to 486 m). The AHT mineralized system consists of: (1) individual Li and W-bearing veins also emplaced within the Beira schists, (2) The Argemela rare-metal granite (Argemela RMG) which forms an intrusion of limited extension presently exploited for quartz and feldspar (UNIZEL MINERAIS, Lda) devoted to ceramic industry and (3) intragranitic Li-Sn-Nb-Ta-W veins which includes the Santa Rita W-bearing vein previously hand-exploited. ATM and AHT disseminated/vein-type mineralization characteristics are described below, and a sequence of mineralizing events is proposed in the Discussion.

III.4.2. Disseminated mineralization

Disseminated mineralization contains Li-, Sn-, Nb-, Ta-bearing minerals in granite bodies (Fig. 2). Two distinct granite bodies showing geochemical characteristics of RMGs can be identified in the AMD area. (i) In the ATM system, such granitic rocks were encountered at the tip of the SA-1 drill core (depth = 482-486 m, Fig. 1b). These granitic rocks show bulk rock enrichment in Nb (76 ppm), Ta (83 ppm) and Sn (586 ppm) and depletion in Ba (31 ppm), all characteristics being typical of RMGs (Table 1). Several deformed granitic dykes were also encountered from 455 to 480 m in the core and are also enriched in metals (27-68 ppm Nb, 21-74 ppm Ta and 48-104 ppm Sn), although to a lesser extent than in typical RMGs (Table 1). Dykes and granitic rocks from the core tip show high Na/K ratio, relatively

low Li content for RMG (105-268 ppm) and intermediate P_2O_5 concentrations (0.32-0.44wt%) (ii) In the AHT system, the namely *Argemela RMG* (see Charoy and Noronha 1996) is very well exposed in a 120 x 80 m operating quarry at the top of the Argemela hill (Fig. 1b). Argemela show bulk rock enrichement in metals (i.e. 35-67 ppm Nb, 39-77 ppm Ta and up to 1118 ppm Sn; Table 1), in Li (up to 4755 ppm) and in P_2O_5 (1.37-1.74 wt%). In both systems, granitic rocks show bulk compositions typical for RMG but geochemical signatures and enrichments strongly differ.

ATM

In the ATM, both the granitic rocks from the end of the tip and the dykes are characterized by millimetric snowball quartz (Qtz) and micas surrounded by a fine-grained white to light grey matrix. The granitic to microgranitic texture is typical of subvolcanic rocks (Müller and Seltmann 1999 and references therein). The ATM granite contains disseminated cassiterite (Cst, Cst1) and columbo-tantalite (CT, Fig. 2f). The Cst1 crystals are between 10 and 40 µm, unzoned and mostly anhedral. The CT crystals are of 30 µm on average, subhedral and show growth zonations. No Li-phosphate minerals of the amblygonite-montebrasite series (Li-P) have been observed in the matrix.

AHT

In the AHT, the Argemela RMG is almost elliptical except for its northeastern border which is affected by the dextral shear zone (see Chapter II) and thus the granite is displaced toward the north (Fig. 1c). It comprises two facies. (1) The main facies shows a granitic to microgranitic (typically subvolcanic) texture with millimetric snowball Qtz and white micas embedded in a fine-grained white matrix. (2) A different facies discontinuously appears along the intrusion's border and is made of alternating aplitic and pegmatitic rocks (Fig. 1c). This facies has been ascribed either to a stocksheider (Charoy and Noronha, 1996) or to unidirectional solidification textures (Inverno, 1998). Except for the northeastern border, the granite is macroscopically isotropic (i.e. underformed/unsheared). All facies from the Argemela RMG contain spread Li-P minerals, Cst and CT (Fig. 2; see also Charoy and Noronha, 1996). The Li-P phases belong to the amblygonite-montebrasite series and form euhedral twinned crystals. The disseminated CT (CT I in the following) crystals are anhedral to subhedral (i.e.,

embayed), appear black in polarized light and clearly show growth zonations (Fig. 2e). Two generations of Cst can be distinguished. The first (Cst I) consists in euhedral crystals which can exceed 1 millimeter in size (Fig. 2a). The latter are always associated with Li-P minerals, appear light brown in polarized light and show growth zonations underlining the euhedral habit of Cst I (Fig. 2c). Large Cst I crystals commonly display inclusions of Li-P (Fig. 2a) and white micas. Another generation of Cst (Cst II) corresponds to skeletal crystals, suggesting fast crystal growth (Fig. 2b). Unlike Cst I, Cst II does not co-crystallize with Li-P but is closely associated with albite crystals (Fig. 2b) suggesting that it postdates Cst I. Cst II is dark brown in polarized light and contains zoned CT crystals (CT II, Fig.2). Inclusions of CT II in Cst II suggest co-crystallization of the two minerals (Fig. 2d).

Table 1

Representative bulk rock analyses of granitic components of the AMD

System	AHT					ATM			
Type	Main facies	Main facies	Main facies	Main facies	Main facies	Aplite	RMG	Dyke	Detection limits (ppm)
Major elements (wt%)	A2	A47	A4	ARGE 4*	ARGE 5*	A11	C25	C21	
SiO_2	68.69	69.98	69.21	69.09	68.59	64.32	72.53	69.78	0.050
TiO_2	-	bdl	-	-	-	-	bdl	bdl	0.100
Al_2O_3	18.27	17.81	18.19	17.85	17.83	19.86	16.36	18.61	0.060
FeO	0.36	0.29	0.32	0.61	0.55	0.15	0.39	0.50	0.030
MnO	0.023	0.03	0.023	0.06	0.05	0.016	bdl	bdl	0.010
MgO	-	bdl	-	-	-	-	0.10	0.09	0.040
CaO	-	0.15	-	0.07	0.04	0.45	0.46	0.24	0.100
Na_2O	4.49	5.83	5.27	5.69	5.94	8.66	7.14	8.00	0.030
K_2O	3.18	2.75	3.81	2.74	2.90	1.04	1.26	1.55	0.080
P_2O_5	1.62	1.55	1.74	1.37	1.54	2.69	0.44	0.32	0.200
F	0.31	0.33	0.29	1.11	1.13	0.27	0.13	0.20	
LOI	2.33	1.35	1.45	1.80	1.91	2.03	1.34	1.16	
Total	98.96	99.74	100.01	99.63	99.74	99.23	100.00	100.26	
Trace elements (ppm)									
B	NA	47.9	NA	NA	29.00	NA	21.0	21.3	
Li	1645	1 649	1731	4395	4755	1688	105	268	
As	28.00	0.88	4.86	NA	NA	21.00	4.33	163.99	0.200
Ba	11.20	9.82	9.70	bdl	bdl	33.40	31.20	45.89	2.000
Be	37.00	45.05	27.50	92.00	75.00	15.80	44.71	13.59	0.090
Ce	0.25	0.25	0.22	318.00	NA	0.13	0.10	0.07	0.020
Cs	30.10	47.18	32.40	300.00	312.00	15.00	22.11	24.04	0.020
Cu	21.60	8.87	6.90	NA	NA	21.70	21.09	42.77	6.000
Eu	0.01	0.01	0.01	4.60	NA	0.01	0.01	0.01	0.002
Ga	42.20	37.94	36.90	31.00	29.00	27.60	28.95	34.92	0.015
Ge	4.43	5.49	4.28	NA	NA	4.48	4.88	5.03	0.050
Hf	2.73	3.02	2.65	2.30	3.10	1.39	2.70	3.11	0.030
La	0.15	0.16	0.12	182.00	NA	0.08	0.08	0.07	0.040
Lu	0.01	-	-	4.20	NA	0.01	-	-	0.001
Nb	34.90	53.58	62.00	67.00	55.00	17.30	76.19	27.75	0.020
Pb	23.90	10.77	27.00	NA	NA	24.10	7.78	10.46	0.350
Rb	1006.00	1141.91	1147.00	2130.00	2175.00	350.00	457.83	550.88	0.200
Sb	0.09	0.12	0.12	NA	NA	0.08	0.16	0.19	0.050
Sn	842.00	1117.98	871.00	635.00	634.00	107.00	586.44	104.20	2.000
Sr	12.60	11.84	12.70	bdl	bdl	132.00	29.27	97.25	0.700
Ta	38.90	64.07	61.80	66.00	77.00	19.60	83.80	21.93	0.002
Th	0.64	0.65	0.57	0.01	0.01	0.17	0.92	0.53	0.010
U	7.31	5.44	5.44	5.50	8.20	8.50	13.55	15.53	0.010
W	3.89	4.46	38.80	3.90	3.80	2.91	bdl	2.58	0.700
Y	0.29	0.34	0.12	NA	NA	0.44	0.14	0.06	0.030
Zn	79.70	59.01	56.80	120.00	116.00	24.60	51.14	134.27	5.000
Zr	14.70	15.26	13.70	13.00	14.00	9.85	14.50	15.41	0.800

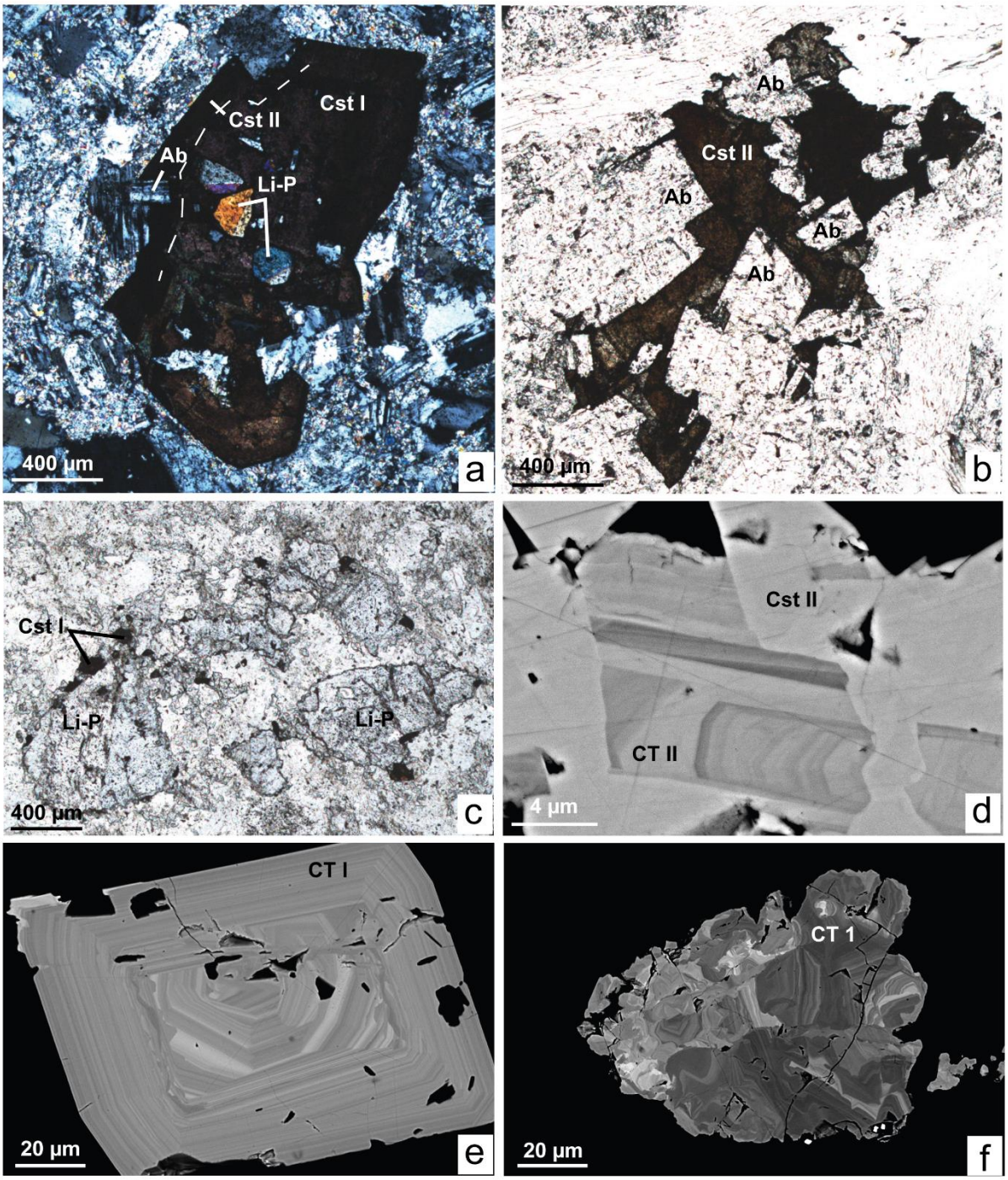

Fig 2 *Disseminated mineralizations in the AHT (a, b, c, d and e) and ATM (f) rare-metal granites (RMGs). (a) Light to dark brown zoned cassiterite (Cst I) enclosing twinned montebrasite (Li-P) and showing an external zone corresponding to Cst II; (b) skeletal Cst II surrounded by albite (Ab) crystals; (c) mutual relationships between Cst I and large Li-P crystals; (d) inclusion of zoned columbite-tantalite (CT II) in Cst II; (e) detail of zonation in CT I; (f) zoned CT 1*

III.4.3. Intragranitic vein-type mineralization

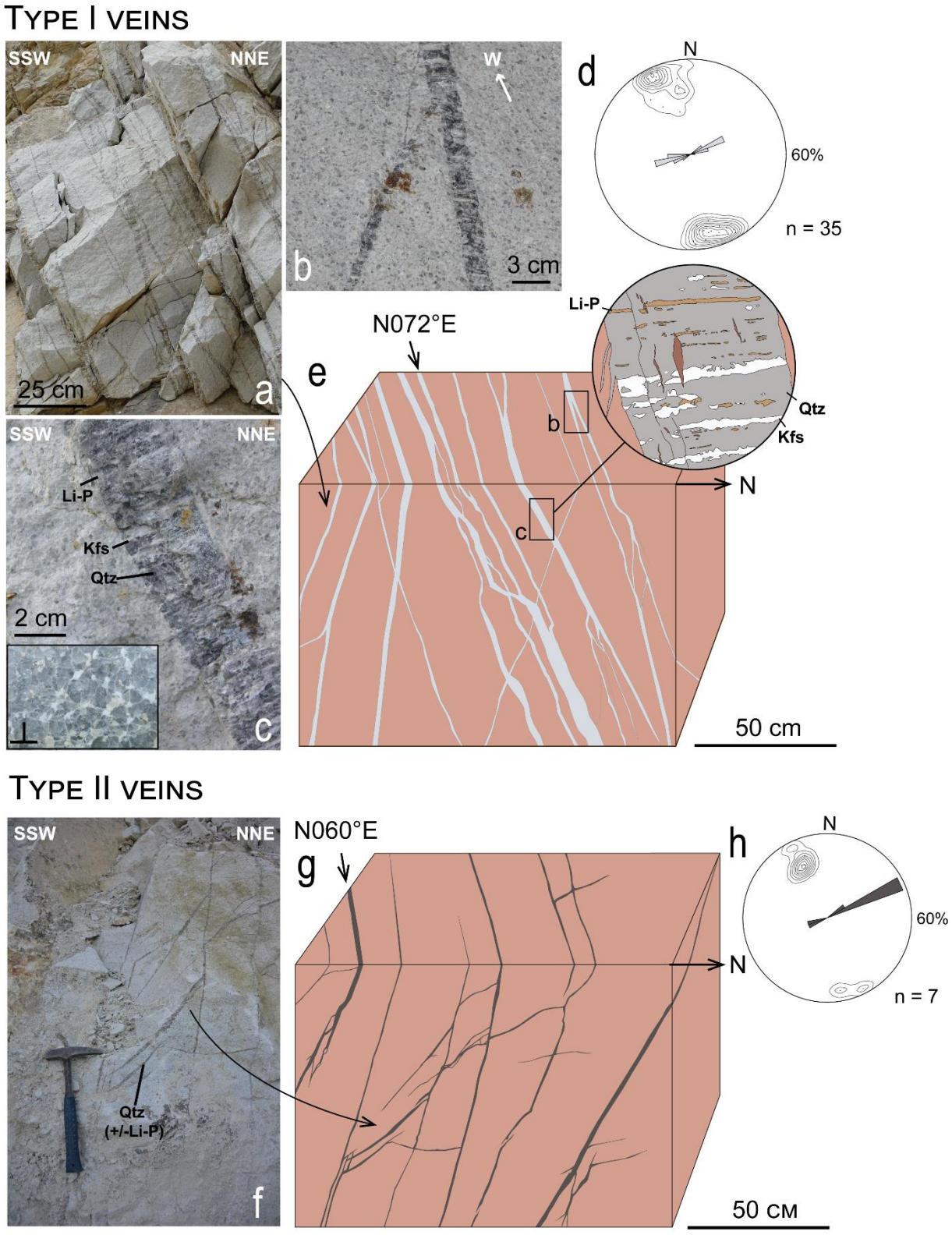

Fig 3 *Geometrical and textural features of Type I (a, b, c, d, e) and Type II (f, g, h) intragranitic veins. (a) undulating veins in cluster with pony tail terminations and branching geometries; (b) vein splitting*

preserving the initial thickness; (c) "bar code" internal texture perpendicular and parallel to vein margin; (d) stereographic and rose plot of vein orientation data; (e) summary 3D diagram; (f) branching geometry of veins in a cluster, (g) stereographic and rose plot of vein orientation data; (h) summary 3D diagram. Same abbreviations as in Fig. 2 and Kfs = alkali feldspar

ATM

Drill cores from the ATM show that the RMG is intersected by pluricentimetric to pluridecimetric veins principally hosting a Qtz-Li-P mineral assemblage. The Li-P minerals occur as large crystals which can exceed several cm in width. These crystals are commonly twinned and subhedral. Qtz occurs as large grains with strongly irregular lobate grain boundaries due to Grain Boundary Migration (GBM) recrystallisation. Some grains show elongate subgrains with undulose extinction.

AHT

The AHT quarry exposes a remarkable network of intragranitic veins. Most of the observations have been made within the quarry in mostly vertical but also horizontal planes; few other observations made around the hill allow extrapolating these results to the entire granite. Detailed analyses reveal three different vein families on the basis of (1) local crosscutting relationships, (2) vein spatial distribution and orientation and (3) type and composition of vein minerals. It is noteworthy that none of the encountered veins was found to spatially extend in the country rocks.

Type I veins (Fig. 3a-e), millimetric to pluricentimetric in size, can be found in the whole quarry (Fig. 1c), and are composed of Qtz, Kfs and Li-P from the amblygonite-montebrasite series (Fig. 3c; e; 5). They are characterized by a peculiar "bar code" texture with alternating Qtz, Li-P and Kfs stripes which form structures elongated perpendicularly to fracture plane (Fig. 3c; e). The vein spatial distribution is more or less clustered. In clusters (Fig. 3a), the distance between veins is of several centimeters and clusters are separated by several ten centimeters to several meters. Veins can also occur isolated. They display either straight or undulating hanging walls with pony tail terminations (Fig. 3a; e). The veins sometimes split into several branches showing slightly oblique orientations but a constant

sub-horizontal orientation of the mineral stripes (Fig. 3b). Locally, the thickness of the vein system is generally preserved when splitting occurs (i.e. the measured cumulated thicknesses of two sub-branches equals the one of the original vein; Fig. 3b). Type I veins trend ENE with a N050°E to N090°E range, N072°E on average (Fig. 3d). The rose diagram and stereographic projection further highlight two evenly distributed sub-populations of NNW and SSE steeply dipping veins. All minerals form elongate blocky anhedral crystals (i.e. stripes) which coarsen toward the center of the veins indicating that mineral growth is perpendicular to the fracture plane (syntaxial growth, Fig. 5a). This suggests a corresponding subhorizontal displacement vector of the fracture which is consistent with extensional type development (Mode I opening, Bons et al., 2012). Discontinuity in mineral growth (especially for Li-P) may indicate several stages of cracks. Qtz displays subgrain domains with irregular boundaries. Some relic grains show undulose extinction in analyzed light and GBM recrystallization. This suggests that Type I veins experienced some but limited deformation.

Type II veins, less common than Type I, can be observed as forming clusters throughout the whole quarry, (Fig. 1c). These latter are composed of dark Qtz and few Li-P (Fig. 3f). They consist in millimetric to centimetric rectilinear and continuous veins with bridges and can show branching geometries (Fig. 3f; g) indicating Mode I brittle failure (Bons et al., 2012). Type II veins are trending ENE (with an average trending to N060°E) and are steeply dipping to the SSE for the most (Fig. 3h). Qtz grains show clear and strong undulose extinction. Some grains are affected by GBM recrystallization, suggesting that Type II vein were affected by late, limited deformation.

Type III veins exist in the whole granite and are of several centimeters wide, sometimes exceeding 15 cm. They show a different and more variable mineralogy than the two first types (Fig. 4). The most common is composed of pinky hyaline Qtz, Kfs and Li-P (Type IIIa, Fig. 4c). In these veins, wolframite (Wf I) can occur in variable amounts (W-Type IIIa, Fig. 4c; 5b). Less commonly, veins contain only Wf (Wf II) present in large amounts and Li-P (Type IIIb, Fig. 4d; 5c). A single vein (Type IIIc, Fig. 4e; 5e) was found containing Cst (Cst III) and large amounts of Wf (Wf III). These veins have a rectilinear simple geometry and do not show any bridge, splitting or other satellite structures as observed for Type I and II veins (Fig. 4b). It is noteworthy that the internal texture varies with the thickness of the vein: (i) most small and medium veins show crystals of Qtz and/or Kfs on the margins

and different infilling mineral assemblages including Kfs, Qtz, Li-P and Wf (e.g. Fig. 5b); (ii) some Wf-Li-P veins show no clear internal texture (e.g. Fig. 5c); (iii) where hanging walls are exposed, large veins generally display asymmetrical growth of Kfs and Li-P suggesting a sinistral component of movement during vein formation (Fig. 4b), though no striae have been observed in the corresponding hanging walls. Type III veins are steeply dipping to the N and show a preferential orientation. Trending directions range between N090°E and N110°E for W-bearing and between N080°E and N110°E for barren veins (Fig. 4a). Thus, despite the variability in mineralogical assemblage and width, all veins show the same range of orientations. In most small/medium size veins, Qtz and Kfs occur as elongate blocky crystals coarsening from the margin toward the center. Kfs are generally euhedral. Inclusion bands, mostly in Qtz, indicate several crack-seal events. In the center of these veins, Qtz occur as blocky grains sometimes having irregular boundaries and showing undulose extinction. Li-P can be observed along the vein border, either coarsening toward the center or as twinned isolated crystals. When Wf I is present, it forms anhedral isolated crystals associated with blocky Qtz and Kfs. Less commonly, both Wf II and Li-P can occur as elongated crystals of up to several millimeters. Li-P are twinned and subhedral. Some Wf II crystals contain inclusions of exsolved CT (CT III, Fig. 5d) and they can pervade into the granite wall rock. This association has exclusively been observed in those veins located close to eastern boundary of the pluton, along the overall N170-175°E trending dextral shear zone (Details in Chapter II). In the Cst-bearing vein, Qtz grains are generally blocky and subhedral. Wf III occurs as large grains while Cst III is almost entirely replaced by stannite (Fig. 5e).

One particular W-bearing vein is the Santa Rita vein (SR), located at the southern rim of the Argemela granite (Fig.1b). This vein has almost entirely been excavated during exploitation making its thickness difficult to estimate. According to Inverno (1998), the SR vein strikes NE to ENE and extends from the granite to within the country rocks. Thus, the SR appears to be the only intragranitic vein with a country rock extension. It shows characteristics similar to Type III veins such as the occurrence of pinky hyaline Qtz (Fig. 4f). Wf (SR) can occur on the vein margins, as isolated inclusions in Qtz and as isolated grains pervading the granite (Fig.4).

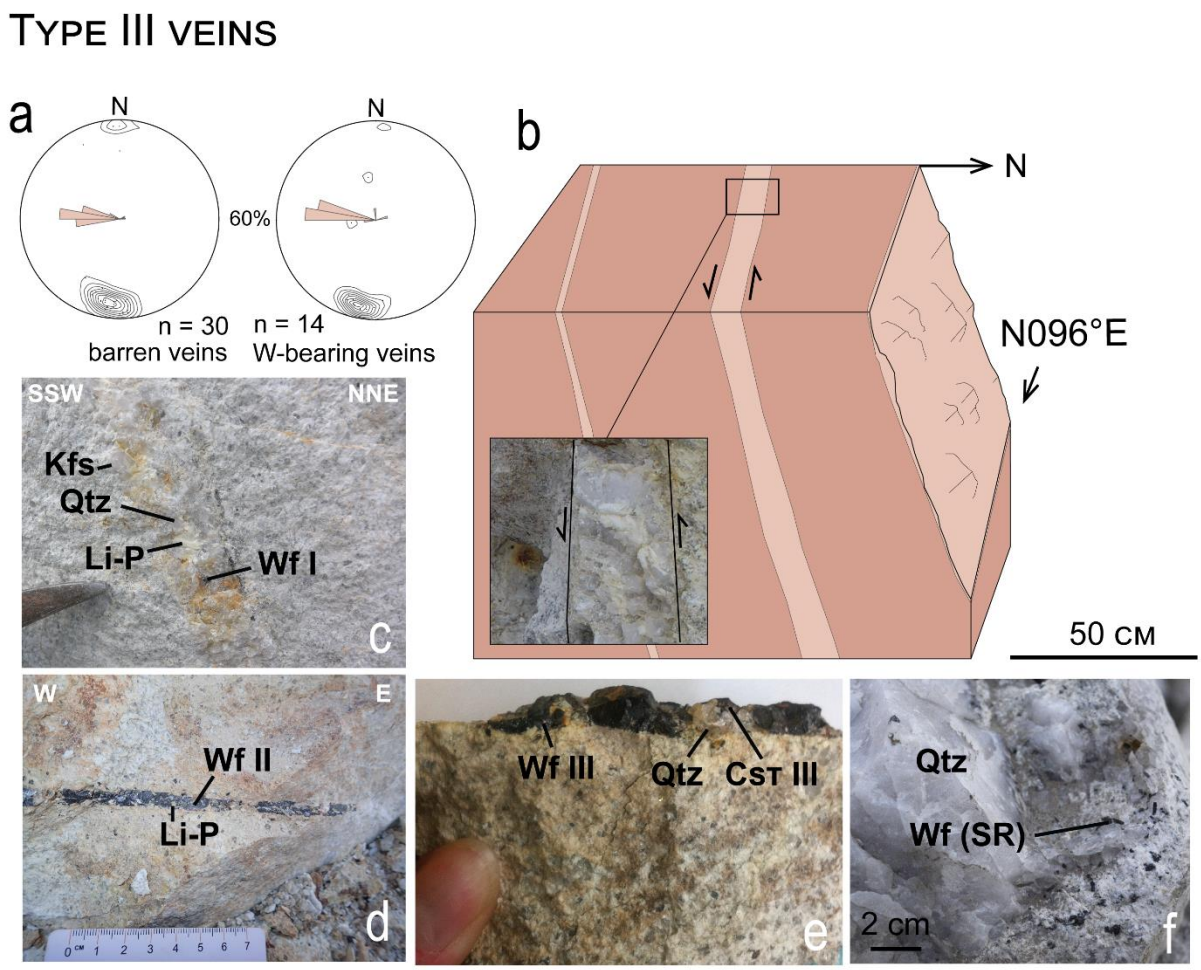

Fig 4 *Geometrical, textural and mineralogical features of Type III intragranitic veins. (a) stereographic and rose plot for barren and W-bearing veins; (b) summary 3D diagram; (c) wolframite (Wf I) present in small amounts together with Li-P, quartz (Qtz) and Kfs in Type IIIa veins; (d) Wf (Wf II) associated with Li-P in Type IIIb vein; (e) Wf (Wf III) associated with Cst (Cst III) and Qtz in Type IIIc vein; (f) Wf associated with Qtz in the the Santa Rita (SR) vein. Other abbreviations as in Fig. 2 and 3*

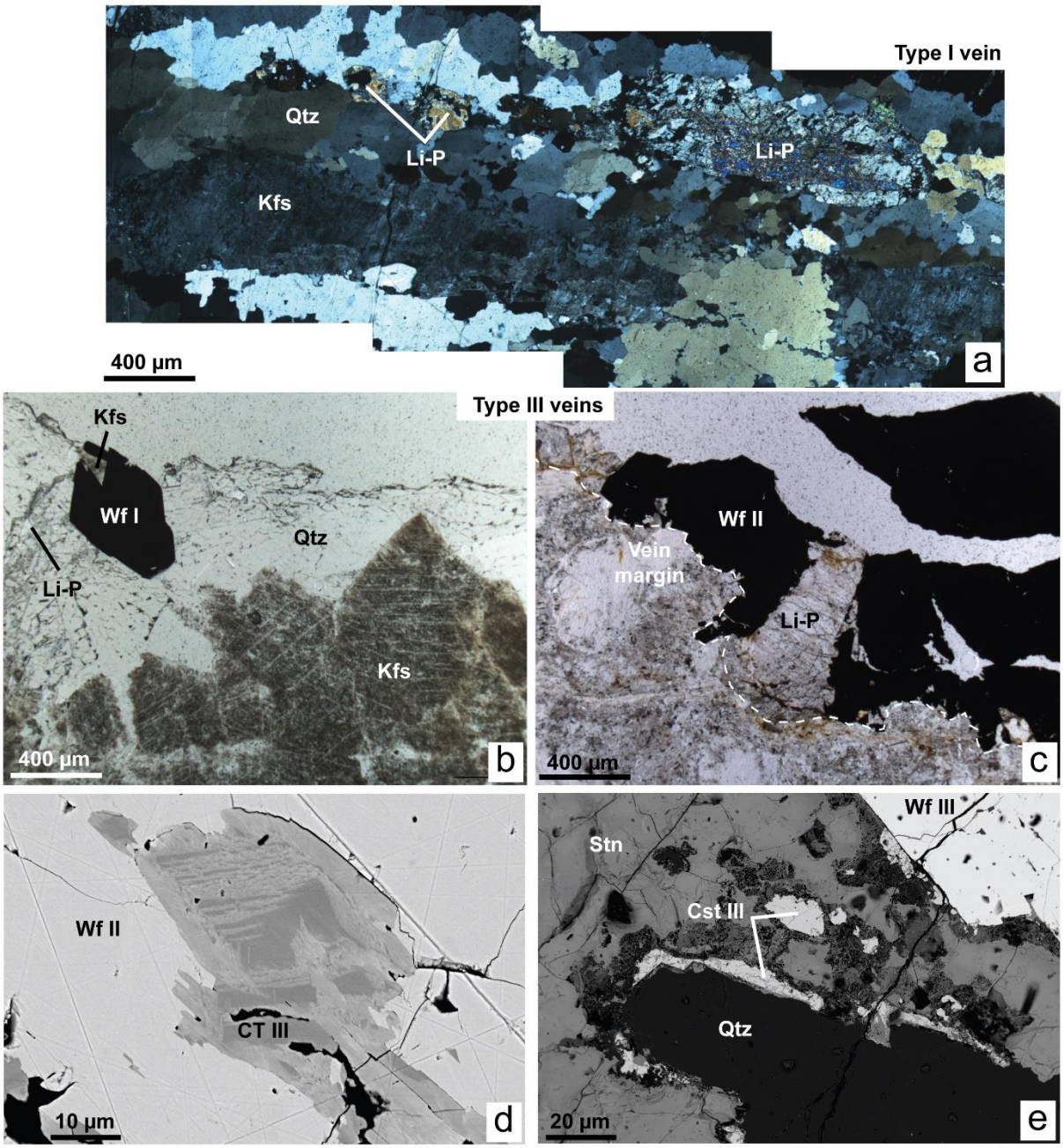

Fig 5 *Mineral textures in Type I and III intragranitic veins. (a) elongated Qtz, Kfs and Li-P in Type I vein; (b) W-Type IIIa vein with elongated Kfs in the margin and Qtz, Kfs, Li-P and Wf I infilling the center of the vein; (c) detail of the association between Wf II and Li-P in a Type IIIb small vein; (d) inclusion of exsolved CT III in Wf II; (e) coexistence of Wf (Wf III), Cst (Cst III) and Qtz in a Type IIIc vein; note that Cst III is almost entirely transformed into stannite (Stn). Other abbreviations as in Fig. 2 and 3*

Thanks to the very good exposure conditions and to the numerous observations made in the quarry, a relative chronology can be established for the intragranitic veins within the Argemela granite. The type I veins are clearly intersected by both the Type II and III. In turn, the Type II are intersected by the Type III veins. Where Type III veins intersect Type I and II, an apparent normal motion is generally observed in vertical planes. According to our observations, Type I and II veins correspond to extensional veins while Type III, at least the large ones are sheared veins. It is important to note that no alteration halos were observed in the granite at veins margins, except for those located on the eastern border which are affected by deposition of late sulphides (detailed below).

III.4.4. Country rock vein-type mineralization

ATM

The emplacement and characteristics of the ATM Sn-Li-bearing veins have been already described, among others in Inverno and Ribeiro (1980) and, formerly, in many exploration and mining internal reports. A structural model of vein formation has been proposed (Inverno and Ribeiro 1980) and is discussed below in the light of our new data.

At the surface, the mineralized veins show a wide range of orientations and several distinct populations can be recognized. At first, the overall structure is that of a single set of slightly oblique veins (Fig. 6). In details, large veins often split into several smaller ones to form an anastomosed system of continuous veins and bridges (Fig. 6a). The cumulated thickness of the vein system appears constant in such configuration. Vein thicknesses range from several cm up to one m and bridges are generally thinner than other more extended veins (Fig. 6). Veins display contrasted deformation amounts depending on their orientation. Most are affected by the regional pervasive subvertical cleavage striking N160°E-N165°E in this area (Fig. 6). All the extended veins are steeply dipping SE while bridge veins are often shallowly dipping to the SSE. Veins display planar or folded structures depending on their trending directions (Fig. 6a-d vs e): planar veins (23 measurements, Fig. 6a, c, d) show an average N069°E trending direction with 35% of them grouped between N060°E and N070°E. The strike

distribution is rather asymmetrical with a slow and continuous frequency decrease from N069°E to N090°E (see rose diagram, Fig. 6b). Folded veins (20 measurements, Fig. 6e-f) strike N073°E on average; their frequency systematically increases from N060°E to N090°E with a maximum between N080°E and N090°E. Directions for folded veins also display a skewed distribution but opposite to the one for planar veins (compare rose diagrams in Fig. 6). As a whole, the data set highlights continuous increasing rate of folding of steeply dipping veins from N069°E (maximum frequency for planar ones) to N090°E (maximum frequency for folded ones). We also observed another population of generally plurimillimetric veins subparallel to the cleavage with a mean computed striking of N162°E and W dipping. Besides, all veins are affected by late fractures which are systematically shallowly (25-30°) dipping either to the ENE or to the WSW. As shown in well exposed vertical planes in this ancient mine (Fig. 6h), fractures clearly display as a conjugate set with angles compatible with subhorizontal NE to ENE striking principal shortening.

The mineralogy of surface veins and of most veins encountered in drill cores consists in Qtz and Li-P from the amblygonite-montebrasite series. Cst (Cst 2) was recognized in only one drill core vein. The internal texture of veins at the surface is difficult to recognize as they are affected by the regional cleavage. In core samples, large Li-P grains are surrounded by Qtz crystals. Quartz is usually observed as large relic grains with irregular lobate boundaries due to slight grain boundary migration (GBM) and recrystallization. Some relic grains show undulose extinction. The Li-P are subhedral and can be up to several cm large. When present, Cst 2 occurs mostly on the margin of the vein as isolated inclusions in Qtz. This Cst 2 is almost totally transformed into stannite and the vein is invaded by late phosphates and sulphides. Qtz in the Cst vein occurs as large relic grains sometimes showing undulose extinction due to the presence of elongate subgrains. These grains have lobate boundaries due to GBM recrystallization. Around some grain interfaces, subgrain domains were observed. Although the mutual chronological relationships between the two types of veins – Cst-bearing and Cst-free – are unclear (only one Cst-bearing vein has been observed), the Cst and Li-P bearing veins may correspond to two different vein generation events according to mineralogy and internal texture.

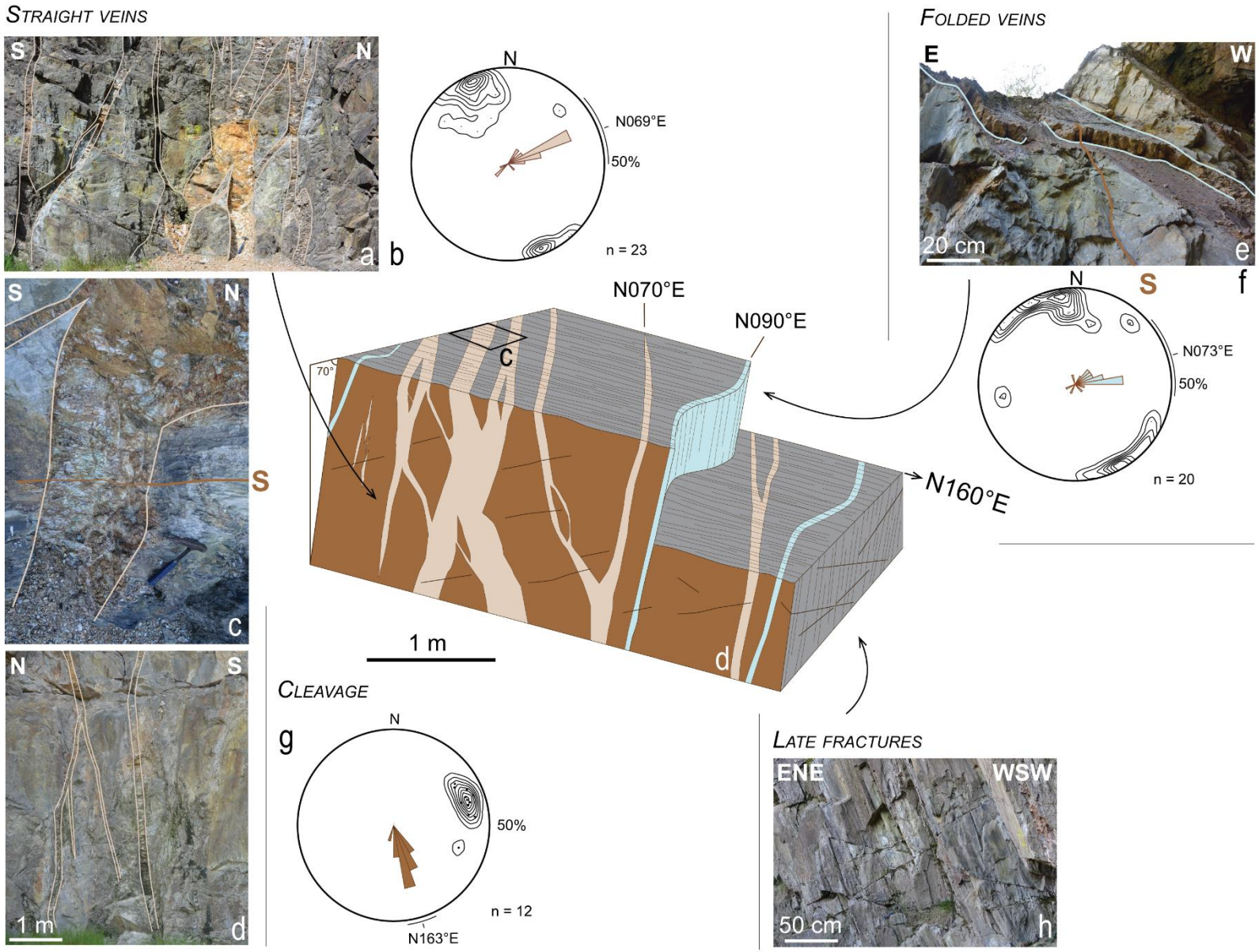
STRAIGHT VEINS
S
N
a
b
N
N069°E
50%
n = 23
FOLDED VEINS
E
W
20 cm
e
f
N
S
N073°E
50%
n = 20
N070°E
N090°E
N160°E
70°
c
1 m
d
S
N
c
N
S
1 m
d
CLEAVAGE
g
N
50%
n = 12
N163°E
LATE FRACTURES
ENE
WSW
50 cm
h

Fig 6 *General characteristics of country rock veins in the vein swarm (ATM). (a) and (d) anastomosed geometries of "straight veins"; (b) stereographic and rose plot of "straight vein" orientations; (c) regional cleavage affecting a "straight vein"; (e) folded vein affected by regional cleavage; (f) stereographic and rose plot of folded veins orientations; (g) stereographic and rose plot of regional cleavage in the area; (h) conjugate late fractures*

AHT

In the AHT, isolated individual veins occur in country rocks at the immediate vicinity of the Argemela granite (Fig. 1c). These include Li-P and Wf-bearing veins, the latter discovered in the surrounding schists about 2 meters away from the northeastern contact of the granite (Fig. 1c). This about 3 cm thick vein is oriented N078°E, 58°N; it is intersected by a dyke derived from the Argemela granite and is thus clearly older than granite emplacement. It consists of milky to geodic Qtz and Wf only (Fig. 7a). Qtz crystals are generally elongated and blocky along the vein margins (Fig. 7b). Crystals tend to be coarser toward the center of the vein which is characteristic of syntaxial veins (Bons et al. 2012). The center of the veins is characterized by blocky Qtz, larger than those near the margin. Quartz is affected by late micro-fractures. Wf is present as large subhedral crystals always spatially associated with blocky Qtz.

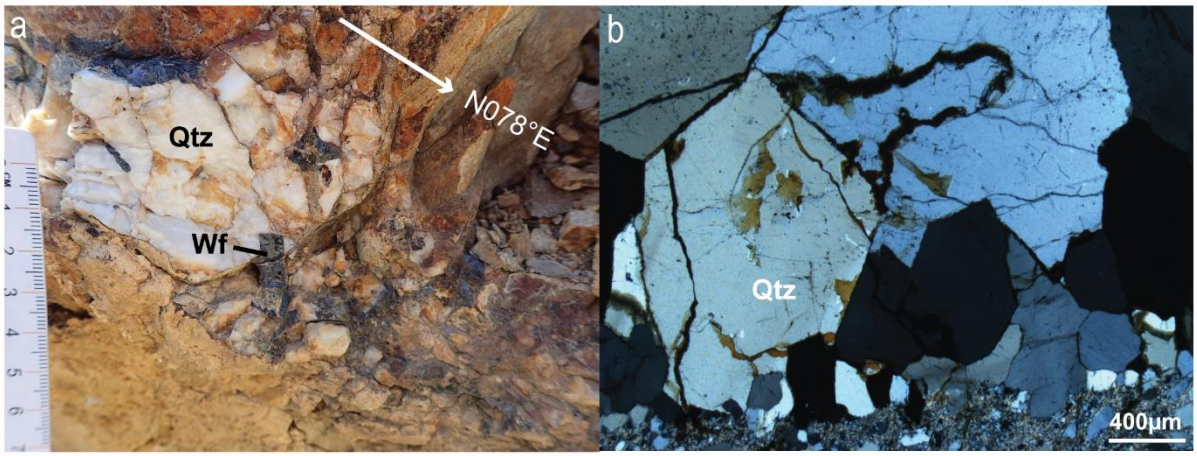

Fig 7 *Detail of the country rock W-bearing vein in the AHT showing (a) the Wf-Qtz mineralogical assemblage and (b) the internal texture of the vein with elongated quartz (Wf is not shown)*

All mineralized components of the AMD are affected by a sulphide deposition stage. In the ATM system, the sulphide stage results in sulphide crystallization in veins and in veinlets intersecting both the country rocks and the RMG. In the AHT system, it is expressed by impregnation of sulphides along subhorizontal fractures and Type III intragranitic veins. This sulphide stage affects only the eastern sheared margin of the granite, where the map scale shear zone is located (Fig. 1c).

III.5. RESULTS: CHEMISTRY OF ORE MINERALS

Ore minerals analyzed in both systems include Cst, CT, Wf and Li-P. Representative analyses are given in Tables 2-5 and mineral compositions are discussed below.

III.5.1. Cassiterites

The mineral chemistry data for all analysed cassiterites (representative individual analyses in Table 2) are plotted on the ternary (Sn+Ti+W)-(Mn+Fe)-(Nb+Ta) (Fig. 8) and binary Nb/Ta-Sn diagrams (Fig. 9).

In the ATM, two generations of Cst have been recognized. The first one (Cst 1, Fig. 8), which corresponds to disseminated Cst in granite, is enriched in Ta_2O_5 (1-12 wt%) and slightly enriched in Nb_2O_5 (0.7-2.6 wt%). The second generation (Cst 2), corresponding to Cst in a vein emplaced in the schists, is almost pure SnO_2 (Fig. 8 and 9).

In the AHT system, the disseminated light brown Cst I crystals in the granite show oscillatory growth zonations underling the euhedral habit of the crystal. Light brown zones are almost pure SnO_2 (0.001 wt% Ta_2O_5 and 0.15 wt% Nb_2O_5) while darker zones have higher Fe, Nb and Ta contents (Table 2 and Fig. 8b). In the latter zones, Ta_2O_5 and Nb_2O_5 can reach 7.4 wt% and 4.2 wt% respectively. Some crystals show dark brown overgrowths surrounding albite and (texturally Cst II) reach up to 10 wt % Ta_2O_5. The typically skeletal Cst II crystals have Ta_2O_5 between 1 and 10 wt% although most analyses are spread between 5 and 10 wt% (Fig. 8b). Nb_2O_5 ranges between 0.5 and 6.1 wt%, mostly between 4 and 6 wt%. The last generation of Cst in Type IIIc intragranitic veins is almost pure SnO_2 (98-100 wt%, Table 2 and Fig. 8b) and contains remarkably high W contents up to 2.4 wt% WO_3.

Table 2

Representative electron microprobe analyses of cassiterites

System	AHT						ATM			
Type	Cst I		Cst II		Cst III		Cst 1		Cst 2	
wt %	Light zone	Dark zone								
TiO_2	bdl	-	0.04	-	-	-	0.65	0.40	-	0.01
MnO	bdl	0.21	0.12	0.11	bdl	-	0.02	-	-	-
FeO	0.19	1.16	1.52	1.20	0.84	1.13	1.28	0.34	0.09	0.09
Nb_2O_5	1.09	2.37	0.74	4.88	bdl	-	2.21	0.73	-	bdl
SnO_2	99.98	91.46	88.56	91.56	98.08	98.82	92.12	97.95	100.39	100.70
Ta_2O_5	0.10	5.66	9.23	2.03	-	-	4.31	1.00	-	bdl
WO_3	bdl	-	NA	NA	1.52	0.21	-	-	0.09	-
Total	101.9	101.3	100.6	100.2	100.9	100.6	101.0	100.9	101.6	101.5
a.p.f.u.										
Ti	-	-	0.001	-	-	-	0.012	0.008	-	-
Mn	-	0.004	0.003	0.002	-	-	-	-	-	-
Fe	0.004	0.024	0.032	0.025	0.017	0.023	0.026	0.007	0.002	0.002
Nb	0.012	0.026	0.008	0.054	-	-	0.025	0.008	-	-
Sn	0.975	0.899	0.887	0.896	0.970	0.979	0.901	0.964	0.991	0.992
Ta	0.001	0.038	0.063	0.014	-	-	0.029	0.007	-	-
W	-	-	-	-	0.010	0.001	-	-	0.001	-
Total	1.005	1.004	1.005	1.003	1.010	1.018	1.007	1.006	1.008	1.007

bdl: below detection limit. Oxides in wt%. NA: not analyzed. Number of cations based on 2 oxygens

It is important to note that, in the two mineralized systems, disseminated Cst are enriched in Ta_2O_5 and Nb_2O_5 compared to Cst from veins which are nearly pure SnO_2. In the ternary diagram, all Cst 1, Cst 2, Cst I and Cst II extend from the Sn-Ti corner along the trend defined by the ideal substitution $(Fe,Mn)^{2+} + 2(Nb,Ta)^{5+} \leftrightarrow 3(Sn,Ti)^{4+}$ (Černy et al., 1985, Fig. 8b). Cst II from the Argemela granite are more enriched in Ta_2O_5 and Nb_2O_5 than Cst I, indicating increased substitution between crystallization of Cst I and Cst II. Cst III from the Argemela intragranitic veins plot on the (Sn+Ti+W)-(Mn+Fe) baseline as compositions are almost Nb- and Ta-free.

In the Nb/Ta-Sn diagram (Fig. 9), Cst I have overall higher Nb/Ta ratio than Cst II as this later is more enriched in Ta on average. Cst III show very low ratio because of the limited amount of both Nb and Ta (i.e., Sn close to 1).

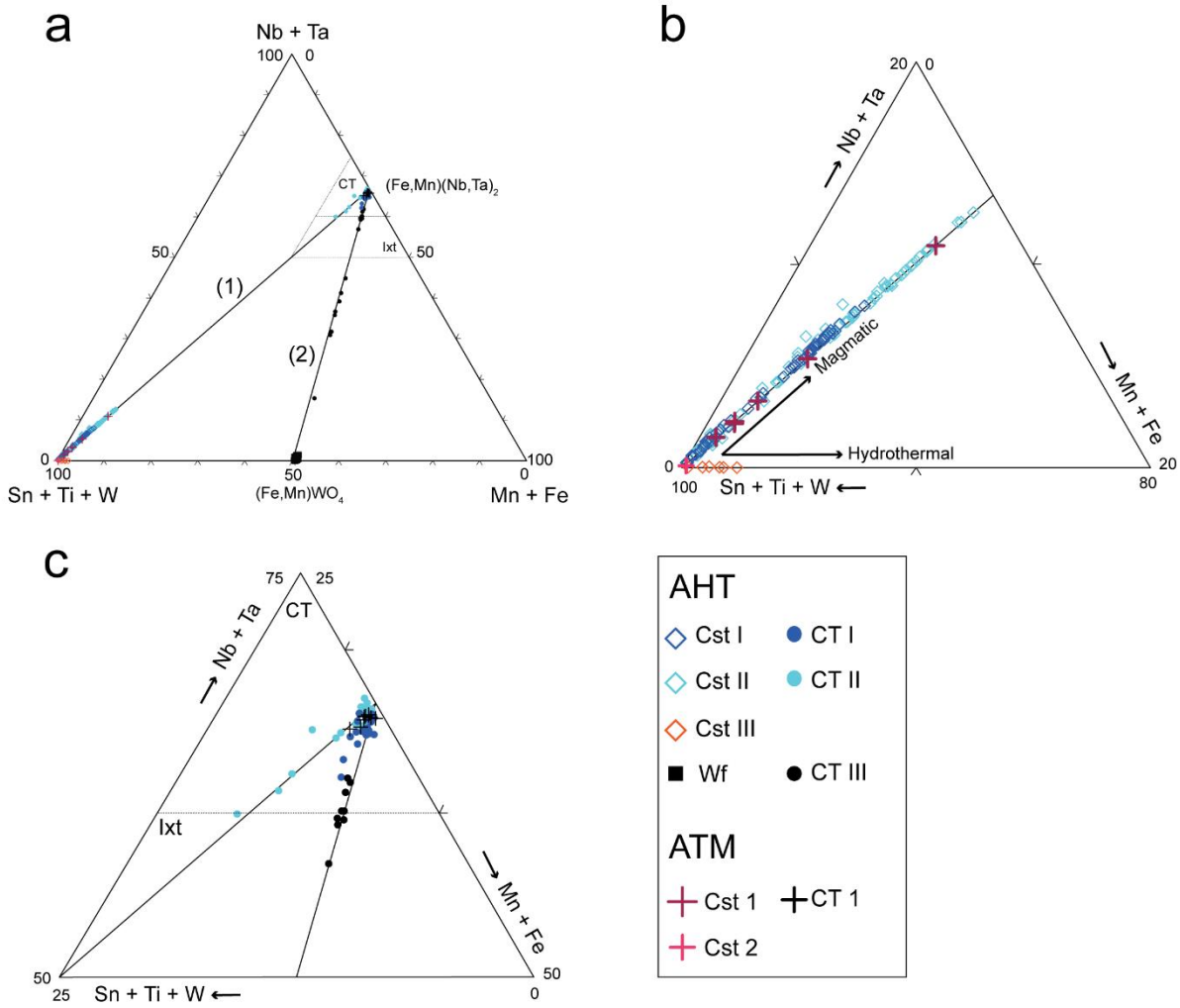

Fig 8 *Cst, CT and Wf compositions plotted in the (Sn+Ti+W)-(Mn+Fe)-(Nb+Ta) ternary diagram. (a) Full scale plot of all data. (1) represents the* $(Fe,Mn)^{2+} + 2(Nb,Ta)^{5+} \leftrightarrow 3(Sn,Ti)^{4+}$ *substitution line after Černý et al (1985) and (2)* $4(Nb,Ta)^{5+} \leftrightarrow Fe^{2+} + 3W^{6+}$ *the substitution line after Suwinonprecha et al. (1995). (b) enlargement on the Sn-Ti-W corner showing details for Cst compositions, magmatic and hydrothermal trends are drawn after Tindle and Breaks (1998) and Breiter et al. (2007); (c) enlargement on CT compositions. Same abbreviations as in Fig. 2 and 3 and Ixt = ixtiolite*

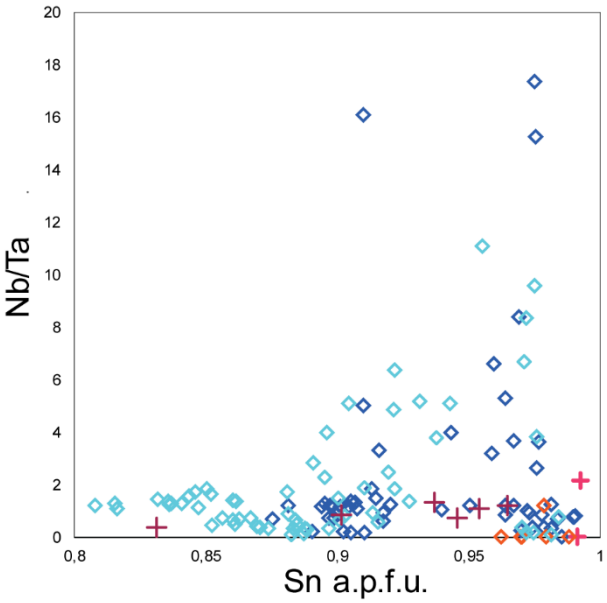

Fig 9 *Nb/Ta-Sn binary diagram showing Cst compositions. Same legend as in Fig. 8*

III.5.2. Columbite-tantalites

CT chemical analyses (Table 3) are plotted in the ternary (Sn+Ti+W)-(Mn+Fe)-(Nb+Ta) (Fig. 8) and binary Ta/(Ta+Nb)-Mn/(Mn+Fe) (Fig. 10) diagrams.

In the ATM system (Fig. 10), the only generation of CT observed in granite consists in disseminated Fe-columbite. Most compositions do not exceed Ta/(Ta+Nb) = 0.4 except one analysis which has Ta/(Ta+Nb) = 0.6 and plots in the Fe-tantalite field. Compositions are homogeneous and plot close to the (Nb+Ta)-(Mn+Fe) baseline in the ternary diagram (Fig. 8c).

In the AHT system, three generations of CT have been recognized (Fig. 10). Disseminated CT I in granite is Mn-columbite with compositions ranging between Mn/(Mn+Fe) = 0.7 and 0.9 and between Ta/(Ta+Nb) = 0.1 and 0.4. CT II in granite (zoned inclusions in Cst II) are Mn-columbites to Mn-tantalites. They have Mn/(Mn+Fe) = 0.6 to 0.8, in the same range as CT I but with a higher Ta/(Ta+Nb) between 0.3 and 0.8. The CT III crystals included in some Wf II from Type IIIb intragranitic veins show only Mn-columbite compositions. These CT have a Mn/(Mn+Fe) ratio ranging from 0.5 and 0.6 and are more enriched in Fe than CT I and CT II. In the ternary (Sn+Ti+W)-(Mn+Fe)-(Nb+Ta) diagram (Fig. 8a and c), disseminated CT I plot close to the (Nb+Ta)-(Mn+Fe) baseline and extend between the two

ideal substitution lines $(Fe,Mn)^{2+} + 2(Nb,Ta)^{5+} \leftrightarrow 3(Sn,Ti)^{4+}$ (Černý et al. 1985) and $4(Nb,Ta)^{5+} \leftrightarrow Fe^{2+} + 3W^{6+}$ (Suwinonprecha et al. 1995; Neiva 1996, Fig. 8a). The data suggest that the two substitutions are responsible for incorporation of W and Sn in CT I. Inclusions of CT II in Sn II plot along the $(Fe,Mn)^{2+} + 2(Nb,Ta)^{5+} \leftrightarrow 3(Sn,Ti)^{4+}$ ideal substitution line. This indicates that this substitution is the main mechanism responsible for incorporation of Sn in CT II. The CT III inclusions in Wf II plot along the wolframite $4(Nb,Ta)^{5+} \leftrightarrow Fe^{2+} + 3W^{6+}$ substitution line suggesting that this mechanism is responsible for W and Fe incorporation in CT III.

Table 3
Representative electron microprobe analyses of colombite-tantalites

System	AHT						ATM	
Type	CT I		CT II		CT III			
TiO_2	0.31	0.62	0.67	0.05	0.39	0.49	0.46	1.18
MnO	16.42	16.21	11.78	13.90	10.41	10.10	8.09	3.54
FeO	2.47	2.98	3.88	4.06	8.91	9.16	9.73	15.78
Nb_2O_5	53.67	55.17	23.37	44.71	45.49	48.24	41.69	56.77
SnO_2	0.07	0.22	1.98	0.35	0.08	0.08	0.19	0.45
Ta_2O_5	26.75	23.93	58.44	36.89	27.29	27.05	40.24	24.12
WO_3	-	0.08	-	-	7.63	5.30	-	-
Total	99.69	99.21	100.13	99.96	100.21	100.41	100.49	101.88
a.p.f.u.								
Ti	0.014	0.029	0.037	0.003	0.019	0.024	0.023	0.054
Mn	0.875	0.858	0.730	0.775	0.570	0.545	0.455	0.182
Fe	0.130	0.156	0.237	0.223	0.482	0.488	0.541	0.800
Nb	1.527	1.559	0.773	1.331	1.329	1.392	1.252	1.557
Sn	0.002	0.006	0.058	0.009	0.002	0.002	0.005	0.011
Ta	0.458	0.407	1.163	0.660	0.480	0.469	0.727	0.398
W	-	0.001	-	-	0.128	0.088	-	-
Total	3.007	3.015	3.000	3.002	3.010	3.008	3.003	3.003

Oxides in wt%. Number of cations based on 6 oxygens

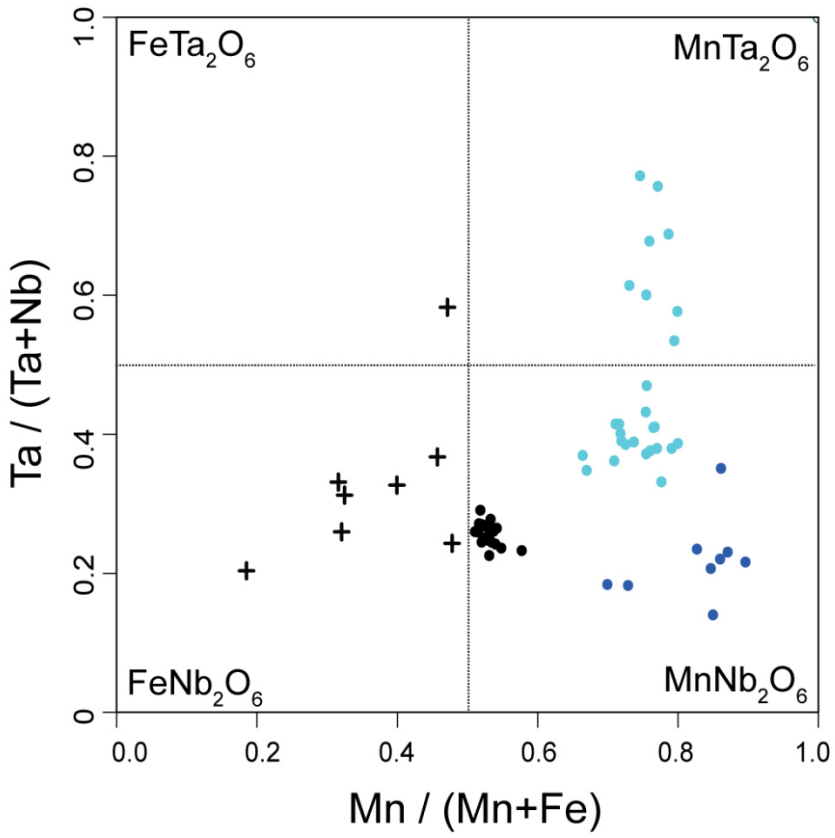

Fig 10 *Ta/(Ta+Nb)-Mn/(Mn+Fe) binary diagram showing CT compositions from this study. Same legend as in Fig. 8*

III.5.3. Wolframites

Wolframite compositions (Table 4) are plotted in the ternary (Sn+Ti+W)-(Mn+Fe)-(Nb+Ta) (Fig. 8) and in the binary H/F-WO_3 diagrams (Fig. 11).

Two generations of wolframites have been recognized, both from the AHT. In the isolated country rock vein, EDS mapping of Fe and Mn reveals a patchy texture (Fig. 12a and b) suggesting two stages of wolframite crystallization (Llorens and Moro 2012). Early wolframite has a H/F ratio (H/F = at. Mn/(Fe+Mn) x 100, Michaud and Pichavant, 2019) of 62% on average (hübnerites) while, for late wolframites, the H/F ratio is of ~10% on average (ferberites, Fig. 11). Wolframites (I-II-III-SR) in Type III intragranitic veins are mostly homogeneous hübnerites (H/F: ~67-75%; Fig. 11). Only some Wf II and SR show a patchy texture (Fig. 12c and d) suggesting an evolution of the wolframite composition

to lower H/F values (55-46%; hübnerite to Mn-rich ferberite, Fig. 11). What is important to note is that, both in the intragranitic and country rock veins, the early stage of wolframite crystallization corresponds to Mn-rich wolframites (hübnerites). Compositions of secondary wolframites are always more Fe-rich than the primary. The major difference between late wolframites occurring within the country rock and late wolframites (Wf II and SR) in intragranitic Type III veins is the Fe content, which is very high in the former compared to the latter. In the ternary diagram, wolframites plot close to the (Sn+Ti+W)-(Mn+Fe) baseline indicating that almost no Nb and Ta are incorporated.

Table 4
Representative electron microprobe analyses of wolframites

Vein type	Country rock vein		Type III intragranitic					
Type			Wf I	Wf II		Wf III	SR	
	Early	Late	Early	Early	Late	Early	Early	Late
TiO_2	-	0.02	-	-	-	-	-	-
MnO	15.17	2.41	17.80	18.02	11.13	16.50	17.90	13.30
FeO	9.25	22.07	6.75	6.37	13.25	7.98	6.18	11.00
Nb_2O_5	0.14	0.19	0.39	0.38	0.52	-	0.47	0.62
SnO_2	bdl	bdl	bdl	-	0.06	-	0.16	0.11
Ta_2O_5	-	-	0.14	-	bdl	-	0.59	0.36
WO_3	76.99	76.98	76.70	76.94	75.95	77.61	76.49	76.39
Total	101.73	101.84	101.83	101.71	101.05	102.10	101.81	101.81
a.p.f.u.								
Ti	0.000	0.001	0.000	0.000	0.000	0.000	0.000	0.000
Mn	0.637	0.101	0.745	0.755	0.470	0.690	0.750	0.557
Fe	0.384	0.915	0.279	0.264	0.552	0.330	0.256	0.455
Nb	0.003	0.004	0.009	0.008	0.012	0.000	0.010	0.014
Sn	0.000	0.000	0.000	0.000	0.001	0.000	0.003	0.002
Ta	0.000	0.000	0.002	0.000	0.000	0.000	0.008	0.005
W	0.990	0.989	0.983	0.987	0.981	0.993	0.981	0.979
Total	2.015	2.014	2.018	2.014	2.018	2.013	2.008	2.012
H/F ratio	62.4	9.9	72.8	74.1	46.0	67.7	74.6	55.0

bdl: below detection limit. Oxides in wt%. Number of cations based on 4 oxygens

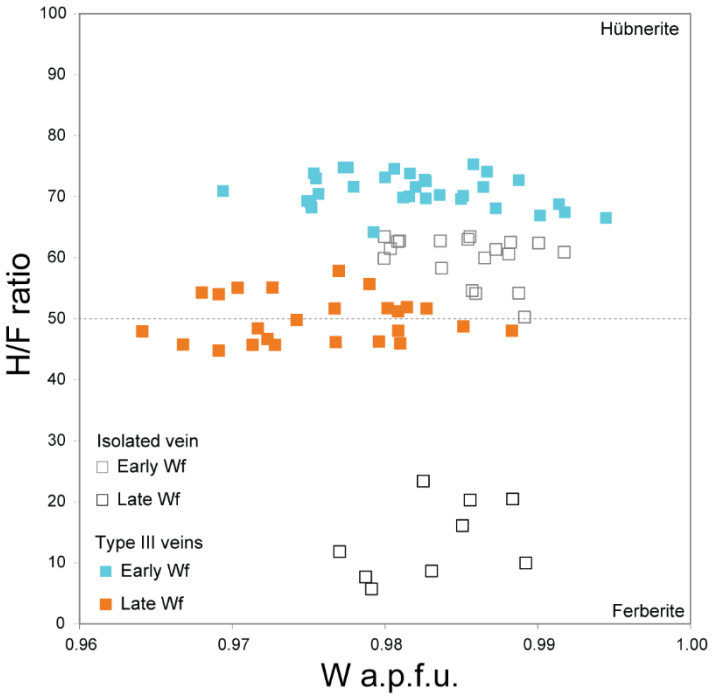

Fig 11 *Compositions of Wf in intragranitic and country rock veins from the AHT. H/F ratio = at. Fe/(Fe+Mn) x 100*

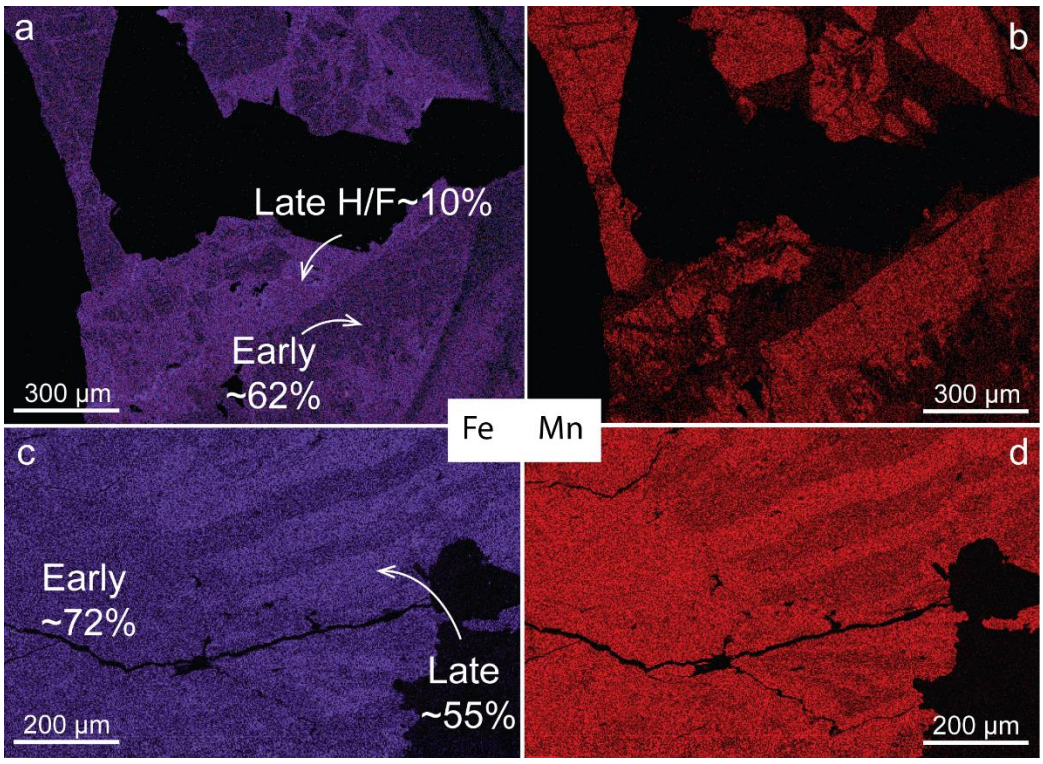

Fig 12 *EDS mapping of Fe and Mn in Wf from the AHT; H/F ratios are indicated. (a) and (b) patchy texture in Wf from the country rock vein; (c) and (d) compositional heterogeneities in Wf II from the Type IIIb intragranitic veins*

III.5.4. Li phosphates

Major element compositions of Li-P do not vary much with the crystallization environment (Table 5); these are mostly montebrasite with OH/F ranging from 1.4 and 3.2 (Dubois et al., 1973). Mtb from hydrothermal veins show only a slight enrichment in F compare to disseminate Mtb. No growth zonation has been observed

Table 5
Representative electron microprobe analyses of montebrasites

System	AHT			ATM			
Type	Dispersed	Type III veins		Intragranitic veins		Country rock veins	
P_2O_5	49.80	48.38	48.84	49.97	48.75	48.97	48.64
Al_2O_3	36.10	34.09	33.78	33.22	33.23	32.99	33.94
MnO	0.01	-	-	-	-	-	-
TiO_2	0.06	-	0.01	0.27	0.32	0.18	0.16
FeO	0.01	-	-	-	0.15	0.15	0.10
MgO	-	-	-	-	-	0.02	0.03
CaO	-	0.02	-	0.04	0.01	0.01	-
Na_2O	0.01	0.02	0.02	0.04	-	-	0.02
K_2O	-	-	-	-	-	-	-
F	3.23	5.38	3.78	3.19	4.43	4.85	4.03
O=F	1.36	2.27	1.59	1.34	1.86	2.04	1.69
Total	87.95	85.65	84.83	85.43	85.03	85.12	85.26
a.p.f.u.							
P	1.971	1.951	1.931	2.028	1.985	1.988	1.979
Al	1.879	1.808	1.862	1.773	1.779	1.761	1.816
Mn	-	-	-	-	-	-	-
Ti	0.002	-	-	0.010	0.012	0.006	0.006
Fe	0.001	-	0.005	-	0.006	0.006	0.004
Mg	-	-	-	-	-	0.001	0.002
Ca	-	0.001	-	0.002	0.001	0.001	-
Na	0.001	0.002	-	0.004	-	-	0.002
K	-	-	0.004	-	-	-	-
F	0.477	0.811	0.735	0.484	0.674	0.736	0.612
OH	1.523	1.189	1.424	1.516	1.326	1.264	1.388
OH/F	3.190	1.465	1.937	3.132	1.968	1.719	2.269

Oxides in wt%. Number of cations based on 8 oxygens

III.6. DISCUSSION

Rare metal Li, Sn, Nb, Ta and W mineralization in the AMD is separated in two spatially disconnected systems which both show disseminated and vein-type deposits. The two mineralized systems share common features, although not developed to the same extent. (i) Both involve a granitic phase with highly specific geochemical and mineralogical features such as the presence of magmatic disseminated Cst and CT. (ii) Hydrothermal intragranitic veins are encountered in both systems, some mineralized in Wf and, more rarely, with Cst and CT. (iii) Hydrothermal Li-P-Cst-bearing veins occur in country rocks although the ATM vein system is more extensively developed; Cst mineralization seems more specific to the ATM and Wf mineralization to the AHT. Taken together, the ATM and AHT have characteristics typical of granite-related magmatic-hydrothermal deposits such as found elsewhere in the Central Iberian Zone (e.g. Argozelo and Panasqueira, Neiva 2008; Cerro de San Cristóbal/Logrosán, Chicharro et al. 2016) and in other parts of the Variscan belt (e.g. north French Massif Central rare metal magmatism belt, Cuney et al. 2002; Podlesi, Müller et al. 2002). No crosscutting relationships can be observed between the two systems and, therefore, their relative chronology is basically unconstrained. However, both the ATM and AHT were emplaced in the same regional geological setting (i.e. Chapter II). Below, the structural and tectonic contexts controlling the development of the two deposits are detailed.

III.6.1. Structural context on emplacement of mineralizations

The metallogenic evolution of the AMD clearly involves a magmatic component represented by the occurrence of RMGs in both the ATM and AHT systems and by a disseminated type of mineralization. It is not possible to constrain the context of emplacement of the ATM RMG which was only encountered in drill cores. This granite can represent either a cupola from a larger and deeper intrusive body similar to that found at Panasqueira (Oosterom et al. 1984) which is unlikely according the gravimetric survey (Chapter II), or a small stock geometrically analoguous to the AHT intrusion and

to other Variscan RMG (reviewed in Černý et al. 2005). In Chapter II, we have shown that the Argemela granite was emplaced in a specific structural context combining the effect of a pressure shadow around the Fundão pluton to a N170°E trending dextral shear corridor. This structural context favored vertical channeling of magma batches, consistent with the pipe-like geometry of the Argemela granite (Chapter II) and the occurrence of subvertical granitic dykes in the ATM cores. Therefore, the different observations all indicate magma ascent and crystallization up to shallow crustal levels as also evidenced by the subvolcanic textures of the two Argemela RMG.

The country rock anastomosed Li-P-bearing veins (mainly observed and exploited in the ATM) are characterized by an E-W preferential striking and steep dipping (~78°S on average, except for the bridges); this is compatible with subhorizontal ~north striking σ3, as suggested by Inverno and Ribeiro (1980). Veins display the same N163°E trending cleavage as the surrounding schists in the area. This rather peculiar cleavage orientation (differing from the ~N135°E striking regional direction) is interpreted (Chapter II) to result from the N170-175°E trending dextral shear corridor. Straight and slightly foliated veins are mostly striking N065°E while more shortened, folded ones are striking ~N080-090°E on average. Besides, stereographic plot of the structural measurements displays continuous directions from N040°E to almost N090°E. The correlated striking and finite strain variations clearly evidence some non-coaxial shear compatible with ~N170-175°E dextral shearing as observed along the nearby shear zone: early sub-vertical veins developed as tension gashes in a ~NE striking and then rotated to ~N80-90°E and folded during simple shear deformation. Later veins show more limited deformation and rotation. Such a model of veins emplacement is consistent with the regional NE-SW shortening and the development of a ~1.5km dextral shear band parallel to the ~N170-175°E trending localized shear zone.

Intragranitic veins from both in the ATM and the AHT form a specific component of the AMD. Although such veins in the ATM were only observed in drill cores, the presence of irregular margins, the range of vein thicknesses and the general vein geometries are common to both systems. Concerning the AHT, the intragranitic veins are confined inside the granite body and do not extend into country rocks. This implies a strong link between granite emplacement, consolidation and vein formation. Type I and II vein show irregular margins, bridges and pony tail terminations. This geometry suggests opening

at the ductile/brittle transition when the granite intrusion is not fully consolidated. Type I steep dipping together with mineral growth perpendicular to margins are compatible with ~N striking subhorizontal σ3 (extensional fractures; Bons et al. 2012). In comparison, the straight geometries of Type III veins suggest pure brittle emplacement, i.e., the surrounding granite has become rigid, in agreement with the relative chronology deduced for the 3 vein types (see above). Assymetrical mineral growth in Type III veins indicates a sinistral component of movement along veins during emplacement (shear fractures; Bons et al. 2012) with $\alpha = 55°$ (angle between σ3 and shear plane; Bons et al. 2012). Regarding orientation, for the ATM system, the link between the dextral shear corridor and regional stress regime is well established (see above). In contrast, no vein folding can be observed in the granite probably due the rigid behavior of the intrusion relative to the surrounding schists. Furthermore, orientations of extensional Type I and II intragranitic veins are not consistent with deformation into a N170-N175°E dextral shear corridor and a NE-SW regional principal shortening direction. This could indicate that the AHT intragranitic veins formed in a structural context different from that specified for the ATM. However, this would imply strain rotation during granite crystallization, a hypothesis which appears unlikely given the short time lapses involved (e.g. ~4 My maximum for a granite body larger than the Argemela RMG, Scaillet et al. 1996). Likewise, the localized dextral shear corridor affects the eastern border of the intrusion suggesting that the two systems developed under the same deformation regime. In fact, localization of the strain along the shear planes bordering the granite shows that the intrusion behaved as a rigid body compared to the surrounding schists where deformation is pervasive. Furthermore, no macroscopic deformation has been observed in the core of the Argemela granite. This, added to the pipe-like geometry of the magmatic body (see Chapter II), suggests that simple dextral shearing could have led to a rigid rotation of the whole intrusion around a vertical axis. In such a setting, the Type I and II veins could have initially opened vertically in a ~NE striking regime, consistent with their extensional type and the regional-scale principal strain orientations. Later, the intrusion and the veins rotated together by about 20° clockwise. Late-magmatic rotations have been observed on bigger intrusions (see Olivier and Améglio 2002 and references therein). If a rotation of ~20° is considered, the coexistence of extensional N075°E type I, N060°E Type II and N096°E shear Type III veins would be consistent with a N170-175°E dextral shear corridor and a NE-SW shortening direction (Chapter II)

acting synchronously during granite emplacement. We conclude that the textural and geometrical specificities between, on the one hand, the Type I and II and, on the other hand, the Type III veins reflect a deformation continuum at the magmatic-hydrothermal transition as the granite intrusion progressively cooled and crystallized.

The structural compatibility between intragranitic and country rock vein sets suggests that both were emplaced contemporaneously, in the same deformation regime. Yet, differences occur in the type of veins developed and in their internal strain (e.g. vein geometries and behaviors during continuous shearing); these mainly result from the contrasted mechanical behavior of the two respective host rocks (granite vs. country rock schists) during continuous simple shearing and vein formation.

III.6.2. Mineralizing events and sequence

Structural, mineralogical data and observations allow distinguishing three main mineralizing episodes in the AMD (Fig. 13). These include (1) disseminated Sn-Nb-Ta-Li mineralizations, (2) vein-type (Sn)-W-Nb-Ta-Li and (3) vein-type Sn-(W)-Li mineralizations which, for the last two, are best represented by the AHT intragranitic and the ATM country rock veins, respectively. These three mineralizing episodes are expressions of a metallogenic evolution initiated at the magmatic stage (disseminated Sn-Nb-Ta-Li mineralizations), pursued during the magmatic-hydrothermal transition (intragranitic vein (Sn)-W-Nb-Ta-Li mineralizations) and ended with the development of hydrothermal circulations in country rocks (Sn-(W)-Li mineralizations). Therefore, an almost complete sequence of ore-forming processes, from magmatic to hydrothermal, is exposed in the AMD and especially in the AHT system. Although geochronological data are lacking for the ATM, the ATM and the AHT sub-systems developed in the same structural context and deformation regime. Therefore, the three main mineralizing episodes juxtaposed in the AMD form part of the same integrated ore-forming process. Below we describe the main steps of this process.

Disseminated mineralizations of magmatic origin are well expressed both in the ATM and AHT granite units. Early generations of Cst (Cst 1 and Cst I) appear as crystals disseminated in the whole

granite mass (Fig.13). In the Argemela RMG, Cst I showing growth zonations is associated with the crystallization of Li-P with, in some cases, Li-P being included in Cst I (Fig. 2). The presence of Li-P is specific of the AHT granite since the ATM granite is Li-P-free (Fig. 13). In contrast, CT is present as disseminated crystals in both granites. In the ATM granite, only Fe-columbite occurs while, in the Argemela RMG, CT I are Mn-columbite (Fig. 10). Disseminated Sn-Nb-Ta-Li mineralizations as in the ATM and AHT RMGs are well known in both Variscan and non-Variscan magmatic-hydrothermal systems (e.g., Cuney et al. 1992; Neiva 1996; Černý et al. 2005; Breiter et al. 2017). These deposits are interpreted as of magmatic origin because (i) ore minerals (Cst, Li-P, CT) appear relatively early in the granite crystallization sequence, (ii) Cst is typically enriched in Nb and Ta (Fig. 8 and 9; Tindle and Breaks 1998; Breiter et al. 2007; Neiva, 2008) and (iii) whole-rock granite rare metal concentrations are in the range of experimental cassiterite and columbo-tantalite solubilities (Linnen et al. 1995; 1996; Linnen and Keppler 1997).

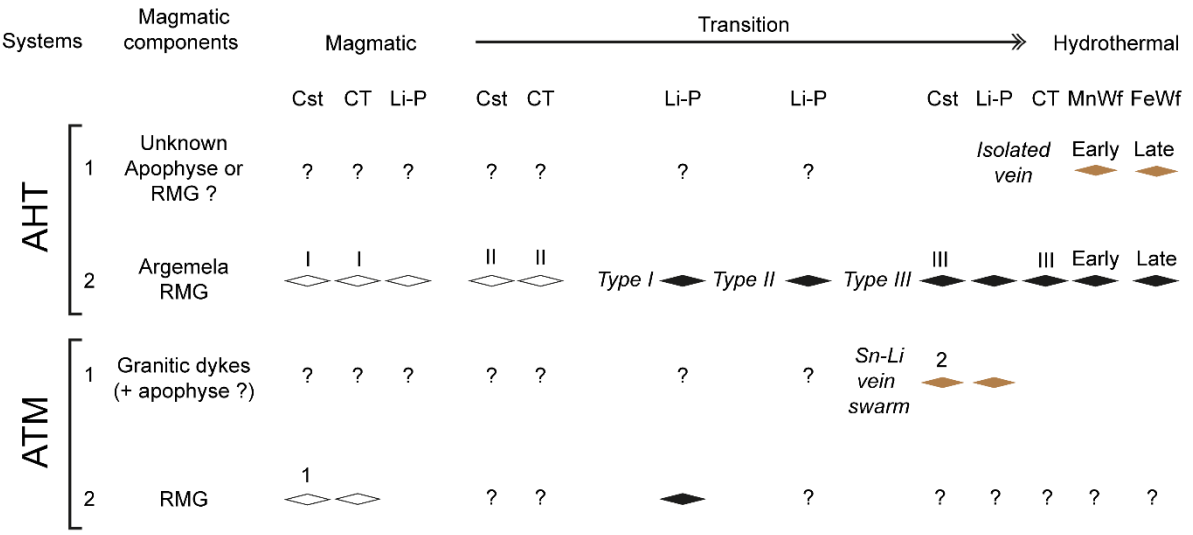

Fig 13 *Paragenetic sequence summarizing the sequence of mineralizing events and ore minerals deposition in the ATM and AHT systems. White diamonds: disseminated mineralization, black diamonds: granite-hosted vein-type mineralization; brown diamonds: schist-hosted vein-type mineralization. Labels next to the diamond symbols refer to the different ore mineral textural types*

distinguished in text. Abbreviations as in Fig. 2-4 and MnWf (Mn-rich wolframite), FeWf (Fe-rich wolframite). See text for details

The second generation of disseminated cassiterite (Cst II) encloses zoned Mn-columbite to Mn-tantalite (CT II) suggesting their co-crystallization (Fig. 2 and 10). The habit of Cst II suggests fast growth possibly assisted by a fluid phase and, therefore, crystallization of disseminated Cst II is the earliest indication for granite crystallization in presence of fluid, i.e., for fluid exsolution from the magma at the beginning of the magmatic-hydrothermal transition (Fig. 13). Crystallization of Cst II and CT within the granite mass indicates that fluid is able to percolate through the crystal mush. The fluid circulation mode then evolves from percolation to channeling leading to the intragranitic vein system exposed in the AHT. Vein emplacement within the Argemela RMG postdates the co-crystallization of Cst II and CT II in the granite mass (Fig. 13). Being confined within the granite with no extension into country rocks, the intragranitic vein system corresponds to magmatic fluids exsolved from the crystallizing body. Type I and II veins possess the strongest magmatic imprint. Type I veins have a coarse granitic-like internal texture (Fig. 3b; d) and a granitic mineralogical composition (presence of abundant alkali feldspars). They lack alteration aureoles at vein margins (this is also the case for the Type II and III veins) indicating chemical equilibrium with the host granite. It is worth stressing that neither cassiterite nor columbite-tantalite crystallizes in Type I and II veins which contain only montebrasite mineralization (Fig. 13). Mineralogical data demonstrates that the magmatic signature becomes progressively diluted from Type I and II to Type III veins (Fig. 13). The Type IIIa and the few wolframite-bearing (Wf I) veins still contain some alkali feldspars. However, veins with a larger amount of wolframite (Wf II and III) are alkali feldspars-free and contain cassiterite (Cst III) depleted in Nb+Ta and Fe-rich compared to Cst I-II. Such cassiterite geochemical signatures are interpreted as typically hydrothermal (Tindle and Breaks 1998; Breiter et al. 2007). Cst III shows an extensive replacement by stannite which is interpreted to indicate the influx of external sulfur-bearing fluids in the intragranitic hydrothermal system. CT III inclusions in wolframites are also more Fe-rich than disseminated columbite-tantalite (Fig. 10). Finally, some Type III and the Santa Rita vein, located E near the contact with the country rocks and close to the dextral shear, record an evolution toward texturally late, more

Fe-rich, wolframite compositions. These mineralogical changes go along with changes in vein geometry (branching/anastomosed vs straight) indicating a variation in host rock behavior from slightly ductile to fully brittle.

Mineralization in country rock veins can be viewed as an extension of the magmatic-hydrothermal system to the granite aureole. This type of mineralization is particularly well represented in the ATM, including montebrasite and, in some cases, cassiterite, but lacking columbite-tantalite and wolframite. Inverno and Ribeiro (1980) have previously interpreted the ATM system as a vein swarm genetically related to a granitic apophyse hidden at depth. The large number of veins together with their size is the mark of a large hydrothermal system. In the AHT, the only recognized country rock vein contains wolframite but no cassiterite. Early crystallizing wolframite are hubnerites in the middle of the range for wolframite in intragranitic veins (Fig. 11). Late crystallizing wolframite are ferberites. These latter compositions contrast with intragranitic veins but are well in the range of country rock veins nearby (Panasqueira, Neiva 2008). At Panasqueira, wolframite deposition involves fluid components coming from the country rocks (Lecumberri-Sanchez et al., 2017). At Argemela, the involvement of a non-magmatic component is also revealed by the presence of a late sulphide stage in both country rock and intragranitic veins. In the ATM, granite in the drill core is intersected by sulphide-bearing veinlets, and sulphides crystallize in veins, replacing cassiterite by stannite. In the AHT, sulphides are restricted to the eastern border of the granite which is affected by the N170-175°E trending dextral shear corridor. They are found in Type III veins as late arsenopyrite and vivianite and as disseminated crystals mostly around Type III veins in the granite.

III.6.3. Contrasted behaviour of Sn and W

The AHT system, where both Cst and Wf occur, provides a perfect example to illustrate the contrasted behaviour of Sn and W in Variscan granite-related mineralizations. In the Argemela RMG, clear evidence for magmatic tin enrichment is provided by the crystallization of disseminated Cst (see above). Both the Cst texture (e.g., growth zoning and inclusions) and chemistry (e.g., significant Nb and

Ta concentrations) indicate a magmatic origin. Whole-rock Sn concentrations in the Argemela granite are elevated and similar to other Variscan RMG (Cuney et al. 1992; Raimbault et al. 1995; Charoy and Noronha 1996; Chapter V; Table 1). They are in the same range than experimental cassiterite solubilities (Linnen et al. 1995; 1996; Bhalla et al. 2005) thus suggesting equilibrium between cassiterite and melt. LA-ICP-MS analyses show that micas from the granite contain significant Sn concentrations, in the 100 - 500 ppm range (see analyses in Chapter V; see also Neiva 1984; Neiva 1996). Magmatic Sn enrichment has been clearly demonstrated in peraluminous volatile-rich obsidians chemically similar to RMG (e.g., Macusani glasses, Pichavant et al. 1987; Richemont rhyolite, Raimbault and Burnol 1998) and in glass inclusions from Variscan magmatic-hydrothermal systems (e.g., Webster et al., 1997; Rickers et al., 2006). In the Argemela granite, magmatic Sn concentration processes led to Cst saturation and deposition as disseminated minerals. The AMD thus provides a clear example of a magmatic source for Sn.

In contrast, for W, no magmatic mineral carrier has been identified in the Argemela granite. Wolframite is absent as a magmatic phase and, in general, the existence of magmatic Wf is currently debated (Che et al. 2013 and references therein). Whole-rock W concentrations in the Argemela granite (Charoy and Noronha 1996; Table 1) are generally much less than experimental Wf solubilities although Wf saturation might be approached if granite crystallization takes place at < 600°C (Che et al. 2013). LA-ICP-MS analyses of micas sporadically show W concentrations in the 20 ppm range (Chapter V). These data consistently suggest that the Argemela granite magma did not reach Wf saturation, at the difference of Cst for Sn. However, this does not rule out the possibility of W concentration at the magmatic stage. Evidence for W concentration in RMG-like melts is provided by the Macusani glasses (Pichavant et al. 1987), the Richemont rhyolite (Raimbault and Burnol 1998) and the Ehrenfriedersdorf inclusions (Rickers et al. 2006). Although the available data on the AMD provides no constraint on W concentration levels in the melt, the mode of Wf mineralizations strongly suggest also a magmatic source for W.

The occurrence of Wf in Type III intragranitic veins constitutes the earliest mineralogical expression of W in the AMD ore-forming sequence. The Wf-bearing veins belong to the Type III veins, chronologically the latest among intragranitic veins. It is reminded here that intragranitic veins

correspond to dominantly magmatic fluids in equilibrium with the granite, and that the stable isotope data, ore mineral assemblages and compositions (see above) indicate that the hydrothermal system was largely isolated from the influence of external fluids derived from country rocks. The fact that Wf crystallized in intragranitic veins at equilibrium with the granite is strongly in favor of W having been supplied by the granite at the magmatic-hydrothermal transition.

This mode of expression of W mineralization markedly differs from what is observed in most Variscan deposits. For example, at Logrosán (Chicharro et al. 2016) and Panasqueira (Neiva 2008), Wf is exclusively deposited from high temperature hydrothermal systems with only indirect link with magmatic activity. At Cligga Head (Smith et al. 1996), there is a clear spatial relation with the magmatic system but the intragranitic Wf-bearing veins are bordered by hydrothermal alteration zones on their margins suggesting disequilibrium between the mineralizing fluids and the host granite. This stresses the specificity of the early Wf deposition stage in the AMD where a clear link with granite crystallization and fluid exsolution is evidenced. This difference between the AMD on the one hand and most Variscan deposits on the other hand is also marked on Wf compositions. Wf from intragranitic veins and the first generation of Wf in country rock vein are hübnerites, similar to most Portuguese pegmatitic and vein-type W-deposits (e.g. Neiva 1996; Neiva 2008). In contrast, Wf from Panasqueira and most deposits from the French Massif Central are ferberites. In the AMD, these compositions are only observed in the second generation of Wf (Fig. 11) and they correspond to Wf recrystallization, i.e., they are related to hydrothermal activity involving a non-magmatic fluid contribution. Therefore, in the AMD and possibly other Variscan deposits, the Fe/Mn ratio of wolframite is a potential marker of the origin and type of fluid involved in W deposition (Michaud and Pichavant, 2019).

III.6.4. Metallogenic model

According to our observations and interpretations, the ATM and the AHT are both composed of two sub-systems (Fig. 13). In the AHT, the isolated Wf-bearing vein intersected by the Argemela RMG marks a first, early, ore-forming stage. As Sn and W deposits involve generally a magmatic

component, we tentatively associate this hydrothermal vein with a hidden granitic apophyse or RMG (Fig. 13) at depth, schematically illustrated in Fig. 14. The second stage in the AHT is represented by the Argemela RMG which shows an entire sequence of mineralizing events from magmatic to hydrothermal. This stage thus differs from the first which exposes only a late hydrothermal event at the surface. In the ATM, the hydrothermal Sn-Li vein swarm is spatially associated with granitic dykes and a granite body. The granite at the tip of the studied core has characteristics of a RMG and it hosts intragranitic veins (Fig. 13). It appears almost isotropic while granitic dykes are strongly deformed. These latter have bulk rock compositions close to the RMG despite certain notable differences (e.g., As, Table 1). For these reasons, we suggest that the two magmatic components of the ATM (dykes and RMG) are not directly genetically related (Fig. 13). In our model, the granitic dykes are related to an apophyse from a hidden granite (see also Charoy and Noronha, 1996). The RMG (with its intragranitic veins) represents a distinct magmatic pulse that followed an independent magmatic-hydrothermal evolution (i.e., magmatic disseminated mineralization and intragranitic hydrothermal veins, Fig. 14). This interpretation is consistent with the size of the Sn-Li vein swarm which calls for large amounts of hydrothermal fluids. Given the restricted volume of RMG in the ATM, an additional magmatic fluid source seems required. This implies (as for the dykes) that the vein swarm is genetically related to the hypothetical granitic apophyse (Fig. 13), in agreement with conclusions from Inverno and Ribeiro (1980). The 4 magmatic-hydrothermal mineralization stages are schematically represented in Fig. 14.

Our observations and interpretations on the Sn-Li vein swarm (ATM) and the Argemela RMG (AHT) sub-systems are integrated in a metallogenic model, schematically illustrated in Figs. 14, 15 and 16. Cross-section of Fig. 14 show common features with the one proposed by Charoy and Noronha (1996), however, the Argemela pipe-like geometry, the mode of expression of deformation and intragranitic veins are detailed. Both sub-systems evolve independently at short distance but in the same structural setting and deformation regime. They are emplaced in a N170-175°E trending dextral shear corridor in the Fundão pluton pressure shadow zone and spotted schists, consistent with regional-scale NE trending principal shortening direction and NW trending principal stretching direction. However, due to differences in host rocks mechanical behavior, the mode of expression of deformation differs. In the Sn-Li vein-swarm, hosted by the Beira schists, the deformation is distributed (i.e. pervasive, Fig. 14;

15). In contrast, in the Argemela RMG sub-system, deformation is strongly localized along the northeastern border while the rest of the granite remains unsheared (Fig. 16b; c). This results in the formation of a dextral shear zone and the clockwise rigid rotation of the intrusion (Fig. 14; 16b; c).

In the ATM sub-system, we propose that the vein swarm emplaced during continuous shearing and in several discrete steps. Veins form as tension gashes in the direction of shortening (Fig. 15b), undergo clockwise rotation (Fig. 15c) and finally bending and shortening (Fig. 15d). Afterwards, new veins form and undergo the same deformational steps while bending and rotation of early veins continue (Fig. 15e; f). Our model for veins emplacement differs from the one of Inverno and Ribeiro (1980) on one point: there is no need to involve the emplacement of a granitic apophyse as the tectonic regime can explain veins orientations and thus is the main controlling factor.

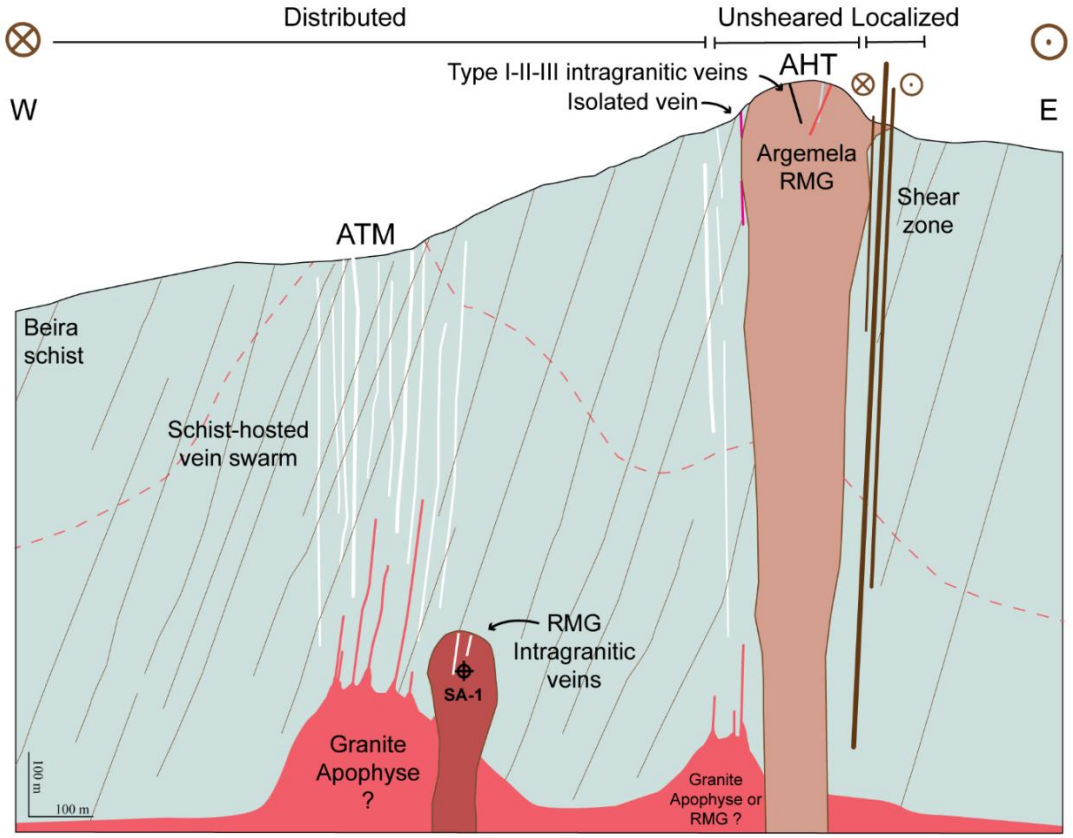

Fig 14 *Schematic cross section illustrating the four different magmatic-hydrothermal mineralization stages identified in the AMD; modified after Charoy and Noronha (1996). See text for explanation of the metallogenic model. Distributed, localized and unsheared refer to the mode of expression of the deformation. Dash-line refers to probable extension of the contact aureole. See text for additional details and explanation of the metallogenic model*

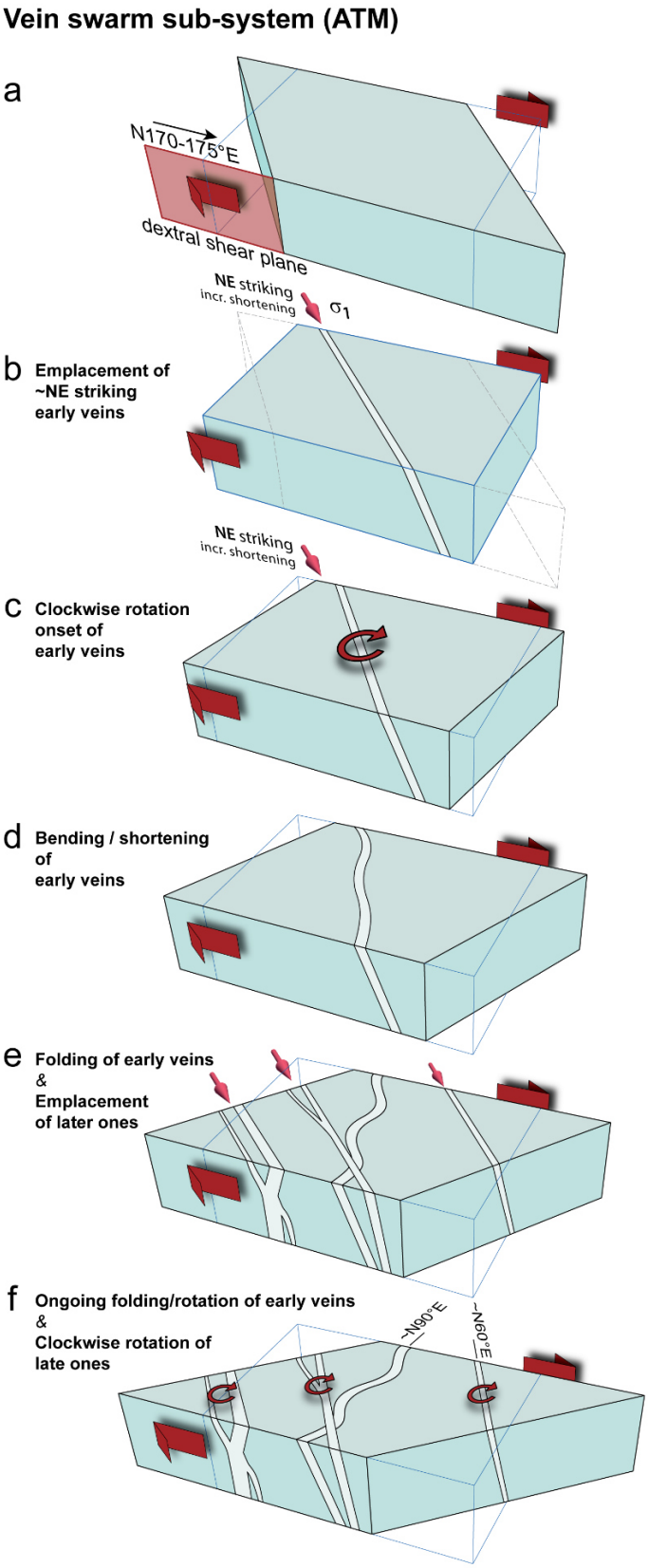

Fig 15 *Multi-stage model illustrating the sequential emplacement the Sn-Li vein swarm in the ATM. See text for explanations*

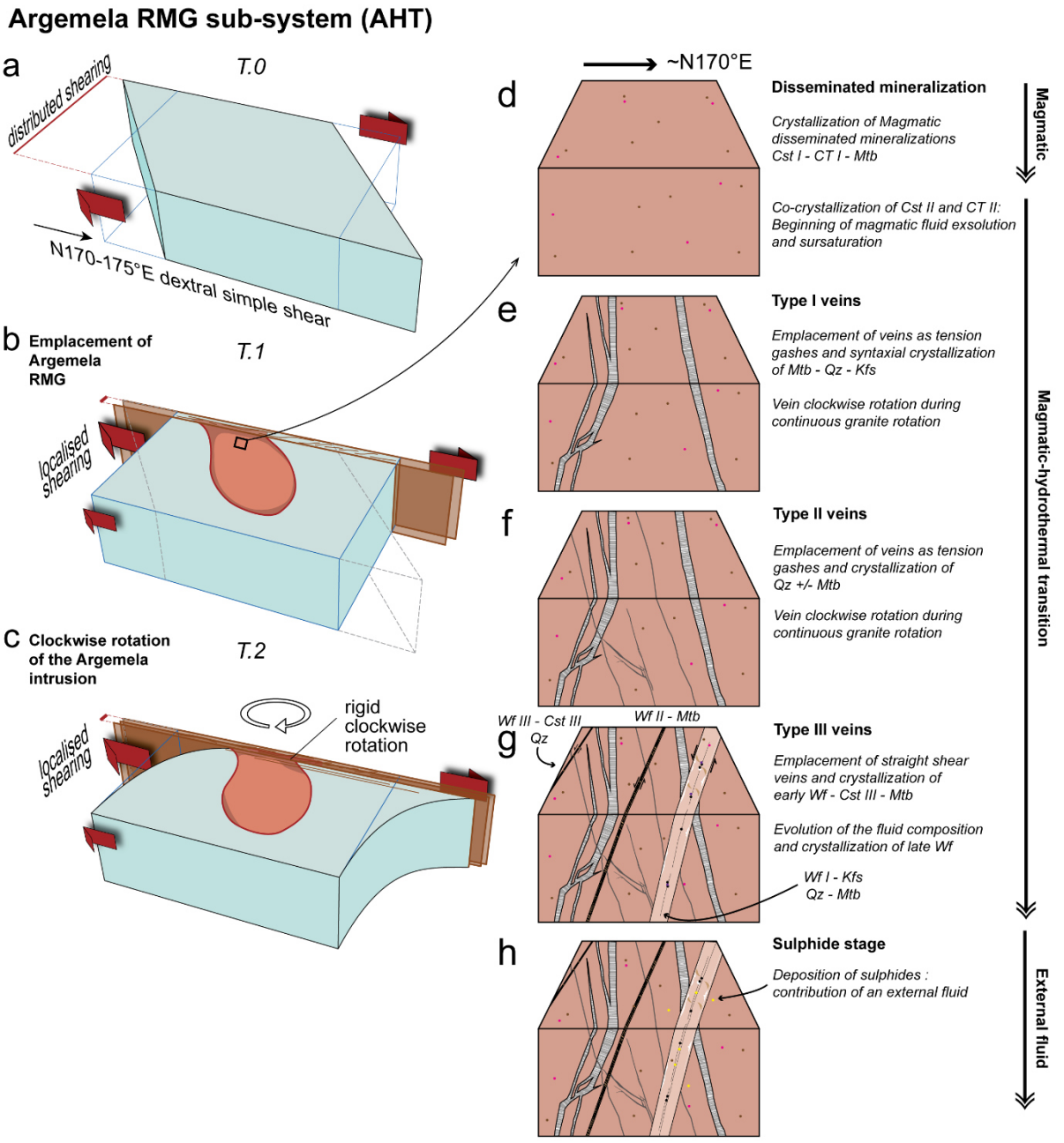

Fig 16 *Multi-stage model illustrating the sequence of mineralization events in the AHT. (a), (b) and (c) localization of deformation on the granite northeastern border and clockwise rigid rotation; (d), (e), (f), (g) and (h) emplacement of disseminated and intragranitic vein-type mineralization within the Argemela RMG. See text for additional explanations*

In the AHT sub-system, mineralization is associated with ~N170-175°E localized continuous dextral shearing and clockwise rigid rotation of the granite (Fig. 16a; b; c). Early magmatic disseminated mineralization including Cst I, CT I and Li-P is followed by the co-crystallization Cst II and CT II which

mark the beginning of fluid exsolution and the magmatic-hydrothermal transition (Fig. 16d). As the intrusion became more and more rigid with continuous crystallization, intragranitic vein replaces disseminated mineralization. Type I veins, with a typically magmatic assemblage and texture (i.e. Kfs and “pegmatitic”), are emplaced as ~N040°E tension gashes and followed by Type II veins. Both Type I and II veins undergo clockwise rotation (i.e. rotation of the entire intrusion) to ~N070°E and ~N060°E respectively (Fig. 16e; f). Then, Type III are emplaced as sinistral shear veins and mark the end of fluid exsolution from the Argemela RMG. They include the crystallization of early and late Wf, CT III and Cst III (Fig. 16g). At last, the sulphide stage marks the contribution of an external fluid (Fig. 16h).

III.7. CONCLUSIONS

Detailed field, structural and mineralogical data on the AMD have been integrated and a metallogenic model developed for this representative Variscan granite-related magmatic-hydrothermal mineralized district. The main key points of this study are as follow:

- The AMD comprises two spatially close mineralized sub-systems (the ATM and the AHT) that developed in the same structural context and deformation regime and thus provide independent information on the metallogenic evolution.

- Field, structural and mineralogical data allow distinguishing three mineralizing episodes in the AMD: (1) disseminated Sn-Nb-Ta-Li mineralizations, (2) intragranitic vein-type (Sn)-W-Nb-Ta-Li and (3) country rock vein-type Sn-(W)-Li mineralizations. These three episodes are markers of a continuous metallogenic sequence initiated at the magmatic stage, pursued during the magmatic-hydrothermal transition and ended with hydrothermal circulations in country rocks. The AMD, and especially the AHT sub-system, is a rare example among Variscan deposits where an entire sequence of mineralizing events from the magmatic to the hydrothermal stages can be observed.

- The structural context and host rock mechanical properties have a key importance in the distribution and expression of mineralizations, especially vein-type. Intragranitic veins are unfolded and either extensional or sheared while country rock veins are folded, despite all being formed in the same structural context.

- Disseminated mineralizations of magmatic origin include montebrasite, cassiterite (Nb-, Ta-rich) and columbite-tantalite of variable composition. Intragranitic veins are mineralized in Li but not in Sn, Nb, Ta, except for the last vein generation in the AHT which also hosts wolframite, colombite-tantalite and cassiterite (almost pure SnO_2). Country rock veins carry Li, Sn (ATM) and locally W (AHT) mineralizations.

- Sn and W show a markedly contrasted behavior in the AMD. Sn enrichment at the magmatic stage is marked by disseminated cassiterite mineralization. In contrast, no magmatic mineral carrier for W is present. The earliest mineralogical expression of W in the ore-forming sequence is Mn-rich

wolframite (hübnerite) present in intragranitic veins. Therefore, wolframite deposition in the AMD can be related to the exsolution of magmatic fluids which is strongly unusual among Variscan W deposits.

CHAPTER IV:

THE H/F RATIO AS AN INDICATOR OF CONTRASTED WOLFRAMITE DEPOSITION MECHANISMS

ABSTRACT

Understanding wolframite deposition mechanisms is a key to develop reliable exploration guides for W. In quartz veins from the Variscan belt of Europe and elsewhere, wolframites have a wide range of compositions, from hübnerite- ($MnWO_4$) to ferberite-rich ($FeWO_4$). Deposition style, source of Mn and Fe, distance from the heat/fluid source and temperature have been proposed to govern the wolframite H/F (hübnerite/ferberite ratio) defined as 100 at. Mn / (Fe + Mn). The Argemela mineralized district, located near the world-class Panasqueira W mine in Portugal, exposes a quartz-wolframite vein system in close spatial and genetic association with a rare-metal granite. Wolframite is absent as a magmatic phase, but W-rich whole-rock chemical data suggest that the granite magma is the source of W. Wolframite occurs as large homogeneous hübnerites (H/F = 64-75%) coexisting with montebrasite, K-feldspar and cassiterite in the latest generation of intragranitic veins corresponding to magmatic fluids exsolved from the granite. Locally, early hübnerites evolve to late more Fe-rich compositions (H/F = 45-55%). In a country rock vein, an early generation of Fe-rich hübnerites (H/F = 50-63%) is followed by late ferberites (H/F = 6-23%). Most Argemela wolframites have H/F ratios higher than at Panasqueira and other Variscan quartz-vein deposits which dominantly host ferberites. In greisens or pegmatitic veins, wolframites generally have intermediate H/F ratios. In those deposits, fluid-rock interactions, either involving country rocks (quartz-veins) or granite (greisens) control W deposition. In contrast, at Argemela, wolframite from intragranitic veins was deposited from a magmatic fluid. Differentiation of highly evolved peraluminous crustal magmas led to high Mn/Fe in the fluid which promoted the deposition of hübnerite. Therefore, the H/F ratio can be used to distinguish between contrasted deposition environments in perigranitic W ore-forming systems. Hübnerite is a simple mineralogical indicator for a strong magmatic control on W deposition.

THE H/F RATIO AS AN INDICATOR OF CONTRASTED WOLFRAMITE DEPOSITION MECHANISMS

Published to Ore Geology Reviews

(see article in Annexe)

IV.1. INTRODUCTION

W is a critical metal, essential for many industrial applications. As for other metals and commodities, exploration for W now focuses on sub-surface to deep contexts in complex geological settings (e.g., Poitrenaud, 2018, www.almonty.com, www.wolfminerals.com.au). Targeting of mineralized systems requires the integration of geological, geophysical and geochemical data sets and their interpretation in the light of an ore deposition model (McCuaig et al., 2010; McCuaig and Hronsky, 2014). With the development of analytical tools, mineralogical compositions of both gangue and ore minerals are increasingly used to footprint the presence of proximal orebodies (Belousova et al., 2002; Codeço et al., 2017; Harlaux et al., 2018a; Neiva, 2008).

W mineral deposits include quartz veins, stockworks, greisens, skarns and breccia pipes spatially associated with granitic bodies, and are thought to result from magmatic and hydrothermal processes, combined (Bobos et al., 2018; Harlaux et al., 2015; Kelly and Rye, 1979; Ramboz et al., 1985; Smith et al., 1996). Although the main parameters controlling the transport of W have been identified (Che et al., 2013; Heinrich, 1990; Wood and Samson, 2000), there is as yet no comprehensive model for W deposition.

Quartz veins such as found in Southeast China and in the Variscan belt of Europe form an important class of W deposits. W, in the form of the dominant ore mineral wolframite ([Fe,Mn]WO4), is generally associated with other metals such as Sn, Cu, Ag. The group of quartz-wolframite deposits is diverse. It includes intragranitic (e.g., Smith et al., 1996) and country rock (e.g., Kelly and Rye, 1979)

veins with a wide range of geometries, widths and extensions (e.g., Giuliani, 1985). Quartz and wolframite can be accompanied by various gangue (e.g., tourmaline, Codeço et al., 2017) and ore (e.g., cassiterite, Noronha et al., 1992) minerals. Wolframites have compositions ranging from hübnerite ($MnWO_4$) to ferberite ($FeWO_4$, e.g., Harlaux et al., 2018a; Lecumberri-Sanchez et al., 2017). Factors of controls of wolframite composition are the subject of an intense debate. The deposition style, source of Mn and Fe, distance from the heat/fluid source and temperature have been proposed to govern the wolframite H/F (i.e., hübnerite/ferberite) ratio, hereafter calculated as 100 at. Mn / (Fe + Mn). Hosking and Polkinghorne (1954) pointed out that wolframites in Cornish pegmatites are relatively Mn-rich while wolframites from quartz veins have high Fe contents. Greisens generally have wolframites with intermediate Fe/Mn (e.g., Breiter et al., 2017; Hosking and Polkinghorne, 1954). Several studies have suggested that Mn-rich wolframites precipitate at higher temperatures than Fe-rich wolframites (e.g., Oelsner 1944, Leutwein 1952, Taylor and Hosking 1970). However, attempts to use the H/F ratio as a geothermometer (Moore and Howie, 1978) have failed as temperature is not the only factor controlling wolframite composition (Amossé, 1978).

Recent studies in the Central Iberian Zone (which includes the world class Panasqueira W deposit) have identified a quartz-wolframite vein system (see details in Chapter V) spatially and genetically associated with a Rare-Metal Granite (RMG), the Argemela granite (Charoy and Noronha, 1996). Field, structural, mineralogical and geochemical evidence suggest that the intragranitic wolframite-bearing veins are the expression of magmatic fluids exsolved from the granite at the magmatic-hydrothermal transition. Below, the main characteristics of the Argemela veins are summarized and compared with other W vein systems. Focus is placed on wolframite compositions, essentially Mn-rich at Argemela and Fe-rich in the neighboring Panasqueira and most other Variscan country rock vein systems. This first-order compositional contrast between wolframites suggests major differences in W deposition mechanisms. It is proposed that the H/F ratio can be used as an exploration tool to help distinguishing between contrasted types of W deposition environments.

IV.2. ANALYTICAL TECHNIQUES

Samples from the Argemela W veins were collected and thin as well as polished sections prepared. Preliminary petrographic and textural observations were conducted with a petrographic microscope. Backscattered electron (BSE) images and EDS element mapping were obtained using a Merlin compact ZEISS Microscope equipped with a Bruker EDS detector and working under an acceleration voltage of 15 kV. Wolframites were analyzed by electron microprobe at ISTO, Orléans (France). Punctual analyses, traverses and elements distribution maps for major and minor elements were obtained with a CAMECA SX Five microprobe operated under an acceleration voltage and a beam current of 20 kV and 40 nA respectively. Standards included SnO_2 (Sn$L\alpha$), Fe_2O_3 (Fe$K\alpha$), $MnTiO_3$ (Mn$K\alpha$ and Ti$K\alpha$) and pure Nb (Nb$L\alpha$), Ta (Ta$L\alpha$) and W (W$L\alpha$) metals. Relative errors for wolframites are calculated as ((standard deviation x 100) / mean) for each major element using a homogeneous population and are: 3.7% for MnO, 8.5% for FeO and 0.6% for WO_3.

IV.3. THE ARGEMELA W VEIN SYSTEM

The Variscan Argemela Mineralized District (AMD) occurs within the Central Iberian Zone (CIZ, Central Portugal) and is divided in two subsystems at < 0.5 km from each other but evolving separately. The first (the Argemela tin mine, ATM) consists of a vein swarm emplaced in low grade metamorphic rocks from the Neoproterozoic Schist and Greywacke Complex (SGC, Meireles et al., 2013). Veins can be up to 2 m wide, are anastomosed and contain Sn and Li mineralization in the form of cassiterite and montebrasite. No W concentration has been recognized. The second (the Argemela Hill Top, AHT) comprises a RMG with disseminated Li, Sn, Nb, Ta mineralization in the form of magmatic montebrasite, cassiterite and columbo-tantalite. The granitic intrusion is associated with a network of intragranitic veins, and a few quartz veins occur in country rocks near the granite contact. Although wolframite is absent as a magmatic phase, W enrichment is marked by granite whole-rock concentrations ranging up to ~20 ppm W (Charoy and Noronha, 1996). Three generations of intragranitic veins occur within the granite. Field evidence (confinement of veins inside the granite), structural (granite and veins are emplaced in the same structural context), mineralogical (veins lack hydrothermal alteration aureoles and the earliest have a “pegmatitic” texture and a granitic mineral assemblage) and stable isotope data indicate that the intragranitic veins are the expression of fluids exsolved from the granite at the magmatic-hydrothermal transition (Chapter V).

Table 1

Representative electron microprobe analyses of wolframite from the Argemela Mineralized District

Major Elements (wt%)	E WI		Mean (19)	σ	L WI		Mean (9)	σ	E WII		Mean (32)	σ	L W II		Mean (25)	σ
	min	max			min	max			min	max			min	max		
MnO	15.40	12.21	14.58	0.92	5.75	1.40	3.37	1.59	18.15	15.59	17.27	0.69	13.26	10.82	12.18	0.93
FeO	8.98	12.24	9.88	0.97	19.08	23.41	21.32	1.50	6.19	8.82	7.17	0.67	10.95	13.53	12.37	0.94
Nb_2O_5	0.59	0.22	0.36	0.15	0.36	0.60	0.40	0.19	0.74	0.49	0.46	0.22	0.74	1.05	0.68	0.25
SnO_2	0.08	0.01	0.04	0.03	-	-	0.02	0.02	-	0.07	0.05	0.07	0.13	0.15	0.10	0.06
Ta_2O_5	0.11	-	0.06	0.06	0.04	0.09	0.04	0.05	-	0.10	0.16	0.25	0.36	0.22	0.18	0.19
WO_3	76.65	76.97	76.95	0.34	76.67	76.81	76.88	0.43	75.62	75.62	76.55	0.63	75.99	75.12	76.05	0.52
Total	101.96	101.81	102.00	0.32	102.04	102.52	102.24	0.39	100.71	100.79	101.68	0.42	101.50	100.96	101.65	0.41
Number of cations based on 4 oxygens																
Mn	0.643	0.513	0.610	0.038	0.241	0.058	0.141	0.067	0.767	0.660	0.724	0.028	0.557	0.456	0.511	0.038
Fe	0.370	0.507	0.408	0.040	0.789	0.964	0.881	0.062	0.258	0.368	0.297	0.028	0.454	0.563	0.513	0.040
Nb	0.013	0.005	0.008	0.003	0.008	0.013	0.009	0.004	0.017	0.011	0.010	0.005	0.017	0.024	0.015	0.006
Sn	0.002	-	0.001	0.001	-	-	-	-	-	0.001	0.001	0.001	0.003	0.003	0.002	0.001
Ta	0.001	-	0.001	0.001	0.001	0.001	0.001	0.001	-	0.001	0.002	0.003	0.005	0.003	0.002	0.003
W	0.980	0.989	0.986	0.003	0.983	0.980	0.985	0.004	0.978	0.979	0.982	0.006	0.977	0.969	0.976	0.006
Total	2.013	2.014	2.014	0.002	2.021	2.017	2.016	0.004	2.020	2.021	2.016	0.004	2.012	2.019	2.019	0.004
H/F	63.5	50.3	59.9	3.9	23.4	5.7	13.8	6.4	74.8	64.2	70.9	2.8	55.1	44.8	49.9	3.8

E: Early and L: Late. WI: wolframite in country rock vein; WII: wolframite in intragranitic vein. For each wolframite type, min and max are compositions that give the minimum and maximum H/F ratios respectively. The H/F ratio is calculated as 100 at. Mn/(Fe+Mn).

Wolframite occurs in variable amounts in the third and latest generation of intragranitic veins which are numerous but of restricted size, never exceeding a 10 cm width. It is mostly associated with quartz, K-feldspar and montebrasite, with quartz and montebrasite only in some other veins, and cassiterite is occasionally present. Wolframites form mostly large homogeneous crystals with hübnerite compositions (early WII, H/F between 64 and 75%, Table 1 and Fig.1). On the eastern border, the granite is affected by a dextral shear zone and the intragranitic veins host wolframites with a patchy texture made of early hübnerites evolving to more Fe-rich compositions (late WII, H/F from 45 to 55%, Table 1, Fig.1, e.g. Baumann 1964). This late wolframite ore deposition stage is followed by sulfides (arsenopyrite) and other phases (vivianite); cassiterite is transformed into stannite.

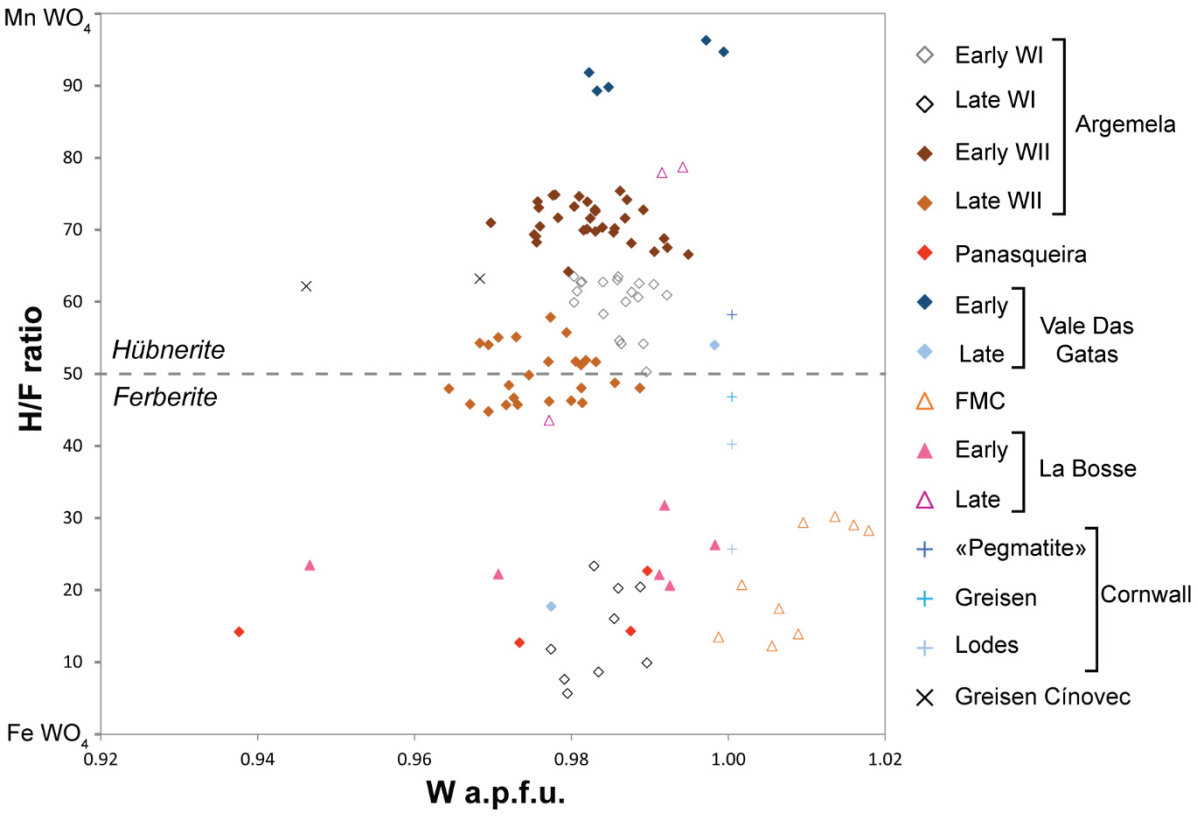

Fig 1 *H/F ratio vs atomic W concentration for wolframites from representative Variscan deposits. Argemela data are from this study (Table 1). For other deposits see references in Table 2*

Table 2

Compositional data for wolframites from representative Variscan deposits

Name	Metallogenic province	Deposit type	Deposition stage	H/F	Mean	σ	W a.p.f.u.	References
Vale Das Gatas	Variscan - Portugal	Intragranitic and country rocks veins	Early	96.2	92.30 (5)	3.05	1.00	Neiva 2008
				89.2			0.98	
			Late	54.0	35.86 (2)	25.62	1.00	
				17.7			0.98	
Panasqueira	Variscan - Portugal	Country rocks veins		22.7	16.00 (4)	4.51	0.99	Neiva 2008
				12.7			0.97	
Enguialès -Leucamp	Variscan - FMC	Country rocks veins		30.2	22.37 (10)	7.53	1.00	Harlaux et al., 2017
				12.3			1.02	
St Goussaud	Variscan - FMC	Intragranitic and country rocks veins		24.7	22.74 (5)	1.66	1.01	Harlaux et al., 2017
				20.4			1.00	
La Bosse	Variscan - FMC	Country rocks veins	Early	31.8	24.43 (6)	4.06	0.99	Aïssa et al., 1987
				20.7			0.99	
			Late	78.7	64.20 (4)	17.10	0.98	
				43.6			0.99	
Le Mazet	Variscan - FMC	Country rocks vein		78.8	-	-	-	Aubert 1969
Gilbert	Variscan - FMC	Country rocks vein		88.2	-	-	-	Aubert 1969
Cornish wolframites	Variscan - Cornwall	"Pegmatitic veins"		58.2	52.5 (2)	8.06	1.00*	Hosking and Polkinghorne 1954
				46.8			1.00*	
		Greisen		46.8	43.52 (2)	4.63	1.00*	
				40.3			1.00*	
		Lodes		40.3	32.97 (2)	10.29	1.00*	
				25.7			1.00*	
Cligga Head	Variscan - Cornwall	Intragranitic veins		35-40+	-	-	-	Unpublished
Cínovec	Variscan - Bohemian Massif	disseminated in greisen		63.6	57.70 (6)	7.45	0.90	Breiter et al., 2017
		quartz veins and greisen		45.8			0.82	

Maximum and minimum H/F values are shown for each type. + data obtained from EDS. *fixed to 1 (no data available).

Wolframite is also present in one country rock vein crosscut by the granite. It appears as large crystals and in variable amounts associated with milky geodic quartz typical of hydrothermal veins in the AMD. In contrast to intragranitic veins, K-feldspar is absent. Wolframite crystals can be homogeneous but most show textural evidence for recrystallization (Fig.2). Early wolframites are Fe-rich hübnerites (early WI, H/F from 50 to 63%, Table 1 and Fig.1). The second generation crystallizes in fractures or near the margins of early wolframites and is a ferberite with high Fe contents (late WI, H/F = 6-23%, Table 1, Fig.1 and 2). This late stage is followed by the deposition of iron oxides.

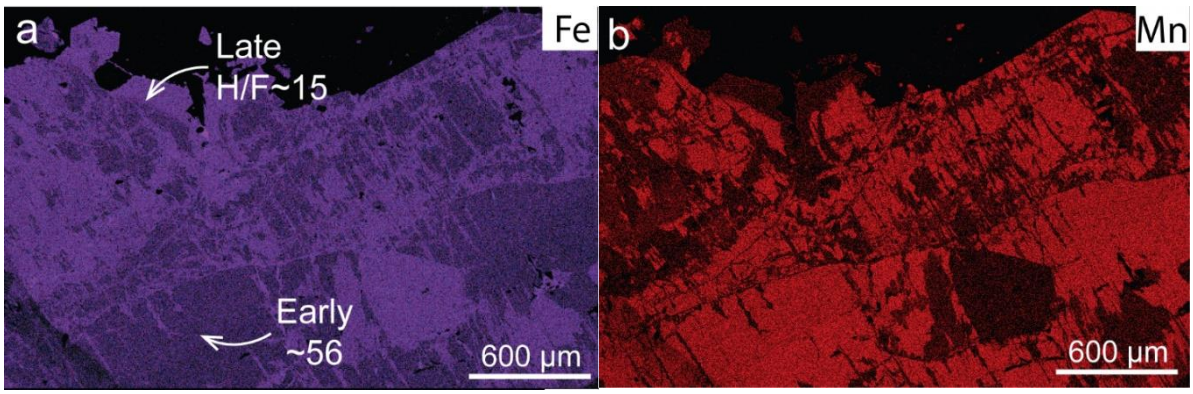

Fig 2 *Patchy texture of Argemela WI (schist-hosted vein) illustrating evolution of the H/F ratio between early and late crystallization stages. EDS map of (a) Fe and (b) Mn*

IV.4. COMPARISON WITH OTHER WOLFRAMITE VEIN-SYSTEMS

Wolframite occurs as the dominant ore mineral in several types of Variscan W deposits and is characterized by highly variable compositions, from hübnerite to ferberite. The Panasqueira W world class mine, located at only 13 km west from Argemela, provides an excellent comparison point with the AMD. The deposit consists of > 1000 nearly horizontal veins emplaced in SGC metamorphic rocks on top of a granite cupola (Neiva, 2008; Foxford et al., 2000). The hydrothermal veins, which can exceed 1 m widths, host wolframite, quartz, muscovite, tourmaline, topaz, arsenopyrite and early cassiterite (Kelly and Rye, 1979, Polya et al., 2000). Wolframites form large chemically homogeneous crystals with H/F ratios generally < 23% (e.g. ferberite), in strong contrast with most AMD wolframites (Table 2 and Fig.1). Same as at Panasqueira, in the French Massif Central (FMC), most Variscan W deposits show wolframites with ferberite compositions (Harlaux et al., 2018 and references therein, Table 2 and Fig.1). For example, the stockwork of La Bosse (north FMC) consists in a network of interconnected subhorizontal quartz veins emplaced in metamorphic rocks; wolframite has H/F ratios between 21 and 32% (Aubert, 1969; Aïssa et al., 1987a, Table 2 and Fig. 1). Other representative examples of ferberite-bearing vein-type W deposits in the FMC include Enguialès, Leucamp and St-Goussaud (e.g., Harlaux et al., 2018 and references therein). Both the Panasqueira and the FMC deposits are representative of perigranitic hydrothermal systems developed in metamorphic country rocks. In the case of Panasqueira, ferberite deposition is controlled by fluid-rock interactions involving SGC country rocks (Lecumberri-Sanchez et al., 2017) and, so, there is a significant non-magmatic contribution to the ore-forming system (e.g., Polya et al., 2000).

Other Variscan W deposits show a closer spatial association with granitic rocks. This is the case of Cligga Head (Cornwall, UK) where wolframite is deposited together with cassiterite, arsenopyrite and other sulfides in a dense network of intragranitic veins (Charoy et al., 1979). Wolframite is ferberite-rich (H/F = 35-40%, Table 2, Charoy, 1979; Michaud, unpublished) and, although the mineralizing fluids have been interpreted as magmatic (Smith et al., 1996), W deposition at Cligga Head is associated with hydrothermal alteration around the veins indicating fluid-granite equilibration at subsolidus

temperatures (300-400°C, Charoy, 1979). At Cínovec (Bohemia, DE and CZ), wolframite occurs disseminated both in greisens and in quartz veins within the host RMG. H/F ratios are intermediate (between 45 and 63%, Table 2 and Fig.1, Breiter et al., 2017) consistent with the presence of sub-equal concentrations of Fe and Mn in fluid inclusions (Korges et al., 2018). Sn-W deposition is associated either with greisenisation of the granite (i.e., with fluid-rock reaction at subsolidus temperatures) or with boiling of the magmatic fluid (Korges et al., 2018). Last, deposits from Cornwall (UK) demonstrate a systematic decrease of H/F ratios from pegmatites and early feldspathic veins (H/F = 47-58), greisens (H/F = 40-47) to quartz lodes (H/F = 26-40, Table 2 and Fig.1, Hosking and Polkinghorne 1954). In the South Crofty Mine, the "pegmatitic vein swarms", mainly composed of quartz, feldspar and other accessory minerals, contain wolframites of intermediate compositions (H/F = 37-60, Taylor and Hosking, 1970).

In some deposits, several wolframite crystallization stages can be identified, indicating distinct deposition mechanisms. For example, the La Bosse stockwork contains a late generation of hübneritic wolframite (H/F = 44-79%, Table 2 and Fig.1) developed in minor amounts on early ferberites (H/F = 21-32%, see above) and attributed to the influence of the late Beauvoir RMG (Aïssa et al., 1987). Isolated hübnerite-bearing veins occur north of the La Bosse deposit (e.g., Le Mazet and Gilbert veins, Table 2) and they have been interpreted as footprints of another Beauvoir-type RMG at depth (Aubert, 1969). In the Portuguese CIZ, the Vale Das Gatas deposit consists of quartz veins cutting the contact between SGC country rocks and a muscovite>biotite granite (Neiva, 2008). The veins are characterized by at least two ore deposition stages, the first involving cassiterite and wolframite and the second only wolframite. Wolframites are mostly hübnerites (H/F = 89-96%) except rims that range from Fe-rich hübnerite to ferberite (H/F = 18-54%, Table 2 and Fig.1).

IV.5. WOLFRAMITE DEPOSITION MECHANISMS

None of the wolframite deposition mechanisms mentioned above is directly applicable to the AMD since none explains the precipitation of hübnerite directly from a magmatic fluid. At Argemela, the W-bearing intragranitic veins show no hydrothermal interaction aureole at their margins. The earliest veins exhibit "pegmatitic" textures and crystallize a granitic mineral assemblage (Chapter V). Quartz in the granite and veins both have high δO^{18} values (respectively 13.7-14.5 and 14.5-15.9 ‰). Therefore, the intragranitic veins formed from fluids exsolved from the crystallizing granite and fluid-granite equilibration was originally established at relatively elevated temperatures. Using solidus temperatures for RMG (Pichavant et al., 1987a) and oxygen isotope thermometry on quartz and muscovite from the granite, magmatic fluids were originally at equilibrium with the granite at temperatures of 500-550°C. Their subsequent evolution within the intragranitic veins most probably followed a fluid-buffered instead of a rock-buffered path (e.g., Heinrich, 1990). There is no evidence for postmagmatic hydrothermal interaction processes such as greisenisation around the veins. Quartz from the relatively late wolframite-bearing veins have the same stable isotope signature (δO^{18}: 15.5-15.9 ‰ ; δD: -25 to -31 ‰) than quartz from the early veins (δO^{18}: 14.5-15 ‰ ; δD: -21 to -35 ‰). Furthermore, the surrounding Beira schists are W-depleted and cannot be the source of W (Charoy and Noronha, 1996). Although the intragranitic vein system was not closed to external non-magmatic contributions (as suggested by the mineralogical data summarized above), wolframite deposition in the Argemela intragranitic veins resulted from cooling of the igneous fluid in isolation from the enclosing rock, in contrast with mechanisms proposed for W deposition in other contexts (e.g., Lecumberri-Sanchez et al., 2017).

Wolframite deposition necessitates a source of Fe and Mn, in addition to W. Amossé (1978) demonstrated that the composition of the deposited wolframite depends essentially on two factors, temperature and aMn/aFe of the ore fluid. The Mn/Fe ratio is always higher (and so the H/F ratio higher) in the deposited wolframite than in the equilibrium fluid. Because lowering temperature slightly increases Mn/Fe in wolframite, Amossé (1978) emphasized the importance of the Mn/Fe ratio of the

mineralizing fluid as the main factor controlling wolframite composition. At Argemela, the Mn/Fe of the ore fluid is defined by fluid/melt partitioning for Mn and Fe. Both elements partition similarly between melt and fluid as shown by their nearly identical ratios in coexisting silicate melt and fluid inclusions from Ehrenfriedersdorf (Zajacz et al., 2008). Thus, the Mn/Fe of the magmatic fluid that deposited hübnerite at Argemela was essentially that of the crystallizing granitic melt. Although this Mn/Fe ratio is unknown, Variscan RMG (e.g., Beauvoir, Raimbault et al., 1995) and pegmatites (Chèdeville, Raimbault, 1998), and equivalent volcanic products (Macusani, Pichavant et al., 1987b), demonstrate a general increase of Mn/Fe during magmatic differentiation. The whole-rock data for the Argemela granite show such an increase (Charoy and Noronha, 1996), also marked in the enrichment of disseminated columbo-tantalites in $MnTa_2O_6$ (Chapter V, see also Raimbault, 1998; Linnen and Cuney, 2005). Therefore, the magmatic evolution of the Argemela RMG led to the exsolution of relatively high Mn/Fe igneous fluids. We suggest that the deposition of hübnerite in perigranitic magmatic-hydrothermal systems is the signature of metals and fluids originating from highly evolved peraluminous crustal magmas similar to the Argemela granite.

Tungsten is known to be transported in hydrothermal fluids as an oxyanion, WO_4^{2-}, complexed with Na+, K+, or H+ (Wood and Samson, 2000; Heinrich, 1990). Substitution of Na for Li does not change wolframite solubilities in granitic melts (all the other parameters being equal, Linnen, 1998) and, so, Li is a W complexing agent with an efficiency comparable to Na. Thus, destabilization of Li-W complexes as a result of precipitation of a Li-bearing phase will cause wolframite deposition. Montebrasite ($LiAlPO_4$ (OH, F)) is a systematic phase in the Argemela intragranitic veins where it is accompanied by K-feldspar (whose crystallization removes K from the fluid). Muscovite never occurs as a mineral in the veins suggesting that the pH of the fluid was never strongly acid. Compositions of montebrasites (details in Chapter V) in K-feldspar-bearing veins show no variations in F content (Loh and Wise 1976) and so deposition was probably not driven by a drastic increase of the fluid pH. However, montebrasites from montebrasite-wolframite veins can have F contents nearly twice as elevated as montebrasites in K-feldspar-bearing veins, which indicates a significant pH decrease (thus counteracting wolframite precipitation). Therefore, a decrease in temperature is probably the main factor controlling wolframite deposition (Heinrich 1990).

One element specific of the Argemela magmatic-hydrothermal system is phosphorus. The Argemela granite, with whole-rock concentrations of up to ~2 wt% P2O5 (Charoy and Noronha, 1996), is a good example of a peraluminous high phosphorus (PHP) rare-metal granite (Linnen and Cuney, 2005). Montebrasite crystallizes as a magmatic phase in the Argemela granite and is also a key phase in intragranitic veins (Charoy and Noronha, 1996). Phosphorus increases wolframite solubility in peraluminous granitic melts (Che et al., 2013). Its influence is however indirect, through the formation of AlPO4 species which increases the availability of Na, K and Li to complex with W. Therefore, removal of such species by phosphate crystallization will cause wolframite deposition. The overall mechanism of wolframite precipitation in the Argemela intragranitic vein system is summarized with the following reaction:

$$\underset{\text{fluid}}{Li\,NaWO_4} + \underset{\text{fluid}}{(Mn, Fe)^{2+}} + \underset{\text{fluid}}{AlPO_4} + \underset{\text{fluid}}{H_2O} = \underset{\text{montebrasite}}{LiAlPO_4OH} + \underset{\text{wolframite}}{(Mn, Fe)WO_4} + \underset{\text{fluid}}{Na^+} + \underset{\text{fluid}}{H^+} \quad (1)$$

An equivalent reaction can be written for the fluorine Li phosphate end-member (amblygonite). Equation (1) is probably driven to the right by a decrease in temperature, i.e., by cooling of the intragranitic vein fluids.

IV.6. DISCUSSION AND IMPLICATIONS FOR EXPLORATION

The model proposed for Argemela emphasizes the differences with other W deposition environments, and has direct implications for exploration. The model applies to hübnerite deposition from a magmatic fluid. Wolframite composition reflects enrichment in Mn relative to Fe in the crystallizing granite which is the source of both W and fluids. Wolframite deposition calls upon a specific chemical environment (presence of both Li and P) in a magmatic-hydrothermal system that evolves under fluid-buffered conditions. Li, together with F and P, is systematically enriched in Variscan granitoïds from the CIZ (Roda-Robles et al., 2018 and references therein). Such anomalies reflect the specific chemistry (Al-, P-, F- and Li-rich, Ca-poor) of the metasedimentary rock sources of granitic magmas (Roda-Robles et al., 2018). The Li- and P-rich geochemical signature exhibited by the Argemela granite is a reflection of such specific crustal sources. Therefore, the W deposition mechanism proposed at Argemela also probably applies to other similar W occurrences in the CIZ.

The model for the AMD differs from others where a magmatic source for W is assumed but fluid interactions with country rocks are considered necessary for W deposition (Lecumberri-Sanchez et al., 2017). One first-order difference between the two types of models is that, in the former case, veins are intragranitic (Argemela) and, in the latter, within country rocks (Panasqueira). Therefore, each corresponds to a specific type of W deposition environment, as reflected by the composition of wolframite, hübnerite in the former and ferberite in the latter (Fig.3). In the case of intragranitic vein systems, a magmatic origin for the ore fluid has been generally proposed (e.g., Korges et al., 2018; Smith et al., 1996). However, one major difference between Argemela and these systems (Cligga Head and Cínovec respectively) is the temperature and mechanism of fluid-rock equilibration. At Argemela, the composition of the ore fluid is defined by fluid/melt equilibrium at near-solidus temperatures; the magmatic fluid evolves along a fluid-buffered path. At Cligga Head and Cínovec, the fluid is buffered by fluid-rock interaction at subsolidus temperatures (greisenisation). Therefore, Argemela can be viewed as a high temperature variant of the Cligga Head and Cínovec cases. Preservation of the high temperature intragranitic vein system at Argemela was probably favored by the small volume of the

granite intrusion which prevented the development of a large long-lived hydrothermal system involving adjacent country rocks and fluids.

Our results suggest that the H/F ratio can be used as an indicator of contrasted W deposition environments in perigranitic ore-forming systems (Fig.3). Hübnerite crystallization is associated with the following key features for exploration: (1) source of W resides in nearby igneous rocks, (2) highly evolved granitic magmas are present, (3) ore fluids have a magmatic origin and (4) a "high temperature" magmatic-hydrothermal stage is preserved. Overall, hübnerite can be viewed as a relatively simple indicator of a strong magmatic control on W deposition. The fact that, in W deposits, ferberite compositions are generally more common than hübnerite could be the consequence of early hübnerite recrystallizing to lower H/F ratios as observed for example in Fig.2. Although, at Argemela hübnerite deposition is the consequence of a high Mn/Fe in the ore fluid, hübnerite crystallization progressively depletes the fluid in Mn (Amossé, 1978) and, therefore, precipitation of wolframites with progressively lower H/F ratios is expected (Fig.3). However, large variations of the H/F ratio within a given deposit (for example at La Bosse, Vale Das Gatas, Argemela, Fig.3) are the mark of a complex multi-phase deposition history involving ore fluids with contrasted Fe/Mn and different, superimposed, wolframite deposition environments. Wolframite can recrystallize to lower H/F ratios (WI in the Argemela country rock vein, Fig.3) when the magmatic-hydrothermal system becomes open to fluids derived from Fe-, S-rich metamorphic country rocks (Lecumberri-Sanchez et al., 2017). Alternatively, overprinting of early low H/F ratios in country rock veins by magmatic fluids derived from a crystallizing RMG can be also observed in the FMC (La Bosse, Fig.3).

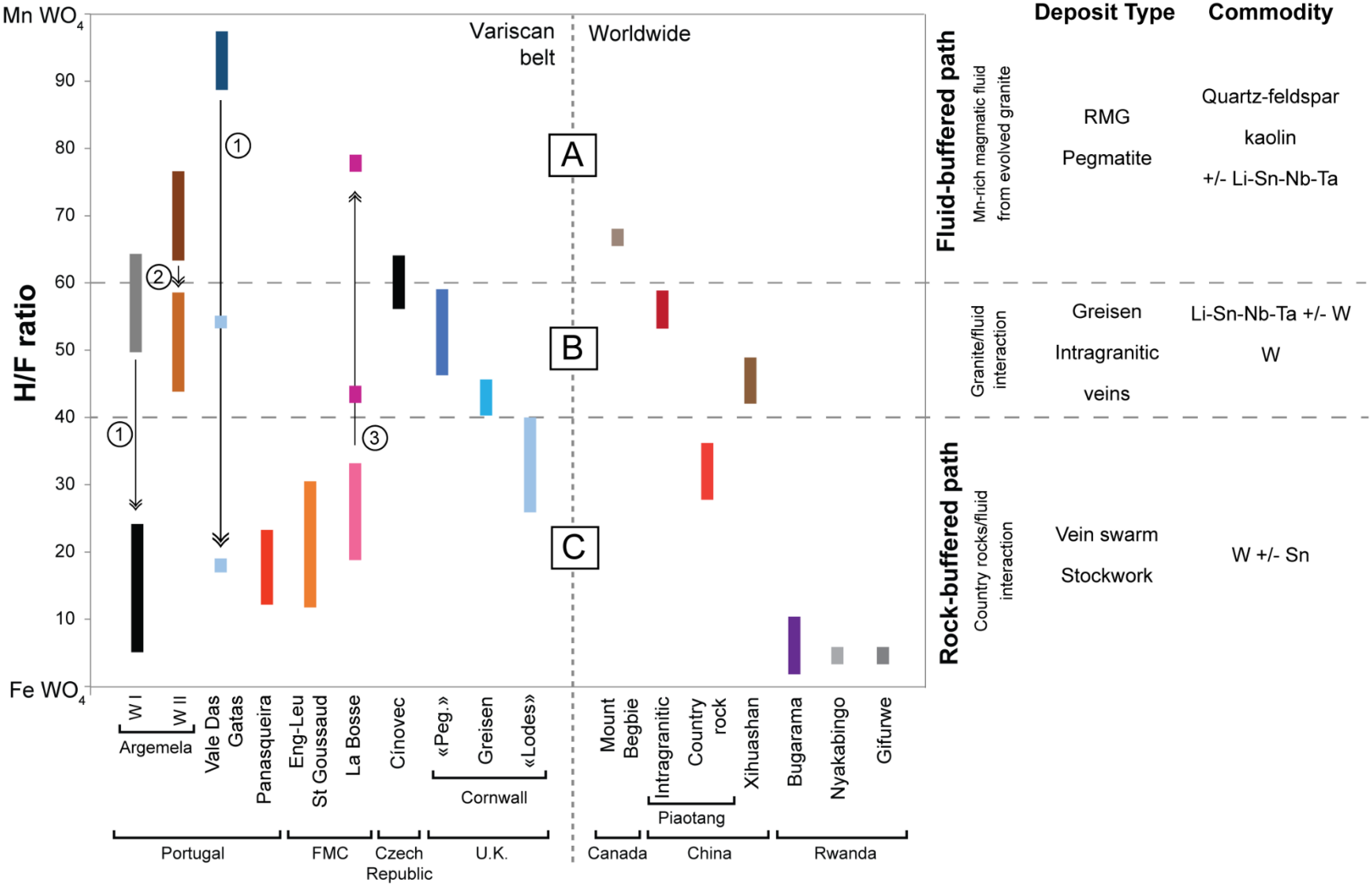
Mn WO4
Fe WO4
H/F ratio
90
80
70
60
50
40
30
20
10
Variscan belt
Worldwide
A
B
C
①
②
③
W I
W II
Argemela
Vale Das Gatas
Panasqueira
Eng-Leu
St Goussaud
La Bosse
Cínovec
«Peg.»
Greisen
«Lodes»
Cornwall
Mount Begbie
Intragranitic
Country rock
Piaotang
Xihuashan
Bugarama
Nyakabingo
Gifurwe
Portugal
FMC
Czech Republic
U.K.
Canada
China
Rwanda
Fluid-buffered path
Mn-rich magmatic fluid from evolved granite
Granite/fluid interaction
Rock-buffered path
Country rocks/fluid interaction
Deposit Type
Commodity
RMG
Pegmatite
Quartz-feldspar
kaolin
+/- Li-Sn-Nb-Ta
Greisen
Intragranitic
veins
Li-Sn-Nb-Ta +/- W
W
Vein swarm
Stockwork
W +/- Sn

Fig 3 *Environments and mechanisms of W deposition as revealed by the H/F ratio for several representative Variscan deposits and extension to worldwide deposits. Source of data in Table 2 for Variscan deposits and see Zhang et al. (2018), Dixon et al. (2014) and Goldmann et al. (2013) for worldwide deposits. Three main H/F domains corresponding to different wolframite deposition mechanisms are identified: (A) for H/F ratio > 60, wolframite precipitates from a Mn-rich magmatic fluid evolving under a fluid-buffered path (Heinrich, 1990); (B) for H/F ratio between 40 and 60, wolframite precipitates from a fluid buffered by granite/fluid interactions (Smith et al., 1996); (C) for H/F ratio < 40, wolframite precipitates from a fluid carrying a significant non magmatic signature derived from country rocks (Lecumberri-Sanchez et al., 2017). Three main mechanisms controlling variations of the H/F ratio in a single deposit are illustrated: (1) step decrease of the H/F ratio resulting from addition of Fe through fluid-rock interactions (Lecumberri-Sanchez et al., 2017); (2) Progressive decrease of the H/F ratio due to Mn removal during hübnerite crystallization (Amossé, 1978) and (3) step increase of the H/F ratio due to influx of Mn-rich magmatic fluid. Deposit type and commodity associated with the three domains are detailed. Eng-Leu: Enguialès-Leucamp; FMC: French Massif Central; "peg": pegmatitic veins (Hosking and Polkinghorne, 1954)*

Hübnerite is a tracer of proximal highly evolved igneous bodies such as RMG and/or pegmatite with potential for commodities such as quartz and feldspar, kaolin and disseminated Li-Sn-Nb-Ta ores (e.g., Aubert, 1969; Fig.3), in addition to W. Wolframite with intermediate H/F ratios is characteristic of medium temperature rock-buffered hydrothermal systems with a strong magmatic signature, both for the fluids and the metals (Fig.3, Smith et al., 1996; Korges et al., 2018). These compositions are typical of greisen-type (both vein and massive) deposits where mostly Li-Sn-Nb-Ta are economically interesting and of intragranitic vein type deposits that follow a rock-buffered path. Lastly, H/F ratios < 40 and down to 0 indicate W deposition environments where a significant non-magmatic contribution to the ore fluid and W deposition is necessary (Fig.3, Lecumberri-Sanchez et al., 2017). Ferberites showing a low H/F ratio are tracers of W-bearing veins/stockwork deposits of great economic importance.

The comparison can be extended to deposits worldwide (Fig. 3). Fractionated Li-bearing pegmatites from Mount Begbie (Bristish Columbia; Dixon et al., 2014) exhibit scarce hübnerites with a high H/F ratio, similar to Argemela (Fig. 3). Intragranitic veins of the Piaotang and Xihuashan W-deposits (Zhang et al., 2018) are characterized by an alteration halo at vein margins which indicates a rock-buffered path (i.e., granite-fluid interaction). These vein systems behave similarly to Cligga Head and both show comparable intermediate H/F ratios. In comparison, Piaotang country rock veins show a lower H/F ratio (Zhang et al., 2018), most probably a consequence of interaction with these rocks. The Bugarama, Nyakabingo and Gifurwe vein-type deposits from the "tungsten belt" of Rwanda are all hosted in country rocks and wolframite shows very low H/F ratio (Goldmann et al., 2013), comparable to the Panasqueira compositions. Thus, the H/F ratio appears as a reliable exploration tool worldwide despite differences in ages and geodynamic contexts between deposits.

IV.7. CONCLUSIONS

Intragranitic veins in the Argemela Mineralized District remarkably illustrate the case of wolframite precipitation directly from relatively “high temperature” magmatic fluids. High H/F ratios wolframites (hübnerites) are characteristic of this specific W deposition environment which contrasts with other mechanisms that lead to intermediate to low H/F ratios. It is proposed that the H/F ratio can be used as an indicator of wolframite deposition style for Variscan deposits (and beyond) and thus as a relevant exploration tool. Lastly, it should be emphasized that the genesis of Variscan W deposits does not only result from locally favorable country rocks, as for Panasqueira (e.g., Lecumberri-Sanchez et al., 2017). Chemically specific source rocks and granite magma types are also necessary.

CHAPTER V:

THE MAGMATIC-HYDROTHERMAL TRANSITION IN RARE-METAL GRANITES: TRACE ELEMENTS AND STABLE ISOTOPE CONSTRAINTS FROM ARGEMELA (CENTRAL PORTUGAL)

ABSTRACT

Rare Metal Granites (RMGs), also designated as tin, topaz, zinnwaldite or Li-F granites, are highly evolved intrusions characterized by a strongly specific signature which vary according to the RMG type. The Argemela granite (CIZ, Portugal) enter in the class of Peraluminous Highly Phosphorous RMG (PHP) regarding the classification of Linnen and Cuney (2005). It is characterized by marked depletion in REE, Y, Zr, Hf, Th, Ca, Fe, Ba and Sr, high concentration in fluxing elements (F, B, P, Li) and metals (Sn, Nb, Ta, W). Origin of the RMG specific signature has been strongly controversial (i.e., metasomatic vs magmatic) as in most RMGs, magmatic features are variably overprinted by subsolidus processes. Furthermore, in most systems, mineralogical, textural and geochemical expressions of the magmatic-hydrothermal transition (i.e. fluid exsolution from the magma and early evolution) are cryptic and only the magmatic and late hydrothermal end-members are preserved. The Argemela RMG is an outstanding example where details of the transition are preserved. In this chapter, we combine major and trace element data on whole-rocks and mineral phases with stable isotopes (O, H) to constraint the transition. This integrated study led to critical results for the understanding of mechanisms at the magmatic-hydrothermal transition with implications for rare elements transport and distribution.

THE MAGMATIC-HYDROTHERMAL TRANSITION IN RARE-METAL GRANITES: TRACE ELEMENTS AND STABLE ISOTOPE CONSTRAINTS FROM ARGEMELA (CENTRAL PORTUGAL)

V.1. INTRODUCTION

Rare Metal Granites (RMGs) are highly evolved granites which occur dispersed across the Variscan belt of Western Europe, from Portugal to the Bohemian Massif (Cuney et al., 1992; Charoy and Noronha, 1996; Breiter et al., 1997). RMGs, also designated as tin, topaz, zinnwaldite or Li-F granites, are characterized by a specific geochemical signature which, although varying with RMG type, strongly differs from most other Variscan granites. Several classifications have been proposed for RMGs such as the one of Linnen and Cuney (2005) based on the alumina saturation index and on specific geochemical and mineralogical characteristics. Peralkaline, metaluminous and peraluminous RMGs have been recognized and, in the peraluminous group, Peraluminous Low, Intermediate and High Phosphorus RMGs (respectively PLP, PIP and PHP) have been distinguished (Linnen and Cuney, 2005). Although peraluminous RMGs share common characteristics, the PHP signature is typical in the western part of the Variscan belt (e.g., Argemela: Charoy and Noronha, 1996; Beauvoir: Cuney et al., 1992). Geochemically, peraluminous RMGs are characterized by marked depletions in REE, Y, Zr, Hf, Th, Ca, Fe, Ba and Sr, high concentrations in fluxing elements (F, B, P, Li) and marked enrichments in rare lithophile elements and metals (Sn, Nb, Ta, Be, Cs, Rb and W). The source of rare elements in peraluminous RMGs and the origin of their geochemical specificities have been strongly controversial topics since the 1960's. Do these evolved granites owe their geochemical signature to a specific magmatic evolution or to late subsolidus processes involving a fluid phase? As an answer to this question, early workers (Beus et al., 1962; Beus and Zhalashkova, 1964; Zhalashkova and Sitnin, 1967;

Hu et al., 1984) have emphasized the role of metasomatic transformations of the crystallized granite by hydrothermal fluids. However, the discovery of volcanic analogues (Kovalenko and Kovalenko, 1976; Pichavant et al. 1988; Raimbault and Burnol, 1998) has demonstrated that magmatic processes are important in the genesis of RMGs.

In most granites and especially in RMGs, the textural, mineralogical and geochemical features resulting from magmatic crystallization are variably overprinted by subsolidus processes (e.g., Pollard et al. 1987; Stemprok, 1987; Kontak, 2006; Muller et al., 2006). Hydrothermal fluids responsible for mineral transformations can have various origins. During magma crystallization, volatile concentrations build up in the residual melt (e.g., Jahns and Burnham, 1969) which leads to the exsolution of a fluid phase of magmatic origin (e.g., Smith et al., 1996; Harlaux et al., 2018; Korges et al., 2018). However, metamorphic and meteoric fluids are commonly found in hydrothermal systems developed in and around granitic plutons (Kelly and Rye, 1979; Fouillac and Rossi, 1991; Polya et al., 2000). In many cases, the hydrothermal evolution is multiphase and several successive discrete stages driven by fluids of various sources can be distinguished (e.g., Sheppard, 1977; Vallance et al., 2001). Whatever the provenance of fluids, geochemical signatures result from magmatic and hydrothermal processes combined, a complexity that is reflected in the common use of "magmatic-hydrothermal" to characterize differentiation processes in RMGs (e.g., Harlaux et al., 2018; Kaeter et al., 2018).

Although the subject of active research, the transition from a melt- to a fluid-dominated differentiation regime (the magmatic-hydrothermal transition, MHT), is still unclear. This transition must occur relatively late during magma crystallization but rather early in the overall cooling and consolidation of the granite body. It controls the transfer of trace elements and metals from the magma towards the fluid phase and modifies magmatic fractionation patterns. One difficulty is that this transition is rarely exposed because most granites keep record of the latest, final, hydrothermal transformations. Therefore, MHT processes are presently constrained mainly from melt and fluid inclusion data (Thomas et al., 2003; 2005; Rickers et al., 2006; Zajacs et al., 2008; Borisova et al., 2012; Harlaux et al., 2018). This approach has brought useful information such as melt-fluid partition coefficients although other aspects have remained controversial. This is the case in particular of the proposal that immiscible H_2O-rich (up to several tens wt% H_2O) melts play a significant role at the

magmatic-hydrothermal transition (e.g., Thomas and Davidson, 2012; 2015; Hulsbosch et al., 2019). Fluid phase separation to vapour and brine is a well-documented mechanism (e.g., Audetat et al., 2000; Korges et al., 2018) but the presence of fluxing element- and metal-rich immiscible hydrous melts at the MHT has so far not found any experimental confirmation (e.g., London, 2015). Because of these difficulties, alternative approaches such as the analysis of element zonation in mineral phases from RMGs and pegmatites (Siegel et al., 2016; Kaeter et al., 2018; Monnier et al., 2018) are increasingly being used to document processes at the MHT. In this paper, a similar approach is applied to a highly representative example of RMG, the Argemela granite (Central Portugal).

The Argemela granite is a small intrusion outcropping in the Central Iberian Zone (Charoy and Noronha, 1996). It forms part of the Argemela Mineralized District (AMD) which comprises both disseminated and vein-type Sn, Li, W, Nb, Ta mineral concentrations (Chapter III). The small size and subvolcanic emplacement of the pipe-like intrusion (See Chapter II) favored the preservation of magmatic, magmatic-hydrothermal and hydrothermal structures which can be directly observed and studied. The Argemela granite has not suffered from late hydrothermal reworking events such as kaolinisation as observed for example at Beauvoir (Cuney et al., 1992), and it constitutes an exceptional source of information on MHT processes. In this paper, we combine major and trace element data on whole-rocks and mineral phases with stable isotope (O, H) constraints and develop a model for the magmatic-hydrothermal transition in PHP-type RMGs.

V.2. GEOLOGICAL SETTING

The Argemela granite (Fig. 1) is a typical PHP RMG (Linnen and Cuney, 2005). It is located in the southern part of the Central Iberian Zone (CIZ), mainly made of autochtonous Gondwanian terranes corresponding to low metamorphic external zones. Occurring ~13 km east of the Panasqueira W mine and ~1.5 km west of the Fundão composite granite, the Argemela granite forms a small almost elliptical body (i.e. 250 x 125 m) in map view and is characterized by a pipe-like geometry in cross-section extending to a maximum depth of 1 km (Chapter I). Contacts of the granite with the surrounding low grade Beira schists (Schist and Greywacke Complex (SGC) of Neo-Proterozoic to Cambrian age) are mostly intrusive but, on the northeastern part, the contact is affected by a dextral shear corridor.

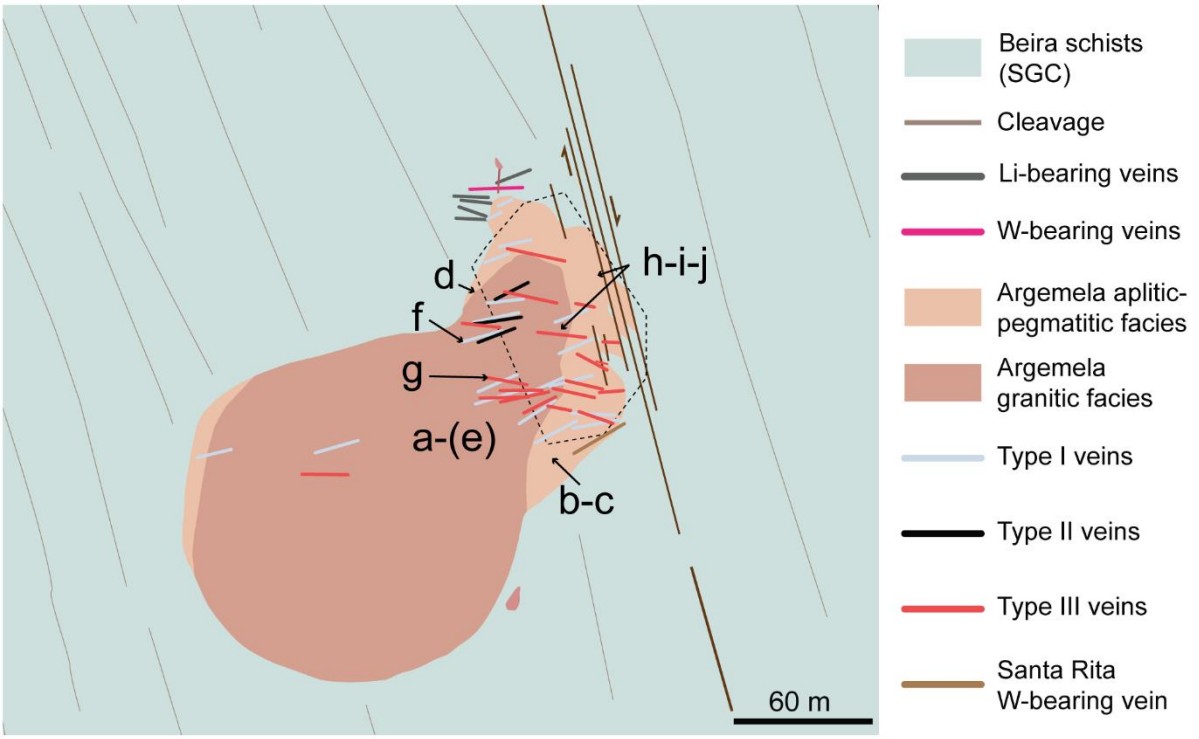

Fig 1 *Geological map of the Argemela RMG. (a)-(j) refers to pictures in Fig. 2*

The Argemela stock is exploited by UNIZEL MINERAIS LDA. as a source of ceramic raw materials, and the quarry (on the northeastern part) provides a well exposed view of the granite. The Argemela intrusion is composed of two main facies: (i) the *granitic* facies (Fig. 1, 2a) which forms the major part of the granite and (ii) the *border* facies (Fig. 1, 2b, c, d). The granitic facies, already described

in Charoy and Noronha (1996), is characterized by a subvolcanic texture. Millimetric phenocrysts of "snowball" euhedral quartz and silverish to greenish micas are embedded in a fined-grained white matrix. The border facies, occurring discontinuously along the contact and mainly found in the quarry, consists in an alternation of aplites (Fig. 2c) and pegmatites (Fig. 2b). In hand samples, the *aplitic* facies is characterized by a very fine-grained white matrix without apparent phenocrysts. Aplites are homogeneous, particularly at the contact with the surrounding Beira Schists and they display bedding in more internal parts. The *pegmatitic* facies consists of large phenocrysts of K-feldspar embedded in a micaceous matrix. In the internal part of the border facies, large K-feldspar crystals form unidirectional solidification textures growing toward the center of the granite.

At the contact between the granitic facies and the border facies, a *micaceous* facies has been observed characterized by the presence of numerous silverish to greenish micas phenocrysts (Fig. 2d). A "ball like" facies has been described by Charoy and Noronha (1996) as an ovoidal mass consisting of very fine-grained material without any apparent phenocrysts. The contact with the granitic facies is said sharp without any apparent modifications. A grey subvertical "dyke-like" facies has also been observed showing sharp contact with the granitic facies (Fig. 2e). Both the granitic, the border facies and the grey facies are intersected by a network of *intragranitic veins* clearly observable in the quarry (see Chapter III). Geometrical relations, structural and mineralogical data enable three generations of veins to be distinguished. The first and earliest generation (Type I, Fig. 2f) is characterized by a pegmatite-like "bar code" internal texture and K-feldspar and montebrasite in addition to quartz. The Type II veins which crosscut the Type I, are K-feldspar-free, being mainly composed of quartz and scarce montebrasite. Type III veins intersect the two previous generations and are mineralogically quite variable, being subdivided in Type IIIa (see Fig. 2g for W-bearing Type IIIa veins), b (Fig. 2h) and c depending on the ore mineral assemblage present. One particular vein (the Santa Rita vein, SR), located on the southeastern part of the granite at the contact with the country rocks, has been hand exploited for tungsten and is described in Inverno (1998).

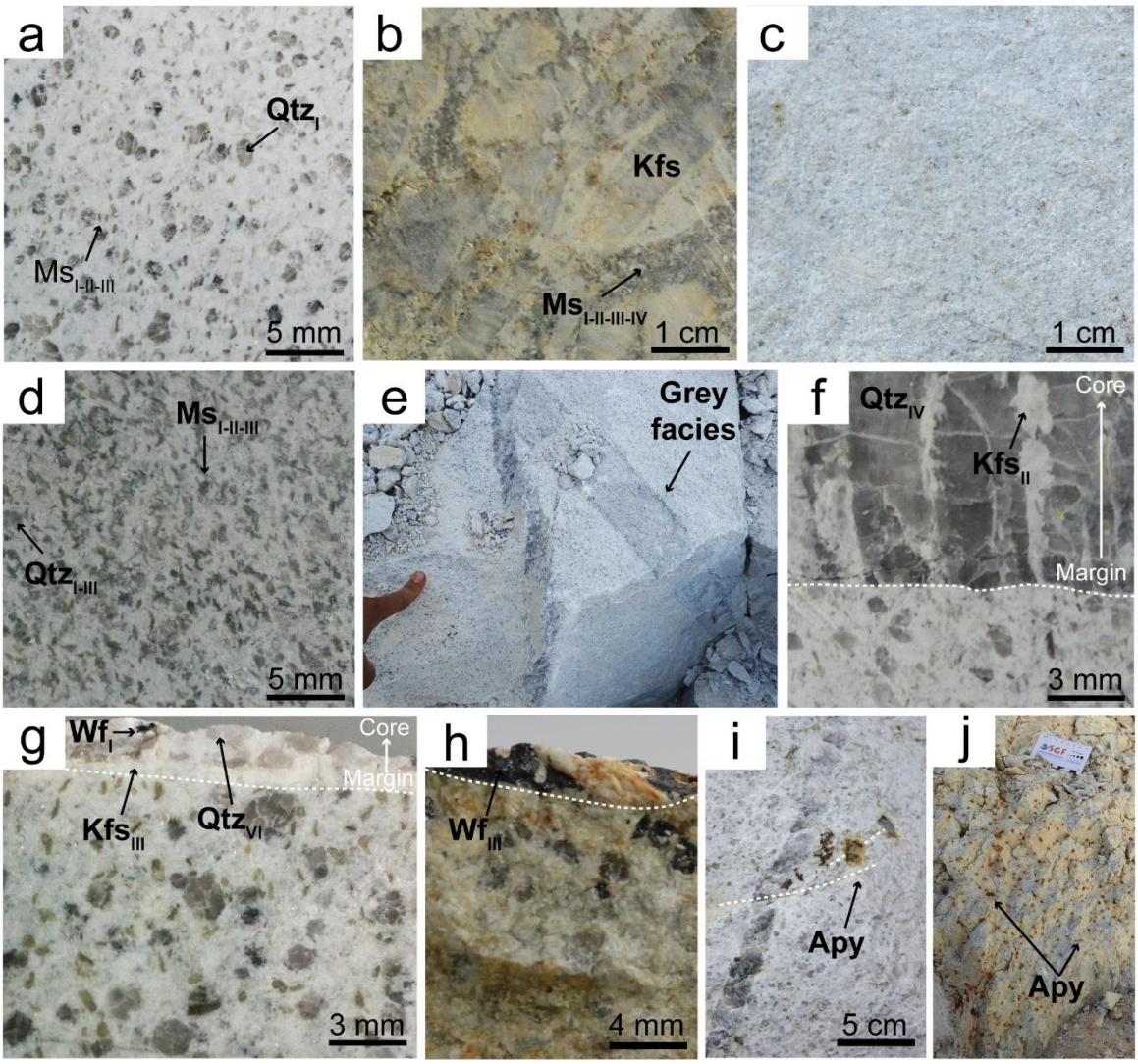

Facies	Characteristics	Rock forming minerals
Granitic facies	Phenocrysts embedded in a fine-grained white matrix	Phenocrysts : Snowball Qz - Ms Matrix: Ab_{I-II} - Li-P_I - $Ms_{I-II-III}$ - $Qtz_{I-II-III}$ +/- Kfs_I Cst_{I-II} - CT_{I-II}
Border facies	Fine-grained aplite without phenocrysts	Ab_{I-II} - Li-P_I - $Ms_{I-II-III-IV}$ - $Qtz_{I-II-III}$ - Kfs_I Cst_{I-II} - CT_{I-II}
	Pegmatitic facies - large phenocrysts embedded in a micaceous matrix	Phenocrysts: Kfs - Ms Matrix = aplite
Type I intragranitic veins	Extensional subvertical veins «bar code» syntaxial growth +/- clustered N072°E on average	Qtz_{IV} - Li-P_{II} - Kfs_{II}
Type II intragranitic veins	Extensional subvertical veins +/- clustered N060°E on average	Qtz_V +/- Li-P_{III}
Type III intragranitic veins	Shear subvertical veins Isolated and straight Internal texture vary with the thickness N090°E - N110°E	IIIa: Qtz_{VI} - Li-P_{IVa} - Kfs_{III}
		W-IIIa: Qtz_{VI} - Li-P_{IVa} - Kfs_{III}- Wf_I
		IIIb: Li-P_{IVa} - Wf_{II} - CT_{III}
		IIIc: Qtz_{VI} - Cst_{III} - Wf_{III}

Fig 2 *Textures, characteristics and mineralogy of the different facies and of intragranitic veins. (a) Subvolcanic texture of the granitic facies with snowball quartz and micas phenocrysts; (b) large K-felspars embedded in a micaceous matrix from the pegmatitic facies; (c) fine-grained texture of the aplitic facies without phenocrysts; (d) Texture of the micaceous facies; (e) the "dyke like" grey facies; (f) Type I intragranitic vein with elongated K-feldspars and quartz crystals; (g) W-bearing Type IIIa vein and its sharp contact with the granite; (h) Type IIIb vein and contact with the granite sampled at the northeastern sheared contact; (i) arsenopyrite crystallizing in small fractures intersecting an intragranitic vein and (j) disseminated sulphides including arsenopyrite at the northeastern border. Table summarizing characteristics of the main features*

V.3. METHODS AND ANALYTICAL TECHNIQUES

V.3.1. Strategy

To track chemical variations during the MHT, whole-rock analyses of representative samples of the Argemela granite are combined with textural studies, electron microprobe, LA ICP-MS and stable isotope (O, H) data for selected mineral phases. Focus is placed on muscovite, quartz, K-feldspar and Li-phosphate phases which have been chosen to monitor chemical changes at the MHT.

V.3.2. Samples

Representative rock samples were collected from in-situ outcrops, including samples of the granitic facies, the border facies and of the three generations of veins. Observation and sampling were conducted in the quarry, in the northeastern part of the intrusion, considered as representative of the whole intrusion. These were prepared to produce 30µm and 100µm thin sections, the thickest sections being prepared specifically for LA-ICP-MS analyses. Preliminary petrographic and textural observations were made using a petrographic microscope. For isotopic analyses, samples of granite and vein were first crushed to obtain a coarse residue and passed three times in a sorting machine to get a representative sampling. From the sorted representative samples, quartz and micas were separated by hand picking under a binocular loupe.

V.3.3. Bulk rock analyses

Bulk rock analyses were carried out at the SARM (CRPG, Nancy, France, Carignan et al., 2001). Samples were analysed using an inductively coupled plasma emission spectrometer (ICP-OES) iCap6500 ThermoFisher for major elements and an inductively coupled plasma mass spectrometry (ICP-MS) iCapQ ThermoFisher for trace elements. The detection limit is calculated as the average plus 6

times the absolute standard deviation on 100 measurements of blank. Detection limits are indicated in Table 1. Samples analyzed include the granitic facies and the border facies. Samples of veins (i.e. core of the veins) and granite at vein margins were also analyzed to track potential chemical variations.

V.3.4. SEM and cathodoluminescence imaging

Backscattered electron (BSE) images and EDS element maps were obtained at the Institut des Sciences de la Terre d'Orléans (ISTO, France) using a Merlin compact ZEISS Microscope equiped with a Bruker EDS detector and working under an acceleration voltage of 15 kV. Cathodoluminesce images were obtained at the BRGM of Orléans (France) using a MIRA TESCAN (FEG) Microscope equipped with a panchromatic (350-660 mm) cathodoluminescence (CL) and working on an acceleration voltage of 20-25kV.

V.3.5. EPMA analyses

Punctual analyses, traverses and elements distribution maps for major and minor elements were obtained using a CAMECA SX Five microprobe operated under an acceleration voltage and a beam current of 15 kV and 6 nA respectively. Standards included albite (Si*Kα* and Na*Kα*), synthetic $MnTiO_3$ (Mn*Kα* and Ti*Kα*), Al_2O (Al*Kα*), Fe_2O_3 (Fe*Kα*), MgO (Mg*Kα*), andradite (Ca*Kα*), orthose (K*Kα*), apatite (P*Kα*) and topaze (F*Kα*). Relative errors for micas are calculated as ((standard deviation x 100) / mean) for each major element using the most homogeneous population (Ms_I; n=62) and are: 2.5% for SiO_2, 5.2% for Al_2O_3, 27.3% for FeO, 31.5% for Na_2O, 10.7% for K_2O and 61.8% for F. Relative errors can be propagated to other populations. For montebrasite, mean values and standard deviations are calculated for each element of each homogeneous populations on the *n* analyses (Table 5). Relative errors for K-feldspars are calculated as ((standard deviation x 100) / mean) for each major element using the most homogeneous population (Kfs_I; n=7) and are: 1.5% for SiO_2, 1.8% for Al_2O_3, 3.7% for K_2O, 47,4% for Na_2O and 34.2% for P_2O_5.

V.3.6. LA-ICP-MS analyses

Micas. Analyses were performed at the LMV (Clermont-Ferrand) using a Resonetics M-50E excimer laser (λ=193 nm) coupled to an Agilent 7500 quadrupole inductively coupled mass spectrometer (ICPMS). Ablation was performed at 2 Hz, at an energy of ~2.8 to 5.65 J.cm^{-2}, and at a beam diameter of 27 µm. NIST612 was used as external (primary) standard, while BCR and NIST610 were used as a control. Al_2O_3 was used as the internal standard. For all samples, Al_2O_3 (wt%) was determined by electron microprobe prior to LA-ICP-MS analyses. Each external standard was analysed two times at the beginning and at the end of each run and one time every ten to twenty sample analyses. 31 isotopes were measured and all data were collected in two sessions. For homogeneous crystals, mean value and standard deviation are calculated on the *n* analyses (Table 3). For single analysis, the 1 sigma error is given in parenthesis under each value (Table 3).

Quartz. Analyses were performed at the BRGM Laboratory (Orléans) using a UVlaser-ablation microsampler CETAC Exite (λ=193 nm) coupled to a ThermoScientific X serie II quadrupole ICPMS. Ablation was performed at 8 Hz, at an energy of ~22.40 J.cm^{-2}, and at a beam diameter of 85 µm. Data were calibrated with the external standard NIST SRM 612 and the internal standard of Si value (4.65 x 10^5 ppm being the stoichiometric concentration of Si in Quartz). Final concentrations were calculated based on the NIST concentrations values given by Pearce et al. (1997). The external standard was analyzed two times at the beginning, every 15 analyses and at the end of a run. Li, Be, B, Na, Al, Ti, Mn, Fe, Ge, As, Rb, Sr, Nb, Sn, Sb, Ta and W isotopes were measured for each quartz sample. For homogeneous crystals, mean value and standard deviation are calculated on the *n* analyses (Table 4). For single analysis, the 1 sigma error is given in parenthesis under each value (Table 4).

Li-phosphates and K-feldspars. Analyses were performed at the IRAMAT-CEB Laboratory (Orléans) using a RESOlution (S-155-E) ArF excimer laser (LA; λ=193 nm) coupled to a Thermo Finnigan Element XR (extended range, high-resolution) ICPMS. Ablation was performed at 10 Hz, at an energy of ~5 J.cm^{-2}, and at a beam diameter of 30 µm. NIST610 was used as external standard, while BCR-2G and NIST612 were used as a control. Al_2O_3 was used as the internal standard. For all samples, Al_2O_3 (wt%) was determined by electron microprobe, while values for external standard and controls

are those of Pearce et al. (1997) and the preferred values from GeoRem (http://georem.mpch-mainz.gwdg.de/), respectively. Primary standards were analyzed two times at the beginning and at the end of each run of ten analyses. 42 isotopes were measured and all data were collected in one 2-day session. Mean value and standard deviation are calculated on the *n* analyses of Li-phosphates (Table 6) and 1 sigma errors are given for single analyses of K-feldspars (Table 8).

Data processing. Raw data were processed off-line using Glitter software where time-resolved signals were examined one-by-one. When the signal was anomalous (e.g., inclusions), the analysis was not considered. Element concentrations were calculated for the initial ~30 s of all ablation signals relative to the gas blank (~20 s), with a linear interpolation across standard analyses.

V.3.7. Stable isotopes

O and H isotopic measurements were carried out at CRPG, Nancy using different procedures.

O isotopes. Oxygen in quartz and micas was extracted by fluorination using BrF_5 in a high-vacuum apparatus similar to those described by Baertschi and Silverman (1951; see also Clayton, 1955; Taylor and Epstein, 1962; Clayton and Mayeda, 1963). Ten mg of each sample was loaded into pure nickel reaction tubes and outgassed under vacuum at room temperature (~30°C) for 1h before reaction with BrF_5 at 550°C for 7 to 10h. Liberated O_2 is then passed through a hot graphite rod for conversion into CO_2. $^{18}O/^{16}O$ isotopes of granite and vein samples were measured using a Thermo-Fisher MAT253 mass spectrometer and values are given in δ in permil relative to Vienna Standard Mean Ocean Water (VSMOW). Analytical precision was quantified at ± 0.1‰ using in-house standard.

H isotopes. The D/H isotopic compositions of muscovite from the granitic and micaceous facies were measured using an Elemental Analyzer (EA) coupled to a VG Isoprime Isotope Ratio Mass Spectrometer (IRMS). Micas powders were dehydrated for 48h, weighted and packed in tin capsules. Tin capsules were then loaded into an automatic sampler carousel pre-flushed with He to avoid atmospheric moisture. Samples were combusted on an EA reaction tube to reduce hydroxyls in H_2. A high temperature of 1450°C (Khantal-Superthal heating element) is necessary for a quick sample reduction avoiding formation of CH_3. Produced gases were separated on a chromatographic column kept

at 60°C prior to introduction of H_2 in the MS source and analyses of D/H. Three different internal standards (muscovite: Mus-D65, phlogopite: Mica-Mg and a fine-grained marine sediment from the bay of Bengal: SO188) were used to consider the instrumental drift. D/H is given as δD and normalized against SMOW. In addition, fluids trapped in quartz from the different facies were extracted and their D/H isotopic composition determined using the same method. To optimize the accuracy of the isotopic measurements, two in-house standards were weakly extracted and analysed. Samples were systematically duplicated; mean values and standard deviations are given in Table 11.

V.4. PETROLOGICAL RESULTS

In the Argemela intrusion, five main units can be distinguished: (i) the granitic facies, (ii) the border facies including the aplitic, the pegmatitic and the micaceous sub-facies, (iii) the Type I intragranitic veins, (iv) the Type II intragranitic veins and (v) the Type III intragranitic veins including the a, b, c and SR sub-types. Petrological features of each main unit are described below.

V.4.1. The granitic facies

The granitic facies, already described by Charoy and Noronha (1996), shows a subvolcanic texture typical of Variscan RMGs (Fig. 2a and 3a). It is characterized by quartz and micas phenocrysts embedded in a fine-grained matrix mainly made of albite, montebrasite and scarce K-feldspar, plus fine-grained disseminated cassiterite and columbite-tantalite.

Two generations of quartz have been recognized (Qtz_I and Qtz_{II}). Quartz phenocrysts, also called snowball quartz (Qtz_I, Fig. 3b, see also Charoy and Noronha, 1996), occur as euhedral crystals up to several mm large. Euhedral albite laths (Ab_I), from several µm to 300 µm in size, form inclusions in Qtz_I where they underline the bipyramidal habit of the host crystal. Inclusions in the inner (Ab_{Ia}) part of Qtz_I are generally less numerous but larger than in the most external part (Ab_{Ib}; Fig. 3c, d). SEM and cathodoluminescence imaging reveal growth zonation in snowball quartz marked by alternating light and dark zones underlined by albite laths (Qtz_{Ia}, Fig. 3c, d). Cores correspond generally to light zones. The external, mostly light grey growth zones and separated from the inner part by numerous tiny albite inclusions, invade the matrix (Qtz_{Ib}, Fig. 3d). A second type of quartz (Qtz_{II}, see also Charoy and Noronha, 1996) occurs within the matrix as polygonal grains never exceeding 100 µm. These grains can form a mosaic in "pockets" replacing early snowball Qtz_I.

White micas occur as phenocrysts of several hundred µm to several mm, appearing either as isolated crystals or in clusters. They can be slightly bent or kinked. SEM imaging reveals a quite complex chemical zonation, illustrated by the mica of Fig. 3e. Several zones corresponding to at least three crystallization steps (I, II, III) can be recognized from core to rim. Contacts between the different zones

are either sharp and irregular. The internal part (Ms_I) is characterized by a light grey core (Ms_{Ia}) and a brighter rim (Ms_{Ib}). The intermediate zone (Ms_{II}), which is darker than Ms_I, also comprises a core (Ms_{IIa}) and a bright rim (Ms_{IIb}). The external part of the mica, darker than the two previous ones, forms an external rim invading the matrix (Ms_{III}). Ms_{III} is not always homogeneous. It generally shows a "patchy" texture and can also be found as thin laths aggregates within the matrix. This mica zonation differs and is more complex than that described by Charoy et al. (1995). Moreover, it is not always equally marked in all granitic facies crystals. Ms_I cores and rims are the most easily identifiable but, for Ms_{II}, the distinction between cores and rims can be difficult. The patchy (Ms_{III}) can form thick rims up to 200 µm wide.

Albite crystals occur either as inclusions in snowball quartz (see above) and as the main minerals of the matrix (Ab_{II}; Fig. 3a). They range from tens to 500 µm in the matrix, are mostly euhedral and show the typical albite twinning.

K-feldspars (Kfs_I) are scarce. When present, they occur as euhedral to subhedral crystals of several hundred µm. Crystals generally show pericline/tartan twinning.

Li-bearing phosphates (Li-P_I, Fig. 3a) from the amblygonite-montebrasite series occur either as large twinned euhedral phenocrysts up to 1 mm in size or as smaller subhedral crystals.

Two generations of disseminated cassiterite are present (details in Chapter III). The first (Cst_I) corresponds to euhedral crystals showing growth zonation from light to dark brown in polarized light. Most are between 10 and 40 µm and closely associated with Li-P_I. The largest crystals, which can be up to 1 mm, contain inclusions of twinned Li-P_I. The second generation (Cst_{II}) occurs as large skeletal crystals of several hundred µm surrounded by albite, i.e., invading the albitic matrix. Cst_{II} is mainly dark brown in polarized light and contains zoned Mn-columbite-tantalite inclusions (Ct_{II}). Ct_I, the other columbite-tantalite generation forms disseminated subhedral Mn-columbite crystals of several tens of µm. Crystals are black in polarized light and strongly zoned in BSE imaging.

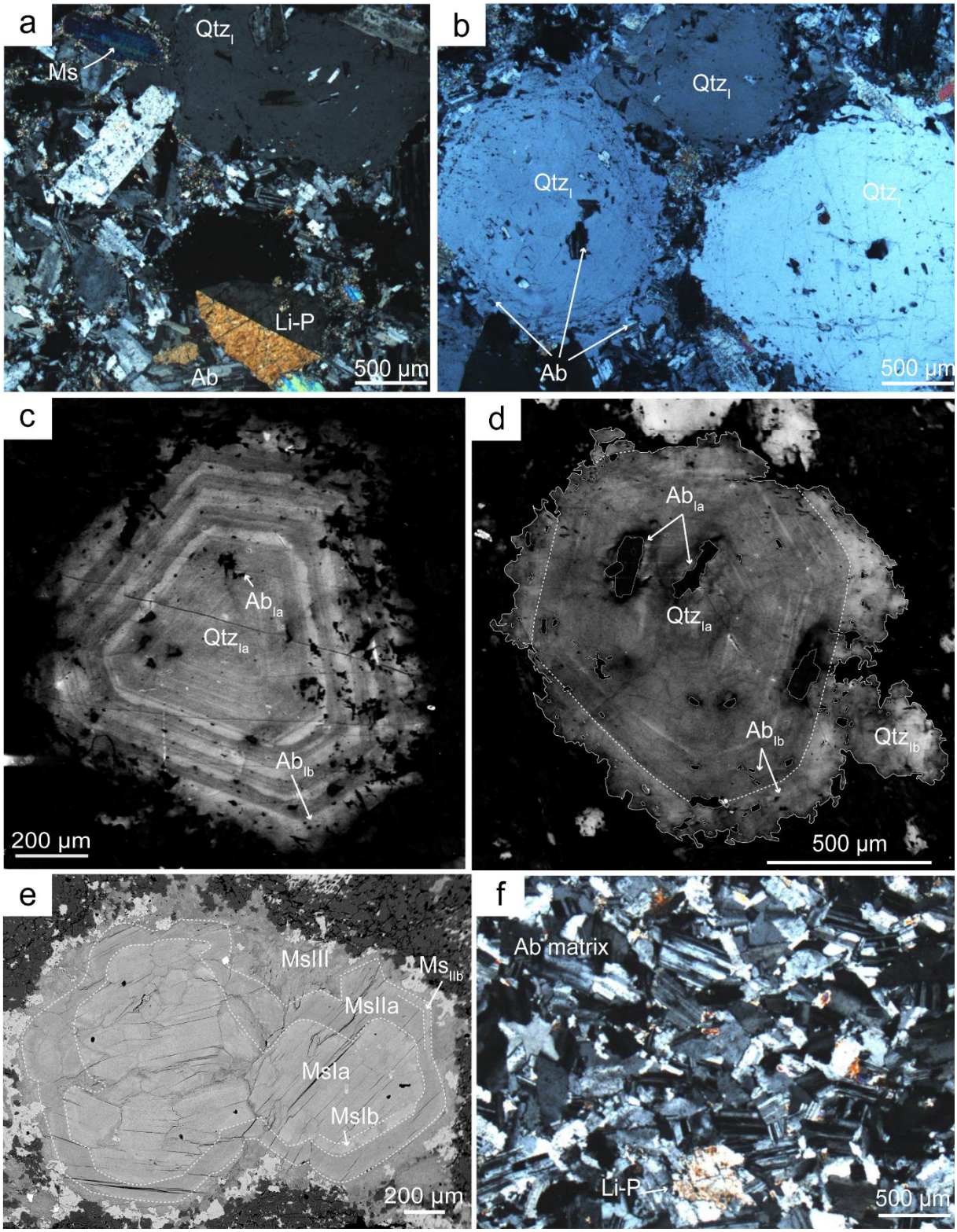

Fig 3 *Petrological features of the granitic and aplitic facies. (a) Texture of the granitic facies showing snowball quartz, twinned Li-phosphates, micas and the albitic matrix; (b) snowball quartz with inclusion of albite; (c) CL image of Qtz_{Ia} zonation underlining the euhedral habit; (d) CL image of zonation in*

QtzIa and external QtzIb zone; (e) BSE image of complex zoning in micas from the granitic facies and (f) microphotograph of the aplitic texture

V.4.2. Border facies

The border facies includes different components (aplitic, pegmatitic, and micaceous) and differs from the granitic facies mainly in texture/grain size and mineralogy. The aplitic facies is characterized by a fine-grained phenocryst-free matrix (Fig. 2c and Fig. 3f) It is composed mainly of euhedral albite crystals ($Ab_{IIaplite}$) rarely exceeding 200 µm. Snowball quartz (Qtz_I) are scarce and has sizes smaller than in the granitic facies. Polygonal Qtz_{II} have not been observed. Li-phosphates form small subhedral to anhedral crystals less numerous than in the granite facies. Micas are also less numerous and of smaller sizes (10-300 µm). Although the zonation observed in the granitic facies is difficult to recognize in the border facies, Ms_I-type cores and darker zones corresponding to Ms_{IIa} are both present, and a new mica generation (Ms_{IVb}) is identified. Ms_{IVb} appears very bright in BSE imaging and occurs either as rims invading Ms_{I-II} or as patchy bright zones within Ms_{I-II}, suggesting disequilibrium between Ms_{IV} and pre-existing micas. The pegmatitic facies, texturally highly variable between samples, is mineralogically more constant (Fig. 2b, Fig. 4a). It is characterized by very large K-feldspar phenocrysts of a few mm to several cm in size (Fig. 4a). Crystals are euhedral, show both the Carlsbad and the pericline twinning and contain numerous inclusions of albite (10-50 µm) and less frequently of mica. The surrounding matrix is made of numerous micas (similar to those encountered in the aplitic facies and including Ms_{IVb}, Fig. 4b), albite (Ab_{IIpeg} euhedral crystals less numerous than in the aplitic facies), quartz (Qtz_I) and Li-phosphates (twinned, euhedral to subhedral). Last, the micaceous facies (Fig. 4c) contains a large amount of mica phenocrysts texturally similar to those described in the aplitic and pegmatitic facies (i.e., Ms_I, Ms_{IIa} and Ms_{IVb}). Snowball Qtz_I are present and a new generation of quartz (Qtz_{III}) occurs as skeletal/interstitial grains within the matrix or as overgrowths on Qtz_I, overprinting its original texture and zonation (Fig. 4d, e). One sample from the rim of the border facies and mineralogically similar to the granitic facies contains a mica (Ms_{IVa}) texturally similar to Ms_{IVb} although less bright on BSE imaging.

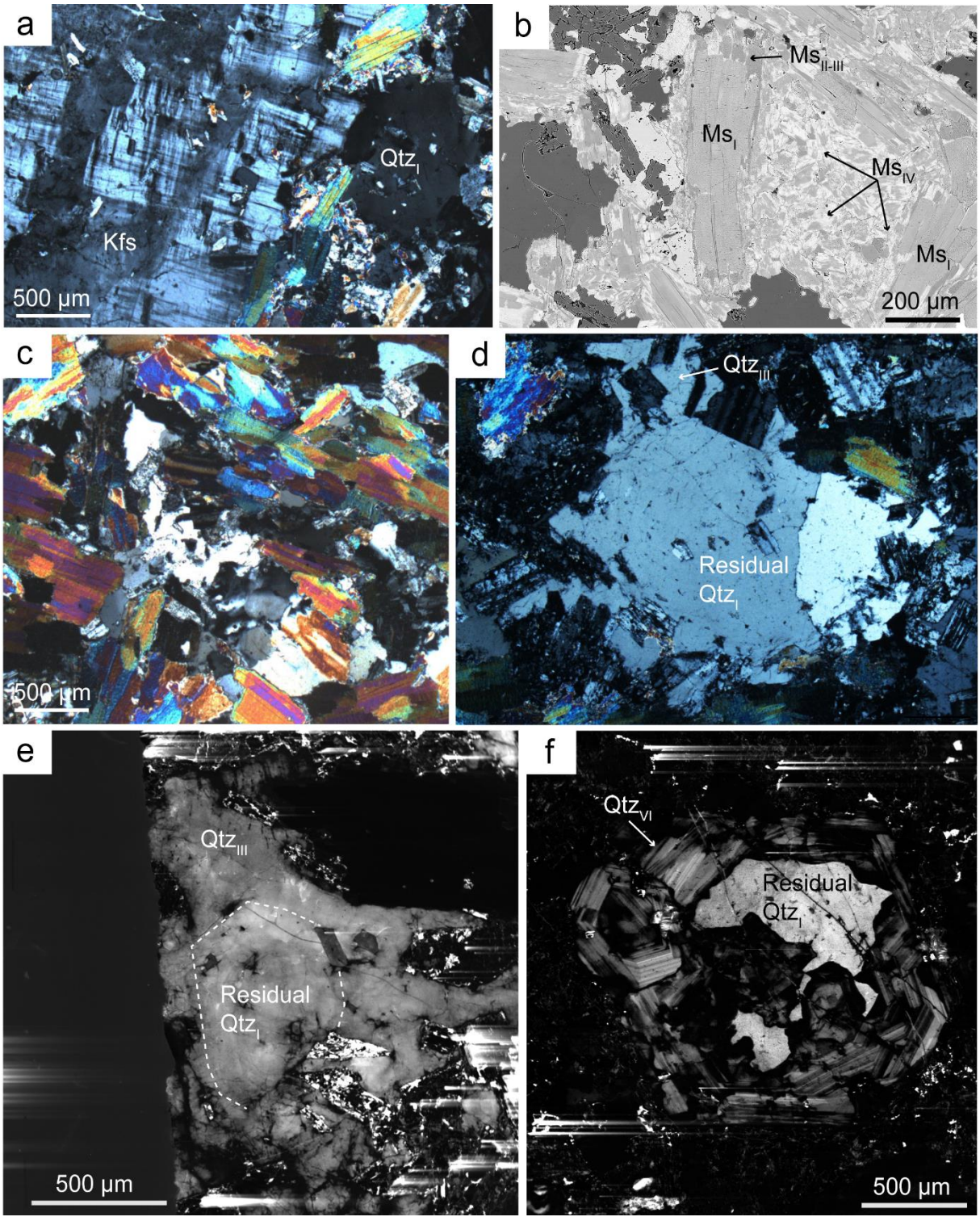

Fig 4 *Petrological features of the pegmatitic and micaceous facies. (a) Large twinned K-felspar occurring in the pegmatitic facies; (b) BSE image showing the patchy texture of* Ms_{IV}*; (c) texture of the micaceous facies; (d) and (e) microphotograph and CL image of skeletal* Qtz_{III} *overgrowing on residual* Qtz_I*; (f) replacement of* Qtz_I *by strongly zoned* Qtz_{VI} *in the granite at Type IIIb vein margin*

V.4.3. Intragranitic veins

The field relations, geometries, structural data and mineralogies of the three generations of intragranitic veins (i.e., Type I, II and III) are detailed in Chapter III. The Type I intragranitic veins consist of N072°E subvertical extensional veins. Millimetric to pluricentimetric in size, they are composed of quartz, K-feldspars and Li-phosphates stripes indicating syntaxial growth perpendicular to the vein margin (Fig. 2f). Most quartz (Qtz_{IV}) and K-feldspars (Kfs_{II}) form elongate anhedral crystals nearly continuous across the vein. Li-phosphates (Li-P_{II}) grow as discontinuous elongate crystals ranging from several tens µm to several mm. The Type II intragranitic veins consist of N060°E (on average) subvertical extensional veins composed of massive quartz (Qtz_V) and scarce subhedral Li-phosphate crystals (Li-P_{III}). Last, the Type III intragranitic veins consist of subvertical N090-110°E shear veins. They display various mineralogical assemblages with unknown mutual chronologies. The most common veins (Type IIIa) are composed of quartz, K-feldspars and Li-phosphates (Li-P_{IVa}) with variable amounts of wolframite. Quartz (Qtz_{VIa}) and K-feldspars (Kfs_{III}) form elongate blocky crystals coarsening toward the center of the vein. Li-phosphates occur as euhedral to subhedral crystals of several hundred µm. When present, wolframite (Wf_I) forms euhedral crystals of several hundred µm, black in polarized light. The second assemblage (Type IIIb) only includes subhedral Li-phosphate crystals (Li-P_{IVb}) of several hundred µm and wolframite (Wf_{II}). EDS mapping of Fe and Mn reveals the patchy texture of wolframite crystals with Mn-rich hübnerite (Wf_{IIa}) recrystallized to Fe-rich hübnerite (Wf_{IIb}; see Chapter III). These wolframites contain inclusions of exsolved Mn-columbite (Ct_{III}). A last type of assemblage (Type IIIc), encountered only in one vein, consists of euhedral quartz of several hundred µm (Qtz_{VIb}), large euhedral wolframite crystals (Wf_{III}) and minor cassiterite (Cst_{III}) almost totally transformed into stannite. In the margins of Type IIIb, in the granite, quartz recrystallizes and cathodoluminescence imaging reveals a new generation of strongly zoned quartz (Qtz_{VII}) associated with relictual Qtz_I.

V.5. GEOCHEMICAL RESULTS

V.5.1. Bulk rock analyses

In the granitic facies, the 8 analyses available yield quite homogeneous results (Table 1). Major elements show relatively small variations (Fig. 5, Table 1; SiO_2: 68-70 wt%, Al_2O_3: 17.5-18.5 wt%, Na_2O: 4.5-6 wt%, K_2O: 2.5-4 wt%, P_2O_5: 1.5-1.75 wt%). Samples are all almost TiO_2-, CaO- and MgO-free and they contain very little FeO and MnO. Similarly, most trace elements (Fig. 6, Table 1; Li: 1600-1750 ppm for 7 analyses, Cs: 23-47 ppm, Nb: 53-57 ppm for 7 analyses, Ta: 60-77 ppm for 7 analyses) are rather homogeneous. Sn (800-1200 ppm) and W (4-40 ppm) both show larger dispersions. As and S, considered as a proxy for external contamination (see below), are quite low, ranging from 0.5 to 28 ppm and from <0.01 to 0.05 ppm. In the border facies, most data concern the aplitic (2 analyses) and the micaceous (1 analysis) facies since the pegmatitic facies was not extensively sampled. Chemical dispersions are significantly higher in the border than in the granitic facies, a consequence of more variable modal compositions in the former than in the latter facies. Major element variations are substantial (SiO_2: 63-67.5 wt%, Na_2O: 3-8.5 wt%, P_2O_5: 1.5-2.7 wt%, Table 1, Fig. 5). Al_2O_3 is systematically higher and SiO_2 and K_2O lower than in the granitic facies. The trace elements also differ, Sn and Li being lower and the Nb/Ta ratio higher in the border than in the granitic facies. Another facies has also been recognized within the granite. It consists of subvertical fine-grained grey “dykes” (i.e. grey facies) and the contacts with the granitic facies is sharp with no modifications at the margin. It is also intersected by the intragranitic veins. This facies show high SiO_2 (71.5 wt%) and K_2O (5.16 wt%) and low Na_2O (2.38 wt%; Table 1, Fig. 5). Most trace element concentrations are in the same range as the granitic facies except for Hf (5.36 ppm) and Sn (1960 ppm) which are almost twice higher, Rb, slightly higher (1442 ppm), Ta (~160 ppm) more than twice higher and Zn (29 ppm) twice lower. Nb/Ta ratio is very low (i.e. 0.3; Fig. 6).

Table 1

Representative bulk rock analyses of the Argemela RMG

Facies	Granitic facies								Grey facies	Border facies		Intragranitic veins margins							Veins		Detection limits (ppm)
										Aplitic-pegmatitic	Aplitic	Mica-ceous	I	II	IIIa	W-IIIa	IIIb	IIIc	I	IIIa	
Major elements (wt %)	A2	A4	A4-2	A5	A6	A43	A47	A89	A8	A20	A13	A11	A9	A46	A45	A6	A61	A49	A49-v	A1	A20R	
SiO_2	68.69	69.21	67.83	68.47	69.79	68.60	69.98	70.04	71.54	62.93	67.54	64.32	65.16	69.40	70.85	69.53	69.13	66.04	65.27	86.16	94.32	0.050
TiO_2	bdl	bdl	bdl	bdl	bdl	bdl	bdl	bdl	bdl	bdl	bdl	bdl	bdl	bdl	bdl	bdl	bdl	bdl	bdl	0.02	1.78	0.100
Al_2O_3	18.27	18.19	18.64	17.87	17.57	18.21	17.81	17.66	16.44	21.02	18.82	19.86	19.24	17.72	16.85	17.93	17.87	19.98	20.12	5.61	0.03	0.060
FeO	0.36	0.32	0.29	0.26	0.27	0.28	0.29	0.22	0.15	0.29	0.32	0.15	0.57	0.33	0.21	0.25	0.28	0.37	0.43	0.09	-	0.030
MnO	0.023	0.023	0.021	0.020	0.020	0.028	0.033	0.021	0.022	0.020	0.031	0.016	0.046	0.05	0.02	0.02	0.05	0.03	0.04	-	-	0.010
MgO	bdl	bdl	bdl	bdl	bdl	bdl	bdl	bdl	bdl	bdl	bdl	bdl	bdl	bdl	bdl	bdl	bdl	bdl	bdl	-	1.12	0.040
CaO	-	-	0.09	-	-	0.50	0.15	0.09	0.03	1.66	0.13	0.45	1.71	0.32	0.05	0.11	0.11	0.33	0.80	-	-	0.100
Na_2O	4.49	5.27	5.43	5.39	5.71	5.96	5.83	6.01	2.38	3.15	7.71	8.66	4.06	6.24	6.01	6.06	6.29	4.85	4.03	0.08	-	0.030
K_2O	3.18	3.81	4.04	3.74	2.92	2.90	2.75	2.65	5.16	4.20	2.15	1.04	2.78	2.12	2.32	2.53	2.23	3.79	4.34	0.53	-	0.080
P_2O_5	1.62	1.74	1.74	1.64	1.49	1.74	1.55	1.87	1.72	1.64	1.57	2.69	2.06	1.76	1.78	1.95	1.92	1.77	1.47	6.46	1.71	0.200
F	0.31	0.29	0.28	0.26	0.29	0.35	0.33	0.26	0.26	0.29	0.33	0.27	0.54	0.43	0.28	0.29	0.45	0.33	0.33	0.45	0.09	
LOI	2.33	1.45	1.69	1.39	1.25	1.35	1.35	1.13	1.97	4.49	1.03	2.03	3.30	1.54	1.17	0.55	1.03	2.50	3.01	0.82	1.21	
O=F	0.13	0.12	0.12	0.11	0.12	0.15	0.14	0.11	0.11	0.12	0.14	0.11	0.23	0.18	0.12	0.12	0.19	0.14	0.14	0.19	0.04	
Total	98.96	100	99.77	98.77	99.03	99.56	99.74	99.69	99.45	99.58	99.29	99.23	98.98	99.48	99.26	98.94	98.92	99.71	99.56	100.13	99.78	
Trace elements (ppm)																						
B	NA	NA	47.70	NA	NA	42.90	47.90	46.10	87.50	51.00	3-	NA	NA	35.80	38.30	47.90	46.60	70.70	83.80	NA	NA	
Li	1645	1731	1746	1607	1684	1650	1649	1904	1774	1161	1358	1688	1445	1788	2026	2026	2462	1041	1027	5962	97.00	
As	28.00	4.86	4.90	2.73	0.75	0.51	0.88	1.23	0.70	19.93	103.86	21.00	0.55	1.00	bdl	0.96	0.91	90.23	99.31	12.30	0.75	0.20
Ba	11.20	9.70	11.54	10.90	6.20	8.67	9.82	6.45	15.05	27.13	7.01	33.40	19.20	8.48	6.77	bdl	7.45	14.71	17.24	2.60	33.70	2.0
Be	37.00	27.50	17.01	34.40	31.90	43.09	45.05	66.18	13.61	30.46	106.18	15.80	62.40	66.99	15.21	150.50	129.76	39.97	56.34	20.50	4.92	0.09

Bi	0.68	0.31	0.27	0.38	0.93	0.20	0.53	0.62	0.68	0.28	0.38	1.35	0.38	0.17	0.49	0.20	1.17	0.11	0.43	1.70	0.17	0.04
Cd	0.05	bdl	0.04	bdl	bdl	0.05	bdl	0.03	bdl	bdl	0.03	bdl	bdl	0.02	0.03	bdl	bdl	0.03	0.05	bdl	bdl	0.04
Ce	0.25	0.22	0.31	0.26	0.15	0.20	0.25	0.17	0.17	1.20	0.12	0.13	0.23	0.13	0.24	0.14	0.17	0.12	0.26	0.14	0.34	0.02
Co	0.12	bdl	bdl	bdl	bdl	0.08	bdl	bdl	0.10	0.27	0.68	0.08	0.10	0.13	0.12	bdl	bdl	0.15	2.15	0.12	0.09	0.075
Cr	1.70	2.20	4.38	2.00	1.70	5.11	2.75	2.29	3.61	2.32	3.86	2.10	1.80	4.42	5.20	3.51	1.72	2.69	3.83	1.90	1.60	0.5
Cs	30.10	32.40	36.01	31.70	29.40	39.32	47.18	23.20	39.22	46.21	32.94	15.00	78.30	50.03	25.35	25.41	49.03	30.63	36.95	8.03	0.53	0.02
Cu	21.60	6.90	30.92	7.20	6.30	9.17	8.87	6.25	11.77	36.64	16.60	21.70	15.40	9.26	9.83	7.19	7.32	16.74	23.88	14.80	bdl	6.0
Dy	0.07	0.02	0.02	0.02	0.01	0.03	0.06	0.02	0.02	0.27	0.03	0.08	0.06	0.06	0.01	0.01	0.02	0.04	0.05	0.02	0.06	0.005
Er	0.04	0.01	0.01	0.01	0.01	0.01	0.03	0.01	0.01	0.08	0.02	0.06	0.04	0.04	0.01	0.01	0.01	0.02	0.03	0.01	0.19	0.001
Eu	0.01	0.01	0.01	0.01	-	0.01	0.01	-	-	0.31	0.01	0.01	0.02	0.01	-	bdl	bdl	0.01	0.01	0.01	0.08	0.002
Ga	42.20	36.90	37.31	34.90	36.30	36.37	37.94	36.22	38.38	36.40	32.17	27.60	39.80	36.23	36.98	37.70	36.43	44.07	44.58	2.88	0.98	0.015
Gd	0.06	0.02	0.02	0.02	0.01	0.02	0.06	0.02	0.02	0.53	0.02	0.06	0.06	0.05	0.01	0.01	0.01	0.04	0.04	0.02	0.11	0.005
Ge	4.43	4.28	4.11	4.36	4.51	5.54	5.49	4.50	4.67	3.34	5.37	4.48	4.98	5.37	4.90	4.66	5.45	3.98	4.03	3.05	2.40	0.05
Hf	2.73	2.65	2.96	3.08	2.36	2.90	3.02	2.87	5.36	2.70	2.14	1.39	2.32	3.03	2.88	2.85	3.43	2.73	1.40	0.17	0.05	0.03
Ho	0.01	-	-	0.01	-	0.01	0.01	-	-	0.04	0.01	0.02	0.01	0.01	-	-	-	0.01	0.01	0.01	0.01	0.001
La	0.15	0.12	0.17	0.15	0.10	0.13	0.16	0.11	0.13	0.61	0.08	0.08	0.14	0.10	0.17	0.12	0.12	0.16	0.16	0.06	0.16	0.04
Lu	0.01	-	-	-	-	-	-	-	bdl	0.01	-	0.01	0.01	0.01	-	-	-	0.01	0.01	-	-	0.001
Nb	34.90	62.00	65.75	58.20	58.70	64.96	53.58	67.86	48.59	22.77	33.34	17.30	44.10	60.06	89.17	63.70	60.94	22.80	18.13	5.60	0.30	0.02
Nd	0.11	0.09	0.13	0.10	0.05	0.10	0.16	0.07	0.05	1.32	0.06	0.08	0.12	0.06	0.08	0.05	0.06	0.07	0.13	0.10	0.28	0.02
Ni	bdl	bdl	4.17	bdl	bdl	2.49	bdl	bdl	3.06	bdl	4.07	bdl	bdl	2.82	3.17	bdl	bdl	5.48	8.31	bdl	bdl	5.0
Pb	23.90	27.00	34.50	24.50	31.00	10.21	10.77	6.72	10	9.40	12.29	24.10	9.93	8.70	34.11	12.17	13.69	5.89	6.38	4.62	5.02	0.35
Pr	0.03	0.03	0.04	0.03	0.02	0.02	0.03	0.02	0.02	0.21	0.02	0.02	0.03	0.02	0.02	0.01	0.02	0.02	0.03	0.02	0.05	0.005
Rb	1006	1147	1311	1116	949	1104	1142	884	1 442	1185	933	350	1211	1068	853	915	1096	1249	1398	179.00	4.86	0.20
S	bdl	bdl	bdl	bdl	bdl	bdl	bdl	bdl	bdl	bdl	bdl	bdl	0.03	bdl	bdl	bdl	bdl	bdl	bdl	bdl	bdl	
Sb	0.09	0.12	0.12	0.10	0.09	0.08	0.12	0.07	0.11	0.24	0.06	0.08	0.24	0.09	0.07	0.10	0.10	0.16	0.15	0.07	0.16	0.05
Sm	0.04	0.02	0.03	0.03	0.01	0.02	0.04	0.02	0.02	0.45	0.02	0.03	0.04	0.02	0.02	0.01	0.01	0.02	0.04	0.03	0.09	0.004
Sn	842	871	1087	880	884	1127	1118	1183	1 960	378	116	107	512	1682	938	1130	1078	1116	837	578.00	8.42	2.0
Sr	12.60	12.70	12.69	12.30	4.60	84.67	11.84	6.54	23.54	143.75	4.88	132.00	677.00	105.11	2.67	7.55	4.67	12.23	16.70	1.50	303.00	0.70

Ta	38.90	61.80	71.93	60.80	62.90	77.41	64.07	76.47	159.62	19.13	27.45	19.60	38.80	78.51	83.98	75.81	81.29	36.16	26.39	13.60	1.59	0.002
Tb	0.01	-	-	-	-	-	0.01	-	-	0.06	-	0.01	0.01	0.01	-	-	-	0.01	0.01	0.01	0.01	0.001
Th	0.64	0.57	0.60	0.57	0.58	0.56	0.65	0.70	1.45	0.30	0.26	0.17	0.43	0.55	0.63	0.53	0.57	0.50	0.45	0.03	0.01	0.01
Tm	0.01	-	-	-	-	-	-	-	bdl	0.01	-	0.01	0.01	0.01	-	-	-	-	-	-	-	0.0005
U	7.31	5.44	6.29	5.86	8.95	15.02	5.44	7.74	9.99	9.21	5.27	8.50	8.28	10.40	6.35	10.93	11.44	5.59	4.33	2.27	0.51	0.01
W	3.89	38.80	6.15	19.00	6.26	5.94	4.46	18.37	4.16	3.58	3.16	2.91	6.16	5.96	3.12	9.96	8.76	25.91	58.80	2.11	1.56	0.70
Y	0.29	0.12	0.13	0.13	0.09	0.17	0.34	0.13	0.093	1.35	0.15	0.44	0.54	0.40	0.11	0.11	0.15	0.18	0.24	0.08	0.37	0.03
Yb	0.05	0.02	0.02	0.02	0.01	0.02	0.03	0.02	-3	0.06	0.02	0.08	0.04	0.03	0.01	0.01	0.02	0.04	0.04	0.01	0.01	0.002
Zn	79.70	56.80	57.33	51.30	51.20	58.76	59.01	51.98	29.23	44.98	49.70	24.60	114.00	58.29	53.56	50.97	65.61	57.67	63.27	bdl	bdl	5.0
Zr	14.70	13.70	15.32	15.70	13.10	15.84	15.26	14.54	15.08	16.13	13.29	9.85	16.20	15.08	15.32	15.17	16.72	15.53	8.35	1.87	1.13	0.80

bdl: below detection limit; NA : not analyzed.

1

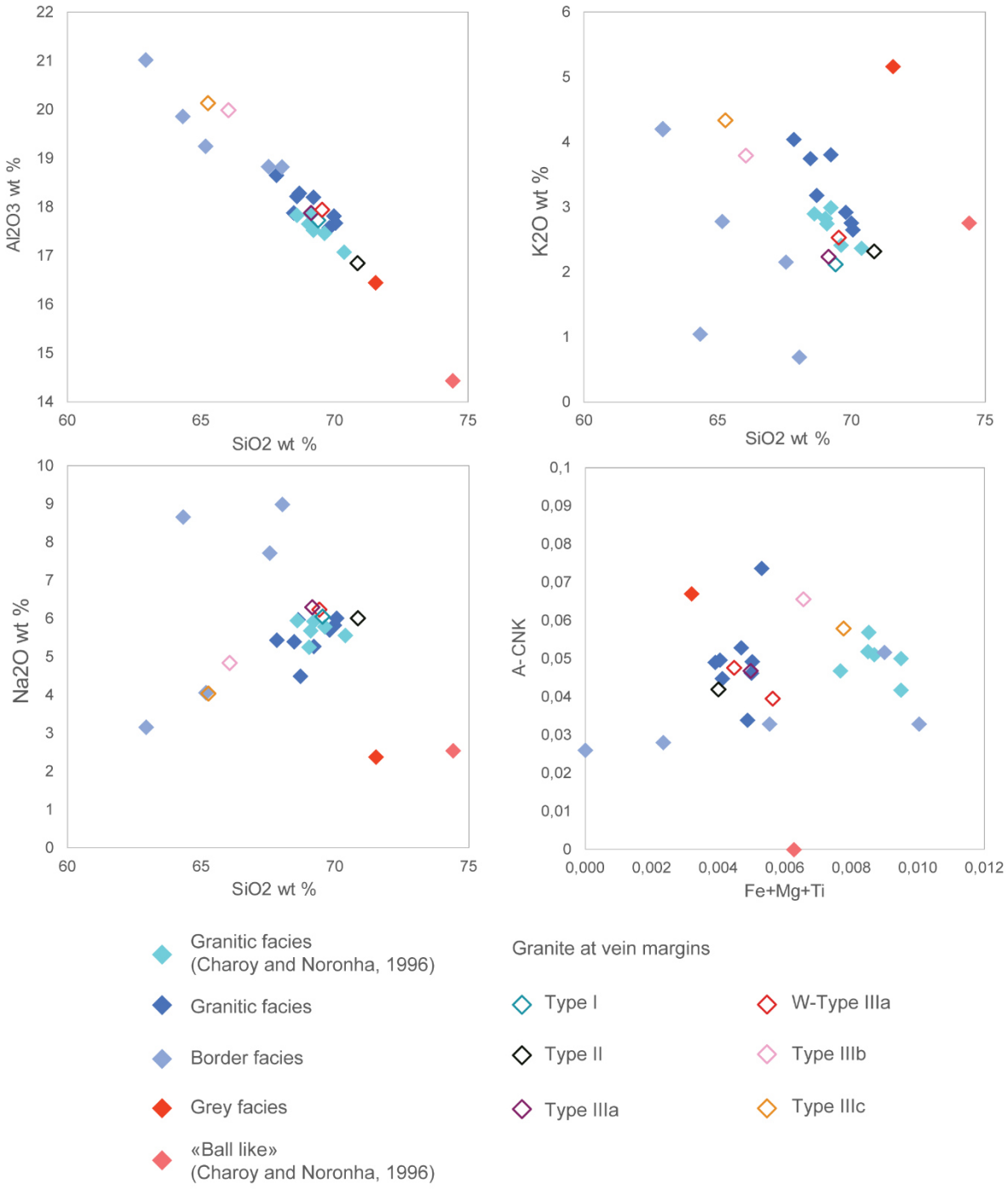

Fig 5 *Comparison of whole rock major element compositions of the different facies, granite at vein margins and intragranitic veins*

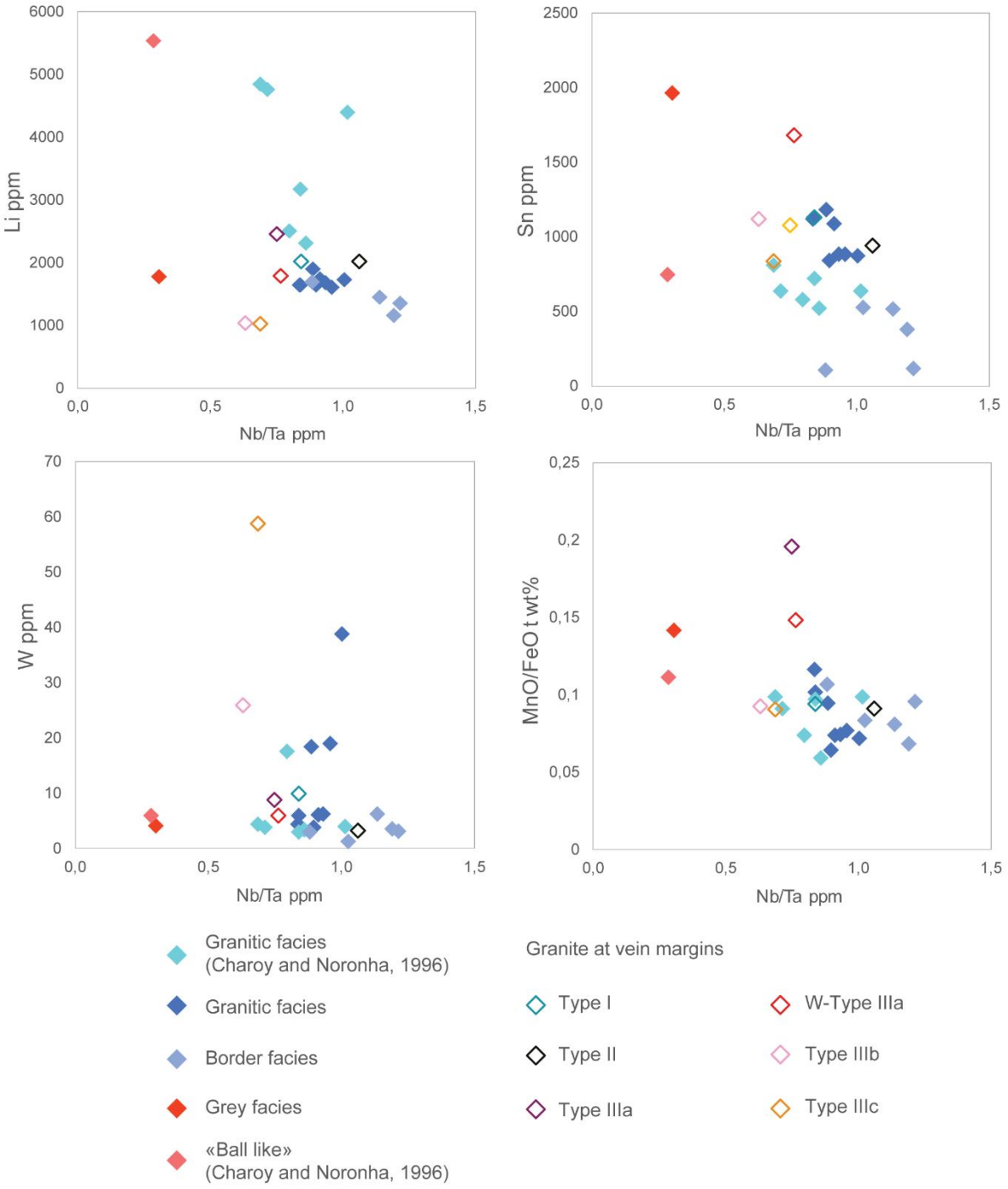

Fig 6 *Comparison of whole rock trace element compositions of the different facies, granite at vein margins and intragranitic veins*

Samples of granite at the margins of Type I, II and IIIa intragranitic veins show the same range of major element variations than samples away from the veins (Table 1, Fig. 5). P_2O_5 is the only major oxide showing a slightly higher concentration (from 1.70 to 1.90 wt%) near the veins. Li (1800-2400 ppm), Nb (60-90 ppm) and Ta (75-84 ppm) are all slightly higher near than away from the veins (Li: 1600-1900 ppm; Nb: 35-68 ppm; Ta: 39-77 ppm). The Nb/Ta ratio is lower at the margins of Type I and IIIa veins (Table 1, Fig. 6). For the granite at the margins of Type IIIb and c veins, collected near the sheared northeastern border of the intrusion, the major element data differ from all other samples, SiO_2 (65-66 wt%) and Na_2O (4-4.8 wt%) being lower and K_2O (3.7-4.3 wt%), Al_2O_3 (~20 wt%), CaO (0.3-0.8 wt%) and FeOt (0.37-0.43 wt%) higher (Table 1, Fig. 5). Sn, Rb and Cs are in the same range while Li shows lower values (1027-1041 ppm) and W is higher (26-58 ppm). As is quite high (90-99 ppm). Type I and W-free Type IIIa veins were also analyzed (Table 1). Both veins show high SiO_2 content (86 and 94 wt% respectively) and low Al_2O_3 (5.6 and 0.3 wt% respectively). P_2O_5 is really high in the Type I vein (~6.5 wt%) and similar to the granitic facies in Type IIIa vein (1.71 wt%). Type I vein is characterized by very high concentration of Li (5962 ppm), intermediate Sn (578 ppm) and low Nb (5.6 ppm). In Type IIIa vein, the metal content is very low (Li: 97 ppm; Nb: 0.3 ppm; Sn: 8.42 ppm; Ta: 1.6 ppm and W: 1.56). For both samples Nb/Ta are very low: 0.41 and 0.19 respectively.

Overall, the granitic facies of Argemela fit with the definition of PHP RMGs defined in Linnen and Cuney (2005), being strongly enriched in P, Rb and rare metals (Li, Sn, Nb, Ta) with low Nb/Ta ratios. The range of concentration in major and trace elements are overall fitting with the data of Charoy and Noronha (1996) for the granitic facies. The border facies is slightly less peraluminous and rare metals (namely Sn and Li) enrichments are lesser. Nb/Ta ratio is higher, but P is high. These geochemical characteristics still fit with the PHP RMGs class. The grey facies represent an extreme regarding enrichment in Sn, Ta, Rb and low Nb/Ta ratio. No strict equivalent of the “ball like” (Charoy and Noronha, 1996) has been recognized even if signature of the grey facies also represents an extreme. No strong apparent modifications are observed at vein margins except for those sampled at the northeastern sheared border. Type I and W-free Type IIIa veins are relatively depleted in metals and Nb/Ta ratios are quite low.

V.5.2. Mineral analyses

Micas. Major and trace elements analyses of the different mica generations are given in Table 2 and 3, respectively. In the binary Mg-Li - Fe+Mn+Ti+AlIV diagram (Fig. 7), Ms_{I} plot mainly in the muscovite field with a slight shift toward the phengite, Li-phengite and Li-muscovite fields. As Ms_{II} can be difficult to distinguish from Ms_{III}, both mica types are plotted with the same symbol, and they fall exclusively in the muscovite field. Thus, mica major element compositions differ little between the $Ms_{I-II-III}$ generations although a general evolution toward pure muscovite can be noted from Ms_{I} to Ms_{II-III}. In the ternary M2+ - Li - Al diagram (not shown), most points are aligned on the muscovite-zinnwaldite join, showing the same tendency toward pure muscovite. Ms_{IVa} and Ms_{IVb} show a more dispersed distribution. The two do not exactly overlap, Ms_{IVa} plotting in the muscovite, phengite, Li-muscovite to Li-phengite and Ms_{IVb} in the Li-muscovite, Li-phengite, zinnwaldite to lepidolite fields (Fig. 7). Therefore, Ms_{IVa} appears as intermediate between compositions within the muscovite field and Ms_{IVb}. In the ternary M2+ - Li - Al diagram (not shown), Ms_{IVa} and Ms_{IVb} compositions plot on the same trend from muscovite to between zinnwaldite and trilithionite. Thus, overall, $Ms_{I-II-III}$ are Li-poor dioctahedral micas and Ms_{IV} Li-rich trioctahedral micas. Compositions of mica cores from Charoy et al. (1995) are similar to the $Ms_{I-II-III}$ group from this study but rims plot outside the Ms_{IVa} and Ms_{IVb} domains (Fig. 7). In the ternary M2+ - Li - Al diagram (not shown), rims from Charoy et al. (1995) plot close to trilithionite on the muscovite - trilithionite join and so have lower M2+ than Ms_{IVa} and Ms_{IVb} from this study.

Table 2

Representatives EPMA major elements analyses of micas

	MsIa		MsIb	MsIIa		MsIIb		MsIII	MsIa	MsII-III	MsIVb	MsI		MsII-III		MsIVa		MsIVb	
Major elements (wt%)												Mean (62)	σ	Mean (30)	σ	Mean (25)	σ	Mean (11)	σ
SiO_2	44.62	46.58	45.64	46.74	46.80	45.93	45.99	45.82	44.49	46.58	49.41	46.62	1.16	47.06	1.19	48.19	1.46	48.10	1.41
TiO_2	-	0.09	-	0.10	-	-	0.08	0.09	0.11	-	0.07	0.04	0.04	0.03	0.04	0.02	0.02	0.01	0.02
Al_2O_3	32.15	32.77	32.55	32.79	33.32	31.87	32.51	33.25	32.98	34.46	21.25	33.65	1.77	33.57	2.23	32.12	2.65	26.68	4.01
FeO	2.59	2.80	2.74	1.81	1.94	2.59	1.53	1.17	2.72	0.69	5.94	2.66	0.73	1.92	0.88	1.86	1.10	4.33	1.34
MnO	0.20	0.04	0.14	-	-	0.21	0.22	0.03	0.08	-	0.64	0.12	0.10	0.16	0.11	0.43	0.29	0.46	0.17
MgO	0.05	0.02	0.04	0.24	0.25	0.10	0.02	0.13	0.07	-	0.01	0.06	0.05	0.06	0.07	0.02	0.02	0.05	0.05
CaO	0.01	-	-	-	-	-	0.02	0.06	-	-	-	0.01	0.02	0.01	0.01	0.02	0.03	bdl	0.01
Na_2O	0.58	0.68	0.60	0.75	0.70	0.55	0.13	0.11	0.68	0.14	0.19	0.48	0.15	0.23	0.21	0.14	0.10	0.16	0.07
K_2O	7.60	7.38	7.65	7.74	7.51	7.78	7.54	7.55	7.86	8.51	7.91	9.14	0.98	9.01	1.14	10.26	0.45	8.35	1.05
P_2O_5	0.20	0.11	-	0.03	0.06	0.06	-	0.11	0.09	0.03	-	0.08	0.07	0.05	0.06	0.04	0.03	0.03	0.04
F	1.74	2.70	2.67	1.79	1.40	3.02	1.91	1.28	1.72	1.35	9.38	1.70	1.05	1.65	0.99	2.68	1.42	7.11	3.36
O=F	0.73	1.14	1.12	0.75	0.59	1.27	0.80	0.54	0.72	0.57	3.95	0.71	0.44	0.69	0.42	1.13	0.60	2.99	1.41
Total	89.69	92.65	91.63	91.86	92.02	91.70	89.84	89.67	90.67	91.83	92.33	94.40	2.34	93.71	2.78	95.44	1.40	93.31	1.92
Number of cations based on 22 O																			
Si	6.10	6.08	6.04	6.21	6.23	6.07	6.22	6.25	6.02	6.20	5.81	6.09	0.07	6.16	0.12	6.08	0.08	5.87	0.20
P	0.02	0.01	-	-	0.01	0.01	-	0.01	0.01	-	-	0.01	0.01	0.01	0.01	bdl	bdl	bdl	bdl
Al IV	1.88	1.91	1.96	1.78	1.76	1.92	1.78	1.74	1.97	1.79	2.19	1.90	0.07	1.84	0.11	1.91	0.08	2.13	0.20
Al VI	3.30	3.13	3.12	3.36	3.46	3.04	3.41	3.60	3.29	3.62	0.76	3.29	0.26	3.34	0.36	2.88	0.45	1.73	0.82
Ti	-	0.01	-	0.01	-	-	0.01	0.01	0.01	-	0.01	bdl	bdl	bdl	bdl	bdl	bdl	bdl	bdl
Fe	0.30	0.31	0.30	0.20	0.22	0.29	0.17	0.13	0.31	0.08	0.58	0.29	0.08	0.21	0.09	0.20	0.11	0.44	0.12
Mn	0.02	-	0.02	-	-	0.02	0.03	-	0.01	-	0.06	0.01	0.01	0.02	0.01	0.05	0.03	0.05	0.02
Mg	0.01	-	0.01	0.05	0.05	0.02	-	0.03	0.01	-	-	0.01	0.01	0.01	0.01	-	-	0.01	0.01
Na	0.15	0.17	0.15	0.19	0.18	0.14	0.04	0.03	0.18	0.04	0.04	0.12	0.04	0.06	0.05	0.04	0.03	0.04	0.02
K	1.33	1.23	1.29	1.31	1.28	1.31	1.30	1.31	1.36	1.45	1.19	1.52	0.16	1.50	0.16	1.65	0.10	1.30	0.19

bdl: below detection limit

Table 3

Representatives LA-ICP-MS trace elements analyses of micas

	MsIa		MsIb	MsIIa		MsIIb		MsIII	MsIa	MsII-III	MsIVb	MsI		MsII-III		MsIVa		MsIVb	
Trace elements (ppm)												Mean (62)	σ	Mean (30)	σ	Mean (25)	σ	Mean (11)	σ
Li	2082 (66.5)	1560 (49.8)	1810 (40.5)	967.27 (31.5)	1266 (40.5)	799.84 (26.2)	683.5 (22.1)	377.64 (12.3)	2718 (91.4)	887.75 (30.3)	22163 (756.9)	2528	1434	3160	3265	8294	3169	10937	3690
Be	20.09 (2.5)	23.44 (2.4)	25.2 (2.7)	26.86 (3.3)	26.97 (2.7)	11.6 (2.4)	23.39 (2.7)	22.31 (2.7)	25.25 (2.4)	27.97 (2.7)	231.62 (15.4)	32.00	7.21	32.35	10.58	47.81	14.01	38.00	10.07
B	61.29 (4.5)	90.77 (5.3)	135.8 (7.18)	129.99 (8.21)	128.62 (7.2)	61.09 (5.0)	353.26 (19.2)	555.52 (30.6)	93 (10.1)	475.35 (53.3)	220.85 (25.3)	142.57	33.57	270.73	138.41	180.43	81.04	128.17	67.13
Sc	5.24 (0.6)	3.85 (0.5)	2.83 (0.5)	5.62 (0.7)	7.21 (0.5)	6.34 (0.7)	3.28 (0.5)	3.47 (0.6)	5.74 0.6)	3.69 (0.7)	4.7 (0.5)	3.77	1.27	4.20	1.91	2.24	0.67	3.96	0.93
Ti	159.86 (12.1)	179.96 (12.8)	169.85 (45.0)	496.32 (41.9)	650.31 (45.0)	35.79 (6.6)	108.49 (9.52)	59.39 (6.7)	414.48 (35.1)	174.4 (16.9)	44.51 (5.7)	233.07	75.14	179.25	118.27	110.16	33.56	82.79	35.15
Mn	710.77 (28.7)	622.28 (25.3)	687.12 (17.4)	360.24 (16.7)	421.07 (17.4)	317.27 (15.0)	968.83 (41.9)	295.19 (13.3)	901.14 (44.5)	999.35 (51.9)	2584 (135.7)	884	335	1313	992	3970	1601	3188	1385
Fe	6899 (304.1)	9478 (423.7)	7985 (235.5)	5540 (298.3)	5565 (253.6)	1625 (91.0)	2640 (130.6)	705.95 (38.0)	9262 (839.3)	3320 (331.3)	6426 (656.0)	8842	2718	6082	3678	7829	2813	10643	3339
Zn	609.47 (24.3)	621.45 (24.7)	939.78 (28.8)	658.55 (28.6)	720.1 (28.8)	66.54 (3.9)	89.68 (4.3)	92.67 (4.5)	933.34 (122.9)	104.63 (14.9)	78.99 (11.4)	982.86	310.12	387.34	429.23	274.71	129.85	387.84	353.78
Ga	131.48 (4.2)	142.95 (4.5)	142.88 (4.3)	127.14 (4.1)	137.18 (4.3)	53.77 (1.9)	138.36 (4.4)	183.7 (5.8)	151.05 (5.9)	110.48 (4.5)	24.91 (1.1)	139.27	13.99	126.73	23.19	117.83	24.52	83.79	24.30
Ge	4.35 (1.6)	3.95 (1.2)	5.73 (1.3)	4.4 (1.7)	6.26 (1.3)	bdl	bdl	4.23 (1.5)	5.4 (1.4)	6.31 (1.6)	13.49 (1.3)	5.73	1.70	5.71	1.48	7.11	1.86	10.53	2.80
Rb	2523 (84.3)	3544 (118.9)	4384 (154.2)	4146 (146.8)	4575 (154.2)	6034 (215.2)	3806 (131.2)	2963 (103.5)	4384 (141.6)	3242 (105.8)	11750 (384.6)	4901	995	5224	1705	7805	1587	8755	2256

Sr	bdl	bdl	bdl	bdl	bdl	bdl	bdl	bdl	bdl	bdl	0.7 (0.1)	0.46	0.08	0.51	0.07	0.78	0.77	bdl	bdl
Zr	bdl	0.74 (0.2)	bdl	bdl	bdl	bdl	bdl	0.79 (0.3)	bdl	bdl	bdl	0.74	0.08	0.76	0.22	0.83	0.12	0.89	0.20
Nb	85.85 (2.8)	123.5 (4.0)	122.32 (3.8)	104.46 (3.6)	115.39 (3.8)	18.39 (0.7)	30.58 (1.0)	14.19 (0.5)	154.47 (5.5)	26.61 (1.0)	28.77 (1.1)	130.71	19.26	85.17	64.78	136.84	51.15	121.40	59.71
Sn	132.45 (5.1)	196.31 (7.4)	274.98 (11.3)	269.91 (11.2)	297.35 (11.3)	88.16 (3.9)	182.66 (7.3)	110.26 (4.5)	245.63 (8.2)	162.02 (5.5)	58.21 (2.1)	296.82	56.52	291.71	90.18	329.77	100.81	319.86	111.15
Cs	40.74 (1.3)	61.37 (2.0)	83.82 (3.2)	87.3 (2.9)	99.73 (3.2)	128.83 (4.3)	80.87 (2.6)	36.94 (1.2)	92.12 (3.4)	54.58 (2.1)	717.5 (27.3)	115.88	54.37	168.48	103.74	326.35	96.72	596.81	274.32
Ba	bdl	bdl	bdl	bdl	4.22 (1.1)	64.57 (3.1)	5.66 (1.2)	6.84 (1.2)	bdl	9.58 (1.5)	34.05 (2.0)	7.11	9.00	11.51	10.46	6.90	7.91	11.10	6.78
Ta	6.72 (0.3)	8.83 (0.3)	9.39 (0.4)	9.99 (0.4)	11.74 (0.4)	3.35 (0.2)	5.2 (0.2)	3.98 (0.2)	11.52 (0.5)	7.01 (0.3)	23.51 (1.0)	10.87	3.31	13.66	6.89	20.90	6.99	97.20	69.89
W	20.61 (1.1)	24.94 (1.1)	18.96 (0.6)	7.1 (0.8)	8.06 (0.6)	3.07 (0.7)	15.91 (0.9)	2.63 (0.6)	26.27 (1.3)	4.96 (0.7)	15.11 (0.8)	16.29	7.07	16.51	8.01	14.79	4.67	27.88	14.64
U	bdl	bdl	bdl	bdl	bdl	1.84 (0.2)	bdl	0.55 (0.2)	bdl	bdl	0.99 (0.1)	0.78	0.49	2.83	4.12	1.11	1.59	0.91	0.60
Nb/Ta	12.78	13.99	13.03	10.46	9.83	5.49	5.88	3.57	13.41	3.80	1.22	12.46	1.85	5.82	2.91	6.36	1.38	2.04	1.49
Mn/Fe	0.10	0.07	0.09	0.07	0.08	0.20	0.37	0.42	0.10	0.30	0.40	0.11	0.06	0.22	0.07	0.50	0.06	0.30	0.11

bdl : below detection limit

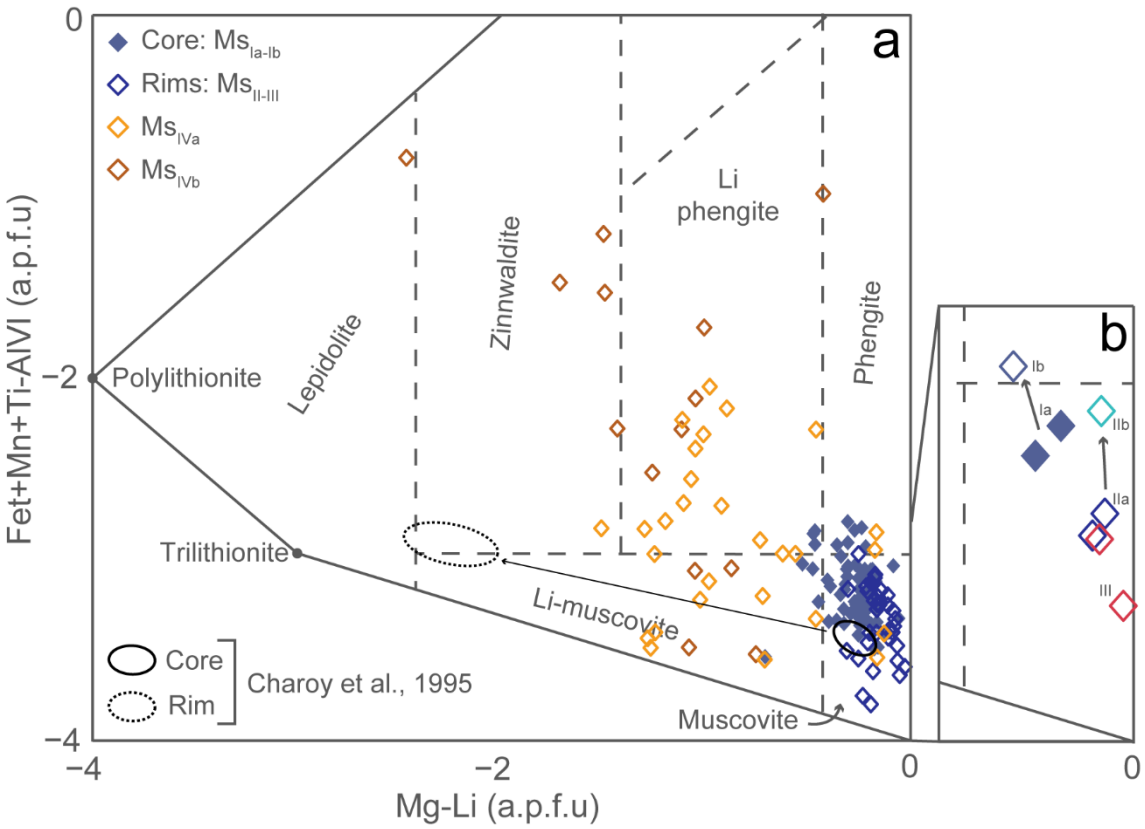

Fig 7 *Geochemical signature of the fourth generations of micas. Nomenclature from Tischendorf (1997). (a) General evolution from Ms$_I$ to Ms$_{IV}$ and (b) zoom on intermediate slight variations between Ms$_I$ and M$_{III}$*

Chemical zonations in micas from the granitic facies are detailed on a representative example (mica A, Fig. 8a, b, c). The major element zonation from Ms$_I$, Ms$_{II}$ to Ms$_{III}$ is minor (Fig. 7). Fe, Li and Mn progressively decrease from core to rim, all passing through a maximum in the Ms$_{Ib}$ zone (Fig. 8a). F is quite constant, slightly increasing from the internal darker (Ms$_{Ia}$ and Ms$_{IIa}$) to the external brighter (Ms$_{Ib}$ and Ms$_{IIb}$) parts in both zones. All trace elements (Sn, B, Nb, Ta) except W increase from Ms$_{Ia}$ to Ms$_{Ib}$ (Fig. 8a). However, the opposite is true for Ms$_{IIa}$ to Ms$_{IIb}$, the Ms$_{IIb}$ zone being characterized by marked depletions in all elements except F. These depletions do not extend into the Ms$_{III}$ zone where a more variable behavior is observed between elements, Fe, Li and F being constant or decreasing and Mn and all trace elements including W increasing to various and sometimes large (i.e., 61 to 454 ppm for B) extents (Fig. 8a).

Granitic facies

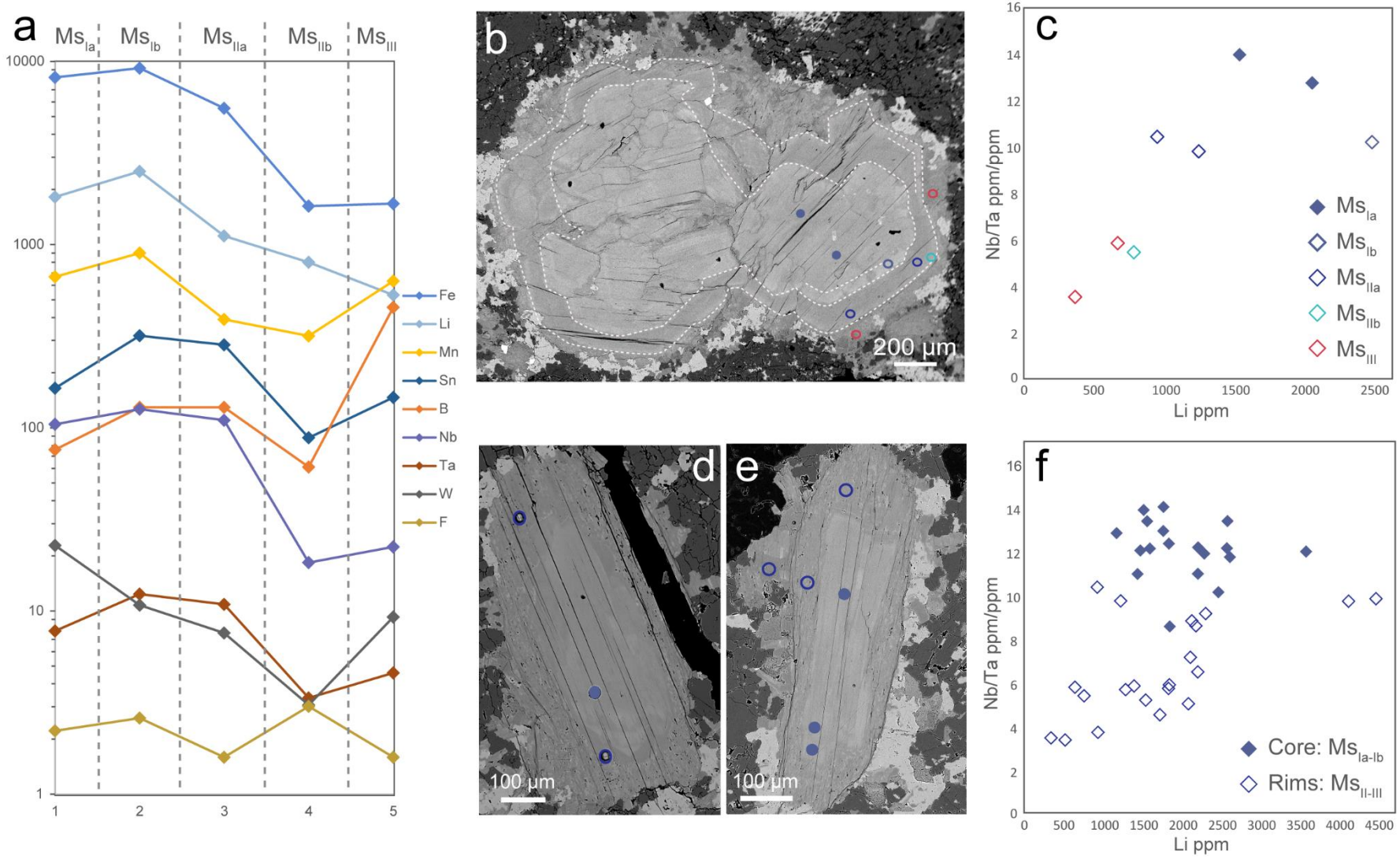

Fig 8 *Chemical characteristics of micas from the granitic facies in relationship with zonation. (a) Chemical variations from core to rim of mica A (see picture b). Numbering 1-5 corresponds to the different zones in (b). (c) Decrease of the Nb/Ta and of the Li content from* Ms_I *to* Ms_{III} *of the mica A. (d) and (e) other micas from the granitic facies where zonations are more difficult to distinguish. (f) Nb/Ta and Li decrease in other micas (i.e., apart from mica A). Analyzed with a 27µm beam. See the text for details*

Other micas from the granitic facies exhibit the same range of concentrations and type of zonation. For example, in mica A from Ms_I to Ms_{III}, the Nb/Ta ratio decreases steadily from ~14 to less than 4 as Li drops from ~2500 to < 400 ppm (Fig. 8c). Other micas (Fig. 8d, e) show the same Nb/Ta (also from ~14 to less than 4) whereas Li decreases from ~4500 to < 400 ppm (Fig. 8f).

In the border facies, micas (Fig. 9a, b, c, d) with intermediate zones are less well represented than in the granitic facies. Cores (corresponding mostly to Ms_{Ia}) have the same range of trace element concentrations than in the granitic facies (i.e., 1500-3000 ppm Li, Nb/Ta between ~15 and 11). Rims, which include Ms_{II} and Ms_{III}, also show similar compositions than Ms_{II-III} from the granitic faces (i.e., 400-900 ppm Li, Nb/Ta from ~5 to < 2). Core-rim zonations are marked by an overall decrease in all elements except Mn and B, as observed from Ms_I to Ms_{III} in the granitic facies (Fig. 9a). Ms_{IVb} strongly contrast with Ms_{I-III} compositions, showing Li and F enrichments up to 22000 ppm and 12 wt% respectively (Fig. 9a, e, f). They are enriched in Ta (from 30 to 200 ppm), W (from 13 to 56 ppm) and B (from 44 to 270 ppm) compared to Ms_{I-III}. Nb/Ta ratios are low to extremely low, from ~4 to less than 1 (Fig. 9e). The transition from Ms_{I-III} to Ms_{IVb} is marked by a decrease in Nb/Ta while Li increases, i.e., the reverse than observed from Ms_I to Ms_{II-III} in the granitic facies. Ms_{IVa} (from the granitic sample near the border facies) are intermediate between Ms_I and Ms_{IVb} and thus less evolved equivalents of Ms_{IVb}. The Mn/Fe - Al_2O_3 diagram (Fig. 9f) highlights two different trends, the first marked by an increase of the Mn/Fe ratio at essentially constant Al_2O_3 content (Ms_I, Ms_{II-III}) and the second by a decrease of Mn/Fe correlated with a decrease of Al_2O_3 (Ms_{IVa}, Ms_{IVb}).

Border facies

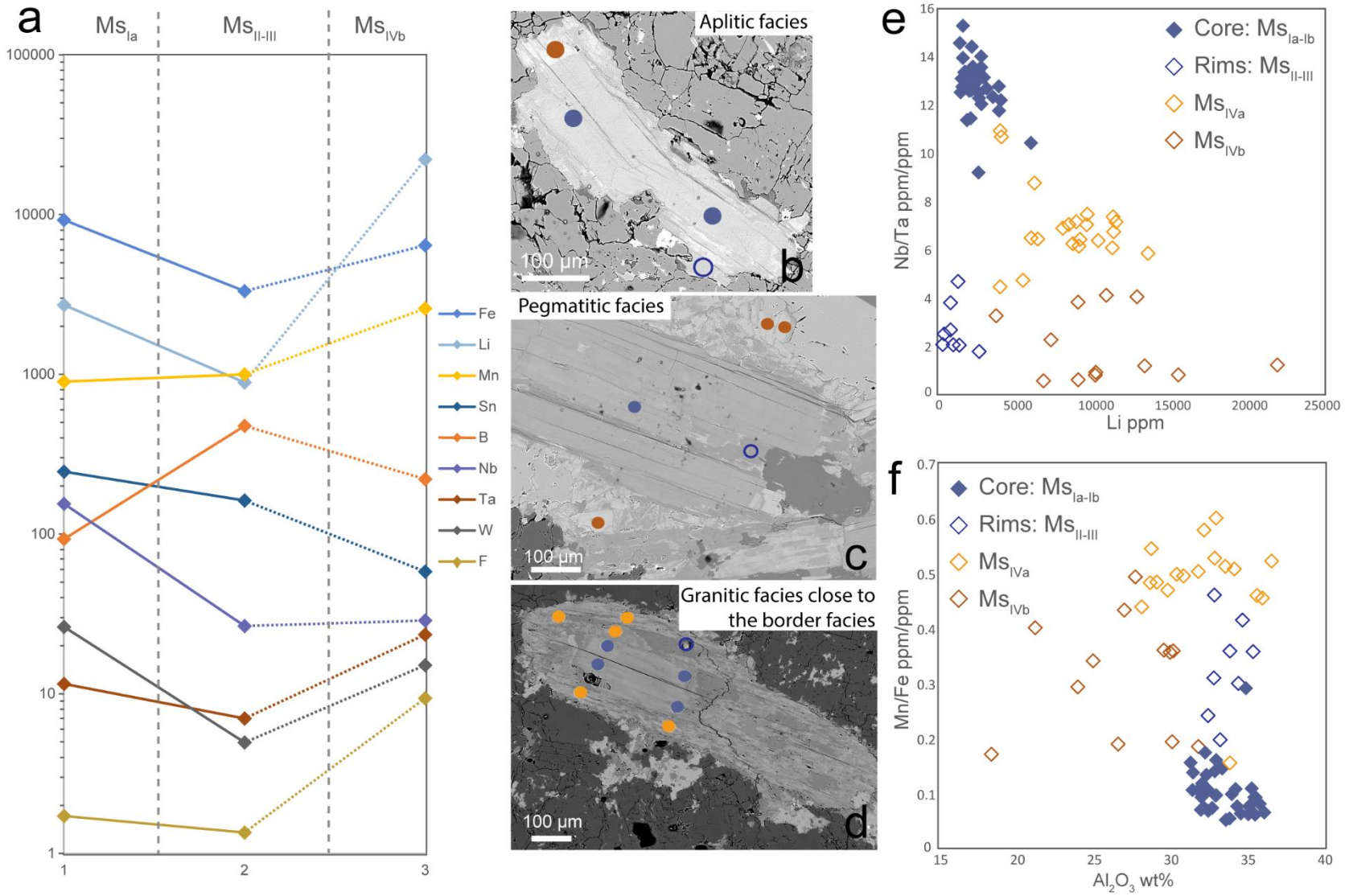

Fig 9 *Chemical characteristics of micas from the border facies in relationship with zonation. (a) Chemical variation from core to rim and apparition of patchy* Ms_{IVb}*; (b) and (c) examples of analyzed micas from the aplitic and the pegmatitic facies showing patchy* Ms_{IVb}*; (d)* Ms_{IVa} *from the granitic facies occurring close to the border facies showing intermediate composition; (e) and (f) Nb/Ta vs Li and Mn/Fe vs* Al_2O_3 *chemical evolution from* Ms_I *to* Ms_{IV}*. Analyzed with a 27µm beam. See text for details*

Quartz. Of the seven quartz generations recognized, four occur disseminated in the granite (Qtz_I, Qtz_{II}, Qtz_{III} and Qtz_{VII}) and three are from intragranitic veins (Qtz_{IV}, Qtz_V and Qtz_{VI}). Data are given in Table 4. In the granitic facies, the zonation from cathodoluminescence imaging on Qtz_{Ia} crystals is weakly marked chemically and only core-rim relations are detailed. Cores are slightly enriched in Al (1300-2050 ppm), Rb (7-26 ppm), Li (50-72 ppm), B (10-17 ppm) and Sn (0.10-0.34 ppm) compared to rims (Al: 640-1010 ppm; Rb: 1.4-5.3 ppm; Li: 25-44 ppm, B: 4.7-6.4 ppm and Sn mostly between 0.10 and 0.14 ppm, Fig. 10a and 11). For most trace elements, concentrations in Qtz_{Ia} extend little modified to Qtz_{Ib} except for Ge, higher in Qtz_{Ib} (10.8 ppm) than in Qtz_{Ia} (<3-7 ppm, Fig. 10b and 11). In the micaceous part of the border facies, skeletal Qtz_{III} is depleted in Al (460-700 ppm), Li (11-13 ppm), Rb (3.2-7.8 ppm) and Sn (0.10-0.16 ppm) compared to residual Qtz_I (Al ~1520 ppm, Rb: 13-13.7 ppm, Li: 36-44 ppm, Sn ~0.3 ppm, Fig. 10c and 11).

Table 4

Representative LA-ICP-MS analyses of trace elements in quartz (ppm)

	QtzIa core		QtzIa rim		QtzIb		Residual QtzI		QtzIII		QtzIV		
	Mean (16)	σ	Mean (16)	σ	Mean (6)	σ	Mean (3)	σ	Mean (5)	σ	1	2	3
Distance from vein margin (mm)											1	2	5
Al	1033.24	546.58	706.98	155.14	791.49	124.83	1153.16	473.18	526.52	101.90	1390.79 (189.1)	1167.88 (158.9)	253.43 (34.5)
Li	48.82	10.16	34.48	6.18	38.03	8.61	32.66	5.77	14.07	2.27	36.55 (3.44)	27.14 (2.6)	4.86 (0.5)
Be	2.34	2.56	0.98	0.06	bdl	bdl	1.60	0.27	bdl	bdl	0.99 (0.1)	bdl	bdl
B	8.56	2.98	6.00	1.26	6.98	1.13	8.59	1.35	6.04	0.71	6.96 (1.1)	8.38 (1.3)	7.37 (1.2)
Ti	4.84	1.92	3.66	0.43	4.10	0.71	3.93	0.84	3.42	0.13	4.31 (0.5)	3.69 (0.4)	3.36 (0.4)
Mn	0.97	0.47	0.97	0.29	1.26	0.34	0.64	0.06	0.86	0.13	bdl	bdl	bdl
Fe	15.29	bdl	68.38	bdl	bdl	bdl	bdl	bdl	24.90	bdl	bdl	bdl	bdl
Ge	4.67	0.76	5.13	0.88	8.57	2.85	4.27	1.03	5.05	1.02	4.51 (0.4)	4.05 (0.5)	3.5 (0.4)
As	0.75	0.47	0.43	0.03	0.46	0.06	0.53	bdl	bdl	bdl	bdl	0.56 (0.2)	bdl
Rb	6.45	6.23	3.91	2.20	7.19	1.16	10.32	3.64	3.53	2.60	3.37 (0.3)	5.19 (0.5)	2.16 (0.2)
Sr	0.79	1.70	0.10	0.05	0.09	0.04	bdl	bdl	0.06	0.01	bdl	0.0713 (0.007)	bdl

Nb	0.19	0.18	0.06	bdl	bdl	bdl	bdl	bdl	bdl	bdl	bdl	bdl	bdl
Sn	0.20	0.09	0.14	0.05	0.21	0.08	0.20	0.10	0.12	0.03	0.143 (0.02)	0.174 (0.02)	0.197 (0.02)
Sb	0.27	0.43	0.12	0.04	0.16	0.09	0.13	0.06	0.16	0.02	0.161 (0.04)	bdl	bdl
Ta	0.05	0.05	0.02	0.01	0.06	0.06	0.01	-	0.02	-	bdl	0.052 (0.01)	0.0185 (0.004)
W	0.96	1.15	0.05	0.04	0.05	-	0.18	bdl	bdl	bdl	bdl	0.0337 (0.008)	bdl

bdl: below detection limit

Continued

			QtzV		QtzVI							QtzVII	
	4	5	Mean (9)	σ	1	2	3	4	5	6	7	Mean	σ
Distance from vein margin (mm)	10	12			0.4	0.6	1.75	2.1	2.55	2.65	3.1		
Al	95.27 (13.0)	214.14 (29.2)	85.38	44.78	843.98 (129.2)	434.73 (66.9)	68.64 (10.6)	64.86 (10.1)	75.4 (11.8)	68.42 (10.8)	64.95 (10.2)	428.35	660.41
Li	3.81 (0.4)	12.15 (1.2)	4.86	6.75	42.31 (4.6)	27.98 (3.1)	1.44 (0.2)	0.99 (0.1)	1.7 (0.2)	0.78 (0.1)	1.24 (0.2)	8.74	6.01
Be	bdl	bdl	bdl	bdl	bdl	bdl	bdl	bdl	bdl	bdl	bdl	bdl	bdl
B	8.37 (1.4)	8.49 (1.4)	5.58	1.25	8.62 (1.6)	7.96 (1.5)	14.87 (2.8)	7.03 (1.4)	5.31 (1.06)	3.97 (0.8)	7.77 (1.6)	6.97	2.12

Ti	3.45 (0.5)	5.72 (0.7)	3.06	0.03	3.33 (0.5)	6.82 (0.9)	bdl	bdl	bdl	bdl	bdl	4.72	1.57
Mn	bdl	0.9 (0.06)	bdl	bdl	0.498 (0.04)	0.547 (0.04)	bdl	bdl	bdl	bdl	bdl	1.76	0.90
Fe	bdl	79.51 (11.8)	bdl	bdl	bdl	bdl	bdl	bdl	bdl	bdl	bdl	10.32	bdl
Ge	3.72 (0.4)	2.54 (0.3)	3.33	0.34	5.1 (0.6)	3.37 (0.4)	2.9 (0.3)	2.72 (0.3)	2.48 (0.3)	2.59 (0.3)	2.83 (0.3)	3.85	0.99
As	0.5 (0.2)	1.04 (0.4)	0.44	-	0.76 (0.3)	bdl	0.9 (0.4)	bdl	bdl	bdl	0.49 (0.2)	3.68	4.50
Rb	0.312 (0.03)	0.794 (0.08)	0.17	0.05	4.1 (0.4)	2.94 (0.3)	0.219 (0.03)	0.101 (0.01)	bdl	bdl	0.189 (0.02)	4.53	6.91
Sr	0.441 (0.04)	0.154 (0.02)	0.08	0.02	0.12 (0.01)	0.094 (0.01)	0.166 (0.02)	bdl	0.096 (0.01)	bdl	bdl	0.18	0.13
Nb	bdl	bdl	bdl	bdl	0.0536 (0.007)	bdl	bdl	bdl	bdl	bdl	bdl	0.13	0.03
Sn	0.162 (0.02)	0.343 (0.04)	0.09	0.01	0.156 (0.02)	0.164 (0.02)	0.114 (0.01)	0.136 (0.02)	bdl	bdl	0.119 (0.02)	0.20	0.11
Sb	0.206 (0.06)	0.53 (0.1)	0.11	0.03	0.14 (0.04))	0.173 (0.05)	0.309 (0.1)	0.103 (0.03)	bdl	bdl	0.178 (0.06)	0.10	0.03
Ta	0.0273 (0.006)	0.129 (0.03)	0.02	0.01	0.0185 (0.005)	0.0256 (0.006)	0.0114 (0.003)	0.0139 (0.004)	bdl	bdl	0.0155 (0.004)	0.05	0.02
W	0.041 (0.01)	0.217 (0.05)	0.13	0.03	0.047 (0.01)	0.69 (0.2)	0.097 (0.03)	0.15 (0.04)	0.037 (0.01)	bdl	0.034 (0.01)	24.96	36.18

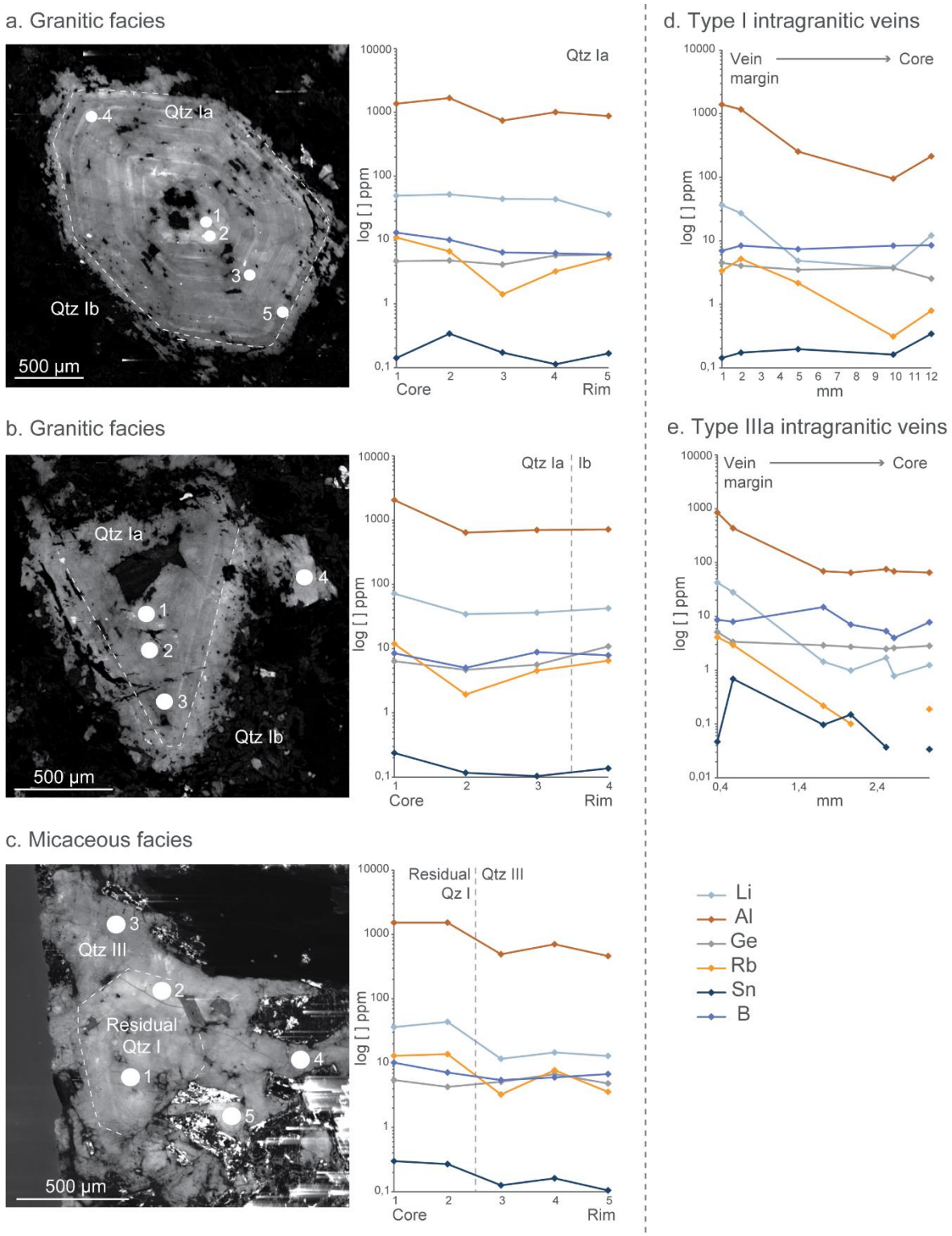

Fig 10 *Chemical characteristics of quartz from the granitic and micaceous facies and of the Type I and IIIa intragranitic veins. CL images of quartz from the granitic facies and chemical variations in QtzIa from core to rim (a) and between QtzIa to QtzIb (b); (c) CL image and chemical variations between residual QtzI and skeletal Qtz III; (d) and (e) chemical variation from margin to core of Type I and IIIa intragranitic veins, respectively. Analyzed with a 85µm beam*

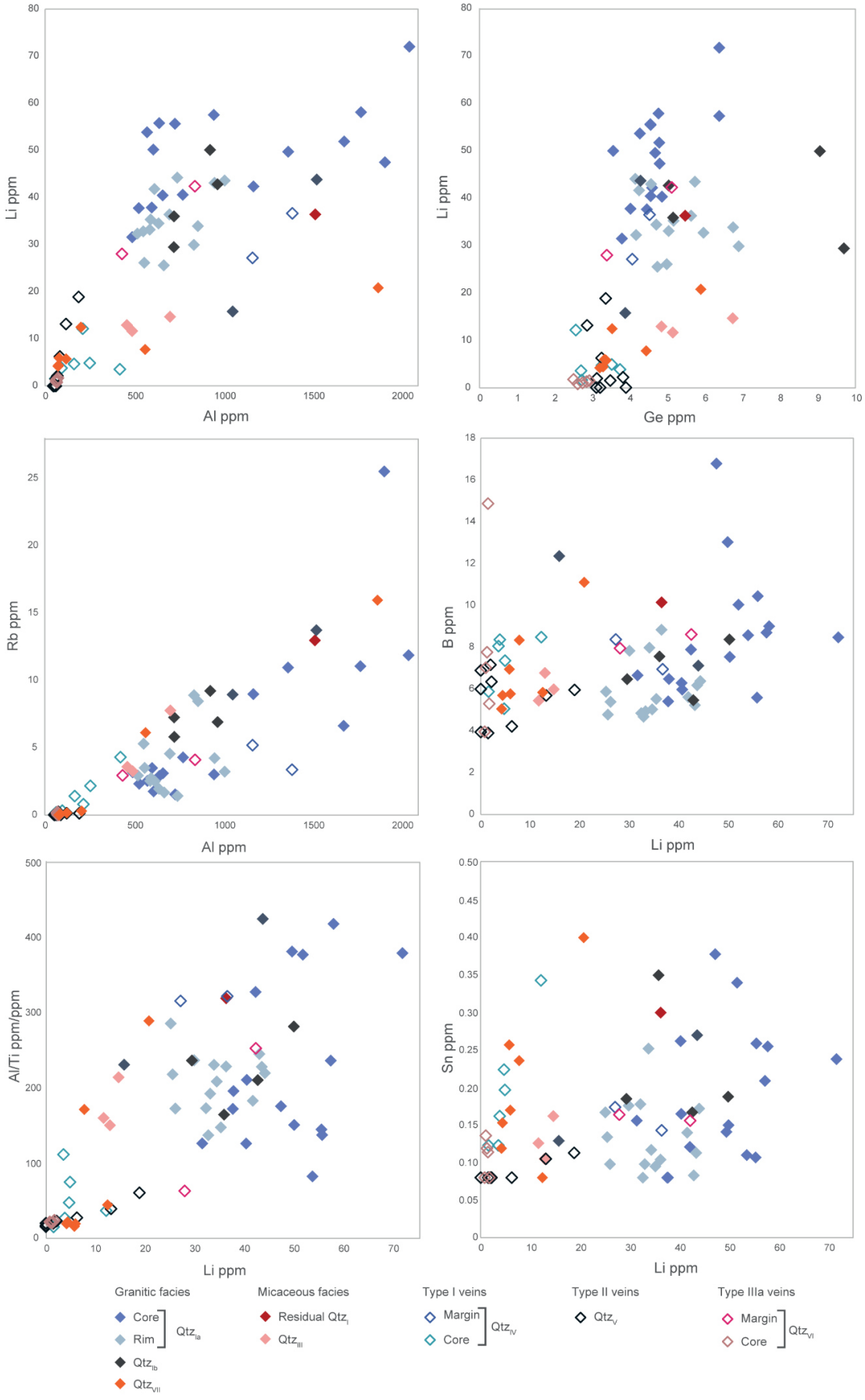

Fig 11 *Trace elements composition of the quartz along the MHT. See text for details*

In comparison with quartz disseminated in the granite, quartz from intragranitic veins show more variable trace element signatures. For the Type I intragranitic veins, Qtz_{IV} at 1 and 2 mm from the margin (i.e., the two first points in Fig. 10d) have trace element contents (Al: 1160-1390 ppm, Rb: 3.4-5.2 ppm, Li: 27-36 ppm) similar to Qtz_{Ia} and Qtz_{Ib}. However, the data in the center of the vein (Fig. 10d) reveal a significant decrease of Al (95-254 ppm), Li (3.8-12.1 ppm) and Rb (0.2-0.8 ppm) contents. A slight increase in Sn (0.11-0.16 ppm) is also observed when compared to concentrations near the margin (Sn ~0.09 ppm). For Qtz_V from the Type II intragranitic veins, data are available only in the center of the vein. Al (50-190 ppm), Rb (0.07-0.1 ppm), Li (0.4-18.8 ppm) and Sn (0.08-0.11 ppm) are very low (Table 3), similar to Qtz_{IV} (middle of the vein) and even lower for Al and Rb. For Qtz_{VI} (Type IIIa intragranitic veins), the Al, Li and Rb contents strongly decrease with increasing distance from the vein margin as found for the Type I veins (Fig. 10e). The data close to the margin reveal relatively high Al (435-844 ppm), Li (28-42 ppm) and Rb (2.95-4.1 ppm) contents. Away from the vein margin (i.e., the three last analyses, Fig. 10e), trace element concentrations are very low (Al: 65-75 ppm, Li: 0.8-1.7 ppm). Compositions of all quartz generations are plotted together for comparison (Fig. 11). *Prima facie*, the data emphasize the compositional contrast between, on the one hand, quartz disseminated in the granite ($Qtz_{Ia,}$, Qtz_{Ib}) and, on the other hand, quartz crystallizing in the center of intragranitic veins (Qtz_{IVcore}, Qtz_V and Qtz_{VIcore}). Residual Qtz_I from the border facies and quartz at the margins of Type I and III intragranitic veins plot in the disseminated quartz domain (Qtz_{Ia} and Qtz_{Ib} compositions). Conversely, Qtz_{VII} (recrystallized quartz in the granite near Type III veins) has very low trace element contents and plots together with quartz from the center of intragranitic veins (Qtz_{IVcore}, Qtz_V and Qtz_{VIcore}). Overall, the data define a trend of systematically decreasing Al, Li, Rb concentrations and Al/Ti from the disseminated to the vein quartz. In comparison, B, Sn and Ti concentrations are relatively constant for all quartz generations.

Li-phosphates. Li-phosphates include disseminated isolated crystals in the granite ($Li\text{-}P_{Ia}$) and inclusions in disseminated cassiterite ($Li\text{-}P_{Ib}$) and are present in the three types of intragranitic veins ($Li\text{-}P_{II}$, $Li\text{-}P_{III}$ and $Li\text{-}P_{IV}$). Major and trace element analyses are listed in Table 5 and 6 respectively. All generations have montebrasite compositions with at. OH/F between 2 and 5.2 (Table 5; Dubois et al.,

1973). No significant variation in major element compositions is observed, most analyses being tightly grouped. The Li content is also quite homogeneous ranging from 44 800 to 54 800 ppm. F ranges from 0.3 to almost 0.6 wt% with no obvious correlation with the generation. Except Sn, Nb, Ta, Ti, Ga, U and Pb, trace elements do not enter the montebrasite structure in significant amounts. The Li-phosphates are all characterized by low Nb/Ta. In Li-P_{Ia} and Li-P_{Ib}, Nb/Ta ranges from <0.4 to ~0. Li-P_{Ib} is enriched in Nb (1.42-7.3 ppm) and Ta (13.8-25.4 ppm) compared to Li-P_{Ia} with Nb ranging from 0.43 to 2.19 and Ta from 2.54 to 14.80 ppm. The Nb/Ta ratio seems to increase from Type I to Type III intragranitic veins. Sn contents can be quite high, up to 200 ppm with an apparent slight decrease from Li-P_{II} to Li-P_{IV}. In the Ti/Ga diagram, Ti decreases with increasing Ga from Li-P_{I} to Li-$P_{II\text{-}III\text{-}IV}$.

Table 5
EPMA averaged major elements analyses of Li-phosphates

	Granitic facies				Type I		Type IIIa		W-Type IIIa	
	Li-PIa		Li-Pib		Li-PII		Li-PIVa		Li-PIVa	
Major elements (wt%)	Mean (9)	σ	Mean (4)	σ	Mean (3)	σ	Mean (4)	σ	Mean (4)	σ
Al_2O_3	36.50	0.71	36.15	0.73	36.03	0.34	35.88	1.79	35.58	0.89
P_2O_5	46.02	1.24	46.82	1.20	45.44	0.76	46.10	0.45	45.10	0.92
F	3.45	1.02	3.42	0.52	3.40	0.97	4.01	0.56	3.03	1.53
O=F	1.45	0.43	1.44	0.22	1.43	0.41	1.69	0.23	1.27	0.64
Total	84.73	0.91	85.14	0.93	83.50	0.64	84.48	1.89	82.56	1.64
Number of cations based on 8 O										
P	1.90	0.04	1.92	0.03	1.90	0.02	1.90	0.02	1.91	0.05
Al	1.98	0.04	1.95	0.05	1.98	0.02	1.95	0.07	1.98	0.02
F	0.53	0.16	0.52	0.08	0.53	0.15	0.62	0.09	0.48	0.24
OH	1.47	0.16	1.48	0.08	1.47	0.15	1.38	0.09	1.52	0.24

Table 6

LA-ICP-MS trace elements analyses of Li-phosphates

	Granitic facies		Type I				Type IIIa		W-Type IIIa	
	Li-PIa		Li-Pib		Li-PII		Li-PIVa		Li-PIVa	
Trace elements (ppm)	Mean (9)	σ	Mean (4)	σ	Mean (3)	σ	Mean (4)	σ	Mean (4)	σ
Li	50973	3238	50751	1848	49447	1919	50274	3756	47389	5671
Be	5.52	2.12	4.50	-	6.00	-	bdl	bdl	37.44	56.97
B	12.25	-	11.92	-	8.64	-	12.12	-	bdl	bdl
Al	36.50	0.71	36.15	0.73	36.03	0.35	35.88	1.79	34.90	1.93
Ti	458.27	88.48	411.71	71.57	318.23	81.20	293.20	27.09	280.60	44.45
Mn	16.49	18.19	5.64	-	37.19	-	bdl	bdl	60.76	-
Fe	189.30	-	294.79	-	bdl	bdl	bdl	bdl	381.48	-
Zn	6.06	-	bdl	bdl	9.61	-	bdl	bdl	24.11	-
Ga	8.25	1.64	6.71	0.20	13.45	1.64	7.02	0.53	11.40	3.37
Rb	18.12	-	bdl	bdl	bdl	bdl	bdl	bdl	bdl	bdl
Sr	2.89	-	0.97	-	6.91	-	bdl	-	12.69	-
Nb	2.60	3.30	4.43	2.40	3.24	2.00	3.08	2.88	1.60	0.77
Sn	88.18	56.24	138.34	31.18	89.45	30.94	179.08	177.48	98.45	71.35
Cs	bdl	bdl	bdl	bdl	bdl	bdl	bdl	bdl	bdl	bdl
Ba	10.22	1.00	2.22	-	8.80	7.51	bdl	bdl	20.70	-
La	0.41	0.35	bdl	bdl	1.13	-	0.15	-	1.55	-
Ce	1.03	-	0.10	-	1.70	-	bdl	bdl	2.75	-
Pr	0.20	-	bdl	bdl	0.19	-	bdl	bdl	0.31	-
Nd	0.52	-	0.22	-	0.75	-	0.35	-	1.43	-
Sm	0.30	0.02	0.20	-	0.28	-	0.17	-	0.27	-
Eu	bdl	bdl	bdl	bdl	bdl	bdl	bdl	bdl	0.25	-
Gd	bdl	bdl	bdl	bdl	bdl	bdl	bdl	bdl	0.61	-
Tb	0.07	-	bdl	bdl	0.17	-	0.13	-	bdl	bdl
Dy	bdl	bdl	0.28	-	bdl	bdl	bdl	bdl	0.25	-
Ho	bdl	bdl	bdl	bdl	0.06	-	bdl	bdl	0.06	-
Er	bdl	bdl	0.07	-	bdl	bdl	0.13	-	bdl	bdl
Tm	bdl	bdl	bdl	bdl	bdl	bdl	bdl	bdl	bdl	bdl
Yb	bdl	bdl	0.26	-	bdl	bdl	bdl	bdl	0.17	-
Lu	0.15	-	bdl	bdl	bdl	bdl	bdl	bdl	bdl	bdl
Hf	0.36	0.05	3.07	4.47	0.58	-	bdl	bdl	1.41	-
Ta	89.72	169.15	17.77	5.24	97.71	119.17	56.03	89.23	7.92	7.74
W	0.53	0.60	0.21	0.04	1.87	2.28	0.24	0.17	1.08	0.80
Th	0.12	0.10	0.06	0.03	0.14	0.19	0.05	0.01	0.72	
U	0.40	0.60	11.50	21.90	3.92	2.28	0.20	0.01	3.17	5.82

bdl: below detection limit; -: only one data is above the detection limit

K-feldspars. K-feldspars occur both as scarce disseminated crystals in the granite (Kfs_I) and is present in Type I (Kfs_{II}) and IIIa intragranitic veins (Kfs_{III}). Major and trace elements analyses are listed in Table 7 and 8 respectively. K-feldspars contain negligible amounts of An, from 0 to 0.6% but significant Ab, up to ~7%. Except two analyses (1.3-2 % Ab), most Kfs_I in the granitic and border facies have Ab (3.8- 6.2 %) higher than K-feldspars in intragranitic veins (0.4-3 %). The Ab content also roughly decreases from Kfs_{II} to Kfs_{III}. K-feldspars have P_2O_5 up to ~0.8 wt%, the highest values being found in the border facies (Fig. 12). Rb contents are high to extremely high, ranging mostly between 5200 and 25000 ppm while Ba concentrations are quite low, never exceeding 40 ppm. Rb contents are lower (4000-7800 ppm) and Ba contents similar to much higher (23-136 ppm, up to 194 ppm) in Kfs_{II-III} than in Kfs_I. In the Ba/Rb diagram, a Ba spike is observed between Kfs_I and Kfs_{II} (Fig. 12). The Sn (mostly 13-42 ppm), Li (16-67 ppm), Ge (8-18 ppm) and Cs (53 to up to 2160 ppm) contents in Kfs_I are generally higher than in Kfs_{II} and Kfs_{III} (Sn: 0.7-1.6 ppm; Li: 7-44 ppm; Ge: 5-11.6 ppm and Cs: 61-480 ppm).

Table 7

EPMA major elements analyses of K-feldspars

	Granitic facies							Type I intragranitic veins				Type IIIa intragranitic veins		
Type	KfsI							KfsII				KfsIII		
Major elements (wt%)														
SiO_2	64.94	64.49	62.69	63.75	62.97	62.35	63.09	64.85	63.67	64.48	63.89	66.53	65.41	65.88
TiO_2	-	0.04	-	0.03	-	-	0.03	-	-	0.02	0.01	-	-	0.02
Al_2O_3	19.06	18.97	18.73	18.47	18.19	18.65	18.25	18.86	18.70	19.08	18.33	19.06	18.79	18.92
FeO	-	-	0.11	-	0.02	-	0.02	-	0.03	0.05	0.05	-	-	0.02
MnO	-	-	-	-	-	-	-	-	-	-	-	-	-	0.04
MgO	-	0.02	-	-	-	0.01	-	0.03	0.02	-	-	-	0.03	0.03
CaO	-	-	-	-	-	0.01	0.11	-	-	-	-	-	0.01	-
Na_2O	0.59	0.45	0.41	0.22	0.72	0.63	0.14	0.10	0.13	0.33	0.32	0.17	0.11	0.19
K_2O	15.52	16.13	15.41	16.39	15.60	14.62	16.02	15.88	15.53	15.92	15.83	15.20	16.00	15.67
P_2O_5	0.39	0.77	0.46	0.42	0.50	0.45	0.24	0.18	0.21	0.47	0.47	0.19	0.29	0.45
Total	101.3	101.6	99.3	99.9	99.5	98.0	98.4	99.9	98.3	100.3	98.9	101.2	100.6	101.2
Number of cations based on 8 O														
Si	2.97	2.95	2.95	2.97	2.96	2.95	2.98	2.98	2.98	2.96	2.97	3.00	2.99	2.98
Ti	-	-	-	-	-	-	-	-	-	-	-	-	-	-
Al	1.03	1.02	1.04	1.01	1.01	1.04	1.02	1.02	1.03	1.03	1.01	1.02	1.01	1.01
Na	0.05	0.04	0.04	0.02	0.07	0.06	0.01	0.01	0.01	0.03	0.03	0.02	0.01	0.02

K	0.91	0.94	0.92	0.97	0.93	0.88	0.96	0.93	0.93	0.93	0.94	0.88	0.93	0.91
P	0.02	0.03	0.02	0.02	0.02	0.02	0.01	0.01	0.01	0.02	0.02	0.01	0.01	0.02
An	-	-	-	-	-	0.11	0.61	-	-	-	-	-	-	-
Ab	5.43	4.08	3.85	2.01	6.60	6.16	1.32	0.96	1.28	3.02	2.99	1.68	0.96	1.74
Or	94.57	95.92	96.15	97.99	93.40	93.74	98.07	99.04	98.72	96.98	97.01	98.32	99.04	98.26

Continued

	W-bearing Type IIIa intragranitic veins									
			KfsIII							
SiO_2	64.01	64.58	64.16	64.18	63.38	64.23	63.76	64.61	63.68	63.45
TiO_2	-	-	-	-	0.01	-	0.04	-	-	-
Al_2O_3	18.63	18.88	17.69	17.10	17.24	17.31	17.74	17.48	17.47	17.33
FeO	-	-	0.01	-	0.07	0.01	-	0.01	0.05	-
MnO	0.01	-	-	-	-	-	-	0.04	0.02	-
MgO	-	0.04	0.01	-	-	-	0.01	-	-	0.02
CaO	0.02	-	-	-	-	-	0.01	0.01	-	-
Na_2O	0.24	0.16	0.14	0.09	0.05	0.11	0.16	0.10	0.14	0.17
K_2O	15.59	15.86	15.96	15.71	15.89	15.95	15.31	15.90	15.77	15.47
P_2O_5	0.35	0.42	0.23	0.06	0.04	0.26	0.39	0.13	0.25	0.19
Total	98.8	99.9	98.7	97.6	97.1	98.3	97.9	98.8	97.9	97.1
Number of cations based on 8 O										
Si	2.98	2.97	3.01	3.04	3.02	3.02	3.00	3.03	3.01	3.02
Ti	-	-	-	-	-	-	-	-	-	-
Al	1.02	1.02	0.98	0.95	0.97	0.96	0.99	0.97	0.97	0.97
Na	0.02	0.01	0.01	0.01	-	0.01	0.01	0.01	0.01	0.02
K	0.93	0.93	0.96	0.95	0.97	0.96	0.92	0.95	0.95	0.94
P	0.01	0.02	0.01	-	-	0.01	0.02	0.01	0.01	0.01
An	0.11	-	-	-	-	-	0.11	-	-	-
Ab	2.32	1.48	1.24	0.94	0.41	1.03	1.50	0.94	1.35	1.68
Or	97.57	98.52	98.76	99.06	99.59	98.97	98.40	99.06	98.65	98.32

Table 8
LA-ICP-MS trace elements analyses of K-feldspars

	Granitic facies							Type I				Type IIIa
Type	KfsI							KfsII				KfsIII
Trace elements (ppm)												
Li	41.45 (5.8)	27.84 (4.5)	68.51 (4.3)	18.37 (3.2)	27.54 (4.4)	66.78 (6.4)	37.03 (3.9)	bdl	bdl	43.98 (5.6)	bdl	bdl
Be	bdl	5.2 (1.0)	5.67 (1.0)	3.63 (0.8)	bdl	5.6 (1.6)	bdl	bdl	bdl	bdl	bdl	bdl
B	9.93 (2.4)	bdl	bdl	bdl	bdl	bdl	bdl	bdl	bdl	bdl	20.25 (2.4)	bdl
Sc	bdl	2.7 (0.9)	7.66 (1.3)	3.68 (1.1)	bdl	5.92 (1.9)	5.91 (1.2)	bdl	bdl	bdl	bdl	bdl
Ga	24.32 (1.1)	18.3 (0.7)	22.07 (0.8)	11.58 (0.5)	19.09 (0.8)	45.94 (1.7)	17.96 (0.7)	24.47 (0.9)	26.29 (1.0)	34.31 (1.4)	51.66 (2.1)	19.17 (0.8)
Ge	bdl	8.49 (2.1)	9.69 (2.6)	18.22 (2.3)	14.29 (3.0)	18.03 (4.1)	8.39 (2.4)	bdl	8.42 (2.4)	10.03 (2.7)	bdl	bdl
Rb	6929 (283.1)	5206 (160.7)	12553 (414.4)	7422 (246.7)	12371 (414.4)	24712 (844.0)	3868 (135.3)	4896 (166.3)	5315 (182.3)	7829 (296.6)	7299 (280.9)	7173 (256.6)
Sr	10.88 (0.6)	bdl	1.27 (0.2)	bdl	bdl	1.55 (0.4)	0.78 (0.3)	bdl	bdl	bdl	9.3 (0.6)	bdl
Zr	16.21 (0.8)	bdl	bdl	bdl	bdl	bdl	bdl	bdl	bdl	bdl	bdl	bdl
Nb	bdl	bdl	bdl	bdl	bdl	bdl	bdl	bdl	bdl	bdl	bdl	bdl
Sn	14.22 (0.9)	20.36 (0.9)	13.01 (0.6)	5.17 (0.4)	15.8 (0.7)	31.12 (1.3)	bdl	1.63 (0.4)	bdl	bdl	bdl	0.86 (0.4)
Cs	199.47 (8.3)	71.53 (2.5)	1176 (42.1)	629.83 (22.8)	1123 (41.3)	2159 (82.0)	53.32 (2.2)	99.49 (4.1)	96.67 (4.1)	477.85 (18.2)	354.58 (13.8)	96.96 (3.9)
Ba	23.97 (1.4)	13.36 (0.9)	1.51 (0.5)	12.95 (0.9)	3.42 (0.7)	bdl	35.04 (1.9)	23.22 (1.2)	41.39 (1.9)	65.41 (2.8)	135.93 (5.3)	33.73 (2.1)
Ta	bdl	0.154 (0.05)	0.167 (0.03)	0.28 (0.04)	bdl	0.104 (0.04)	bdl	0.205 (0.04)	0.243 (0.05)	bdl	bdl	0.227 (0.05)
W	0.76 (0.1)	bdl	bdl	0.259 (0.09)	bdl	bdl	bdl	0.304 (0.07)	bdl	bdl	bdl	0.45 (0.1)
Th	0.376 (0.05)	bdl	0.0161 (0.008)	bdl	0.024 (0.01)	bdl	bdl	0.0107 (0.006)	bdl	-	bdl	bdl
U	0.199 (0.03)	0.508 (0.04)	1.379 (0.08)	0.0107 (0.005)	-	-	bdl	0.237 (0.02)	0.095 (0.02)	bdl	bdl	0.998 (0.08)
Pb 206	3.02 (0.3)	1.07 (0.2)	40.05 (1.9)	2.25 (0.2)	16.9 (0.9)	38.59 (2.1)	1.33 (0.2)	2.47 (0.2)	2.49 (0.3)	7.76 (0.6)	19.02 (1.0)	28.86 (1.6)
Pb 207	2.38 (0.3)	1.03 (0.2)	35.97 (1.6)	2.86 (0.3)	15.6 (0.8)	39.58 (2.0)	0.86 (0.2)	1.7 (0.2)	2.54 (0.3)	8.41 (0.6)	17.2 (1.0)	27.03 (1.5)
Pb 208	2.61 (0.2)	1.34 (0.1)	39.42 (1.9)	2.47 (0.2)	16.26 (0.8)	37.53 (2.0)	1.13 (0.2)	1.43 (0.2)	2.44 (0.2)	8.49 (0.5)	17.18 (0.9)	27.51 (1.3)

bdl: below detection limit

Continued

	W-bearing Type IIIa											
	KfsIII											
Li	bdl	14.36 (3.4)	21.66 (4.5)	17.66 (4.7)	31.28 (3.5)	17.61 (3.4)	bdl	38.71 (3.7)	30.87 (9.0)	11.48 (3.5)	12.55 (3.2)	bdl
Be	bdl	bdl	4.65 (1.1)	bdl	bdl	3.24 (0.8)	bdl	bdl	bdl	bdl	2.84 (0.8)	3.19 (1.0)
B	18.9 (2.0)	bdl	59.05 (3.5)	bdl	bdl	bdl	bdl	bdl	bdl	bdl	bdl	bdl
Sc	bdl	bdl	bdl	2.69 (1.1)	bdl	bdl	bdl	5.31 (1.0)	bdl	bdl	bdl	bdl
Ga	26.38 (0.9)	31.1 (1.1)	32.82 (1.1)	25.18 (1.0)	22.16 (0.8)	28.66 (1.0)	20.03 (0.7)	17.26 (0.7)	28.34 (1.3)	24.77 (0.9)	17.31 (0.6)	18.07 (0.7)
Ge	8.34 (2.0)	bdl	6.9 (2.3)	5.9 (2.4)	bdl	bdl	6.2 (1.5)	8.7 (2.1)	bdl	8.35 (1.9)	bdl	bdl
Rb	4777 (168.7)	5358 (194.2)	4686 (154.1)	5378 (175.8)	4577 (139.8)	4959 (151.7)	4822 (174.6)	5456 (181.0)	4033 (134.8)	4538 (152.5)	4417 (149.6)	4215 (144.1)
Sr	0.92 (0.3)	1.59 (0.3)	4.85 (0.4)	bdl	bdl	3.33 (0.3)	bdl	0.68 (0.3)	51.03 (2.0)	bdl	bdl	1.79 (0.3)
Zr	bdl	bdl	4.88 (0.3)	bdl	bdl	bdl	bdl	bdl	83.97 (3.3)	bdl	bdl	bdl
Nb	bdl	bdl	bdl	bdl	bdl	bdl	bdl	bdl	1.15 (0.2)	0.262 (0.07)	bdl	bdl
Sn	bdl	bdl	1.57 (0.4)	bdl	bdl	bdl	bdl	bdl	20.59 (1.4)	bdl	bdl	bdl
Cs	96.78 (3.8)	74.18 (3.0)	100.8 (3.9)	98.87 (3.8)	71.16 (3.3)	84.18 (4.0)	86.43 (4.3)	66.99 (2.4)	72.74 (2.9)	74.8 (2.7)	61.08 (1.3)	44.53 (1.7)
Ba	77.33 (3.9)	94.4 (5.0)	108.8 (4.0)	78.13 (3.3)	23.74 (1.3)	70.83 (3.3)	42.82 (2.1)	29.48 (1.6)	99.19 (5.2)	34.78 (1.8)	35.72 (1.8)	43.77 (2.2)
Ta	bdl	0.08 (0.02)	0.078 (0.03)	0.238 (0.06)	bdl	0.078 (0.03)	0.094 (0.03)	0.077 (0.03)	0.198 (0.09)	0.109 (0.03)	0.176 (0.04)	0.151 (0.03)
W	bdl	0.206 (0.07)	0.37 (0.08)	0.29 (0.1)	bdl	2.6 (0.2)	0.175 (0.06)	0.74 (0.1)	0.36 (0.2)	bdl	bdl	bdl
Th	0.019 (0.009)	bdl	0.1 (0.03)	0.017 (0.012)	bdl	0.013 (0.007)	bdl	bdl	2.06 (0.2)	bdl	bdl	bdl
U	bdl	0.123 (0.02)	bdl	0.48 (0.05)	0.01	-	bdl	0.037 (0.01)	2.11 (0.2)	0.431 (0.04)	bdl	0.741 (0.05)
Pb 206	10.28 (0.6)	18.75 (1.0)	20.6 (0.8)	4.55 (0.4)	13.61 (0.6)	48.48 (1.8)	1.64 (0.2)	1.42 (0.2)	5.29 (0.6)	8.01 (0.5)	4.4 (0.3)	2.02 (0.2)
Pb 207	10.49 (0.6)	17.12 (0.9)	18.83 (0.8)	4.34 (0.4)	12.64 (0.6)	41.99 (1.7)	1.81 (0.2)	1.54 (0.2)	3.09 (0.6)	6.89 (0.4)	3.87 (0.3)	1.59 (0.2)
Pb 208	10.1 (0.5)	17.71 (0.8)	19.6 (0.7)	4.04 (0.3)	13.58 (0.6)	42.42 (1.7)	1.53 (0.1)	1.62 (0.2)	4.18 (0.4)	6.68 (0.3)	3.98 (0.2)	1.23 (0.1)

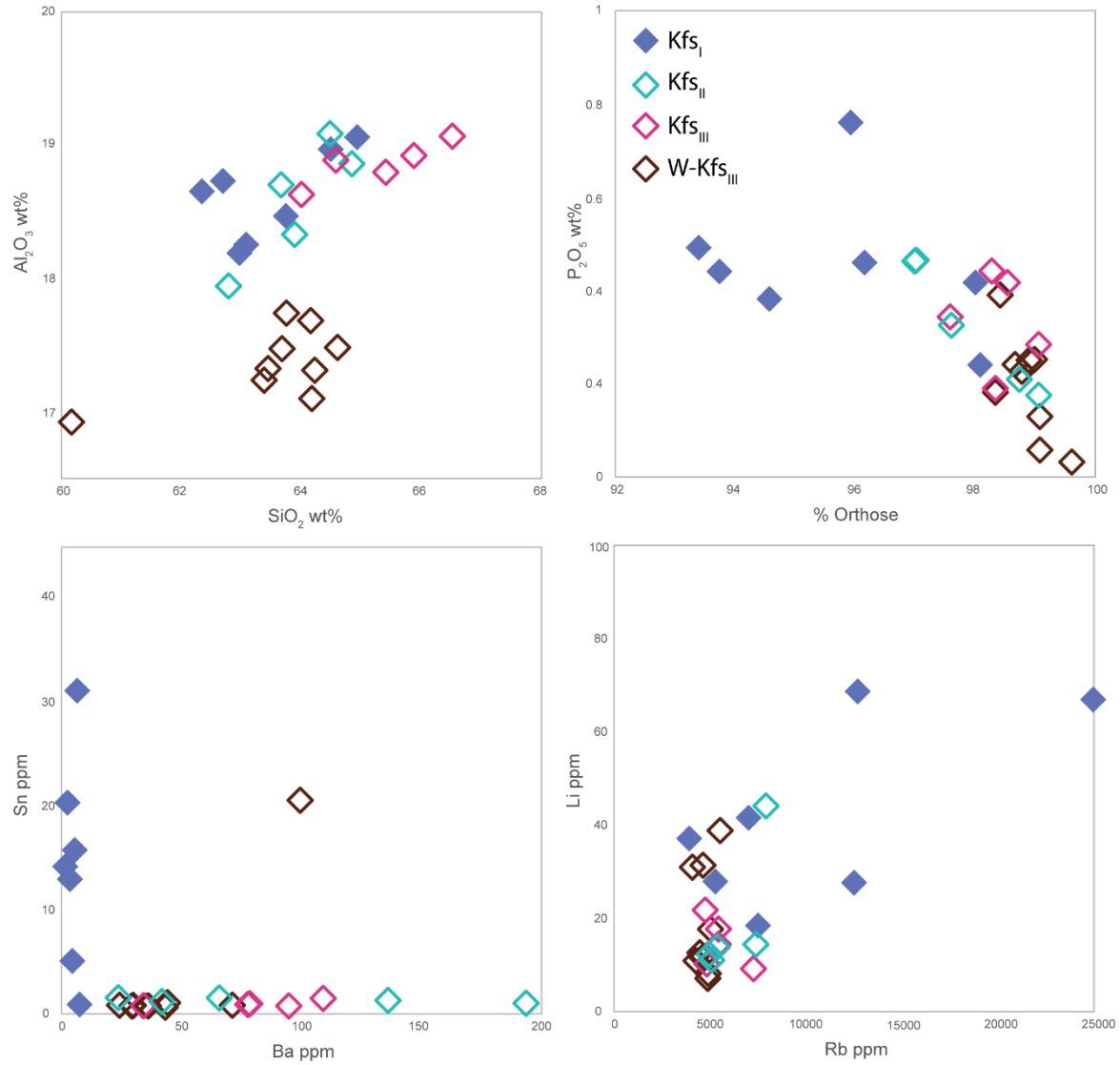

Fig 12 *Major and trace element variations of K-feldspars. See text for description*

Albite. Albite crystals, only analyzed for major elements (Table 9), occur either as inclusions in the core (Ab_{Ia}) and rim (Ab_{Ib}) of snowball Qtz_I or as the main mineral of the matrix (Ab_{II}). Ab_{Ia} show slightly higher concentration of Al (1.01-1.06 apfu), higher An (0.41-0.91 %) and P_2O_5 (0.33-0.83 wt%) and slightly lower Or (mostly 0.41-0.72 %) compared to Ab_{Ib} (Al: mainly 1.01-1.04 apfu; An: 0-0.3 % with two higher values; P_2O_5: mainly 0.01-0.4 wt% and Or: 0.32-0.87 %). Differences with Ab_{II} of the granitic facies are more pronounced (Al: 0.99-1.02 apfu; An: mainly 0-0.3 %; P_2O_5: mainly 0-0.34 wt% and Or: 0.4-0.87 %). $Ab_{IIaplite}$ plot in the same range compared to Ab_{II} of the granitic facies while Ab_{IIpeg}

show a wider range of variations. Concentrations evolve from concentrations similar to those of Ab_{II} of the granitic facies to values in the same range of Ab_{Ia}.

Table 9

Average EPMA analyses of albites

Facies	Granitic facies						Border facies					
Type	Ab_{Ia}		Ab_{Ib}		$Ab_{IIgranite}$		$Ab_{IImicaceous}$		$Ab_{IIaplite}$		$Ab_{IIpegmatite}$	
Major elements (wt%)	Mean (8)	σ	Mean (6)	σ	Mean (32)	σ	Mean (4)	σ	Mean (3)	σ	Mean (13)	σ
SiO_2	67.60	0.75	68.37	0.72	68.58	0.74	69.14	0.78	68.94	0.43	67.80	1.17
TiO_2	0.02	0.02	0.01	0.01	0.01	0.01	0.02	0.02	0.04	0.07	0.01	0.02
Al_2O_3	20.27	0.39	20.22	0.32	19.70	0.26	19.81	0.20	19.73	0.35	20.03	0.42
FeO	0.01	0.02	-	-	0.02	0.04	0.01	0.01	-	-	0.03	0.04
MnO	0.01	0.01	0.02	0.03	0.02	0.03	0.01	0.01	0.01	0.01	0.01	0.01
MgO	0.02	0.02	0.01	0.01	0.01	0.01	0.03	0.02	0.01	0.02	0.01	0.01
CaO	0.10	0.05	0.06	0.06	0.02	0.02	0.03	0.03	-	-	0.06	0.05
Na_2O	11.34	0.54	11.39	0.36	11.07	1.71	11.24	0.10	11.93	0.12	11.11	0.89
K_2O	0.10	0.05	0.10	0.03	0.66	1.72	0.07	0.04	0.10	0.01	0.53	1.16
P_2O_5	0.61	0.16	0.24	0.29	0.11	0.11	0.13	0.14	0.03	0.02	0.57	0.41
Total	100.08	0.62	100.42	0.51	100.21	0.89	100.49	0.93	100.80	0.61	100.15	1.47
Number of cations based on 8 O												
Si	2.94	0.02	2.97	0.02	2.99	0.01	2.99	0.01	2.99	0.01	2.96	0.03
Al	1.04	0.01	1.04	0.02	1.01	0.01	1.01	0.01	1.01	0.02	1.03	0.02
Na	0.96	0.05	0.96	0.03	0.94	0.14	0.94	0.02	1.00	0.01	0.94	0.07
K	0.01	-	0.01	-	0.04	0.10	-	-	0.01	-	0.03	0.06
P	0.02	0.01	0.01	0.01	-	-	-	-	-	-	0.02	0.02
An	0.49	0.25	0.26	0.28	0.09	0.11	0.16	0.18	-	-	0.30	0.25
Ab	98.96	0.37	99.20	0.45	95.62	11.50	99.45	0.34	99.47	0.05	96.69	6.47
Or	0.55	0.28	0.54	0.19	4.29	11.52	0.40	0.23	0.53	0.05	3.02	6.54

V.6. STABLE ISOTOPE RESULTS

O and H isotopic data have been determined mostly for quartz and a few analyses are available for micas. Analyzed quartz correspond to snowball quartz (Qtz_I) from the granitic facies, to residual quartz with skeletal rims (Qtz_{I-III}) from the micaceous facies and to quartz ($Qtz_{IV-V-VI}$) from each generation of intragranitic veins (Type I, II, IIIa and b). The analyzed micas correspond to micas crystallizing in the granitic and the micaceous facies (Ms_{I-III}).

V.6.1. Oxygen isotope data

Oxygen isotope data for both quartz and micas are given in Table 10 and shown in Fig. 13.

Table 10
$\delta^{18}O$ data of quartz and micas (‰)

Facies	Qz	Micas	ΔQtz-Mu
Granitic	+13,7	+11,7	2
Micaceous	+14,5	+11,7	2,8
Type I	+14,7		
Type II	+15,6		
Type IIIa	+15,5		
Type IIIc	+15,9		
Type IIISR	+16,0		

Mica from both the granitic and micaceous facies yield identical $\delta^{18}O$ (11.7‰). Unlike mica, quartz (Qtz_I and Qtz_{I-III}) yields different $\delta^{18}O$, +13.7 and +14.5‰ respectively in the same two facies. The highest value found in the micaceous facies probably reflects analysis of a mixture between Qtz_I and Qtz_{III}. The quartz-muscovite O isotope fractionation factor (ΔQtzMu) is 2 when calculated for Qtz_I of the granitic facies and 2.8 for Qtz_{I-III} of the micaceous facies. Using the thermometric equations of Zhanget al. (1989) and O'Neil and Taylor (1969), this yields temperatures of equilibration between quartz and muscovite in the range 500-800°C.

For quartz in intragranitic veins, $\delta^{18}O$ ranges from +14.5 to +16‰ and progressively increases with the vein type, from Qtz_{IV}, Qtz_V to Qtz_{VI}. Quartz from Type I veins (Qtz_{IV}) have $\delta^{18}O$ of +14.5 and

+15‰, the lowest value being identical to Qtz_{I-III} in the micaceous facies. Qtz_V from Type II veins has a $\delta^{18}O$ of +15.6‰ while Qtz_{VIa} (Type IIIa veins) and Qtz_{VIb} (Type IIIc veins) have the highest $\delta^{18}O$ values, respectively +15.5‰ and +15.9‰.

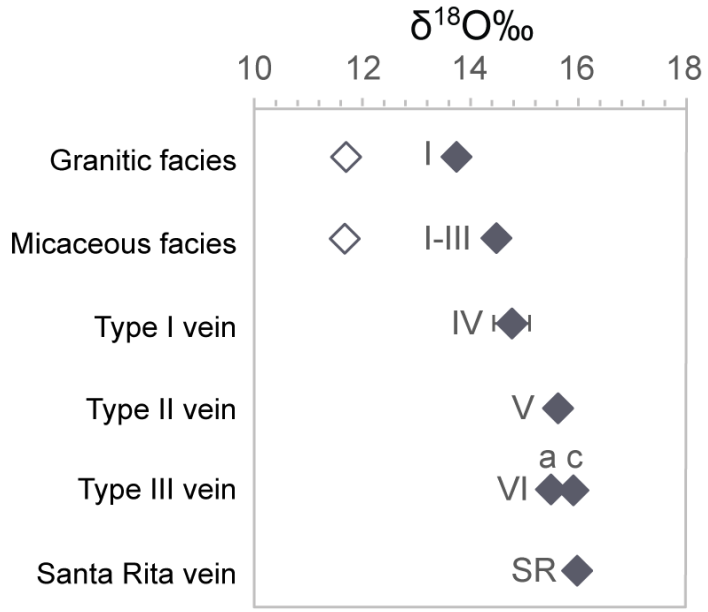

Fig 13 *$\delta^{18}O$ values of micas (white lozenges) and quartz (black lozenges) along the MHT*

V.6.2. Hydrogen isotope data

Hydrogen isotope data are given in Table 11 and shown in Fig. 14. Muscovite of the granitic facies yield δD values of -64.7‰ and -65‰ (H_2O content: 3.85 and 3.87 wt% respectively) while muscovite of the micaceous facies gives slightly lower values (-66.9‰ and -67.4‰) with lower H_2O content (3.57 and 3.55 wt%). Mean values are calculated for the two facies and give -64.9 ± 0.2‰ for the granitic facies and -67.1 ± 0.4‰ for the micaceous facies. For fluids trapped in quartz (i.e., δD of the fluid), δD range between -20.2 and -52.1‰. δD of fluid in equilibrium with Qtz_I of the granitic range between -26.1 and -48.5‰ (for 7 analyses) with a mean value of -35.4 ± 7‰. The micaceous facies yield δD of -39.4 to -46.5‰ (n=3) with a mean value of -41.9 ± 3‰ higher than for the granitic facies. Fluids in equilibrium with Qtz_{IV} show δD between -21.2 and -34.9‰ (n=13) with a mean value of -28.5 ± 4.4‰ while δD of fluid for Qtz_V range between -20.2 and -52.1‰ (n=6) with a mean value of -33.5 ±

12‰. Finally, fluids in equilibrium with Qtz_{VI} yield δD between -25 and -30.9‰ (n=3) with a mean value of -28.2 ± 3‰. δD of fluid in Qtz_{SR} have also been measured and are between -35.3 and -43.9‰ (n=4) with a mean value of -38.9 ± 4‰. Overall, δD mean values of quartz in the granitic and micaceous facies are lower than for intragranitic veins except for the Santa Rita vein.

Table 11
δD data of micas and of fluid in quartz

Micas	Data (‰)	Mean (‰)	σ	Quartz	Data (‰)	Mean (‰)	σ
Granitic	-64.7	-64.9	0.2	Granitic	-38.0	-35.4	7.0
	-65.0				-48.5		
Micaceous	-67.4	-67.1	0.3		-32.2		
	-66.9				-26.1		
					-33.3		
					-31.7		
					-37.6		
				Micaceous	-39.4	-41.9	4.0
					-39.8		
					-46.5		
				Type I	-32.4	-28.5	4.4
					-27.4		
					-21.2		
					-21.5		
					-27.5		
					-33.0		
					-28.7		
					-25.1		
					-26.5		
					-34.4		
					-27.5		
					-30.1		
					-34.9		
				Type II	-31.2	-33.5	11.9
					-23.7		
					-52.1		
					-31.1		
					-42.5		
					-20.2		
				Type IIIa	-28.6	-28.2	3.0
					-25.0		
					-30.9		
				SR	-35.3	-38.9	3.8
					-43.9		
					-40.0		
					-36.5		

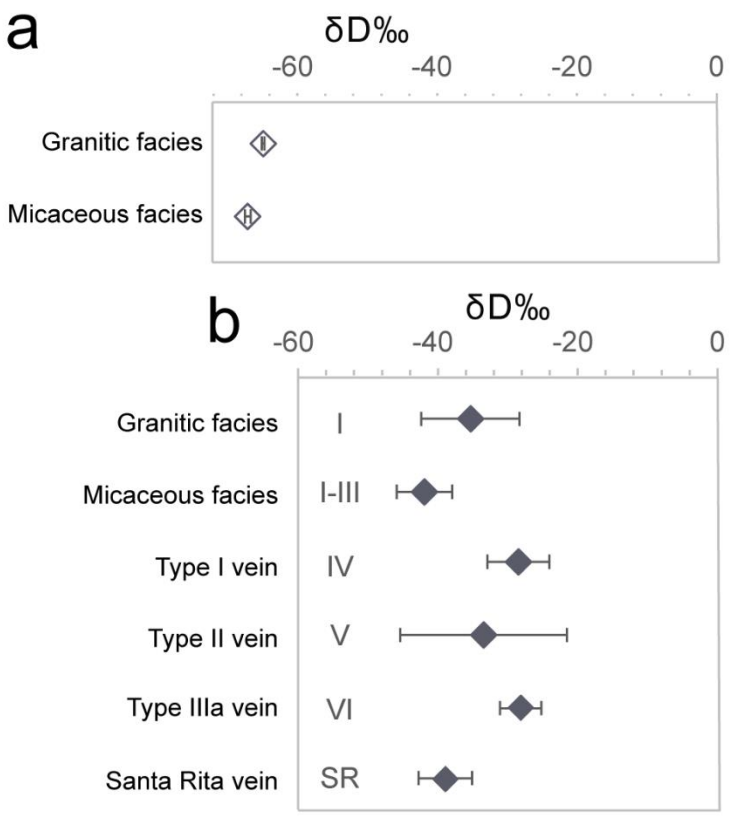

Fig 14 *δD data. (a) δD of micas and (b) δD of fluid inclusions in quartz*

V.7. DISCUSSION

Several lines of evidence demonstrate that the Argemela granite results from the crystallization of a highly evolved rare-metal magma (see also Charoy and Noronha, 1996). This includes: (1) the pipe-like shape of the intrusion consistent with an origin from a vertically ascending small magma batch (see Chapter II); (2) the subvolcanic texture and presence of snowball quartz crystals which indicates crystallization at shallow levels although the textural variability of the border facies reveals more complex mechanisms; (3) the presence of a two feldspars plus quartz mineral assemblage which calls for a parental granitic melt; (4) the strongly peraluminous character, high whole-rock P_2O_5 concentrations and the specific magmatic mineralogy (presence of muscovite as the sole mica, of montebrasite, cassiterite and columbo-tantalite) which shows that the Argemela granite is a representative example of a PHP RMG as found elsewhere in the Variscan belt. However, several features of the Argemela intrusion cannot be explained with a purely magmatic model. This is most clearly illustrated by the network of intragranitic quartz veins. In the same way, mineralogical features such as the late compositionally specific mica generation and the trace element evolutions recorded by mica, quartz and other phases require interpretations. Below, we argue that all these features are the manifestations, at different scales of observation, of the magmatic-hydrothermal transition.

V.7.1. The intragranitic veins as markers of the exsolution of magmatic fluids

Geometrical, structural and mineralogical studies performed on the intragranitic vein system well exposed in the quarry (see above and Chapter III) have identified several important points pertaining to their origin. (1) The field relations show unambiguous evidence for the veins being confined inside the granite and for not extending into the country rocks, indicating that the fluids have their origin within the intrusion. (2) Structural analysis shows that both the granite and veins were emplaced in the same deformation regime (Chapter II). The Type I and II are extensional and the Type III shear veins, indicating fluid overpressure during opening of, at least, the two earliest vein generations.

(3) Mineralogically, hydrothermal alteration assemblages and aureoles are absent in the granite near the veins. The bulk rock data show that the chemical changes in the granite near the Type I, II, IIIa veins are restricted to slight increases in P_2O_5, Li, Nb and Ta. (In comparison, granite near Type IIIb and c veins at the northeastern sheared part of the intrusion is more chemically modified). Quartz at the margins of Type I and III intragranitic veins have trace element contents very close to disseminated quartz in the granitic facies (Fig. 6). Type I veins have a pegmatite-like texture and a granitic mineral assemblage (quartz, K-feldspar) suggesting that minerals in the vein grew from a fluid in chemical equilibrium with the enclosing granite.

The stable isotope data provide additional constraints. The quartz $\delta^{18}O$ values demonstrate a progressive increase from early magmatic quartz (Qtz_I), quartz from the micaceous facies (Qtz_{I-III}) to hydrothermal quartz (Qtz_{IV}, Qtz_V to Qtz_{VI}) in the intragranitic veins. The lowest $\delta^{18}O$ value in Qtz_{IV} is identical to that in Qtz_{I-III} from the micaceous facies, consistent with the mineralogical and trace element evidence for equilibration between the earliest intragranitic veins and the granite. We note that, in the intragranitic veins, the increase in $\delta^{18}O$ is in the same order as the relative chronology between veins (i.e., $\delta^{18}O$ Qtz_{IV} < $\delta^{18}O$ Qtz_V < $\delta^{18}O$ Qtz_{VI}). This variation in $\delta^{18}O$ is attributed to a progressive change in conditions with time at the MHT and can be interpreted in two possible ways, (1) progressive cooling or (2) increase in ^{18}O content of the fluid. The first interpretation is supported by the H isotopic data (-20.2 and -52.1‰ for fluid in equilibrium with quartz). There is no evidence in our dataset for different fluid reservoirs that would be revealed by highly variable δD values. Nearby at Panasqueira, the anomalously low δD fluids (Kelly and Rye, 1979; Polya et al., 2000) have been interpreted to trace interaction between the magmatic-hydrothermal fluid (with a meteoric-dominated meteoric-magmatic signature) and fluids derived from organic-rich metasediments. Such anomalous δD are not observed at Argemela. In addition, the second interpretation requires that the fluid (or the different fluids) progressively evolves toward higher, and not lower, $\delta^{18}O$, as expected in the case of a non-magmatic (i.e., meteoric) fluid contribution. High $\delta^{18}O$ quartz values such as found in this study are generally interpreted as evidence for the involvement of fluids enriched in ^{18}O at levels greater than normally expected for meteoric waters (Kelly and Rye, 1979; Polya et al., 2000). Therefore, the alternative appears to be between a unique fluid with high $\delta^{18}O$ and a mixture of several fluids all with high $\delta^{18}O$.

Additional analyses and a much larger dataset would be needed to test the latter hypothesis. Consequently, the progressive $\delta^{18}O$ increase observed along the MHT at Argemela is interpreted to reflect the cooling of a unique fluid.

To more fully characterize this fluid, $\delta^{18}O$ of fluids in equilibrium with quartz and muscovite were calculated from the mineral-water equilibrium equations of Zhang et al. (1989) and O'Neil and Taylor (1969) respectively. To do so, different temperatures (500, 600°C) were considered. The temperature range determined above for quartz and muscovite O isotopic equilibration in the Argemela granite (500-800°C) is quite large. Experimental phase equilibria show that coexistence of quartz and muscovite in RMG magmas requires temperatures < 800°C (Pichavant et al., 1987; Pichavant, unpub.). Conversely, 500°C is quite low, possibly the consequence of different mica generations (Ms_I, Ms_{II} and Ms_{III}) being mixed in the analyzed mineral separate. Yet, the 500-800°C range obtained indicates quartz-muscovite isotopic equilibration mostly under magmatic conditions since ~550°C is the solidus temperature for the Beauvoir RMGs (Pichavant et al., 1987). For temperatures of 500, 550 and 600°C, calculated $\delta^{18}O$ of equilibrium fluids are 10.8‰, 11.5‰ and 12.1‰ (Qtz_I), 11.6‰, 12.3‰ and 12.8‰ ($Qtz_{I\text{-}III}$) and, for fluids at equilibrium with muscovites, 11.6‰, 12.1‰ and 12.5‰, respectively (Table 12; Fig. 15). These $\delta^{18}O$ values all plot within the range (9-13‰) of magmatic waters defined by Sheppard (1977), see also Smith et al. (1996; Fig. 15). A narrower range of $\delta^{18}O$ for magmatic waters (11 ± 1‰) is given by Polya et al. (2000) for the nearby Panasqueira system, overlapping with most of the $\delta^{18}O$ signature inferred for the earliest fluids at Argemela at 550°C (Fig. 15), the $\delta^{18}O$ of fluids in equilibrium with $Qtz_{I\text{-}III}$ being slightly higher. δD of fluids in equilibrium with muscovite were calculated from O'Neil and Taylor (1969). For a temperature of 550°C (i.e. intermediate between 500 and 600°C), δD are -52.2‰ for the granitic facies and -54.4‰ for the micaceous facies. δD of fluids in equilibrium with muscovite reflect signature of the primary magmatic fluid as water is part of the mica structure. These primary fluids plot in the range of magmatic waters defined by Sheppard (1977; -40 to -65‰) and by Polya et al. (2000; -40 to -80‰), thus representing the early magmatic signature. The mean δD value of fluids in equilibrium with $Qtz_{I\text{-}III}$ also plots within the magmatic boxes while Qtz_I yields values higher than the magmatic range. For quartz from intragranitic veins, all fluid δD values plot higher than magmatic waters and in the field for pegmatites and skarns defined by Alderton and Harmon (1992; see

also Smith et al., 1996), this latter being close to the domain for Sn-W mineralization in SW England (Alderton and Harmon, 1992). The evolution between early magmatic (constrained by muscovite) and hydrothermal (constrained by vein quartz) signatures define a vertical trend from lower to higher δD (Fig. 15). Such a trend has been recognized in other similar systems worldwide (Shieh and Zhang, 1991; Bettencourt et al., 2005; Chicharro et al., 2016; Van Daele et al., 2018). For example, in the Dajishan Mine (Jiangxi Province, Southeast China, Shieh and Zhang, 1991), the fluid δD values increase (at nearly constant $\delta^{18}O$) from the magmatic (defined by minerals from the muscovite granite) to the main Sn-W ore stage (defined by minerals from the veins). A late hydrothermal stage also involves fluids having δD - $\delta^{18}O$ signatures of local meteoric waters. In this system, the isotopic compositions of the main ore fluids are interpreted as the result of isotopic equilibration with the granitic magma at a very low water/rock ratio (i.e., granite-buffered fluid compositions, Shieh and Zhang, 1991). The δD signature in the Argemela intragranitic veins is interpreted in an analogous way. Such "vertical" evolutions with δD values extending to lighter values at constant $\delta^{18}O$ have been also attributed to either outgassing of earlier fluids from the magma (Taylor, 1986), depletion of late-magmatic fluids in deuterium (Carten et al., 1988), variations linked to fluid-magma isotope effects (Rye et al., 1990) or minor admixtures of meteoric waters (Heinrich, 1990). All these interpretations accept a dominantly magmatic origin for the fluids.

Table 12
$\delta^{18}O$ and δD of micas and quartz and fluid in equilibrium

Minerals	Facies	T °C	$\delta^{18}O$ mineral (‰)	$\delta^{18}O$ fluid (‰)	δD mineral (‰)	δD fluid (‰)	σ (‰)
Micas	Granitic	550	+11.7	+12.1	-64.9	-52.2	0.2
	Micaceous	550	+11.7	+12.1	-67.1	-54.4	0.4
Quartz	Granitic	550	+13.7	+11.5		-35.4	7.0
	Micaceous	550	+14.5	+12.3		-41.9	4.0
	Type I	504	+14.8	+12.0		-28.5	4.4
	Type II	454	+15.6	+12.0		-33.5	11.9
	Type IIIa	459	+15.5	+12.0		-28.2	3.0
	Type IIIc	437	+15.9	+12.0			
	Type IIISR	432	+16.0	+12.0		-38.9	3.8

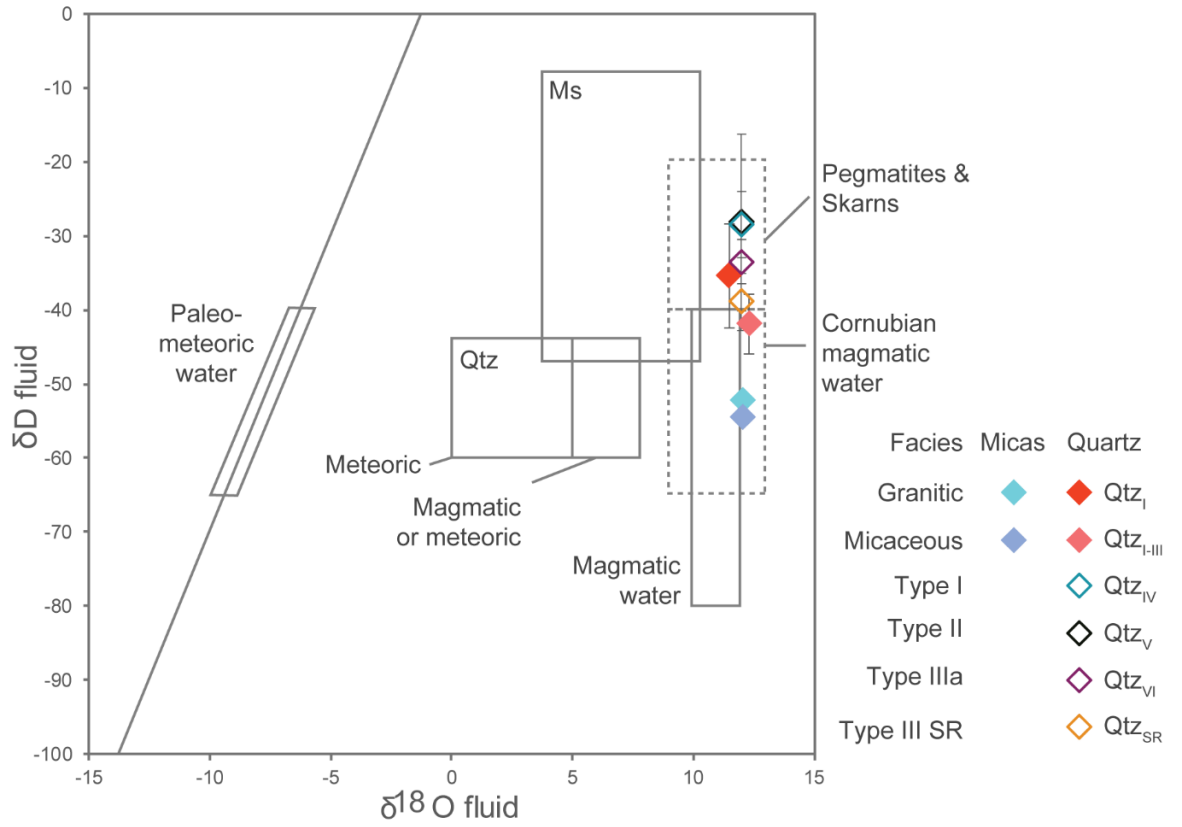

Fig 15 *Evolution of the fluid isotopic composition throughout the MHT. Magmatic and meteoric water boxes are from Sheppard, 1986; see also Polya et al. (2000). Cornubian magmatic water and minerals from pegmatites and skarn are from Sheppard, 1977 and Alderton and Harmon (1992), respectively; see also Smith et al. (1996). Quartz and muscovite boxes correspond to the $\delta^{18}O$ and δD range in minerals of Panasqueira (Kelly and Rye, 1979).*

Temperatures have been calculated for quartz-fluid and muscovite-fluid equilibration by assuming that the magmatic fluid exsolved at the MHT has a $\delta^{18}O$ of +12‰ (see the calculations above using Qtz_I, Qtz_{I-III} and muscovite). In the granitic and micaceous facies, results range from 595 to 526°C for quartz and 541°C is obtained for muscovite (Table 12). For the intragranitic veins, temperatures range from 526 to 491°C for the Type I, 454°C for the Type II to 459-437°C for the Type III veins (Table 12). This temperature range is viewed as reasonable given the recent thermometric determinations (up to ~450°C from topaz-muscovite equilibrium and fluid inclusion data, Halter and William-Jones, 1999; Mateus et al., 2018) for the Panasqueira magmatic-hydrothermal system. They provide an *a posteriori* validation of the interpretation of the $\delta^{18}O$ trend. As an information, if Type I, II

III intragranitic vein quartz were assumed to have all crystallized at the same temperature (526°C), the fluid would have a $\delta^{18}O$ of +12 to +13.4‰, which is higher than most magmatic waters (Fig. 15).

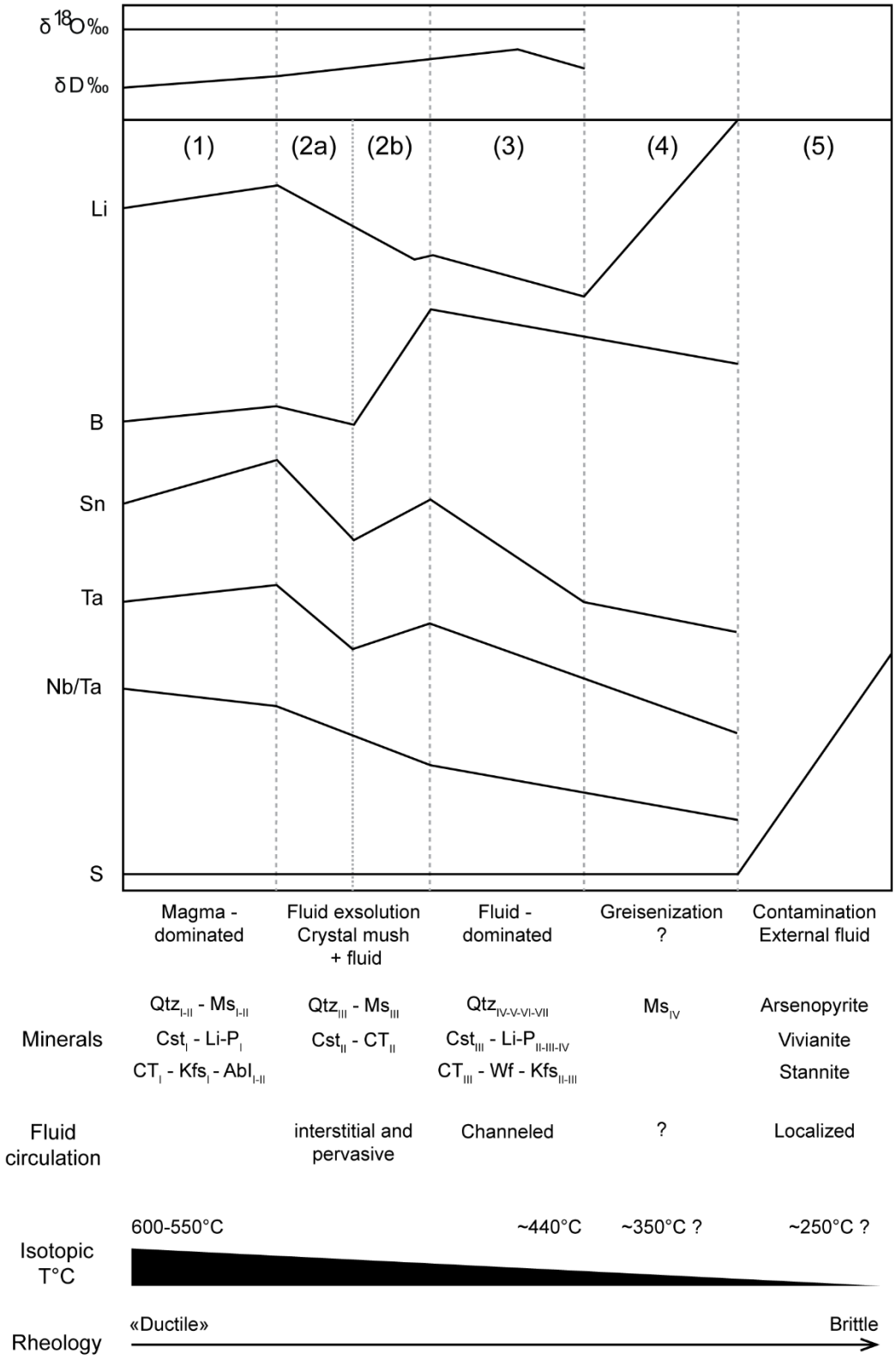

Fig 16 *Model of evolution of the magma and fluid signature and circulation. See text for descriptions*

Overall, the magmatic-hydrothermal transition is interpreted to have occurred in an essentially closed system. Early fluids have a clear magmatic composition and hydrothermal fluids from the veins have granite-buffered isotopic signatures. No addition of external fluids (i.e., metamorphic or meteoric) can be clearly detected clearly from the isotopic data and, so, the intragranitic veins can be considered as the expression of the exsolution of magmatic fluids. Nevertheless, late crystallization of sulfides (e.g., stannite, vivianite and arsenopyrite) is observed in Type III intragranitic veins, but only at the northeastern sheared border of the intrusion. This suggests a localized influx of a S-Fe-As-rich fluid indicating that the hydrothermal system was open to external contributions at the very end.

V.7.2. Mechanisms at the magmatic-hydrothermal transition

Detailed studies of mineral zonations, geochemical data and textural and structural characteristics provide evidence for the mechanisms involved at the MTM. At least five stages can be identified (Fig. 16): (1) early magma-dominated stage involving crystallization of mostly anhydrous minerals (except micas and montebrasite), (2) magmatic-hydrothermal stage corresponding to the exsolution of the magmatic fluid and its coexistence with the crystallizing magma, (3) early hydrothermal stage postdating granite crystallization and corresponding to fluid circulation in the intragranitic vein system and (4) late hydrothermal stage marked by the crystallization of sulfides and influx of an external fluid in the intragranitic vein system.

(1) The magmatic stage is associated with the crystallization of Qtz_I, Ms_{I-III}, Kfs_I, Li-P_I, Ab_I, Cst_I and CT_I in the Argemela granite. Growth zonation is found in snowball Qtz_I, being marked by alternating light and dark zones which underline the bipyramidal habit; there is no evidence for mineral dissolution or recrystallization. The chemical signatures of Qtz_I vary only slightly between light and dark zones indicating no first-order change in the crystallization environment. The zoning pattern of snowball Qtz_I suggests crystallization in situ in a static magma. The trigonal quartz habitus could indicate crystallization at temperatures < 600°C (Müller and Seltmann, 1999) which is consistent with isotopic temperatures and the type of zonation external fluctuations (i.e., over self-organizing growth) in an open system due to periodic degassing during melt cooling (e.g., Plimer, 1977; Holten et al., 1997; Müller

and Seltmann, 1999). The strong enrichment in Al and Li in Qtz_I, together with the depletion in Ti, is characteristic of highly evolved and flux-enriched magmas crystallizing at low temperatures (e.g., Breiter and Müller, 2009; Breiter et al., 2013; Müller et al., 2018). High Li and Al concentrations in the melt are necessary for their incorporation in the quartz lattice (Breiter et al., 2017; Müller et al., 2018) even if the correlation between Al in quartz and magma peraluminous character is still debated (Breiter and Müller, 2009). Ab_{Ia}, included in snowball cores, do not show the same signature than Ab_{Ib}, found in external zones. Early albite is enriched in P_2O_5, anorthite and Al_2O_3 (i.e., correlation of Al and P following the substitution mechanism: Al + P = 2 Si. In Ab_{Ib}, the relative depletions in P_2O_5 and Al_2O_3 could indicate syncrystallization with micas and/or montebrasite. Kfs_I are also relatively enriched in P2O5 which, together with a similar enrichment in early albite, implies high P contents in the parental melt which is a key characteristic of PHP magmas (Simpson, 1977; London et al., 1990; 1999). These K-feldspars show a significant albitic component which suggests a partial only reequilibration to low temperatures and corroborates their early crystallization. Cst_I, closely associated with Li-P_I crystallization, show an alternating zoning pattern underlining its euhedral habit. This feature is comparatively similar to what is observed in Qtz_I and thus indicates the same steady conditions of crystallization.

(2) The transition between the magma-dominated and the magmatic-hydrothermal stage is marked by micas and other phases from the granite which record the beginning of fluid exsolution. From Ms_I to Ms_{III}, the F (and Al) variations show alternating low and high values suggesting no first order change in the growth environment. The high metal (Li, Sn, Nb, Ta, W) contents in early micas, especially in Ms_I, are strongly in favor of a primary magmatic enrichment for these elements. However, from Ms_{IIa} to Ms_{III}, a strong drop is observed for most elements including metals, together with a marked increase in B between Ms_{IIb} and Ms_{III}. This indicates a major modification in the system, interpreted as indicating fluid exsolution from the magma and transfer of elements and metals toward the fluid phase. Qtz_{III} and Cst_{II} with inclusions of CT_{II} show features similar to Ms_{III} regarding metal concentrations. From Qtz_I to Qtz_{III}, Li, Al and Sn concentrations show the same decreasing evolution as observed in micas together with a slight increase of the B content. The high B content and slight re-increase of concentrations in some metals from Ms_{IIb} and Ms_{III} reflect the chemical imprint of the magmatic fluid. B is known to be

preferentially partitioned toward the fluid rather than in the melt (e.g., Pichavant, 1981) and the Argemela granite contains no phase such as tourmaline that could trap B. Texturally, Ms_{III} is specific compared to other micas (i.e., no zonation pattern, occurrence as overgrowth on early micas or invading the matrix) which suggests fast fluid-assisted growth. Similarly, Qtz_{III} and Cst_{II} are characterized by a skeletal habit invading the preexisting matrix, either overgrowing on earlier crystals or crystallizing in isolation. The evolution of the Nb/Ta ratio corroborates this interpretation (e.g., Ballouard et al., 2016) as the Nb/Ta ratio decreases from Ms_I to Ms_{III}. The Nb/Ta of both Cst_{II} and CT_{II} strongly decreases compared to the first generations and are very low (See Chapter III). Overall, both the chemical and textural characteristics of Ms_{III}, but also of Qtz_{III}, Cst_{II} and CT_{II}, consistently indicate granite crystallization under fluid-present conditions. From a structural and rheological point of view, the magmatic fluid during the magmatic-hydrothermal stage is able to percolate through the crystal mush as the granite still behaves as a "ductile" body. The grey facies, occurring as subvertical "dykes", marks the starting point of channeling of residual fluid-melt mixtures in weakness zones. This geometry represents an intermediate between fluid percolation in "ductile" granite and vein opening in a more brittle environment.

(3) The early hydrothermal stage is clearly marked in the field by the intragranitic quartz vein system. However, Type I and II intragranitic veins show mostly undulating margins, bridges and ponytail terminations suggesting a still "ductile" behavior. In contrast, Type III veins are straight with sharp contacts with the granite (Chapter III) indicating emplacement in a brittle regime. This clearly shows that vein emplacement occurs at the transition between a slightly "ductile" to brittle rheological regime and emphasizes the genetic link between the early veins and the magmatic evolution. For both Type I and W-bearing IIIa veins (since the data for Type II veins are limited), quartz close to vein margins show similar ranges of Li and Al concentrations than early Qtz_I. However, the data in vein cores demonstrate a strong decrease of these elements. This might be due to montebrasite crystallization mobilizing both Al and Li from the fluid and buffering incorporation of these elements in quartz. High concentrations of Li at the beginning of vein opening indicate that, despite crystallization of Li-P_I, a high amount of Li is available and transported by the magmatic fluid together with Al (e.g., essential for incorporation in quartz through the berlinite substitution; Breiter et al., 2006; Müller et al., 2018). Low

Al and Li contents and decreasing Ge in quartz have also been observed in other RMG-related vein systems (e.g. Cínovec/Zinnwald, Müller et al., 2018). The decrease in Ge can be explained by the decreasing solubility of Ge in fluids with decreasing temperature (Pokrovskii and Schott, 1998). Compositions of K-feldspars also evolve systematically from Type I to Type III intragranitic veins. Ba contents decrease and, as for quartz, the decrease in Li and P is probably related to montebrasite crystallization. Complementary to the mineral data, the bulk rock analyzes of Type I veins reveal a significant amount of Sn as well as some Nb, Ta and W which means that the hydrothermal fluid circulating in the veins carries metals in high concentrations, despite ore minerals being absent. Such elevated whole-rock metal concentrations are not observed in the Type III veins. The most likely explanation is that crystallization of Cst_{III}, Wf and CT_{III} (as observed) has depleted the fluid in the corresponding metals.

(4) Crystallization of Ms_{IV} does not fit easily in the above model. We recall here that Ms_{IV} differ from earlier micas both texturally (i.e., patchy habit invading earlier micas) and chemically (i.e., zinnwaldite to lepidolite compositions). In other similar systems (e.g., Cínovec: Breiter et al., 2017; Beauvoir: Cuney et al., 1992), zinnwaldite and lepidolite are very often associated with greisens. Although at Argemela Ms_{IV} occur only in and near the border facies, their Li- and F-rich chemistries bears a strong magmatic imprint inconsistent with an origin involving fluids external to the intrusion. Therefore, they are interpreted to mark a late crystallization event within the intrusion, earlier than the sulfide stage (5) which corresponds to the influx of external fluids in the intragranitic vein system (see below). Ms_{IV} crystallization markedly contrasts with the general trend of progressively decreasing Li during the MHT as recorded by micas and quartz from the granite and intragranitic veins. Therefore, the Ms_{IV} crystallization stage could be related to the late extreme enrichments found in the grey/"ball like" facies which can be very Li-rich (Charoy and Noronha, 1996). However, the textural and geometrical evidence does not confirm this hypothesis since the crystallization of Ms_{IV} is pervasive and the grey/"ball like" facies have dike or ovoïdal geometries. Yet, Ms_{IV} marks a local late Li-rich probably subsolidus crystallization stage that partially transforms and replaces earlier mineral assemblages. It is worth emphasizing here that metasomatic transformations of early phases are of minor importance at Argemela and restricted to the border facies.

(5) The late hydrothermal stage is marked by the crystallization of sulfides such as arsenopyrite, vivianite and stannite replacing cassiterite. The S-rich mineral assemblage is viewed as an indication for the involvement of fluids external to the intrusion since the granite is very poor in S (whole S contents mostly below detection limit, Table 1). External contamination occurs only at the northeastern border of the intrusion, close to the sheared contact. Sulphides crystallize in late little fractures, disseminated mainly around/inside Type III veins. This suggests that the influence of the S-Fe-As-bearing fluid is of restricted importance and superimposed to earlier hydrothermal processes in the veins.

V.7.3. Fractionation mechanisms at the MHT

Analysis of mineral chemical trends during the different stages above provide constraints on fractionation mechanisms at the MHT (Fig. 16). The *early* evolution (marked by Ms_I, Qtz_I and feldspars from stage (1) corresponds to high and either constant or slightly increasing Li, Sn, Nb, Ta, P, Ge, Al, Fe, Mn, W. These elements were initially present at significant levels and became slightly concentrated in residual melts as crystallization progressed. CstI, CTI and Li-P most probably crystallized from such melts (thus buffering their Sn, Nb, Ta, Li and P concentrations) and so appeared slightly later than the main phases in the crystallizing magma. The *intermediate* evolution corresponds to an important and progressive decrease in element concentrations, particularly well recorded in Ms_{IIb} and Qtz_{III} from stage (2). This evolution affects all elements uniformly (except for Rb and Cs which remain stable) including those not sequestered in ore minerals such as CstI and CTI. Therefore, it indicates non-selective element loss from the crystallizing magma, attributed to element partitioning toward the fluid phase (2a; Fig. 16). Transfer of elements in the magmatic fluid must be combined with a mechanism of extraction of the fluid to explain the observed depletions as crystallization continued. The *late* evolution (Ms_{III} from stage, 2b, Fig. 16) corresponds to a back increase of Sn, W, Mn and Ta concentrations accompanied by a drastic rise of the B concentration. It is followed in the intragranitic vein system (stage (3)) by a trend of progressive depletions of all elements (Fig. 16).

The late enrichment observed contrasts with the intermediate evolution which is characterized by element depletions. Yet, we note that similar enrichments also appear in the grey facies (Table 1).

The Ms_{IV} stage (4) also locally testifies of a late enriched crystallization environment. This enrichment trend could indicate a change in the fluid hydrodynamic regime from open- (intermediate evolution) to closed- (late evolution) system, the late fluids becoming confined. However, efficient draining of late-magmatic fluids out of the crystallizing magma is demonstrated by the intragranitic vein system. Late-stage processes such as greisenisation are associated with positive (and not negative) permeability changes. Quartz from intragranitic veins also do not show the enrichments recorded in Ms_{III} from the granite. As an alternative explanation, it is possible that the intermediate and late fractionation trends observed involve two different types of magmatic fluids. Several recent studies have called upon the existence of immiscible H_2O-rich melts, in addition to fluids with more conventional properties, at the MHT (e.g., Thomas and Davidson, 2012; 2015; Kaeter et al., 2018; Hulsbosch et al., 2019). These immiscible melts have been proposed to play an important role in the partitioning of elements and the transport of metals at the MHT (Thomas and Davidson, 2012). However, the very existence of such immiscible melts is strongly questioned (London, 2015; Thomas and Davidson, 2016). Yet, magmatic fluids at equilibrium with evolved magmas such as RMGs are dense phases that carry several wt% dissolved silicates in addition to fluxing elements and metals (e.g., Pichavant, 1981; London, 2018). Cooling and/or depressurization of such fluids might lead to condensation of solute material, as observed experimentally (Pichavant, 1981; London, 2018). Elemental fractionations are to be expected between condensate solutes and the residual, low density, fluids. Thus, it is possible that the late enriched fractionation trend observed is the mark of such dense condensates. The highly enriched granite facies (grey facies in this study and “ball like” facies in Charoy and Noronha, 1996) could also be representative of this type of material. Yet, it should be emphasized that this specific phase is of restricted importance in volume as only a few occurrences of the grey facies have been found. The late enrichment trend is also limited to the outer rim of micas.

V.8. IMPLICATIONS FOR RARE-METAL GRANITES

Stable isotope, whole rock, mineral and textural data indicate that the geochemical signature of the Argemela RMG depends on essentially two factors, the melt composition (i.e., controlled by early magmatic processes) and mechanisms at the MHT. For example, the concentrations, transportation and distribution of rare elements (e.g., Sn, Li, Nb, Ta, W) are controlled by their initial concentration levels in the melt, then by exsolution of magmatic fluids, melt-fluid partitioning and fluid extraction and, finally, by the chemical evolution of the fluid in the intragranitic vein system as temperature decreases and the intrusion becomes rigid. Locally, condensation of the magmatic fluid results in the *in-situ* crystallization of rare element-enriched facies and/or minerals. At Argemela, the magmatic-hydrothermal evolution is well documented because the late hydrothermal transformations (i.e., greisenization, kaolinization) are limited. In particular, the transition between the magmatic, the magmatic-hydrothermal and the early hydrothermal stages is preserved. The fluids involved at the MHT are clearly demonstrated to have a magmatic origin (i.e., no external fluid contribution is identified except at the late end). In comparison, in others RMGs of the Variscan belt, magmatic fluid exsolution and early hydrothermal evolution (i.e., the "intermediate" stages) are generally overprinted by late hydrothermal alteration events and only the two extreme signatures (i.e., the magmatic and late hydrothermal stages) are preserved.

On the magmatic side, clear differences are to be noted between RMGs. For example, the Zinnwaldite granite at Cínovec has lower P and rare element contents and a lower peraluminosity than at Argemela. Magmatic quartz in the former has lower Al and Li than in the latter. Lower Li, Al and P contents in the melt are also highlighted by the absence of montebrasite as a magmatic phase, zinnwaldite being the main Li-bearing mineral. In contrast with zonation patterns in Argemela micas, the zinnwaldite crystals at Cinovec are homogeneous (Breiter et al., 2017) and, so, the "intermediate" stages have been largely erased in the Zinnwaldite granite. This is also the case at Beauvoir where the RMG hosts mostly homogeneous Li-rich micas (lepidolite, Cuney et al., 1992) and muscovite fringe interpreted as the result of greisenization. On the late hydrothermal side, at Cinovec, intense hydrothermal alteration is observed as marked by the common presence of greisens and of late veins

(Breiter et al., 2017). At Beauvoir, greisenization is only local at the difference of Cinovec, but kaolinization is strongly marked and there is evidence for a significant contribution of meteoric fluids during the MHT (Fouillac and Rossi, 1991). Chemical signatures of quartz in the Beauvoir granite and apex veins show that only the magmatic and late hydrothermal stages are preserved (Monnier et al., 2018). Early magmatic quartz share common features with Qtz_I at Argemela while apex veins quartz are strongly enriched in Li suggesting crystallization in a highly enriched environment similar to Ms_{IV} at Argemela. Thus, Argemela represents a rare case where early hydrothermal mechanisms are preserved.

Another important aspect to be emphasized is that chemical fractionation trends are not necessarily amplified by these "intermediate" processes. Geochemical patterns during the MHT at Argemela include a depletion trend uniformly marked on all elements, associated with fluid/melt element partitioning and extraction of the fluid phase. This depletion trend is followed by enrichments having a more local significance and, therefore, in detail, several types of fractionation mechanisms take place during the MHT. This suggests that, in other RMGs, the element enrichments are mostly associated with late hydrothermal events (i.e., remobilization of rare elements in greisens or late veins). Cínovec is a good example where greisenization processes led to elevated rare elements concentrations and the formation of an economic deposit despite low rare element contents in the melt compared to Argemela.

V.9. SYNTHESIS AND CONCLUSIONS

A synthesis of mechanisms occurring at Argemela during the MHT is represented on Fig. 16. The geochemical evolutions go along with changes in magma crystallinity. A rheological transition from ductile to brittle impacts fluid extraction and circulation and the repartition of the mineralized veins in the intrusion. The early stage is dominated by crystallization down to a temperature of ~550°C as the RMG magma evolves towards a crystal mush. Minerals crystallizing during stage (1) are characterized by significant concentrations in Li, Ta, Nb, Sn, suggesting that the specific rare-metal enriched signature of the Argemela granite has a primary magmatic origin. Crystallization of anhydrous minerals promotes fluid exsolution from the magma resulting in the crystal mush coexisting with a magmatic fluid (stage (2)). The fluid partitions elements from the crystallizing melt and becomes extracted from the mush, forming the intragranitic vein system. Fluid circulation, accompanied by temperature and pressure changes, locally results in condensation of the fluid, thought to be responsible for selective element increases in micas and crystallization of the Sn-Li-Ta-rich grey facies (2a, Fig. 16). The grey facies, its dyke-like geometry together with its highly enriched chemistry, is a marker of the beginning of fluid channeling as temperature decreases and the rheology of the intrusion evolves (2b, Fig. 16). The intragranitic veins (stage (3)) represent outstanding evidence for fluid channeling. Their geometries demonstrate emplacement in an environment that changes from slightly ductile to more brittle. During vein formation, the observed decrease of element concentrations is due to mineral precipitation and fluid dispersion. The Ms_{IV} crystallization stage (4) corresponds to a local late hydrothermal Li remobilization event. Finally, the late crystallization of sulfides in veins at the sheared northeastern border of the intrusion testifies of contamination of the magmatic system by an external fluid at the very end of the evolution (stage (5)).

The main points of this study are as follow:

1. The rare element (especially Sn, Nb, Ta, Li) concentrations in the Argemela granite have a primary magmatic origin as testified by the crystallization of cassiterite, columbo-tantalite and montebrasite as magmatic minerals.

2. The field observations, structural data, mineralogical and geochemical constraints, complemented by the stable isotope (O, H) data, establish the magmatic origin of the fluid circulating in the intragranitic veins. The magmatic-hydrothermal system is locally open to a minor late influx of external S-rich fluids.

3. The Argemela RMG provides an outstanding record of processes and fractionation mechanisms at the MHT.

4. Exsolution of the magmatic fluid and its extraction are marked by a general decrease in trace element concentrations. It is followed by a selective enrichment trend attributed to the local condensation of the magmatic fluid.

5. At Argemela, the overall evolution during the MHT corresponds to a decrease of rare element concentrations as metals are transferred from the magma toward the hydrothermal system. This contrasts with enrichments commonly observed in other Variscan RMGs which are attributed to the influence of late hydrothermal events not observed at Argemela.

6. Highly evolved magmas do not necessarily result in the formation of an economic deposit. Intensity of late hydrothermal alteration will trigger rare elements concentration.

CHAPTER VI:

LOW DEGREE PARTIAL MELTING AS A MECHANISM OF METAL CONCENTRATION AND GENESIS OF RARE METAL MAGMAS: AN EXPERIMENTAL APPROACH.

ABSTRACT

Partial melting experiments were conducted to investigate the origin of evolved magmas such as RMGs enriched in Li, Sn, Nb, Ta and W. One model for the origin of Variscan RMGs involves low degree of partial melting of crustal protoliths. To test this model aH_2O and temperature were adjusted to simulate the generation of low degree partial melts (< 20%). Two different natural protoliths were selected as starting materials: a paragneiss (bt, pl, qtz, grt, kfs, ms) and an orthogneiss (ms, pl, kfs, qtz, bt) both from the metamorphic series of La Dronne (Limousin, FMC) and containing variable concentrations of metals (especially Sn and W). Plurimillimetric microcores cut perpendicular to the natural cleavage and sealed into gold capsules were melted at 800 and 850°C and 4kbars for 2 weeks in an internally heated vessel pressurizd with an Ar-H_2 mixture (initial pH_2=6bars) to control the fO_2. No water was added to the capsule to promote dehydration melting. Experimental charges were quenched isobarically. At 850°C, degrees of melting are of ~18 and ~20% for the paragneiss and the orthogneiss, respectively and of ~8 and ~13% at 800°C. Melt distribution between the two protoliths strongly differs due to micas repartition and melting mechanisms, however, major element composition of glass are quite homogeneous and are close to peraluminous granite whole rock compositions. Muscovite and biotite dehydration melting results in the formation of peritectic phases, later called restite. Trace element composition of the melt can strongly vary and at both 850 an 800°C rare elements are only little partitioned into the melt except for Li. It is showed that most metals made available by micas breakdown are sequestered into the restite. Overall, our experiments show that a one stage low degree dehydration melting is not an efficient mechanism to preconcentrate rare-elements in the generated melt. A multistage melting model, involving the destabilization of enriched restites is proposed instead to generate rare metal magmas.

LOW DEGREE PARTIAL MELTING AS A MECHANISM OF METALS CONCENTRATION AND GENESIS OF RARE METAL MAGMAS: AN EXPERIMENTAL APPROACH

VI.1. INTRODUCTION

Rare Metal Granites (RMGs) are highly evolved granites occurring worldwide (e.g., China: Belkasmi et al., 2000; Zhu et al., 2001; Finland: Haapala and Likkari, 2005; Algeria: Kesraoui et al., 2000; Namibia: Schmitt et al., 2000; Nigeria: Kinnaird et al., 1985; Egypt: Renno, 1997; Canada: Kontak, 1990, Pillet et al., 1992; Russia: Raimbault et al., 1995; Mongolia: Kovalenko et al., 1995). Among others, numerous RMGs have been recognized dispersed across the Variscan belt of Western Europe, from the Bohemian Massif - northeastward - to Iberia - southeastward - (Aubert, 1969; Manning and Hill, 1990; Cuney et al., 1992; Charoy and Noronha, 1996; Breiter et al., 1997; Raimbault, 1998; Breiter et al., 2017; López-Moro et al., 2017). Variscan RMGs are mainly peraluminous (A/CNK > 1) to highly peraluminous (A/CNK > 1.3) except for some Cornish examples that are metaluminous to slightly peralkaline (A/CNK $\leq$ 1; Manning and Hill, 1990). The classification of Linnen and Cuney (2005) divides RMGs into three main groups according to the alumina saturation index and based on geochemical/mineralogical specificities: peralkaline (PLK; ASI < 1), metaluminous to peraluminous low phosphorous (PLP; P_2O_5 < 0.1 wt%) and peraluminous highly phosphorous (PHP; P_2O_5 > 1wt%); peraluminous intermediate phosphorous types have also been considered (PIP; 0.1< P_2O_5 <1 wt%). Several outstanding examples of Variscan PHP are used as references, namely the Beauvoir (French Massif Central; Cuney et al., 1992; Raimbault, 1995), the Cínovec (Bohemian Massif, Breiter et al., 2017) and the Argemela granites (Central Iberian Zone; Charoy and Noronha, 1996). Regarding their specific common geochemical signature, these granites are characterized by a marked depletion in REE, Y, Zr, Hf, Th, Ca, Fe, Ba and Sr, high concentration in fluxing elements (F, B, Li, P) and marked enrichment in rare lithophile elements and metals (Sn, Nb, Ta, Be, Cs, Rb, and W). The source of rare

elements in RMGs and the origin of their peculiar geochemical signature have been much debated since the 60's and remain controversial. Do these granites owe their geochemical signature and metal enrichment to a specific magmatic evolution or to late subsolidus processes involving a fluid phase? Early workers (Beus et al., 1962; Beus and Zhalashkova, 1964; Zhalashkova and Sitnin, 1967; Hu et al., 1984) have emphasized the role of subsolidus metasomatic transformations of the granite by incompatible elements-enriched hydrothermal fluids. However, studies on volcanic analogues (Kovalenko and Kovalenko, 1976; Pichavant et al. 1988; Raimbault and Burnol, 1998) demonstrated the importance of magmatic processes in RMGs genesis and their metal enrichment. A magmatic origin is thus widely accepted by the scientific community, thought it does not exclude a late fluid-assisted remobilization.

Regarding the role of magmatic processes in the specific signature of RMGs, two main models stand out. Numerous authors (e.g., Jahn and Burnham, 1969; Raimbault, 1987; Černȳ, 1991b, Černȳ 1992a; Raimbault et al., 1995; Breaks et al., 2005; Černȳ et al., 2005; Roda-Robles et al., 2018) consider that rare metal magmas result from extreme fractionation of a peraluminous crustal magma (i.e., a parental granite magma), since fluxing, lithophile and metallic elements are preferentially partitioned in the residual melt during crystallization. This model implies a direct genetic link between peraluminous granite and RMGs. Rossi et al. (1988) have concluded from the study of Sn-W granites that fractional crystallization from a monzogranite to leucogranites can achieve an enrichment of one order of magnitude in Sn and W. Raimbault (1987) suggests a similar process for rare metal magmas. However, it has also been noted that crystallization-differentiation cannot account for such high rare metal concentrations. Furthermore, the spatial and chronological relationships between peraluminous granites and RMGs are not always consistent with derivation of the latter from the former. Therefore, direct partial melting of the crust has been proposed as an alternative model to generate fractionated melts (e.g., Christiansen et al., 1986; Cuney, 1990; Cuney et al., 1992; Cerny et al., 2005). This process would depend on several factors such as the degree of melting, nature of the protolith (i.e., ortho- vs. para-derived), degree of geochemical specialization of source rocks, type of minerals responsible for the metal enrichments and their behavior during melting. The role of micas, for example, is of importance

as they could represent the main metal carriers, muscovite being generally considered more enriched in metals than biotite.

Partial melting results in the redistribution of elements in the crust and allows concentration of rare elements in the melt. It is of growing interest to better understand melting mechanisms and the role of the degree of partial melting on the rare element concentration of the formed melt. Low degree partial melting has been proposed as a possible mechanism to generate rare metal magmas because the rare elements become concentrated in a small volume of melt. This mechanism also requires that the source is fertile (i.e., it initially contains minimum amounts of metals), that the rare-elements-bearing minerals are broken down during the melting reaction and that the partition coefficients for the rare elements are in favor of the melt. For a given source rock, conditions of partial melting (e.g., temperature) and type of melting reaction (i.e., dehydration vs. fluid-present melting) are the main factors controlling the degree of melting.

Several experimental melting studies have been performed over the years (e.g., Icenhower and London, 1995; Patiño Douce and Harris, 1997; Tumarkina et al., 2011; Konzett et al., 2018). However, experimental data for low degree melts (e.g., partition coefficients for major and trace elements between rock forming minerals and melt) are limited. Most experiments have focused on the behavior of major elements and synthetic starting materials have been commonly used as protoliths instead of natural rocks. For example, Icenhower and London (1995) used a synthetic metapelite powder (i.e., a synthetic mixture of natural minerals) as starting material. Experiments were conducted at 650-750°C and 2kbars. Degrees of melting in these experiments were quite high and trace elements (Ba, Rb, Cs, Li) were given minor attention in comparison to major elements. In contrast, recently, low degree partial melting experiments were performed at 7kbars, 650-750°C, with and without added water, on staurolite-garnet-muscovite-biotite gneisses from the Texel Complex (Konzett et al., 2018). The study was centered on the role of staurolite as a source of Li in the resulting melt but no trace element data was reported. Theoretical trace element pelite melting models have been elaborated (Harris et al., 1992: Harris and Inger, 1995) but they concern Ba, Sr and Rb and not rare metals such Sn, W, Nb, Ta, Li. The behavior of Sn during partial melting has been recently explored from geochemical data obtained on migmatite samples, combined with calculation of conditions and degrees of melting (Wolf et al., 2018). However,

Li, W, Nb and Ta were not detailed, and the modelling was performed on theoretical protolith compositions.

VI.2. STRATEGY

This study focuses on testing low degree partial melting as a mechanism for rare metal (Sn, W, Nb, Ta, Li) magma genesis and concentration. All experiments detailed below were performed under fluid absent conditions which is known to be a relevant mechanism at the scale of the crust and commonly tested in other studies (e.g., Vielzeuf and Holloway, 1988; Harris et al., 1995; Patiño Douce and Harris, 1997; Konzett et al., 2018). Companion experiments were performed under fluid-present conditions but they yielded generally high degrees of melting and are not considered below. The fluid absent experiments were performed at 400 MPa for two temperatures (800, 850°C), all under reducing redox conditions.

Natural samples are used to favorize natural melting mechanisms at different temperatures. Two classical lithologies were chosen representing end members: a para- and ortho-derived gneisses. Metasedimentary lithologies are generally acclaimed as sources of peraluminous magmas, however, regarding melting mechanism of both end-members is more realistic. An orthogneissic source is, besides, invoked for "A-type" rare metal magmas production. Melting a mixed source (i.e., mixing para- and orth-derived gneisses) is another alternative. The use of natural samples also favorize low degree melting compared to powders and minerals involved in the melting reaction can be identified.

Microcores cut perpendicularly to the cleavage allow the preservation of natural texture and microtextures. Initial texture (i.e., rock cleavage) and mineral distribution are main controlling factors for melting reaction and melt distribution.

Another key feature is the variation of protolith mineralogies. The variation of micas proportion and especially the biotite/muscovite ratio is one of the major important parameters. Muscovite and biotite behaviors during melting and according to temperature are contrasted. Micas are also the main metal-bearing minerals, thus, their behavior during melting will largely control metal redistribution. A

biotite-rich paragneiss and muscovite-rich orthogneiss were thus chosen in order to constrain their contrasted behaviors and effects on melting degree, reaction, metal redistribution.

The two protoliths show different whole rock and mineral compositions which allow varying the fertility of the source. As an example, the orthogneiss show significant Sn, Li and W content compared to the paragneiss, however, biotite of the paragneiss is the main micas and contains higher Li, Nb, Ta than muscovite. Changing the initial trace element content in whole rock and even more in minerals such as micas, will help to emphasized Sn, Nb, Ta, W and Li behavior during melting. No similar studies have been conducted before and there are thus no *a priori* on the results.

VI.3. METHODS AND ANALYTICAL TECHNIQUES

VI.3.1. Starting materials

The melting experiments were performed on two gneisses from the La Dronne metamorphic series in the southwestern part of the French Massif Central. Building of the Variscan orogen is the consequence of a nappe stacking event between 360 to 320 Ma. This resulted in the superposition of 4 units, from top to bottom, the Thiviers-Payzac Unit (TPU), the Upper Gneiss Unit (UGU), the Lower Gneiss Unit (LGU) and finally the Autochthonous Unit (PAU) (e.g. Faure et al, 2009). The La Dronne metamorphic series belong to the PAU unit. This nappe stacking episode was followed by a collisional stage, collapse of the belt from 330 Ma to about 300 Ma, crustal melting and by generation of peraluminous granitic bodies which intruded the upper nappes. Rocks from the La Dronne metamorphic series have been classically considered as possible protoliths of the peraluminous granites (e.g., Turpin et al., 1990). Two gneisses, one orthogneiss and one paragneiss, representative of the La Dronne lithological diversity, were sampled. Both rocks are strongly deformed and finely banded and they show no indications for extensive mobilization and partial melting. The orthogneiss is muscovite-rich, containing also quartz, alkali feldspar, plagioclase, minor biotite and garnet whereas the paragneiss (quartz, plagioclase, alkali feldspar, biotite, garnet, kyanite, sillimanite, oxides) almost totally lacks muscovite. Therefore, the two samples differ in the nature of the mica phase present. Thermobarometric estimations with Perple_X using bulk rock and mineral compositions have yielded conditions of metamorphic equilibration of 600-650°C and 400-500 MPa for the two rocks.

Whole rock analyses. The whole rock geochemical signature of two starting materials differs. Data and detection limits are given in Table 1. The paragneiss shows higher FeO (4.60 wt%), Na_2O (3.40 wt%), TiO_2 (0.81 wt%), MgO (1.76 wt%) and lower SiO_2 (69.29 wt%), CaO (1.25 wt%), K_2O (2.68 wt%), P_2O_5 (0.20 wt%) and F (0.05 wt%) content than the orthogneiss (FeO: 1.04 wt%; Na_2O: 1.66; TiO_2: 0.30 wt%; MgO: 0.44 wt%; SiO_2: 72.03 wt%; CaO: 1.48 wt%; K_2O: 5.94 wt%; P_2O_5: 1.25 wt% and F:0.35 wt%). The trace element contents also differ between the two samples and especially

the rare elements. The paragneiss is relatively enriched in Ta (1.78 ppm) and Nb (16.70 ppm) and depleted in Li (48 ppm), Sn (2.81 ppm) and W (2.66 ppm) compared to the orthogneiss (Ta: 0.93 ppm; Nb: 11.12 ppm; Li: 95 ppm; W: 16.96 ppm) being strongly enriched in Sn (217.9 ppm).

Table 1

Whole rock analyses of the starting materials

Major elements (wt%)	Paragneiss	Orthogneiss	Detection limits
SiO_2	69.29	72.03	0.05
TiO_2	0.81	0.30	0.02
Al_2O_3	13.72	13.56	0.04
FeO	4.60	1.04	0.015
MnO	0.06	0.02	0.015
MgO	1.76	0.44	0.03
CaO	1.25	1.48	0.03
Na_2O	3.40	1.66	0.02
K_2O	2.68	5.94	0.03
P_2O_5	0.20	1.25	0.10
F	0.05	0.35	
LOI	0.89	2.05	
Total	99.22	99.89	
Trace elements (ppm)			
Li	48.00	95.00	
Be	2.21	6.46	0.05
As	11.98	16.56	0.50
Ba	844.10	745.20	5.5
Bi	0.18	0.20	0.045
Cd	0.35	0.24	0.02
Ce	102.10	66.62	0.03
Co	9.27	1.50	0.08
Cr	109.00	96.00	0.50
Cs	6.64	34.50	0.02
Cu	10.73	bdl	2.0
Dy	5.03	5.74	0.004
Er	2.68	2.95	0.002
Eu	1.44	1.34	0.002
Ga	19.15	22.40	0.02
Gd	5.99	6.07	0.005
Ge	1.97	2.11	0.04
Hf	11.77	5.00	0.03
Ho	0.95	1.11	0.001
In	0.08	bdl	0.03
La	55.59	37.93	0.02
Lu	0.46	0.39	0.001
Mo	bdl	3.30	0.50

Nb	16.70	11.12	0.015
Nd	43.35	35.52	0.016
Ni	23.42	47.66	2.0
Pb	20.26	26.87	0.45
Pr	12.00	9.41	0.004
Rb	110.20	245.70	0.15
Sc	12.04	4.16	0.6
Sb	0.27	2.02	0.06
Sm	7.75	7.66	0.005
Sn	2.81	217.90	0.30
Sr	175.80	98.00	0.70
Ta	1.78	0.93	0.004
Tb	0.90	0.98	0.001
Th	17.33	14.50	0.015
Tm	0.42	0.43	0.001
U	3.92	2.57	0.01
V	90.88	17.41	0.85
W	2.66	16.96	0.80
Y	27.74	31.44	0.02
Yb	2.87	2.73	0.002
Zn	82.59	25.08	7.0
Zr	537.10	185.60	1.50

bdl: below detection limit

Minerals major elements. Representative analyses of rock forming minerals from the two starting rocks are given in Table 2 (data from Arnaud Villaros). Data are not available for all minerals yet, but work is in progress. Garnets from both the paragneiss and the orthogneiss are almandine-rich, the garnet from the orthogneiss being richer in manganese and more depleted in magnesium than in the paragneiss. Biotites from the paragneiss are magnesian (MgO: 7.92-8.03 wt%; FeO: 17.47-18.03 wt%) while biotites of the orthogneiss are more ferrous (MgO: 2.91-3.45 wt%; FeO: 26.11-27.37 wt%). Plagioclase from the paragneiss has a significant CaO content (3.67 wt%), corresponding to An 13-16.

Table 2

Representative EPMA major element analyses of rock forming minerals from the starting materials

	Paragneiss							Orthogneiss							
Major elements (wt%)	Ky	Bt			Grt	Pl	Qtz	Bt			Kfs	Grt	Ms		
SiO_2	37.16	35.24	35.73	35.40	37.93	64.24	98.25	33.84	34.54	34.54	64.79	36.92	48.36	47.88	47.35
TiO_2	-	3.54	3.99	3.76	-	-	-	2.26	2.47	2.57	0.01	0.01	0.62	0.51	0.78
Al_2O_3	61.05	18.51	18.52	18.92	20.46	21.17	-	17.10	16.69	16.88	17.71	20.55	32.46	32.51	32.48
FeO	0.19	17.69	17.47	18.03	33.54	-	-	27.37	26.11	26.29	-	34.76	2.98	3.24	2.97
MnO	-	0.06	0.13	0.11	3.41	-	0.03	0.35	0.30	0.31	0.02	4.22	-	0.11	0.02
MgO	0.02	8.03	8.18	7.92	3.05	0.02	0.02	2.91	3.38	3.45	0.01	0.92	0.73	0.67	0.67
CaO	0.02	-	-	-	1.05	3.67	-	-	-	0.01	-	1.73	0.03	0.02	-
Na_2O	0.01	0.09	0.16	0.19	0.01	8.83	-	0.04	0.03	0.08	0.72	0.02	0.44	0.39	0.36
K_2O	0.01	9.55	9.31	9.47	-	0.18	0.05	9.14	8.89	9.04	15.50	0.03	9.59	8.98	9.66
P_2O_5	0.05	0.15	-	0.04	0.06	-	-	0.04	0.01	0.15	0.05	-	-	0.02	0.05
F	-	0.15	0.16	0.14	0.05	-	-	0.35	0.40	0.40	-	-	0.16	0.27	0.19
Total	98.52	92.99	93.65	93.98	99.55	98.12	98.34	93.39	92.81	93.70	98.81	99.16	95.36	94.59	94.53

Table 3

Representative LA-ICP-MS trace element analyses of rock forming minerals from the starting materials

Trace elements (ppm)	Paragneiss							Orthogneiss							
	Ky	Bt			Grt	Pl	Qtz	Bt			Kfs	Grt	Ms		
Li	0.40	218.65	188.69	163.22	37.11	0.20	9.14	58.52	178.26	209.07	3.13	46.44	74.22	87.86	78.73
Be	bdl	0.97	0.85	0.92	bdl	6.56	0.13	1.85	2.10	0.95	0.26	0.70	2.59	2.43	2.47
B	bdl	2.99	3.85	5.32	bdl	2.06	2.14	3.84	1.04	1.68	4.34	1.45	7.40	6.71	7.06
Sc	4.01	36.04	36.95	36.34	206.39	4.92	9.85	25.03	19.38	16.90	5.19	71.96	38.10	42.46	38.54
Ti	215.62	21034	21444	21074	962.41	11.50	28.87	5773	18861	14128	112.60	31.94	3815	4033	4147
V	211.74	393.57	361.14	349.06	105.52	0.09	0.13	48.72	66.59	69.41	1.65	14.44	50.77	53.26	57.47

Zn66	bdl	346.25	349.92	310.31	72.13	0.88	0.43	28.70	411.46	461.34	2.68	75.02	32.75	37.39	32.71
Zn68	bdl	300.39	317.02	300.24	49.87	23.71	31.47	40.73	206.44	179.10	84.22	36.49	46.14	50.49	43.52
Rb	0.83	488.70	495.91	466.11	18.93	0.42	0.05	558.28	1034	1029	423.20	93.99	583.81	682.77	565.39
Sr	bdl	1.56	1.49	1.85	bdl	85.35	0.06	2.66	2.81	1.53	86.18	0.96	5.03	3.74	4.64
Y	bdl	0.47	0.23	0.28	253.81	0.63	bdl	0.07	37.64	21.55	0.09	754.69	0.06	0.11	0.58
Zr	bdl	1.69	0.97	1.58	1.91	0.06	bdl	2.68	10.86	2.95	0.03	5.39	2.70	2.64	3.30
Nb	0.18	56.48	126.52	119.02	4.13	bdl	0.03	86.97	227.83	125.95	1.64	0.12	80.68	81.88	76.64
Sn	0.29	11.37	10.68	10.22	0.65	0.10	0.05	48.26	30.53	18.64	2.02	1.98	66.24	58.74	63.67
Cs	bdl	31.14	30.84	29.31	1.19	bdl	0.04	4.54	36.17	36.18	2.03	7.94	5.45	7.63	5.42
Ba	8.72	2133	1996	1947	87.60	12.26	0.58	231.84	162.23	179.37	634.34	8.86	246.09	283.98	235.86
La	bdl	0.14	0.04	0.03	bdl	3.36	bdl	bdl	7.19	3.00	1.16	1.09	bdl	bdl	0.11
Ce	bdl	0.29	0.05	0.10	0.15	5.21	bdl	bdl	6.51	3.11	0.89	1.77	bdl	bdl	0.11
Pr	bdl	0.04	bdl	0.02	bdl	0.46	bdl	bdl	1.98	0.88	0.04	0.39	bdl	bdl	0.03
Nd	bdl	0.14	bdl	bdl	bdl	1.32	bdl	bdl	9.40	4.33	0.07	1.73	bdl	bdl	0.09
Sm	bdl	bdl	bdl	bdl	bdl	0.22	bdl	bdl	2.25	1.13	bdl	1.12	bdl	bdl	bdl
Eu	bdl	0.07	0.05	0.06	0.17	0.68	bdl	0.03	0.38	0.21	0.54	0.17	0.04	0.04	0.05
Gd	bdl	0.13	bdl	0.08	1.57	0.23	bdl	bdl	3.52	1.88	bdl	9.57	bdl	bdl	bdl
Tb	bdl	0.02	bdl	bdl	1.21	0.03	bdl	bdl	0.62	0.35	bdl	6.13	bdl	bdl	bdl
Dy	bdl	0.13	bdl	bdl	21.07	0.17	bdl	bdl	4.28	2.42	bdl	86.06	bdl	bdl	0.07
Ho	bdl	0.03	bdl	bdl	8.90	0.03	bdl	bdl	0.93	0.53	bdl	24.93	bdl	bdl	bdl
Er	bdl	0.10	0.04	0.04	42.87	0.06	bdl	bdl	2.58	1.39	bdl	84.78	bdl	bdl	0.06
Tm	bdl	bdl	bdl	bdl	8.44	bdl	bdl	bdl	0.37	0.17	bdl	13.49	bdl	bdl	0.01
Yb	bdl	0.08	bdl	bdl	66.29	bdl	bdl	0.06	2.38	1.03	bdl	93.97	0.09	0.11	0.11
Lu	bdl	0.02	bdl	bdl	9.06	bdl	bdl	0.02	0.33	0.14	0.01	11.47	bdl	0.02	0.04
Hf	bdl	0.12	0.08	0.07	bdl	bdl	bdl	0.17	0.57	0.21	bdl	0.30	0.18	0.19	0.29
Ta	bdl	3.25	11.73	9.14	0.37	bdl	bdl	2.88	10.33	6.01	0.05	0.02	2.05	2.54	2.22
W	bdl	11.84	11.71	12.23	0.57	bdl	bdl	51.25	4.65	5.34	1.85	0.13	103.38	68.53	73.84
Pb208	bdl	3.91	3.55	3.58	0.27	19.65	bdl	1.54	3.56	2.08	70.87	1.46	3.22	2.21	2.73

bdl: below detection limit

0

Minerals trace elements. Representative analyses of rock forming minerals are given in Table 2 (Data are from Arnaud Villaros). Biotites from both starting materials are enriched in Li, with values ranging from 163 to 218 ppm in the paragneiss and between 58 and 209 ppm in the orthogneiss. A significant content of Nb is recorded though being quite variable. Nb ranges from 56-126 ppm in the paragneiss and from 86-227 ppm in the orthogneiss. Sn content in biotites from the paragneiss is quite homogeneous (~10-11 ppm). In the orthogneiss, biotites are enriched in Sn compared to the paragneiss but concentrations are quite variable (18-48 ppm). Ta content is variable, ranging from 3 to 11 ppm in the paragneiss and from 2 to 10 ppm in the orthogneiss. W is homogenous in the paragneiss biotites (~11 ppm) while being highly variable in orthogneiss biotites (4-51 ppm). Muscovites in the orthogneiss show lower Li (74-87 ppm), Ta (~2 ppm) and Nb (76-81 ppm) content than all biotites confounded, however, Sn (58-66 ppm) and W (68-103 ppm) are enriched. Regarding trace element analyses, biotites and muscovite are the main rare-metal bearing minerals. Thus, their behaviour during partial melting will be a significant controlling factor for rare-metal partitioning.

VI.3.2. Experimental methodology

For each rock, cores (10-15 mm length, 2.5 mm diameter; Fig. 1) were drilled perpendicularly to the cleavage and then kept in an oven before use. These were loaded without any additional volatile in Au capsules (15-25 mm length, 2.5 mm diameter), subsequently welded shut. Capsules for both the orthogneiss and the paragneiss were placed in the pressure vessel and ran together in the same experiment so that results are directly comparable.

Two experiments were performed at 800 and 850°C and for a constant pressure of 400 MPa. Each lasted for two weeks. They were performed in an internally heated pressure vessel operating vertically and pressurized with Ar-H_2 gas mixtures (Scaillet et al., 1995). The proportion of H_2 in the pressurizing mixture was adjusted to generate a moderately reducing redox environment in the experiments. Experimental fH_2 were measured from CoPd solid sensor capsules (Taylor et al., 1992) which were prepared and placed in the vessel together with the experimental capsules. At the end of the experiment, the composition of the CoPd alloy was determined and the sensor fO2 and the experimental

fH_2 determined (e.g., Scaillet et al., 1995). These experimental fH_2 generate fO_2 within experimental capsules of around FMQ - 0.5. During the experiments, total pressure was permanently recorded and is known to better than +/- 20 bar. Temperature was continuously measured by three thermocouples with an uncertainty of +/- 5°C. At the end of the experiment, the power to the furnace was switched off and temperature dropped by about 300°C during the first 5 mn. Simultaneously, Ar was pumped inside the vessel to keep pressure approximatively constant during quench. Capsules were checked for leaks by weighting and opened. Experimental charges were embedded in epoxy and polished.

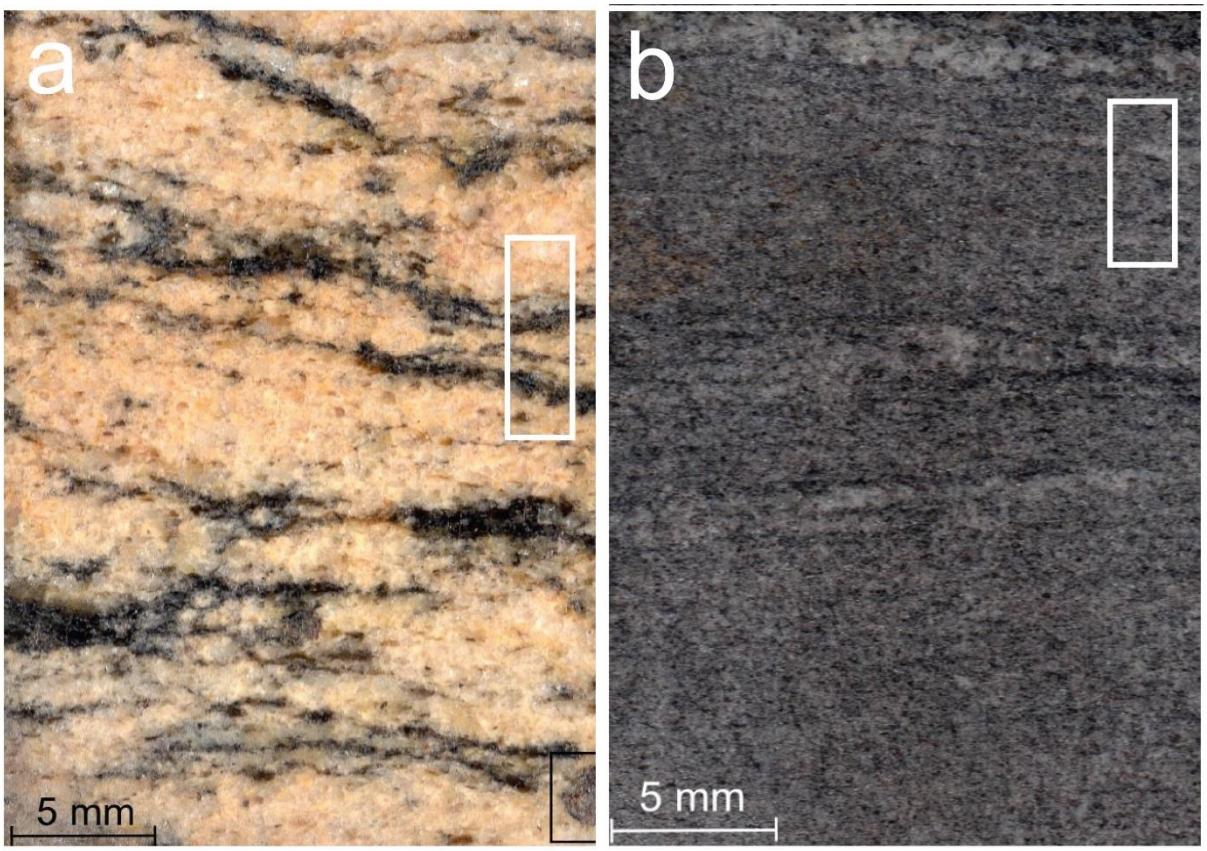

Fig. 1 *Texture of the starting materials. White rectangles represent the size of µmicores of the 800°C experiment. (a) orthogneiss and (b) paragneiss*

VI.3.4. Analytical techniques

SEM. Backscattered electron (BSE) images and EDS element maps were obtained at the Institut des Sciences de la Terre d'Orléans (ISTO, France) using a Merlin compact ZEISS Microscope equiped

with a Bruker EDS detector and working under an acceleration voltage of 15 kV. Panoramas of the whole experimental Charges were also performed to have an overall view of the results.

Calculation of degrees of melting. Degrees of melting were calculated from 2D image processing. High resolution panoramas of each experimental samples were used together with element distribution maps which served to locate the melt pools. Melt zones were manually outlined and black and white images produced. Pixel counting of the melt proportion was performed using the ImageJ software. The melting degree considers only melt; for melt-peritectic phases mixture zones, a melt average proportion has been calculated. Degree is calculated as a ratio of pixels (i.e., melt pixels over all pixels of the sample).

EPMA. Point analyses, traverses and element distribution maps for major and minor elements were obtained using a CAMECA SX Five microprobe operated under an acceleration voltage and a beam current of 15 kV and 6 nA respectively. Standards included albite (Si$K\alpha$ and Na$K\alpha$), synthetic $MnTiO_3$ (Mn$K\alpha$ and Ti$K\alpha$), Al_2O (Al$K\alpha$), Fe_2O_3 (Fe$K\alpha$), MgO (Mg$K\alpha$), andradite (Ca$K\alpha$), orthose (K$K\alpha$), apatite (P$K\alpha$) and topaz (F$K\alpha$). For glass analyses, mean values and standard deviations were calculated and are given in Table 4. For biotites, a secondary standard was used, and standard deviations were calculated on the 12 analyses. Standard deviations are as follow: 0.5wt% for SiO_2, 0.7wt% for TiO_2, 0.7wt% for Al_2O_3, 3.1wt% for FeO, 0.08wt% for MnO, 2.1wt% for MgO, 0.02wt% for CaO, 0.1wt% for Na_2O, 0.3 for K_2O and 0.06 for P_2O_5. Mean values and standard deviations were calculated on the 17 and 10 analyses of peritectic feldspars and spinel, respectively, of the Orthogneiss 800°C. Data are given in Table 7. Standard deviations are calculated on the 3 available analyses of peritectic orthopyroxene of the Paragneiss 850°C and are as follow: 1.3wt% for SiO_2, 0.7wt% for TiO_2, 0.8wt% for Al_2O_3, 0.4wt% for FeO, 0.1wt% for MnO, 0.2wt% for MgO, 0.01wt% for CaO, 0.05wt% for Na_2O, 0.09wt% for K_2O and 0.01wt% for P_2O_5. Standard deviations are calculated on the 2 available analyses of garnet overgrowths of the Paragneiss 850°C and are as follow: 1.2wt% for SiO_2, 0.06wt% for TiO_2, 0.2wt% for Al_2O_3, 1wt% for FeO, 0.08wt% for MnO, 0.3wt% for MgO, 0.09wt% for CaO, 0.02wt% for Na_2O, 0.01wt% for K_2O and 0.03wt% for P_2O_5.

LA-ICP-MS. Analyses of glass and glass-peritectic minerals mixture zones were performed at the IRAMAT-CEB Laboratory (Orléans). A RESOlution (S-155-E) ArF excimer laser (LA; λ=193 nm) coupled to a Thermo Finnigan Element XR (extended range, high-resolution) ICPMS was used. Ablation was performed at 5 Hz, at an energy of ~5 $J.cm^{-2}$. A beam diameter of 30µm was used for the residual minerals. Glass pockets were analysed with a spot size of both 15 and 50µm for comparison. Spot of 50µm were also performed on peritectic clusters to average the trace element composition. NIST610 was used as external standard, while BCR-2G and NIST612 were used as a control. Al_2O_3 was used as the internal standard. For all samples, Al_2O_3 (wt%) was determined by electron microprobe, while values for external standard and controls are those of Pearce et al. (1997) and the preferred values from GeoRem (http://georem.mpch-mainz.gwdg.de/), respectively. Primary standards were analyzed two times at the beginning and at the end of each run of ten analyses. 15 isotopes were measured, and raw data were processed off-line using Glitter software where time-resolved signals were examined one-by-one. Element concentrations were calculated for the initial ~30 s of all ablation signals relative to the gas blank (~20 s), with a linear interpolation across standard analyses. The 1 sigma error is given in parenthesis under each value for glass analyses (Table 5) and for glass-peritectic minerals mixture zone analyses (Table 9)

Micro X-ray fluorescence analysis. Analyses were performed on the DIFFABS beam line at SOLEIL synchrotron facility, Saclay. Both element distribution maps and element concentrations were obtained. Processing of the data is still in progress.

VI.4. RESULTS

VI.4.1. Texture and microtextures

Results of the 2D image processing show lower degrees of melting at 800 than at 850°C and lower ones for the paragneiss than the orthogneiss. At 800°C, the orthogneiss and paragneiss have degrees of melting of ~12.8 and ~8% while at 850°C they are of ~19.8 and ~17.8% respectively. Even if calculation are rough estimations (i.e., 2D calculation), it shows that melting is limited, especially at 800°C where percentages are lower than most previous studies.

Paragneiss. In the paragneiss samples (i.e., at 800 and 850°C), melt forms a continuous network at grains boundaries without preferential association with mineral layering (Fig. 2). At 800°C, the few scarce muscovites are broken down and replaced by peritectic phases (e.g., biotite, spinel, sillimanite ilmenite and mullite) underlining the initial habit of the mica (i.e., muscovite ghost; Fig. 3a). Newly formed biotites occur as euhedral rectangular crystals aligned along what was formerly the muscovite cleavages. Sillimanite, spinel, ilmenite and mullite form small micrometric crystals. Biotites (residual in Fig. 3) are only slightly affected by melting (Fig. 3a, b, c, d). Melt pools + peritectics (neoformed in Fig. 3) form along cleavages and along boundaries. Newly formed ilmenite occurs either within melt pools along cleavage and on boundaries as stocky micrometric needles. Spinel form micrometric euhedral crystals occurring preferentially in melt pools (Fig. 3d). Quartz and plagioclase crystals are rounded and generally surrounded by the melt (Fig. 3b, c, d). It must be noted that the formation of peritectic phases is mainly associated to biotite breakdown. At 850°C, the melting reaction is more advanced. Residual biotites appear more reacted, showing numerous melting gulfs, rounded boundaries and bigger melt pools along cleavage (Fig. 3f, g). Peritectic phases are numerous and of larger size. Spinel crystals are pluri-micrometers and orthopyroxene appear as euhedral thickset crystals of several microns to tens of microns (Fig. 3f, g, h). Orthopyroxenes seem to grow perpendicularly to the biotite boundaries. Residual garnets are rounded and show overgrowth with a different composition (i.e., darker

rims; Fig. 3h) with inclusions of ilmenite needles. K-feldspars overgrowths on residual plagioclases have also been highlighted (Fig. 3i).

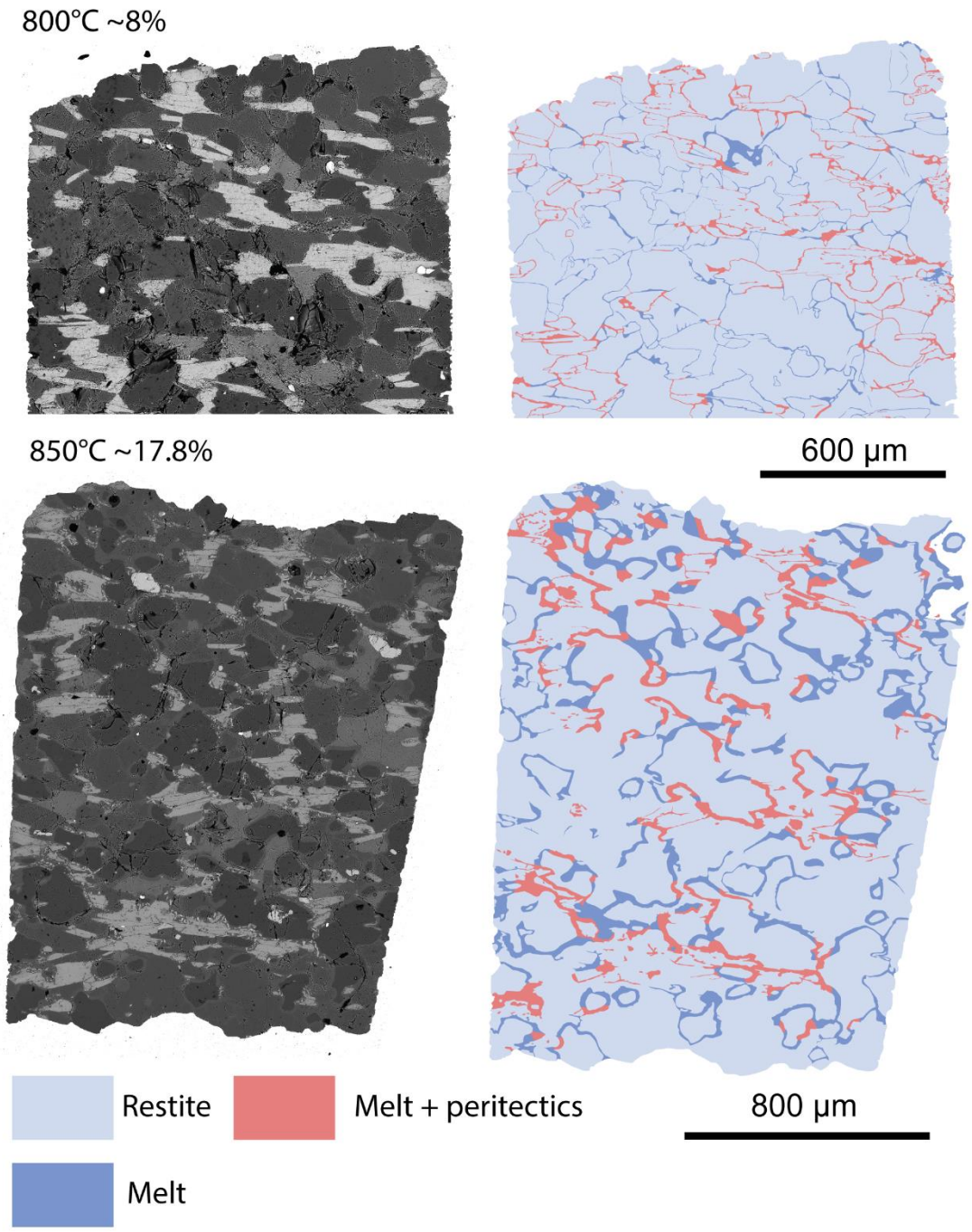

Fig. 2 *BSE panoramas of paragneiss experimental charges at 800 and 850°C and melt distribution. See text for details*

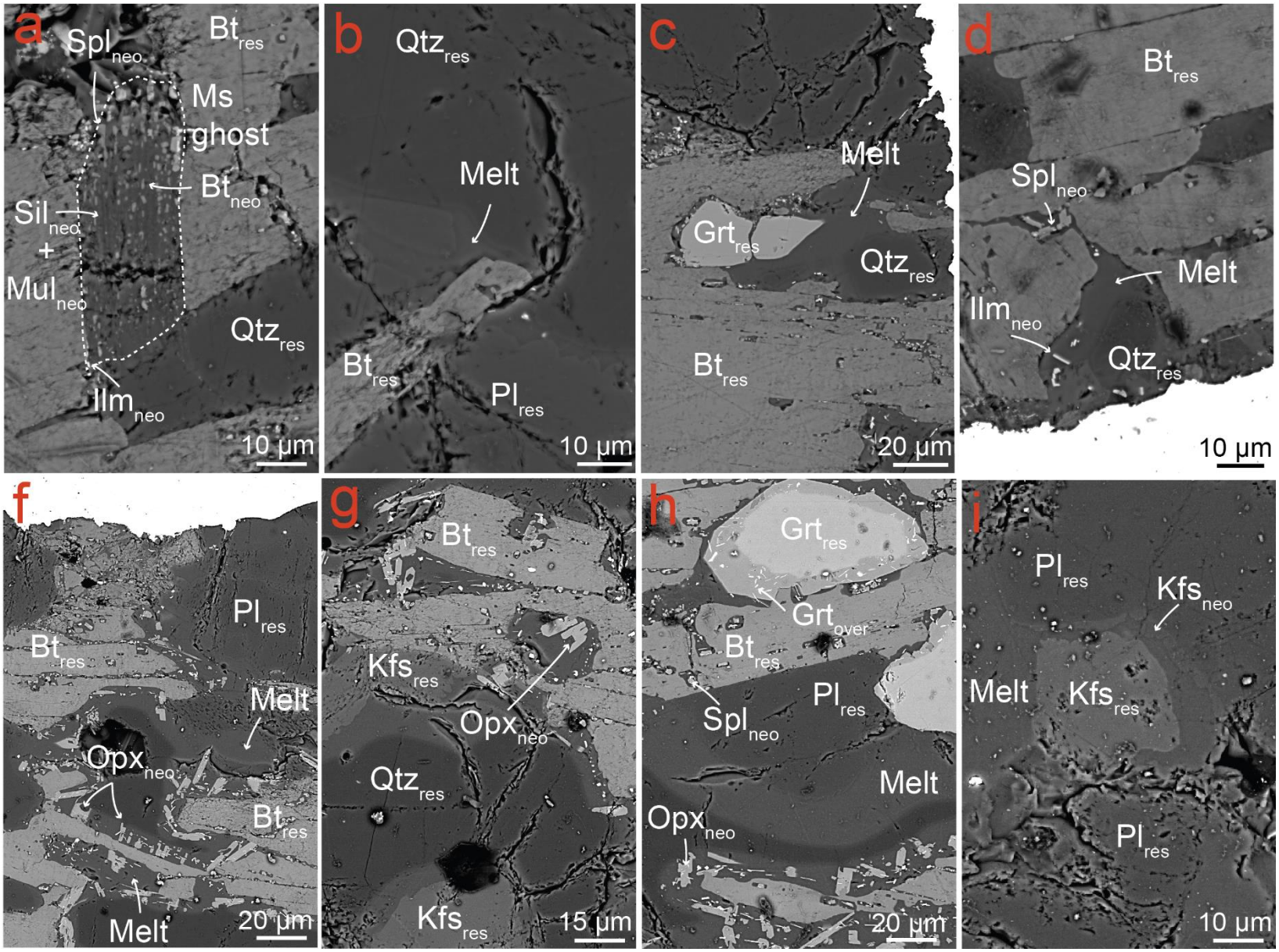
a
Spl neo
Bt res
Ms ghost
Bt neo
Sil neo + Mul neo
Qtz res
Ilm neo
10 µm
b
Qtz res
Melt
Bt res
Pl res
10 µm
c
Melt
Grt res
Qtz res
Bt res
20 µm
d
Bt res
Spl neo
Melt
Ilm neo
Qtz res
10 µm
f
Pl res
Bt res
Melt
Opx neo
Bt res
Melt
20 µm
g
Bt res
Kfs res
Opx neo
Qtz res
Kfs res
15 µm
h
Grt res
Grt over
Bt res
Pl res
Spl neo
Melt
Opx neo
20 µm
i
Pl res
Kfs neo
Melt
Kfs res
Pl res
10 µm

Fig 3 *BSE images illustrating texture and microtextures of the paragneiss experimental charges. (a) to (d) are from the 800°C experiment and (f)-(i) are from the 850°C. res: residual; neo: neoformed; over: overgrowth; Qtz: quartz; Bt: biotite; Pl: plagioclase; Kfs: potassic feldspar; Grt: garnet; Spl: spinel; Sil: sillimanite; Mul: mullite; Ilm: ilmenite; Opx: orthopyroxene. See text for description*

Orthogneiss. The melt distribution (Fig. 4) is similar between the orthogneiss melted at 850 and 800°C. Melt pools are heterogeneously distributed and occur preferentially associated with muscovite reaction zones, marking the initial cleavage and mineral layering. At 800°C (Fig. 5), the orthogneiss shows peritectic phases mainly associated with muscovite (Fig. 5a, b, c). Muscovites are entirely broken down while scarce residual biotites still occur. Peritectic phases replacing muscovites (i.e., muscovite ghosts, Fig.5a, c) include µm ilmenite needle and stocky crystals, euhedral to subhedral crystals of biotite and spinel, sillimanite needles and skeletal crystals of mullite (Fig. 5d). Newly formed spinels and biotites often occur as chaplets while sillimanite and mullite crystals are clustered (Fig. 5c). In some cases, a small amount of melt coexists with peritectic mullite needles and euhedral K-feldspars (Fig. 5d). In melt zones, occurring at quartz and K-feldspars or plagioclase grain boundaries, peritectic euhedral K-feldspars and sometimes plagioclases often overgrow on residual feldspars (Fig. 5e, f, g). Quartz always show rounded shapes (Fig. 5a) and in some rare cases, melt pockets occur isolated in quartz residual crystals. Residual biotites show typical melting habit with gulfs and melt pools + peritectic phases mostly occurring along crystals cleavages (Fig. 5a, h). Peritectic phases associated to biotite destabilization are mainly euhedral spinels and ilmenites cluster or isolated crystals (Fig. 5h). At 850°C, melting is more advanced. Biotite crystals are more affected, and orthopyroxene occur as a new peritectic phase related to biotite breakdown.

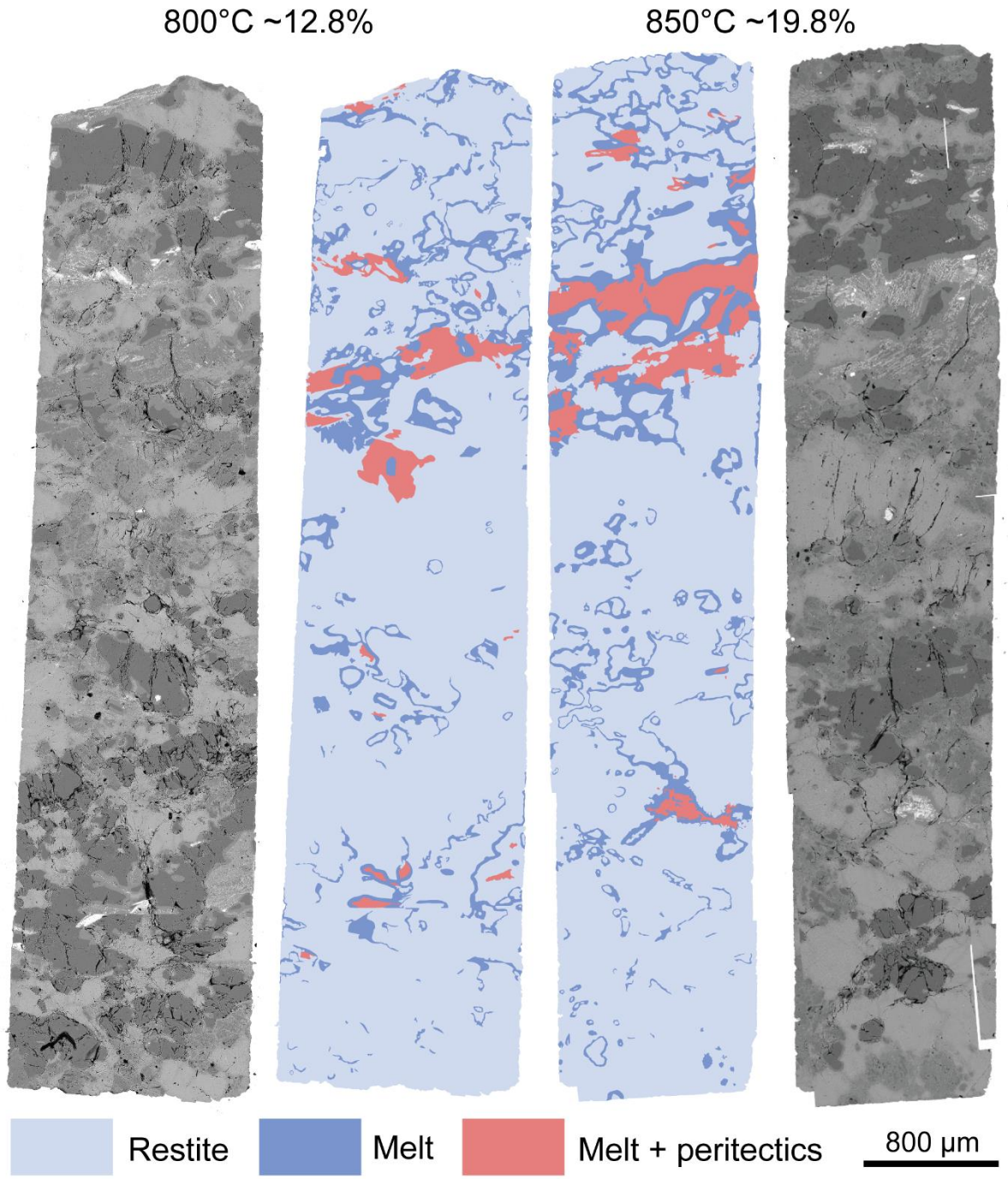

Fig 4 *BSE panoramas of orthogneiss experimental Charges at 800 and 850°C and melt distribution. See details in text*

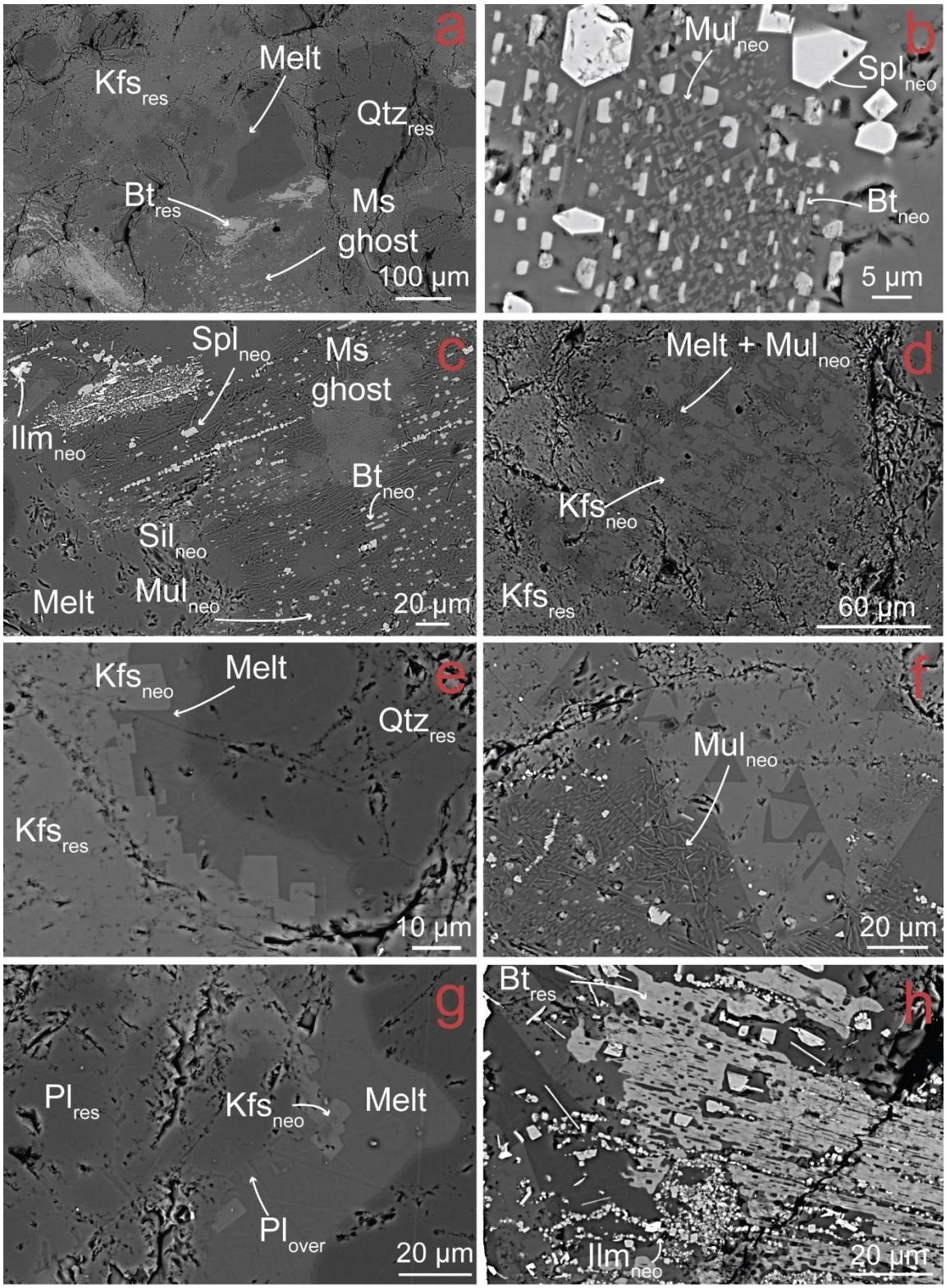

Fig 5 *BSE images of the orthogneiss experimental charge at 800°C illustrating melting texture and microtextures. res: residual; neo: neoformed; over: overgrowth; Qtz: quartz; Bt: biotite; Pl: plagioclase; Kfs: potassic feldspar; Grt: garnet; Spl: spinel; Sil: sillimanite; Mul: mullite; Ilm: ilmenite. See text for description*

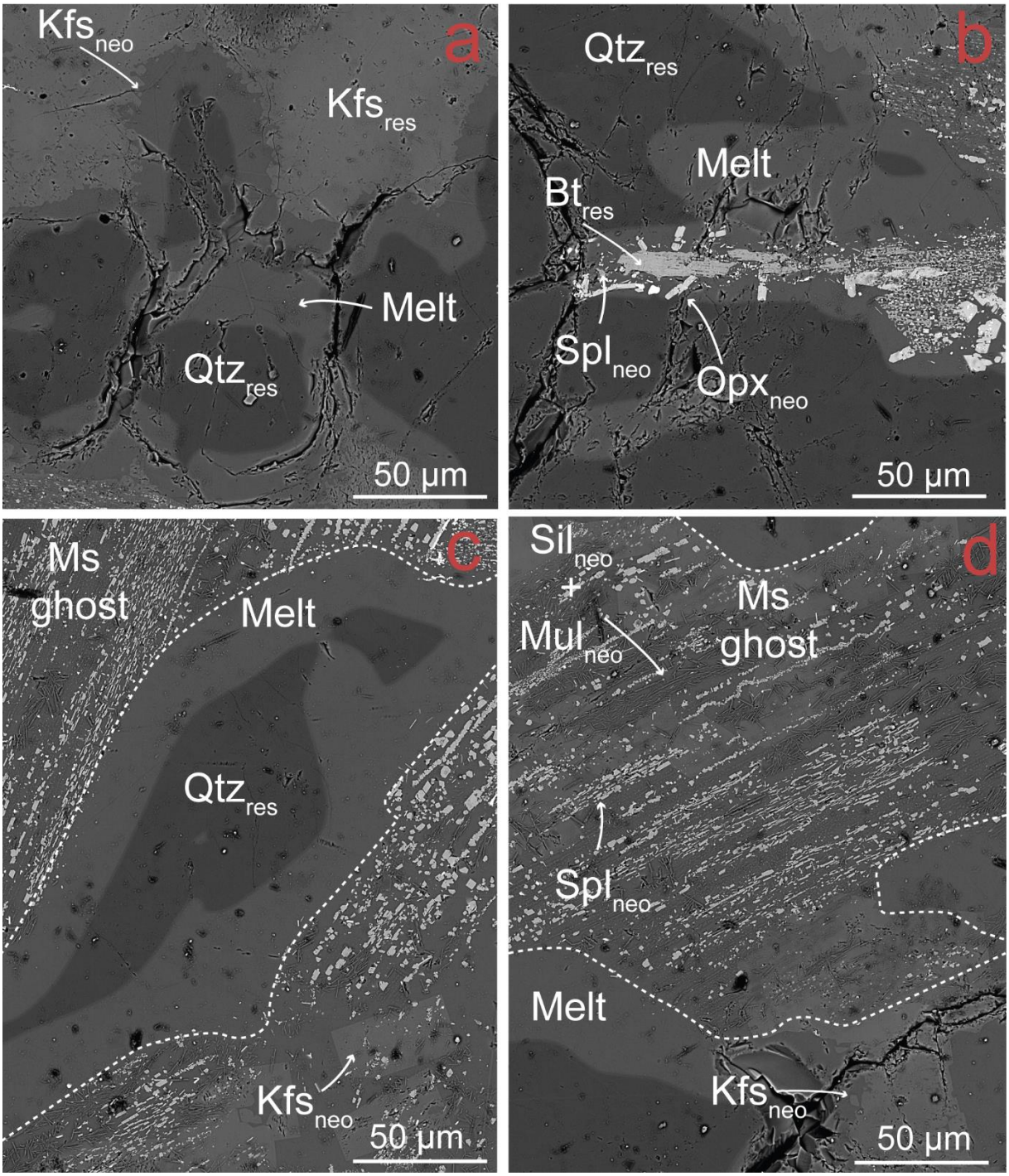

Fig 6 *BSE images of the orthogneiss experimental load at 850°C illustrating melting texture and microtextures. res: residual; neo: neoformed; over: overgrowth; Qtz: quartz; Bt: biotite; Pl: plagioclase; Kfs: potassic feldspar; Grt: garnet; Spl: spinel; Sil: sillimanite; Mul: mullite; Ilm: ilmenite; Opx: orthopyroxene. See text for description*

VI.4.2. Phase compositions

Glass. No significant variations are highlighted for glass major element compositions. For each experimental charge, the data are clustered and quite homogenous. Major element data normalized to 100% are given in Table 4 and illustrated in Fig. 7. Regarding the orthogneiss charges, average concentrations of Al_2O_3 (14.0 ± 0.3 wt%), Na_2O (2.88 ± 0.26 wt%) and A/CNK (1.18 ± 0.05) are slightly higher for the 800°C experiment than the 850°C (i.e., Al_2O_3: 13.8 ± 0.3 wt%; Na_2O: 2.79 ± 0.3 wt%; A/CNK: 1.15 ± 0.04). Conversely, K_2O (5.58 ± 0.23 wt%), FeOt (1.20 ± 0.29 wt%) and CaO (0.30 ± 0.08 wt%) are slightly lower at 800°C than at 850°C (i.e., K_2O: 5.70 ± 0.18 wt%; FeOt: 1.34 ± 0.36 wt%; CaO: 0.33 ± 0.04 wt%). However, most values are clustered and identical within the standard deviations. Similar trends are observed for the paragneiss charges between 800°C and 850°C. Some noticeable differences can be highlighted between the compositions of the paragneiss and orthogneiss melts. K_2O and Na_2O concentrations are slightly lower while FeO and P_2O_5 content are higher, up the almost 0.4 wt% on average at 800°C, in the paragneiss than in the orthogneiss charges. Melt from the paragneiss are more peraluminous with average A/CNK close to 1.3 at 800°C. Variations in the degree of melting do not correspond to systematic changes in the major element composition of the melts. Total of major element analyses are between 94 and 97% which means that a significant amount of dissolve H_2O might be present in the melt.

Table 4

Representative analyses of glass major elements normalized to 100

Major elements (wt%)	Paragneiss 800 °C		Mean (6)	σ	850°C		Mean (14)	σ
SiO_2	75.61	73.42	74.51	0.91	74.86	74.21	75.17	0.61
TiO_2	0.23	0.25	0.24	0.14	0.17	0.17	0.22	0.05
Al_2O_3	13.81	14.62	14.10	0.39	13.83	14.41	13.92	0.30
FeO	1.09	1.87	1.53	0.39	1.45	1.22	1.64	0.40
MnO	0.03	0.03	0.05	0.02	-	0.13	0.03	0.06
MgO	0.20	0.26	0.30	0.16	0.27	0.26	0.27	0.06
CaO	0.28	0.30	0.29	0.03	0.36	0.62	0.39	0.08
Na_2O	2.60	2.62	2.63	0.19	2.47	3.51	2.68	0.45
K_2O	5.17	5.02	5.15	0.09	5.27	5.13	5.34	0.17
P_2O_5	0.11	0.78	0.38	0.38	0.30	0.34	0.17	0.16
F	-	0.04	0.03	0.02	1.00	-	0.13	0.31
A/CNK	1.26	1.35	1.29	0.05	1.25	1.06	1.21	0.09
Fe + Mg +Ti	0.02	0.04	0.03	0.01	0.03	0.03	0.03	0.01

Major elements (wt%)	Orthogneiss 800°C		Mean (25)	σ	850°C		Mean (21)	σ
SiO_2	75.46	75.49	75.37	0.45	76.04	74.96	75.40	0.63
TiO_2	-	0.16	0.12	0.09	0.12	0.23	0.15	0.09
Al_2O_3	14.03	13.74	14.01	0.31	13.64	14.02	13.82	0.28
FeO	1.30	1.19	1.20	0.30	1.85	1.47	1.34	0.36
MnO	0.17	-	0.04	0.06	-	-	0.04	0.05
MgO	0.14	0.14	0.14	0.04	0.13	0.15	0.14	0.03
CaO	0.21	0.32	0.30	0.08	0.34	0.38	0.33	0.04
Na_2O	2.71	3.11	2.88	0.26	2.34	3.04	2.79	0.30
K_2O	5.70	5.79	5.58	0.23	5.53	5.59	5.70	0.18
P_2O_5	-	0.05	0.04	0.05	-	0.05	0.06	0.09
F	0.26	-	0.28	0.32	-	-	0.18	0.28
A/CNK	1.23	1.09	1.18	0.05	1.23	1.13	1.15	0.04
Fe + Mg +Ti	0.02	0.02	0.02	-	0.03	0.03	0.02	0.01

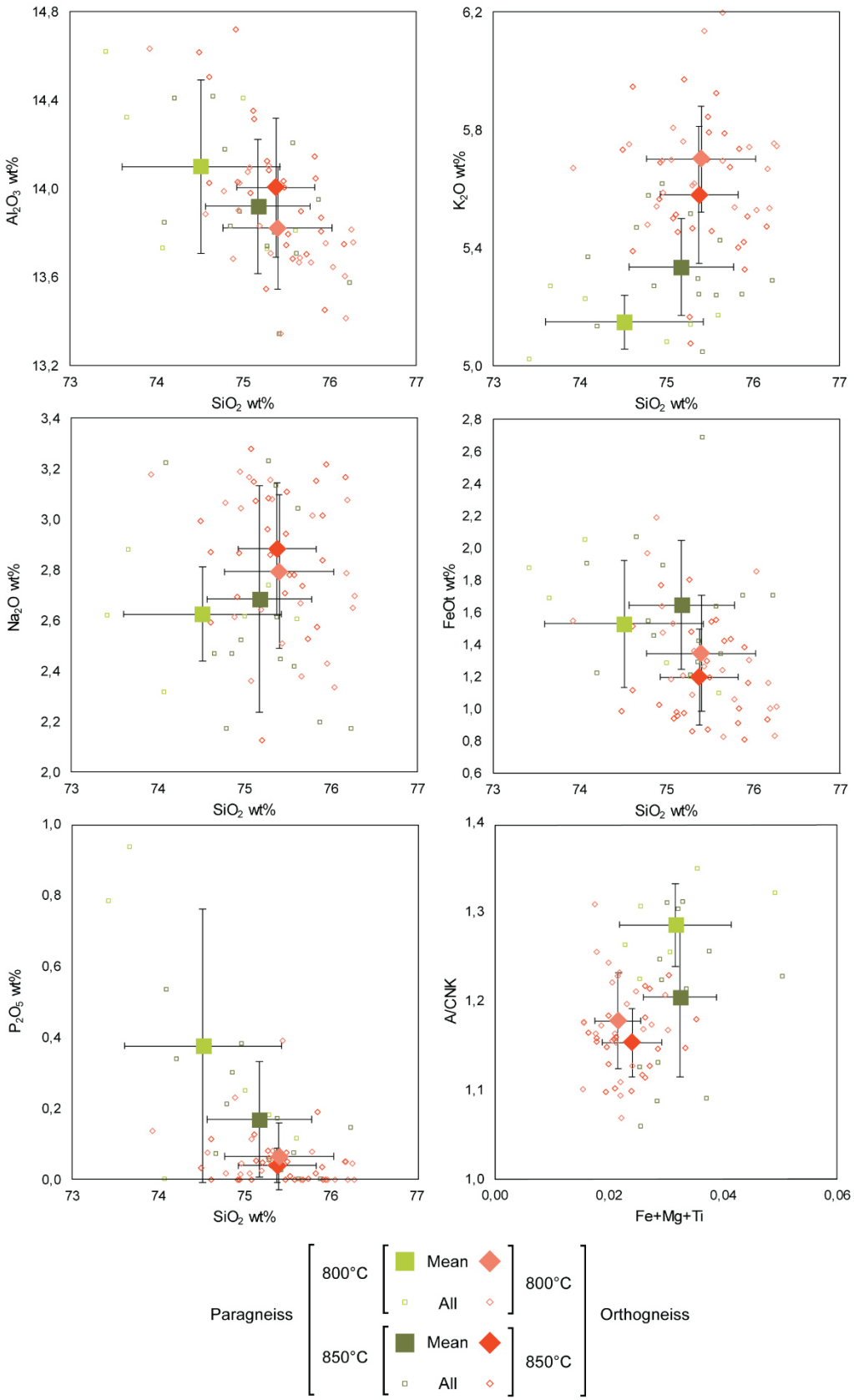

Fig 7 *Major element composition of glass for experiments at 800 and 850°C for the two starting materials. See text for comment*

Table 5

Representative trace element analyses of glass

	Paragneiss		Orthogneiss															
	850°C		800°C									850°C						
Spot size	15	15	15	15	15	15	15	15	15	15	15	50	15	15	15	15	15	15
Trace elements (ppm)																		
Li	197.6 (17.9)	167.7 (17.4)	103.8 (17)	74.01 (13.1)	76.99 (9.1)	53.75 (6.9)	80.31 (10.3)	61.97 (8.8)	103.9 (14.9)	65.87 (10.4)	67.95 (11.0)	57.49 (1.9)	72.37 (6.8)	119.4 (10.2)	85.5 (8.0)	95.66 (10.9)	97.92 (9.0)	98.97 (8.9)
Be	2.37 (0.8)	bdl	2.94 (0.9)	3.71 (1.1)	bdl	3.32 (0.7)	3.14 (0.8)	3.94 (0.9)	2.67 (0.7)	2 (0.8)	bdl	2.75 (0.2)	2.47 (0.8)	3.73 (0.8)	3.23 (0.8)	4.3 (1.0)	bdl	3.12 (0.7)
B	8.46 (2.4)	11.11 (2.6)	9.44 (2.9)	13.39 (3.9)	19.98 (2.5)	bdl	bdl	7.31 (2.4)	11.26 (2.2)	bdl	bdl	8.72 (0.4)	12.84 (2.7)	13.07 (2.6)	bdl	11.49 (3.0)	7.9 (2.6)	9.42 (2.3)
Rb	273.1 (23.6)	250.5 (24.5)	472.1 (90.7)	471.9 (94.1)	358.8 (19.6)	370.4 (20.6)	485.0 (28.3)	455.9 (27.3)	414.1 (27.7)	349.2 (24.2)	393.4 (28.0)	430.0 (15.1)	428.9 (25.9)	444.7 (28.2)	431.9 (28.2)	459.3 (36.3)	464.0 (36.4)	400.1 (31.9)
Nb	9.05 (1.0)	12.29 (1.4)	224.9 (46.6)	51.81 (11.2)	46.13 (2.7)	12.37 (0.8)	28.43 (1.9)	30.07 (2.0)	36.68 (2.6)	46.15 (3.3)	28.06 (2.2)	44.62 (1.7)	27.09 (2.1)	39.75 (3.1)	24.87 (2.0)	37.3 (3.6)	39.22 (3.4)	36.09 (3.2)
Sn	bdl	bdl	bdl	3.06 (1.2)	9.33 (1.2)	5.55 (1.0)	4.27 (1.2)	6.26 (1.2)	5.99 (1.0)	3.84 (1.0)	2.98 (1.0)	7.79 (0.4)	11.31 (1.5)	9.23 (1.4)	8.79 (1.3)	15.15 (2.0)	5.96 (1.2)	3.93 (1.0)
Cs	21.02 (2.2)	16.4 (2.1)	15.49 (3.4)	19.14 (4.2)	6.37 (1.4)	6.54 (1.3)	8.49 (1.6)	6.67 (1.6)	8.06 (1.4)	7.65 (1.5)	5.2 (1.4)	10.41 (0.4)	18.56 (2.0)	17.45 (1.9)	13.25 (1.8)	11.91 (2.0)	15.43 (1.9)	13.35 (1.6)
Ta	0.53 (0.1)	1.22 (0.2)	16.22 (.5)	3.89 (0.9)	1.59 (0.2)	0.313 (0.08)	1.21 (0.2)	0.6 (0.1)	0.439 (0.1)	1.84 (0.2)	0.43 (0.1)	1.89 (0.1)	0.8 (0.1)	1.45 (0.2)	0.55 (0.1)	1.21 (0.2)	1.62 (0.2)	1.68 (0.2)
W	6.08 (0.8)	6.61 (0.8)	43.14 (8.2)	45.3 (8.9)	52.56 (2.6)	9.72 (0.8)	23.35 (1.6)	33.46 (2.0)	38.88 (2.1)	51.67 (2.6)	29.91 (1.9)	34.83 (1.4)	27.79 (3.2))	34.18 (4.0)	18.26 (2.3)	33.7 (4.9)	37.94 (2.6)	30.63 (2.1)
U	0.392 (0.1)	0.4 (0.08)	4.22 (0.8)	4.29 (0.9)	0.542 (0.09)	2.5 (0.2)	2.35 (0.2)	1.21 (0.2)	1.32 (0.2)	1.12 (0.1)	1.29 (02)	18.43 (0.8)	4.32 (0.6)	7.16 (1.0)	5.4 (0.8)	6.43 (1.1)	18.77 (1.1)	13.51 (0.8)
^{64}Zn	31.8 (4.7)	19.59 (4.1)	99.6 (22.3)	146.8 (33.9)	56.11 (5.5)	11.83 (3.3)	21.14 (4.2)	10.15 (4.0)	8.55 (3.4)	19.93 (3.8)	10.23 (3.3)	138.5 (8.5)	13.64 (3.9)	22.94 (3.9)	13.4 (3.7)	9.74 (4.2)	26.92 (4.6)	16.76 (3.7)

^{66}Zn	NA	NA	30.63 (7.2)	152.3 (29.0)	38.96 (6.0)	13.42 (4.1)	bdl	11.82 (5.0)	15.82 (4.5)	bdl	bdl	131.0 (5.9)	bdl	bdl	bdl	bdl	28.36 (6.2)	bdl
^{138}Ba	761.1 (52.5)	633.2 (48.6)	17.12 (3.4)	18.95 (3.9)	35.89 (2.6)	14.65 (1.3)	15.66 (1.5)	17.05 (1.6)	21.18 (2.0)	26.47 (2.5)	14.43 (42.6)	60.39 (2.5)	41.3 (4.7)	46.06 (5.5)	74.09 (9.1)	75.11 (11.2)	64.94 (4.3)	55.69 (3.8)
^{137}Ba	NA	NA	19.08 (4.6)	14.12 (3.9)	39.66 (2.4)	10.26 (2.3)	21.97 (3.0)	18.45 (2.8)	16.75 (2.5)	30.49 (3.3)	16.25 (2.6)	59.63 (2.3)	42.38 (4.9)	40.11 (4.7)	71.88 (8.1)	68.86 (9.2)	70.49 (7.0)	58.67 (5.9)
Sr	39.4 (3.9)	31.81 (3.6)	4.09 (1.1)	2.3 (1.1)	4.95 (0.8)	3.16 (0.8)	5.49 (1.1)	2.52 (1.0)	3.2 (0.9)	2.36 (0.9)	4.18 (0.9)	5.74 (0.3)	5.54 (0.9)	7.97 (0.9)	7.85 (1.0)	8.02 (1.2)	6.88 (1.1)	5.84 (1.0)
Nb/Ta	17.1	10.1	13.9	13.3	29.0	39.5	23.5	50.1	83.5	25.01	65.2	23.6	33.9	27.4	45.2	30.8	24.2	21.5

bdl: below detection limit; NA: not analyzed

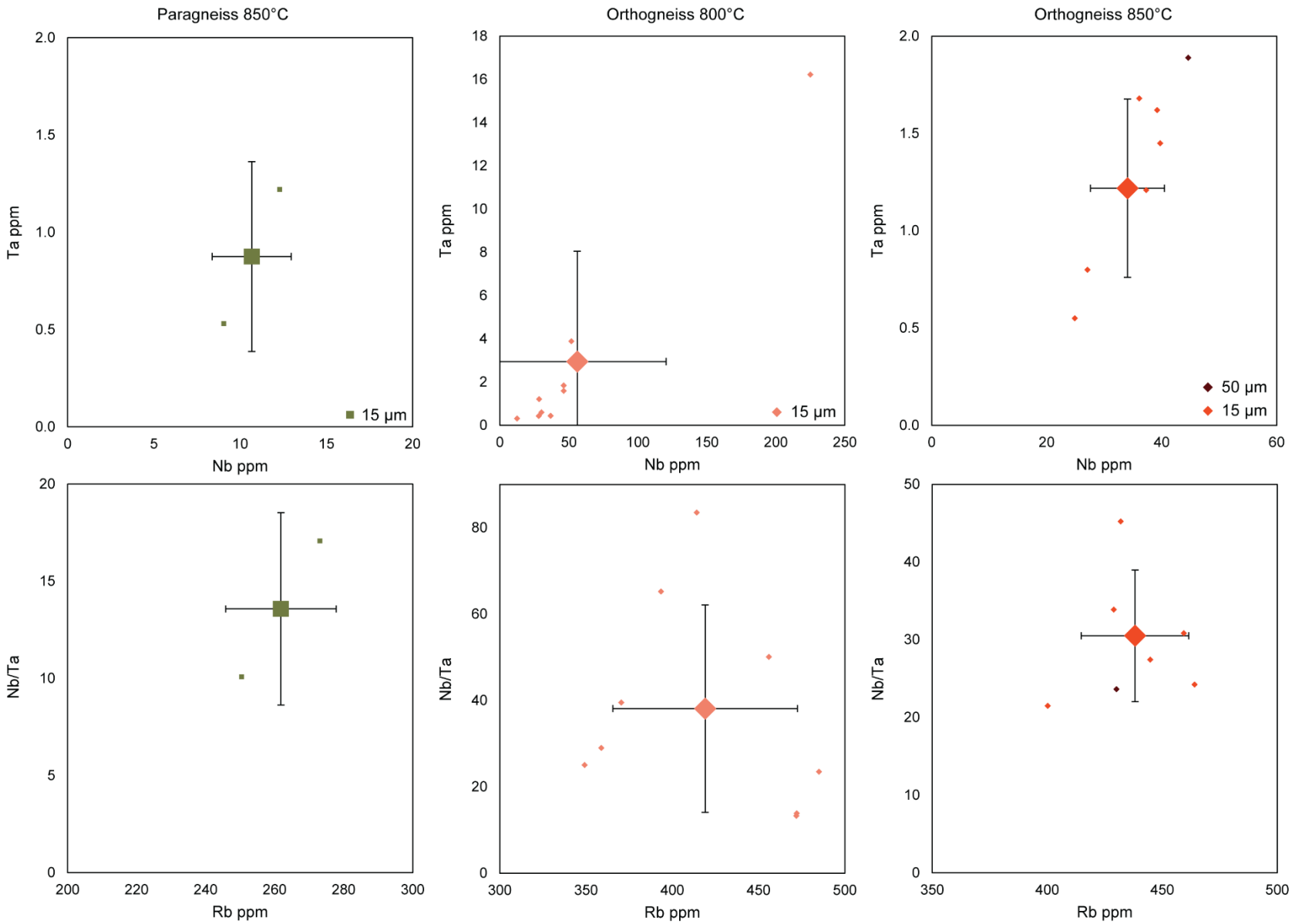
Paragneiss 850°C
Orthogneiss 800°C
Orthogneiss 850°C
Ta ppm
Nb ppm
Nb/Ta
Rb ppm
15 µm
50 µm

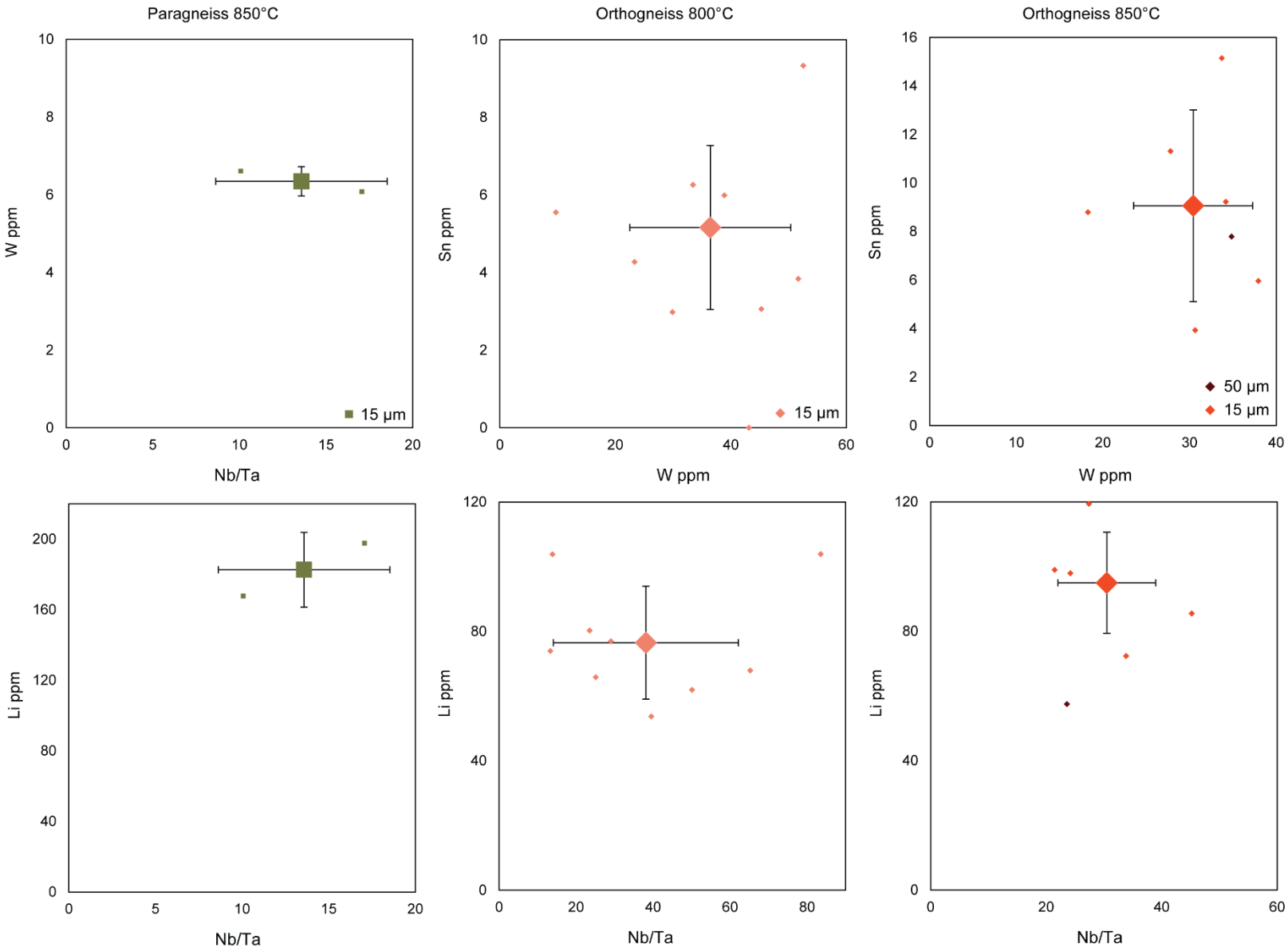
Paragneiss 850°C
Orthogneiss 800°C
Orthogneiss 850°C
W ppm
Sn ppm
Sn ppm
Nb/Ta
W ppm
W ppm
15 µm
15 µm
50 µm
15 µm
Li ppm
Li ppm
Li ppm
Nb/Ta
Nb/Ta
Nb/Ta

Fig 8 *Ta, Nb, Nb/Ta and Rb concentrations in glass from the paragneiss charge at 850 and from the orthogneiss charges at 800 and 850°C. See text below for description*

Fig 9 *W, Sn and Li concentrations in glass from the paragneiss charge at 850 and from the orthogneiss charges at 800 and 850°C. See below for description*

In contrast, there are important variations in trace element contents. Trace element compositions are given in Table 5 and shown in Fig. 8 and 9. In most cases, a spot size of 15µm was used because of the small size of melt pockets. One analysis (orthogneiss at 850°C) was performed with a spot size of 50 µm for comparison. No data for the paragneiss charge at 800°C are available as the melt zones were too small to be analyzed. The Ta content (Fig. 8) ranges from 0.53 to 1.22 ppm in the paragneiss glass, between 0.3 and 3.9 ppm in the orthogneiss glass at 800°C and between 0.55 and 1.9 ppm in the orthogneiss glass at 850°C. Nb ranges from 9 to 12.3 ppm in the paragneiss glass, from 12 to 51.8 ppm in the orthogneiss glass at 800°C (with one outlier at 225 ppm) and between 24.9 and 44.6 ppm in the orthogneiss glass at 850°C. In the paragneiss glass, Ta is doubled as Nb less than double; in the orthogneiss glass at 800°C, Ta double when Nb increase by almost 50 and in the 850°C orthogneiss glass the correlation is about 1:1. The Nb/Ta ratio in the paragneiss glass varies from 10.1 to 17.1; it ranges from 13.3 to 83.6 in the 800°C orthogneisss glass and from 21.5 to 45.2 in the 850°C orthogneiss. Rb contents range from 250.5 to 273.1 ppm, 350 to 585 ppm and from 400 to 464 ppm in the paragneiss and 800°C and 850°C orthogneisses, respectively. Sn content in the paragneiss glass is under detection limit and, it varies from below detection limit to 9 ppm at 800°C and from 3.9 to 15.1 ppm at 850°C. W and Li contents vary respectively from 6.1 to 6.6 and 167.6 to 197.6 ppm (paragneiss glass), from 23 to 53 and 53 to 103 ppm (orthogneiss glass, 800°C) and from 18 to 38 and 57 to 119 ppm (orthogneiss glass, 850°C).

Peritectic phases.

Major element analyses of peritetic phases of the paragneiss and the orthogneiss are given in Tables 6-8. Note that the number of analyses is not comprehensive, data acquisition is still in progress.

Table 6
Major element analyses of peritectic and reequilibrated granet

	Paragneiss 800°C	850°C			
wt%	Spinel	Opx		Garnet overgrowths	
SiO_2	2.47	46.07	45.87	36.21	37.97
TiO_2	1.80	1.53	3.08	0.38	0.47
Al_2O_3	54.59	6.41	6.53	21.59	21.83
FeO	33.67	32.43	29.99	33.19	31.70
MnO	0.13	0.25	0.26	0.40	0.52
MgO	4.97	14.11	12.99	7.91	8.37
CaO	0.10	0.09	0.16	0.77	0.90
Na_2O	0.22	0.02	0.20	0.04	-
K_2O	0.36	0.05	0.49	0.04	0.06
P_2O_5	0.18	0.01	0.08	0.24	0.70
Total	98.53	100.96	100.08	101.28	102.54

Table 7
Major element analyses of peritectic phases in the Orthogneiss at 800°C

wt%	Feldspars		Mean (17)	σ	Biotite	Spinel	Mean (10)	σ	Ilmenite
SiO_2	66.55	64.86	65.36	0.46	41.73	0.13	1.45	2.86	0.14
TiO_2	0.02	-	0.01	0.02	5.15	0.61	0.36	0.17	51.24
Al_2O_3	17.21	19.15	18.60	0.49	19.02	55.50	55.86	2.76	0.24
FeO	0.23	0.22	0.17	0.10	17.34	40.71	38.05	2.24	43.02
MnO	-	0.01	0.03	0.04	0.15	0.16	0.16	0.10	0.17
MgO	0.01	-	0.01	0.02	7.73	2.41	3.15	1.08	1.51
CaO	0.30	0.85	0.43	0.26	-	0.07	0.02	0.03	0.02
Na_2O	2.44	3.96	3.28	0.37	0.80	0.06	0.08	0.15	-
K_2O	10.59	9.68	11.24	0.84	8.75	0.06	0.12	0.18	0.10
P_2O_5	-	-	0.02	0.03	0.04	-	0.02	0.04	0.12
Total	97.35	98.73	99.32	0.84	100.88	99.70	99.50	0.67	98.11
An	2.75	6.20	3.24	1.86					
Ab	40.00	51.99	45.33	3.21					
Or	57.25	41.80	51.43	4.87					

Table 8
Major element analyses of peritectic phases of the Orthogneiss at 850°C

wt%	Feldspars		Opx		Ilmenite		Spinel			
SiO_2	64.07	64.05	43.23	44.67	0.04	0.04	0.38	0.18	0.10	1.11
TiO_2	-	-	0.21	0.29	51.49	51.90	0.27	0.34	0.37	0.36
Al_2O_3	19.20	19.15	4.76	4.08	0.30	0.24	59.13	59.20	56.31	58.77
FeO	0.23	0.27	39.17	44.74	46.28	43.68	34.34	34.64	35.74	32.49
MnO	0.09	0.03	0.50	0.26	0.41	0.25	0.17	0.09	0.19	-
MgO	0.04	0.02	6.94	5.82	1.32	1.30	5.24	5.47	3.55	6.34
CaO	0.42	0.64	0.26	0.19	0.01	-	0.04	-	0.02	0.01
Na_2O	3.31	3.54	0.47	0.11	0.01	-	0.01	-	0.06	0.05
K_2O	11.51	11.13	0.15	0.04	0.10	0.05	0.08	0.08	0.07	0.12
P_2O_5	0.10	0.20	-	-	-	0.01	0.03	-	-	-
Total	99.02	99.18	95.77	100.22	100.01	99.25	99.69	100.09	101.09	99.44
An	3.21	4.74								
Ab	45.19	46.81								
Or	51.60	48.44								

The bulk trace element contents of the melt-peritectic phases mixture zones in the orthogneiss charges at both 800 and 850°C were determined using a spot size of 50 µm since the size of the peritectic phases was too small for individual analysis. The data are given in Table 9 and shown on Fig. 10.

Table 9
Bulk trace element composition of peritectic mix from muscovite breakdown

	Orthogneiss							
	800 °C					850°C		
Spot size	50	50	50	50	50	50	50	50
Trace elements (ppm)								
Li	35.11 (1.3)	64.31 (2.3)	64.54 (2.3)	62.19 (2.3)	66.58 (2.5)	66.38 (2.3)	59.75 (2.1)	52.13 (1.8)
Be	1.85 (0.2)	3.73 (0.3)	3.59 (0.3)	4.36 (0.3)	5.3 (0.4)	3.06 (0.2)	2.3 (0.2)	3.14 (0.2)
B	8.77 (0.6)	11.17 (0.6)	11.27 (0.7)	12.04 (0.6)	12.04 (0.7)	10.97 (0.7)	8.96 (0.6)	7.23 (0.5)
Rb	428.8 (15.3)	441.3 (16.1)	380.8 (14.1)	401.5 (15.0)	391.3 (15.0)	424.4 (14.6)	411.2 (14.3)	445.0 (15.7)
Nb	56.04 (2.2)	68.62 (2.7)	87.78 (3.6)	82.3 (3.4)	50.52 (2.2)	113.8 (4.2)	47.92 (1.8)	146.63 (5.6)
Sn	2.03 (0.2)	2.33 (0.2)	12.36 (0.7)	11.33 (0.6)	9.77 (0.6)	18.75 (0.9)	9.28 (0.5)	6.35 (0.4)
Cs	5.33 (0.3)	13.24 (0.6)	6.25 (0.4)	5.96 (0.3)	6.14 (0.4)	10.98 (0.5)	10.91 (0.5)	9.86 (0.5)
Ta	3.15 (0.2)	4.66 (0.2)	2.25 (0.1)	2.25 (0.1)	1.79 (0.1)	2.97 (0.2)	2.41 (0.1)	7.18 (0.4)

W	31.42 (1.4)	49.84 (2.2)	84.88 (3.7)	64.55 (2.9)	32.89 (1.6)	66.41 (2.7)	37.87 (1.6)	58.47 (2.4)
U	3.16 (0.2)	4.32 (0.2)	0.837 (0.06)	1.339 (0.08)	2.15 (0.1)	9.8 (0.4)	25.05 (1.1)	104.5 (4.6)
^{64}Zn	293.0 (18.9)	385.3 (26.2)	39.74 (2.9)	78.62 (5.7)	62.51 (4.8)	166.2 (9.7)	470.6 (28.3)	593.89 (32.3)
^{66}Zn	288.6 (13.4)	402 (19.2)	21.41 (1.4)	54.74 (2.9)	45.15 (2.6)	124.73 (5.6)	462.8 (20.4)	545.0 (24.7)
^{138}Ba	442.0 (19.0)	47.92 (2.2)	180.8 (8.2)	116.7 (5.4)	86.97 (4.2)	63.63 (2.6)	79.91 (3.3)	73.97 (3.1)
^{137}Ba	445.3 (16.6)	48.6 (2.0)	181.3 (7.2)	120.5 (4.9)	85.9 (3.6)	62.99 (2.5)	80.59 (3.1)	71.41 (2.8)
Sr	37.62 (1.7)	3.4 (0.2)	10.57 (0.5)	2.77 (0.2)	3.5 (0.2)	6.39 (0.3)	6.15 (0.3)	7.42 (0.3)
Nb/Ta	17.8	14.7	39.0	36.6	28.2	38.3	19.9	20.4

Nb and Ta contents of peritectic phases mostly decrease with decreasing temperature and degree of melting. The Ta content ranges from 1.8 to 4.7 ppm in the 800°C charge, from 2.4 and 7.2 ppm in the 850°C charge. Nb ranges from 50.5 to 87.8 ppm and from 47.9 to 146.6 ppm at 800 and 850°C, respectively. Nb/Ta ratios are between 17.8 and 39 but mean values are similar (i.e., ~ 26.5) for both temperatures. Rb and Li contents are also similar, ranging from 380.8 to 441.3 ppm and 411.2 and 445 ppm for Rb, and from ~ 63 (with an extreme value at 35.11 ppm) and 52 to 66 ppm at 800 and 850°C, respectively. Sn varies from 2 to 11.3 ppm at 800°C and from 6.3 to 18.7 ppm at 850°C. Finally, W ranges from 31.4 to 84.8 ppm at 800°C and from 37.9 to 66.4 ppm at 850°C.

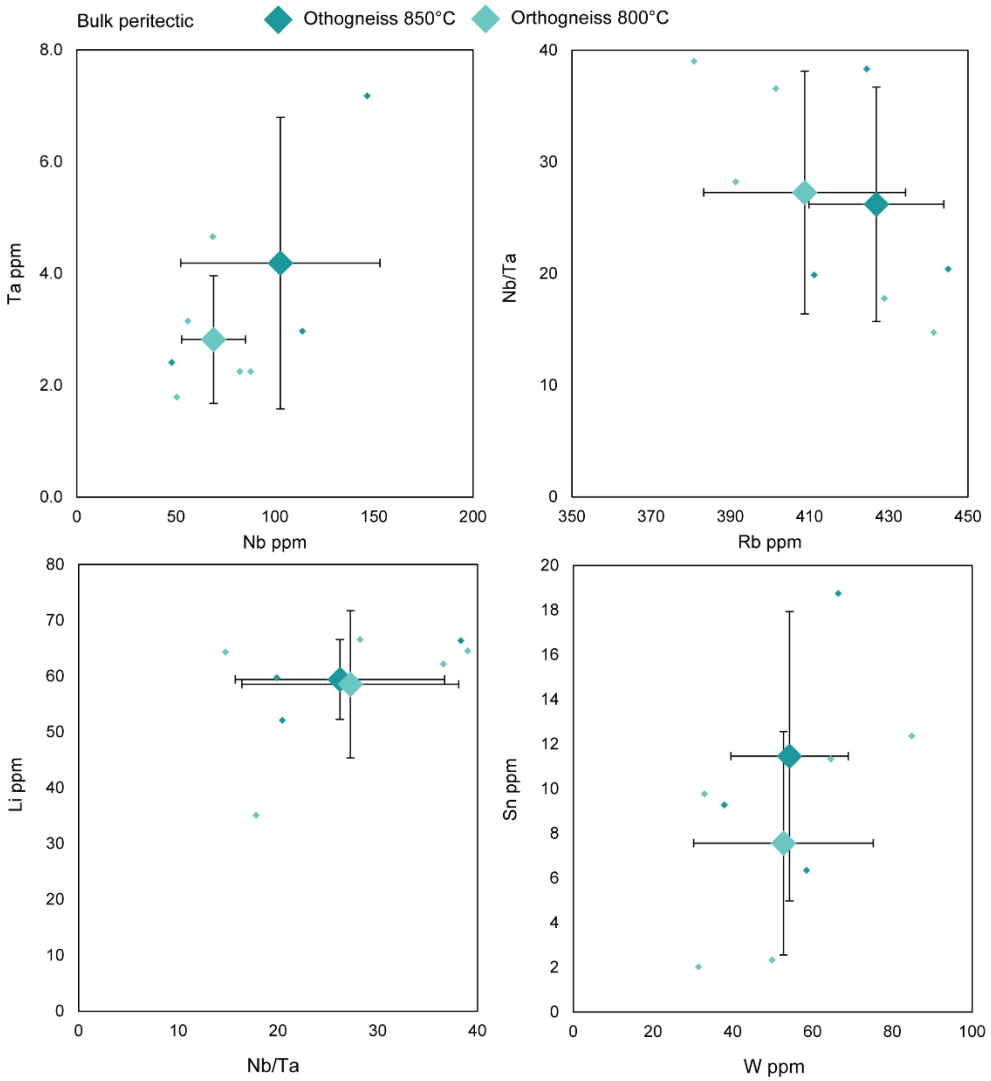

Fig 10 *Trace element compositions of melt-peritectic phases mixture zones replacing muscovite in the orthogneiss 800 and 850°C experiments. Analyses were performed with a beam size of 50 µm to average the concentrations. See text for details*

VI.5. DISCUSSION

In the following discussion, the term "residual" will be used for mineral phases that persist in reaction products and are assumed to correspond to phases essentially stable under the experimental conditions. Residual phases include congruently (e.g., quartz) and incongruently (e.g., biotite) melting minerals and they can reequilibrate chemically during the experiment (e.g., garnet). The term "restite" will be reserved for newly formed peritectic phases appearing as breakdown products of incongruently melting minerals (e.g., muscovite, biotite). "Melt" or "glass" will refer to a phase made of 100% silicate liquid, the peritectic phases being excluded.

VI.5.1. Melting mechanisms

Melt distribution, melting texture and microtextures differ strongly between the paragneiss and the orthogneiss charges suggesting distinct melting mechanisms. In the *paragneiss*, melt is homogeneously distributed at grain boundaries and forms a continuous network without preferential association with any mineral. However, limited crystallization of peritectic phases (i.e., restite) takes place and is mostly related to the destabilization of a few scarce muscovites and to the onset of biotite destabilization. At 800°C, the paragneiss is only slightly reacted since the degree of partial melting is low (i.e., ~8%). The scarce muscovites are the only phases being totally broken down and replaced by the *in-situ* crystallization of sillimanite, spinel, ilmenite biotite and K-feldspar peritectic phases. This means that the muscovite dehydration-melting reaction (Spear, 1995) was overstepped at 800°C. On the other hand, biotite is only slightly affected, showing rounded edges and melt pools formed along cleavages. Limited destabilization of biotite results in the crystallization of mainly euhedral hercynitic spinel in pools (e.g., Brearley, 1987b, Table 6) and of ilmenite in the surrounding melt along residual mineral boundaries. Thus, biotite breakdown is only incipient at 800°C and so the biotite dehydration-melting reaction (Spear, 1995) is not overstepped. As muscovite occurs as small and scarce isolated crystals in the starting material, muscovite dehydration-melting cannot be the main melting mechanism. Furthermore, this would not explain the observed melt distribution. The other hydrous phase, biotite, is only slightly reacted and,

so, the contribution of biotite to melt production is limited. Under fluid absent melting conditions, a quartz-K-feldspar-plagioclase assemblage would melt at approximately 980°C at 400 MPa (Luth, 1969; see also Brearley and Rubie, 1990). However, all quartz and feldspars exhibit melting textures in the 800°C experiment. Therefore, a source of water other than micas appears necessary. Given the melt distribution, one likely possibility is that interstitial water present at grain boundaries promotes melting of the paragneiss at 800°C. If interstitial water is the main control on the melting mechanism, the amount available at grain boundaries will limit the extent of the reaction. All the available water will partition into the melt and further melting will be inhibited, consistent with the very low degree of melting at 800°C (~8%). The reaction describing the melting of the paragneiss at 800°C can be written as follows:

$$Bt + Qtz + Pl + Kfs + Grt + Ky \pm Ms + \text{interstitial } H_2O \longrightarrow \text{melt} + Hc + Ilm + Bt + Kfs + Mul + Sil \quad (1)$$

In (1), the restitic/peritectic phases are present in small amounts since the contribution of muscovite and biotite to the reaction is considered minor compared to the role played by interstitial water.

At 850°C, the melt distribution in the paragneiss is very close to what is observed at 800°C. The melt is homogeneously distributed at grain boundaries forming a continuous network in the whole sample. Thus, the melting mechanisms are similar at 850°C and 800°C. However, the degree of melting is more than twice higher at 850°C (i.e., ~17.8%) than at 800°C (~8%). In the 850°C experimental charge, biotite is strongly destabilized although not totally reacted out. This is demonstrated by the crystallization of large euhedral orthopyroxene crystals that appear in addition to the other previously described restitic phases. This probably indicates that the biotite dehydration melting reaction is about to be overstepped. Thus, biotite dehydration melting and presence of interstitial water are considered as the major melting mechanisms at 850°C according to the following melting reaction:

$$Bt + Qtz + Pl + Kfs + Grt + Ky \pm Ms + \text{interstitial } H_2O \longrightarrow \text{melt} + Opx + Hc + Ilm\ (Bt + Kfs + Mul + Sil?) \quad (2)$$

In (2), the main change compared to (1) concerns the appearance of orthopyroxene in the restite mineral assemblage.

In the 800°C *orthogneiss* charge, the melt distribution strongly differs compared to the paragneiss. Melt is preferentially associated to muscovite reaction zones. In this experiment, muscovite is totally broken down and replaced by the *in-situ* crystallization of restitic phases including biotite (more Mg-rich than the starting biotite), sillimanite, mullite, ilmenite, K-feldspar and hercynitic spinel. The peritectic phases outline the contour of the starting muscovite. This suggests that, as for the paragneiss, the muscovite dehydration melting curve (Spear, 1995) has been overstepped. However, muscovite is an essential mineral in the orthogneiss. Thus, muscovite dehydration melting must be considered as a major melting mechanism. This explains the higher melting degree in the orthogneiss (~12.8%) compared to the paragneiss (~8%) at 800°C and also the melt distribution observed in the orthogneiss. Indeed, muscovites are not homogeneously distributed and underline the initial metamorphic layering and cleavage which is also reflected in the distribution of the melt pockets resulting from muscovite dehydration melting. In muscovite-free zones, melting textures of the quartz-plagioclase-K-feldspar assemblage are also observed suggesting that an additional melting mechanism is involved. Interstitial water present at grain boundaries probably plays a similar role than in the paragneiss. However, the presence of interstitial water has less importance in the orthogneiss than in the paragneiss because muscovite dehydration melting accounts for an important part of melt production. The scarce biotites initially present in the orthogneiss are from unreacted to slightly affected at 800°C which indicates that the biotite dehydration melting curve has not been passed. The melting reaction for the orthogneiss at 800°C can be written as follows:

$$Ms + Qtz + Pl + Kfs \pm Bt + Ms\ H_2O\ (\pm \text{interstitial } H_2O) \longrightarrow \text{melt} + Hc + Ilm + Bt + Kfs + Mul + Sil \quad (3)$$

In (3), the textures of newly formed K-feldspar and their compositions (higher Na and lower K than in starting and residual minerals) demonstrates that it belongs to the restitic assemblage. In this reaction, muscovite dehydration is considered as the main melting mechanism.

At 850°C, the scarce biotites initially present in the orthogneiss are almost entirely broken-down meaning that the biotite dehydration melting curve is very close to be overstepped. Since biotite is a minor phase in the orthogneiss, biotite dehydration melting remains a minor melt production mechanism. Biotite breakdown is indicated by the appearance of orthopyroxene which joins the restitic phase assemblage at 850°C. At this

temperature, muscovites are entirely broken-down as at 800°C and muscovite dehydration melting still represents the main melt production mechanism because of the modal importance of muscovite in the starting rock. In muscovite-free zones, melting is still enhanced, and melt pockets have greater sizes compared to 800°C experiment. This suggests that interstitial water also contribute to the melting mechanism. The melting reaction for the 850°C experiment can be expressed as follows:

$$Ms + Qtz + Pl + Kfs \pm Bt + Ms\ H_2O + \text{interstitial } H_2O \longrightarrow \text{melt} + Opx + Hc + Ilm + Bt + Kfs + Mul + Sil \quad (4)$$

The main melting mechanism in the orthogneiss at 850°C is still muscovite dehydration but biotite dehydration and interstitial water should also be taken into consideration.

Overall, our results underline differences in the melting mechanisms between the two protoliths investigated. However, muscovite and biotite show the same respective behavior in the paragneiss and the orthogneiss. Interstitial water also plays a similar role in the two types of charges. It is worth emphasizing that the dehydration melting reactions (1) – (4) above are similar to those proposed in simple systems (e.g., Brearley and Rubie, 1990; Patiño Douce and Harris, 1998; Vielzeuf and Holloway, 1988). The temperature ranges suggested for muscovite and biotite dehydration melting in our experiments is consistent with previous results on the partial melting of crustal rocks (Vielzeuf and Holloway, 1988; Patiño Douce and Harris, 1999).

VI.5.2. Major element compositions of experimental melts and Variscan RMGs

One result of the experiments is that melt major element compositions only slightly differ between the paragneiss and the orthogneiss. For each group of charges, there are no large compositional variations with temperature from 800 to 850°C. Melt pockets analyzed at different locations in the same charge yield homogeneous melt compositions. Melting kinetics are known to be sluggish (Patiño Douce and Harris, 1999) and melt equilibration must overcome difficulties due to low melt fractions and local melting mechanisms. Yet, the experiments do not show compositional heterogeneities at the scale of the charge. In the same way, one could have expected more marked compositional differences between melts from the paragneiss and orthogneiss

charges, given their contrasted mineral modes. However, muscovite and biotite show the same respective behaviour in two protoliths and this, together with the presence of interstitial water in both cases, probably explains the converging melt compositions for the two protoliths. Patiño Douce and Harris (1999) also observed that the composition of leucogranitic melts were little dependent of the starting material in their partial melting experiments performed at 700-900°C and 6-10kbars.

P_2O_5 and A/CNK are both slightly higher in the paragneiss than in the orthogneiss and they will be used as indicators to compare experimental glass and whole rock compositions of Variscan peraluminous granites and RMG (Fig. 11). In so doing, we recognize that granite whole rock analyses do not necessarily reflect melt compositions due to the expulsion of magmatic fluids at the magmatic-hydrothermal transition and the possibility of crystal accumulation. However, in Fig. 11, glass compositions of both the paragneiss and the orthogneiss plot in the peraluminous field (A – CNK > 1). Glasses from the orthogneiss overlap with the composition of some RMGs from Cornwall and Erzgebirge (e.g., Cínovec: Breiter et al., 2017; Tregonning and Hensbarrow topaz granites: Manning and Hill, 1990 and references therein). Glasses from the paragneiss are slightly more peraluminous than in the orthogneiss but their ferro-magnesian contents are also higher. All glass compositions plot away from the composition of highly fractionated RMGs such as Argemela (see Chapter V for whole rock data). The P_2O_5 content of orthogneiss glasses is low and in the same range as Cínovec which belongs to the low phosphorous class of RMGs (Linnen and Cuney, 2005). The paragneiss glasses plot in the range of intermediate phosphorous RMGs (Linnen and Cuney, 2005). At 800°C, the paragneiss glass shows a quite high P_2O_5 content close to Podlesí and Cornish RMGs. All glass compositions are far from the high phosphorous field which include the Argemela RMG.

Overall, low degree melting allows generation of peraluminous melts with variable P_2O_5 content which are comparable to peraluminous granites and to composition of some RMGs. However, they are distinct from compositions of the most peraluminous, high phosphorous RMGs.

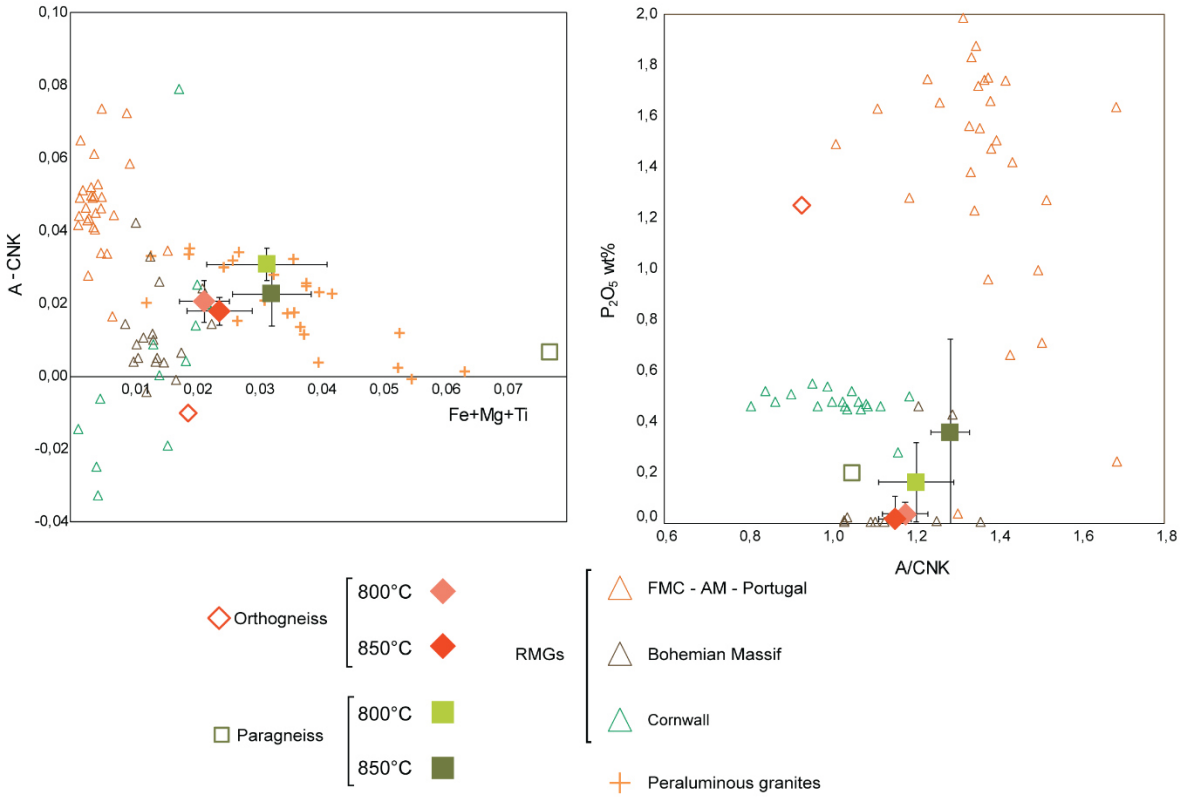

Fig 11 *Major element compositions of experimental glasses compared with peraluminous granites and RMGs from the Variscan belt. Data from this study and Raimbault et al., 1995; Breiter et al., 2017; Breiter et al., 2005; Müller et al., 2005; Chauris 1988; Raimbault et al., 1987; Manning and Hill, 1990. See text for discussion*

VI.5.3. Partitioning of Sn-Li-Nb-Ta-W between glass and restite

Glass trace elements compositions are highly variable between the paragneiss and the orthogneiss charges and the differences depend on the element considered (Fig. 12). There are also marked differences with temperature in the orthogneiss charges. We recall here that glass trace element concentrations were not determined in the paragneiss charge at 800°C due to the small size of the melt pockets and that compositions of melt-peritectic phases mixture zones are only available for the orthogneiss charges. In the paragneiss at 850°C, Ta and Nb glass concentrations are depleted compared to their concentrations in the protolith. W is slightly enriched while Li is more than 6 times higher in the melt. In the orthogneiss at 800°C and 850°C, Ta is slightly enriched in the melts compared to its concentration in the protolith while W and Nb are 1.5 to 2 times higher, respectively. However, Li is depleted in the glass at 800°C and its concentration is equivalent to that of the

protolith at 850°C. All glasses show low Sn contents, despite tin being strongly enriched in the starting orthogneiss (Sn ~220 ppm, Table 1). We attribute this Sn depletion (which is at odds with what is observed for the other elements) to Sn loss to the capsule (e.g., Linnen et al., 1995). In the restite-rich mixture zones of the orthogneiss, which correspond to muscovite reaction zones, Nb is 7 to 10 times (at 800 and 850°C, respectively) more enriched than in the protolith. When compared to the melt, the restite-rich zones are only slightly enriched at 800°C and 3 times higher at 850°C. Similarly, Ta is 3 to 4 times higher in the restite compared to the protolith. The Ta contents are similar in the restite and the melt at 800°C while the restite is 3 times more enriched than the melt at 850°C. W is 2.5 times higher in the restite than in the protolith and also higher than in the melt. By opposite, Li is depleted in the restite compared to concentrations in both the protolith and the melt. Thus, the data demonstrate a difference in the behaviour of Nb, Ta and W on the one hand (preferentially sequestered in the peritectic phases forming the restite than in the melt) and of Li on the other hand (preferentially partitioned into the melt than in the restite).

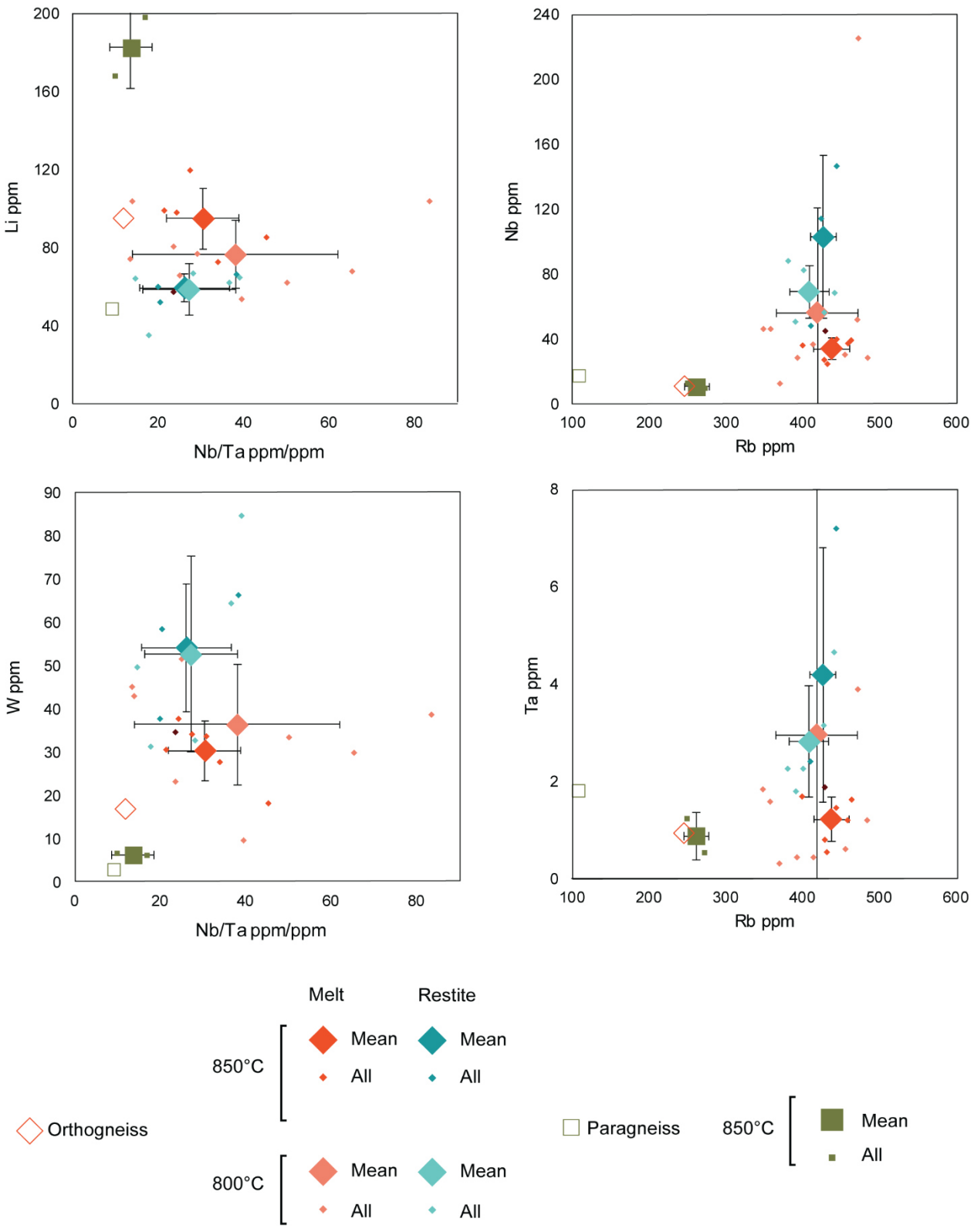

Fig 12 *Trace element compositions of experimental glass and restite-rich zones, and comparison with trace element compositions of the protoliths. See text for discussion*

VI.5.4. Metal concentrations in melts: comparison with Variscan RMGs

The low W content in the paragneiss 850°C is comparable to whole rock W concentrations in Variscan granites such as the Argemela, Beauvoir and Cornish RMGs (Fig. 13). Tungsten is partly partitioned into the orthogneiss melt at either 800°C and 850°C even is concentrations in restites show higher values. W in the melt is in the range of W content in the Argemela and Beauvoir granites Ta content of either glass and restite of all experiments is quite low and plot away from the RMG field (Fig.13). Niobium in glass of the paragneiss 850°C is low and not comparable to RMG content while Nb in glass of the orthogneiss are in the RMG range, the glass at 800°C showing higher values. In the restite, Nb is higher and plot in highest range of RMGs. The Nb/Ta ratio of the paragneiss is closer to Nb/Ta of RMGs than glass and restite of the orthogneiss whatever the temperature, their Nb/Ta ratio being more than twice higher. The Li content in both the restite and the glass of the orthogneiss is quite low, being mainly partitioned into the melt. On the other hand, the highest enrichment (up to 180 ppm) occurs in the paragneiss glass. Such a value is in the range of Cornish granites but, however, is far to attain concentration levels such as found in the Argemela and Beauvoir granites. Glass and restite of the orthogneiss show significant content of Rb getting close to Rb value of Cornish granite, though far from Rb content observed for Argemela and Beauvoir showing extreme concentrations. Overall, this comparison must be taken with caution as whole rock metal content of RMGs do not reflect the magma composition as a significant amount of rare elements must have partitioned into the magmatic fluid (e.g., Chapter V).

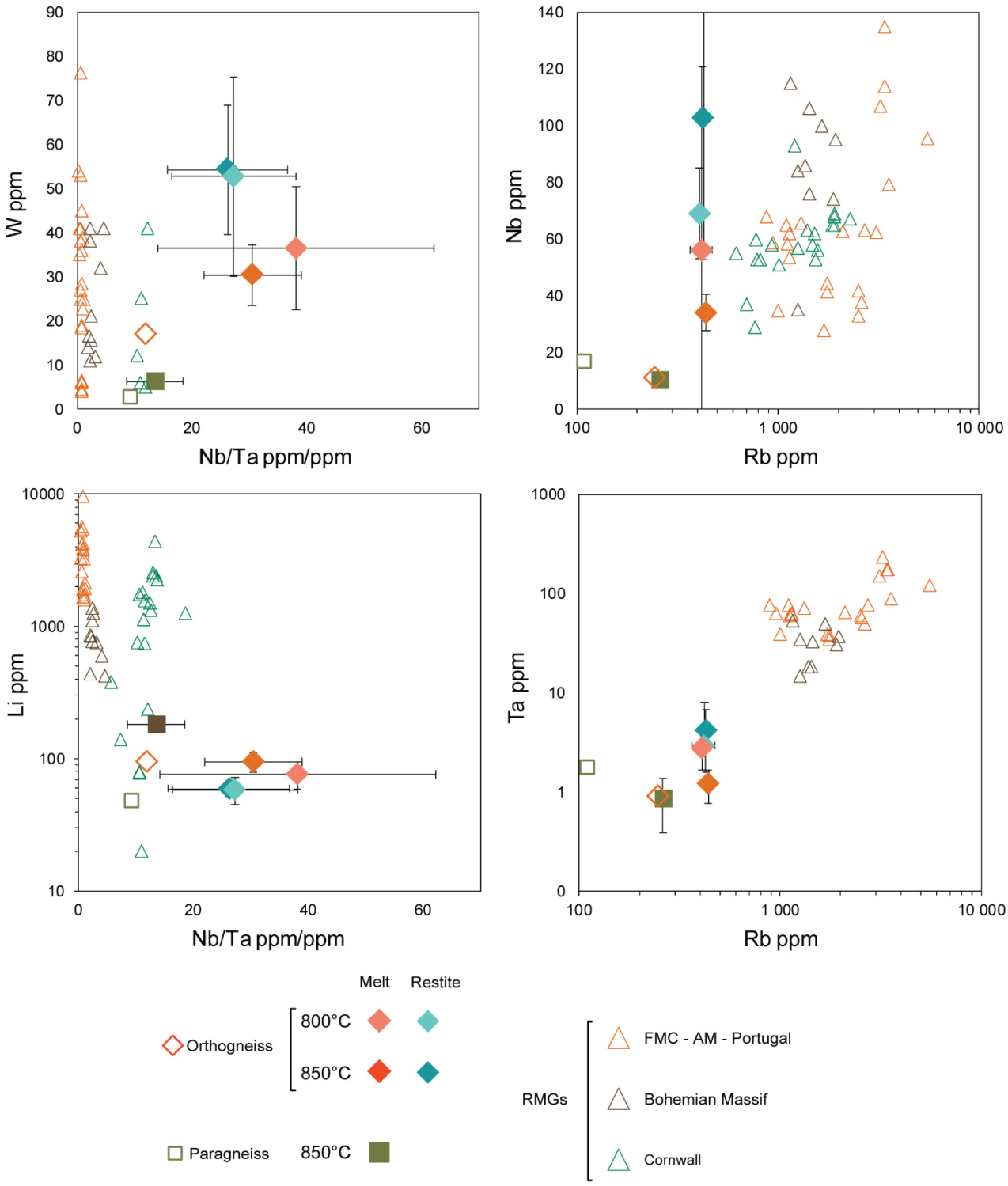

Fig 13 *Trace element compositions of experimental glasses compared with whole-rock compositions of Variscan RMGs. Data from this study and Raimbault et al., 1995; Breiter et al., 2017; Breiter et al., 2005; Müller et al., 2005; Chauris 1988; Raimbault et al., 1987; Manning and Hill, 1990. See text for explanations and discussion*

VI.5.5. Behaviour of Sn-Li-Nb-Ta-W during partial melting

Protolith mineralogy, composition and temperature are fundamental factors controlling melting mechanisms, reactions and degrees of melting and, therefore, the partitioning and distribution of rare elements between reactant and product phases. At 800°C, the main process affecting the orthogneiss is muscovite dehydration melting. As muscovite is the essential mineral carrier for Li, Sn, Nb, Ta, W in this protolith, muscovite breakdown releases these rare metals which leads to their enrichment in the partial melt. However, since muscovite is an incongruently melting phase, the melting reaction involves the crystallization of a peritectic/restitic assemblage that includes Al silicates, biotite, ilmenite and hercynitic spinel as the main phases. These phases have the potential to concentrate certain elements (W, Nb, Ta, Li) although selectively. Therefore, during dehydration melting of muscovite, W, Nb, Ta and Li are partitioned between melt and the restitic phases. The elemental enrichments observed in the restite-rich zones demonstrate that the partition coefficients for W, Nb and Ta are in favour of the restitic minerals, although, with our data, it is impossible to say which mineral from the restite has the strongest influence. At 800°C, biotite does not appreciably react, thus Li from the scarce residual biotites is immobilized and, so, the melt Li concentration reflects mobilization of Li initially present in the muscovite. The fact that the Li concentration in the restite-rich zones is lower than in the melt can be interpreted either by a low proportion of biotite in the restite assemblage or a biotite-melt Li partition coefficient close to 1 (Icenhower and London, 1995; Pichavant et al., 2016).

At 850°C, the degree of melting has substantially increased. In addition to muscovite dehydration melting, biotite dehydration melting takes place as marked by the appearance of orthopyroxene in the restitic assemblage. As a result, metals coming from biotite will add to metals from muscovite and, so, higher metal concentrations would be expected in the melt. However, this effect is counterbalanced by the degree of melting significantly higher at 850 than at 800°C and which would lead to dilution of metals in the melt. The fact that Nb, Ta and W are more enriched in the 850°C than in the 800°C restite-rich zones can be explained neither by a change in the restite mineral assemblage nor by significant variations in the relative proportions of the restitic minerals, which have not been observed. This effect could be attributed to increases of the restitic mineral-melt partition coefficients for W, Nb and Ta as temperature increases.

For the paragneiss at 850°C, the reaction is mainly controlled by biotite dehydration melting as reflected by the appearance of orthopyroxene. W, Nb and Ta are depleted in the melt, although Li is strongly enriched. Clearly, such an elevated melt Li concentration reflects a major contribution of biotite to the Li budget. Biotite is the main mineral carrier for Li in the paragneiss and, so, the results (when compared to the data for orthogneiss) demonstrate the key influence of biotite relative to muscovite in the control of the melt Li concentration.

VI.6. IMPLICATIONS

VI.6.1. Role of metal preconcentration in the protolith

Our results allow to explore the role of metal pre-concentration in the protolith since one of the starting samples (the orthogneiss) is quite enriched in Sn, W, Li, Be whereas the other (the paragneiss) only shows normal concentrations for crustal rocks. However, high concentrations of metals in the protolith do not necessarily result in their enrichment in the melt, even if the degree of partial melting is low. In fact, the distribution of metals is strongly controlled by the melting mechanisms which are similar for both protoliths although they do not have the same importance due to contrasted mineralogical compositions. Indeed, at 800°C, conditions for muscovite dehydration melting are overstepped and this (in addition to the influence of interstitial water) leads to a higher degree of melting in the orthogneiss than in the paragneiss because the former has higher muscovite content than the latter. Even if degrees of melting are kept low in the two types of charges (respectively ~8 and ~13% in the paragneiss and the orthogneiss), results for the orthogneiss show that metals distribute between melt (where they are only slightly enriched) and restitic phases (which sequester most of them). Therefore, restitic mineral-melt partition coefficients, and not the protolith trace element composition, exert the main control on the incorporation of metals in the melt and concentrations. For the paragneiss and although the melt trace element data are lacking, muscovite is present in minor amounts and biotite is mostly stable and, so, it is expected that metals (including Li) will be present at low concentration levels in the melt.

At 850°C, conditions for biotite dehydration melting are attained and probably close to be overstepped judging from the extensive biotite breakdown textures and the appearance of orthopyroxene as a restitic phase. In the orthogneiss, the melt is less enriched in W, Nb and Ta at 850 than at 800°C. This is probably due to a metal dilution effect, as the degree of melting has increased significantly (from ~ 13 to ~20%). However, a significant amount of metals are still sequestered in the restite which means that metal mobilization from the mineral carriers initially present in the protolith (mainly muscovite) actually took place. The behaviour of Li differs from the other rare elements. Indeed, it is never appreciably sequestered in the restite probably as a result of an unsufficient modal abundance of biotite in the restitic assemblage. It is more enriched in the 850°C than

in the 800°C melt because additional Li is available from biotite dehydration melting, despite biotite being present in low amounts in the orthogneiss. In the paragneiss, biotite is a major rock forming mineral and the behaviour of metals is strongly affected by biotite dehydration melting, as marked by the extreme enrichment of Li in the melt. Therefore, for the paragneiss as for the orthogneiss, factors such as the initial metal pre-concentration in the protolith and the degree of melting appear of subordinate importance in comparison with the role played by the melting reaction and the partitioning of metals between residual and restitic minerals and the anatectic melt.

VI.6.2. Restites and metal enrichment

As emphasized previously, the observed degrees of metal enrichment in our experimental melts are significant but not very substantial, being < 1 order of magnitude. Average enrichments in the melt referenced to each respective protolith are illustrated in Fig. 14. For the orthogneiss at 800°C, Nb and Ta are enriched by a facor of 3.15 and 3.18, W by 2.09 and Li is depleted (-0.81) At 850°C, the melt show degrees of enrichment of 3.2 for Nb, 1.42 for Ta and 1.83 for W while Li is even more depleted (-0.94). In the paragneiss, only Li and W are enriched, by 3.81 and 2.38, respectively. Degrees of enrichment are higher at 800°C for the orthogneiss reminding that no data are available for the paragneiss. In comparison, degrees of enrichment in the restite are higher than in the melt. At 850°C, they are of 9.26 for Nb, 4.51 for Ta and 3.2 for W (at 800°C, Nb: 6.22, Ta, 3.04 and W: 3.11). Thus, Nb, Ta and W become preferentially enriched in the restite than in the melt when temperature is increased from 800 to 850°C. Meanwhile, Li is preferentially partitioned to the melt. Assuming that RMGs are representative of compositions of their parental anatectic melts, these results suggest that, even for low degrees of partial melting and pre-enriched sources, rare metal concentration by direct partial melting is not efficient enough to reach levels of enrichment as seen in the most fractionated RMGs.

From our results, one possibility that needs to be considered for the generation of RMG is multistage melting. A metal-rich restite left after a first stage of partial melting appears as an appealing protolith if subject to a second partial melting event. It is quite possible that a low degree of partial melting of a metal-enriched residual rock could produce a strong enrichment of the melt in rare metals. However, this would require that no

minerals with the potential to sequester rare elements crystallize during the second-stage melting reaction. Muscovite dehydration melting promotes relatively high degree of melting and the partitioning of metals in the restite. Biotite dehydration melting can also potentially result in the crystallization of peritectics sequestering the metals although this remains to be tested experimentally. However, it seems possible that melting of a restitic rock where biotite is the only metal carrier and under conditions exceeding dehydration melting could produce strongly enriched magmas, assuming that the restitic assemblage is dominated by phases (such as orthopyroxene) with low mineral-melt partition coefficients for the rare metals. Although our experiments do not provide information on the behaviour of Sn, Wolf et al. (2018) emphasized that Sn preferentially partitions into the restite which would imply that the restite left after a first stage of partial melting is Sn, Nb, Ta and W-rich. Wolf et al. (2018) also considered the possibility of multistage melting for rare metal magma generation. However, this possibility leads to difficulties in the case of Li which seems to partition preferentially in the melt than in the restite. Therefore, and although elements such as Sn, Nb, Ta and W show similar restite-melt partitioning behaviour, it is probably necessary to consider the behaviour of each rare element individually.

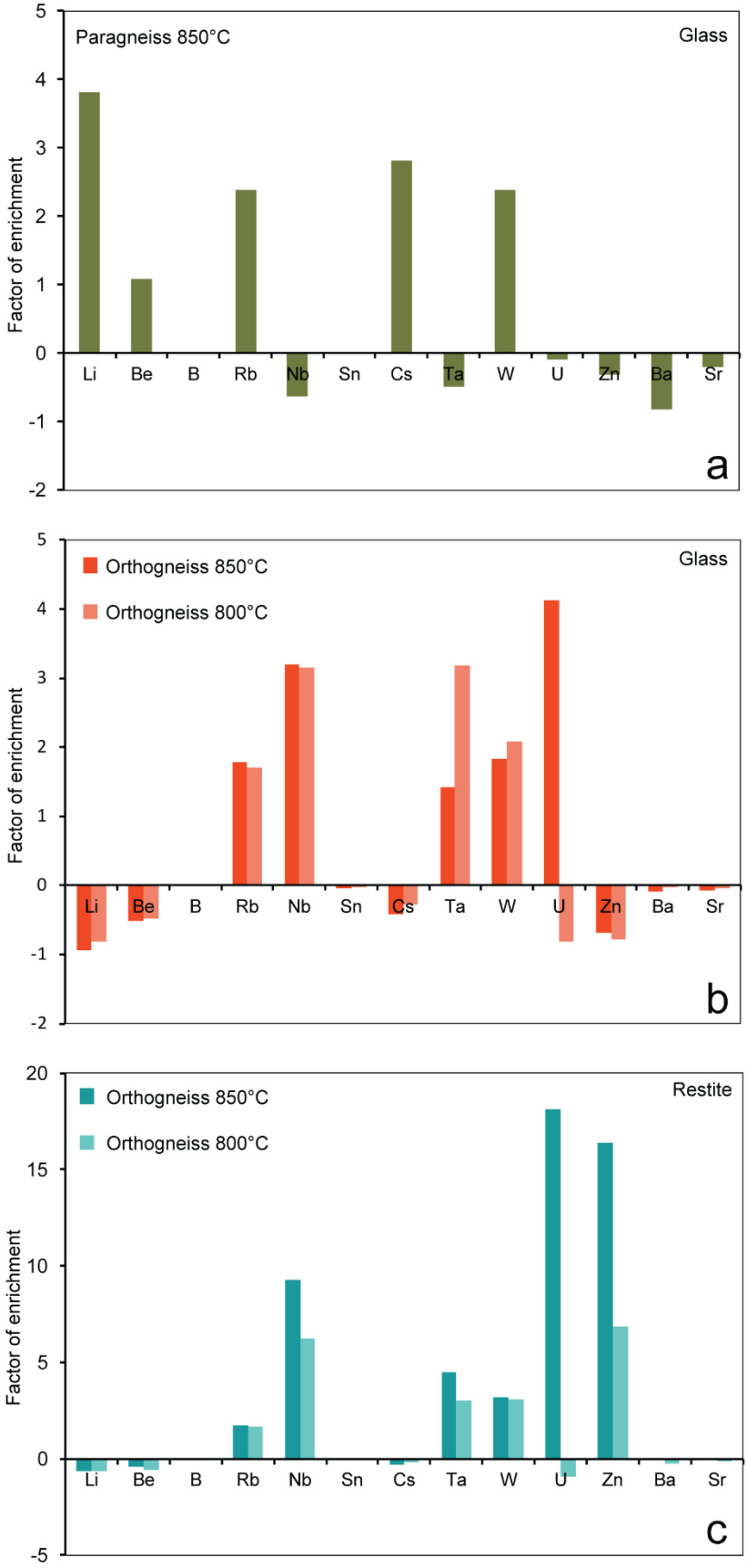

Fig 14 *Factors of enrichment in glass of the paragneiss 850°C and the orthogneiss and restite of the orthogneiss*

VI.6.3. Implications for RMGs

Single episode melting, involving either muscovite and/or biotite dehydration melting mechanisms, is not efficient to preconcentrate rare metals. Preconcentration of metals in minerals of the protoliths and low degree melting are important controlling factors on metals distribution, however, according to our experiments and other studies (e.g., Wolf et al., 2018) most of the available rare elements are sequestered in the restite. Single episode melting allows the generation of slightly enriched melts having similar major composition compared to peraluminous granite and to the less evolved RMGs. On the other hand, trace element content never reaches the strong enrichment observed for highly evolved RMGs such as Beauvoir (FMC) and Argemela (Portugal). Multistage melting, as suggested in Wolf et al., (2018), could explain both rare element enrichment in highly evolved RMGs and the continuum with peraluminous granites genesis. The large amount of peraluminous granites occurring within the Variscan belt emplace at the end of the Variscan orogeny during the post-collisional exhumation, suggesting that metamorphic rocks follow a roughly adiabatic decompression path. Muscovite dehydration melting have often been proposed as the main mechanism for peraluminous magma generation (e.g. Castro et al., 2000) and our experimental results support this assumption. This means that restitic rocks resulting from this melting episode might be metal enriched. Further melting assuming pressure decrease at almost constant temperature could ensue in biotite dehydration of the pre-enriched restitic rocks and in the genesis of rare metal magma. Thereby, such multistage melting mechanism would be strongly dependent on the P-T path followed by the metamorphic rocks. This would suggest a relative continuity between peraluminous magma and rare metal magma generation rather than two distinct melting episodes. Though being very little constrained for the time being and must be debated, a multistage melting model can be proposed with: (1) Muscovite dehydration melting leading to the generation of a significant amount of peraluminous magmas over a time span of 20-30 Ma; rare elements being mostly sequestered in the biotite-bearing restitic rocks at that stage. This could result in large amount (e.g., Saint-Sylvestre granitic complex, FMC) to moderate amount (e.g., Chateauponsac and Sagne intrusions, FMC) of magmas through continuous melting with time. (2) Biotite dehydration inducing low degree melting of the metal-rich restitic rocks and producing rare-element concentration in the magma. Taking the example of the Limousin (northwestern part of the FMC), multistage

melting could have resulted in the emplacement, through time, of: (i) the Saint-Sylvestre granitic complex (~325 Ma, Hollinger et al., 1986); (ii) the Chateauponsac and the main Blond intrusion of restricted size compared to the Saint-Sylvestre complex (~319 Ma for the Blond granite, Alexandrov et al., 2000); (iii) the evolved metal-bearing units of the Blond massif (~301 Ma, Duthou et al., 1984).

VI.7. CONCLUDING REMARKS

This experimental study allowed significative advances on the understanding of rare metal magmas generation. The main concluding remarks are as follow:

- The use of natural samples in the form of microcores rather than powder permitted to evidence variations in melt distribution and to better stick to natural processes,

- Melting mechanisms involved for the two protoliths are similar even if the initial mineralogy and chemistry strongly differ. At 800°C, experiments show that both the orthogneiss and the paragneiss are affected by muscovite dehydration melting and intertitial water at grain boundary, though not in the same proportions (i.e., modal amount of muscovites). At 850°C, muscovite and biotite dehydration occur,

- Different metals enrichement in the protoliths allowed evaluating the role of metal preconcentration. High concentrations of metals in the protolith do not necessarily result in their enrichment in the melt, even if the degree of partial melting is low, evidencing the importance of melting mechanisms,

- Micas breakdown lead to the formation of restitic phases sequestrating the metals (not Li) which results in low rare elements concentration in the melt,

- Experimental results show that one stage of direct low degree dehydration melting is not an efficient mechanism to concentrate rare elements in the melt. A multistage melting can be, though, efficient to produce rare metal magmas, assuming that the restite is metal enriched and are melted.

CHAPTER VII:

SYNTHESIS AND CONCLUSIONS

SYNTHESIS AND CONCLUSIONS

Based on a multiscale approach and combining diverse methods, this study results in a comprehensive understanding of the magmatic, hydrothermal and tectonic features controlling the specificity of evolved granites. The Argemela is a clear outstanding example allowing to address the overall issues controlling RMGs. Furthermore, the experimental study, although preliminary, gave significative insights for rare metal magma generation. The main results coming out from this thesis manuscript are summarized below.

VII.1. STRUCTURAL CONTEXT OF EMPLACEMENT OF THE ARGEMELA MINERALIZED DISTRICT

Field structural study, regional-scale strain field analysis and gravity modelling allowed constraining the structure/geometry of the Argemela RMG and the mechanical context leading to its emplacement (Fig. 1).

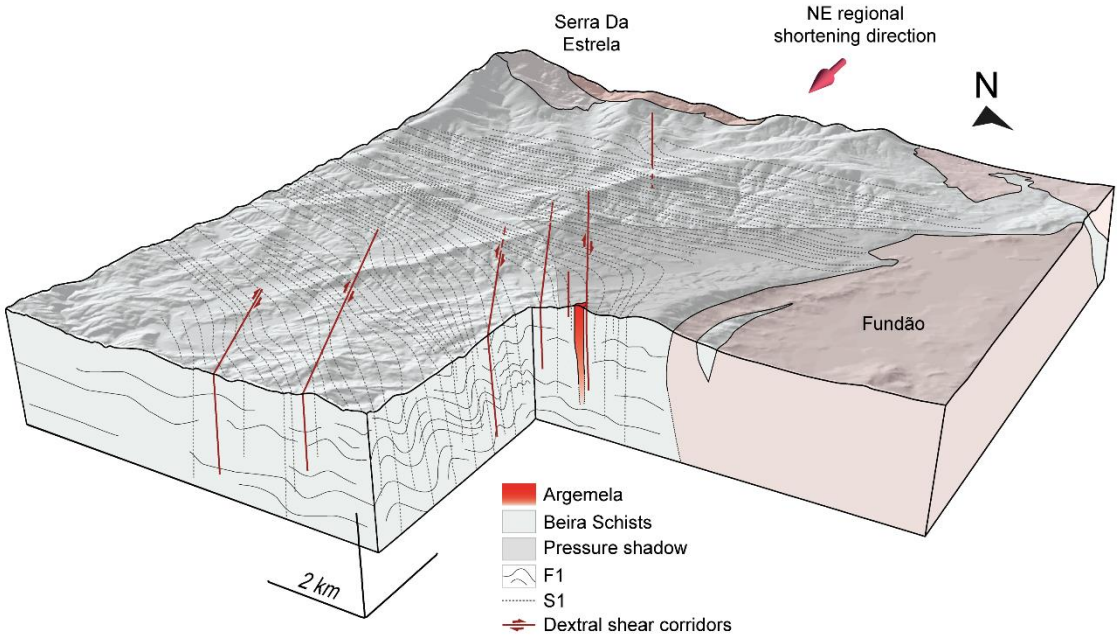

Fig 1 *Synthetic 3D block stressing the special structural context of emplacement of the Argemela RMG and illustrating its unusual geometry*

The field structural analysis highlights key features of the main deformational events affecting the Argemela district and the special environment of emplacement. The main outcomes are listed below.

- At the regional scale, well preserved sedimentary bedding is affected by regional-scale and homogeneous coaxial NE trending compression. S0 displays systematic N130-140°E upright folds (F1) from decimeter to multi-kilometer scale as outlined by the Armorican quartzite layers. S1 formed as a penetrative steeply-dipping ~N135°E trending axial-planar cleavage.

- The Argemela district emplace in a regional kilometer-scale pressure shadow evidenced by the reorientation of S1 cleavage around the Fundão pluton and its metamorphic aureole (Fig. 1). This implies that the Fundão intrusion predate the emplacement of the Argemela RMG. The pressure shadow, acting as a stress release zone during Variscan deformation, has played an important role for Argemela emplacement favoring magma channeling and ascent in this peculiar location. Efficiency of such zones to promote magma channeling has been demonstrated and should be considered in further studies.

- A pipe-like geometry has been revealed by gravity modelling for the Argemela RMG which is consistent with vertical magma ascent to subvolcanic levels of emplacement and with intrusive steep contacts between Argemela and the surrounding rocks (Fig. 1).

- N170°E-NS subvertical dextral shear zones superimpose to the regional-scale pressure shadow, consistent with a NE shortening direction. At a regional-scale, shear zones leaded to the formation of some F2 folds with steeply dipping axes and locally a S2 axial-planar cleavage has been recognized. Within the Beira schists, localized strain along shear planes results in S1 passive reorientation. The northeastern border of the Argemela intrusion is affected by such shear zone playing a significant role at least during the late stages of emplacement. The shear zone is better expressed than those occurring within the country rocks and strongly localizes along the contact which illustrate the role of the rheological behavior on strain localization. Furthermore, strain localization could have leaded to the clockwise rotation of the pipe-like intrusion (Fig. 2).

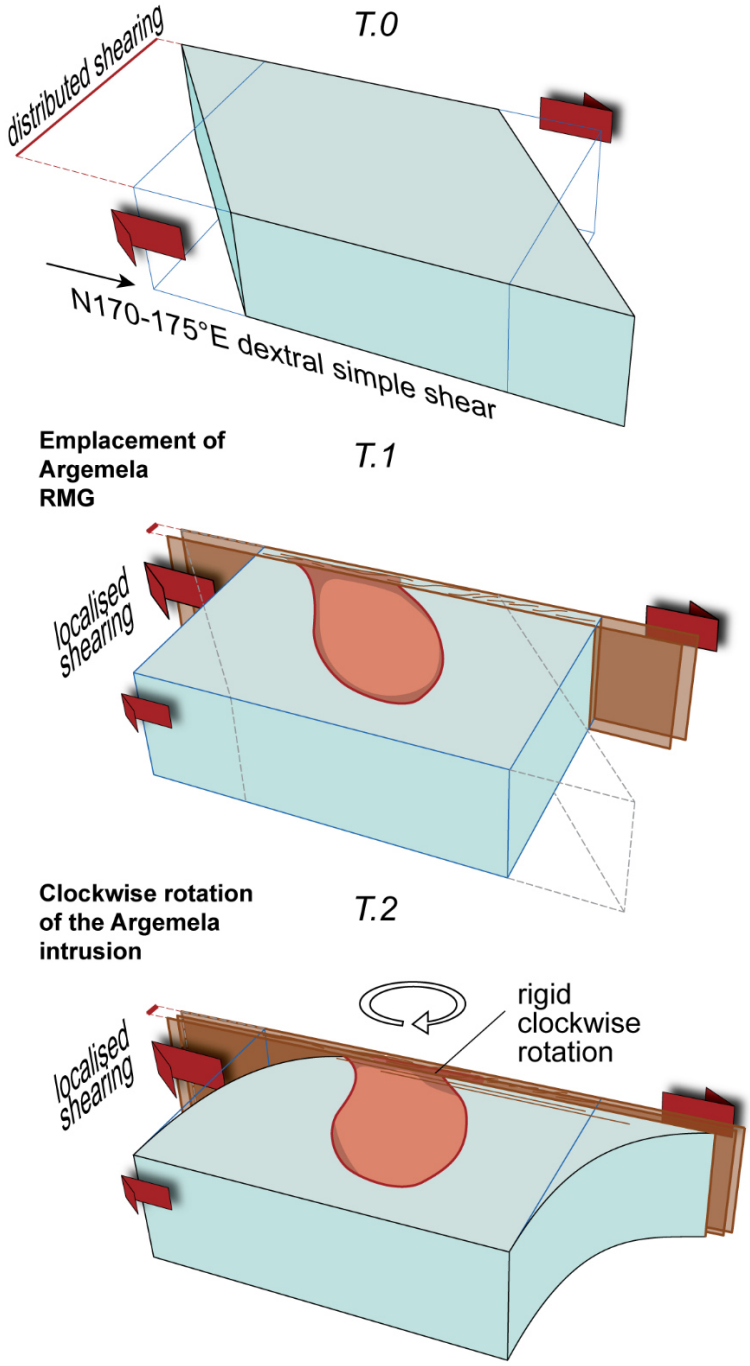

Fig 2 *Multi-stages model illustrating the clockwise rotation of Argemela under shearing conditions and during intragranitic vein emplacement*

- Strain localization along shear zones within the CIZ has been described in previous studies and these structures were attributed to the Late Carboniferous deformational event. The Argemela RMG is synchronous to such deformation and thus emplaced during Late Carboniferous which is consistent with available datations.

- At the scale of the gravity modelling, the intrusion is unrooted on the shear which suggest only shape modification at the emplacement level. These dextral shear corridors may have, thought, deeper continuation and might be branched on larger structures which would have also promoted magma channeling.

- Subvolcanic level of emplacement has been suggested has a specific characteristic of RMG. Geometrical and textural criterias of Argemela strongly suggest fast channeled upward rise of the magma to shallow levels of the crust. This is also consistent with low viscosity generally ascribed to rare metal magmas. Other RMGs show similar small magma volumes and geometries suggesting vertical magma channeling, therefore, it is proposed that rare metal magmas have common mechanical behavior inhibiting horizontal flows typicaly observed for other granites in the Variscan belt. Overall, such integrated study demonstrates the importance of structural mechanisms and their implications for granitic-magma ascent.

- In the AMD system, mode of emplacement of the vein systems fit with the regional deformational environment. The intragranitic vein system limited to the Argemela RMG is composed of three vein generations. The two first types show extensional characteristics opening as tension gashes and evidenced the still slightly ductile behavior of the cooling intrusion. On the other hand, the Type III veins exhibit sharp contact with the granite and apparent sinistral shearing (i.e., shear veins) which suggest a more brittle behavior of the surrounding granite. It has been noted that in its actual striking the vein set is not consistent with the regional NE shortening direction. As the Argemela RMG is affected by a shear zone also consistent with this deformation regime and strain axes orientation, it is proposed that the entire Argemela granite undergone a ~20° clockwise rotation around vertical axis during the non-coaxial shearing (Fig. 2); this latter behaved as a rigid body compared to the surrounding schists. Such rotation was described on bigger granitic bodies. On the other hand, striking directions and evolving geometries of the veins of the ATM are also consistent with the development of simple shear in a NE incremental shortening direction (Fig. 3). The correlated striking and finite strain variations of the system evidenced non-coaxial shear compatible with the N170°E-NS dextral shear zones. Veins opened as tension gashes and rotate and fold during simple shear deformation, folding being allowed by the ductile behavior of the surrounding schist. Therefore, it is emphasized that the behavior of host rocks plays an important role on the deformation distribution and on the development and finite stucture of vein-type mineralization.

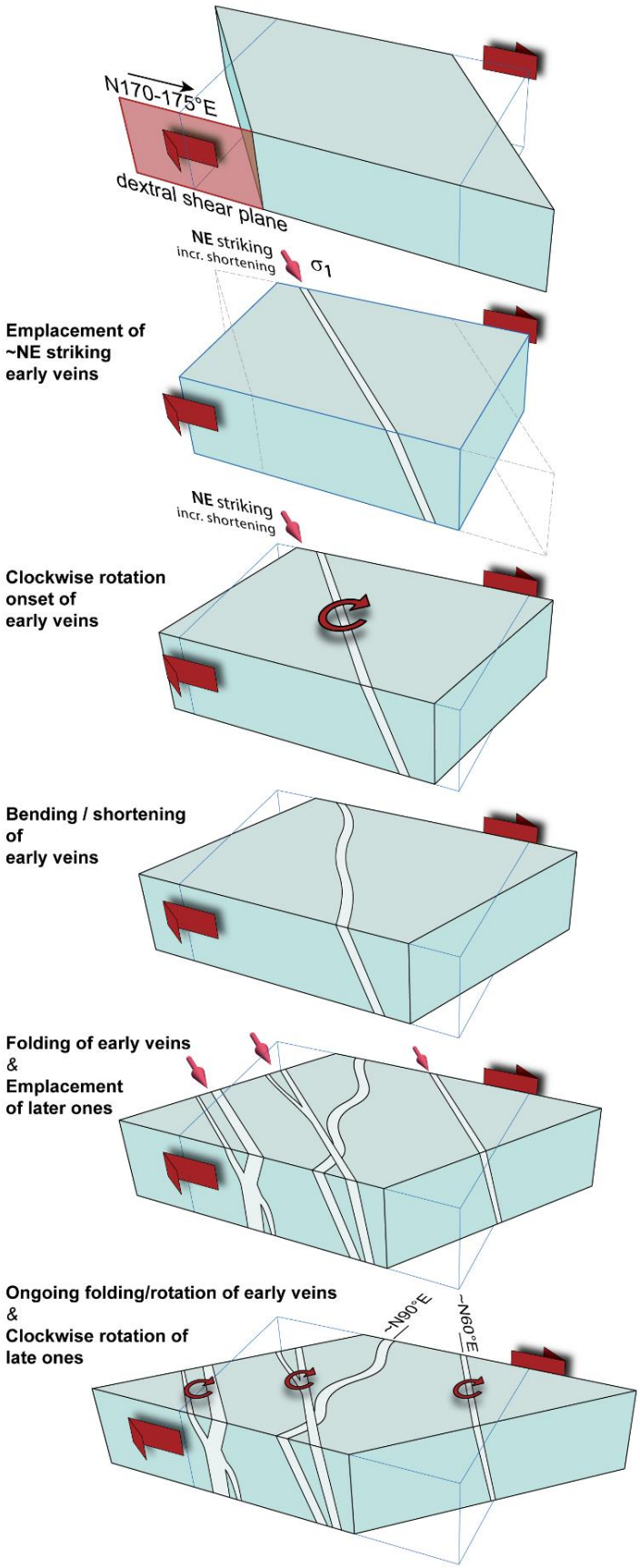

Fig 3 *Multi-stages model of vein emplacement within the country rock*

VII.2. FROM MAGMATIC TO HYDROTHERMAL

The Argemela RMG provide an exceptional opportunity to observe the expression of magmatic to hydrothermal processes and to better understand the role of this transition on metal transport/distribution and mineralization deposition. Field observations were combined with a petrological study, major and trace elements geochemical analyses of rocks and minerals and stable isotopes (O, H). Field study allowed the recognition of three main facies intersected by three types of intragranitic veins. Clear field intersection relationships allowed the determination of a detailed chronology: (1) granitic and border facies, (2) "dyke-like" grey facies, (3) Type I intragranitic veins, (4) Type II veins, (5) Type III veins and (6) sulfides. The stable isotope study (O, H) performed on micas and quartz, together with mineralogical and geochemical features, strongly suggest the magmatic affinity of the fluid with no external contribution (i.e., metamorphic or meteoric), except at the northeastern sheared border. Whole rock geochemistry and recognition of zonation together with major and trace elements analyses of key minerals - occurring either in the granite or the veins - (except for micas) permitted decipher five main stages along the magmatic-hydrothermal transition (4).

(1) The early magma-dominated stage (Fig. 4) corresponds to the crystallization of mostly anhydrous magmatic phases (except for micas and montebrasite) to form up to 90% of the granitic mass. The transition between a magma-dominated system and crystal mush most probably impact the mechanical behavior of the intrusion. Mineral zoning pattern suggest *in-situ* crystallization of the magma and no first-order change in the crystallization environment. Micas and quartz significant rare elements content - namely Sn, Li, Nb, Ta, W and P - indicate that concentration occur *via* magmatic processes in the first place. Zoning pattern, chemical signature and textures of the first generations of cassiterite and columbite-tantalite suggest that their crystallization occur during the magmatic stage. Indeed, all minerals record metal enrichment meaning that the crystallization environment was concentrated at that stage.

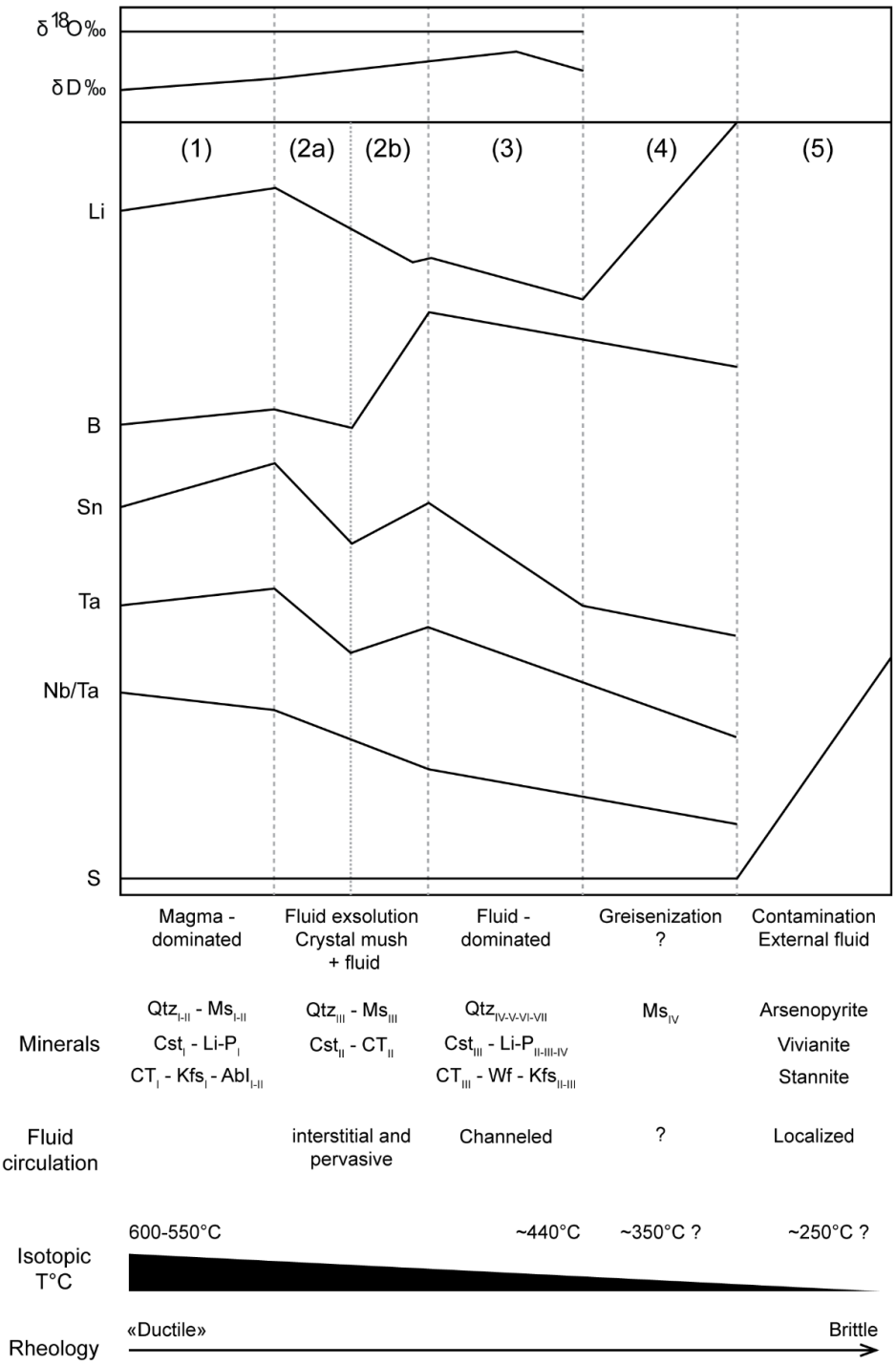

Fig 4 *Illustration of the five main stage occurring at the magmatic hydrothermal transition*

(2) The second stage represent a turning point in the magmatic-hydrothermal transition (Fig. 4). This stage is mainly stressed by strong changes in micas composition. A uniform drop of concentration is observed for all elements - namely Sn, Li, Nb, Ta, W - (except for Rb and Cs remained stable) which indicates a strong modification in the crystallization environment. This together with textural and chemical evidences on other

minerals (Qtz_{III}, Cst_{II}, CT_{II}) consistently indicate granite crystallization under fluid present conditions. Therefore, the strong change in the crystallization environment marks the beginning of magmatic fluid exsolution and that rare-elements are partitioned to the fluid phase (2a, Fig. 4). At this stage, crystallization of skeletal crystal indicates that mechanically fluid is still able to percolate through the crystal mush. After this strong decrease, a selective back increase of elements is observed (namely Sn, Nb, Ta, Mn) accompanied by a drastic rise of B. One possible explanation is that cooling and/or depressurization of fluid lead to condensation of solute-rich material as observed in experimental studies. This would explain element fractionation and the crystallization of the abnormally rich granitic-like grey facies. Apart from that, the grey facies occurs as steeply dipping "dyke-like" structures sign the beginning of fluid channeling being an intermediate between fluid percolation within the crystal mush and vein opening.

(3) This stage corresponds to the emplacement of intragranitic veins. Fluid is now totally channeled and no longer interacts with the granite as suggested by whole rock analyses at vein margins. The intrusion is totally crystallized but geometries of Type I and II veins suggest a transitional mechanical behavior with the granite rock no yet fully brittle. Analyses and mineralogy of veins indicate that rare elements are transported within the magmatic fluid phase. However, quartz from Type I to Type III veins register an overall decrease of these elements being removed by mineral crystallization or lost due to fluid extraction.

(4) This stage is interpreted to be the restricted expression of late hydrothermal alteration. The strong Li-F enrichment of the last generation of micas must be the expression of element remobilization and subsolidus crystallization.

(5) Sulfide crystallization, restricted at the northeastern sheared border, marks the late contribution of a S-As-rich external fluid.

The detailed study of the petrographic and geochemical evolution at the magmatic-hydrothermal transition also allows proposing a sequence of mineralizing events which emphasized the contrasted behaviors of Sn and W along with this transition. Cassiterite crystallizes mostly as a magmatic phase or early in the

transition and wolframite, only in the latest hydrothermal veins as generally observed in other W-systems. Therefore, Sn and W-bearing minerals result from contrasted deposition mechanisms. Besides, wolframite composition comes out as a key feature to understand deposition mechanisms. Indeed, our results suggest that the H/F ratio can be used as an indicator of contrasted W deposition environments in perigranitic ore-forming systems. It has been proposed that wolframite composition can be a useful tool for exploration, Mn-rich wolframite tracing the presence of RMGs and pegmatite mainly exploited for ceramic raw material, Li and Nb, Ta, Sn as by products and Fe-rich wolframite tracing large W-bearing hydrothermal systems of economic importance (Fig. 5).

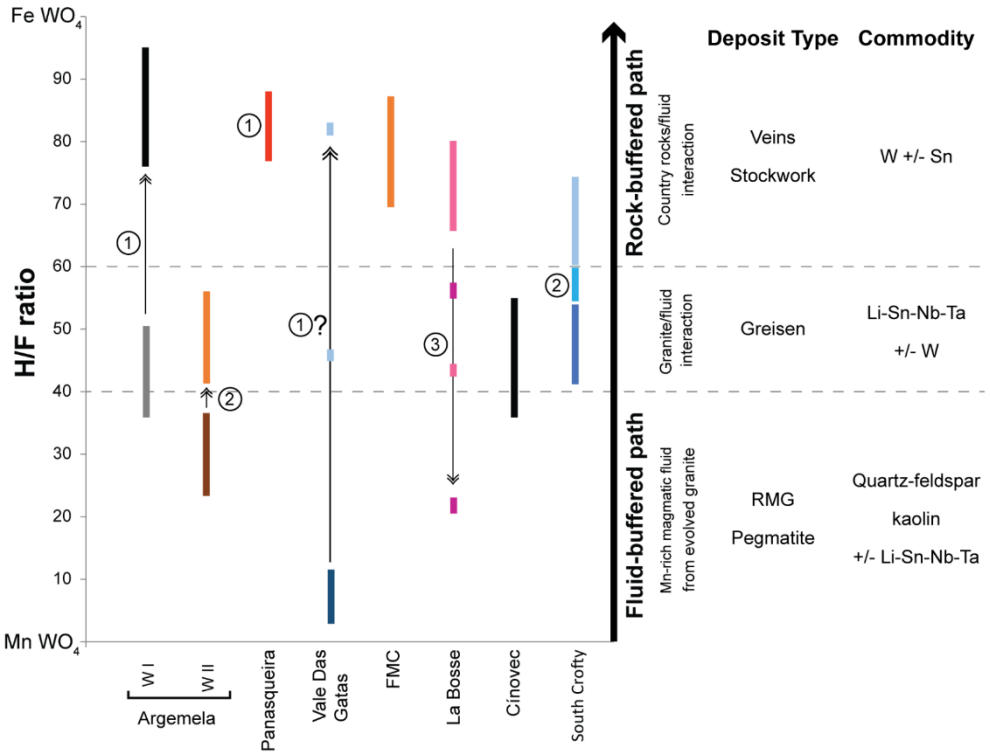

Fig 5 *Environments and mechanisms of W deposition as revealed by the H/F ratio for several representative Variscan deposits and extension to worldwide deposits*

VII.3. METALLOGENIC POTENTIAL

RMGs are classically exploited to produce ceramic raw materials (e.g., quartz, feldspars, kaolin), as their Fe content is very low avoiding oxidation stains. They commonly show strong enrichment in rare elements concentrated by magmatic processes. However, despite an initial strong enrichment, our results suggest that the fluid exsolution from the magma engender an overall loss (i.e., dispersion) of rare elements. Most RMGs are affected by strong late hydrothermal alteration sometimes involving external fluids. The Zinnwaldite granite of Cínovec is affected by intense greisenization and despite a lower initial content in rare elements compared to Argemela, these are remobilized and focused leading to the formation of a rich ore-deposit. In Beauvoir, kaolinization enhanced the transformation of the granite into clay and metric massive quartz form containing pluricentrimetric crystals of cassiterite. Therefore, late hydrothermal alteration stands out as the most important process in RMG able to produce economic concentration of metals and kaolin. Others RMGs such as Argemela which are only slightly affected by hydrothermal alteration can though be exploited for quartz and feldspars as raw ceramic materials, but metals are not of economical interest. Besides, at Argemela, fluids are channeled leading to the concentration of W crystallizing as Mn-rich wolframite in Type III veins but veins are not of economic importance. Nevertheless, Mn-rich wolframite of the Mazet (FMC, north of Beauvoir) were formerly exploited. Exsolution of magmatic fluids from RMGs can thus, result in the formation of W-rich veins but as these are isolated, they are no longer economic nowadays. On the other hand, providing Li in Europe is of growing importance and RMGs represent potential reserves. Greisen and the Zinnwaldite granite of Cínovec are currently explored to produce Li. However, it is difficult to extract Li from micas, montebrasite being absent.

VII.4. RARE METAL MAGMAS: NEW INSIGHTS

The experimental study allowed to test the efficiency of low degree partial melting to generate rare metal magmas and dehydration melting as main mechanism for metal redistribution. Uses of natural samples having natural mineral distribution, different mineralogical and geochemical characteristics, permitted to better stick to natural processes. We have highlighted the significant role of the mineralogical assemblage, mineral distribution and structure of the protolith (i.e., cleavage) on melt distribution, being highly variable between the paragneiss and the orthogneiss. For different initial mineralogies and chemistries, melting mechanisms are similar at the same temperature conditions. On the other hand, the initial proportion of biotite and muscovite is a main factor controlling the melting degree and metal redistribution, micas being the main metal carriers. This study also shows that high metal concentration in the protolith and in micas do not necessarily results in metal enrichment in the generated melt. Only slight enrichments were evidenced even for the lower melting degrees, metals being sequestered in the restitic phases. This has major implications for rare metal magma generation, suggesting that a one stage melting cannot produce significative metal enrichments. However, multistage melting involving the destabilization of enriched restites could result in greater enrichements in the melt. Multistage melting needs to be considered as an efficient mechanism in the Variscan belt to produce successively: large volume of peraluminous magmas, smaller volume of slightly evolved magmas and finally, reduce volume of rare metal magmas.

VII.5. CONCLUSIONS AND PERSPECTIVES

This study points out the necessity to combine different approaches, at different scales, to get a comprehensive overview and understanding of mineralized systems. RMGs results from a combination of magmatic, hydrothermal and structural processes, all playing an important role. As one process will influence the others, it clearly stresses the primary importance of perform integrated studies on such objects.

Several perspectives arise. The integrated structural and gravimetric study of Argemela gave significant results with strong implications for granitic-magma ascent and should be applied to other RMGs. As the magmatic-hydrothermal transition is now well constrained for Argemela, a melt/fluid inclusion study should be performed with analyses of metals to better understand and quantify element partitioning during these processes. Further work must also be carried out on the role of fluid condensates using an experimental approach. A complementary study of wolframite compositions in other systems is necessary to wider the scope of the H/F ratio approach described here. Finally, the experimental study gives strong insights for rare metal magma generation by low degree direct melting. The next step is to test multistage melting as a powerful mechanism to concentrate rare elements experimentally. To do this, they are two main options: (i) the melting of a naturally enriched restite or multistage melting of a protolith with magma extraction at each step.

REFERENCES

- A -

Ábalos B, Carreras J, Druguet E, Escuder Viruete J, Gómez Pugnaire MT, Alvarez SL, Quesada C, Rodríguez Fernández LR, Gil-Ibarguchi JI (2002) Variscan and Pre-Variscan tectonics. The Geology of Spain, Gibbons W, Moreno T. 155-183

Aïssa M, Marignac C, Weisbrod A, (1987a) Le stockwork à ferbérite d'Echassières : évolution spatiale et temporelle ; cristallochimie des ferbérites. In Cuney M, Autran A, Géologie profonde de la Franche Echassières : le forage scientifique. Une clé pour la compréhension des mécanismes magmatiques et hydrothermaux associées aux granites à métaux rares. Géologie de la France, 2-3:311-333

Alderton D H M, Harmon R S (1991) Fluid inclusion and stable isotope evidence for the origin of mineralising fluids in south-west England. Mineral. Mag., 55 :605-611

Alexandrov P, Cheilletz A, Deloule E, Cuney M (2000) 319 ± 7 Ma crystallization age for the Blond granite (northwest Limousin, French Massif Central) obtained by U-Pb ion-probe dating of zircons. C. R. Acad. Sci. Paris, 330 :617-622

Amossé J, (1978) Physicochemical study of the hubnerite-ferberite (MnWO4-FeWO4) zonal distribution in wolframite ($Mn_X Fe_{(1-X)} WO_4$) deposits. Phys Chem Minerals, 3:331–341

Aranguren A, Cuevas J, Tubía J M, Román-Berdiel T, Casas-Sainz A, Casas-Ponsati A (2003) Granite laccolith emplacement in the Iberian arc : AMS and gravity study of the La Tojiza pluton (NW Spain). Journal of the Geological Society, London, 160:435-445

Arthaud F, Matte P (1975) Les decrochements tardi-hercyniens du sud-ouest de l'europe. Geometrie et essai de reconstitution des conditions de la deformation. Tectonophysics, 25 :139–171. https://doi.org/10.1016/0040-1951(75)90014-1

Aubert G (1962) Données nouvelles sur le gîte de lithium et étain de Montebras (Creuse). C. R. Soc. Géol., Fr., n°1

Aubert G, Autran A, Burnol L (1965) L'albite quartzitique à lépidolite de Beauvoir. C. R. Acad. Sci., Fr., 260 :6158-6161

Aubert G (1969) Les coupoles granitiques de Montebras et d'Échassières:(Massif Central français) et la genèse de leurs minéralisations en étain, lithium, tungstène et béryllium. Éditions BRGM

Audrain J, Vigneresse J-L, Cuney M, Friedrich M (1989) Modèle gravimétrique et mise en place du complexe granitique hyperalumineux de Saint-Sylvestre (Massif Central Français). Comptes Rendus de l'Académie des Sciences Paris, 309, II :1907-1914

Autran, A, Cogné J (1980) La zone interne de l'orogène varisque dans l'Ouest de la France et sa place dans le développement de la chaîne hercynienne. Mémoires du BRGM 191–202

- B -

Baertschi P, Silverman S R (1951) Ein neues Verfahren zur Messung der Unterschiede im O18-Gehalt von Silikatgesyeinen. Helv. Chim. Acta, 35:1748-1751

Ballèvre M, Bosse V, Ducassou C, Pitra P (2009) Paleozoic hystory of the Armorican Massif: Models of the tectonic evolution of the suture zones. C. R. Geosciences Tectonics, 341:174-201

Ballèvre M, Bosse V, Dabard M-P, Ducassou C, Fourcade S, Paquette J-L, Peucat J-J, Pitra P (2013) Histoire géologique du Massif Armoricain : actualité de la recherche. Bull. Soc. Minéral. Bretagne, 10-11 :5-96

Ballèvre M, Martinez-Catalan J R, Lopez-Carmona A, Pitra P, Abati J, Diez-Fernandez R, Ducassou C, Arenas R, Bosse V, Castineiras P, Fernandez-Suarez J, Gomez Barreiro J, Paquette J-L, Peucat J-J, Poujol M, Ruffet G, Sanchez-Martinez S (2014) Correlation of the nappe stack in the Ibero-Armorican arc across the Bay of Biscay: a joint French-Spanish project. in: Schulmann K, OG (Eds, Martinez Catalan JR, Lardeaux JM, Vanouzek V (Ed), The Variscan Orogeny: Extent, Timescale and the Formation of the European Crust, Geological Society, London, Special Publications, n°405 Geological Society of London, 77–113. https://doiorg/101144/SP40513

Ballouard C, Poujol M, Boulvais P, Branquet Y, Tartèse R, Vigneresse J-L (2016) Nb-Ta fractionation in peraluminous granites; a marker of the magmatic-hydrothermal transition. Geology, Geological Society of America. doi:10.1130/G37475.1

Bard J-P, Burg J-P, Matte P, Ribeiro A (1980) La chaine hercynienne d'Europe occidentale en termes de

tectonique des plaques. Géologie de l'Europe 108:233–46

Bartels A, Vetere F, Holtz F, Behrens H, Linnen R (1991) Viscosity of flux-rich pegmatitic melts. Contrib. Mineral Petrol., 162:51-60

Bartels A, Bejrens, Holtz F, Schmidt B C, Fechtelkord M, Knipping J, Crede L, Baasner A, Pukallus N (2013) The effect of fluorine, boron and phosphorous on the viscosity of pegmatite forming melts. Chemical Geology 346:184-198

Baumann L, Starke R, (1964) Breitag zur Verteilung der H/F Koeffizienten minerhalb der Wolframitlagerstätte Pechtelgrün auf Gund neuer röntgenographischer Untersuchungen : Bergakademie, 16:79-82

Belkasmi M, Cuney M, Pollard P J, Bastoul A (2000) Chemistry of the Ta-Nb-Sn-W oxide minerals from the Yichun rare metal granite (SE China): genetic implications and comparison with Moroccan and French Hercynian examples. Mineralogical Magazine, 64:507-523

Belousova E A, Griffin W L, O'Reilly S Y, Fisher N I, (2002) Apatite as an indicator mineral for mineral exploration: trace-element compositions and their relationship to host rock type. Journal of Geochemical Exploration, 76:45–69

Berthé D, Choukroune P, Gapais D, (1979) Orientations préférentielles du quartz et orthogneissification progressive en régime cisaillant : l'exemple du cisaillement sud-armoricain. Bulletin de Minéralogie 102:265–272. https://doi.org/10.3406/bulmi.1979.7287

Beus A A, Severov V A, Sitnin A A, and Subbotin K D (1962) Albitized and greisenized granites (apogranites): Moscow, Akademiia Nauk USSR, 196 p. (in Russian)

Beus A A, Zhalashkova N Y (1964) Postmagmatic high temperature metasomatic processes in granitic rocks: International Geology Review, 6: 668-681

Beus A A (1982) Metallogeny of Precambrian rare-metal granitoids. Rev. Bras. Geosci, 12:410-413

Béziat P, Prouhet JP, Tollon F (1980) Le district de Montredon-Labessonnié (Tarn), 26 Congres International de Géologie. E7

Bhalla P, Holtz F, Linnen RL, Behrens H (2005) Solubility of cassiterite in evolved granitic melts: effect of T, fO2, and additional volatiles. Lithos 80:387–400

Bobos I, Noronha F, Mateus A (2018) Fe-, Fe,Mn- and Fe,Mg-chlorite: A genetic linkage to W, (Cu,Mo) - mineralization in the magmatic-hydrothermal system of Borralha, Northern Portugal. Mineralogical

Magazine 1–35

Bons P D, Elburg MA, Gomez-Rivas E (2012) A review of the formation of tectonic veins and their microstructures. Journal of Structural Geology 43:33–62

Borisova A Y, Thomas R, Salvi S, Candaudap F, Lanzanova A, Chmeleff J (2012) Tin and associated metal and metalloid geochemistry by femtosecond LA-ICP-QMS microanalysis of pegmatite-leucogranite melt and fluid inclusions: new evidence for melt-melt-fluid immiscibility. Mineralogical Magasine, 76:91-113

Bosse V, Feraud G, Ruffet G, Ballèvre M, Peucat J-J, De Jong K (2000) Late Devonian subduction and early-orogenic exhumation of eclogite-facies rocks from the Champtoceaux Complex (Variscan belt, France). Geological Journal, 35:297–325

Bouchez J L, Bernier S, Rochette P, Guineberteau B (1987) Logs des susceptibilité magnétiques et anisotropies de susceptibilité dans le granite de Beauvoir : conséquences pour sa mise en place. Géologie de la France, 2-3:223-232

Bray C J, Spooner E T C (1983) Sheeted vein Sn-W mineralization and greisenization associated with economic kaolinization, Goonbarrow China Clay Pit, St. Austell, Cornwall, England: geologic relationships and geochronology. Economic Geology, 78:1064-1089

Breaks F W, Selway J B, Tindle A C (2005) Fertile peraluminous granites and related rare-element pegmatites, Superior Province of Ontario. in "Rare-Element Geochemistry and Mineral Deposits", R L Linnen & I M Sampson, eds. Geol. Soc. Can. Short Course Notes, St. Catharines, 17:87-125

Brearley F W (1987b) An experimental and kinetic study of the breakdown of aluminous biotite at 800°C: reaction microstructures and mineral chemistry. Bull. Miner., 110:513-532

Brearley A J, Rubie D C (1990) Effects of H_2O on the Disequilibrium breakdown of muscovite+quartz. Journal of Petrology, 31, 4:925-956

Breiter K, Fryda J, Seltmann R, Thomas R, (1997) Mineralogical evidence for two magmatic stages in the evolution of an extremely fractionated R-rich Rare-metal granite: the Podlesi stock, Krusne Hory, Czech Republic. Journal of Petrology 38, 12:1728-1739

Breiter K, Müller A, Leichmann J, Gabašová (2005) Textural and chemical ecolution of a fractionated granitic system: The Podlesí stock, Czech Republic. Lithos, 80:323-345

Breiter K, Föster H-J, Škoda R (2006) Extreme P-, Bi-, Nb-, Sc-, U- and F-rich zircon from fractionated perphosphorous granites: the peraluminous Podlesí granite system, Czech Republic. Lithos, 88:15-34

Breiter K, Škoda R, Uher P (2007) Nb-Ta-Ti-W-Sn-oxide minerals as indicators of a peraluminous P- and F-rich granitic system evolution: Podlesí, Czech Republic. Mineralogy and Petrology 91:225-248

Breiter K, Müller A (2009) Evolution of rare-metal granitic magmas documented by quartz chemistry. Eur. J. Mineral., 21:335-346

Breiter K, Ackerman L, Svojtka M, Müller A (2013) Behavior of trace elements in quartz from plutons of different geochemical signature: a case study from the Bohemian Massif, Czech Republic. Lithos, 175-176:54-67

Breiter K, Ďurišová J, Hrstka T, Korbelová Z, Hložková Vaňková M, Vašinová Galiová M, Kanický, V, Rambousek P, Knésl I, Dobeš P, Dosbaba M (2017) Assessment of magmatic vs metasomatic processes in rare-metal granites: A case study of the Cínovec/Zinnwald Sn–W–Li deposit, Central Europe. Lithos, 292–293:198–217

Burchardt S, Tanner D, Krumbholz M (2012) The Slaufrudalur pluton, southeast Iceland – an example of shallow magma emplacement by couple cauldron subsidence and magmatic stoping. Geological Society of America Bulletin, 124:213-227

Burg J-P, Balé P, Brun J-P, Girardeau J (1987) Stretching lineation and transport direction in the Ibero-Armorican arc during the Siluro-Devonian collision. Geodynamica Acta, 1:71-87

Burg J-P, Van Den Driessche J, Brun J-P (1994) Syn- to post-thickenning extension in the Variscan belt of Western Europe: Modes and structural consequences. Géologie de la France, 3:33-51

Burnham C W, Nekvasil H (1986) Equilibrium properties of granite pegmatite magmas. American Mineralogist, 71: 239-263

Burt D M, Sheridan M F, Bikun J V, Christiansen E H (1982) Topaz rhyolites - distribution origin and significance for exploration. Econ. Geol., 77:1818-1836

- C -

Calcagno P, Chilès P, J, Courrioux G, Guillen A (2008) Geological modelling from field data and geological

knowledge: part I. Modelling method coupling 3D potential field interpolation and geological rules. Phys. Earth Planet. Inter., 171:147-157

Cameron J (1951) The geology of Hemerdon wolfram mine, Devon. Transactions of the Institute of Mining and Metallurgy 61:1-14

Carten R B, Rye R O, Landis G P (1988) Effects of igneous and hydrothermal processes on the composition of ore-forming fluids; stable isotope and fluid inclusion evidence, Henderson molibdenum deposit, Colorado. Abstracts with Programs-Geological Society of America, 19, A94

Castro A (1986) Structural pattern and ascent model in the Central Extremadura batholith, Hercynian belt, Spain. Journal of Structural Geology, 8, 6:633-645

Castro A, Corretgé G L, El-Biad M, El-Hmid H, Fernández C, Patiño Douce A E (2000) Experimental constraints on Hercynian anatexis in the Iberian Massif, Spain. Journal of Petrology, 41, 10:1471-1488

Cathelineau M, Boiron MC, Holliger P, Poty B (1990) Metallogenesis of the French part of the Variscan orogen. Part II: Time-space relationships between U, Au and Sn-W ore deposition and geodynamic events—mineralogical and U-Pb data. Tectonophysics 177:59–79

Černý P, Roberts WL, Ercit TS, Chapman R (1985) Wodginite and associated oxide minerals from the Perless pegmatite, Pennington County, South Dakota. American Mineralogist 70:1044–1049

Černý P (1991) Rare-element granitic pegmatites. Part 1: Anatomy and internal evolution of pegmatite deposits. Part 2: Regional to global environments and petrogenesis. Geosci. Canada, 18:49-81

Černý P (1992a) Geochemical and petrogenetic features of mineralization in rare-element granitic pegmatites in the light of current research. Applied Geochemistry 7:393–416

Černý P, Blevin PL, Cuney M, London D (2005) Granite-related ore deposits. Economic Geology 100:337–370

Černý P, Masau M, Goad B E, Ferreira K (2005) The Greer Lake leucogranite, Manitobe, and the origin of lepidolite-subtype granitic pegmatites. Lithos, 80:305-321

Charoy B (1979) Greisenisation, minéralisation et fluides associés à Cligga Head, Cornwall (sud-ouest de l'Angleterre). Bulletin de Minéralogie 102:633-641

Charoy B, Noronha F (1991) The Argemela granite-porphyry (Central Portugal): the subvolcanic expression of a high-fluorine, rare-element pegmatite magma. In: Source, Transport and Deposition of Metals (eds.)

Pagel & Leroy, 741-744

Charoy B, Noronha F (1996) Multistage growth of a rare-element, volatile-rich microgranite at Argemela (Portugal). Journal of Petrology 37:73–94

Chauris L (1988) Les leucogranites à béryl de Bretagne méridionale. 113e Congrès National des Sociétés Savante, Strasbourg, Sciences de la Terre, 37-49

Che X D, Linnen RL, Wang R C, et al (2013) Tungsten solubility in evolved granitic melts: An evaluation of magmatic wolframite. Geochimica et Cosmochimica Acta 106:84–98

Cheilletz A, Archibald D A, Cuney M, Charoy B (1992) Ages 40Ar-39Ar du leucogranite à topaze-lépidolite de Beauvoir et des pegmatites sodolithiques de Chédeville (Nord du Massif Central, France). Signification pétrologique et géodynamique. Comptes Rendus de l'Académie des Sciences Paris, 315, II :329-336

Chicharro E, Martín-Crespo T, Gómez-Ortiz D, López-García J A, Oyarzun R, Villaseca C (2015) Geology and gravity modelling of the Logrosán Sn-(W) ore deposits (Central Iberian Zone, Spain). Ore Geology Reviews, 65:294-307

Chicharro E, Boiron M-C, López-García JÁ, et al (2016) Origin, ore forming fluid evolution and timing of the Logrosán Sn–(W) ore deposits (Central Iberian Zone, Spain). Ore Geology Reviews 72:896–913

Christiansen E H, Sheridan M F, Burt D M (1986) The geology and geochemistry of Cenozoic topaz rhyolite from the western United Stated. Geol. Soc. America Spec. Paper, 205 :1-82

Ciancaleoni L, Marquer D (2006) Syn-extension leucogranite deformation during convergence in the Eastern Central Alps: example of the Novate intrusion. Terra Nova, 18:170-180

Clayton R N (1955) Variations in oxygen isotope abundances in rock minerals. Ph.D. thesis, California Institute of Technology

Clayton R N, Mayeda T K (1963): The use of bromine pentafluoride in the extraction of oxygen from oxides and silicates for isotopic analysis. Geochim. Cosmochim. Ada, 27:43-57

Cochelin B, (2016) Champ de déformation du socle Paléozoïque des Pyrénées (Doctorat). Université de Toulouse, Toulouse.

Cochelin B, Gumiaux C, Chardon D, Denèle Y, Le Bayon B (2018) Multi-scale strainfield analysis using geostatistics: Invertigating the rheological behavior of the hot Variscan crust of the Pyrenees (Axial Zone). Journal of Structural Geology, "from hot to cold" special issue. Doi:10.1016/j.jsg.2018.07.024

Codeço M S, Weis P, Trumbull R B, Pinto F, Lecumberri-Sanchez P, Wilke F D H (2017) Chemical and boron isotopic composition of hydrothermal tourmaline from the Panasqueira W-Sn-Cu deposit, Portugal. Chemical Geology, 468:1–16

Courrioux G, (1983) Exemple de mise en place d'un leucogranite pendant le fonctionnement d'une zone de cisaillement; le granite hercynien de Puentedeume (Galice, Espagne). Bulletin de la Société Geologique de France S7–XXV :301–307. https://doi.org/10.2113/gssgfbull.S7-XXV.3.301

Cuney M, Autran A, (1987) Objectifs généraux du projet GPF Echassières n°1 et résultats essentiels acquis par le forage de 900m sur le granite albitique à topaze-lépidolite de Beauvoir. Géologie de la France, 2-3:7-24

Cuney M, Friedrich M, Blumenfeld P, et al (1990) Metallogenesis in the French part of the Variscan orogen. Part I: U preconcentrations in pre-Variscan and Variscan formations—a comparison with Sn, W and Au. Tectonophysics 177:39–57

Cuney M, Marignac C, Weisbrod A (1992) The Beauvoir topaz-lepidolite albite granite (Massif Central, France); the disseminated magmatic Sn-Li-Ta-Nb-Be mineralization. Economic Geology 87:1766–1794

Cuney M, Alexandrov P, Le Carlier de Veslud C, Cheilletz A, Raimbault L, Ruffet G, Scaillet S (2002) The timing of W-Sn-rare metals mineral deposit formation in the Western Variscan chain in their orogenic setting : the case of the Limousin area (Massif Central, France). Geological Society of London, Special Publications 204:213-228

Cuney M, Barbey P (2014) Uranium, rare metals, and granulite-facies metamorphism. Geosciences Frontiers 1-17

- D -

Darbyshire D P F, Sheperd T J (1985) Chronology of granite magmatism and associated mineralization, SW England. J. geol. Soc. London, 142 :1159-1177

Demange M, Nicolas VA, Soler P, Giouse H (1988) Le gisement tungstifère de Leucamp (Cantal, France): contrôle géologiques et minéralisations. Bulletin de la Société Géologique de France 4:559-570

De San Jose M A, Pieren A P, Garcia-Hidalgo J F, Vilas L, Herranz P, Pelaez J R, Perejon A (1990) Central Iberian Zone. Autochthonous sequences. Ante-Ordovician Stratigraphy. in: Dallmeyer R D, Martinez Garcia E (Eds.), Pre-Mesozoic Geology of Iberia. Springer-Verlag, Berlin, Heidelberg, 147–159

Dias R, Ribeiro A (1995) The Ibero-Armorican arc: a collisional effect against an irregular continent ? Tectonophysics 246:113-128

Diez Balda M A, Vegas R, Gonzalez Lodeiro F, (1990) Central Iberian Zone. Autochthonous sequences. Structure. in: Dallmeyer R D, Martinez Garcia E (Eds.), Pre-Mesozoic Geology of Iberia. Springer-Verlag, Berlin, Heidelberg, 172–188

Dixon A, Cempírek J, Groat L A (2014) Mineralogy and geochemistry of pegmatites on Mount Begbie, British Columbia. The Canadian Mineralogist, 52:129-164

Dominy S C, Camm G S, Bussell M A, Bennett TS (1995) The structure and paragenetic evolution of cassiterite mineralized veins at Rosevale Mine, Zennor, West Cornwall. Proceedings of the Ussher Society 8:374-378

Druguet E, Hutton D H W, (1998) Syntectonic anatexis and magmatism in mid-crustal transpressional shear zone: an example from the Hercynian rocks of the eastern Pyrenees. Journal of Structural Geology, 20:905-916

Dubois J, Marchand J, Bourguignon P (1973) Données minéralogiques sur la série amblygonite-montebrasite. Annales de la Société Géologique de Belgique, 95:285-310

Ducassou C, Poujol M, Ruffet G, Bruguier O, Ballèvre M (2014) Relief variation and erosion of the Variscan belt: detrital geochronology of the Palaeozoic sediments from the Mauges Unit (Armorican Massif, France). Geological Society, London, Special Publications, 405:137–167. https://doi.org/10.1144/SP405.6

Duthou J-L, Pin C (1987) Etude isotopique Rb/Sr de l'apex granitique d'Echassières. Geol. Fr., 2-3:63-67

Duthou J-L, Cantagrel J-M, Didier J, Vialette Y (1984) Paleozoic granitoids from the French Massi Central: age and origin studied by $^{87}Rb/^{87}Sr$ system. Phys Earth Planet. In., 35:131-144

- F -

Falster A U, Simmons Wm B, Webber K L (1997) The origin of evolved LCT-type granitic pegmatites in the Hoskin Lake granite-pegmatite field, Florence Co., Wisconsin. IAVCEI General Assembly, Jan. 1997, Puerto Vallarta, Mexico, Programme, 118

Faure M, Pons J (1991) Crustal thinning recorded by the shape of the Namurian-Westphalian leucogranite in the Variscan belt of the northwest Massif Central. Geology, 19:730-733

Faure M (1995) Late orogenic carboniferous extensions in the Variscan French Massif Central. Tectonics 14:132–153

Faure M, Leloix C, Roig JY (1997) L'évolution polycyclique de la chaîne hercynienne. Bulletin de la Société Géologique de France 168,6:695-705

Faure M, Bé Mézèmé E, Duguet M, Cartier C, Talbot J-Y (2005) Paleozoic tectonic evolution of medio-europa from the example of the french massif central and massif armoricain. J Virtual Explor Electron Edit 19(5):1–26

Faure M, Bé Mézèmé E, Cocherie A, Rossi P, Chemenda A, Boutelier D (2008) Devonian geodynamic evolution of the Variscan Belt, insights from the French Massic Central and Massif Armoricain. Tectonics, 27. doi:10.1029/2007TC002115

Ferreira M P, Macedo C R, Alves E I (1985) A zonalidade interna de um plutonito. Estruturas condicionantes e idades de evoluçào (Plutonio do Fundão, Portugal Central). Memorias e Noticias Publicadas pelo Musell do Laboratorio de Mineralogia e Geologia da Universidade de Coimbra 99:167-186

Förster H-J (2001) The radioactive accessory-mineral assemblage of the Podlesi granite-pegmatite system, western Krušne hory: Implications to intrusion age and magmatic/hydrothermal fluid-rock interaction. In: Breiter K. (ed) Phosphorus- and Fluorine-rich Granites. Abstracts – Excursion guide – Program. Int. Workshop Podlesi, Czech Geol. Surv., Praha, 14–15

Fouillac A M, Rossi P (1991) Near-solidus 18O depletion in a Ta-Nb-bearing albite granite: the Beauvoir granite, France. Economic Geology, 86:1704-1720

Foxford K A, Nicholson R, Polya D A, Hebblethwaite R P B (2000) Extensional failure and hydraulic valving at Minas da Panasqueira, Portugal: evidence from vein spatial distributions, displacements and geometries. Journal of Structural Geology, 22:1065-1086

Franke W, Żelaźniewicz A (2000) The eastern termination of the Variscides: terrane correlation and kinematic evolution. In: Franke W, Haak V, Oncken O, Tanner D (eds) Orogenic processes: quantification and modelling in the Variscan Belt. Geol Soc Lond Spec Pub, 179:63–86

Franke W (2000) The mid-European segment of he Variscides: tectonostratigraphic units, terrane boundaries and plate tectonic evolution. In: Franke W, Haak V, Oncken O, Tanner D (eds) Orogenic processes: quantification and modelling in the Variscan belt. Geol Soc Lond Spec Publ 179: 35–61

Franke W, Żelaźniewicz A (2002) Structure and evolution of the Bohemian Arc. In: Winchester J, Pharaoh TC, Verniers J (eds) Palaeozoic amalgamation of central Europe. Geol Soc Lond Spec Pub, 201: 279–294

Franke W (2014) Topography of the Variscan orogen in Europe: failed-not collapsed. Int. J. Earth Sci (Geol Rundsch), 103:1471-1499

- G -

Gapais D, Lagarde J-L, Le Corre C, Audren C, Jégouzo P, Casas Saintz A, Van Den Driessche J (1993) La zone de cisaillement de Quiberon : témoin d'extension de la chaîne varisque en Bretagne méridionale au Carbonifère. Comptes Rendus de l'Académie des Sciences - Series IIA - Earth and Planetary Science, 316:1123–1129

Gapais D, Brun J-P, Gumiaux C, Cagnard F, Ruffet G, Veslud C L C D (2015) Extensional tectonics in the Hercynian Armorican belt (France). An overview. BSGF, 186:117–129. https://doi.org/10.2113/gssgfbull.186.2-3.117

Giuliani G, (1985) Le gisement de tungstène de Xihuashan (Sud-Jiangxi, Chine): Relations granites, altérations deutériques-hydrothermales, minéralisations. Mineral. Deposita 20, 107–115.

Goldmann S, Melcher F, Gäbler H-E, Dewaele S, De Clercq F, Muchez P (2013) Mineralogy and Trace Element Chemistry of Ferberite/Reinite from Tungsten Deposits in Central Rwanda. Minerals, 3:121-144

Gómez-Ortiz D, Agarwal B N P, Tejero R, Ruiz J (2011) Crustal structure from gravity signatures in the Iberian Peninsula. Geological Society of America, 123:1247-1257

Guillen A, Calcagno P, Courrioux G, Joly A, Ledru P (2008) Geological modelling from field data and geological knowledge: part II. Modelling validation using gravity and magnetic data inversion. Phys. Earth Planet. Inter 171 :158-169

Gumiaux C, Gapais D, Brun J-P (2003) Geostatistics applied to best-fit interpolation of orientation data. Tectonophysics, 376:241-259

Gutierrez Marco J-C, de San Jose M A, Pieren A P (1990) Central Iberian Zone. Autochthonous sequences. Post-Cambrian Palaeozoic Stratigraphy. in: Dallmeyer R D, Martinez Garcia E (Eds.), Pre-Mesozoic Geology of Iberia. Springer-Verlag, Berlin, Heidelberg, 160–171

- H -

Haapala I, Lukkari S (2005) Petrological and geochemical evolution of the Kymi stock, a topaz granite cupola within the Wiborg rapakivi batholith, Finland. Lithos, 80:347-362

Halter W E, William-Jones A E (1999) Application of Topaz-Muscovite F-OH exchange as a geothermeter. Economic Geology, 94:1249-1258

Hammer S (1939) Terrain corrections for gravimeter stations. Geophysics, 4:184-194

Harlaux M, Marignac C, Cuney M, Mercadier J, Magott R, Mouthier B (2015) Nb-ti-y-hree-w-u Oxide Minerals with Uncommon Compositions Associated with the Tungsten Mineralization in the Puy-les-vignes Deposit (Massif Central, France): Evidence For Rare-metal Mobilization By Late Hydrothermal Fluids with a Peralkaline Signature. The Canadian Mineralogist 53:653–672

Harlaux M, Romer R, Mercadier J, Morlot C, Marignac C, Cuney M (2017) 40 Ma of hydrothermal W mineralization during the Variscan orogenic evolution of the French Massif Central revealed by U-Pb dating of wolframite. Mineralium Deposita 1-31

Harlaux M, Mercadier J, Marignac C, Peiffert C, Cloquet C, Cuney M (2018) Tracing metal sources in peribatholitic hydrothermal W deposits based on the chemical composition of wolframite: The example of the Variscan French Massif Central. Chemical Geology

Harris N B W, Inger S (1992) Trace element modelling of pelite-derived granites. Contrib. Mineral. Petrol., 110:46-56

Harris N B W, Ayres M, Massey J (1995) Geochemistry of granitic melts produced during the incongruent melting of muscovite: Implications for the extraction of Himalayan leucogranite magmas. Journal of Geophysical Research, 100, B8:14,767-15,777

Heinrich CA (1990) The chemistry of hydrothermal tin (-tungsten) ore deposition. Economic Geology 85:457–481

Hofmann M, Linnemann U, Gerdes A, Ullrich B, Schauer M (2009) Timing of dextral strike-slip processes and basement exhumation in the Elbe Zone (Saxo-Thuringian Zone): the final pulse of the Variscan Orogeny in the Bohemian Massif constrained by LA-SF-ICP-MS U-Pb zircon data. Geological Society, London, Special Publications, 327:197-214

Holder M T, Leveridge B E (1986) Correlation of the Rhenohercynian Variscides. Journal of the Geological Society, London, 143:141-147

Hollinger P, Cuney M, Friedrich M, Turpin L (1986) Géochimie et géochronologie isotopiques. Age Carbonifère de l'unité Brame du complexe peralumineux de Saint-Sylvestre (N.O. Massif Central) défini par les données isotopiques U-Pb sur zircon et monazite. C. R. Acad. Sc. Paris, 303, II, 14:1309-1314

Holten T, Jamtveit B, Meakin P, Cortini M, Blundy J, Austrheim H (1997) Statistical characteristics and origin of oscillatory zoning in crystals. American Mineralogist, 82:596-606

Holtz F, Dingwell D B, Behrens H (1993) Effects of F, B2O3 and P2O5 on the solubility of water in haplogranite melts compared to natural silicate melts. Contributions to Mineralogy and Petrology, 113:492–501

Hosking K F G, Polkinghorne J P R (1954) The significance of the variable iron content of the "Wolframites" of the west of England. Royal Geological Society of Cornwall, 18.

Hu S, Sun M, Yan Z, Xu J, Cao X, Ye Y (1984) An important metallogenetic model for W, Sn and rare granitophile elements ore deposits related to metasomatically altered granites: Geology of Granites and Their Metallogenetic Relations. International Symposium, Nanjing University, Nanjing, October 26-30, 1982, Proceedings, 519-537

Hulsbosch N (2019 in press) Nb-Ta-Sn-W distribution in granite-related ore systems: fractionation mechanisms and examples from the Karagwe-Ankole Belt of Central Africa. In: Decrée S, Robb L (Eds.), Ore Deposits Origin Exploration and Exploitation. Wiley

Hutton D H W (1988) Granite emplacement mechanisms and tectonic controls: interferences from deformation studies. Transaction of the Royal Society of Edinburgh; Earth Sciences, 19 :245-255

- I -

Icenhower J, London D (1995) An experimental study of element partitioning among biotite, muscovite, and coexisting peraluminous silicic melt at 200 MPa (H2O). Am. Mineral. 80:1229–1251

Inverno C, Ribeiro M L (1980) Fracturação e cortejo filoneano nas Minas da Argemela (Fundão). Commission Serviços Geológicos de Portugal 66:185-193

Inverno C (1998) Comments on the new findings on the geology, geochemistry and mineralization of Argemela, central Portugal. Commission Instituto Geológico e Mineiro 85:73-79

- J -

Jacquot T, Gagny C (1987) Pétrologie structurale du granite de Beauvoir : données et interprétation à son niveau apical. Géologie de la France, 2-3:57-62

Jahns R H, Burnham C W (1969) Experimental studies of pegmatite genesis: I. A model for the derivation and crystallization of granitic pegmatites. Econ. Geol., 64:843-864

Jégouzo P (1980) The South Armorican Shear Zone. Journal of Structural Geology, Shear zones in rocks, 2:39–47. https://doi.org/10.1016/0191-8141(80)90032-2

Jones K A, Brown M (1990) High-temperature “clockwise” P-T paths and melting in the development of regional migmatites: an example from southern Brittany, France. Journal of Metamorphic Geology, 8:551–578. https://doi.org/10.1111/j.1525-1314.1990.tb00486.x

- K -

Kaeter D, Barros R, Menuge J F, Chew D M (2018) The magmatic-hydrothermal transition in rare-element pegmatites from the southeast Ireland: LA-ICP-MS chemical mapping of muscovite and columbite-tantalite. Geochemica et Cosmochemica Acta, 240:98-130

Kelly W C, Rye R O (1979) Geologic, fluid inclusion, and stable isotope studies of the tin-tungsten deposits of Panasqueira, Portugal. Economic Geology 74:1721–1822

Kesraoui M, Marignac C, Verkaeren J (2000) L'évolution tardi-magmatique des granites à métaux rares : l'exemple de la coupole de Tin-Amzi (Hoggar-Algérie). Bulletin de la Société Géologique de l'Algérie, 11, 2 :195-216

Kinnaird J, Bowden P, Ixer R A, Odling N W A (1985) Mineralogy, geochemistry and mineralization of the Ririwai complex, northern Nigeria. Journal of African Earth Sciences, 3:185-222

Kontak D J (1990) The East Kemptville topaz-muscovite leucogranite, Nova Scotia; I. Geological setting and whole-rock geochemistry. The Canadian Mineralogist, 28, 4:787-825

Kontak D (2006) Nature and origin of an LCT-suite pegmatite with late-stage sodium enrichment, Brazil Lake, Yarmouth County, Nova Scotia. I. Geological setting and petrology. The Canadian Mineralogist, 44:563-598

Konzett J, Hauzenberger C, Ludwig T, Stalder R (2018) Anatectic granitic pegmatites from the eastern Alps: a case study of variable rare metal enrichment during high-grade regional metamorphism. II. Pegmatite staurolite as an indicator of anatectic pegmatite parent melt formation - a field and experiment study. The Canadian Mineralogist, 56:603-624

Korges M, Weis P, Lüders V, Laurent O (2018) Depressurization and boiling of a single magmatic fluid as a mechanism for tin-tungsten deposit formation. Geology, 46:75–78

Kovalenko V I, Kuz'min M I, Letnikov F A (1970) Magmatic origin of lithium and fluorine bearing rare metal granites: Doklady Akademii Nauk SSSR, Earth Sciences Section, 190:189-192

Kovalenko V I, Kovalenko N I (1976) Ongonites (topaz bearing quartz keratophyre) – subvolcanic analogues of rare metal Li-F granites: Nauka, Moskva, 124 p. (in Russian)

Kovalenko V I, Tsaryeva G M, Goreglyad A V, Yarmolyuk V V, Troitsky V A, Hervig R L, Farmer G L (1995) The peralkaline granite-related Khaldzan-Buregtey rare metal (Zr, Nb, REE) deposit, western Mongolia. Economic Geology, 90:530-547

Kroner U, Hahn T, Romer RL, Linnemann U (2007) The Variscan orogeny in the Saxo-Thuringian Zone—Heterogeneous overprint of Cadomian/Paleozoic Peri-Gondwana crust. In: Linnemann U, Nance RD,

Kraft P, Zulauf G (eds) The evolution of the Rheic Ocean: from Avalonian-Cadomian active margin to Alleghenian- Variscan collision. Geol Soc Am Spec Pap, 423:153–172

Kroner U, Romer R L (2013) Two plates - Many subduction zones: The Variscan orogeny reconsidered. Gondwana Research, 24:298-329

- L -

Lagarde J L, Capdevila R, Fourcade S (1992) Granites et collision continentale ; l'exemple des granitoides carboniferes dans la chaine hercynienne ouest-europeenne. Bulletin de la Société Géologique de France, 163:597–610

Lagarde J-L, Dallain C, Ledru P, Courrioux G (1994) Strain patterns within the late Variscan granitic dome of Velay, French Massif Central. Journal of Structural Geology, 16:839–852. https://doi.org/10.1016/0191-8141(94)90149-X

Lajaunie C, Courrioux G, Manuel L (1997) Foliation fields and 3D cartography in geology: principles of a method based on potential interpolation. Math. Geol. 29:571-584

LeBoutillier N G (2002) The tectonics of Variscan magmatism and mineralisation in South West England. Thesis, University of Exeter

Lehmann B (1990) Metallogeny of Tin

Lecumberri-Sanchez P, Vieira R, Heinrich C A, Pinto F, Wälle M (2017) Fluid-rock interaction is decisive for the formation of tungsten deposits. Geology, 45:579–582

Ledru P, Lardeaux J-M, Santallier D, Autran A, Quenardel J-M, Floc'h J-P, Lerouge G, Maillet N, Marchand J, Ploquin A (1989) Où sont les nappes dans le Massif central français ? Bull. Soc. Géol. France, 3 :605-618

Lerouge C, Bouchot V, Guerrot C (2000) Fluids and the W (+/-As, Au) ore deposits of the Enguilès-Leucamp District, La Châtaigneraie, French Massif Central. Journal of Geochemical Exploration, 69-70:343-347

Leutwein F (1952) Die Wolframit Grappe. Freiberg Forschungsh, C3:8-19

Linnen R L, Pichavant M, Holtz F, Burgess S (1995) The effect of fo2 on the solubility, diffusion, and speciation of tin in haplogranitic melt at 850°C and 2 kbar. Geochimica et Cosmochimica Acta 59:1579–1588

Linnen R L, Keppler H (1997) Columbite solubility in granitic melts: consequences for the enrichment and fractionation of Nb and Ta in the Earth's crust. Contrib Mineral Petrol 128:213–227

Linnen R L (1998) The solubility of Nb-Ta-Zr-Hf-W in granitic melts with Li and Li + F; constraints for mineralization in rare metal granites and pegmatites. Economic Geology, 93:1013–1025

Linnen R L, Cuney M (2005) Granite-related rare-element deposits and experimental constraints on Ta-Nb-W-Sn-Zr-Hf mineralization, in Linnen RL and Samson IM, eds., rare-element geochemistry and mineral deposits. In: Geological Association of Canada, GAC, Short CourseLoh, S.E., Wise, W.S., 1976. Synthesis and fluorine-hydroxyl exchange in the amblygonite series. Cananadian Mineralogist 14, 357-363

Llorens T, Moro M C (2012a) Oxide minerals in the granitic cupola of the Jálama Batholith, Salamanca, Spain. Part I: accessory Sn, Nb, Ta and Ti minerals in leucogranites, aplites and pegmatites. Journal of Geosciences 57:25

Llorens T, Moro M C (2012b) Oxide minerals in the granitic cupola of the Jálama Batholith, Salamanca, Spain. Part II: Sn, W and Ti minerals in intra-granitic quartz veins. Journal of Geosciences 57:155

London D, Černȳ P, Loomis J L, Pan J J (1990) Phosphorous in alkali feldspars of rare-elemetn granitic pegmatites. Canadian Mineralogist, 28:771-786

London D, Wolf M B, George B M VI, Gallego Garrido M (1999) Experimental silicate-phosphate equilibria in peraluminous granitic magmas, with a case study of the Alburquerque Batholith at Tres Arroyos, Badajoz, Spain. Journal of Petrology, 40,1:215-240

London D (2015) Reply to Thomas and Davidson on "A petrologic assessment of internal zonation in granitic pegmatites" (London 2014a). Lithos, 212-215:469-484

London D (2018) Ore-forming processes within granitic pegmatites. Ore Geology Reviews, 101:349-383

López-Moro F J, García Polonio F, Llorens González T, Sanz Contreras J L, Fernández Fernández A, Candelas Moro Benito M (2017) Ta and Sn concentration by muscovite fractionation and degassing in a lens-like granite body: The case study of the Penouta rare-metal albite granite (NW Spain). Ore Geology Reviews, 82:10-30

Lotout C, Pitra P, Poujol M, Anczkiewicz R, Van Den Driessche J (2018) Timing and duration of Variscan high-pressure metamorphism in the French Massif Central: A multimethod geochronological study

from the Najac Massif. Lithos, 308–309, 381–394. https://doi.org/10.1016/j.lithos.2018.03.022

Luth W C (1969) The system $NaAlSi_3O_8$-SiO_2 and $KAlSi_3O_8$ to 20kb and the relationship between H_2O content pH_2O and p_{total} in granitic magmas. Am. J. Sci. 267A:325-341

- M -

Manning D A C, Hill P I (1990) The petrogenetic and metallogenetic significance of topaz granite from the Southwest England orefield: Geological Society of America Special Paper, 246:51-69

Marignac C, Cuney M (1999) Ore deposits of the French Massif Central: insight into the metallogenesis of the Variscan collision belt. Mineralium Deposita 34:472–504

Marignac C, Cathelineau M (2009) The nature of ore-forming fluids in peri-batholitic Sn-W deposits and a classification. In: Smart science for exploration and mining, Proceedings Xth Biennial SGA Meeting, Townsville 245–247

Martelet G, Debeglia N, Brun J-P (2002) Updating and validating the French gravity terrain corrections out to a distance of 167 km. Comptes Rendus Geoscience, 334:449-454

Martínez Catalán J R, Fernández-Suárez J, Jenner J, Belousova G A, Díes Montes A (2004) Provenance constraints from detrital zircon U-Pb ages in the NW Iberian Massif: implications for Paleozoic plate configuration and Variscan evolution. Journal of the Geological Society, London, 2:63-68

Martínez Catalán J R (2011) Are the oroclines of the Variscan belt related to late Variscan strike-slip tectonics? Terra Nova 23:241–247

Martínez Catalán J R, Arenas R, Días García F, González Cuadra P, Gómez-Barreiro J, Abati J, Castiñeiras P, Fernández-Suárez J, Sánchez Martínez S, Andonaegui P, González Clavijo E, Díes Montes A, Rubio Pascual F J, Valle Aguado B (2007) Space and tome in the tectonic evolution of the northwestern Iberian Massif: Implications ofr the Variscan belt. The Geological Society of America, 200:403-423

Martínez-Moreno F J, Galindo-Zaldívar J, Pedrera A, Teixidó T, Peña J A, Gonzáles-Castillo L (2015) Regional and residual anomaly separation in microgravity maps for cave detection: the case study of Gruta de las Maravilhas (SW Spain). Journal of Applied Geology, 114:1-11

Martínez Poyatos D, Carbonell R, Palomeras I, Simancas J F, Ayarza P, Martí D, Azor A, Jabaloy A, González Cuadra P, Tejero R, Martín Parra L M, Matas J, González Lodeiro F, Pérez-Estaún A, García Lobón J L, Mansilla L (2012) Imaging the crustal structure of the Central Iberian Zone (Variscan Belt): The ALCUDIA deep seismic reflection transect: ALCUDIA DEEP SEISMIC REFLECTION TRANSECT. Tectonics 31. https://doi.org/10.1029/2011TC002995

Martínez Poyatos D, Nieto F, Azor A, Simancas J F (2001) Relationships between very low-grade metamorphism and tectonic deformation: examples from the southern Central Iberian Zone (Iberian Massif, Variscan Belt). Journal of the Geological Society, 158:953–968. https://doi.org/10.1144/0016-764900-206

Mateus A et al. (2018) The Panasqueira lode system ; new insights from detailed petrography and mineral chemistry. NewOres Porto Meeting

Matte P (1986) La chaine varisque parmi les chaines paleozoiques peri atlantiques, modele d'evolution et position des grands blocs continentaux au Permo-Carbonifere. BSGF, II :9–24. https://doi.org/10.2113/gssgfbull.II.1.9

Matte P (1991) Accretionary history and crustal evolution of the Variscan belt in Western Europe. Tectonophysics, 196:309–337. https://doi.org/10.1016/0040-1951(91)90328-P

Matte P (2001) The Variscan collage and orogeny (480–290 Ma) and the tectonic definition of the Armorica microplate: a review. Terra Nova 13(2):122–128

Matte P (2007) Variscan thrust nappes, detachments, and strike-slip faults in the French Massif Central: interpretation of the lineations. In: Hatcher R D Jr, Carslon M P, McBride J H, Martinez- Catalan J R (eds) 4D framework of continental crust. Geol Soc Am Mem, 200:391–402

McCuaig T C, Beresford S, Hronsky J (2010) Translating the mineral systems approach into an effective exploration targeting system. Ore Geology Reviews, Mineral Prospectivity Analysis and Quantitative Resource Estimation, 38:128–138

McCuaig T C, Hronsky J M A (2014) The mineral system concept: the key to exploration targeting. SEG Special Publication, 18:153-175

Meireles C, Sequeira A J D, Castro P, Ferreira N (2013) New data on the lithostratigraphy of Beiras Group (Schist Greywacke Complex) in the region of Gois-Arganil-Pampilhosa da Serra (Central Portugal). Cadernos Lab. Xeoloxico de Laxe, 37:105–124

Melleton J, Gloaguen E, Frei D (2011) Rare-elements (Li-Be-Ta-Sn-Nb) magmatism in the European Variscan belt, a review. 13th SGA biennial Meeting 2:807-810

Michaud J A-S, and Pichavant M (2019) The H/F ratio as an indicator of contrasted wolframite deposition mechanisms. Ore Geology Reviews, 104:266-272. https://doi.org/10.1016/j.oregeorev.2018.10.015

Miller J A, Mohr P A (1964) Potassium-argon measurements on the granites and some associated rocks from southwest England. Geol. J., 4, 1:105-126

Mingram B, Kröner A, Hegner, Krentz O (2004) Zircon ages, geochemistry, and Nd isotopic systematics of pre-Variscan orthogneisses from the Erzgebirge, Saxony (Germany), and geodynamic interpretation. Int J Earth Sci (Geol Rundsch), 93:706-727

Monnier L, Lach P, Salvi S, Melleton J, Bailly L, Béziat D, Monnier Y, Gouy S (2018) Quartz trace-element composition by LA-ICP-MS as proxy for granite differentiation, hydrothermal episodes, and related mineralization: The Beauvoir granite (Echassières district), France. Lithos, 320-321:355-377

Moore F, Howie R A (1978) On the application of the hübnerite:ferberite ratio as a geothermometer. Mineral. Deposita, 13:391–397

Müller A, Seltmann R (1999) The genetic significance of snowball quartz in high fractionated tin granites of the Krušne Hory/Erzgebirge. In Mineral deposits: processes to processing 1:409-412

Müller A, Kronz A, Breiter K (2002) Trace elements and growt patterns in quartz: a fingerprint of theevolution of the subvolcanic Podlesí Granite System (Krušné hory Mts., Czech Republic). Bulletin of the Czech Geological Survey 77:135-145

Müller A, Williamson B J, Smith M (2005) Origin of quartz cores in tourmaline from Roche Rock, SW England. Mineralogical Magazine, 69, 4:381-401

Müller A, Seltmann R, Halls C, Siebel W, Dulski P, Jeffries T, Spratt J, Kronz A (2006) The magmatic evolution of the Land's End pluton, Cornwall, and associated pre-enrichment of metals. Ore Geology Reviews, 28-329-367

Müller A, Leiss B, Ullemeyer K, Breiter K (2011) Lattice-preferred orientations of late-Variscan granito%ids

derived from neutron diffraction data: implications for magma emplcament mechanisms. Int. J. Earth Sci. (Geol Rundsch), 100:1515-1532

Müller A, Herklotz G, Giegling H (2018) Chemistry of quartz related to the Zinnwald/Cínovec Sn-W-Li greisen-type deposit, Eastern Erzgebirge, Germany. Journal of Geochemical Exploration, 190:357-373

Myers J S (1975) Cauldron subsidence and fluidization: mechanisms of intrusion of the Coastal Batholith of Peru into its own volcanic ejecta. Geological Society of America Bulletin, 86:1209-1220

- N -

Nabelek P I, Russ-Nabelek C, Denison J R (1992a) The generation and crystallization conditions of the Proterozoic Harney Peak Leucogranite, Black Hills, South Dakota, USA: Petrologic and geochemical constraints. Contrib. Mineral. Petrol., 110:173-191

Nabelek P I, Russ-Nabelek C, Haeussler G T (1992b) Stable isotope evidence for the petrogenesis and fluid evolution in the Proterozoic Harney Peak leucogranite, Black Hills, South Dakota. Geochim. Cosmochim. Acta, 56:403-417

Neiva A M R (1984) Geochemistry of tin-bearing granitic rocks. Chemical Geology 43:241–256

Neiva A M R (1996) Geochemistry of cassiterite and its inclusions and exsolution products from tin and tungsten deposits in Portugal. The Canadian Mineralogist 34:745–768

Neiva A M R (2008) Geochemistry of cassiterite and wolframite from tin and tungsten quartz veins in Portugal. Ore geology reviews 33:221–238

Noronha F, Doria A, Dubessy J, Charoy B (1992) Characterization and timing of the different types of fluids present in the barren and ore-veins of the W-Sn deposit of Panasqueira, Central Portugal. Mineral. Deposita, 27:72–79

Noronha F, Ribeiro M A, Almeida A, Dória A, Guedes A, Lima A, Martins H C, Sant'Ovaia H, Nogueira P, Martins T, Ramos R, Vieira R (2013) Jazigos filonianos hidrotermais e aplitopegmatíticos espacialmente associados a granitos (Norte Portugal). in: Geologia de Portugal Vol. I, Geologia Pré-Mesozoica de Portugal (Eds) Dias R, Araùjo A, Terrinha P, Kulberg J C C K, Escolar E Editora

Noyé F, Weisbrod A (1988) Les indices stanno-wolframifères de Saint-Mélany (Cévennes médianes, Ardèche,

Massif Central Français). Bulletin du BRGM 158:175–194

- O -

Oelsner O (1944) Über arzebirge Wolframite: Ber. Freib.Geol. Ges., 20:44-49

Olivier P, Améglio L (2002) Structure et mise en régime décrochant puis rotation tardi-magmatique des plutons granitiques hercyniens du Veinazès et de Marcolès (Châtaigneraie, Massif Central Français). Bulletin de la Société Géologique de France 173 :207-218

O'Neil J R, Taylor H P Jr (1969) Oxygen isotope equilibrium between muscovite and water: Jour. Geophys. Research, 74:6012-6022

Oosterom M G, Bussink R W, Vriend S P (1984) Lithogeochemical studies of aureoles around the Panasqueira tin-tungsten deposit, Portugal. Mineralium Deposita 19:283-288

Ordóñez Casado, B., Gebauer, D., Schäfer, H.J., Ibarguchi, J.I.G., Peucat, J.J., 2001. A single Devonian subduction event for the HP/HT metamorphism of the Cabo Ortegal complex within the Iberian Massif. Tectonophysics 332, 359–385. https://doi.org/10.1016/S0040-1951(00)00210-9

- P -

Paquette J-L, Ballèvre M, Peucat J-J, Cornen G (2017) From opening to subduction of an oceanic domain constrained by LA-ICP-MS U-Pb zircon dating (Variscan belt, Southern Armorican Massif, France). Lithos, 294–295:418–437. https://doi.org/10.1016/j.lithos.2017.10.005

Paterson S R, Schimdt K L (1999) Is there a close spatial relationship between faults and plutons? Journal of Structural Geology, 21:1131-1142

Patiño Douce A E, Harris N (1998) Experimental constraints on Himalayan anatexis. Journal of Petrology, 39:689-710

Patiño Douce A E (1999) What do experiment tell us about relative contributions of crust and mantle to the origin of granitic magmas ? Geological Society, London, Special Publications, 168:55-75

Pereira E, Ribeiro A, Meireles C (1993) Cisalhamentos hercínicos et control das mineralizações de Sn-W, Au

e U na zona Centro-Ibérica, em Portugal. Cuaderno Lab. Xeolóxico de Laxe 18 :89-119

Petford N, Cruden A R, McCaffrey K J W, Vigneresse JL (2000) Granite magma formation, transport and emplacement in the Earth's crust. Nature, 408:669-673

Pichavant M (1981) An experimental study of the effect of boron on a water saturated haplogranite at 1Kbar vapour pressure. Contributions to Mineralogy and Petrology, 76, 4:430-439

Pichavant M, Boher M, Stenger JF, Aïssa M, Charoy B (1987a) Relations de phase des granites de Beauvoir à 1 et 3kbar en conditions de saturation en H_2O. Géologie de la France, 1:77-85

Pichavant M (1987b) The Macusani glasses, SE Peru : evidence of chemical fractionation in peraluminous magmas. Magmatic Process : Physicochemical Principles. Geochem. Soc. Spec. Publ., 1:359–373.

Pichavant M, Manning, D (1984) Petrogenesis of tourmaline granites and topaz granites; the contribution of experimental data. Physics of the Earth and Planetary Interiors, 35:31-50

Pichavant M, Kontak D J, Valencia Herrera J, Clark A H (1988a) The Miocene-Pliocene Macusani Volcanics, SE Peru. I. Mineralogy and magmatic evolution of a two-mica aluminosilicate-bearing ignimbrite suite. Contrib. Mineral Petrol., 100:300-324

Pichavant M, Villaros A, Deveaud S, Scaillet B, Lahlafi M (2016) The influence of Redox state on mica crystallization in leucogranitic and pegmatitic liquids. The Canadian Mineralogist, 54, 3:559-581

Pillet D, Chevenoy M, Bélanger M (1992) Pétrologie du granite peralcalin du lac Brisson, Labrador central, Nouveau-Québec. 1. Mode de mise en place et évolution chimique. Revue Canadienne des Sciences de la Terre, 29:353-372

Pin C, Duthou J-L (1990) Sources of Hercynian granitoids from the French Massif Central: Interferences from Nd isotopes and consequences for crustal evolution. Chemical Geology, 83:281-296

Pitra P, Ballèvre M, Ruffet G (2010) Inverted metamorphic field gradient towards a Variscan suture zone (Champtoceaux Complex, Armorican Massif, France). Journal of Metamorphic Geology, 28:183–208. https://doi.org/10.1111/j.1525-1314.2009.00862.x

Plimer I R (1987) Fundamental parameters for the formation of granite-related tin deposits. Geol. Rundschau 76/1:23-40

Poitrenaud T (2018) Le gisement périgranitique à tungstène et or de Salau (Pyrénées, France). Histoire polyphasée d'un système minéralisé varisque. Thèse, Univ. Orléans, 487 p.

Pokrovski GS, Schott J (1998a) Thermodynamic properties of aqueous Ge (IV) hydroxide complexes from 25 to 350 °C: Implications for the behavior of germanium and the Ge / Si ratio in hydrothermal fluids. Geochim Cosmochim Acta 62:1631−1642

Pokrovski GS, Schott J (1998b) Experimental study of the complexation of silicon and germanium with aqueous organic species: Implications for germanium and silicon transport and Ge / Si ratio in natural waters. Geochim Cosmochim Acta 62:3413−3428

Pollard P J, Pichavant M, Charoy B (1987) Contrasting evolution of fluorine- and boron-rich tin systems. Mineralium Deposita, 22, 4:315-321

Polya D A, Foxford K A, Stuar, F, Boyce A, Fallick A E (2000) Evolution and paragenetic context of low δD hydrothermal fluids from the Panasqueira W-Sn deposit, Portugal: new evidence from microthermometric, stable isotope, noble gas and halogen analyses of primary fluid inclusions. Geochimica et Cosmochimica Acta, 64:3357–3371

Poutiainen M, Scherbakova T F (1998) Fluid and melt inclusion evidence for the origin of idiomorphic quartz crystals in topaz-bearing granite from the Salmi batholith, Karelia, Russia. Lithos, 44:141-151

Pownall J M, Waters D J, Searle M P, Shail R K, Robb L J (2013) Shallow laccolithic emplacement of the Land's End and Tregonning granites, Cornwall, UK: Evidence from aureole field relations and P-T modeling of cordierite-anthophyllite hornfels. Geological Society of America, 1467-1504

- R -

Raimbault L (1987) Genèse des granites à métaux rares : Revue comparative des modèles géochimiques. Géologie de la France, 3 101-108

Raimbault L, Charoy B, Cuney M, Pollard P J (1991) Comparative geochemistry of Ta-bearing granites. In: Source, Transport and Deposition of Metals (eds.) Pagel & Leroy, 793-796

Raimbault L, Cuney M, Azencott C, Duthou J-L, Joron J L (1995) Geochemical evidence for a multistage magmatic genesis of Ta-Sn-Li mineralization in the granite at Beauvoir, French Massif Central. Economic Geology, 90:548–576

Raimbault L (1998) Composition of complex lepidolite-type granitic pegmatites and of constituent columbite-

tantalite, Chedeville, Massif Central, France. The Canadian Mineralogist, 36:563–583

Raimbault L, Burnol L (1998) The Richemont rhyolite dyke, Massic Central, France: a subvolcanic equivalent of rare-metal granites. The Canadian Mineralogist, 36:265-282

Ramboz C, Schnapper D, Dubessy J (1985) The P-V̄-T-X-f O2 evolution of H2O-CO2-CH4-bearing fluid in a wolframite vein: Reconstruction from fluid inclusion studies. Geochimica et Cosmochimica Acta, 49:205–219

Ramsay J G, Huber M I (1983) The techniques of Modern Structural Geology, Vol. 1: Strain Analysis. Academic Press London, 307pp

Renno A (1997) Zur Petrogenese der Albitgranite von Abu Dabbab und Nuweibi, Central Eastern Desert, Ägypten. Unpublished PhD Thesis, TechnischeUniversität Berlin, Berlin, 216 p.

Ribeiro A, Pereira E, Dias R (1990) Central Iberian Zone. Allochthonous sequences. Structure in the Northwest of the Iberian Peninsula. in: Dallmeyer R D, Martinez Garcia E (Eds.), Pre-Mesozoic Geology of Iberia. Springer-Verlag, Berlin, Heidelberg, 220–236

Ribeiro R F (2017) Gravimetric modelling and Geological interpretation of Argemela-Panasqueira area. MSc, Faculdade de Ciências do Porto

Rickers K, Thomas R, Heinrich W (2006) The behavior of trace elements during the chemical evolution of the H_2O-, B-, and F-rich granite–pegmatite–hydrothermal system at Ehrenfriedersdorf, Germany: a SXRF study of melt and fluid inclusions. Mineralium Deposita 41:229–245

Roda E, Pesquera A, Velasco F, Fontan F (1999) The granitic pegmatites of the Fregeneda area (Salamanca, Spain): characteristics and petrogenesis. Mineral. Mag., 63:535-556

Roda-Robles E, Villaseca C, Pesquera A, Gil-Crespo P P, Vieira R, Lima, A, Garate-Olave I (2018) Petrogenetic relationships between Variscan granitoids and Li-(F-P)-rich aplite-pegmatites in the Central Iberian Zone: Geological and geochemical constraints and implications for other regions from the European Variscides. Ore Geology Reviews, 95:408-430

Roger F, Matte P (2005) Early Variscan HP metamorphism in the western Iberian Allochthon—A 390 Ma U–Pb age for the Bragança eclogite (NW Portugal). Int J Earth Sci (Geol Rundsch), 94:173–179. https://doi.org/10.1007/s00531-005-0466-3

Rolin P, Marquer D, Cartannaz C, Rossi P (2014) Carboniferous magmatism related to progressive pull-apart opening in the western French Massif Central. Bull. Soc. Géol. France, 185, 3:171-189

Román-Berdiel T, Gapais D, Brun JP (1997) Granite intrusion along strkie-slip zones in experiment and nature. American Journal of Science, 297:651-678

Romão J, Ribeiro A, Pereira E, Fonseca P, Rodrigues J, Mateus A, Noronha F, Dias R (2009) Interplate versus intraplate strike-slip deformed belts: examples from SW Iberia Variscides. Trabajos de Geologia, Universidad de Oviedo, 29:671–677

Romer R L, Kroner U (2016) Phanerozoic tin and tungsten mineralization—tectonic controls on the distribution of enriched protoliths and heat sources for crustal melting. Gondwana Research 31:60–95

Rossi P, Cocherie A, Meyer G, Fouillac A M, Autran A (1988) Metallogenic W and Sn granites: genesis and main distinguishing features. In: Boissonna Js, Omenetto P, eds., Mineral deposits within the European community: Berlin, Springer-Verlag, 3-28

Rye R O, Lufkin J L, Wasserman M D (1990) Genesis of the rhyolite-hosted tin ocurrences in the black range, New Mexico, as indicated by stable isotope studies. Geological Society of America Special Paper, 246:233– 250

- S -

Sánchez Martínez S, Arenas R, García F D, Catalán J R M, Gómez-Barreiro J, Pearce J A (2007) Careón ophiolite, NW Spain: Suprasubduction zone setting for the youngest Rheic Ocean floor. Geology, 35:53–56. https://doi.org/10.1130/G23024A.1

Sant'Ovaia H, Olivier P, Ferreira N, Noronha F, Leblanc D (2010) Magmatic structures and kinematics emplacement of the Variscan granites from Central Portugal (Serra da Estrela and Castro Daire areas). Journal of Structural Geology, 32:1450-1465

Scaillet B, Pichavant M, Roux J (1995) Experimental crystallization of leucogranite magmas. Journal of Petrology, 36, 3:663-705

Scaillet S, Cheilletz A, Cuney M, Farrar E, Archibald DA (1996) Cooling pattern and mineralization history of the Saint-Sylvestre and western Marche leucogranite pluton, French Massif Central : I. $^{40}Ar/^{39}Ar$

isotopic constraints. Geochimica et Cosmochimica Acta 60:4653-4671

Scaillet S, Cuney M, Le Carlier de Veslud C, Cheilletz A, Royer J J (1996) Cooling pattern and mineralization history of the Saint-Sylvestre and western Marche leucogranite pluton, French Massif Central : II. Thermal modelling and implications for the mechanisms of uranium mineralization. Geochimica et Cosmochimica Acta 60:4673-4688

Schmitt A K, Emmermann R, Trumbull R B, Bühn B (2000) Petrogenetic aspects of metalumi-nous and per-alkaline granites in the Brandberg anorogenic complex, Namibia: Evidence for major mantle contribution. J. Petrol., 41:1207-1239

Sheppard S M F (1977) The Cornubian batholith, S.W. England: D/H and 180/16O studies of kaolinite and other alteration minerals. Geol. Soc, 133:573-591

Sheppard S M F (1986) Characterization and isotopic variations in natural waters. Rev. Mineral., 16:165–184

Shieh Y-N, Zhang G-X (1991) Stable isotope studies of quartz-vein type tungsten deposits in Dajishan Mine, Jiangxi Province, Southeast China. In: Stable Isotope Geochemistry: A tribute to Samuel Epstein (ed) Taylor H P, O'Neil J R Jr, Kaplan I R, The Geochemical Society, Special Publication 3

Siegel K, Wagner T, Trumbull R B, Jonsson Erik, Matalin G, Wälle M, Heinrich C A (2016) Stable Isotope (B, H, O) and mineral-chemistry constraints on the magmatic to hydrothermal evolution of the Varuträsk rare-element pegmatite (Northern Sweden). Chemical Geology, 421:1-16

Simmons Wm B, Foord E E, Falster A U, King V T (1995) Evidence for an anatectic origin of granitic pegmatites, western Maine, USA. Geol. Soc. Amer. Ann. Mtng., New Orleans, LA, Abstr. Prog., 27, A411

Simmons Wm B, Foord E E, Falster A U (1996) Anatectic origin of granitic pegmatites, western Maine, USA. GAC-MAC Ann. Mtng., Winnipeg, Abstr. Prog., A87

Simpson D R (1977) Aluminum phosphate variants of feldspar. American Mineralogist, 62:351-355

Siqueira-Corrêa R, Gouveía de Olivera C, Vidotti R M, Da Silva Souza V (2015) Regional-scale pressure shadow-controlled mineralization in the Príncipe Orogenic Gold Deposit, Central Brazil. Ore Geology Reviews, 71:273-304

Smith M, Banks D A, Yardley B W, Boyce A (1996) Fluid inclusion and stable isotope constraints on the genesis of the Cligga Head Sn-W deposit, SW England. European Journal of Mineralogy 8:961–974

Spear F S (1995) Metamorphic Phase Equilibria and Pressure-Temperature-Time Paths. *2*nd ed., Mineralogical Society of America, Washington, D.C.

Štemprok M (1987) Greisenization (a review). Geologische Rundschau, Stuttgart, 76/1:169-175

Štemprok M, Seltmann R, Breiter K (1995) The Cínovec/Zinnwald Sn–W–Li deposit. Ore mineralizations of the Krušné hory Mts (Erzgebirge): Excursion Guide, Prague, Czech Geological Survey 77–83

Štemprok M, Blecha V (2015) Variscan Sn–W–Mo metallogeny in the gravity picture of the Krušné hory/Erzgebirge granite batholith (Central Europe). Ore Geology Reviews 69:285–300

Shaw J, Johnston S T, Gutierrez-Alonso G, Weil A B (2012) Oroclines of the Variscan orogen of Iberia: paleocurrent analysis and palaeogeographic implications. Earth Planet Sci Lett 329–330:60–70

Stosch H-G, Lugmair G W (1990) Geochemistry and evolution of MORB-type eclogites from the Münchberg Massif, southern Germany. Earth and Planetary Science Letters, 99:230–249. https://doi.org/10.1016/0012-821X(90)90113-C

Suwinonprecha M N, Černý P, Friedrich G (1995) Rare metal mineralization related to granites and pegmatites, Phuket, Thailand. Economic Geology 90:603-615

- T -

Tartèse R, Boulvais, P, Poujol M, Vigneresse J-L (2011) Granite petrogenesis revealed by combined gravimetric and radiometric imaging. Textonophysics, 501:98-103

Taylor H P, Epstein S (1962) The relationship between O18/O16 ratios in coexisting minerals of igneous and metamorphic rocks. Bull. Geol. Soc. Amer., 73:461-480

Taylor B E (1986) Magmatic volatiles; isotopic variation of C, H, and S. In: Valley, J.W., Taylor Jr., H.P., O'Neil, J.R. (Eds.), Stable Isotopes in High Temperature Geological Processes, Reviews in Mineralogy, Mineralogical Society of America, 6:185– 220

Taylor R G, Hosking K F G (1970) Manganese-Iron ratios in wolframite, South Crofty Mine, Cornwall. Economic Geology 65:47-53

Taylor J R, Wall V J, Pownceby M I (1992) The calibration and application of accurate redox sensors. American Mineralogist, 77:284-295

Thomas R, Webster J D (2000) Strong tin enrichment in a pegmatite-forming melt. Mineralium Deposita, 35:570-582

Thomas R, Föster H-J, Heinrich W (2003) The behaviour of boron in a peraluminous granite-pegmatite system and associated hydrothermal solutions: a melt and fluid-inclusion study. Contrib. Mineral Petrol., 144:457-472. Doi : 10.1007/s00410-002-0410-5

Thomas R, Föster H-J, Rickers K, Webster J D (2005) Formation of extremely F-rich hydrous melt fractions and hydrothermal fluids during differentiation of highly evolved tin-granite magmas: a melt-fluid-inclusions study. Contrib. Mineral Petrol., 148:582-601

Thomas R, Webster J D, Rhede D, Seifert W, Rickers K, Föster H-J, Heinrich W, Davidson P (2006) The transition from peraluminous to peralkaline granitic melts: Evidence from melt inclusions and accessory minerals. Lithos, 91:137-149

Thomas R, Davidson P (2012b) Evidence of a water-rich silica gel state during the formation of a simple pegmatite. Mineral. Mag., 76:2785–2801

Thomas R, Davidson P (2016) Revisiting complete miscibility between silicate melts and hydrous fluids, and the extreme enrichment of some elements in the supercritical state - Consequences for the formation of pegmatites and ore deposits. Ore Geology Reviews, 72:1088-1101

Tindle A G, Breaks F W (1998) Oxide minerals of the separation rapids rare-element granitic pegmatite group, Northwestern Ontario. The Canadian Mineralogist 36:609-635

Tischendorf G, Gottesmann B, Föster H-J, Trumbull R B (1997) On Li-bearing micas: estiating Li from electron microprobe analyses and an improved diagram for graphical representation. Mineralogical Magazine, 61:809-834

Tumarkina E, Misra S, Burlini L, Conolly J A D (2011) An experimental study of the role of shear deformation on partial melting of a synthetic metapelite. Tectonophysics, 503:92-99

Turrillot P, Augier R, Faure M (2009) The top-to-the-southeast Sarzeau shear zone and its place in the late-orogenic extensional tectonics of southern Armorica. Bulletin de la Société Géologique de France, 180 :247–261. https://doi.org/10.2113/gssgfbull.180.3.247

Turpin L, Leroy J L, Sheppard S M F (1990) Isotopic (O, H, C, Sr, Nd) of superimposed barren and U-bearing hydrothermal systems in a Hercynian granite, Massif Central, France. Chemical Geology, 88:85-98

- U -

Upton G J G, Fingleton B (1989) Spatial Data Analysis by Example, vol. 2. Wiley, New York. 416 pp.

- V -

Vallance J, Cathelineau M, Marignac C, Boiron M-C, Fourcade S, Martineau F, Fabre C (2001) Microfracturing and fluid mixing in granites: W-(Sn) ore deposition at Vaulry (NW French Massif Central). Tectonophysics, 336:43-61

Van Daele J, Hulsbosch N, Dawaele S, Boiron M-C, Piessens K, Boyce A, Muchez P (2018) Mixing of magmatic-hydrothermal and metamorphic fluids and the origin of peribatholitic Sn vein-type deposits in Rwanda. Ore Geology Reviews, 101:481-501

Vielzeuf D, Holloway J R (1988) Experimental determination of the fluid-absent melting relations in the pelitic system: consequences for crustal differentiation/ Contrib. Mineral. Petrol., 98:257– 276

Vigneresse J-L, Brun J-P (1983) Les leucogranites armoricains marqueurs de la deformation régionale ; apport de la gravimetrie. Bulletin de la Societe Geologique de France S7–XXV:357–366. https://doi.org/10.2113/gssgfbull.S7-XXV.3.357

Vigneresse J-L (1988) Forme et volume des plutons granitiques. Bulletin de la Société Géologique de France, IV:897–906. https://doi.org/10.2113/gssgfbull.IV.6.897

Vigneresse J-L (1995) Control of granite emplacement by regional deformation. Tectonophysics 249:173-186

Vigneresse J-L, Bouchez J-L (1997) Successive granitic magma batches during pluton emplacement: the case of Cabeza de Araya (Spain). Journal of Petrology, 38, 12:1767-1776

Vigneresse J-L (1999) Intrusion level of granitic massifs along the Hercynian belt: balancing the eroded crust. Tectonophysics, 307:277-295

Vigneresse J-L (2004) A new paradigm for granite generation. Transactions of the Royal Society of Edinburgh, Earth Sciences, 95:11-22

Vigneresse J-L (2007) The role of discontinuous magma imput in felsic magma and ore generation. Ore Geology Reviews, 30:181-216

Vilas L, de San Jose M A (1990) Central Iberian Zone. Autochthonous sequences. Stratigraphy, in: Dallmeyer, R.D., Martinez Garcia, E. (Eds.), Pre-Mesozoic Geology of Iberia. Springer-Verlag, Berlin, Heidelberg, 145–146

Villaseca C, Pérez-Soba C, Merino E, Orejana D, López-García J A, Billstrom K (2008) Contrasting crustal sources for peraluminous granites of the segmented Montes de Toledo batholith (Iberian Variscan Belt). Journal of Geosciences 53:263-280

- W -

Webster J D, Thomas R, Rhede D, et al (1997) Melt inclusions in quartz from an evolved peraluminous pegmatite: Geochemical evidence for strong tin enrichment in fluorine-rich and phosphorus-rich residual liquids. Geochimica et Cosmochimica Acta 61:2589-2604

Weidner J R, Martin R F (1987) Phase equilibrium of a fluorine-rich leucogranite from the St. Austell pluton, Cornwall. Geochemica et Cosmochimica Acta, 51, 6:1591-1597

Weinberg R F, Sial A N, Marino G (2004) Close spatial relationship between plutons and shear zones. Geological society of America, 32, 5:377-380. doi: 10.1130/G20290.1

Wolf M, Romer R L, Franz L, López-Moro F J (2018) Tin in granitic melts: The role of melting temperature and protolith composition. Lithos, 310-311:20-30

Wood S A, Samson I M (2000) The Hydrothermal Geochemistry of Tungsten in Granitoid Environments: I. Relative Solubilities of Ferberite and Scheelite as a Function of T, P, pH, and mNaCl. Economic Geology, 95:143–182

- Z -

Zajacz Z, Halter W E, Pettke T, Guillong M (2008) Determination of fluid/melt partition coefficients by LA-ICPMS analysis of co-existing fluid and silicate melt inclusions: Controls on element partitioning. Geochimica et Cosmochimica Acta, 72:2169–2197

Zhalashkova N Y, Sitnin A A (1967) Features of the distribution of rare elements in tatalum-bearing apogranites and biotite granites. Geochemistry International, 4:1013-1025

Zhang L F, Liu J F, Chen Z S (1989) Oxygen isotope fractionation in the quartz-water-salt system. *Econ. Geol,* 84:1643-1650

Zhang Q, Zhang R-Q, Gao J-F, Lu J-J, Wu J-W (2018) In-situ LA-ICP-MS trace element analyses of scheelite and wolframite: Contraints on the genesis of veinlet-disseminated and vein-type tungsten depostis, South China. Ore Geology Reviews, 99:166-179

Zhu J-C, Li R-K, Li F-C, Xiong X-L, Zhou F-Y, Huang X-L (2001) Topaz-albite granites and rare-metal mineralization in the Limu District, Guangxi Province, southeast China. Mineralium Deposita, 36, 5:393-405

FIGURES

CHAPTER I:

CHAPTER II:

CHAPTER III:

CHAPTER IV:

CHAPTER V:

CHAPTER VI:

CHAPTER VII:

TABLES

CHAPTER III:

CHAPTER IV:

CHAPTER V:

CHAPTER VI:

ANNEXE

Ore Geology Reviews 104 (2019) 266–272

Contents lists available at ScienceDirect

Ore Geology Reviews

journal homepage: www.elsevier.com/locate/oregeorev

Short communication

The H/F ratio as an indicator of contrasted wolframite deposition mechanisms

Julie Anne-Sophie Michaud*, Michel Pichavant

Université d'Orléans/CNRS/ISTO/BRGM, UMR 7327, 1A rue de la Férollerie, 45100 Orléans, France

ARTICLE INFO

Keywords:
Wolframite
Hübnerite
W deposition
Magmatic control
W ore deposit
Veins

ABSTRACT

Understanding wolframite deposition mechanisms is a key to develop reliable exploration guides for W. In quartz veins from the Variscan belt of Europe and elsewhere, wolframites have a wide range of compositions, from hübnerite- ($MnWO_4$) to ferberite-rich ($FeWO_4$). Deposition style, source of Mn and Fe, distance from the heat/fluid source and temperature have been proposed to govern the wolframite H/F (hübnerite/ferberite ratio) defined as 100 at. Mn/(Fe + Mn). The Argemela mineralized district, located near the world-class Panasqueira W mine in Portugal, exposes a quartz-wolframite vein system in close spatial and genetic association with a rare-metal granite. Wolframite is absent as a magmatic phase, but W-rich whole-rock chemical data suggest that the granite magma is the source of W. Wolframite occurs as large homogeneous hübnerites (H/F = 64–75%) co-existing with montebrasite, K-feldspar and cassiterite in the latest generation of intragranitic veins corresponding to magmatic fluids exsolved from the granite. Locally, early hübnerites evolve to late more Fe-rich compositions (H/F = 45–55%). In a country rock vein, an early generation of Fe-rich hübnerites (H/F = 50–63%) is followed by late ferberites (H/F = 6–23%). Most Argemela wolframites have H/F ratios higher than at Panasqueira and other Variscan quartz-vein deposits which dominantly host ferberites. In greisens or pegmatitic veins, wolframites generally have intermediate H/F ratios. In those deposits, fluid-rock interactions, either involving country rocks (quartz-veins) or granite (greisens) control W deposition. In contrast, at Argemela, wolframite from intragranitic veins was deposited from a magmatic fluid. Differentiation of highly evolved peraluminous crustal magmas led to high Mn/Fe in the fluid which promoted the deposition of hübnerite. Therefore, the H/F ratio can be used to distinguish between contrasted deposition environments in perigranitic W ore-forming systems. Hübnerite is a simple mineralogical indicator for a strong magmatic control on W deposition.

1. Introduction

W is a critical metal, essential for many industrial applications. As for other metals and commodities, exploration for W now focuses on sub-surface to deep contexts in complex geological settings (e.g., Poitrenaud, 2018, www.almonty.com, www.wolfminerals.com.au). Targeting of mineralized systems requires the integration of geological, geophysical and geochemical data sets and their interpretation in the light of an ore deposition model (McCuaig et al., 2010; McCuaig and Hronsky, 2014). With the development of analytical tools, mineralogical compositions of both gangue and ore minerals are increasingly used to footprint the presence of proximal orebodies (Belousova et al., 2002; Codeço et al., 2017; Harlaux et al., 2018; Neiva, 2008).

W mineral deposits include quartz veins, stockworks, greisens, skarns and breccia pipes spatially associated with granitic bodies, and are thought to result from magmatic and hydrothermal processes, combined (Bobos et al., 2018; Harlaux et al., 2015; Kelly and Rye, 1979; Ramboz et al., 1985; Smith et al., 1996). Although the main parameters controlling the transport of W have been identified (Che et al., 2013; Heinrich, 1990; Wood and Samson, 2000), there is as yet no comprehensive model for W deposition.

Quartz veins such as found in Southeast China and in the Variscan belt of Europe form an important class of W deposits. W, in the form of the dominant ore mineral wolframite ([Fe,Mn]WO4), is generally associated with other metals such as Sn, Cu, Ag. The group of quartz-wolframite deposits is diverse. It includes intragranitic (e.g., Smith et al., 1996) and country rock (e.g., Kelly and Rye, 1979) veins with a wide range of geometries, widths and extensions (e.g., Giuliani, 1985). Quartz and wolframite can be accompanied by various gangue (e.g., tourmaline, Codeço et al., 2017) and ore (e.g., cassiterite, Noronha

* Corresponding author.
E-mail address: julie.michaud@univ-orleans.fr (J.A.-S. Michaud).

https://doi.org/10.1016/j.oregeorev.2018.10.015
Received 25 July 2018; Received in revised form 11 October 2018; Accepted 22 October 2018
Available online 23 October 2018
0169-1368/

Table 1
Representative electron microprobe analyses of wolframite from the Argemela Mineralized District.

Major elements (wt%)	E WI		Mean (19)	σ	L WI		Mean (9)	σ	E WII		Mean (32)	σ	L W II		Mean (25)	σ
	min	max			min	max			min	max			min	max		
MnO	15.40	12.21	14.58	0.92	5.75	1.40	3.37	1.59	18.15	15.59	17.27	0.69	13.26	10.82	12.18	0.93
FeO	8.98	12.24	9.88	0.97	19.08	23.41	21.32	1.50	6.19	8.82	7.17	0.67	10.95	13.53	12.37	0.94
Nb_2O_5	0.59	0.22	0.36	0.15	0.36	0.60	0.40	0.19	0.74	0.49	0.46	0.22	0.74	1.05	0.68	0.25
SnO_2	0.08	0.01	0.04	0.03	0.00	0.00	0.02	0.02	0.00	0.07	0.05	0.07	0.13	0.15	0.10	0.06
Ta_2O_5	0.11	0.00	0.06	0.06	0.04	0.09	0.04	0.05	0.00	0.10	0.16	0.25	0.36	0.22	0.18	0.19
WO_3	76.65	76.97	76.95	0.34	76.67	76.81	76.88	0.43	75.62	75.62	76.55	0.63	75.99	75.12	76.05	0.52
Total	101.96	101.81	102.00	0.32	102.04	102.52	102.24	0.39	100.71	100.79	101.68	0.42	101.50	100.96	101.65	0.41
Number of cations based on 4 oxygens																
Mn	0.643	0.513	0.610	0.038	0.241	0.058	0.141	0.067	0.767	0.660	0.724	0.028	0.557	0.456	0.511	0.038
Fe	0.370	0.507	0.408	0.040	0.789	0.964	0.881	0.062	0.258	0.368	0.297	0.028	0.454	0.563	0.513	0.040
Nb	0.013	0.005	0.008	0.003	0.008	0.013	0.009	0.004	0.017	0.011	0.010	0.005	0.017	0.024	0.015	0.006
Sn	0.002	0.000	0.001	0.001	0.000	0.000	0.000	0.000	0.000	0.001	0.001	0.001	0.003	0.003	0.002	0.001
Ta	0.001	0.000	0.001	0.001	0.001	0.001	0.001	0.001	0.000	0.001	0.002	0.003	0.005	0.003	0.002	0.003
W	0.980	0.989	0.986	0.003	0.983	0.980	0.985	0.004	0.978	0.979	0.982	0.006	0.977	0.969	0.976	0.006
Total	2.013	2.014	2.014	0.002	2.021	2.017	2.016	0.004	2.020	2.021	2.016	0.004	2.012	2.019	2.019	0.004
H/F	63.5	50.3	59.9	3.9	23.4	5.7	13.8	6.4	74.8	64.2	70.9	2.8	55.1	44.8	49.9	3.8

E: Early and L: Late. WI: wolframite in country rock vein; WII: wolframite in intragranitic vein. For each wolframite type, min and max are compositions that give the minimum and maximum H/F ratios respectively. The H/F ratio is calculated as 100 at. Mn/(Fe + Mn).

et al., 1992) minerals. Wolframites have compositions ranging from hübnerite ($MnWO_4$) to ferberite ($FeWO_4$, e.g., Harlaux et al., 2018; Lecumberri-Sanchez et al., 2017). Factors of controls of wolframite composition are the subject of an intense debate. The deposition style, source of Mn and Fe, distance from the heat/fluid source and temperature have been proposed to govern the wolframite H/F (i.e., hübnerite/ferberite) ratio, hereafter calculated as 100 at. Mn/(Fe + Mn). Hosking and Polkinghorne (1954) pointed out that wolframites in Cornish pegmatites are relatively Mn-rich while wolframites from quartz veins have high Fe contents. Greisens generally have wolframites with intermediate Fe/Mn (e.g., Breiter et al., 2017; Hosking and Polkinghorne, 1954). Several studies have suggested that Mn-rich wolframites precipitate at higher temperatures than Fe-rich wolframites (e.g., Oelsner, 1944, Leutwein, 1952, Taylor and Hosking, 1970). However, attempts to use the H/F ratio as a geothermometer (Moore and Howie, 1978) have failed as temperature is not the only factor controlling wolframite composition (Amossé, 1978).

Recent studies in the Central Iberian Zone (which includes the world class Panasqueira W deposit) have identified a quartz-wolframite vein system (Michaud et al., 2018) spatially and genetically associated with a Rare-Metal Granite (RMG), the Argemela granite (Charoy and Noronha, 1996). Field, structural, mineralogical and geochemical evidence suggest that the intragranitic wolframite-bearing veins are the expression of magmatic fluids exsolved from the granite at the magmatic-hydrothermal transition. Below, the main characteristics of the Argemela veins are summarized and compared with other W vein systems. Focus is placed on wolframite compositions, essentially Mn-rich at Argemela and Fe-rich in the neighboring Panasqueira and most other Variscan country rock vein systems. This first-order compositional contrast between wolframites suggests major differences in W deposition mechanisms. It is proposed that the H/F ratio can be used as an exploration tool to help distinguishing between contrasted types of W deposition environments.

2. Analytical techniques

Samples from the Argemela W veins were collected and thin as well as polished sections prepared. Preliminary petrographic and textural observations were conducted with a petrographic microscope. Backscattered electron (BSE) images and EDS element mapping were obtained using a Merlin compact ZEISS Microscope equipped with a Bruker EDS detector and working under an acceleration voltage of 15 kV. Wolframites were analyzed by electron microprobe at ISTO, Orléans (France). Punctual analyses, traverses and elements distribution maps for major and minor elements were obtained with a CAMECA SX Five microprobe operated under an acceleration voltage and a beam current of 20 kV and 40nA respectively. Standards included SnO_2 (Sn*Lα*), Fe_2O_3 (Fe*Kα*), $MnTiO_3$ (Mn*Kα* and Ti*Kα*) and pure Nb (Nb*Lα*), Ta (Ta*Lα*) and W (W*Lα*) metals.

3. The Argemela W vein system

The Variscan Argemela Mineralized District (AMD) occurs within the Central Iberian Zone (CIZ, Central Portugal) and is divided in two subsystems at < 0.5 km from each other but evolving separately. The first (the Argemela tin mine, ATM) consists of a vein swarm emplaced in low grade metamorphic rocks from the Neoproterozoic Schist and Greywacke Complex (SGC, Meireles et al., 2013). Veins can be up to 2 m wide, are anastomosed and contain Sn and Li mineralization in the form of cassiterite and montebrasite. No W concentration has been recognized. The second (the Argemela Hill Top, AHT) comprises a RMG with disseminated Li, Sn, Nb, Ta mineralization in the form of magmatic montebrasite, cassiterite and columbo-tantalite. The granitic intrusion is associated with a network of intragranitic veins, and a few quartz veins occur in country rocks near the granite contact. Although wolframite is absent as a magmatic phase, W enrichment is marked by granite whole-rock concentrations ranging up to ~20 ppm W (Charoy and Noronha, 1996). Three generations of intragranitic veins occur within the granite. Field evidence (confinement of veins inside the granite), structural (granite and veins are emplaced in the same structural context), mineralogical (veins lack hydrothermal alteration aureoles and the earliest have a “pegmatitic” texture and a granitic mineral assemblage) and stable isotope data indicate that the intragranitic veins are the expression of fluids exsolved from the granite at the magmatic-hydrothermal transition (Michaud et al., 2018). Wolframite occurs in variable amounts in the third and latest generation of intragranitic veins which are numerous but of restricted size, never exceeding a 10 cm width. It is mostly associated with quartz, K-feldspar and montebrasite, with quartz and montebrasite only in some other veins, and cassiterite is occasionally present. Wolframites form mostly large homogeneous crystals with hübnerite compositions (early WII, H/F between 64 and 75%, Table 1 and Fig. 1). On the eastern border, the granite is affected by a dextral shear zone and the intragranitic veins host wolframites with a patchy texture made of early hübnerites

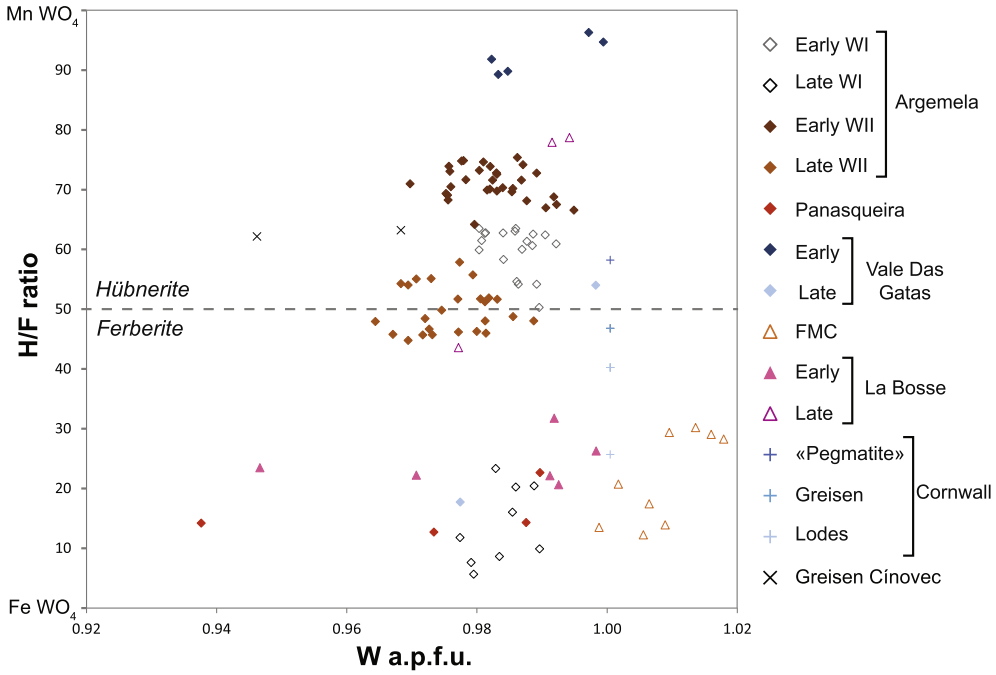

Fig. 1. H/F ratio vs atomic W concentration for wolframites from representative Variscan deposits. Argemela data are from this study (Table 1). For other deposits see references in Table 2.

evolving to more Fe-rich compositions (late WII, H/F from 45 to 55%, Table 1, Fig. 1, e.g. Baumann, 1964). This late wolframite ore deposition stage is followed by sulfides (arsenopyrite) and other phases (vivianite); cassiterite is transformed into stannite.

Wolframite is also present in one country rock vein crosscut by the granite. It appears as large crystals and in variable amounts associated with milky geodic quartz typical of hydrothermal veins in the AMD. In contrast to intragranitic veins, K-feldspar is absent. Wolframite crystals can be homogeneous but most show textural evidence for recrystallization (Fig. 2). Early wolframites are Fe-rich hübnerites (early WI, H/F from 50 to 63%, Table 1 and Fig. 1). The second generation crystallizes in fractures or near the margins of early wolframites and is a ferberite with high Fe contents (late WI, H/F = 6–23%, Table 1, Figs. 1 and 2). This late stage is followed by the deposition of iron oxides.

4. Comparison with other wolframite vein systems

Wolframite occurs as the dominant ore mineral in several types of Variscan W deposits and is characterized by highly variable compositions, from hübnerite to ferberite. The Panasqueira W world class mine, located at only 13 km west from Argemela, provides an excellent comparison point with the AMD. The deposit consists of > 1000 nearly horizontal veins emplaced in SGC metamorphic rocks on top of a granite cupola (Neiva, 2008; Foxford et al., 2000). The hydrothermal veins, which can exceed 1 m widths, host wolframite, quartz, muscovite, tourmaline, topaz, arsenopyrite and early cassiterite (Kelly and Rye, 1979, Polya et al., 2000). Wolframites form large chemically homogeneous crystals with H/F ratios generally < 23% (e.g. ferberite), in strong contrast with most AMD wolframites (Table 2 and Fig. 1). Same as at Panasqueira, in the French Massif Central (FMC), most Variscan W deposits show wolframites with ferberite compositions (Harlaux et al., 2018 and references therein, Table 2 and Fig. 1). For example, the stockwork of La Bosse (north FMC) consists in a network of interconnected subhorizontal quartz veins emplaced in metamorphic rocks; wolframite has H/F ratios between 21 and 32% (Aubert, 1969; Aïssa et al., 1987, Table 2 and Fig. 1). Other representative examples of ferberite-bearing vein-type W deposits in the FMC include Enguialès, Leucamp and St-Goussaud (e.g., Harlaux et al., 2018 and references therein). Both the Panasqueira and the FMC deposits are representative of perigranitic hydrothermal systems developed in metamorphic country rocks. In the case of Panasqueira, ferberite deposition is controlled by fluid-rock interactions involving SGC country rocks (Lecumberri-Sanchez et al., 2017) and, so, there is a significant non-magmatic contribution to the ore-forming system (e.g., Polya et al., 2000).

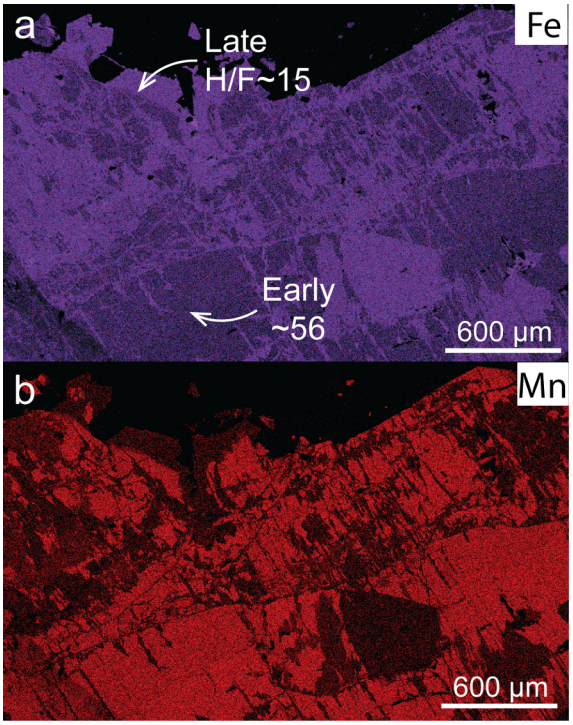

Fig. 2. Patchy texture of Argemela WI (schist-hosted vein) illustrating evolution of the H/F ratio between early and late crystallization stages. EDS map of (a) Fe and (b) Mn.

Other Variscan W deposits show a closer spatial association with

Table 2
Compositional data for wolframites from representative Variscan deposits.

Name	Metallogenic province	Deposit type	Deposition stage	H/F	Mean	σ	W a.p.f.u.	References
Vale Das Gatas	Variscan - Portugal	Intragranitic and country rocks veins	Early	96.2 89.2	92.30 (5)	3.05	1.00 0.98	Neiva (2008)
			Late	54.0 17.7	35.86 (2)	25.62	1.00 0.98	
Panasqueira	Variscan - Portugal	Country rocks veins		22.7 12.7	16.00 (4)	4.51	0.99 0.97	Neiva (2008)
Enguialès-Leucamp	Variscan - FMC	Country rocks veins		30.2 12.3	22.37 (10)	7.53	1.00 1.02	Harlaux et al. (2018)
St Goussaud	Variscan - FMC	Intragranitic and country rocks veins		24.7 20.4	22.74 (5)	1.66	1.01 1.00	Harlaux et al. (2018)
La Bosse	Variscan - FMC	Country rocks veins	Early	31.8 20.7	24.43 (6)	4.06	0.99 0.99	Aïssa et al. (1987)
			Late	78.7 43.6	64.20 (4)	17.10	0.98 0.99	
Le Mazet	Variscan - FMC	Country rocks vein		78.8	–	–	–	Aubert (1969)
Gilbert	Variscan - FMC	Country rocks vein		88.2	–	–	–	Aubert (1969)
Cornish wolframites	Variscan - Cornwall	"Pegmatitic veins"		58.2 46.8	52.5 (2)	8.06	1.00* 1.00*	Hosking and Polkinghorne (1954)
		Greisen		46.8 40.3	43.52 (2)	4.63	1.00* 1.00*	
		Lodes		40.3 25.7	32.97 (2)	10.29	1.00* 1.00*	
Cligga Head	Variscan - Cornwall	Intragranitic veins		35–40+	–	–	–	Unpublished
Cínovec	Variscan - Bohemian Massif	disseminated in greisen quartz veins and greisen		63.6 45.8	57.70 (6)	7.45	0.90 0.82	Breiter et al. (2017)

Maximum and minimum H/F values are shown for each type. +data obtained from EDS. *fixed to 1 (no data available).

granitic rocks. This is the case of Cligga Head (Cornwall, UK) where wolframite is deposited together with cassiterite, arsenopyrite and other sulfides in a dense network of intragranitic veins (Charoy, 1979). Wolframite is ferberite-rich (H/F = 35–40%, Table 2, Charoy, 1979; Michaud, unpublished) and, although the mineralizing fluids have been interpreted as magmatic (Smith et al., 1996), W deposition at Cligga Head is associated with hydrothermal alteration around the veins indicating fluid-granite equilibration at subsolidus temperatures (300–400 °C, Charoy, 1979). At Cínovec (Bohemia, DE and CZ), wolframite occurs disseminated both in greisens and in quartz veins within the host RMG. H/F ratios are intermediate (between 45 and 63%, Table 2 and Fig. 1, Breiter et al., 2017) consistent with the presence of sub-equal concentrations of Fe and Mn in fluid inclusions (Korges et al., 2018). Sn-W deposition is associated either with greisenisation of the granite (i.e., with fluid-rock reaction at subsolidus temperatures) or with boiling of the magmatic fluid (Korges et al., 2018). Last, deposits from Cornwall (UK) demonstrate a systematic increase of H/F ratios from pegmatites and early feldspathic veins (H/F = 47–58), greisens (H/F = 40–47) to quartz lodes (H/F = 26–40, Table 2 and Fig. 1, Hosking and Polkinghorne, 1954). In the South Crofty Mine, the "pegmatitic vein swarms", mainly composed of quartz, feldspar and other accessory minerals, contain wolframites of intermediate compositions (H/F = 37–60, Taylor and Hosking, 1970).

In some deposits, several wolframite crystallization stages can be identified, indicating distinct deposition mechanisms. For example, the La Bosse stockwork contains a late generation of hübneritic wolframite (H/F = 44–79%, Table 2 and Fig. 1) developed in minor amounts on early ferberites (H/F = 21–32%, see above) and attributed to the influence of the late Beauvoir RMG (Aïssa et al., 1987). Isolated hübnerite-bearing veins occur north of the La Bosse deposit (e.g., Le Mazet and Gilbert veins, Table 2) and they have been interpreted as footprints of another Beauvoir-type RMG at depth (Aubert, 1969). In the Portuguese CIZ, the Vale Das Gatas deposit consists of quartz veins cutting the contact between SGC country rocks and a muscovite > biotite granite (Neiva, 2008). The veins are characterized by at least two ore deposition stages, the first involving cassiterite and wolframite and the second only wolframite. Wolframites are mostly hübnerites (H/F = 89–96%) except rims that range from Fe-rich hübnerite to ferberite (H/F = 18–54%, Table 2 and Fig. 1).

5. Wolframite deposition mechanism

None of the wolframite deposition mechanisms mentioned above is directly applicable to the AMD since none explains the precipitation of hübnerite directly from a magmatic fluid. At Argemela, the W-bearing intragranitic veins show no hydrothermal interaction aureole at their margins. The earliest veins exhibit "pegmatitic" textures and crystallize a granitic mineral assemblage (Michaud et al., 2018). Quartz in the granite and veins both have high δO^{18} (respectively 13.7–14.5 and 14.5–15.9‰). Therefore, the intragranitic veins formed from fluids exsolved from the crystallizing granite and fluid-granite equilibration was originally established at relatively elevated temperatures. Using solidus temperatures for RMG (Pichavant et al., 1987a) and oxygen isotope thermometry on quartz and muscovite from the granite, magmatic fluids were originally at equilibrium with the granite at temperatures of 500–550 °C. Their subsequent evolution within the intragranitic veins most probably followed a fluid-buffered instead of a rock-buffered path (e.g., Heinrich, 1990). There is no evidence for postmagmatic hydrothermal interaction processes such as greisenisation around the veins. Quartz from the relatively late wolframite-bearing veins have the same stable isotope signature (δO^{18}: 15.5–15.9‰; δD: −25 to −31‰) than quartz from the early veins (δO^{18}: 14.5–15‰; δD: −21 to −35‰). Furthermore, the surrounding Beira schists are W-depleted and cannot be the source of W (Charoy and Noronha, 1996). Although the intragranitic vein system was not closed to external non-magmatic contributions (as suggested by the mineralogical data summarized above), wolframite deposition in the Argemela intragranitic veins resulted from cooling of the igneous fluid in isolation from the enclosing rock, in contrast with mechanisms proposed for W deposition in other contexts (e.g., Lecumberri-Sanchez

et al., 2017).

Wolframite deposition necessitates a source of Fe and Mn, in addition to W. Amossé (1978) demonstrated that the composition of the deposited wolframite depends essentially on two factors, temperature and aMn/aFe of the ore fluid. The Mn/Fe ratio is always higher (and so the H/F ratio higher) in the deposited wolframite than in the equilibrium fluid. Because lowering temperature slightly increases Mn/Fe in wolframite, Amossé (1978) emphasized the importance of the Mn/Fe ratio of the mineralizing fluid as the main factor controlling wolframite composition. At Argemela, the Mn/Fe of the ore fluid is defined by fluid/melt partitioning for Mn and Fe. Both elements partition similarly between melt and fluid as shown by their nearly identical ratios in coexisting silicate melt and fluid inclusions from Ehrenfriedersdorf (Zajacz et al., 2008). Thus, the Mn/Fe of the magmatic fluid that deposited hübnerite at Argemela was essentially that of the crystallizing granitic melt. Although this Mn/Fe ratio is unknown, Variscan RMG (e.g., Beauvoir, Raimbault et al., 1995) and pegmatites (Chèdeville, Raimbault, 1998), and equivalent volcanic products (Macusani, Pichavant et al., 1987b), demonstrate a general increase of Mn/Fe during magmatic differentiation. The whole-rock data for the Argemela granite show such an increase (Charoy and Noronha, 1996), also marked in the enrichment of disseminated columbo-tantalites in $MnTa_2O_6$ (Michaud et al., 2018, see also Raimbault, 1998; Linnen and Cuney, 2005). Therefore, the magmatic evolution of the Argemela RMG led to the exsolution of relatively high Mn/Fe igneous fluids. We suggest that the deposition of hübnerite in perigranitic magmatic-hydrothermal systems is the signature of metals and fluids originating from highly evolved peraluminous crustal magmas similar to the Argemela granite.

W is known to be transported in hydrothermal fluids as an oxyanion, WO_4^{2-}, complexed with Na+, K+, or H+ (Wood and Samson, 2000; Heinrich, 1990). Substitution of Na for Li does not change wolframite solubilities in granitic melts (all the other parameters being equal, Linnen, 1998) and, so, Li is a W complexing agent with an efficiency comparable to Na. Thus, destabilization of Li-W complexes as a result of precipitation of a Li-bearing phase will cause wolframite deposition. Montebrasite ($LiAlPO_4$ (OH, F)) is a systematic phase in the Argemela intragranitic veins where it is accompanied by K-feldspar (whose crystallization removes K from the fluid). Muscovite never occurs as a mineral in the veins suggesting that the pH of the fluid was never strongly acid. Compositions of montebrasites (Michaud et al., 2018) in K-feldspar-bearing veins show no variations in F content (Loh and Wise, 1976) and so deposition was probably not driven by a drastic increase of the fluid pH. However, montebrasites from montebrasite-wolframite veins can have F contents nearly twice as elevated as montebrasites in K-feldspar-bearing veins, which indicates a significant pH decrease (thus counteracting wolframite precipitation). Therefore, a decrease in temperature is probably the main factor controlling wolframite deposition (Heinrich, 1990).

One element specific of the Argemela magmatic-hydrothermal system is phosphorus. The Argemela granite, with whole-rock concentrations of up to ~ 2 wt% P2O5 (Charoy and Noronha, 1996), is a good example of a peraluminous high phosphorus (PHP) rare-metal granite (Linnen and Cuney, 2005). Montebrasite crystallizes as a magmatic phase in the Argemela granite and is also a key phase in intragranitic veins (Charoy and Noronha, 1996). Phosphorus increases wolframite solubility in peraluminous granitic melts (Che et al., 2013). Its influence is however indirect, through the formation of AlPO4 species which increases the availability of Na, K and Li to complex with W. Therefore, removal of such species by phosphate crystallization will cause wolframite deposition. The overall mechanism of wolframite precipitation in the Argemela intragranitic vein system is summarized with the following reaction:

$$\underset{\text{fluid}}{Li}\,\underset{\text{fluid}}{NaWO_4} + \underset{\text{fluid}}{(Mn, Fe)^{2+}} + \underset{\text{fluid}}{AlPO_4} + \underset{\text{fluid}}{H_2O} = \underset{\text{montebrasite}}{LiAlPO_4OH} + \underset{\text{wolframite}}{(Mn, Fe)WO_4} + \underset{\text{fluid}}{Na^+} + \underset{\text{fluid}}{H^+} \quad (1)$$

An equivalent reaction can be written for the fluorine Li phosphate end-member (amblygonite). Eq. (1) is probably driven to the right by a decrease in temperature, i.e., by cooling of the intragranitic vein fluids.

6. Discussion and implications for exploration

The model proposed for Argemela emphasizes the differences with other W deposition environments, and has direct implications for exploration. The model applies to hübnerite deposition from a magmatic fluid. Wolframite composition reflects enrichment in Mn relative to Fe in the crystallizing granite which is the source of both W and fluids. Wolframite deposition calls upon a specific chemical environment (presence of both Li and P) in a magmatic-hydrothermal system that evolves under fluid-buffered conditions. Li, together with F and P, is systematically enriched in Variscan granitoïds from the CIZ (Roda-Robles et al., 2018 and references therein). Such anomalies reflect the specific chemistry (Al-, P-, F- and Li-rich, Ca-poor) of the metasedimentary rock sources of granitic magmas (Roda-Robles et al., 2018). The Li- and P-rich geochemical signature exhibited by the Argemela granite is a reflection of such specific crustal sources. Therefore, the W deposition mechanism proposed at Argemela also probably applies to other similar W occurrences in the CIZ.

The model for the AMD differs from others where a magmatic source for W is assumed but fluid interactions with country rocks are considered necessary for W deposition (Lecumberri-Sanchez et al., 2017). One first-order difference between the two types of models is that, in the former case, veins are intragranitic (Argemela) and, in the latter, within country rocks (Panasqueira). Therefore, each corresponds to a specific type of W deposition environment, as reflected by the composition of wolframite, hübnerite in the former and ferberite in the latter (Fig. 3). In the case of intragranitic vein systems, a magmatic origin for the ore fluid has been generally proposed (e.g., Korges et al., 2018; Smith et al., 1996). However, one major difference between Argemela and these systems (Cligga Head and Cínovec respectively) is the temperature and mechanism of fluid-rock equilibration. At Argemela, the composition of the ore fluid is defined by fluid/melt equilibrium at near-solidus temperatures; the magmatic fluid evolves along a fluid-buffered path. At Cligga Head and Cínovec, the fluid is buffered by fluid-rock interaction at subsolidus temperatures (greisenisation). Therefore, Argemela can be viewed as a high temperature variant of the Cligga Head and Cínovec cases. Preservation of the high temperature intragranitic vein system at Argemela was probably favored by the small volume of the granite intrusion which prevented the development of a large long-lived hydrothermal system involving adjacent country rocks and fluids.

Our results suggest that the H/F ratio can be used as an indicator of contrasted W deposition environments in perigranitic ore-forming systems (Fig. 3). Hübnerite crystallization is associated with the following key features for exploration: (1) source of W resides in nearby igneous rocks, (2) highly evolved granitic magmas are present, (3) ore fluids have a magmatic origin and (4) a “high temperature” magmatic-hydrothermal stage is preserved. Overall, hübnerite can be viewed as a relatively simple indicator of a strong magmatic control on W deposition. The fact that, in W deposits, ferberite compositions are generally more common than hübnerite could be the consequence of early hübnerite recrystallizing to lower H/F ratios as observed for example in Fig. 2. Although, at Argemela hübnerite deposition is the consequence of a high Mn/Fe in the ore fluid, hübnerite crystallization progressively depletes the fluid in Mn (Amossé, 1978) and, therefore, precipitation of wolframites with progressively lower H/F ratios is expected (Fig. 3). However, large variations of the H/F ratio within a given deposit (for example at La Bosse, Vale Das Gatas, Argemela, Fig. 3) are the mark of a

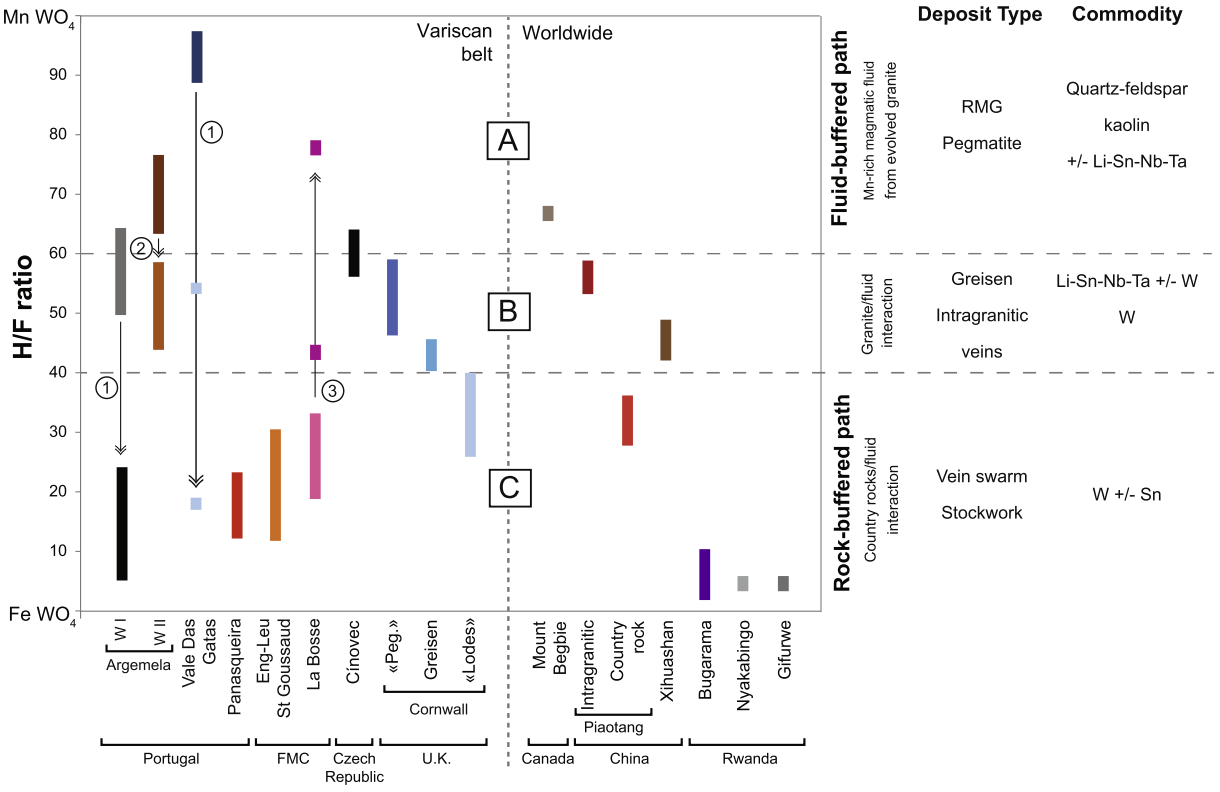

Fig. 3. Environments and mechanisms of W deposition as revealed by the H/F ratio for several representative Variscan deposits and extension to worldwide deposits. Source of data in Table 2 for Variscan deposits and see Zhang et al. (2018), Dixon et al. (2014) and Goldmann et al. (2013) for worldwide deposits. Three main H/F domains corresponding to different wolframite deposition mechanisms are identified: (A) for H/F ratio > 60, wolframite precipitates from a Mn-rich magmatic fluid evolving under a fluid-buffered path (Heinrich, 1990); (B) for H/F ratio between 40 and 60, wolframite precipitates from a fluid buffered by granite/fluid interactions (Smith et al., 1996); (C) for H/F ratio < 40, wolframite precipitates from a fluid carrying a significant non magmatic signature derived from country rocks (Lecumberri-Sanchez et al., 2017). Three main mechanisms controlling variations of the H/F ratio in a single deposit are illustrated: (1) step decrease of the H/F ratio resulting from addition of Fe through fluid-rock interactions (Lecumberri-Sanchez et al., 2017); (2) Progressive decrease of the H/F ratio due to Mn removal during hübnerite crystallization (Amossé, 1978) and (3) step increase of the H/F ratio due to influx of Mn-rich magmatic fluid. Deposit type and commodity associated with the three domains are detailed. Eng-Leu: Enguialès-Leucamp; FMC: French Massif Central; "peg": pegmatitic veins (Hosking and Polkinghorne, 1954).

complex multi-phase deposition history involving ore fluids with contrasted Fe/Mn and different, superimposed, wolframite deposition environments. Wolframite can recrystallize to lower H/F ratios (WI in the Argemela country rock vein, Fig. 3) when the magmatic-hydrothermal system becomes open to fluids derived from Fe-, S-rich metamorphic country rocks (Lecumberri-Sanchez et al., 2017). Alternatively, overprinting of early low H/F ratios in country rock veins by magmatic fluids derived from a crystallizing RMG can be also observed in the FMC (La Bosse, Fig. 3).

Hübnerite is a tracer of proximal highly evolved igneous bodies such as RMG and/or pegmatite with potential for commodities such as quartz and feldspar, kaolin and disseminated Li-Sn-Nb-Ta ores (e.g., Aubert, 1969; Fig. 3), in addition to W. Wolframite with intermediate H/F ratios is characteristic of medium temperature rock-buffered hydrothermal systems with a strong magmatic signature, both for the fluids and the metals (Fig. 3, Smith et al., 1996; Korges et al., 2018). These compositions are typical of greisen-type (both vein and massive) deposits where mostly Li-Sn-Nb-Ta are economically interesting and of intragranitic vein type deposits that follow a rock-buffered path. Lastly, H/F ratios < 40 and down to 0 indicate W deposition environments where a significant non-magmatic contribution to the ore fluid and W deposition is necessary (Fig. 3, Lecumberri-Sanchez et al., 2017). Ferberites showing a low H/F ratio are tracers of W-bearing veins/stockwork deposits of great economic importance.

The comparison can be extended to deposits worldwide (Fig. 3). Fractionated Li-bearing pegmatites from Mount Begbie (Bristish Columbia; Dixon et al., 2014) exhibit scarce hübnerites with a high H/F ratio, similar to Argemela (Fig. 3). Intragranitic veins of the Piaotang and Xihuashan W-deposits (Zhang et al., 2018) are characterized by an alteration halo at vein margins which indicates a rock-buffered path (i.e., granite-fluid interaction). These vein systems behave similarly to Cligga Head and both show comparable intermediate H/F ratios. In comparison, Piaotang country rock veins show a lower H/F ratio (Zhang et al., 2018), most probably a consequence of interaction with these rocks. The Bugarama, Nyakabingo and Gifurwe vein-type deposits from the "tungsten belt" of Rwanda are all hosted in country rocks and wolframite shows very low H/F ratio (Goldmann et al., 2013), comparable to the Panasqueira compositions. Thus, the H/F ratio appears as a reliable exploration tool worldwide despite differences in ages and geodynamic contexts between deposits.

7. Conclusions

Intragranitic veins in the Argemela Mineralized District remarkably illustrate the case of wolframite precipitation directly from relatively "high temperature" magmatic fluids. High H/F ratios wolframites (hübnerites) are characteristic of this specific W deposition environment which contrasts with other mechanisms that lead to intermediate to low H/F ratios. It is proposed that the H/F ratio can be used as an indicator of wolframite deposition style for Variscan deposits (and beyond) and thus as a relevant exploration tool. Lastly, it should be emphasized that the genesis of Variscan W deposits does not only result from locally favorable country rocks, as for Panasqueira (e.g., Lecumberri-Sanchez et al., 2017). Chemically specific source rocks and

granite magma types are also necessary.

Acknowledgements

The authors acknowledge P. Moutela and P. Ferraz for field access and I. Di Carlo for assistance with the electron microprobe and SEM. This work was supported by the Labex VOLTAIRE (ANR-10-LABX-100-01), the ERAMIN project NewOres and the ANR project VARPEG (ANR-15-CE01-0001). We acknowledge P. Lecumberri-Sanchez for her constructive remarks.

References

Aïssa, M., Marignac, C., Weisbrod, A., 1987. Le stockwork à ferbérite d'Echassières : évolution spatiale et temporelle; cristallochimie des ferbérites. In Cuney, M., Autran, A., Géologie profonde de la Franche Echassières : le forage scientifique. Une clé pour la compréhension des mécanismes magmatiques et hydrothermaux associées aux granites à métaux rares. Géol. Fr. 2–3, 311–333.

Amossé, J., 1978. Physicochemical study of the hubnerite-ferberite (MnWO4-FeWO4) zonal distribution in wolframite ($Mn_X\ Fe_{(1-X)}\ WO_4$) deposits. Phys. Chem. Miner. 3, 331–341.

Aubert, G., 1969. Les coupoles granitiques de Montebras et d'Échassières:(Massif Central français) et la genèse de leurs minéralisations en étain, lithium, tungstène et béryllium. Éditions BRGM.

Baumann, L., Starke, R., 1964. In: Breitag zur Verteilung der H/F Koeffizienten minerhalb der Wolframitlagerstätte Pechtelgrün auf Gund neuer röntgenographischer Untersuchungen. Bergakademie, pp. 79–82.

Belousova, E.A., Griffin, W.L., O'Reilly, S.Y., Fisher, N.I., 2002. Apatite as an indicator mineral for mineral exploration: trace-element compositions and their relationship to host rock type. J. Geochem. Explor. 76, 45–69.

Bobos, I., Noronha, F., Mateus, A., 2018. Fe-, Fe, Mn- and Fe, Mg-chlorite: a genetic linkage to W, (Cu, Mo) - mineralization in the magmatic-hydrothermal system of Borralha. Northern Portugal. Mineral. Mag. 1–35.

Breiter, K., Ďurišová, J., Hrstka, T., Korbelová, Z., Hložková Vaňková, M., Vašinová Galiová, M., Kanický, V., Rambousek, P., Knésl, I., Dobeš, P., Dosbaba, M., 2017. Assessment of magmatic vs. metasomatic processes in rare-metal granites: a case study of the Cínovec/Zinnwald Sn–W–Li deposit, Central Europe. Lithos 292–293, 198–217.

Charoy, B., 1979. Greisenisation, minéralisation et fluides associés à Cligga Head, Cornwall (sud-ouest de l'Angleterre). Bull. Minér. 102, 633–641.

Charoy, B., Noronha, F., 1996. Multistage growth of a rare-element, volatile-rich microgranite at Argemela (Portugal). J. Petrol. 37, 73–94.

Che, X.D., Linnen, R.L., Wang, R.C., Aseri, A., Thibault, Y., 2013. Tungsten solubility in evolved granitic melts: an evaluation of magmatic wolframite. Geochim. Cosmochim. Acta 106, 84–98.

Codeço, M.S., Weis, P., Trumbull, R.B., Pinto, F., Lecumberri-Sanchez, P., Wilke, F.D.H., 2017. Chemical and boron isotopic composition of hydrothermal tourmaline from the Panasqueira W-Sn-Cu deposit, Portugal. Chem. Geol. 468, 1–16.

Dixon, A., Cempírek, J., Groat, L.A., 2014. Mineralogy and geochemistry of pegmatites on Mount Begbie, British Columbia. Can. Mineral. 52, 129–164.

Foxford, K.A., Nicholson, R., Polya, D.A., Hebblethwaite, R.P.B., 2000. Extensional failure and hydraulic valving at Minas da Panasqueira, Portugal: evidence from vein spatial distributions, displacements and geometries. J. Struct. Geol. 22, 1065–1086.

Giuliani, G., 1985. Le gisement de tungstène de Xihuashan (Sud-Jiangxi, Chine): relations granites, altérations deutériques-hydrothermales, minéralisations. Mineral. Deposita 20, 107–115.

Goldmann, S., Melcher, F., Gäbler, H.-E., Dewaele, S., De Clercq, F., Muchez, P., 2013. Mineralogy and trace element chemistry of ferberite/reinite from tungsten deposits in central Rwanda. Minerals 3, 121–144.

Harlaux, M., Marignac, C., Cuney, M., Mercadier, J., Magott, R., Mouthier, B., 2015. Nb-ti-y-hree-w-u oxide minerals with uncommon compositions associated with the tungsten mineralization in the Puy-les-vignes Deposit (Massif Central, France): evidence for rare-metal mobilization by late hydrothermal fluids with a peralkaline signature. Can. Mineral. 53, 653–672.

Harlaux, M., Mercadier, J., Marignac, C., Peiffert, C., Cloquet, C., Cuney, M., 2018. Tracing metal sources in peribatholitic hydrothermal W deposits based on the chemical composition of wolframite: the example of the Variscan French Massif Central. Chem. Geol.

Heinrich, C.A., 1990. The chemistry of hydrothermal tin (-tungsten) ore deposition. Econ. Geol. 85, 457–481.

Hosking, K.F.G., Polkinghorne, J.P.R., 1954. The significance of the variable iron content of the "Wolframites" of the west of England. R. Geol. Soc. Cornwall 18.

Kelly, W.C., Rye, R.O., 1979. Geologic, fluid inclusion, and stable isotope studies of the tin-tungsten deposits of Panasqueira, Portugal. Econ. Geol. 74, 1721–1822.

Korges, M., Weis, P., Lüders, V., Laurent, O., 2018. Depressurization and boiling of a single magmatic fluid as a mechanism for tin-tungsten deposit formation. Geology 46, 75–78.

Lecumberri-Sanchez, P., Vieira, R., Heinrich, C.A., Pinto, F., Wälle, M., 2017. Fluid-rock interaction is decisive for the formation of tungsten deposits. Geology 45, 579–582.

Leutwein, F., 1952. Die Wolframit Grappe. Freiberg Forschungsh C3, 8-19.

Linnen, R.L., 1998. The solubility of Nb-Ta-Zr-Hf-W in granitic melts with Li and Li + F; constraints for mineralization in rare metal granites and pegmatites. Econ. Geol. 93, 1013–1025.

Linnen, R.L., Cuney, M., 2005. Granite-related rare-element deposits and experimental constraints on Ta-Nb-W-Sn-Zr-Hf mineralization. In: Linnen, R.L., Samson, I.M. (Eds.), Rare-Element Geochemistry and Mineral Deposits. Geological Association of Canada, GAC Short Course.

Loh, S.E., Wise, W.S., 1976. Synthesis and fluorine-hydroxyl exchange in the amblygonite series. Can. Mineral. 14, 357–363.

McCuaig, T.C., Beresford, S., Hronsky, J., 2010. Translating the mineral systems approach into an effective exploration targeting system. Ore Geol. Rev. Miner. Prospectivity Anal. Quant. Resour. Estimation 38, 128–138.

McCuaig, T.C., Hronsky, J.M.A., 2014. The Mineral System Concept: The Key to Exploration Targeting. SEG Special Publication, pp. 153–175.

Meireles, C., Sequeira, A., Castro, P., Ferreira, N., 2013. New data on the lithostratigraphy of Beiras Group (Schist Greywackes Complex) in the region of Góis-Arganil-Pampilhosa da Serra (Central Portugal). Cuaderno Lab. Xeolóxico de Laxe, pp. 105–124.

Michaud, J. A-S., Gumiaux, C., Pichavant, M., Gloaguen, E., Marcoux, E., 2018. From magmatic to hydrothermal Sn-Li-Nb-Ta-W mineralization: the Argemela District (Portugal). Accepted to Mineralium Deposita.

Moore, F., Howie, R.A., 1978. On the application of the hübnerite:ferberite ratio as a geothermometer. Mineral. Deposita 13, 391–397.

Neiva, A.M.R., 2008. Geochemistry of cassiterite and wolframite from tin and tungsten quartz veins in Portugal. Ore Geol. Rev. 33, 221–238.

Noronha, F., Doria, A., Dubessy, J., Charoy, B., 1992. Characterization and timing of the different types of fluids present in the barren and ore-veins of the W-Sn deposit of Panasqueira, Central Portugal. Mineral. Deposita 27, 72–79.

Oelsner, O., 1944. Über arzebirge Wolframite. Ber. Freib. Geol. Ges. 20, 44–49.

Pichavant, M., Boher, M., Stenger, J.F., Aïssa, M., Charoy, B., 1987a. Relations de phase des granites de Beauvoir à 1 et 3kbar en conditions de saturation en H_2O. Géol. Fr. 1, 77–85.

Pichavant, M., 1987b. The Macusani glasses, SE Peru : evidence of chemical fractionation in peraluminous magmas. Magmatic process: physicochemical principles. Geochem. Soc. Spec. Publ. 1, 359–373.

Poitrenaud, T., 2018. Le gisement périgranitique à tungstène et or de Salau (Pyrénées, France). Histoire polyphasée d'un système minéralisé varisque. Thèse, Univ. Orléans, p. 487.

Polya, D.A., Foxford, K.A., Stuart, F., Boyce, A., Fallick, A.E., 2000. Evolution and paragenetic context of low δD hydrothermal fluids from the Panasqueira W-Sn deposit, Portugal: new evidence from microthermometric, stable isotope, noble gas and halogen analyses of primary fluid inclusions. Geochim. Cosmochim. Acta 64, 3357–3371.

Raimbault, L., 1998. Composition of complex lepidolite-type granitic pegmatites and of constituent columbite-tantalite, Chedeville, Massif Central, France. Can. Mineral. 36, 563–583.

Raimbault, L., Cuney, M., Azencott, C., Duthou, J.-L., Joron, J.L., 1995. Geochemical evidence for a multistage magmatic genesis of Ta-Sn-Li mineralization in the granite at Beauvoir, French Massif Central. Econ. Geol. 90, 548–576.

Ramboz, C., Schnapper, D., Dubessy, J., 1985. The P-v -T-X-f O2 evolution of H2O-CO2-CH4-bearing fluid in a wolframite vein: reconstruction from fluid inclusion studies. Geochim. Cosmochim. Acta 49, 205–219.

Roda-Robles, E., Villaseca, C., Pesquera, A., Gil-Crespo, P.P., Vieira, R., Lima, A., Garate-Olave, I., 2018. Petrogenetic relationships between Variscan granitoids and Li-(F-P)-rich aplite-pegmatites in the Central Iberian Zone: geological and geochemical constraints and implications for other regions from the European Variscides. Ore Geol. Rev. 95, 408–430.

Smith, M., Banks, D.A., Yardley, B.W., Boyce, A., 1996. Fluid inclusion and stable isotope constraints on the genesis of the Cligga Head Sn-W deposit, SW England. Eur. J. Mineral. 8, 961–974.

Taylor, R.G., Hosking, K.F.G., 1970. Manganese-iron ratios in wolframite, South Crofty Mine, Cornwall. Econ. Geol. 65, 47–53.

Wood, S.A., Samson, I.M., 2000. The Hydrothermal Geochemistry of Tungsten in Granitoid Environments: I. Relative Solubilities of Ferberite and Scheelite as a Function of T, P, pH, and mNaCl. Econ. Geol. 95, 143–182.

Zajacz, Z., Halter, W.E., Pettke, T., Guillong, M., 2008. Determination of fluid/melt partition coefficients by LA-ICPMS analysis of co-existing fluid and silicate melt inclusions: controls on element partitioning. Geochim. Cosmochim. Acta 72, 2169–2197.

Zhang, Q., Zhang, R.-Q., Gao, J.-F., Lu, J.-J., Wu, J.-W., 2018. In-situ LA-ICP-MS trace element analyses of scheelite and wolframite: constraints on the genesis of veinlet-disseminated and vein-type tungsten depostis, South China. Ore Geol. Rev. 99, 166–179.

JULIE MICHAUD

LES GRANITES A METAUX RARES : ORIGINE, MISE EN PLACE ET MECANISMES DE LA TRANSITION MAGMATIQUE-HYDROTHERMALE

Résumé :

Les granites à métaux rares sont issus de la cristallisation de magmas très évolués enrichis en volatiles et fondants (F, Li, P, B) et en métaux tels que Sn, Nb, Ta et W. Dans la chaîne Varisque d'Europe de l'Ouest, ils résultent d'un magmatisme tardi-orogénique spécifique. Depuis les années 60, de nombreuses études se sont intéressées à la signature géochimique de ces granites et différents modèles de genèse ont pu être proposés. Malgré cela, plusieurs questions subsistent; le contexte et les mécanismes de mise en place de ces granites particuliers ne sont que rarement abordés. Afin d'avoir une vision complète des processus et mécanismes responsables de (i) la genèse des magmas à métaux rares, (ii) la géométrie et la mise en place de ces granites, (iii) leur signature géochimique et leur enrichissement en métaux, une étude multi-approches et multi-échelles a été menée sur l'exemple du granite à métaux rares d'Argemela (Zone Centro-Ibérique, Portugal). Elle a été complétée par une étude expérimentale portant sur la genèse des magmas. Les résultats de l'étude structurale montrent que l'intrusion d'Argemela se met en place dans un contexte particulier. Plusieurs critères suggèrent une remontée verticale rapide et chenalisée du magma jusqu'à un niveau très superficiel, subvolcanique. L'étude pétrologique et géochimique du granite et des minéralisations associées a permis de mettre en évidence les évènements clés et les processus mis en jeu durant la transition magmatique-hydrothermale. Ceci a également permis d'appréhender les processus de concentration/transport des métaux et les mécanismes de dépôt des minéralisations. L'étude expérimentale indique qu'un seul stade de fusion partielle à faible taux ne permet pas de générer des magmas suffisamment enrichis en métaux. Cependant, un mécanisme de refusion de restites enrichies, qui reste encore à tester, pourrait produire les concentrations en métaux requises. Enfin, cette étude démontre la nécessité de combiner les approches car l'ensemble des processus sont interdépendants dans ce type de systèmes minéralisés.

Mots clés : granites à métaux rares, Argemela, minéralisations, mise en place, fusion partielle, enrichissement

RARE METAL GRANITES: ORIGIN, EMPLACEMENT AND MECHANISMS OF THE MAGMATIC-HYDROTHERMAL TRANSITION

Abstract :

Rare metal granites result from the crystallization of highly evolved magmas enriched in volatiles and fluxing elements (F, Li, P, B) and in metals such as Sn, Nb, Ta and W. In the Western Europe Variscan belt, these granites are attributed to a late orogenic episode of rare metal magmatism. Since the 60's, numerous studies have focused on the specific geochemical signature of rare metal granites and several models have been proposed for their genesis. However, several questions remain and, in particular, the context and mechanisms of magma emplacement have been only rarely addressed. In order to build a comprehensive understanding of magmatic, hydrothermal and tectonic processes and mechanisms responsible for (i) rare metal magma generation, (ii) magma emplacement and geometry, (iii) specific geochemical signature and metal enrichment, a multi-approach and multi-scale study has been performed on the example of the rare metal granite of Argemela (Central Iberian Zone, Portugal). It has been complemented by an experimental study on the genesis of rare metal magmas. Results of the structural analysis highlighted the special structural context of emplacement of the Argemela intrusion. Several criteria suggest a fast vertical and channelled magma ascent up to shallow subvolcanic levels. The petrological and geochemical study of the granite and related mineralization allow the identification of key events and processes involved during the magmatic-hydrothermal transition. Mechanisms of concentration/transportation and deposition of metals have been also specified. The experimental study indicates that a single step low degree partial melting is not efficient enough to produce rare metal magmas, since most are sequestered into the restite. However, remelting of enriched restitic assemblages, a mechanism which remains to be tested, could well produce the required rare metal concentrations. Finally, this study demonstrates the necessity to combine several approaches, since processes and mechanisms are interrelated in these mineralized systems.

Keywords: rare metal granites, Argemela, mineralization, emplacement, partial melting, enrichment

Institut des Sciences de la Terre d'Orléans
CNRS/ISTO, UMR 7327, 1A rue de la Férollerie,
45071 Orléans, France